ISBN 978-82-326-5689-9 (printed ver.)
ISBN 978-82-326-6336-1(electronic ver.)
ISSN 1503-8181 (printed ver.)
ISSN 2703-8084 (electronic ver.)

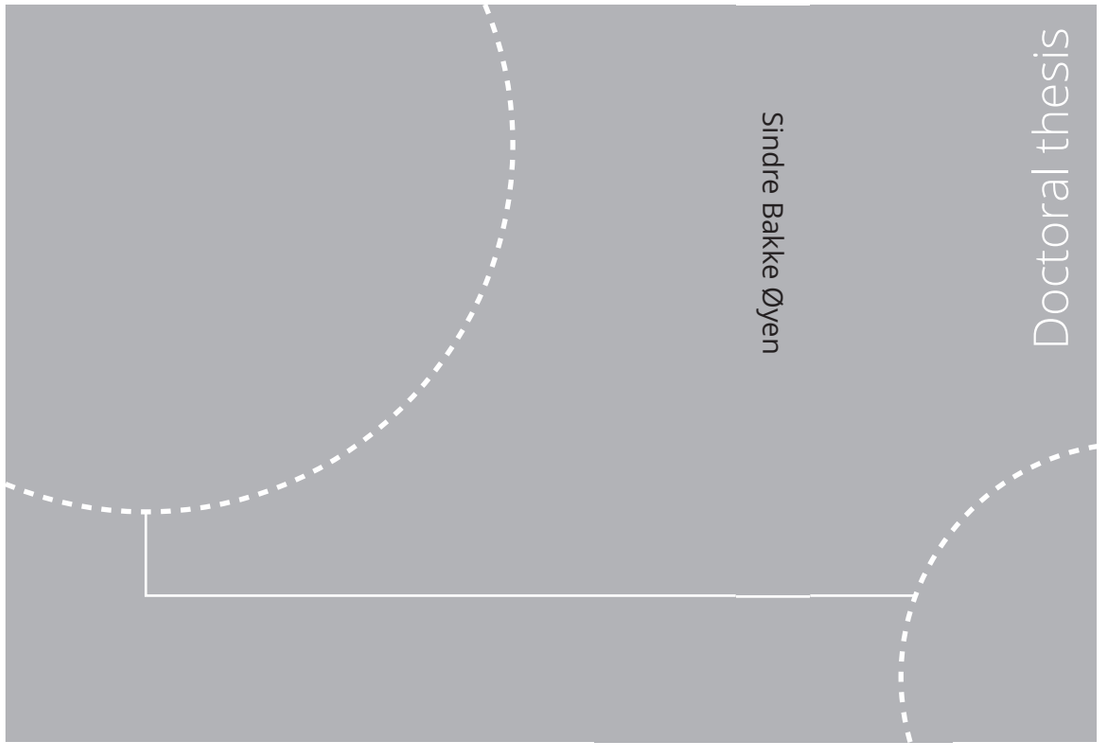

Doctoral theses at NTNU, 2023:87

Sindre Bakke Øyen

Unifying Transport Phenomena and Thermodynamic Equilibrium Models

A theoretical study of current and novel equilibrium based models in transport phenomena

Doctoral theses at NTNU, 2023:87

NTNU
Norwegian University of Science and Technology

NTNU
Norwegian University of
Science and Technology
Thesis for the degree of
Philosophiae Doctor
Faculty of Natural Sciences
Department of Chemical Engineering

NTNU
Norwegian University of Science and Technology

Sindre Bakke Øyen

Unifying Transport Phenomena and Thermodynamic Equilibrium Models

A theoretical study of current and novel equilibrium based models in transport phenomena

Thesis for the degree of Philosophiae Doctor

Trondheim, March 2023

Norwegian University of Science and Technology
Faculty of Natural Sciences
Department of Chemical Engineering

NTNU
Norwegian University of
Science and Technology

NTNU
Norwegian University of Science and Technology

Thesis for the degree of Philosophiae Doctor

Faculty of Natural Sciences
Department of Chemical Engineering

ISBN 978-82-326-5689-9 (printed ver.)
ISBN 978-82-326-6336-1 (electronic ver.)
ISSN 1503-8181 (printed ver.)
ISSN 2703-8084 (electronic ver.)

Doctoral theses at NTNU, 2023:87

PRINTED IN NORWAY
NO - 1598

NORDIC SWAN ECOLABEL
Printed matter
2041 0731

Printed by Skipnes Kommunikasjon AS

Abstract

Transport phenomena are based on the conservation of mass, momentum, and energy, and provide equations that give insight into the motion of fluids, the driving force behind this motion, and the dissipation of such driving forces. The rigorous governing transport equations are functions of space and time. On the other hand, thermodynamics is another field of science that focuses mainly on equilibrium states, which are neither functions of space nor time. Thermodynamics can be used to describe the behavior of pressure, density, and chemical potential. Moreover, chemical and phase equilibrium are central topics within thermodynamics.

The focus of this dissertation is placed on the intersection between transport phenomena and thermodynamics. This intersection is here seen as i) the pressure field, ii) the density field, iii) the transport equation for energy, iv) chemical reaction in the transport equation for species mass, and v) mass transfer in multifluid flow in the transport equation for total and species mass. The work is twofold, in which the first part focuses primarily on point iv), while the second part focuses mainly on point v). Both parts require points i), ii), and iii) to be considered.

The first part of this work employs transport equations for mass, species mass, momentum, and energy for a reactive gas in a fixed bed of porous catalysts. In the transport equation for species mass, the source/sink term originating from the chemical reaction is computed from chemical equilibrium rather than reaction kinetics. The chemical equilibrium is computed by minimizing Gibbs or Helmholtz energy at every numerical discretization point. For the Gibbs energy approach, the minimization is performed while holding the temperature and pressure constant at the numerical discretization points. For the Helmholtz energy, the minimization is performed while holding the temperature and volume constant at the numerical discretization points. The volume to be utilized has two alternatives: i) the volume may be obtained from the iteration of the equation of state (EoS), and ii) by discretizing in space with the finite volume method where the volume may be obtained from the numerical grid. For the Helmholtz energy approach,

the numerical solution obtained by utilizing the volume from alternatives i) and ii) were compared and revealed identical result. Moreover, the Gibbs and the Helmholtz energy minimization methods also gave identical results. On the other hand, the Gibbs energy method spent less computational time than the Helmholtz energy method to converge the set of equations. In the transport equation for energy, the heat capacity and the molar heat of reaction were computed from the EoS with residual functions denoting the departure from the ideal gas state.

The procedure above was performed for the Soave–Redlich–Kwong EoS, and the virial expansion truncated after the second term. Furthermore, two different chemical processes were investigated: the steam–methane reforming (SMR) and the methanol (MeOH) process. It is emphasized that the reactor concept investigated in the first part of this dissertation is not intended to replace reaction kinetics. The reaction rate expressions developed through rigorous catalytic kinetics experiments should be used when they are available, and if no reaction rate expression is available, the equilibrium-based reactor investigated here could serve as an alternative in process design studies.

The second part of this work derives a set of mass transfer equations that have their basis in the continuity of mass fluxes through the interphase separating two adjoining phases. Contrary to the common practice, which employs Henry's law, the mass transfer equations developed here feature a complete phase equilibrium description that incorporates all components, including the component that is commonly referred to as the solvent (the component in excess). The phase equilibrium description at the surface allows for a flexible framework, where the thermodynamic model can be chosen to best fit the components in the process investigated. It has been shown that the new framework is a generic case of the commonly employed Henry's law, and it is illustrated for three different EoSs and two different processes. The Soave–Redlich–Kwong EoS was employed for the single-cell protein process, and the Peng–Robinson and the perturbed-chain statistical association fluid theory (PC-SAFT) EoSs were employed for the Fischer–Tropsch synthesis. For the complex Fischer–Tropsch synthesis process, the novel phase equilibrium based mass transfer equations were preferable due to Henry's law coefficients being unavailable for many species in the Fischer–Tropsch synthesis process. On the other hand, Henry's law coefficients were available for all species for the SCP process.

The mass transfer expressions based on the Henry's law and the complete phase equilibrium were qualitatively and quantitatively different for both processes. The mass transfer of the solvent was not modeled with Henry's

law in either of the processes, and the differences in mass fractions were seen to vary by, at most, 150% (relatively) in the SCP process. In the Fischer–Tropsch synthesis process, several weaknesses were described for the method based on Henry's law, e.g., i) mass transfer being a function of the chosen solvent, ii) the solvent as a concept being imprecise and ambiguous, and iii) the mass transfer of the solvent is implicitly computed since the Henry's law coefficient does not exist for this component. These weaknesses were not present for the phase equilibrium based method. However, the increase in computational cost accompanied by solving a complete phase equilibrium problem is not to be disregarded. For instance, the mass transfer expression based on the PC-SAFT EoS was found to be 260 times slower than the equivalent mass transfer expression based on Henry's law. On the other hand, the mass transfer expression based on the Peng–Robinson EoS was only 5 times slower than the equivalent mass transfer expression based on Henry's law. Hence, there are large variations in the computational requirements of the new mass transfer expression based on the complexity of the EoS employed.

Acknowledgments

First and foremost, I would like to thank the Department of Chemical Engineering at NTNU, Faculty of Natural Sciences. None of this would be possible without the financial grant provided for this research project. The supervision by Prof. Jannike Solsvik has been instrumental in the direction and completion of this research project. Her advice and insight into transport phenomena and thermodynamics have been a keystone throughout this work, and her availability for questions has proven invaluable.

The co-supervision by Prof. Hugo A. Jakobsen was deeply appreciated. His passion for transport phenomena is reflected through his comprehensive understanding of modeling, numerical methods, and implementation. Furthermore, he cares for his Ph.D. students. He spends more time than expected on ensuring his students' progress towards submitting their dissertations. His assistance will not go unnoticed.

Associate prof. Tore Haug-Warberg, you have been essential for my thermodynamic education. Furthermore, we've had plenty of fruitful discussions in your offices about methods and thermodynamics properties that are not taught elsewhere. Your approach in your field of science is unique and generic, and I was fortunate to be your student for over 3 years.

I would like to thank my colleagues and fellow Ph.D. students, especially Ida, Mathias, and Eirik, for contributing to an excellent social environment at the offices. We've had some great discussions, both academic ones but also non-academic ones. You've kept me both encouraged and sharp throughout my work at the department, even amid the pandemic, when it was hard to maintain social ties.

A special thanks go to my family and friends. You have all been very supportive and encouraging that I would be able to submit this dissertation. I would specifically like to thank Eskild, Kristine, Frida, Petter, Haakon, Fatbardha, Hallvard, and Joachim for their care and energizing interest in the progress of this work. Moreover, thank you mom and dad for giving me the strength and endurance to keep pushing towards the finish line when my motivation was low, and for everything else you've done; it means the

world to me. Finally, and most importantly, my partner Anja. You have always been there and believed in me and that I would be able to finish my dissertation. You've encouraged, comforted, helped me plan, and so much more. I am forever grateful for your kindness, and for that, I dedicate this book to you.

List of Publications and Presentations

Publications in Journals

Paper I Øyen, S. B., Jakobsen, H. A., Haug-Warberg, T., & Solsvik, J. (2020). Differential Gibbs and Helmholtz reactor models for ideal and non-ideal gases: Applications to the SMR and methanol processes. Chemical Engineering Science, 234, 116257.
https://doi.org/10.1016/j.ces.2020.116257

CRediT: **Øyen, S. B.**: Software, Validation, Investigation, Writing - Original Draft, Writing - Review & Editing, Visualization; **Solsvik, J.**: Conceptualization, Methodology, Supervision, Funding acquisition, Writing - Review & Editing; **Jakobsen, H. A.**: Supervision, Writing - Review & Editing; **Haug-Warberg, T.**: Supervision, Writing - Review & Editing

Paper II Øyen, S. B., Jakobsen, H. A., Haug-Warberg, T., & Solsvik, J. (2021). Interface Mass Transfer in Reactive Bubbly Flow: A Rigorous Phase Equilibrium-Based Approach. Industrial & Engineering Chemistry Research, 60(48), 17705–17732.
https://doi.org/10.1021/acs.iecr.1c03131

CRediT: **Øyen, S. B.**: Software, Validation, Methodology, Investigation, Writing - Original Draft, Writing - Review & Editing, Visualization; **Solsvik, J.**: Conceptualization, Supervision, Funding acquisition, Writing - Review & Editing; **Jakobsen, H. A.**: Conceptualization, Methodology, Supervision, Writing - Review & Editing; **Haug-Warberg, T.**: Conceptualization, Methodology, Supervision, Writing - Review & Editing

Paper III Øyen, S. B., Jakobsen, H. A., Haug-Warberg, T., & Solsvik, J. (2022). Mass transfer modeling and sensitivity study of low-temperature Fischer–Tropsch synthesis. Chemical Engineering Science, 259, 117774. https://doi.org/10.1016/j.ces.2022.117774

CRediT: **Øyen, S. B.**: Methodology, Software, Validation, Investigation, Writing - Original Draft, Writing - Review & Editing, Visualization, Data Curation; **Solsvik, J.**: Conceptualization, Supervision, Funding acquisition, Writing - Review & Editing; **Jakobsen, H. A.**: Supervision, Writing - Review & Editing; **Haug-Warberg, T.**: Supervision

Presentations and Posters at Conferences

Presentation Øyen, S. B., Jakobsen, H. A., Haug-Warberg, T., Solsvik, J. (2020). Unifying the framework of fluid dynamics and chemical reaction equilibrium for non-ideal systems in a numerical study. *14th International Conference on Computational Fluid Dynamics In the Oil & Gas, Metallurgical and Process Industries, Trondheim, Norway, Virtual conference, October 12–14, 2020.*

Poster Øyen, S. B., Jakobsen, H. A., Haug-Warberg, T., Solsvik, J. (2019). Differential Gibbs And Helmholtz Reactors. *12th European Congress of Chemical Engineers, Florence, Italy, September 15–19, 2019.*

Contents

Chapter 1

Introduction

1.1 Background

Transport phenomena is a major field of science with a vast application area. Examples include but are not limited to fire simulations, metallurgy, pipeline transportation, reactor technology, and multiphase fluid flow. Moreover, the application area is increasing as the available computational power has increased over the recent decades.

Transport phenomena have a solid mathematical foundation where conservation equations for mass, momentum, and energy are formulated for an arbitrary control volume. The physical phenomena are accounted for by their interaction with the control volume, and where necessary, constitutive equations are employed to close the set of equations.

Although transport phenomena base on a solid framework for determining the spatial and transient changes of the chemical composition, it relies heavily on thermodynamics. Particularly important quantities include the enthalpy, the heat capacity, and the internal energy, as they are vital for the energy equation. Furthermore, for compressible fluids, a thermodynamic relation is required to compute the density or pressure of the fluid flow. Moreover, for reactions of reversible character, the reaction rate expression usually incorporates the chemical equilibrium to describe how the net reaction rate ultimately vanishes and approaches zero. On the other hand, the driving force for mass transfer between two fluid phases is believed to be related to thermodynamic phase equilibrium.

Combining transport phenomena and thermodynamics is non-trivial. In thermodynamics, the species composition resulting from chemical reactions are computed from chemical equilibrium. The chemical equilibrium concept is constrained to time-independent systems. Furthermore, the com-

putation is performed by minimizing an energy potential, typically Gibbs or Helmholtz energy. For Gibbs energy, the temperature and pressure are held constant under the minimization. For Helmholtz energy, the temperature and volume are held constant under the minimization. Regardless of which thermodynamic potential is chosen for the idealized equilibrium calculation, it is difficult to realize constant temperature or pressure profiles in real fluid flow problems. On the other hand, in transport phenomena, the reactions are typically computed through kinetic reaction rate expressions that are fitted to experiments [Fogler, 2016]. Whenever kinetic reaction rate expressions are unavailable, chemical equilibrium provides different means of computing the change in composition in a chemical reactor. This may be helpful for chemical reactors that operate close to chemical equilibrium and process design studies, albeit not for accurately representing the change in composition.

In mass transfer phenomena, two fluid phases share a common interface over which mass transfer occurs. It is commonly assumed that phase equilibrium prevails at the interface. In the literature, the phase equilibrium is (to the author's knowledge) computed using the Henry's law exclusively, where the Henry's law has several inherent limitations that are impractical to mend. First, the relation is valid for poorly soluble solutes in a specific solvent, and computing the mass transfer of the solvent is thus impossible. Second, an infinite dilution limit is employed, meaning that Henry's law is valid when a solute is practically insoluble in the specified solvent. For solutes that are not poorly soluble, Henry's law is impractical. Third, Henry's law requires the identification of a single solvent. Henry's law can provide different results based on which solvent is chosen in systems where no compound is clearly in excess and easily identified as the solvent. The Fischer–Tropsch synthesis represents this situation, where hydrocarbons are present in various chain lengths and concentrations.

In thermodynamics, phase equilibrium is an overarching principle that is generic and independent of the models chosen. The phase equilibrium prevailing at the phase boundary could thus be represented by *any* thermodynamic model. Therefore, it is crucial to choose a thermodynamic model that represents the phase equilibrium satisfactorily. For some systems, Henry's law provides an adequate representation of the phase equilibrium. For other systems, the theoretical foundation of Henry's law is violated, and Henry's law is unwarranted. Regardless, Henry's law remains the common practice, and a vast number of thermodynamic models remain unexplored in mass transfer modeling.

1.2 Research Objectives

The main goal of this dissertation is to unify thermodynamic equilibrium and transport phenomena. This work is twofold: first, chemical equilibrium is treated in a packed bed reactor operated at steady state with non-uniform temperature and pressure fields. Thus, the minimization of the Gibbs or Helmholtz energy is performed at all discrete points in space, yielding local instantaneous chemical equilibrium. Furthermore, transport equations for mass, momentum, and energy are employed to compute the spatial variations of velocity, temperature, and pressure. This approach attempts to improve classical equilibrium reactors where the temperature and pressure fields are fixed and spatial variations are not considered. Ideal and non-ideal gases are considered, and the models are implemented thermodynamically consistent. The reactor concept is to be used in the *absence* of kinetic reaction rate expressions and for processes that are believed to operate close to equilibrium.

Second, the phase equilibrium at the phase boundary of two adjoining fluid phases is treated in a bubble column reactor. Rather than using Henry's law to close the mass transfer problem, a rigorous phase equilibrium-based approach is attempted. The novel driving force for mass transfer is generic, and in contrast to Henry's law, the novel concept i) allows the mass transfer of *all* components (including the solvent), ii) is not limited to the infinite dilution limit, and iii) does not require the identification of a single solvent. Emphasis is placed on solution strategy, numerical properties, convergence, and quantitative differences in the converged composition profiles. Furthermore, the choice of solvent and its implications are highlighted for mass transfer based on Henry's law.

1.3 Dissertation Outline

An introduction to classical thermodynamics is given in Chapter 2, and also mathematical prerequisites and optimization algorithms are described therein. In Chapter 3, the different attempts to formulate a novel mass transfer expression are described, and some remarks on heat and momentum transfer induced by mass transfer are given. The published papers, and hence the results of this dissertation, are given in Chapter 4. Concluding remarks and suggestions for further work are given in Chapter 5.

Chapter 2

Thermodynamics

2.1 Mathematical Prerequisites

2.1.1 Optimization

Optimization is a central topic within thermodynamics due to how equilibrium problems are formulated. Hence, a brief introduction to optimization problems, their formulations, solution strategies, and the conditions to be satisfied at a located trial solution is given here.

Optimization is the minimization of an objective function subject to a set of constraints. Let $f(\boldsymbol{x})$ denote the objective function and let $\boldsymbol{x}$ denote the decision variables. Assume that there are only linear equality constraints and non-negative inequality constraints. The equality constraints are represented by the matrix $\boldsymbol{A}$ and the vector $\boldsymbol{b}$. The problem may then be formulated as the following optimization problem:

$$\begin{aligned} \min_{\boldsymbol{x}} \quad & f(\boldsymbol{x}) \\ \text{s.t.} \quad & \boldsymbol{A}\boldsymbol{x} = \boldsymbol{b} \\ & \boldsymbol{x} \geq \boldsymbol{0}. \end{aligned} \tag{2.1}$$

The problem may be solved by the method of Lagrange multipliers. The Lagrangian function is formulated as (see e.g. Nocedal and Wright [2006], Taylor [2010])

$$\mathcal{L}(\boldsymbol{x}, \boldsymbol{\lambda}) = f(\boldsymbol{x}) - \boldsymbol{\lambda}^\top (\boldsymbol{A}\boldsymbol{x} - \boldsymbol{b}), \tag{2.2}$$

where $\boldsymbol{\lambda}$ are the Lagrange multipliers. At the optimum these multipliers reflect the decrease of the objective function as a result of perturbing the right-hand side of the equality constraints by one unit. That is, if b_i is decreased by 1, then the objective function value is decreased by λ_i. The

Lagrange multipliers are therefore referred to as shadow prices in operational analysis.

The stationary point of the Lagrangian function will have the desirable property of both minimizing (or maximizing) f and satisfying all equality constraints. To iterate the feasible set towards a stationary point, a search direction is to be specified. Among these, the *Newton step* is frequently used in optimization, primarily due to its quadratic convergence rate. By a Taylor expansion around $\boldsymbol{x}, \boldsymbol{\lambda}$ gives:

$$\begin{aligned}\mathcal{L}(\boldsymbol{x}+\boldsymbol{p}_{\boldsymbol{x}}, \boldsymbol{\lambda}+\boldsymbol{p}_{\boldsymbol{\lambda}}) \approx \mathcal{L}(\boldsymbol{x}, \boldsymbol{\lambda}) + \nabla\mathcal{L}(\boldsymbol{x}, \boldsymbol{\lambda})^\top \boldsymbol{p} \\ + \frac{1}{2}\boldsymbol{p}^\top \nabla\nabla^\top \mathcal{L}(\boldsymbol{x}, \boldsymbol{\lambda})\boldsymbol{p} + O(\|\boldsymbol{p}^3\|),\end{aligned} \tag{2.3}$$

where $\boldsymbol{p} = (\boldsymbol{p}_{\boldsymbol{x}}, \boldsymbol{p}_{\boldsymbol{\lambda}})$ is the search direction vector. As a result of truncating the Taylor expansion after the second term, an error of third order is introduced. This error is denoted $O(\|\boldsymbol{p}^3\|)$.

Setting the derivative of eq. (2.3) with respect to $\boldsymbol{p}$ equal to 0 yields the Newton step

$$O(\|\boldsymbol{p}^2\|) + \boldsymbol{H}_{\mathcal{L}}(\boldsymbol{x}^\nu, \boldsymbol{\lambda}^\nu)\boldsymbol{p}^{\nu+1} = -\boldsymbol{J}_{\mathcal{L}}(\boldsymbol{x}^\nu, \boldsymbol{\lambda}^\nu). \tag{2.4}$$

In the above notation, $\boldsymbol{H}_{\mathcal{L}}(\boldsymbol{x}^\nu, \boldsymbol{\lambda}^\nu)$ is the Hessian matrix and $\boldsymbol{J}_{\mathcal{L}}(\boldsymbol{x}^\nu, \boldsymbol{\lambda}^\nu)$ is the Jacobi vector of the Lagrangian function at iteration ν. By differentiating eq. (2.2) twice, inserting into eq. (2.4), and omitting the error notation

$$\begin{pmatrix} \boldsymbol{H}_f & -\boldsymbol{A}^\top \\ -\boldsymbol{A} & \boldsymbol{0} \end{pmatrix}^\nu \begin{pmatrix} \boldsymbol{p}_{\boldsymbol{x}} \\ \boldsymbol{p}_{\boldsymbol{\lambda}} \end{pmatrix}^{\nu+1} = -\begin{pmatrix} \nabla_{\boldsymbol{x}} f(\boldsymbol{x}) - \boldsymbol{A}^\top \boldsymbol{\lambda} \\ \boldsymbol{b} - \boldsymbol{A}\boldsymbol{x} \end{pmatrix}^\nu. \tag{2.5}$$

Here $\nabla_{\boldsymbol{x}}$ is used to denote the gradient with respect to the decision variables. The first line in the matrix equation above is highlighted to show cancelling terms. By noting that $\boldsymbol{p}_{\boldsymbol{x}} = \boldsymbol{x}^{\nu+1} - \boldsymbol{x}^\nu$ and $\boldsymbol{p}_{\boldsymbol{\lambda}} = \boldsymbol{\lambda}^{\nu+1} - \boldsymbol{\lambda}^\nu$, the equation reads

$$\begin{aligned}
&\boldsymbol{H}_f^\nu(\boldsymbol{x}^{\nu+1} - \boldsymbol{x}^\nu) - A^\top(\boldsymbol{\lambda}^{\nu+1} - \cancel{\boldsymbol{\lambda}^\nu}) &&= -\nabla_{\boldsymbol{x}} f(\boldsymbol{x}) + \cancel{A^\top \boldsymbol{\lambda}^\nu} \\
&\boldsymbol{H}_f^\nu(\boldsymbol{x}^{\nu+1} - \boldsymbol{x}^\nu) - A^\top \boldsymbol{\lambda}^{\nu+1} &&= -\nabla_{\boldsymbol{x}} f(\boldsymbol{x}) \quad | \, (-\boldsymbol{I}) \\
-&\boldsymbol{H}_f^\nu \boldsymbol{p}_{\boldsymbol{x}}^{\nu+1} + A^\top \boldsymbol{\lambda}^{\nu+1} &&= \nabla_{\boldsymbol{x}} f(\boldsymbol{x}) \\
&\boldsymbol{H}_f^\nu(-\boldsymbol{p}_{\boldsymbol{x}}^{\nu+1}) + A^\top \boldsymbol{\lambda}^{\nu+1} &&= \nabla_{\boldsymbol{x}} f(\boldsymbol{x}).
\end{aligned} \tag{2.6}$$

In the second line, the whole equation was multiplied by the negative 1. This is done by left multiplication by the negative identity matrix. It is easy to show that the last line in the matrix equation eq. (2.5) can be written

$\boldsymbol{A}(-\boldsymbol{p}_{\boldsymbol{x}}^{\nu+1}) = \boldsymbol{A}\boldsymbol{x}^{\nu} - \boldsymbol{b}$. As such, eq. (2.5) is identical to

$$\begin{pmatrix} \boldsymbol{H}_f & \boldsymbol{A}^\top \\ \boldsymbol{A} & \boldsymbol{0} \end{pmatrix}^{\nu} \begin{pmatrix} -\boldsymbol{p}_{\boldsymbol{x}} \\ \boldsymbol{\lambda} \end{pmatrix}^{\nu+1} = \begin{pmatrix} \nabla_{\boldsymbol{x}} f(\boldsymbol{x}) \\ \boldsymbol{A}\boldsymbol{x} - \boldsymbol{b} \end{pmatrix}^{\nu}. \tag{2.7}$$

The decision variables in the next step are extracted as $\boldsymbol{x}^{\nu+1} = \boldsymbol{x}^{\nu} + \boldsymbol{p}_{\boldsymbol{x}}^{\nu+1}$. To ensure that the step $\boldsymbol{p}_{\boldsymbol{x}}^{\nu+1}$ stays feasible (does not violate any inequality constraints), the step is shortened appropriately. If the current iterate $\boldsymbol{x}^{\nu}$ is feasible and $\boldsymbol{p}_{\boldsymbol{x}}^{\nu+1} \geq \boldsymbol{0}$, then $\boldsymbol{x}^{\nu+1} = \boldsymbol{x}^{\nu} + \boldsymbol{p}_{\boldsymbol{x}}^{\nu+1} \geq \boldsymbol{0}$, since both terms are positive. However, if the current iterate $\boldsymbol{x}^{\nu}$ is feasible and $p_{x_i}^{\nu+1} < 0$ for some variable x_i, then $x_i^{\nu+1}$ is not necessarily feasible, since $|p_{x_i}^{\nu+1}|$ might be greater than x_i^{ν}. Therefore, whenever $p_{x_i}^{\nu+1} < 0$ for some i, necessary actions must be taken. This is implemented as $x_i^{\nu+1} = x_i^{\nu} + \alpha^{\nu} p_{x_i}^{\nu+1} \geq 0, \forall i$. This equation is rearranged so that $\alpha^{\nu} \leq -\frac{x_i^{\nu}}{p_{x_i}^{\nu+1}}, \forall i$ (inequality flipped since $p_{x_i}^{\nu+1} < 0$). Hence,

$$\alpha^{\nu} = \min\left(1, \min \frac{-x_i^{\nu}}{p_{x_i}^{\nu+1}}, \quad \forall p_{x_i} < 0\right). \tag{2.8}$$

In eq. (2.8) either the full step is taken by $\alpha = 1$ or it is shortened. The latter is done by going through all negative steps in $\boldsymbol{p}_{\boldsymbol{x}}^{\nu+1}$ and shortening the "most violating" step. That is, the $p_{x_i}^{\nu+1}$ that results in an $x_i^{\nu+1}$ that is most negative. The step in $\boldsymbol{\lambda}$ must be shortened accordingly, so that eq. (2.7) is satisfied. Consequently, $\boldsymbol{\lambda}^{\nu+1} = \boldsymbol{\lambda}^{\nu} + \alpha^{\nu} \boldsymbol{p}_{\boldsymbol{\lambda}}^{\nu+1}$ as well.

At the optimal solution, the first order necessary conditions known as the Karush–Kuhn–Tucker (KKT) conditions have to be satisfied

$$\nabla_{\boldsymbol{x}} \mathcal{L}(\boldsymbol{x}^*, \boldsymbol{\lambda}^*) = 0 \tag{2.9a}$$
$$c_i(\boldsymbol{x}^*) = 0, \qquad \text{for all } i \in \mathcal{E} \tag{2.9b}$$
$$c_i(\boldsymbol{x}^*) \geq 0, \qquad \text{for all } i \in \mathcal{I} \tag{2.9c}$$
$$\lambda_i^* \geq 0, \qquad \text{for all } i \in \mathcal{I} \tag{2.9d}$$
$$\lambda_i^* c_i(\boldsymbol{x}^*) = 0, \qquad \text{for all } i \in \mathcal{E} \cup \mathcal{I}. \tag{2.9e}$$

Here c_i is constraint i, * indicates the trial solution (which is optimal when eq. (2.9) is satisfied) and $\mathcal{E}$ and $\mathcal{I}$ are the set of equality and inequality constraints, respectively.

2.1.2 The Internal Energy and Entropy

Considerable time has been spent in the last centuries on the conservation of energy. A somewhat confusing result is the existence of kinetic and potential

energy at both the macroscopic and microscopic level. The former refers to energies in Newtonian mechanics, and thus the kinetic energy relates to the center of mass of the system and the potential energy relates to the gravitational potential energy. The microscopic kinetic and internal energy, on the other hand, is collectively referred to as the *internal energy* (see Elliott and Lira [2012], Helbæk and Kjelstrup [2006]).

It was shown by Joule in one of his experiments that when a non-reacting substance is enclosed by adiabatic walls, then it is possible to measure the energy of the system by measuring the mechanical work done. If the energy can be measured adiabatically, then the heat can be measured diabatically. The heat is then the difference between the energy and the mechanical work.

Since the amount of work and heat depend on the path taken, their differentials will be assigned the symbol đ instead of the symbol d normally used for differentials. The former are referred to as *inexact differentials* and the latter are referred to as *exact differentials*. From the previous discussion the differential heat transferred is

$$đQ = (\mathrm{d}U)_{\boldsymbol{n}} - đW, \tag{2.10}$$

where $(\mathrm{d}U)_{\boldsymbol{n}}$ is the exact differential of the internal energy at constant mole number vector $\boldsymbol{n} = (n_1, n_2, \ldots, n_C)$, and $đW$ is the inexact differential of the mechanical work. Going from state A to state B through process P, the integrated form of eq. (2.10) is

$$U_B - U_A = Q + W. \tag{2.11}$$

This is commonly referred to as the *first law of thermodynamics*, however there is no mathematical proof that eq. (2.11) is generally valid. It is merely based on empirical results. There is no evidence that disputes eq. (2.11), and it is therefore generally accepted.

It was mentioned in the context of eq. (2.10) that the differential of the internal energy is *exact* without any further comments. Consider conversely that the differential is *not* exact, and that internal energy depends on the path taken. If the system is taken from state A to B through path P_1, and then back from B to A through path P_2, then $\Delta U_{\text{total}} = \oint \mathrm{d}U = \int_A^B \mathrm{d}U^{P_1} + \int_B^A \mathrm{d}U^{P_2} = \Delta U^{P_1}_{A\to B} + \Delta U^{P_2}_{B\to A} \neq 0$. This means that whenever the two changes in internal energy are unequal, the energy conservation is violated. Consider for instance the same circular process where the subprocesses $\Delta U^{P_1}_{A\to B} = 1\,\mathrm{J}$ and $\Delta U^{P_2}_{B\to A} = -2\,\mathrm{J}$. By going from A to B through path P_1, 1 J is consumed. Going back to A through P_2 releases 2 J. Hence, there is a net release of 1 J. This creates the idea of a perpetual motion machine which has not yet been (and probably will not ever be) invented. This

is not a proof that the internal energy is a *state function* (path independent), but rather a comment on its likeliness.

Before further remarks can be given about the internal energy, three postulates are given. If V denotes the volume, then the postulates read (see Callen [1985])

1. There exists a function $S(U, V, \boldsymbol{n})$ (called entropy) defined for all equilibrium states. The values of $U, V, \boldsymbol{n}$ are those that maximize S, given the set of constraints imposed on the system.

2. The entropy of a composite system is additive over constituent subsystems. The entropy is continuous and differentiable and is a monotonically increasing function of the energy.

3. The entropy is zero when $\left(\frac{\partial U}{\partial S}\right)_{V,\boldsymbol{n}} = 0$.

From the second postulate, the entropy can be inverted for the internal energy. The result is a single-valued, continuous and differentiable function of $S, V, \boldsymbol{n}$. By writing the total differential of $U(S, V, \boldsymbol{n})$

$$\mathrm{d}U = \left(\frac{\partial U}{\partial S}\right)_{V,\boldsymbol{n}} \mathrm{d}S + \left(\frac{\partial U}{\partial V}\right)_{S,\boldsymbol{n}} \mathrm{d}V + \sum_{i=1}^{C} \left(\frac{\partial U}{\partial n_i}\right)_{S,V,n_{j\neq i}} \mathrm{d}n_i, \tag{2.12}$$

where C denotes the number of components present. The partial derivatives at the right-hand side will be *defined* as T, $-p$ and μ_i, respectively. These quantities are called temperature, negative pressure and chemical potential. For a reversible process $đW^{\mathrm{rev}} = -p\,\mathrm{d}V$. By comparing eq. (2.10) and eq. (2.12) at constant composition, it is concluded that $T\,\mathrm{d}S = đQ^{\mathrm{rev}}$.

2.1.3 Euler Homogeneous Functions

Euler homogeneous functions put strict conditions on the relations between different energy surface functions, on their partial derivatives, and even on the relations between those partial derivatives. In the following, a generic foundation is formulated, which is shown to be valid for all relevant energy surface functions within thermodynamics.

A function $f(\boldsymbol{x}, \boldsymbol{\xi})$, where $\boldsymbol{x}$ and $\boldsymbol{\xi}$ are vectors, is homogeneous of degree k if

$$F := f(\boldsymbol{X}, \boldsymbol{\xi}) = \lambda^k f(\boldsymbol{x}, \boldsymbol{\xi}) \tag{2.13}$$

$$\boldsymbol{X} := \lambda \boldsymbol{x}. \tag{2.14}$$

That is, $f(\boldsymbol{x}, \boldsymbol{\xi})$ is homogeneous if $f(\lambda \boldsymbol{x}, \boldsymbol{\xi})$ is proportional to λ^k. The variables $\boldsymbol{X}$ and $\boldsymbol{\xi}$ are in thermodynamic applications often referred to as extensive and intensive variables, respectively. That is, $\boldsymbol{X}$ scales with the size of the system denoted by λ, whereas $\boldsymbol{\xi}$ does not. For instance, let $F = m\boldsymbol{v}$ be the momentum, with units $\mathrm{kg\,m\,s^{-1}}$. Here, $X = m$ is the mass transplaced at velocity $\xi = \boldsymbol{v}$. By taking $\lambda = V$ as the volume, then $f = \rho v$ is the volumetric momentum, and $x = X/\lambda = m/V = \rho$ is the mass density.

By taking the total differential of eq. (2.13) and making use of $\mathrm{d}\boldsymbol{X} = \lambda\,\mathrm{d}\boldsymbol{x} + \boldsymbol{x}\,\mathrm{d}\lambda$

$$\mathrm{d}F = \left(\frac{\partial F}{\partial \boldsymbol{X}}\right)_{\boldsymbol{\xi}}^{\top} \boldsymbol{x}\,\mathrm{d}\lambda + \lambda \left(\frac{\partial F}{\partial \boldsymbol{X}}\right)_{\boldsymbol{\xi}}^{\top} \mathrm{d}\boldsymbol{x} + \left(\frac{\partial F}{\partial \boldsymbol{\xi}}\right)_{\boldsymbol{X}}^{\top} \mathrm{d}\boldsymbol{\xi}. \tag{2.15}$$

Another form of the total differential is obtained by utilizing the definition of $F = \lambda^k f$ to get

$$\mathrm{d}F = k\lambda^{k-1} f\,\mathrm{d}\lambda + \lambda^k df = k\lambda^{k-1} f\,\mathrm{d}\lambda + \lambda^k \left(\frac{\partial f}{\partial \boldsymbol{x}}\right)_{\boldsymbol{\xi}}^{\top} \mathrm{d}\boldsymbol{x} + \lambda^k \left(\frac{\partial f}{\partial \boldsymbol{\xi}}\right)_{\boldsymbol{x}}^{\top} \mathrm{d}\boldsymbol{\xi}. \tag{2.16}$$

The two differentials for $\mathrm{d}F$ in eq. (2.15) and eq. (2.16) are equivalent. Comparing the coefficients for the differentials $\mathrm{d}\lambda$, $\mathrm{d}\boldsymbol{x}$ and $\mathrm{d}\boldsymbol{\xi}$ lead to three relations

$$\left(\frac{\partial F}{\partial \boldsymbol{X}}\right)_{\boldsymbol{\xi}}^{\top} \boldsymbol{X} = kF \tag{2.17a}$$

$$\left(\frac{\partial F}{\partial \boldsymbol{X}}\right)_{\boldsymbol{\xi}} = \lambda^{k-1} \left(\frac{\partial f}{\partial \boldsymbol{x}}\right)_{\boldsymbol{\xi}} \tag{2.17b}$$

$$\left(\frac{\partial F}{\partial \boldsymbol{\xi}}\right)_{\boldsymbol{X}} = \lambda^k \left(\frac{\partial f}{\partial \boldsymbol{\xi}}\right)_{\boldsymbol{x}}. \tag{2.17c}$$

Equation (2.17a) is referred to as Euler's theorem for homogeneous functions (see Euler [2000] for the same result but with different notation). This result has great importance and is frequently used in thermodynamics. Given the total differential of F, the function F itself can be found through eq. (2.17a). This process is referred to as *Euler integration*.

As seen in eq. (2.17b), the derivative of an Euler homogeneous function of degree 1 with respect to an extensive variable is Euler homogeneous of degree 0. In eq. (2.17c) it is seen that the derivative of the same function, but with respect to an intensive variable is Euler homogeneous of degree 1.

Differentiating eq. (2.17a) yields

$$\boldsymbol{X}^{\top} \mathrm{d}\left(\frac{\partial F}{\partial \boldsymbol{X}}\right)_{\boldsymbol{\xi}} + \left(\frac{\partial F}{\partial \boldsymbol{X}}\right)_{\boldsymbol{\xi}}^{\top} \mathrm{d}\boldsymbol{X} = k \left(\frac{\partial F}{\partial \boldsymbol{X}}\right)_{\boldsymbol{\xi}}^{\top} \mathrm{d}\boldsymbol{X} + k \left(\frac{\partial F}{\partial \boldsymbol{\xi}}\right)_{\boldsymbol{X}}^{\top} \mathrm{d}\boldsymbol{\xi}, \tag{2.18}$$

and by noting that the differential in the first term in eq. (2.18)

$$\mathrm{d}\left(\frac{\partial F}{\partial \boldsymbol{X}}\right)_{\boldsymbol{\xi}} = \left(\frac{\partial^2 F}{\partial \boldsymbol{X}\partial \boldsymbol{X}^\top}\right)_{\boldsymbol{\xi}} \mathrm{d}\boldsymbol{X} + \left(\frac{\partial^2 F}{\partial \boldsymbol{X}\partial \boldsymbol{\xi}^\top}\right) \mathrm{d}\boldsymbol{\xi}, \tag{2.19}$$

we obtain (with $k = 1$)

$$\boldsymbol{X}^\top \left(\frac{\partial^2 F}{\partial \boldsymbol{X}\partial \boldsymbol{X}^\top}\right)_{\boldsymbol{\xi}} \mathrm{d}\boldsymbol{X} + \boldsymbol{X}^\top \left(\frac{\partial^2 F}{\partial \boldsymbol{X}\partial \boldsymbol{\xi}^\top}\right) \mathrm{d}\boldsymbol{\xi} = \left(\frac{\partial F}{\partial \boldsymbol{\xi}}\right)_{\boldsymbol{X}} \mathrm{d}\boldsymbol{\xi}. \tag{2.20}$$

By first setting $\mathrm{d}\boldsymbol{\xi} = \boldsymbol{0}$ and then setting $\mathrm{d}\boldsymbol{X} = \boldsymbol{0}$, it can be concluded that

$$\left(\frac{\partial^2 F}{\partial \boldsymbol{X}\partial \boldsymbol{X}^\top}\right)_{\boldsymbol{\xi}} \boldsymbol{X} = \boldsymbol{0} \tag{2.21a}$$

$$\left(\frac{\partial^2 F}{\partial \boldsymbol{\xi}\partial \boldsymbol{X}^\top}\right) \quad \boldsymbol{X} = \left(\frac{\partial F}{\partial \boldsymbol{\xi}}\right)_{\boldsymbol{X}}, \tag{2.21b}$$

respectively.

The relations in eq. (2.21) provide both means of calculating some of the first derivatives given the mixed second derivatives (see eq. (2.21b)), but it also offers useful tests for internal consistency within thermodynamics, see Section 2.3.

As an example of the use of Euler's theorem for homogeneous functions, consider the internal energy $F = U(S, V, \boldsymbol{n})$, $\boldsymbol{X} = (S, V, \boldsymbol{n})$ and $\xi = \emptyset$. This is an Euler homogeneous function of degree one. Using Euler's theorem on eq. (2.12) yields:

$$\begin{aligned} U &= \left(\frac{\partial U}{\partial S}\right)_{V,\boldsymbol{n}} S + \left(\frac{\partial U}{\partial V}\right)_{S,\boldsymbol{n}} V + \left(\frac{\partial U}{\partial \boldsymbol{n}}\right)_{S,V}^\top \boldsymbol{n} \\ &= TS - pV + \boldsymbol{\mu}^\top \boldsymbol{n}, \end{aligned} \tag{2.22}$$

where the earlier definitions were inserted for T, $-p$ and μ_i. By using eq. (2.21a)

$$\left(\frac{\partial^2 U}{\partial S^2}\right)_{V,\boldsymbol{n}} S + \left(\frac{\partial^2 U}{\partial S\partial V}\right)_{\boldsymbol{n}} V + \left(\frac{\partial^2 U}{\partial S\partial \boldsymbol{n}}\right)_{V}^\top \boldsymbol{n} = 0 \tag{2.23a}$$

$$\left(\frac{\partial^2 U}{\partial V\partial S}\right)_{\boldsymbol{n}} S + \left(\frac{\partial^2 U}{\partial V^2}\right)_{S,\boldsymbol{n}} V + \left(\frac{\partial^2 U}{\partial V\partial \boldsymbol{n}}\right)_{S}^\top \boldsymbol{n} = 0 \tag{2.23b}$$

$$\left(\frac{\partial^2 U}{\partial \boldsymbol{n}\partial S}\right)_{V} S + \left(\frac{\partial^2 U}{\partial \boldsymbol{n}\partial V}\right)_{S} V + \left(\frac{\partial^2 U}{\partial \boldsymbol{n}\partial \boldsymbol{n}^\top}\right)_{S,V} \boldsymbol{n} = \boldsymbol{0}. \tag{2.23c}$$

The $C + 2$ equations given by eq. (2.23) put strict conditions on the thermodynamic energy function U. If eqs. (2.22) and (2.23) hold, it is likely to develop a thermodynamically consistent internal energy function. Furthermore, when a thermodynamically consistent internal energy function is implemented, eqs. (2.22) and (2.23) should be checked to minimize the risk of implementation errors.

2.1.4 Relations Between Partial Derivatives

In order to derive relations for an energy surface function in practical coordinate sets, it is essential to be able to handle transitions between these different coordinate sets. For instance, the internal energy function is written in $S, V, \boldsymbol{n}$; however this coordinate set has proven impractical due to the entropy not being measurable. Typically, the entropy is replaced by temperature to have a fully measurable coordinate set. Handling transitions of this kind is not trivial and requires attention given in the following. Further usages of the manipulations given in the following include relations between partial derivatives of the equation of state.

If m variables $x, y, z, \boldsymbol{w}$ are interrelated by $f(x, y, z, \boldsymbol{w}) = 0$, $m - 1$ of them may be chosen as independent such that, e.g., $z = g(x, y, \boldsymbol{w})$. The total differential of z is

$$\mathrm{d}z = \left(\frac{\partial z}{\partial x}\right)_{y,\boldsymbol{w}} \mathrm{d}x + \left(\frac{\partial z}{\partial y}\right)_{x,\boldsymbol{w}} \mathrm{d}y + \sum_{i=1}^{m-3} \left(\frac{\partial z}{\partial w_i}\right)_{x,y,w_{j\neq i}} \mathrm{d}w_i. \tag{2.24}$$

Setting $\mathrm{d}z = 0$ and $\mathrm{d}\boldsymbol{w} = \boldsymbol{0}$ results in the two relations

$$\left(\frac{\partial z}{\partial x}\right)_{y,\boldsymbol{w}} \left(\frac{\mathrm{d}x}{\mathrm{d}y}\right)_{z,\boldsymbol{w}} + \left(\frac{\partial z}{\partial y}\right)_{x,\boldsymbol{w}} = 0 \tag{2.25a}$$

$$\left(\frac{\partial z}{\partial x}\right)_{y,\boldsymbol{w}} + \left(\frac{\partial z}{\partial y}\right)_{x,\boldsymbol{w}} \left(\frac{\mathrm{d}y}{\mathrm{d}x}\right)_{z,\boldsymbol{w}} = 0. \tag{2.25b}$$

Since all variables but x and y are kept constant in $\mathrm{d}x/\,\mathrm{d}y$, it is identical to its partial derivative. Replacing the differentials by their partial derivatives yields

$$\left(\frac{\partial z}{\partial x}\right)_{y,\boldsymbol{w}} \left(\frac{\partial x}{\partial y}\right)_{z,\boldsymbol{w}} + \left(\frac{\partial z}{\partial y}\right)_{x,\boldsymbol{w}} = 0 \tag{2.26a}$$

$$\left(\frac{\partial z}{\partial x}\right)_{y,\boldsymbol{w}} + \left(\frac{\partial z}{\partial y}\right)_{x,\boldsymbol{w}} \left(\frac{\partial y}{\partial x}\right)_{z,\boldsymbol{w}} = 0. \tag{2.26b}$$

Using either of the above, rearranging and dividing by the derivatives, the following *triple rule* is obtained

$$\left(\frac{\partial z}{\partial x}\right)_{y,\boldsymbol{w}}\left(\frac{\partial x}{\partial y}\right)_{z,\boldsymbol{w}}\left(\frac{\partial y}{\partial z}\right)_{x,\boldsymbol{w}}=-1. \tag{2.27}$$

As an example of the usage of the triple rule, consider $f(T,p,V,\boldsymbol{n})=0$. At $\mathrm{d}V=0$ and $\mathrm{d}\boldsymbol{n}=\boldsymbol{0}$, the following holds

$$\left(\frac{\partial V}{\partial T}\right)_{p,\boldsymbol{n}}\left(\frac{\partial T}{\partial p}\right)_{V,\boldsymbol{n}}\left(\frac{\partial p}{\partial V}\right)_{T,\boldsymbol{n}}=-1. \tag{2.28}$$

Thus, by rearranging, the useful relation

$$\left(\frac{\partial V}{\partial T}\right)_{p,\boldsymbol{n}}=-\frac{\left(\frac{\partial p}{\partial T}\right)_{V,\boldsymbol{n}}}{\left(\frac{\partial p}{\partial V}\right)_{T,\boldsymbol{n}}} \tag{2.29}$$

is obtained.

Consider now a function $g(x,y,\boldsymbol{w})$, where $y=h(x,\boldsymbol{w},z)$, then

$$\mathrm{d}g=\left(\frac{\partial g}{\partial x}\right)_{y,\boldsymbol{w}}\mathrm{d}x+\left(\frac{\partial g}{\partial y}\right)_{x,\boldsymbol{w}}\mathrm{d}y+\sum_i\left(\frac{\partial g}{\partial w_i}\right)_{x,y,w_{j\neq i}}\mathrm{d}w_i. \tag{2.30}$$

The total differential of y

$$\mathrm{d}y=\left(\frac{\partial y}{\partial x}\right)_{z,\boldsymbol{w}}\mathrm{d}x+\left(\frac{\partial y}{\partial z}\right)_{x,\boldsymbol{w}}\mathrm{d}z+\sum_i\left(\frac{\partial y}{\partial w_i}\right)_{x,z,w_{j\neq i}}\mathrm{d}w_i \tag{2.31}$$

is then substituted into eq. (2.30) to yield

$$\begin{aligned}\mathrm{d}g=&\left(\left(\frac{\partial g}{\partial x}\right)_{y,\boldsymbol{w}}+\left(\frac{\partial g}{\partial y}\right)_{x,\boldsymbol{w}}\left(\frac{\partial y}{\partial x}\right)_{z,\boldsymbol{w}}\right)\mathrm{d}x\\&+\left(\left(\frac{\partial g}{\partial y}\right)_{x,\boldsymbol{w}}\left(\frac{\partial y}{\partial z}\right)_{x,\boldsymbol{w}}\right)\mathrm{d}z\\&+\sum_i\left(\left(\frac{\partial g}{\partial w_i}\right)_{x,y,w_{j\neq i}}+\left(\frac{\partial g}{\partial y}\right)_{x,\boldsymbol{w}}\left(\frac{\partial y}{\partial w_i}\right)_{x,z,w_{j\neq i}}\right)\mathrm{d}w_i.\end{aligned} \tag{2.32}$$

A particularly useful result is obtained at $\mathrm{d}z=0$, $\mathrm{d}\boldsymbol{w}=\boldsymbol{0}$ and dividing by $\mathrm{d}x$

$$\left(\frac{\partial g}{\partial x}\right)_{z,\boldsymbol{w}}=\left(\frac{\partial g}{\partial x}\right)_{y,\boldsymbol{w}}+\left(\frac{\partial g}{\partial y}\right)_{x,\boldsymbol{w}}\left(\frac{\partial y}{\partial x}\right)_{z,\boldsymbol{w}}. \tag{2.33}$$

A demonstration of the use of eq. (2.33) is in its place. Consider again the internal energy $U = g(S, V, \boldsymbol{n})$, where its derivative with respect to the volume at constant $T, \boldsymbol{n}$ is required. Then $x = V$, $\boldsymbol{w} = \boldsymbol{n}$, $z = T$ and $y = S(T, V, \boldsymbol{n})$. Inserted into eq. (2.33)

$$\begin{aligned}\left(\frac{\partial U}{\partial V}\right)_{T,\boldsymbol{n}} &= \left(\frac{\partial U}{\partial V}\right)_{S,\boldsymbol{n}} + \left(\frac{\partial U}{\partial S}\right)_{V,\boldsymbol{n}} \left(\frac{\partial S}{\partial V}\right)_{T,\boldsymbol{n}} \\ &= -p + T\left(\frac{\partial S}{\partial V}\right)_{T,\boldsymbol{n}}.\end{aligned} \tag{2.34}$$

2.1.5 Legendre Transformations

An important mathematical concept is the Legendre transformation. For a function $f(x_1, x_2, \ldots, x_N)$, one of its independent variables may be replaced by its derivative with respect to that variable, i.e., x_i can be replaced by $\left(\frac{\partial f}{\partial x_i}\right)_{x_{j\neq i}}$. The new function, f_i has the same independent variables as f except for x_i which is replaced by the derivative. In terms of equations, a Legendre transformation is defined as

$$\begin{aligned}f_i(\xi_i, x_j, x_k, \ldots, x_N) &:= f(x_i, x_j, x_k, \ldots, x_N) - \xi_i x_i \\ \xi_i &:= \left(\frac{\partial f}{\partial x_i}\right)_{x_{m\neq i}}.\end{aligned} \tag{2.35}$$

Utilizing the defined Legendre transformation on the thermodynamic function U results in the thermodynamic functions H (enthalpy), A (Helmholtz energy), and G (Gibbs energy) in their canonical (natural) variable sets. This means that by specifying a state in the respective coordinate set, U, H, A and G contain all thermodynamic information that can be acquired about the system. Such a relation is called a *fundamental relation*. The Legendre transformations are shown in Table 2.1.

2.1.6 Maxwell Relations

For a function $f : \mathbb{R}^n \to \mathbb{R}$ with continuous second partial derivatives Schwartz' theorem states that (see Schwarz [1890])

$$\left(\frac{\partial^2 f}{\partial x_i \partial x_j}\right)_{x_{k\neq i,j}} = \left(\frac{\partial^2 f}{\partial x_j \partial x_i}\right)_{x_{k\neq i,j}}. \tag{2.36}$$

This may seem obvious, but it has important consequences in both mathematics and thermodynamics. First, it ensures that a Hessian matrix is

Table 2.1: Legendre transformations for the internal energy.

Function	Integral form	Differential form
$U(S, V, \boldsymbol{n})$	$TS - pV + \boldsymbol{\mu}^\top \boldsymbol{n}$	$T\,\mathrm{d}S - p\,\mathrm{d}V + \boldsymbol{\mu}^\top\,\mathrm{d}\boldsymbol{n}$
$H(S, -p, \boldsymbol{n})$	$U + pV$	$T\,\mathrm{d}S + V\,\mathrm{d}p + \boldsymbol{\mu}^\top\,\mathrm{d}\boldsymbol{n}$
$A(T, V, \boldsymbol{n})$	$U - TS$	$-S\,\mathrm{d}T - p\,\mathrm{d}V + \boldsymbol{\mu}^\top\,\mathrm{d}\boldsymbol{n}$
$G(T, -p, \boldsymbol{n})$	$U - TS + pV$	$-S\,\mathrm{d}T + V\,\mathrm{d}p + \boldsymbol{\mu}^\top\,\mathrm{d}\boldsymbol{n}$

always symmetric. Second, it leads to the *Maxwell relations*. For the thermodynamic functions U, H, A, G the Maxwell relations can be deduced by utilizing eq. (2.36) on the differential forms given in Table 2.1. The results are listed in Table 2.2. In the case of a compositional derivative, i.e., a derivative with respect to n_i, all $n_{j\neq i}$ are to be held constant. However, for brevity of notation, this is omitted.

Table 2.2: Maxwell relations for the internal energy, enthalpy, Helmholtz energy, and Gibbs energy.

Function	#1	#2	#3
U	$\left(\frac{\partial T}{\partial V}\right)_{S,\boldsymbol{n}} = -\left(\frac{\partial p}{\partial S}\right)_{V,\boldsymbol{n}}$	$\left(\frac{\partial \mu_i}{\partial S}\right)_{V,\boldsymbol{n}} = \left(\frac{\partial T}{\partial n_i}\right)_{S,V}$	$\left(\frac{\partial \mu_i}{\partial V}\right)_{S,\boldsymbol{n}} = -\left(\frac{\partial p}{\partial n_i}\right)_{S,V}$
H	$\left(\frac{\partial T}{\partial p}\right)_{S,\boldsymbol{n}} = \left(\frac{\partial V}{\partial S}\right)_{p,\boldsymbol{n}}$	$\left(\frac{\partial T}{\partial n_i}\right)_{S,p} = \left(\frac{\partial \mu_i}{\partial S}\right)_{p,\boldsymbol{n}}$	$\left(\frac{\partial V}{\partial n_i}\right)_{S,p} = \left(\frac{\partial \mu_i}{\partial p}\right)_{S,\boldsymbol{n}}$
A	$\left(\frac{\partial S}{\partial V}\right)_{T,\boldsymbol{n}} = \left(\frac{\partial p}{\partial T}\right)_{V,\boldsymbol{n}}$	$\left(\frac{\partial \mu_i}{\partial T}\right)_{V,\boldsymbol{n}} = -\left(\frac{\partial S}{\partial n_i}\right)_{T,V}$	$\left(\frac{\partial \mu_i}{\partial V}\right)_{T,\boldsymbol{n}} = -\left(\frac{\partial p}{\partial n_i}\right)_{T,V}$
G	$\left(\frac{\partial V}{\partial T}\right)_{p,\boldsymbol{n}} = -\left(\frac{\partial S}{\partial p}\right)_{T,\boldsymbol{n}}$	$\left(\frac{\partial \mu_i}{\partial T}\right)_{p,\boldsymbol{n}} = -\left(\frac{\partial S}{\partial n_i}\right)_{T,p}$	$\left(\frac{\partial V}{\partial n_i}\right)_{T,p} = \left(\frac{\partial \mu_i}{\partial p}\right)_{T,\boldsymbol{n}}$

2.2 Thermodynamic Descriptions and Derivations

2.2.1 Equations of State

A relationship that expresses an intensive variable in terms of independent extensive variables is called an *equation of state* (EoS), see Callen [1985]. For instance, the internal energy is a function of the extensive variables $S, V, \boldsymbol{n}$. An equation of state may then express the temperature as a function of these variables, i.e., $T = f(S, V, \boldsymbol{n})$. When all EoSs are specified, they define the

right-hand side of eq. (2.17a) for a thermodynamic function. The ideal gas law is one such EoS, and it states that

$$pV = nRT, \tag{2.37}$$

where p is the pressure, V is the volume, n is the total number of moles, R is the gas constant and T is the temperature. There are many equations of state, but in chemical engineering most of them have the form $p = f(T, V, \boldsymbol{n})$.

The Virial Equation of State

The virial expansion is an EoS generalizing the ideal gas law. It is formulated as a power series in molar density, however it can also be formulated as a similar power series in pressure. The two expansions read (see Elliott and Lira [2012] for the former)

$$\frac{pV}{nRT} = 1 + \sum_{i=1}^{\infty} B_{i+1}(T)\rho^i \tag{2.38a}$$

$$\frac{pV}{nRT} = 1 + \sum_{i=1}^{\infty} B'_{i+1}(T)p^i, \tag{2.38b}$$

respectively, where B, ρ and B' are virial coefficient, molar density, and virial coefficient in pressure expansion, respectively. The virial coefficients are related to each other, see Epstein [1952] for the first five.

The virial expansion in pressure for pure components (truncated after the second term) reads

$$\frac{pV}{nRT} = 1 + \frac{b_2(T)}{RT}p, \tag{2.39}$$

where b_2 (from now on called b) is the same temperature-dependent virial coefficient as that for the density expansion. For charge-symmetric particles, this (pure component) coefficient is related to the pair-potential, $\phi(r)$, through (see Hirschfelder et al. [1964])

$$b(T) = 2\pi N_A \int_0^{\infty} \left(1 - \exp\left(-\frac{\phi(r)}{k_B T}\right)\right) r^2 dr, \tag{2.40}$$

and has the units of $\mathrm{cm}^3\,\mathrm{mol}^{-1}$ (or another volumetric unit per mole). Here Avogadro's number and Boltzmann's constant are denoted N_A and k_B, respectively.

The pair-potential used to model the behavior of the second virial coefficient could be hard sphere, square well, or the Lennard–Jones (12-6)

potential among others. The simplest potential is the hard sphere potential which only consists of repulsive forces. This repulsion occurs when the inelastic hard spheres touch, more specifically when their separation is equal to their hard sphere diameter, σ. The potential has the following form

$$\phi^{\text{hs}}(r) = \begin{cases} \infty, & r \leq \sigma \\ 0, & r > \sigma, \end{cases} \tag{2.41}$$

where "hs" denotes hard sphere. If eq. (2.41) is inserted into eq. (2.40), it gives the hard sphere virial coefficient

$$b^{\text{hs}} = \frac{2}{3}\pi N_A \sigma^3. \tag{2.42}$$

Please note that this virial coefficient is temperature *independent*.

The square well potential is one of the simplest potentials with the form

$$\phi(r) = \begin{cases} \infty, & r \leq \sigma \\ -\varepsilon, & \sigma < r \leq \lambda\sigma \\ 0, & \lambda\sigma < r. \end{cases} \tag{2.43}$$

The name of the potential as well as its mathematical form reveal the shape of the function. When the particles cannot get closer due to their hard sphere volumes the potential rises to infinite, just as for the hard sphere potential. This separation is denoted σ. On the other hand, when particles are far from each other, they do not affect each other. In between these extremes, the particles attract each other. At some separation, there is a maximum attraction. This is the bottom of the potential "well", and the minimum has the value $-\varepsilon$. From the name of the potential, the well is square and $\lambda > 1$ is used to select the width of the bottom of the well, and hence select at what separations the particles interact. By inserting eq. (2.43) into eq. (2.40) the result is

$$\begin{aligned} b(T) &= \frac{2}{3}\pi N_A \sigma^3 \left[1 + \left(1 - \lambda^3\right)\left(\exp\left(\frac{\varepsilon}{k_B T}\right) - 1\right)\right] \\ &= b^{\text{hs}} \left[1 + \left(1 - \lambda^3\right)\left(\exp\left(\frac{\varepsilon}{k_B T}\right) - 1\right)\right]. \end{aligned} \tag{2.44}$$

For a mixture, b needs mixing rules. A theoretical mixing rule derived from statistical mechanics is

$$nB(T, \boldsymbol{n}) = n^2 b_{\text{mix}}(T, \boldsymbol{n}) = \sum_{i=1}^{C} n_i \sum_{j=1}^{C} n_j b_{ij}(T), \tag{2.45}$$

where $b_{ij}(T)$ is the cross coefficient found from integrating the pair-potential for components i and j. Whenever $i = j$, the pair-potential is the pure component pair-potential as first discussed. When $i \neq j$, the pair-potential is that for unlike components. This potential is denoted $\phi_{ij}(r; \sigma_{ij}, \varepsilon_{ij}, \lambda_{ij})$, and it is a function of the separation distance and the square well parameters. Different combining rules can be employed to find the unlike pair-potentials. Lorentz [1881] proposed for hard spheres that the pair diameter is the arithmetic mean

$$\sigma_{ij} = \frac{1}{2}(\sigma_{ii} + \sigma_{jj}). \tag{2.46}$$

The width, λ_{ij}, and the depth, ε_{ij}, of the potential well for the unlike parameters can either be correlated to experiments or derived from theory. Only the theoretical approach is discussed here.

By solely integrating the attractive part of the pair-potential and equating it to the London dispersion forces, the depth of the potential is obtained (see Haslam et al. [2008] for derivation and London [1937] for theoretical background)

$$\varepsilon_{ij} = 2\frac{\sigma_{ii}^3\sigma_{jj}^3}{\sigma_{ij}^6}\left(\frac{(\lambda_{ii}^3 - 1)^{1/2}(\lambda_{jj}^3 - 1)^{1/2}}{\lambda_{ij}^3 - 1}\right)\left(\frac{(I_iI_j)^{1/2}}{I_i + I_j}\right)(\varepsilon_{ii}\varepsilon_{jj})^{1/2}. \tag{2.47}$$

Here I_i is the ionization energy of molecule i. At this point, assumptions must be made about the combining rules for the width of the potential. For instance, the weighted arithmetic mean

$$\lambda_{ij} = \frac{\sigma_{ii}\lambda_{ii} + \sigma_{jj}\lambda_{jj}}{\sigma_{ii} + \sigma_{jj}} \tag{2.48}$$

can be used to close the set of equations.

The combining rules for the width and the depth of the potential well can subsequently be fitted to experiments by introducing a $(1 - k_{ij})$ and $(1 - l_{ij})$, respectively. This will capture deviations in the theoretically derived combining rules. This procedure is not to be confused with the method of correlating the parameters to experiments. Further remarks on the topic are not given here.

The EoS for the mixture now reads

$$p(T, V, \boldsymbol{n}) = \frac{nRT}{V - B(T, \boldsymbol{n})}, \tag{2.49}$$

where B is determined from the previous discussion.

Cubic Equations of State

The most known among the cubic EoSs is the van der Waals EoS

$$p = \frac{nRT}{V - B} - \frac{D}{V^2}, \tag{2.50}$$

where B and D represent excluded volume and attraction, respectively. This EoS has poor accuracy and has mostly historical value. A class of cubic EoSs can be captured by introducing two parameters, δ_1 and δ_2, and extending the van der Waals expression:

$$p = \frac{nRT}{V - B} - \frac{D}{(V + \delta_1 B)(V + \delta_2 B)}. \tag{2.51}$$

By choosing $\delta_1 = 1$ and $\delta_2 = 0$ the Soave–Redlich–Kwong (see Soave [1972]) EoS is retrieved and by choosing $\delta_1 = 1 + \sqrt{2}$ and $\delta_2 = 1 - \sqrt{2}$ the Peng–Robinson (see Peng and Robinson [1976]) EoS is obtained. For pure components $B = b$ and $D = a(T)$. The a and b parameters were by van der Waals [2010] thought of as constants determined to fit experimental measurements. This is also the case for b for the Soave–Redlich–Kwong and Peng–Robinson, however, a is made temperature dependent. The two are calculated by

$$a = a_c\Big(1 + m\Big(1 - \sqrt{T/T_c}\Big)\Big)^2 \tag{2.52a}$$

$$b = b_c, \tag{2.52b}$$

where

$$a_c = \Omega_a \frac{(RT_c)^2}{p_c} \tag{2.53a}$$

$$b_c = \Omega_b \frac{RT_c}{p_c} \tag{2.53b}$$

$$m = \alpha + \beta\omega + \gamma\omega^2, \tag{2.53c}$$

with ω being the acentric factor, and $\Omega_a, \Omega_b, \alpha, \beta, \gamma$ being parameters fitted to experimental vapor pressures.

For mixtures, however, $B = f(\boldsymbol{n})$ and $D = g(T, \boldsymbol{n})$. The classical mixing rules are

$$D = n^2 a_{\text{mix}} = \sum_{i=1}^{C} n_i \sum_{j=1}^{C} n_j a_{ij} \tag{2.54a}$$

$$nB = n^2 b_{\text{mix}} = \sum_{i=1}^{C} n_i \sum_{j=1}^{C} n_j b_{ij} \tag{2.54b}$$

with

$$a_{ij} = a_{ji} = \sqrt{a_{ii}a_{jj}}(1 - k_{ij}) \tag{2.55a}$$

$$b_{ij} = b_{ji} = \frac{1}{2}(b_{ii} + b_{jj})(1 - l_{ij}). \tag{2.55b}$$

Above, k_{ij} and l_{ij} are normally referred to as binary interaction parameters, and it is often assumed that $l_{ij} = 0$. In that case, the mixing rules for B reduce to

$$B = \sum_{i=1}^{C} n_i b_{ii}. \tag{2.56}$$

The PC-SAFT Equation of State

The perturbed-chain statistical association fluid theory (PC-SAFT) is an EoS that is based on statistical mechanics, similar to the virial expansion. It was formulated by Gross and Sadowski [2001] as a SAFT model that accounts for hard-chain and attractive (dispersive) contributions. The molecules are viewed as hard, interacting spheres. Initially, $\bar{m}$ hard spheres are assigned a reduced hard sphere Helmholtz energy. This energy is denoted $\tilde{a}^{\text{hs}}$. Subsequently, the hard spheres move closer together, and the attraction (dispersion) energy is denoted $\tilde{a}^{\text{disp}}$. The hard spheres are assumed to form chains when they are sufficiently close, and the hard chains are assigned a hard chain contribution to the Helmholtz energy, denoted by $\tilde{a}^{\text{chain}}$. Then, the hard chains are given interaction sites where two or more hard chains may associate (e.g., through hydrogen bonding). The energy associated with this is denoted $\tilde{a}^{\text{assoc}}$.

The PC-SAFT EoS is given on Helmholtz energy form by summing all residual molar Helmholtz energy contributions (see Section 2.2.3 for more information on residual thermodynamic functions):

$$\tilde{a}^{\text{r,v}}(T, v, \boldsymbol{x}) = \frac{A^{\text{r,v}}(T, V, \boldsymbol{N})}{N k_B T} = \bar{m}\tilde{a}^{\text{hs}} + \tilde{a}^{\text{chain}} + \tilde{a}^{\text{disp}} + \tilde{a}^{\text{assoc}}. \tag{2.57}$$

Here, $N = \sum_{i=1}^{C} N_i$ denotes the total number of *molecules*, $v = V/N$ denotes the *molecular* volume, and $x_i = N_i/N$ denotes the mole fraction. Moreover, A denotes the extensive Helmholtz energy. Also note that the associative contribution to the Helmholtz energy potential was not considered here, as it was not part of the original formulation of the PC-SAFT EoS [Gross and Sadowski, 2001], but was rather introduced in a later revision of the EoS (see [Gross and Sadowski, 2002]).

In the original work of Gross and Sadowski [2001], the EoS was given on dimensionless form. However, the EoS was rewritten in this dissertation into the canonical variable set $T, V, \boldsymbol{N}$. The EoS is then given as

$$A^{\mathrm{r,v}} = \bar{m}A^{\mathrm{hs}} + A^{\mathrm{chain}} + A^{\mathrm{disp}} + A^{\mathrm{assoc}}, \tag{2.58}$$

$$A^{\mathrm{hs}}(T, V, \boldsymbol{N}) = \frac{Nk_BT}{\xi_0}\left[\frac{3\xi_1\xi_2}{1-\xi_3} + \frac{\xi_2^3}{\xi_3(1-\xi_3)^2} + \left(\frac{\xi_2^3}{\xi_3^2} - \xi_0\right)\ln(1-\xi_3)\right], \tag{2.59}$$

where ξ_i is an auxiliary variable. Furthermore,

$$A^{\mathrm{chain}}(T, V, \boldsymbol{N}) = -k_BT\sum_{i=1}^{C} N_i(m_i - 1)\ln g_{ii}^{\mathrm{hs}}, \tag{2.60}$$

where g_{ij}^{hs} is the radial distribution function between components. The dispersive terms are given as:

$$A^{\mathrm{disp}}(T, V, \boldsymbol{N}) = A_1 + A_2, \tag{2.61}$$

$$A_1(T, V, \boldsymbol{N}) = -\frac{2\pi k_BT}{V}I_1\sum_{i=1}^{C}\sum_{j=1}^{C} N_iN_jm_im_j\left(\frac{\varepsilon_{ij}}{k_BT}\right)\sigma_{ij}^3, \tag{2.62}$$

$$A_2(T, V, \boldsymbol{N}) = -\frac{\pi k_BT}{V}\bar{m}C_1I_2\sum_{i=1}^{C}\sum_{j=1}^{C} N_iN_jm_im_j\left(\frac{\varepsilon_{ij}}{k_BT}\right)^2\sigma_{ij}^3. \tag{2.63}$$

Here, I_1 and I_2 are integral approximations, and C_1 denotes a compressibility expression.

The molecular model is a modified square well potential similar (but not identical) to eq. (2.43). The modified square well potential is given by

$$\phi(r) = \begin{cases} \infty, & r < (\sigma - s_1) \\ 3\varepsilon, & (\sigma - s_1) \leq r < \sigma \\ -\varepsilon, & \sigma \leq r < \lambda\sigma \\ 0, & \lambda\sigma \leq r, \end{cases} \tag{2.64}$$

where $s_1/\sigma = 0.12$ was assumed. The temperature dependent segment diameter is thus given as:

$$\begin{aligned} d_i(T) &= \int_0^{\infty}\left[1 - \exp\left(-\frac{\phi(r)}{k_BT}\right)\right]dr \\ &= \sigma_i\left[1 - 0.12\exp\left(-3\frac{\varepsilon_i}{k_BT}\right)\right] \end{aligned} \tag{2.65}$$

The other additional relations required for the PC-SAFT EoS are given by

$$\bar{m}(\boldsymbol{N}) = \sum_{i=1}^{C} x_i m_i \tag{2.66}$$

$$\xi_n(T, V, \boldsymbol{N}) = \frac{\pi}{6V} \sum_{i=1}^{C} N_i m_i d_i^n, \tag{2.67}$$

$$g_{ij}^{\text{hs}}(T, V, \boldsymbol{N}) = \frac{1}{1-\xi_3} + \frac{d_i d_j}{d_i + d_j} \frac{3\xi_2}{(1-\xi_3)^2} + \left(\frac{d_i d_j}{d_i + d_j}\right)^2 \frac{2\xi_2^2}{(1-\xi_3)^3} \tag{2.68}$$

$$C_1(T, V, \boldsymbol{N}) = \left[1 + \bar{m} \frac{8\xi_3 - 2\xi_3^2}{(1-\xi_3)^4} + (1-\bar{m}) \frac{20\xi_3 - 27\xi_3^2 + 12\xi_3^3 - 2\xi_3^4}{(1-\xi_3)^2(2-\xi_3)^2}\right]^{-1} \tag{2.69}$$

$$I_1(T, V, \boldsymbol{N}) = \sum_{i=0}^{6} a_i \xi_3^i \tag{2.70}$$

$$I_2(T, V, \boldsymbol{N}) = \sum_{i=0}^{6} b_i \xi_3^i \tag{2.71}$$

$$a_i(\boldsymbol{N}) = a_{0i} + \frac{\bar{m}-1}{\bar{m}} a_{1i} + \frac{\bar{m}-1}{\bar{m}} \frac{\bar{m}-2}{\bar{m}} a_{2i} \tag{2.72}$$

$$b_i(\boldsymbol{N}) = b_{0i} + \frac{\bar{m}-1}{\bar{m}} b_{1i} + \frac{\bar{m}-1}{\bar{m}} \frac{\bar{m}-2}{\bar{m}} b_{2i}. \tag{2.73}$$

Here, a_i and b_i are model constants for the EoS. The combining rule for the segment diameter is given by the Lorentz [1881] combining rule

$$\sigma_{ij} = \frac{1}{2}(\sigma_i + \sigma_j) \tag{2.74}$$

and the combining rule for the well depth is given by the Berthelot [1898] combining rule:

$$\varepsilon_{ij} = \sqrt{\varepsilon_i \varepsilon_j}(1 - k_{ij}). \tag{2.75}$$

2.2.2 Changes of State at Constant Composition

In many chemical processes a change of state at constant composition proves useful. The discussion is also a prerequisite for the discussion to follow in Section 2.2.3. The canonical variable sets of internal energy and enthalpy involve the entropy, S. However, for this to be useful, it is required to have knowledge of the other state variables as a function of entropy. The entropy is not measurable or easily manipulable and for experimental studies this

quantity has not been much used. Hence, EoSs are rarely developed in the form $x(S, y_1, y_2, \ldots, y_N)$, where x and $\boldsymbol{y}$ are other quantities of interest.

One solution to the above is to move away from the canonical variable sets and work in other more practical variable sets. The most common involve T, V and T, p. Since $(\mathrm{d}U)_{\boldsymbol{n}} = T\,\mathrm{d}S - p\,\mathrm{d}V$ and $(\mathrm{d}H)_{\boldsymbol{n}} = T\,\mathrm{d}S + V\,\mathrm{d}p$ in canonical coordinates, a total differential for the entropy must be formulated in terms of T, V or T, p, depending on which coordinate set the user sees fit. The total differentials of the entropy in these coordinates read

$$\begin{aligned}(\mathrm{d}S(T, V, \boldsymbol{n}))_{\boldsymbol{n}} &= \left(\frac{\partial S}{\partial T}\right)_{V,\boldsymbol{n}} \mathrm{d}T + \left(\frac{\partial S}{\partial V}\right)_{T,\boldsymbol{n}} \mathrm{d}V \\ &:= \frac{C_V}{T}\,\mathrm{d}T + \left(\frac{\partial p}{\partial T}\right)_{V,\boldsymbol{n}} \mathrm{d}V \qquad (2.76a)\\ (\mathrm{d}S(T, p, \boldsymbol{n}))_{\boldsymbol{n}} &= \left(\frac{\partial S}{\partial T}\right)_{p,\boldsymbol{n}} \mathrm{d}T + \left(\frac{\partial S}{\partial p}\right)_{T,\boldsymbol{n}} \mathrm{d}p \\ &:= \frac{C_p}{T}\,\mathrm{d}T - \left(\frac{\partial V}{\partial T}\right)_{p,\boldsymbol{n}} \mathrm{d}p. \qquad (2.76b)\end{aligned}$$

In the above, heat capacity definitions were used and Maxwell relations (see Table 2.2) for Helmholtz and Gibbs energy were utilized to convert the volume and pressure derivatives, respectively.

As a result of the discussion above, the total differential for entropy in T, V-coordinates can be substituted to yield the total differential of internal energy in T, V-coordinates. If both $\mathrm{d}S$ and $\mathrm{d}V$ is formulated in T, p-coordinates, then $\mathrm{d}U$ can be formulated in T, p-coordinates as well. Thus, the differential of U in T, V is obtained by utilizing eq. (2.76a), and the differential of U in T, p is obtained by combining

$$(\mathrm{d}V)_{\boldsymbol{n}} = \left(\frac{\partial V}{\partial T}\right)_{p,\boldsymbol{n}} \mathrm{d}T + \left(\frac{\partial V}{\partial p}\right)_{T,\boldsymbol{n}} \mathrm{d}p \qquad (2.77)$$

with eq. (2.76b). The two differentials read

$$\begin{aligned}(\mathrm{d}U(T, V, \boldsymbol{n}))_{\boldsymbol{n}} &= T(\mathrm{d}S(T, V, \boldsymbol{n}))_{\boldsymbol{n}} - p\,\mathrm{d}V \\ &= C_V\,\mathrm{d}T + \left(T\left(\frac{\partial p}{\partial T}\right)_{V,\boldsymbol{n}} - p\right)\mathrm{d}V \qquad (2.78a)\end{aligned}$$

$$
\begin{aligned}
(\mathrm{d}U(T,p,\boldsymbol{n}))_{\boldsymbol{n}} &= T(\mathrm{d}S(T,p,\boldsymbol{n}))_{\boldsymbol{n}} - p(\mathrm{d}V(T,p,\boldsymbol{n}))_{\boldsymbol{n}} \\
&= \left(C_p - p\left(\frac{\partial V}{\partial T}\right)_{p,\boldsymbol{n}}\right)\mathrm{d}T \\
&\quad - \left(T\left(\frac{\partial V}{\partial T}\right)_{p,\boldsymbol{n}} + p\left(\frac{\partial V}{\partial p}\right)_{T,\boldsymbol{n}}\right)\mathrm{d}p. \qquad (2.78\mathrm{b})
\end{aligned}
$$

The canonical enthalpy differential is $(\mathrm{d}H)_{\boldsymbol{n}} = T\,\mathrm{d}S + V\,\mathrm{d}p$. Hence, the pressure differential must be substituted to get $\mathrm{d}H(T,V,\boldsymbol{n})$ whereas the differential $\mathrm{d}H(T,p,\boldsymbol{n})$ does not need any further modifications apart from inserting the total differential for entropy in T,p-coordinates. The pressure differential is

$$
(\mathrm{d}p)_{\boldsymbol{n}} = \left(\frac{\partial p}{\partial T}\right)_{V,\boldsymbol{n}}\mathrm{d}T + \left(\frac{\partial p}{\partial V}\right)_{T,\boldsymbol{n}}\mathrm{d}V, \qquad (2.79)
$$

and therefore

$$
\begin{aligned}
(\mathrm{d}H(T,V,\boldsymbol{n}))_{\boldsymbol{n}} &= T(\mathrm{d}S(T,V,\boldsymbol{n}))_{\boldsymbol{n}} + V(\mathrm{d}p(T,V,\boldsymbol{n}))_{\boldsymbol{n}} \\
&= \left(C_V + V\left(\frac{\partial p}{\partial T}\right)_{V,\boldsymbol{n}}\right)\mathrm{d}T \\
&\quad + \left(T\left(\frac{\partial p}{\partial T}\right)_{V,\boldsymbol{n}} + V\left(\frac{\partial p}{\partial V}\right)_{T,\boldsymbol{n}}\right)\mathrm{d}V \qquad (2.80\mathrm{a}) \\
(\mathrm{d}H(T,p,\boldsymbol{n}))_{\boldsymbol{n}} &= T(\mathrm{d}S(T,p,\boldsymbol{n}))_{\boldsymbol{n}} + V\,\mathrm{d}p \\
&= C_p\,\mathrm{d}T + \left(V - T\left(\frac{\partial V}{\partial T}\right)_{p,\boldsymbol{n}}\right)\mathrm{d}p. \qquad (2.80\mathrm{b})
\end{aligned}
$$

The non-canonical representation of the energy potentials U and H is not completely unproblematic. The canonical representation of the energy potentials contains a complete thermodynamic description of the system. They are therefore fundamental relations, meaning that all thermodynamic information that can be acquired about the system rests in the canonical description. Alternatively, if all equations of state are known, they may be substituted into the Euler relation eq. (2.17a) to recover the fundamental relation. This major strength of the canonical coordinate set is lost when the energy potentials are formulated in another, non-canonical coordinate set. As a result, additional descriptions are required, such as entropy in the same non-canonical coordinates. The chemical potential is also more troublesome to obtain in the non-canonical world.

2.2.3 Residual Functions

Residual or departure functions are defined as the deviation of some quantity M from ideal gas at the same $T, V, \boldsymbol{n}$ or $T, p, \boldsymbol{n}$, hence, $M^{\mathrm{r,v}} = M(T, V, \boldsymbol{n}) - M^{\mathrm{ig}}(T, V, \boldsymbol{n})$ or $M^{\mathrm{r,p}} = M(T, p, \boldsymbol{n}) - M^{\mathrm{ig}}(T, p, \boldsymbol{n})$. The notation r,v and r,p denotes that the state is specified in $T, V, \boldsymbol{n}$ or $T, p, \boldsymbol{n}$, respectively. The ideal gas limit is either seen as $V \to \infty$ or $p \to 0$. Both of these provide important starting points for this discussion, since the residuals vanish at these limits. This is due to the transition between a real fluid and ideal gas, which happens at the mentioned limits.

Assume $M(T, V, \boldsymbol{n})$ has an EoS defined by $\left(\frac{\partial M}{\partial V}\right)_{T,\boldsymbol{n}}$. The corresponding EoS for an ideal gas is given by $\left(\frac{\partial M^{\mathrm{ig}}}{\partial V}\right)_{T,\boldsymbol{n}}$. When $V \to \infty$ the EoS specifies the same value as the ideal gas EoS. Therefore, the argument is zero-valued at $V \to \infty$. Assuming that the integrated difference vanish at $V \to \infty$, the residual function of M is defined by integrating along an isotherm from ∞ to the volume of interest V

$$M^{\mathrm{r,v}}(T, V, \boldsymbol{n}) = \int_{\infty}^{V} \left(\left(\frac{\partial M(T, \nu, \boldsymbol{n})}{\partial \nu} \right)_{T,\boldsymbol{n}} - \left(\frac{\partial M^{\mathrm{ig}}(T, \nu, \boldsymbol{n})}{\partial \nu} \right)_{T,\boldsymbol{n}} \right) \mathrm{d}\nu, \tag{2.81}$$

which, by the discussion above, is finite.

The discussion for $M^{\mathrm{r,p}}$ is similar to the one for $M^{\mathrm{r,v}}$: the integrand is zero-valued at the $p \to 0$. Assuming the integrated difference between the EoSs vanish at $p \to 0$, the integral along an isotherm from 0 to the pressure of interest defines the residual at $T, p, \boldsymbol{n}$:

$$M^{\mathrm{r,p}}(T, p, \boldsymbol{n}) = \int_{0}^{p} \left(\left(\frac{\partial M(T, \pi, \boldsymbol{n})}{\partial \pi} \right)_{T,\boldsymbol{n}} - \left(\frac{\partial M^{\mathrm{ig}}(T, \pi, \boldsymbol{n})}{\partial \pi} \right)_{T,\boldsymbol{n}} \right) \mathrm{d}\pi. \tag{2.82}$$

It is stressed that whether the system is specified in $T, p, \boldsymbol{n}$ or $T, V, \boldsymbol{n}$, the value of M should be the same (given the pressure, p, corresponds to the volume, V). Thus, $M(T, p, \boldsymbol{n}) = M(T, V, \boldsymbol{n})$, and a difference in the residuals above must therefore come from a different ideal gas state. For an ideal gas, the temperature is $T = \frac{p_0 V_0}{NR}$, where p_0 and V_0 is the pressure and volume where the gas becomes ideal. At this state the thermodynamic function assumes the value of $M^{\mathrm{ig}}(p_0, V_0, \boldsymbol{n})$. Any of the two first arguments may be replaced by the corresponding temperature to give $M^{\mathrm{ig}}(T, V_0, \boldsymbol{n}) = M^{\mathrm{ig}}(T, p_0, \boldsymbol{n})$. Hence, the function value is the same irrespective of whether p_0 or V_0 is specified.

Whenever the pressure (or volume) assumes some other value than the ideal gas limit, there is a difference in the function value. This difference

comes from the integral from V_0 to V and p_0 to p. Inserting for ideal gas in eq. (2.80a) and eq. (2.80b) results in the coefficients for $\mathrm{d}V$ and $\mathrm{d}p$ canceling. Therefore, the enthalpy is only a function of temperature and composition for ideal gas. When holding these quantities constant, i.e., $\mathrm{d}T = 0$ and $\mathrm{d}\boldsymbol{n} = 0$, the differentials $(\mathrm{d}H^{\mathrm{ig}}(T, V, \boldsymbol{n}))_{T,\boldsymbol{n}} = (\mathrm{d}H^{\mathrm{ig}}(T, p, \boldsymbol{n}))_{T,\boldsymbol{n}} = 0$. The same argument holds for internal energy. Consequently,

$$\int_{V_0}^{V} \left(\frac{\partial H^{\mathrm{ig}}(T, \nu, \boldsymbol{n})}{\partial \nu} \right)_{T,\boldsymbol{n}} \mathrm{d}\nu = 0 \tag{2.83a}$$

$$\int_{p_0}^{p} \left(\frac{\partial H^{\mathrm{ig}}(T, \pi, \boldsymbol{n})}{\partial \pi} \right)_{T,\boldsymbol{n}} \mathrm{d}\pi = 0, \tag{2.83b}$$

and whether the residual is given at $T, V, \boldsymbol{n}$ or $T, p, \boldsymbol{n}$, they are equal, i.e.

$$H^{\mathrm{r,v}} = H^{\mathrm{r,p}}, \text{ and} \tag{2.84}$$

$$U^{\mathrm{r,v}} = U^{\mathrm{r,p}}. \tag{2.85}$$

These are special cases that appear from canceling terms in the total differentials when inserted for ideal gas.

The Helmholtz Approach

The equalities in eq. (2.84) and eq. (2.85) do not apply for all thermodynamic functions. For instance, Helmholtz energy has two different residuals. The most natural choice is to evaluate the residual at the canonical variable set $(T, V, \boldsymbol{n})$. However, most discussions in literature happen in $T, p, \boldsymbol{n}$ and as such, $A^{\mathrm{r,p}}$ has gained more attention than $A^{\mathrm{r,v}}$, even though both notations

are equally uncommon. The differences come from

$$\begin{aligned}
A^{\mathrm{ig}}(T,V,\boldsymbol{n}) - A^{\mathrm{ig}}(T,V(p),\boldsymbol{n}) & \\
&= \int_{V_0}^{V} \left(\frac{\partial A^{\mathrm{ig}}}{\partial \nu}\right)_{T,\boldsymbol{n}} \mathrm{d}\nu - \int_{p_0}^{p} \left(\frac{\partial A^{\mathrm{ig}}}{\partial \pi}\right)_{T,\boldsymbol{n}} \mathrm{d}\pi \\
&= -\int_{V_0}^{V} p(\nu)\,\mathrm{d}\nu + \int_{p_0}^{p} \pi \left(\frac{\partial V}{\partial \pi}\right)_{T,\boldsymbol{n}} \mathrm{d}\pi \\
&= -NRT \ln \frac{V}{V_0} - \int_{p_0}^{p} \frac{NRT}{\pi}\,\mathrm{d}\pi \\
&= -NRT \ln \frac{V}{V_0} - NRT \ln \frac{p}{p_0} \\
&= -NRT \ln \frac{pV}{p_0 V_0} \\
&= -NRT \ln \frac{ZNRT}{NRT} \\
&= -NRT \ln Z,
\end{aligned} \tag{2.86}$$

where $Z = \frac{pV}{NRT}$ is the compressibility factor. Here the actual pressure and volume of the fluid are denoted p and V and the ideal gas pressure and volume are denoted p_0 and V_0.

From

$$\begin{aligned}
A &= A^{\mathrm{r,v}}(T,V,\boldsymbol{n}) + A^{\mathrm{ig}}(T,V,\boldsymbol{n}) \\
&= A^{\mathrm{r,p}}(T,V(p),\boldsymbol{n}) + A^{\mathrm{ig}}(T,V^{\mathrm{ig}}(p),\boldsymbol{n}),
\end{aligned} \tag{2.87}$$

the differences between the residual Helmholtz energy at $T,p,\boldsymbol{n}$ and $T,V,\boldsymbol{n}$ are

$$\begin{aligned}
A^{\mathrm{r,p}} &= A^{\mathrm{r,v}} + A^{\mathrm{ig}}(T,V,\boldsymbol{n}) - A^{\mathrm{ig}}(T,V^{\mathrm{ig}}(p),\boldsymbol{n}) \\
&= A^{\mathrm{r,v}} - NRT \ln Z.
\end{aligned} \tag{2.88}$$

This is a result that is frequently encountered. A similar procedure may be applied for entropy to obtain

$$S^{\mathrm{r,p}} = S^{\mathrm{r,v}} + NR \ln Z. \tag{2.89}$$

The important results of eq. (2.84) and eq. (2.89) along with the two Legendre transformations

$$H = A + TS + pV \tag{2.90}$$

$$G = H - TS \tag{2.91}$$

yield

$$\begin{aligned} G^{\mathrm{r,p}} &= H^{\mathrm{r,p}} - TS^{\mathrm{r,p}} \\ &= H^{\mathrm{r,v}} - TS^{\mathrm{r,p}} \\ &= A^{\mathrm{r,v}} + TS^{\mathrm{r,v}} + p^{\mathrm{r,v}}V - T(S^{\mathrm{r,v}} + NR\ln Z) \\ &= A^{\mathrm{r,v}} + pV - NRT - NRT\ln Z. \end{aligned} \tag{2.92}$$

All thermodynamic energy functions and their possible forms have relations as defined originally. For instance, $\left(\frac{\partial G}{\partial p}\right)_{T,\boldsymbol{n}} = V$ and $\left(\frac{\partial G^{\mathrm{ig}}}{\partial p}\right)_{T,\boldsymbol{n}} = V^{\mathrm{ig}}$. Therefore, $\left(\frac{\partial G^{\mathrm{r,p}}}{\partial p}\right)_{T,\boldsymbol{n}} = \left(\frac{\partial G}{\partial p}\right)_{T,\boldsymbol{n}} - \left(\frac{\partial G^{\mathrm{ig}}}{\partial p}\right)_{T,\boldsymbol{n}} = V - V^{\mathrm{ig}} = V^{\mathrm{r,p}}$. Similarly,

$$S^{\mathrm{r,v}} = -\left(\frac{\partial A^{\mathrm{r,v}}}{\partial T}\right)_{V,\boldsymbol{n}} \tag{2.93a}$$

$$C_V^{\mathrm{r,v}} = -T\left(\frac{\partial^2 A^{\mathrm{r,v}}}{\partial T^2}\right)_{V,\boldsymbol{n}} \tag{2.93b}$$

for the Helmholtz function.

The residual isobaric heat capacity can be found by first applying eq. (2.33) to the entropy $S(T,V,\boldsymbol{n})$, and then removing the ideal gas contribution:

$$\begin{aligned} C_p &= T\left(\frac{\partial S}{\partial T}\right)_{p,\boldsymbol{n}} \\ &= T\left(\left(\frac{\partial S}{\partial T}\right)_{V,\boldsymbol{n}} + \left(\frac{\partial S}{\partial V}\right)_{T,\boldsymbol{n}}\left(\frac{\partial V}{\partial T}\right)_{p,\boldsymbol{n}}\right) \\ &= C_V + T\left(\frac{\partial p}{\partial T}\right)_{V,\boldsymbol{n}}\left(\frac{\partial V}{\partial T}\right)_{p,\boldsymbol{n}} \\ &= C_V - T\frac{\left(\frac{\partial p}{\partial T}\right)^2_{V,\boldsymbol{n}}}{\left(\frac{\partial p}{\partial V}\right)_{T,\boldsymbol{n}}}. \end{aligned} \tag{2.94}$$

Here a Maxwell's relation was utilized for the entropy derivative, and the triple rule was used to transform the volume derivative. By inserting ideal gas in the pressure derivatives, eq. (2.94) yields $C_p^{\mathrm{ig}} - C_V^{\mathrm{ig}} = NR$. By subtracting this result from the original equation eq. (2.94)

$$C_p^{\mathrm{r,p}} - C_V^{\mathrm{r,v}} = -T\frac{\left(\frac{\partial p}{\partial T}\right)^2_{V,\boldsymbol{n}}}{\left(\frac{\partial p}{\partial V}\right)_{T,\boldsymbol{n}}} - NR. \tag{2.95}$$

The Fugacity Coefficient

An important concept in chemical engineering is the fugacity coefficient, which is a shorthand notation for the residual chemical potential at specified $T, p, \boldsymbol{n}$, i.e.

$$\ln \varphi_i := \frac{1}{RT}\mu_i^{\mathrm{r,p}} = \frac{1}{RT}\left(\frac{\partial G^{\mathrm{r,p}}}{\partial n_i}\right)_{T,p}. \tag{2.96}$$

Please note that all $n_{j\neq i}$ are also held constant under the derivation but are omitted for brevity, as will be the case further into this discussion as well. Equation (2.96) requires the usage of temperature and pressure and does not simplify calculations in any way. However, it is common practice and hence it is also introduced here.

If the Helmholtz energy potential is to be used to obtain $\ln \varphi_i$, caution must be exercised. Since one of the variables held constant under the differentiation is pressure, this implicitly defines the volume of the fluid and the volume of the corresponding ideal gas. This means that $Z = \frac{V}{V^{\mathrm{ig}}}$ is in turn also held constant under the differentiation, and eq. (2.96) is expressed as

$$\begin{aligned}\ln \varphi_i &= \frac{1}{RT}\left(\frac{\partial A^{\mathrm{r,p}}}{\partial n_i}\right)_{T,V(p),V^{\mathrm{ig}}(p)} \\ &= \frac{1}{RT}\left(\frac{\partial A^{\mathrm{r,v}}}{\partial n_i}\right)_{T,V} - \ln Z.\end{aligned} \tag{2.97}$$

This argument also provides an alternative way of arriving at eq. (2.89).

The derivatives of the fugacity coefficient are derived by utilizing the triple rule (see eq. (2.27)), eq. (2.33), and eq. (2.97). Hence,

$$\begin{aligned}&\left(\frac{\partial \ln \varphi_i}{\partial T}\right)_{p,\boldsymbol{n}} = \\ &\quad \frac{\partial}{\partial T}\left(\frac{1}{RT}\left(\frac{\partial A^{\mathrm{r,v}}}{\partial n_i}\right)_{T,V} - \ln Z\right)_{p,\boldsymbol{n}} \\ &= \frac{\partial}{\partial T}\left(\frac{1}{RT}\left(\frac{\partial A^{\mathrm{r,v}}}{\partial n_i}\right)_{T,V} - \ln Z\right)_{V,\boldsymbol{n}} \\ &+ \frac{\partial}{\partial V}\left(\frac{1}{RT}\left(\frac{\partial A^{\mathrm{r,v}}}{\partial n_i}\right)_{T,V} - \ln Z\right)_{T,\boldsymbol{n}}\left(\frac{\partial V}{\partial T}\right)_{p,\boldsymbol{n}}\end{aligned}$$

$$= \frac{1}{RT^2}\left(T\left(\frac{\partial^2 A^{\mathrm{r,v}}}{\partial T \partial n_i}\right)_V - \left(\frac{\partial A^{\mathrm{r,v}}}{\partial n_i}\right)_{T,V}\right) - \frac{T}{p}\frac{T\left(\frac{\partial p}{\partial T}\right)_{V,\boldsymbol{n}} - p}{T^2}$$
$$+ \left(\frac{1}{RT}\left(\frac{\partial^2 A^{\mathrm{r,v}}}{\partial V \partial n_i}\right)_T - \frac{1}{pV}\left(V\left(\frac{\partial p}{\partial V}\right)_{T,\boldsymbol{n}} + p\right)\right)\left(\frac{\partial V}{\partial T}\right)_{p,\boldsymbol{n}}. \tag{2.98}$$

At this point, the triple rule eq. (2.27) is employed to replace $\left(\frac{\partial p}{\partial T}\right)_{V,\boldsymbol{n}}$. Two further uses of the triple rule are also shown, because they are utilized in the subsequent derivation

$$\left(\frac{\partial p}{\partial T}\right)_{V,\boldsymbol{n}} = -\left(\frac{\partial p}{\partial V}\right)_{T,\boldsymbol{n}}\left(\frac{\partial V}{\partial T}\right)_{p,\boldsymbol{n}}, \text{ constant } \boldsymbol{n} \tag{2.99a}$$
$$\left(\frac{\partial p}{\partial n_i}\right)_{T,V} = -\left(\frac{\partial p}{\partial T}\right)_{V,\boldsymbol{n}}\left(\frac{\partial T}{\partial n_i}\right)_{p,V}, \text{ constant } V \tag{2.99b}$$
$$\left(\frac{\partial V}{\partial T}\right)_{T,\boldsymbol{n}} = -\left(\frac{\partial V}{\partial n_i}\right)_{T,p}\left(\frac{\partial n_i}{\partial T}\right)_{p,V}, \text{ constant } p. \tag{2.99c}$$

When eq. (2.99a) is inserted into eq. (2.98), the result is

$$\left(\frac{\partial \ln \varphi_i}{\partial T}\right)_{p,\boldsymbol{n}} =$$
$$\frac{1}{RT^2}\left(T\left(\frac{\partial^2 A^{\mathrm{r,v}}}{\partial T \partial n_i}\right)_V - \left(\frac{\partial A^{\mathrm{r,v}}}{\partial n_i}\right)_{T,V}\right)$$
$$+ \frac{1}{p}\cancel{\left(\frac{\partial p}{\partial V}\right)_{T,\boldsymbol{n}}\left(\frac{\partial V}{\partial T}\right)_{p,\boldsymbol{n}}} + \frac{1}{T}$$
$$- \left(\frac{1}{RT}\left(\frac{\partial p^{\mathrm{r,v}}}{\partial n_i}\right)_{T,V} + \frac{1}{p}\cancel{\left(\frac{\partial p}{\partial V}\right)_{T,\boldsymbol{n}}} + \frac{1}{RT}\left(\frac{\partial p^{\mathrm{ig}}}{\partial n_i}\right)_{T,V}\right)\left(\frac{\partial V}{\partial T}\right)_{p,\boldsymbol{n}}$$
$$= \frac{1}{RT^2}\left(T\left(\frac{\partial^2 A^{\mathrm{r,v}}}{\partial T \partial n_i}\right)_V - \left(\frac{\partial A^{\mathrm{r,v}}}{\partial n_i}\right)_{T,V}\right) + \frac{1}{T}$$
$$- \frac{1}{RT}\left(\frac{\partial p}{\partial n_i}\right)_{T,V}\left(\frac{\partial V}{\partial T}\right)_{p,\boldsymbol{n}}$$
$$= \frac{1}{RT^2}\left(T\left(\frac{\partial^2 A^{\mathrm{r,v}}}{\partial T \partial n_i}\right)_V - \left(\frac{\partial A^{\mathrm{r,v}}}{\partial n_i}\right)_{T,V}\right) + \frac{1}{T} - \frac{\overline{V}_i}{RT}\left(\frac{\partial p}{\partial T}\right)_{V,\boldsymbol{n}}. \tag{2.100}$$

The triple rule in eq. (2.99) was used on line three and six: at line three, eq. (2.99a) was used, and at line six, eq. (2.99b) and eq. (2.99c) were used.

Also, a new notation is introduced: $\overline{M}_i = \left(\frac{\partial M}{\partial n_i}\right)_{T,p}$ which is the *partial molar* property of M. Hence, $\overline{V}_i$ is the partial molar volume of the mixture.

The pressure derivative is found by using the fundamental theorem of calculus on eq. (2.82). The fundamental theorem of calculus is given as [Adams and Essex, 2013]:

$$f(x) = \frac{\mathrm{d}}{\mathrm{d}x}\int_a^x f(t)\mathrm{d}t. \tag{2.101}$$

By inserting $M = G$ into eq. (2.82) and employing eq. (2.101) with $x = p$, we obtain

$$\left(\frac{\partial G^{\mathrm{r,p}}}{\partial p}\right)_{T,\boldsymbol{n}} = \left(\frac{\partial G}{\partial p}\right)_{T,\boldsymbol{n}} - \left(\frac{\partial G^{\mathrm{ig}}}{\partial p}\right)_{T,\boldsymbol{n}} = V - \frac{nRT}{p}. \tag{2.102}$$

Taking the compositional derivative of eq. (2.102) and dividing through by RT yields:

$$\left(\frac{\partial \ln \varphi_i}{\partial p}\right)_{T,\boldsymbol{n}} = \frac{\overline{V}_i}{RT} - \frac{1}{p}. \tag{2.103}$$

Finally, the same procedure as for the temperature derivative is employed for composition, which yields:

$$\left(\frac{\partial \ln \varphi_i}{\partial n_j}\right)_{T,p} = \frac{1}{RT}\left(\frac{\partial^2 A^{\mathrm{r,v}}}{\partial n_i \partial n_j}\right)_{T,V} + \frac{1}{N} + \frac{1}{RT}\frac{\left(\frac{\partial p}{\partial n_i}\right)_{T,V}\left(\frac{\partial p}{\partial n_j}\right)_{T,V}}{\left(\frac{\partial p}{\partial V}\right)_{T,\boldsymbol{n}}}. \tag{2.104}$$

Partial Molar Quantities

It was previously mentioned that partial molar quantities are defined as $\overline{M}_i = \left(\frac{\partial M}{\partial n_i}\right)_{T,p}$. This is also a concept that requires the usage of $T, p, \boldsymbol{n}$, but it has for historical reasons received its own notation. Specifically important are the partial molar enthalpy, entropy and Gibbs energy. The partial molar enthalpy indicates how much heat is absorbed or released when a small amount of a component is added to a mixture at constant temperature and pressure. The partial molar Gibbs energy is by definition the chemical potential and this is highly relevant for equilibrium calculations. The partial molar entropy can at least be used as a consistency check, since $\overline{G}_i = \overline{H}_i - T\overline{S}_i$.

The partial molar enthalpy can be derived from its definition $\overline{H}_i = \left(\frac{\partial H}{\partial n_i}\right)_{T,p}$. The residual of this quantity is found by using eq. (2.33)

$$
\begin{aligned}
\overline{H}_i^{\mathrm{r,p}} &= \frac{\partial}{\partial n_i}\left(A^{\mathrm{r,v}} + TS^{\mathrm{r,v}} + pV - NRT\right)_{T,p} \\
&= \frac{\partial}{\partial n_i}\left(A^{\mathrm{r,v}} + TS^{\mathrm{r,v}} + pV - NRT\right)_{T,V} \\
&+ \frac{\partial}{\partial V}\left(A^{\mathrm{r,v}} + TS^{\mathrm{r,v}} + pV - NRT\right)_{T,\boldsymbol{n}} \left(\frac{\partial V}{\partial n_i}\right)_{T,p} \\
&= \left(\frac{\partial A^{\mathrm{r,v}}}{\partial n_i}\right)_{T,V} - T\left(\frac{\partial^2 A^{\mathrm{r,v}}}{\partial T \partial n_i}\right)_V + \cancel{V\left(\frac{\partial p}{\partial n_i}\right)_{T,V}} - RT \\
&+ \left(\left(\frac{\partial A^{\mathrm{r,v}}}{\partial V}\right)_{T,\boldsymbol{n}} - T\left(\frac{\partial^2 A^{\mathrm{r,v}}}{\partial T \partial V}\right)_{\boldsymbol{n}} + p + \cancel{V\left(\frac{\partial p}{\partial V}\right)_{T,\boldsymbol{n}}}\right)\left(\frac{\partial V}{\partial n_i}\right)_{T,p} \\
&= \left(\frac{\partial A^{\mathrm{r,v}}}{\partial n_i}\right)_{T,V} - T\left(\frac{\partial^2 A^{\mathrm{r,v}}}{\partial T \partial n_i}\right)_V - RT \\
&+ \left(-p^{\mathrm{r,v}} - T\left(\frac{\partial^2 A^{\mathrm{r,v}}}{\partial T \partial V}\right)_{\boldsymbol{n}} + p\right)\left(\frac{\partial V}{\partial n_i}\right)_{T,p} \\
&= \left(\frac{\partial A^{\mathrm{r,v}}}{\partial n_i}\right)_{T,V} - T\left(\frac{\partial^2 A^{\mathrm{r,v}}}{\partial T \partial n_i}\right)_V - RT \\
&+ T\left(\frac{p^{\mathrm{ig}}}{T} + \left(\frac{\partial p^{\mathrm{r,v}}}{\partial T}\right)_{V,\boldsymbol{n}}\right)\left(\frac{\partial V}{\partial n_i}\right)_{T,p} \\
&= \left(\frac{\partial A^{\mathrm{r,v}}}{\partial n_i}\right)_{T,V} - T\left(\frac{\partial^2 A^{\mathrm{r,v}}}{\partial T \partial n_i}\right)_V - RT + T\overline{V}_i\left(\frac{\partial p}{\partial T}\right)_{V,\boldsymbol{n}} \\
&= -\left(T\left(\frac{\partial^2 A^{\mathrm{r,v}}}{\partial T \partial n_i}\right)_V - \left(\frac{\partial A^{\mathrm{r,v}}}{\partial n_i}\right)_{T,V} + RT - T\overline{V}_i\left(\frac{\partial p}{\partial T}\right)_{V,\boldsymbol{n}}\right).
\end{aligned}
\tag{2.105}
$$

By dividing eq. (2.105) through by RT^2 it is seen that

$$
\frac{\overline{H}_i^{\mathrm{r,p}}}{RT^2} = -\left(\frac{\partial \ln \varphi_i}{\partial T}\right)_{p,\boldsymbol{n}}. \tag{2.106}
$$

By definition

$$
\frac{\overline{G}_i^{\mathrm{r,p}}}{RT} = \ln \varphi_i, \tag{2.107}
$$

and

$$
\overline{S}_i^{\mathrm{r,p}} = \frac{\overline{H}_i^{\mathrm{r,p}} - \overline{G}_i^{\mathrm{r,p}}}{T}. \tag{2.108}
$$

The Gibbs Approach

If the equation of state can be written as $V = g(T, p, \boldsymbol{n})$, then the residual Gibbs energy may be evaluated by inserting $M = G$ in eq. (2.82)

$$\begin{aligned} G^{\mathrm{r,p}}(T, p, \boldsymbol{n}) &= \int_0^p \left(\left(\frac{\partial G}{\partial \pi} \right)_{T,\boldsymbol{n}} - \left(\frac{\partial G}{\partial \pi} \right)^{\mathrm{ig}}_{T,\boldsymbol{n}} \right) \mathrm{d}\pi \\ &= \int_0^p (V - V^{\mathrm{ig}})\, \mathrm{d}\pi. \end{aligned} \tag{2.109}$$

As discussed in the Helmholtz approach, normal relations for thermodynamics apply to the residual Gibbs energy as well. Thus,

$$S^{\mathrm{r,p}}(T, p, \boldsymbol{n}) = -\left(\frac{\partial G^{\mathrm{r,p}}}{\partial T} \right)_{p,\boldsymbol{n}} \tag{2.110a}$$

$$C_p^{\mathrm{r,p}}(T, p, \boldsymbol{n}) = -T \left(\frac{\partial^2 G^{\mathrm{r,p}}}{\partial T^2} \right)_{p,\boldsymbol{n}} \tag{2.110b}$$

$$C_V^{\mathrm{r,p}} - C_p^{\mathrm{r,p}} = T \frac{\left(\frac{\partial V}{\partial T} \right)^2_{p,\boldsymbol{n}}}{\left(\frac{\partial V}{\partial p} \right)_{T,\boldsymbol{n}}} + NR \tag{2.110c}$$

$$H^{\mathrm{r,p}}(T, p, \boldsymbol{n}) = G^{\mathrm{r,p}} + TS^{\mathrm{r,p}}. \tag{2.110d}$$

Since partial molar quantities are defined as compositional derivatives at constant T, p, their derivations are readily in terms of Gibbs energy

$$\overline{G}_i^{\mathrm{r,p}} = \left(\frac{\partial G^{\mathrm{r,p}}}{\partial n_i} \right)_{T,p} := \mu_i^{\mathrm{r,p}} := RT \ln \varphi_i \tag{2.111a}$$

$$\overline{S}_i^{\mathrm{r,p}} = -\left(\frac{\partial^2 G^{\mathrm{r,p}}}{\partial T \partial n_i} \right)_p \tag{2.111b}$$

$$\overline{H}_i^{\mathrm{r,p}} = \overline{G}_i^{\mathrm{r,p}} + T\overline{S}_i^{\mathrm{r,p}}. \tag{2.111c}$$

2.2.4 Residual Derivatives for Selected Equations of State

So far, all considerations of residual properties are especially concerned with the Helmholtz and Gibbs energies. The discussion did not consider a specified EoS, and the relations are therefore general and valid for any EoS that can be written in the form $V(T, p, \boldsymbol{n})$ or $p(T, V, \boldsymbol{n})$. In this subsection, some selected EoSs are chosen and their first and second derivatives are shown. The chosen EoSs were presented in Section 2.2.1 and are the virial EoS truncated after the second term, a class of cubic EoSs, and the PC-SAFT EoS.

The Virial Equation of State

The virial equation of state is, if truncated after the second term, one of the very few EoSs that lets itself rewrite from a pressure-explicit form to a volume-explicit form. For this reason, two explicit implementations can be made: one $T, V, \boldsymbol{n}$-implementation in Helmholtz energy, and one $T, p, \boldsymbol{n}$-implementation in Gibbs energy. Both eq. (2.81) and eq. (2.82) may be used for the corresponding canonical energy surface, that is Helmholtz and Gibbs energy, respectively.

$\underline{T, V, \boldsymbol{n}}$

By utilizing eq. (2.81), residual Helmholtz energy may be calculated. Noting that p is given by the virial EoS

$$\begin{aligned} A^{\mathrm{r,v}}(T, V, \boldsymbol{n}) &= \int_{\infty}^{V} \left(\left(\frac{\partial A}{\partial \nu} \right)_{T,\boldsymbol{n}} - \left(\frac{\partial A^{\mathrm{ig}}}{\partial \nu} \right)_{T,\boldsymbol{n}} \right) \mathrm{d}\nu \\ &= \int_{\infty}^{V} (p^{\mathrm{ig}} - p)\, \mathrm{d}\nu \\ &= \int_{\infty}^{V} \left(\frac{NRT}{\nu} - \frac{NRT}{\nu - B(T, \boldsymbol{n})} \right) \mathrm{d}\nu \\ &= -NRT \ln \frac{V - B(T, \boldsymbol{n})}{V}. \end{aligned} \tag{2.112}$$

The first order derivatives are

$$\left(\frac{\partial A^{\mathrm{r,v}}}{\partial T} \right)_{V,\boldsymbol{n}} = -NR \left(\ln \frac{V - B}{V} - \frac{T}{V - B} \left(\frac{\partial B}{\partial T} \right)_{\boldsymbol{n}} \right) \tag{2.113a}$$

$$\left(\frac{\partial A^{\mathrm{r,v}}}{\partial V} \right)_{T,\boldsymbol{n}} = -NRT \frac{B}{V(V - B)} \tag{2.113b}$$

$$\left(\frac{\partial A^{\mathrm{r,v}}}{\partial n_i} \right)_{T,V} = -RT \left(\ln \frac{V - B}{V} - \frac{N}{V - B} \left(\frac{\partial B}{\partial n_i} \right)_{T} \right) \tag{2.113c}$$

where

$$\left(\frac{\partial B}{\partial T} \right)_{\boldsymbol{n}} = \frac{1}{N} \sum_{i=1}^{C} n_i \sum_{j=1}^{C} n_j \frac{\mathrm{d}b_{ij}}{\mathrm{d}T} \tag{2.114a}$$

$$\left(\frac{\partial B}{\partial n_i} \right)_{T} = \frac{2 \sum_{j=1}^{C} n_j b_{ij} - B}{N}, \tag{2.114b}$$

and the second order derivatives are

$$\left(\frac{\partial^2 A^{\mathrm{r,v}}}{\partial T^2}\right)_{V,\boldsymbol{n}} = \frac{NR}{V-B}\Big(2\left(\frac{\partial B}{\partial T}\right)_{\boldsymbol{n}} + \frac{T}{V-B}\left(\frac{\partial B}{\partial T}\right)_{\boldsymbol{n}}^2 + T\left(\frac{\partial^2 B}{\partial T^2}\right)_{\boldsymbol{n}}\Big) \tag{2.115a}$$

$$\left(\frac{\partial^2 A^{\mathrm{r,v}}}{\partial V^2}\right)_{T,\boldsymbol{n}} = \frac{NRTB}{V(V-B)}\Big(\frac{1}{V} + \frac{1}{V-B}\Big) \tag{2.115b}$$

$$\left(\frac{\partial^2 A^{\mathrm{r,v}}}{\partial n_i \partial n_j}\right)_{T,V} = \frac{RT}{V-B}\Big(\left(\frac{\partial B}{\partial n_i}\right)_T + \left(\frac{\partial B}{\partial n_j}\right)_T + \frac{N}{V-B}\left(\frac{\partial B}{\partial n_i}\right)_T\left(\frac{\partial B}{\partial n_j}\right)_T + N\left(\frac{\partial^2 B}{\partial n_i \partial n_j}\right)_T\Big) \tag{2.115c}$$

$$\left(\frac{\partial^2 A^{\mathrm{r,v}}}{\partial T \partial V}\right)_{\boldsymbol{n}} = -\frac{NR}{V-B}\Big(\frac{B}{V} + \frac{T}{V-B}\left(\frac{\partial B}{\partial T}\right)_{\boldsymbol{n}}\Big) \tag{2.115d}$$

$$\left(\frac{\partial^2 A^{\mathrm{r,v}}}{\partial T \partial n_i}\right)_V = -R\Big(\ln\frac{V-B}{V} - \frac{N}{V-B}\left(\frac{\partial B}{\partial n_i}\right)_T - \frac{T}{V-B}\Big(\left(\frac{\partial B}{\partial T}\right)_{\boldsymbol{n}} + N\Big(\left(\frac{\partial^2 B}{\partial T \partial n_i}\right) + \frac{\left(\frac{\partial B}{\partial n_i}\right)_T \left(\frac{\partial B}{\partial T}\right)_{\boldsymbol{n}}}{V-B}\Big)\Big)\Big) \tag{2.115e}$$

$$\left(\frac{\partial^2 A^{\mathrm{r,v}}}{\partial V \partial n_i}\right)_T = -\frac{RT}{V-B}\Big(\frac{B}{V} + \frac{N}{V-B}\left(\frac{\partial B}{\partial n_i}\right)_T\Big) \tag{2.115f}$$

where

$$\left(\frac{\partial^2 B}{\partial T^2}\right)_{\boldsymbol{n}} = \frac{1}{N}\sum_{i=1}^{C} n_i \sum_{j=1}^{C} n_j \frac{\mathrm{d}^2 b_{ij}}{\mathrm{d}T^2} \tag{2.116a}$$

$$\left(\frac{\partial^2 B}{\partial n_i \partial n_j}\right)_T = \frac{2b_{ij} - \left(\frac{\partial B}{\partial n_i}\right)_T - \left(\frac{\partial B}{\partial n_j}\right)_T}{N} \tag{2.116b}$$

$$\left(\frac{\partial^2 B}{\partial T \partial n_i}\right) = \frac{2\sum_{j=1}^{C} n_j \frac{\mathrm{d}b_{ij}}{\mathrm{d}T} - \left(\frac{\partial B}{\partial T}\right)_{\boldsymbol{n}}}{N}. \tag{2.116c}$$

The integrated pair-potential of components i and j results in the virial

coefficients $b_{ij}(T)$. The temperature derivatives of these are

$$\frac{\mathrm{d}b_{ij}}{\mathrm{d}T} = -b_{ij}^{\mathrm{hs}}\varepsilon_{ij}\frac{(1-\lambda_{ij}^3)}{kT^2}\exp\left(\frac{\varepsilon_{ij}}{kT}\right) \tag{2.117a}$$

$$\begin{aligned}\frac{\mathrm{d}^2 b_{ij}}{\mathrm{d}T^2} &= -b_{ij}^{\mathrm{hs}}\varepsilon_{ij}(1-\lambda_{ij}^3)\left(\frac{-\frac{\varepsilon_{ij}}{kT^2}\exp\left(\frac{\varepsilon_{ij}}{kT}\right)kT^2 - 2kT\exp\left(\frac{\varepsilon_{ij}}{kT}\right)}{(kT^2)^2}\right) \\ &= -\frac{\mathrm{d}b_{ij}}{\mathrm{d}T}\frac{\varepsilon_{ij}+2kT}{kT^2}.\end{aligned} \tag{2.117b}$$

$\underline{T, p, \boldsymbol{n}}$
The residual Gibbs energy is written

$$\begin{aligned}G^{\mathrm{r,p}}(T,p,\boldsymbol{n}) &= \int_0^p \left(\left(\frac{\partial G}{\partial \pi}\right)_{T,\boldsymbol{n}} - \left(\frac{\partial G}{\partial \pi}\right)_{T,\boldsymbol{n}}^{\mathrm{ig}}\right)\mathrm{d}\pi \\ &= \int_0^p (V - V^{\mathrm{ig}})\,\mathrm{d}\pi \\ &= \int_0^p \left(\frac{NRT}{\pi} + B - \frac{NRT}{\pi}\right)\mathrm{d}\pi \\ &= Bp.\end{aligned} \tag{2.118}$$

The first order derivatives are

$$\left(\frac{\partial G^{\mathrm{r,p}}}{\partial T}\right)_{p,\boldsymbol{n}} = p\left(\frac{\partial B}{\partial T}\right)_{\boldsymbol{n}} \tag{2.119a}$$

$$\left(\frac{\partial G^{\mathrm{r,p}}}{\partial p}\right)_{T,\boldsymbol{n}} = B \tag{2.119b}$$

$$\left(\frac{\partial G^{\mathrm{r,p}}}{\partial n_i}\right)_{T,p} = p\left(\frac{\partial B}{\partial n_i}\right)_{T}, \tag{2.119c}$$

and the second derivatives are

$$\left(\frac{\partial^2 G^{\mathrm{r,p}}}{\partial T^2}\right)_{p,\boldsymbol{n}} = p\left(\frac{\partial^2 B}{\partial T^2}\right)_{\boldsymbol{n}} \tag{2.120a}$$

$$\left(\frac{\partial^2 G^{\mathrm{r,p}}}{\partial p^2}\right)_{T,\boldsymbol{n}} = 0 \tag{2.120b}$$

$$\left(\frac{\partial^2 G^{\mathrm{r,p}}}{\partial n_i \partial n_j}\right)_{T,p} = p\left(\frac{\partial^2 B}{\partial n_i \partial n_j}\right)_{T} \tag{2.120c}$$

$$\left(\frac{\partial^2 G^{\mathrm{r,p}}}{\partial T \partial p}\right)_{\boldsymbol{n}} = \left(\frac{\partial B}{\partial T}\right)_{\boldsymbol{n}} \tag{2.120d}$$

$$\left(\frac{\partial^2 G^{\mathrm{r,p}}}{\partial T \partial n_i}\right)_{p} = p\left(\frac{\partial^2 B}{\partial T \partial n_i}\right) \tag{2.120e}$$

$$\left(\frac{\partial^2 G^{\mathrm{r,p}}}{\partial p \partial n_i}\right)_{T} = \left(\frac{\partial B}{\partial n_i}\right)_{T}. \tag{2.120f}$$

The first and second derivatives of the virial coefficient of the mixture, $B(T, \boldsymbol{n})$, are given by eq. (2.114) and eq. (2.116), and the derivatives of the cross virial coefficients, $b_{ij}(T)$, are given by eq. (2.117).

Cubic Equations of State

$\underline{T, V, \boldsymbol{n}}$
Let $p(T, V, \boldsymbol{n})$ be given by eq. (2.51). Then

$$\begin{aligned} A^{\mathrm{r,v}}(T, V, \boldsymbol{n}) &= \int_{\infty}^{V} \left(\left(\frac{\partial A}{\partial \nu}\right)_{T,\boldsymbol{n}} - \left(\frac{\partial A^{\mathrm{ig}}}{\partial \nu}\right)_{T,\boldsymbol{n}} \right) \mathrm{d}\nu \\ &= \int_{\infty}^{V} (p^{\mathrm{ig}} - p)\, \mathrm{d}\nu \\ &= \int_{\infty}^{V} \left(\frac{NRT}{\nu} - \left(\frac{NRT}{V - B} - \frac{D}{(V + \delta_1 B)(V + \delta_2 B)} \right) \right) \mathrm{d}\nu \\ &= -NRT \ln \frac{V - B}{V} - \frac{D(T)}{B(\delta_1 - \delta_2)} \ln \frac{V + \delta_1 B}{V + \delta_2 B}. \end{aligned} \tag{2.121}$$

The following implementation is based on Michelsen and Mollerup [2007]. Let the reduced residual Helmholtz energy be given as

$$F = F(T, V, N, B, D) = \frac{A^{\mathrm{r,v}}}{RT} = -Ng(V, B) - \frac{D(T, \boldsymbol{n})}{T} f(V, B), \tag{2.122}$$

where

$$g(V,B) = \ln \frac{V-B}{V} \tag{2.123a}$$

$$f(V,B) = \frac{1}{RB(\delta_1-\delta_2)} \ln \frac{V+\delta_1 B}{V+\delta_2 B}. \tag{2.123b}$$

The first order derivatives are

$$\left(\frac{\partial F}{\partial T}\right)_{V,\boldsymbol{n}} = F_T + F_D D_T \tag{2.124a}$$

$$\left(\frac{\partial F}{\partial V}\right)_{T,\boldsymbol{n}} = F_V \tag{2.124b}$$

$$\left(\frac{\partial F}{\partial n_i}\right)_{T,V} = F_N + F_B B_i + F_D D_i, \tag{2.124c}$$

where

$$F_T = \frac{D}{T^2} \tag{2.125a}$$

$$F_V = -N g_V - \frac{D}{T} f_V \tag{2.125b}$$

$$F_N = -g \tag{2.125c}$$

$$F_B = -N g_B - \frac{D}{T} f_B \tag{2.125d}$$

$$F_D = -\frac{f}{T} \tag{2.125e}$$

$$g_V = \frac{B}{V(V-B)} \tag{2.125f}$$

$$g_B = -\frac{1}{V-B} \tag{2.125g}$$

$$f_V = -\frac{1}{R(V+\delta_1 B)(V+\delta_2 B)} \tag{2.125h}$$

$$f_B = -\frac{f + V f_V}{B}. \tag{2.125i}$$

The second order derivatives are given as

$$\left(\frac{\partial^2 F}{\partial T^2}\right)_{V,\boldsymbol{n}} = F_{TT} + 2F_{TD} + F_D D_{TT} \tag{2.126a}$$

$$\left(\frac{\partial^2 F}{\partial V^2}\right)_{T,\boldsymbol{n}} - = F_{VV} \tag{2.126b}$$

$$\left(\frac{\partial^2 F}{\partial n_i \partial n_j}\right)_{T,V} = F_{NB}(B_i + B_j) + F_{BD}(B_i D_j + B_j D_i) + F_B B_{ij} + F_{BB} B_i B_j + F_D D_{ij} \tag{2.126c}$$

$$\left(\frac{\partial^2 F}{\partial T \partial V}\right)_{\boldsymbol{n}} = F_{TV} + F_{VD} D_T \tag{2.126d}$$

$$\left(\frac{\partial^2 F}{\partial T \partial n_i}\right)_{V} = (F_{TB} + F_{BD} D_T) B_i + F_{TD} D_i + F_D D_{Ti} \tag{2.126e}$$

$$\left(\frac{\partial^2 F}{\partial V \partial n_i}\right)_{T} = F_{VN} + F_{VB} B_i + F_{VD} D_i, \tag{2.126f}$$

where

$$F_{TT} = -2\frac{F_T}{T} \tag{2.127a}$$

$$F_{VV} = -N g_{VV} - \frac{D}{T} f_{VV} \tag{2.127b}$$

$$F_{BB} = -N g_{BB} - \frac{D}{T} f_{BB} \tag{2.127c}$$

$$F_{TV} = \frac{D}{T^2} f_V \tag{2.127d}$$

$$F_{TB} = \frac{D f_B}{T^2} \tag{2.127e}$$

$$F_{TD} = \frac{f}{T^2} \tag{2.127f}$$

$$F_{VN} = -g_V \tag{2.127g}$$

$$F_{VB} = -N g_{VB} - \frac{D}{T} f_{VB} \tag{2.127h}$$

$$F_{VD} = -\frac{f_V}{T} \tag{2.127i}$$

$$F_{NB} = -g_B \tag{2.127j}$$

$$F_{BD} = -\frac{f_B}{T} \tag{2.127k}$$

$$g_{VV} = -\frac{1}{(V-B)^2} + \frac{1}{V^2} \tag{2.127l}$$

$$g_{BB} = -\frac{1}{(V-B)^2} \tag{2.127m}$$

$$g_{VB} = \frac{1}{(V-B)^2} \tag{2.127n}$$

$$f_{VV} = \frac{1}{RB(\delta_1-\delta_2)}\left(-\frac{1}{(V+\delta_1 B)^2}+\frac{1}{(V+\delta_2 B)^2}\right) \tag{2.127o}$$

$$f_{BB} = -\frac{2f_B + Vf_{VB}}{B} \tag{2.127p}$$

$$f_{VB} = -\frac{2f_V + Vf_{VV}}{B}. \tag{2.127q}$$

In this modular implementation components can be exchanged with relative ease without having to do a new implementation.

$\underline{T, p, \boldsymbol{n}}$

The cubic EoS is explicit in $T, V, \boldsymbol{n}$ and hence, a single value for pressure is obtained by specifying the coordinate set $T, V, \boldsymbol{n}$. The resulting implementation of $A^{\mathrm{r,v}}$ given above is thus explicit. An alternative to the approach with $T, V, \boldsymbol{n}$ as independent variables is to choose $T, p, \boldsymbol{n}$. This means that the $T, V, \boldsymbol{n}$ relation must be inverted. Due to the cubic nature of the EoS, three values exist for V when specifying the coordinate set $T, p, \boldsymbol{n}$.

For a given temperature, pressure and composition, the volume can be calculated. Cubic EoSs can be solved analytically, however, a general approach is to find the volume by Newton–Raphson iteration on the pressure equation. This volume can be used to initialize the $T, V, \boldsymbol{n}$-implementation, and the residuals at $T, p, \boldsymbol{n}$ are then available from the previous discussion in Section 2.2.3. In other words, $M^{\mathrm{r,p}}$ can be computed when $M^{\mathrm{r,v}}$ is known.

The volume, V, ranges from B to ∞, however, $\beta := B/V \in (0, 1]$. The Newton–Raphson iteration scheme can therefore be applied on β, and V can be retrieved from B/β. The pressure equation on residual form reads

$$h(T, p, V, \boldsymbol{n}) = \frac{NRT}{V} - RT\left(\frac{\partial F}{\partial V}\right)_{T,\boldsymbol{n}} - p = 0. \tag{2.128}$$

This is expressed in terms of β by multiplying by B/NRT

$$h(T, p, \beta, \boldsymbol{n}) = \beta + B\left(g_V + \frac{D}{NT}f_V\right) - \frac{pB}{NRT} = 0, \tag{2.129}$$

where its derivative with respect to β is

$$\left(\frac{\partial h}{\partial \beta}\right)_{T,p,\boldsymbol{n}} = 1 - \left(\frac{B}{\beta}\right)^2\left(g_{VV} + \frac{D}{NT}f_{VV}\right). \tag{2.130}$$

The expression for a Newton–Raphson iteration

$$\beta^{\nu+1} = \beta^{\nu} - \frac{h(T, p, \beta, \boldsymbol{n})}{\left(\frac{\partial h}{\partial \beta}\right)_{T,p,\boldsymbol{n}}} \tag{2.131}$$

along with eq. (2.129) and eq. (2.130) will find the volume, given a reasonable initial volume is provided, see e.g., eq. (16) from Paper I in Chapter 4. Assuming the mixture is a gas phase, a good initial estimate is ideal gas, hence $\beta_0 = pB/(NRT)$.

The PC-SAFT Equation of State

$\underline{T, V, \boldsymbol{n}}$

For the PC-SAFT EoS, $A^{\mathrm{r,v}}(T, V, \boldsymbol{N})$ is given rather than $p(T, V, \boldsymbol{N})$. The expressions were given previously in Section 2.2.1, and consists of eqs. (2.58) to (2.60), (2.62), (2.63) and (2.65) to (2.73). Since the expression for $A^{\mathrm{r,v}}$ is involved, the derivatives also became lengthy. For readability, the derivatives are split into sections for each of its independent variables.

It is noted that there are a few similarities with the derivations in this work and those of Gross and Sadowski [2001]. This only applies to the first derivatives, since no higher order derivatives were given in the original work. The similarities are related to those of the auxiliary variables given in eqs. (2.65) to (2.73). Since Gross and Sadowski [2001] differentiated with respect to mole fractions without respecting $\sum_{i=1}^{C} x_i = 1$, their mole fraction derivatives take a similar form as the compositional derivatives given here. On the other hand, the Helmholtz energy function derivatives with respect to temperature and composition given here are different from the ones given by Gross and Sadowski [2001] due to containing the term Nk_BT. Furthermore, an additional auxiliary variable was introduced by Gross and Sadowski [2001], namely C_2. This variable has not been utilized in this work.

Derivatives with respect to T:

$$A_T^{\mathrm{r,v}} = \bar{m} A_T^{\mathrm{hs}} + A_T^{\mathrm{chain}} + A_{1T} + A_{2T}, \tag{2.132}$$

$$\begin{aligned} A_T^{\mathrm{hs}} = \frac{A^{\mathrm{hs}}}{T} + \frac{Nk_BT}{\xi_0}\Bigg[&\frac{3\xi_{1T}\xi_2}{1-\xi_3} + \frac{3\xi_1\xi_{2T}}{1-\xi_3} + \frac{3\xi_1\xi_2\xi_{3T}}{(1-\xi_3)^2} \\ &+ \frac{3\xi_2^2\xi_{2T}}{\xi_3(1-\xi_3)^2} - \frac{\xi_2^3\xi_{3T}}{\xi_3^2(1-\xi_3)^2} + \frac{2\xi_2^3\xi_{3T}}{\xi_3(1-\xi_3)^3} \\ &+ \left(\frac{3\xi_2^2\xi_{2T}}{\xi_3^2} - \frac{2\xi_2^3\xi_{3T}}{\xi_3^3}\right)\ln(1-\xi_3) - \left(\frac{\xi_2^3}{\xi_3^2} - \xi_0\right)\frac{\xi_{3T}}{1-\xi_3}\Bigg] \end{aligned} \tag{2.133}$$

$$A_T^{\text{chain}} = \frac{A^{\text{chain}}}{T} - k_B T \sum_{i=1}^{C} N_i (m_i - 1) \frac{g_{iiT}^{\text{hs}}}{g_{ii}^{\text{hs}}} \tag{2.134}$$

$$A_{1T} = \frac{I_{1T}}{I_1} A_1 \tag{2.135}$$

$$A_{2T} = -\frac{A_2}{T} + \frac{C_{1T}}{C_1} A_2 + \frac{I_{2T}}{I_2} A_2 \tag{2.136}$$

Furthermore, the derivatives concerning T of the additional relations are:

$$d_{iT} = \frac{3\varepsilon_i}{k_B T^2}(d_i - \sigma_i), \tag{2.137}$$

$$\xi_{nT} = \frac{\pi}{6V} \sum_{i=1}^{C} N_i m_i n d_i^{n-1} d_{iT} \tag{2.138}$$

$$\begin{aligned} g_{ijT}^{\text{hs}} = {} & \frac{\xi_{3T}}{(1-\xi_3)^2} \\ & + \Big[\frac{d_{iT} d_j}{d_i + d_j} + \frac{d_i d_{jT}}{d_i + d_j} - \frac{d_i d_j d_{iT}}{(d_i + d_j)^2} - \frac{d_i d_j d_{jT}}{(d_i + d_j)^2}\Big] \frac{3\xi_2}{(1-\xi_3)^2} \\ & + \frac{d_i d_j}{d_i + d_j}\Big[\frac{3\xi_{2T}}{(1-\xi_3)^2} + \frac{6\xi_2 \xi_{3T}}{(1-\xi_3)^3}\Big] \\ & + \frac{d_i d_j}{d_i + d_j}\Big[\frac{d_{iT} d_j}{d_i + d_j} + \frac{d_i d_{jT}}{d_i + d_j} - \frac{d_i d_j d_{iT}}{(d_i + d_j)^2} - \frac{d_i d_j d_{jT}}{(d_i + d_j)^2}\Big] \frac{4\xi_2^2}{(1-\xi_3)^3} \\ & + \Big(\frac{d_i d_j}{d_i + d_j}\Big)^2 \Big[\frac{4\xi_2 \xi_{2T}}{(1-\xi_3)^3} + \frac{6\xi_2^2 \xi_{3T}}{(1-\xi_3)^4}\Big] \end{aligned} \tag{2.139}$$

$$\begin{aligned} C_{1T} = {} & -C_1^2 \Big[4\bar{m}\xi_{3T}\Big(\frac{2-\xi_3}{(1-\xi_3)^4} + \frac{8\xi_3 - 2\xi_3^2}{(1-\xi_3)^5}\Big) \\ & + 2\xi_{3T}(1-\bar{m})\Big(\frac{10 - 27\xi_3 + 18\xi_3^2 - 4\xi_3^3}{(1-\xi_3)^2(2-\xi_3)^2} \\ & + \frac{20\xi_3 - 27\xi_3^2 + 12\xi_3^3 - 2\xi_3^4}{(1-\xi_3)^3(2-\xi_3)^2} + \frac{20\xi_3 - 27\xi_3^2 + 12\xi_3^3 - 2\xi_3^4}{(1-\xi_3)^2(2-\xi_3)^3}\Big)\Big] \end{aligned} \tag{2.140}$$

$$I_{1T} = \sum_{i=0}^{6} i a_i \xi_3^{i-1} \xi_{3T} \tag{2.141}$$

$$I_{2T} = \sum_{i=0}^{6} i b_i \xi_3^{i-1} \xi_{3T} \tag{2.142}$$

Derivatives with respect to V:

$$A_V^{\mathrm{r,v}} = \bar{m} A_V^{\mathrm{hs}} + A_V^{\mathrm{chain}} + A_{1V} + A_{2V}, \tag{2.143}$$

$$\begin{aligned} A_V^{\mathrm{hs}} = &-\frac{\xi_{0V}}{\xi_0} A^{\mathrm{hs}} + \frac{N k_B T}{\xi_0}\Big[\frac{3\xi_{1V}\xi_2}{1-\xi_3} + \frac{3\xi_1\xi_{2V}}{1-\xi_3} + \frac{3\xi_1\xi_2\xi_{3V}}{(1-\xi_3)^2} \\ &+ \frac{3\xi_2^2\xi_{2V}}{\xi_3(1-\xi_3)^2} - \frac{\xi_2^3\xi_{3V}}{\xi_3^2(1-\xi_3)^2} + \frac{2\xi_2^3\xi_{3V}}{\xi_3(1-\xi_3)^3} \\ &+ \Big(\frac{3\xi_2^2\xi_{2V}}{\xi_3^2} - \frac{2\xi_2^3\xi_{3V}}{\xi_3^3} - \xi_{0V}\Big)\ln(1-\xi_3) - \Big(\frac{\xi_2^3}{\xi_3^2} - \xi_0\Big)\frac{\xi_{3V}}{1-\xi_3}\Big], \end{aligned} \tag{2.144}$$

$$A_V^{\mathrm{chain}} = -k_B T \sum_{i=1}^{C} N_i (m_i - 1) \frac{g_{iiV}^{\mathrm{hs}}}{g_{ii}^{\mathrm{hs}}}, \tag{2.145}$$

$$A_{1V} = -\frac{A_1}{V} + \frac{I_{1V}}{I_1} A_1, \tag{2.146}$$

$$A_{2V} = -\frac{A_2}{V} + \frac{C_{1V}}{C_1} A_2 + \frac{I_{2V}}{I_2} A_2. \tag{2.147}$$

Furthermore, the derivatives concerning V of the additional relations are:

$$\xi_{nV} = -\frac{\xi_n}{V} \tag{2.148}$$

$$\begin{aligned} g_{ijV}^{\mathrm{hs}} = &\frac{\xi_{3V}}{(1-\xi_3)^2} + \frac{d_i d_j}{d_i + d_j}\Big[\frac{3\xi_{2V}}{(1-\xi_3)^2} + \frac{6\xi_2\xi_{3V}}{(1-\xi_3)^3}\Big] \\ &+ \Big(\frac{d_i d_j}{d_i + d_j}\Big)^2\Big[\frac{4\xi_2\xi_{2V}}{(1-\xi_3)^3} + \frac{6\xi_2^2\xi_{3V}}{(1-\xi_3)^4}\Big] \end{aligned} \tag{2.149}$$

$$\begin{aligned} C_{1V} = &-C_1^2\Big[4\bar{m}\xi_{3V}\Big(\frac{2-\xi_3}{(1-\xi_3)^4} + \frac{8\xi_3 - 2\xi_3^2}{(1-\xi_3)^5}\Big) \\ &+ 2\xi_{3V}(1-\bar{m})\Big(\frac{10 - 27\xi_3 + 18\xi_3^2 - 4\xi_3^3}{(1-\xi_3)^2(2-\xi_3)^2} \\ &+ \frac{20\xi_3 - 27\xi_3^2 + 12\xi_3^3 - 2\xi_3^4}{(1-\xi_3)^3(2-\xi_3)^2} + \frac{20\xi_3 - 27\xi_3^2 + 12\xi_3^3 - 2\xi_3^4}{(1-\xi_3)^2(2-\xi_3)^3}\Big)\Big] \end{aligned} \tag{2.150}$$

$$I_{1V} = \sum_{i=0}^{6} i a_i \xi_3^{i-1} \xi_{3V} \tag{2.151}$$

$$I_{2V} = \sum_{i=0}^{6} i b_i \xi_3^{i-1} \xi_{3V} \tag{2.152}$$

Derivatives with respect to N_k:

$$A_k^{\mathrm{r,v}} = \bar{m}A_k^{\mathrm{hs}} + A^{\mathrm{hs}}\bar{m}_k + A_k^{\mathrm{chain}} + A_{1k} + A_{2k}, \tag{2.153}$$

$$\begin{aligned} A_k^{\mathrm{hs}} = \frac{A^{\mathrm{hs}}}{N} - \frac{\xi_{0k}}{\xi_0}A^{\mathrm{hs}} + \frac{Nk_BT}{\xi_0}\Big[&\frac{3\xi_{1k}\xi_2}{1-\xi_3} + \frac{3\xi_1\xi_{2k}}{1-\xi_3} + \frac{3\xi_1\xi_2\xi_{3k}}{(1-\xi_3)^2} \\ &+ \frac{3\xi_2^2\xi_{2k}}{\xi_3(1-\xi_3)^2} - \frac{\xi_2^3\xi_{3k}}{\xi_3^2(1-\xi_3)^2} + \frac{2\xi_2^3\xi_{3k}}{\xi_3(1-\xi_3)^3} \\ &+ \Big(\frac{3\xi_2^2\xi_{2k}}{\xi_3^2} - \frac{2\xi_2^3\xi_{3k}}{\xi_3^3} - \xi_{0k}\Big)\ln(1-\xi_3) - \Big(\frac{\xi_2^3}{\xi_3^2} - \xi_0\Big)\frac{\xi_{3k}}{1-\xi_3}\Big], \end{aligned} \tag{2.154}$$

$$A_k^{\mathrm{chain}} = -k_BT(m_k-1)\ln g_{kk}^{\mathrm{hs}} - k_BT\sum_{i=1}^{C} N_i(m_i-1)\frac{g_{iik}^{\mathrm{hs}}}{g_{ii}^{\mathrm{hs}}}, \tag{2.155}$$

$$A_{1k} = \frac{I_{1k}}{I_1}A_1 - \frac{4\pi k_BT}{V}I_1\sum_{i=1}^{C} N_im_im_k\left(\frac{\varepsilon_{ik}}{k_BT}\right)\sigma_{ik}^3, \tag{2.156}$$

$$\begin{aligned} A_{2k} = &\frac{\bar{m}_k}{\bar{m}}A_2 + \frac{C_{1k}}{C_1}A_2 + \frac{I_{2k}}{I_2}A_2 \\ &- \frac{2\pi k_BT}{V}\bar{m}C_1I_2\sum_{i=1}^{C} N_im_im_k\left(\frac{\varepsilon_{ik}}{k_BT}\right)^2\sigma_{ik}^3, \end{aligned} \tag{2.157}$$

Furthermore, the derivatives concerning N_k of the additional relations are:

$$\bar{m}_k = \frac{m_k - \bar{m}}{N} \tag{2.158}$$

$$\xi_{nk} = \frac{\pi}{6V}m_kd_k^n \tag{2.159}$$

$$\begin{aligned} g_{ijk}^{\mathrm{hs}} = &\frac{\xi_{3k}}{(1-\xi_3)^2} + \frac{d_id_j}{d_i+d_j}\Big[\frac{3\xi_{2k}}{(1-\xi_3)^2} + \frac{6\xi_2\xi_{3k}}{(1-\xi_3)^3}\Big] \\ &+ \Big(\frac{d_id_j}{d_i+d_j}\Big)^2\Big[\frac{4\xi_2\xi_{2k}}{(1-\xi_3)^3} + \frac{6\xi_2^2\xi_{3k}}{(1-\xi_3)^4}\Big] \end{aligned} \tag{2.160}$$

$$\begin{aligned} C_{1k} = -C_1^2\Big[&4\bar{m}\xi_{3k}\Big(\frac{2-\xi_3}{(1-\xi_3)^4} + \frac{8\xi_3 - 2\xi_3^2}{(1-\xi_3)^5}\Big) \\ &+ 2\xi_{3k}(1-\bar{m})\Big(\frac{10 - 27\xi_3 + 18\xi_3^2 - 4\xi_3^3}{(1-\xi_3)^2(2-\xi_3)^2} \\ &+ \frac{20\xi_3 - 27\xi_3^2 + 12\xi_3^3 - 2\xi_3^4}{(1-\xi_3)^3(2-\xi_3)^2} + \frac{20\xi_3 - 27\xi_3^2 + 12\xi_3^3 - 2\xi_3^4}{(1-\xi_3)^2(2-\xi_3)^3}\Big) \\ &+ 2\bar{m}_k\frac{4\xi_3 - \xi_3^2}{(1-\xi_3)^4} - \bar{m}_k\frac{20\xi_3 - 27\xi_3^2 + 12\xi_3^3 - 2\xi_3^4}{(1-\xi_3)^2(2-\xi_3)^2}\Big] \end{aligned} \tag{2.161}$$

$$I_{1k} = \sum_{i=0}^{6} [a_{ik}\xi_3^i + i a_i \xi_3^{i-1}\xi_{3k}] \tag{2.162}$$

$$I_{2k} = \sum_{i=0}^{6} [b_{ik}\xi_3^i + i b_i \xi_3^{i-1}\xi_{3k}] \tag{2.163}$$

$$a_{ik} = \frac{\bar{m}_k}{\bar{m}^2} a_{1i} + \Big(\frac{3\bar{m}_k}{\bar{m}^2} - \frac{4\bar{m}_k}{\bar{m}^3}\Big) a_{2i} \tag{2.164}$$

$$b_{ik} = \frac{\bar{m}_k}{\bar{m}^2} b_{1i} + \Big(\frac{3\bar{m}_k}{\bar{m}^2} - \frac{4\bar{m}_k}{\bar{m}^3}\Big) b_{2i} \tag{2.165}$$

Derivatives with respect to V, V:

$$A_{VV}^{\mathrm{r,v}} = \bar{m} A_{VV}^{\mathrm{hs}} + A_{VV}^{\mathrm{chain}} + A_{1VV} + A_{2VV}, \tag{2.166}$$

$$\begin{aligned} A_{VV}^{\mathrm{hs}} = &-\frac{\xi_{0VV}}{\xi_0} A^{\mathrm{hs}} - 2\frac{\xi_{0V}}{\xi_0} A_V^{\mathrm{hs}} + \frac{N k_B T}{\xi_0}\Big[\frac{3\xi_{1VV}\xi_2}{1-\xi_3} + \frac{6\xi_{1V}\xi_{2V}}{1-\xi_3} \\ &+ \frac{6\xi_{1V}\xi_2\xi_{3V}}{(1-\xi_3)^2} + \frac{3\xi_1\xi_{2VV}}{1-\xi_3} + \frac{6\xi_1\xi_{2V}\xi_{3V}}{(1-\xi_3)^2} + \frac{3\xi_1\xi_2\xi_{3VV}}{(1-\xi_3)^2} + \frac{6\xi_1\xi_2\xi_{3V}^2}{(1-\xi_3)^3} \\ &+ \frac{6\xi_2\xi_{2V}^2}{\xi_3(1-\xi_3)^2} + \frac{3\xi_2^2\xi_{2VV}}{\xi_3(1-\xi_3)^2} - \frac{6\xi_2^2\xi_{2V}\xi_{3V}}{\xi_3^2(1-\xi_3)^2} + \frac{12\xi_2^2\xi_{2V}\xi_{3V}}{\xi_3(1-\xi_3)^3} \\ &- \frac{\xi_2^3\xi_{3VV}}{\xi_3^2(1-\xi_3)^2} + \frac{2\xi_2^3\xi_{3V}^2}{\xi_3^3(1-\xi_3)^2} - \frac{4\xi_2^3\xi_{3V}^2}{\xi_3^2(1-\xi_3)^3} + \frac{2\xi_2^3\xi_{3VV}}{\xi_3(1-\xi_3)^3} \\ &+ \frac{6\xi_2^3\xi_{3V}^2}{\xi_3(1-\xi_3)^4} + \Big(\frac{6\xi_2\xi_{2V}^2}{\xi_3^2} + \frac{3\xi_2^2\xi_{2VV}}{\xi_3^2} - \frac{12\xi_2^2\xi_{2V}\xi_{3V}}{\xi_3^3} - \frac{2\xi_2^3\xi_{3VV}}{\xi_3^3} \\ &+ \frac{6\xi_2^3\xi_{3V}^2}{\xi_3^4} - \xi_{0VV}\Big)\ln(1-\xi_3) - 2\Big(\frac{3\xi_2^2\xi_{2V}}{\xi_3^2} - \frac{2\xi_2^3\xi_{3V}}{\xi_3^3} \\ &- \xi_{0V}\Big)\frac{\xi_{3V}}{1-\xi_3} - \Big(\frac{\xi_2^3}{\xi_3^2} - \xi_0\Big)\Big(\frac{\xi_{3VV}}{1-\xi_3} + \frac{\xi_{3V}^2}{(1-\xi_3)^2}\Big)\Big], \end{aligned} \tag{2.167}$$

$$A_{VV}^{\mathrm{chain}} = -k_B T \sum_{i=1}^{C} N_i(m_i - 1)\left[\frac{g_{iiVV}^{\mathrm{hs}}}{g_{ii}^{\mathrm{hs}}} - \left(\frac{g_{iiV}^{\mathrm{hs}}}{g_{ii}^{\mathrm{hs}}}\right)^2\right] \tag{2.168}$$

$$A_{1VV} = 2\frac{A_1}{V^2} - 2\frac{I_{1V}}{I_1 V} A_1 + \frac{I_{1VV}}{I_1} A_1, \tag{2.169}$$

$$A_{2VV} = 2\frac{A_2}{V^2} - 2\frac{C_{1V}}{C_1 V} A_2 - 2\frac{I_{2V}}{I_2 V} A_2 + 2\frac{C_{1V}}{C_1}\frac{I_{2V}}{I_2} A_2 + \frac{C_{1VV}}{C_1} A_2 + \frac{I_{2VV}}{I_2} A_2 \tag{2.170}$$

Furthermore, the derivatives concerning V, V of the additional relations are:

$$\xi_{nVV} = 2\frac{\xi_n}{V^2} \tag{2.171}$$

$$\begin{aligned}
g^{\mathrm{hs}}_{ijVV} = {} & \frac{\xi_{3VV}}{(1-\xi_3)^2} + \frac{2\xi_{3V}^2}{(1-\xi_3)^3} \\
& + \frac{d_i d_j}{d_i + d_j}\Big[\frac{3\xi_{2VV}}{(1-\xi_3)^2} + \frac{12\xi_{2V}\xi_{3V}}{(1-\xi_3)^3} + \frac{6\xi_2\xi_{3VV}}{(1-\xi_3)^3} + \frac{18\xi_2\xi_{3V}^2}{(1-\xi_3)^4}\Big] \\
& + \Big(\frac{d_i d_j}{d_i + d_j}\Big)^2\Big[\frac{4\xi_{2V}^2}{(1-\xi_3)^3} + \frac{4\xi_2\xi_{2VV}}{(1-\xi_3)^3} + \frac{24\xi_2\xi_{2V}\xi_{3V}}{(1-\xi_3)^4} \\
& + \frac{6\xi_2^2\xi_{3VV}}{(1-\xi_3)^4} + \frac{24\xi_2^2\xi_{3V}^2}{(1-\xi_3)^5}\Big]
\end{aligned} \tag{2.172}$$

$$\begin{aligned}
C_{1VV} = {} & \frac{2C_{1V}^2}{C_1} - C_1^2\Big[4\bar{m}\xi_{3VV}\Big(\frac{2-\xi_3}{(1-\xi_3)^4} + \frac{8\xi_3 - 2\xi_3^2}{(1-\xi_3)^5}\Big) \\
& + 4\bar{m}\xi_{3V}^2\Big(-\frac{1}{(1-\xi_3)^4} + 8\frac{2-\xi_3}{(1-\xi_3)^5} + 5\frac{8\xi_3 - 2\xi_3^2}{(1-\xi_3)^6}\Big) \\
& + 2\xi_{3VV}(1-\bar{m})\Big(\frac{10 - 27\xi_3 + 18\xi_3^2 - 4\xi_3^3}{(1-\xi_3)^2(2-\xi_3)^2} \\
& + \frac{20\xi_3 - 27\xi_3^2 + 12\xi_3^3 - 2\xi_3^4}{(1-\xi_3)^3(2-\xi_3)^2} + \frac{20\xi_3 - 27\xi_3^2 + 12\xi_3^3 - 2\xi_3^4}{(1-\xi_3)^2(2-\xi_3)^3}\Big) \\
& + 2\xi_{3V}^2(1-\bar{m})\Big(\frac{-27 + 36\xi_3 - 12\xi_3^2}{(1-\xi_3)^2(2-\xi_3)^2} \\
& + 2\frac{20 - 54\xi_3 + 36\xi_3^2 - 8\xi_3^3}{(1-\xi_3)^3(2-\xi_3)^2} + 2\frac{20 - 54\xi_3 + 36\xi_3^2 - 8\xi_3^3}{(1-\xi_3)^2(2-\xi_3)^3} \\
& + 3\frac{20\xi_3 - 27\xi_3^2 + 12\xi_3^3 - 2\xi_3^4}{(1-\xi_3)^4(2-\xi_3)^2} + 3\frac{20\xi_3 - 27\xi_3^2 + 12\xi_3^3 - 2\xi_3^4}{(1-\xi_3)^2(2-\xi_3)^4} \\
& + 4\frac{20\xi_3 - 27\xi_3^2 + 12\xi_3^3 - 2\xi_3^4}{(1-\xi_3)^3(2-\xi_3)^3}\Big)\Big]
\end{aligned} \tag{2.173}$$

$$I_{1VV} = \sum_{i=0}^{6} i a_i[(i-1)\xi_3^{i-2}\xi_{3V}^2 + \xi_3^{i-1}\xi_{3VV}] \tag{2.174}$$

$$I_{2VV} = \sum_{i=0}^{6} i b_i[(i-1)\xi_3^{i-2}\xi_{3V}^2 + \xi_3^{i-1}\xi_{3VV}] \tag{2.175}$$

Derivatives with respect to V, N_k:

$$A^{\mathrm{r,v}}_{Vk} = \bar{m}A^{\mathrm{hs}}_{Vk} + A^{\mathrm{hs}}_{V}\bar{m}_k + A^{\mathrm{chain}}_{Vk} + A_{1Vk} + A_{2Vk}, \tag{2.176}$$

$$
\begin{aligned}
A_{Vk}^{\mathrm{hs}} = &\Big(\frac{1}{N} - \frac{\xi_{0k}}{\xi_0}\Big)A_V^{\mathrm{hs}} - \frac{\xi_0 V}{\xi_0}A_k^{\mathrm{hs}} + \Big(\frac{\xi_0 V}{Nt\xi_0} - \frac{\xi_{0Vk}}{\xi_0}\Big)A^{\mathrm{hs}} \\
&+ \frac{Nk_BT}{\xi_0}\Big[\frac{6\xi_2^3\xi_{3V}\xi_{3k}}{\xi_3(1-\xi_3)^4} + \frac{6\xi_2^2\xi_{2V}\xi_{3k}}{\xi_3(1-\xi_3)^3} + \frac{2\xi_2^3\xi_{3V}\xi_{3k}}{\xi_3^3(1-\xi_3)^2} - \frac{4\xi_2^3\xi_{3V}\xi_{3k}}{\xi_3^2(1-\xi_3)^3} \\
&- \frac{3\xi_2^2\xi_{2k}\xi_{3V}}{\xi_3^2(1-\xi_3)^2} + \frac{6\xi_2^2\xi_{2k}\xi_{3V}}{\xi_3(1-\xi_3)^3} - \frac{3\xi_2^2\xi_{2V}\xi_{3k}}{\xi_3^2(1-\xi_3)^2} + \frac{6\xi_1\xi_2\xi_{3V}\xi_{3k}}{(1-\xi_3)^3} \\
&+ \frac{6\xi_2\xi_{2V}\xi_{2k}}{\xi_3(1-\xi_3)^2} + \Big(\frac{6\xi_2\xi_{2V}\xi_{2k}}{\xi_3^2} + \frac{3\xi_2^2\xi_{2Vk}}{\xi_3^2} - \frac{6\xi_2^2\xi_{2k}\xi_{3V}}{\xi_3^3} \\
&- \frac{6\xi_2^2\xi_{2V}\xi_{3k}}{\xi_3^3} - \frac{2\xi_2^3\xi_{3Vk}}{\xi_3^3} + \frac{6\xi_2^3\xi_{3V}\xi_{3k}}{\xi_3^4} - \xi_{0Vk}\Big)\ln(1-\xi_3) \\
&- \Big(\frac{3\xi_2^2\xi_{2V}}{\xi_3^2} - \frac{2\xi_2^3\xi_3 V}{\xi_3^3} - \xi_{0V}\Big)\frac{\xi_{3k}}{1-\xi_3} + \frac{3\xi_{1k}\xi_{2V}}{1-\xi_3} + \frac{3\xi_{1Vk}\xi_2}{1-\xi_3} \\
&+ \frac{3\xi_1\xi_{2Vk}}{1-\xi_3} + \frac{3\xi_{1V}\xi_{2k}}{1-\xi_3} - \Big(\frac{\xi_2^3}{\xi_3^2} - \xi_0\Big)\Big(\frac{\xi_{3Vk}}{1-\xi_3} + \frac{\xi_{3V}\xi_{3k}}{(1-\xi_3)^2}\Big) \\
&+ \frac{2\xi_2^3\xi_{3Vk}}{\xi_3(1-\xi_3)^3} - \frac{\xi_2^3\xi_{3Vk}}{\xi_3^2(1-\xi_3)^2} + \frac{3\xi_1\xi_2\xi_{3Vk}}{(1-\xi_3)^2} + \frac{3\xi_2^2\xi_{2Vk}}{\xi_3(1-\xi_3)^2} \\
&+ \frac{3\xi_{1k}\xi_2\xi_{3V}}{(1-\xi_3)^2} + \frac{3\xi_1\xi_{2k}\xi_{3V}}{(1-\xi_3)^2} + \frac{3\xi_{1V}\xi_2\xi_{3k}}{(1-\xi_3)^2} + \frac{3\xi_1\xi_2 V\xi_{3k}}{(1-\xi_3)^2} \\
&- \Big(\frac{3\xi_2^2\xi_{2k}}{\xi_3^2} - \frac{2\xi_2^3\xi_{3k}}{\xi_3^3} - \xi_{0k}\Big)\frac{\xi_{3V}}{1-\xi_3}\Big],
\end{aligned}
\tag{2.177}
$$

$$
A_{Vk}^{\mathrm{chain}} = -k_BT(m_k-1)\frac{g_{kkV}^{\mathrm{hs}}}{g_{kk}^{\mathrm{hs}}} - k_BT\sum_{i=1}^{C}Ni(m_i-1)\Big(\frac{g_{iiVk}^{\mathrm{hs}}}{g_{ii}^{\mathrm{hs}}} - \frac{g_{iiV}^{\mathrm{hs}}g_{iik}^{\mathrm{hs}}}{(g_{ii}^{\mathrm{hs}})^2}\Big) \tag{2.178}
$$

$$
A_{1Vk} = \frac{I_{1k}}{I_1}A_{1V} + \Big(\frac{I_{1V}}{I_1} - \frac{1}{V}\Big)A_{1k} + \Big(\frac{I_{1Vk}}{I_1} - 2\frac{I_{1V}I_{1k}}{I_1^2} + \frac{I_{1k}}{VI_1}\Big)A_1 \tag{2.179}
$$

$$
\begin{aligned}
A_{2Vk} = &\Big(\frac{\bar{m}_k}{\bar{m}} + \frac{C_{1k}}{C_1} + \frac{I_{2k}}{I_2}\Big)A_{2V} + \Big(\frac{C_{1V}}{C_1} + \frac{I_{2V}}{I_2} - \frac{1}{V}\Big)A_{2k} \\
&+ \Big[\frac{C_{1Vk}}{C_1} - \frac{C_{1V}C_{1k}}{C_1^2} + \frac{I_{2Vk}}{I_2} - \frac{I_{2V}I_{2k}}{I_2^2} \\
&- \Big(\frac{\bar{m}_k}{\bar{m}} + \frac{C_{1k}}{C_1} + \frac{I_{2k}}{I_2}\Big)\Big(\frac{C_{1V}}{C_1} + \frac{I_{2V}}{I_2} - \frac{1}{V}\Big)\Big]A_2
\end{aligned}
\tag{2.180}
$$

Furthermore, the derivatives concerning V, N_k of the additional relations are:

$$
\xi_{nVk} = -\frac{\pi}{6V^2}m_k d_k^n \tag{2.181}
$$

$$
\begin{aligned}
g^{\mathrm{hs}}_{ijVk} &= 2\frac{\xi_{3k}}{1-\xi_3}g^{\mathrm{hs}}_{ijV} + 2\frac{\xi_{3V}}{1-\xi_3}g^{\mathrm{hs}}_{ijk} - 2\frac{\xi_{3V}\xi_{3k}}{(1-\xi_3)^2}g^{\mathrm{hs}}_{ij} + \frac{\xi_{3Vk}}{(1-\xi_3)^2} \\
&+ \frac{d_i d_j}{d_i+d_j}\Big[3\frac{\xi_{2Vk}}{(1-\xi_3)^2} + 6\frac{\xi_2\xi_{3Vk}}{(1-\xi_3)^3}\Big] \\
&+ \Big(\frac{d_i d_j}{d_i+d_j}\Big)^2\Big[4\frac{\xi_{2V}\xi_{2k}}{(1-\xi_3)^3} + 4\frac{\xi_2\xi_{2Vk}}{(1-\xi_3)^3} + 4\frac{\xi_2\xi_{2k}\xi_{3V}}{(1-\xi_3)^4} \\
&+ 4\frac{\xi_2\xi_{2V}\xi_{3k}}{(1-\xi_3)^4} + 6\frac{\xi_2^2\xi_{3Vk}}{(1-\xi_3)^4} + 4\frac{\xi_2^2\xi_{3V}\xi_{3k}}{(1-\xi_3)^5}\Big]
\end{aligned} \tag{2.182}
$$

$$
\begin{aligned}
C_{1Vk} &= \frac{2C_{1V}C_{1k}}{C_1} - C_1^2\Big[4\bar{m}\xi_{3Vk}\Big(\frac{2-\xi_3}{(1-\xi_3)^4} + \frac{8\xi_3-2\xi_3^2}{(1-\xi_3)^5}\Big) \\
&+ 4\bar{m}\xi_{3V}\xi_{3k}\Big(-\frac{1}{(1-\xi_3)^4} + 8\frac{2-\xi_3}{(1-\xi_3)^5} + 5\frac{8\xi_3-2\xi_3^2}{(1-\xi_3)^6}\Big) \\
&+ 2\xi_{3Vk}(-\bar{m}+1)\Big(\frac{10-27\xi_3+18\xi_3^2-4\xi_3^3}{(1-\xi_3)^2(2-\xi_3)^2} \\
&+ \frac{20\xi_3-27\xi_3^2+12\xi_3^3-2\xi_3^4}{(1-\xi_3)^3(2-\xi_3)^2} + \frac{20\xi_3-27\xi_3^2+12\xi_3^3-2\xi_3^4}{(1-\xi_3)^2(2-\xi_3)^3}\Big) \\
&+ 2\xi_{3V}\xi_{3k}(-\bar{m}+1)\Big(\frac{-27+36\xi_3-12\xi_3^2}{(1-\xi_3)^2(2-\xi_3)^2} \\
&+ 4\frac{10-27\xi_3+18\xi_3^2-4\xi_3^3}{(1-\xi_3)^3(2-\xi_3)^2} + 4\frac{10-27\xi_3+18\xi_3^2-4\xi_3^3}{(1-\xi_3)^2(2-\xi_3)^3} \\
&+ 3\frac{20\xi_3-27\xi_3^2+12\xi_3^3-2\xi_3^4}{(1-\xi_3)^4(2-\xi_3)^2} + 4\frac{20\xi_3-27\xi_3^2+12\xi_3^3-2\xi_3^4}{(1-\xi_3)^3(2-\xi_3)^3} \\
&+ 3\frac{20\xi_3-27\xi_3^2+12\xi_3^3-2\xi_3^4}{(1-\xi_3)^2(2-\xi_3)^4}\Big) + 2\bar{m}_k\xi_{3V}\Big(\frac{4-2\xi_3}{(1-\xi_3)^4} \\
&+ 4\frac{4\xi_3-\xi_3^2}{(1-\xi_3)^5} - \frac{10-27\xi_3+18\xi_3^2-4\xi_3^3}{(1-\xi_3)^2(2-\xi_3)^2} \\
&- \frac{20\xi_3-27\xi_3^2+12\xi_3^3-2\xi_3^4}{(1-\xi_3)^3(2-\xi_3)^2} - \frac{20\xi_3-27\xi_3^2+12\xi_3^3-2\xi_3^4}{(1-\xi_3)^2(2-\xi_3)^3}\Big)\Big]
\end{aligned} \tag{2.183}
$$

$$
I_{1Vk} = \sum_{i=0}^{6}[ia_{ik}\xi_3^{i-1}\xi_{3V} + ia_i[(i-1)\xi_3^{i-2}\xi_{3V}\xi_{3k} + \xi_3^{i-1}\xi_{3Vk}]] \tag{2.184}
$$

$$
I_{2Vk} = \sum_{i=0}^{6}[ib_{ik}\xi_3^{i-1}\xi_{3V} + ib_i[(i-1)\xi_3^{i-2}\xi_{3V}\xi_{3k} + \xi_3^{i-1}\xi_{3Vk}]] \tag{2.185}
$$

Derivatives with respect to Nk, Nl:

$$
A^{\mathrm{r,v}}_{kl} = \bar{m}A^{\mathrm{hs}}_{kl} + \bar{m}_l A^{\mathrm{hs}}_k + \bar{m}_k A^{\mathrm{hs}}_l + \bar{m}_{kl}A^{\mathrm{hs}} + A^{\mathrm{chain}}_{kl} + A_{1kl} + A_{2kl} \tag{2.186}
$$

$$
\begin{aligned}
A_{kl}^{\mathrm{hs}} &= \Big(\frac{1}{N}-\frac{\xi_{0l}}{\xi_0}\Big)A_k^{\mathrm{hs}}+\Big(\frac{1}{N}-\frac{\xi_{0k}}{\xi_0}\Big)A_l^{\mathrm{hs}}+\Big(\frac{\xi_{0k}}{\xi_0 N}+\frac{\xi_{0l}}{\xi_0 N}-\frac{2}{N^2}\Big)A^{\mathrm{hs}}\\
&+\frac{Nk_BT}{\xi_0}\Big[\frac{3\xi_{1k}\xi_{2l}}{1-\xi_3}+\frac{3\xi_{1k}\xi_2\xi_{3l}}{(1-\xi_3)^2}+\frac{3\xi_{1l}\xi_{2k}}{1-\xi_3}+\frac{3\xi_{1}\xi_{2k}\xi_{3l}}{(1-\xi_3)^2}+\frac{3\xi_{1l}\xi_2\xi_{3k}}{(1-\xi_3)^2}\\
&+\frac{3\xi_1\xi_{2l}\xi_{3k}}{(1-\xi_3)^2}+\frac{6\xi_1\xi_2\xi_{3k}\xi_{3l}}{(1-\xi_3)^3}+\frac{6\xi_2\xi_{2k}\xi_{2l}}{\xi_3(1-\xi_3)^2}-\frac{3\xi_2^2\xi_{2k}\xi_{3l}}{\xi_3^2(1-\xi_3)^2}\\
&+\frac{6\xi_2^2\xi_{2k}\xi_{3l}}{\xi_3(1-\xi_3)^3}-\frac{3\xi_2^2\xi_{3k}\xi_{2l}}{\xi_3^2(1-\xi_3)^2}+\frac{2\xi_2^3\xi_{3k}\xi_{3l}}{\xi_3^3(1-\xi_3)^2}-\frac{4\xi_2^3\xi_{3k}\xi_{3l}}{\xi_3^2(1-\xi_3)^3}\\
&+\frac{6\xi_2^2\xi_{3k}\xi_{2l}}{\xi_3(1-\xi_3)^3}+\frac{6\xi_2^3\xi_{3k}\xi_{3l}}{\xi_3(1-\xi_3)^4}\\
&+\Big(\frac{6\xi_2\xi_{2k}\xi_{2l}}{\xi_3^2}-\frac{6\xi_2^2\xi_{2k}\xi_{3l}}{\xi_3^3}-\frac{6\xi_2^2\xi_{3k}\xi_{2l}}{\xi_3^3}+\frac{6\xi_2^3\xi_{3k}\xi_{3l}}{\xi_3^4}\Big)\ln(1-\xi_3)\\
&-\Big(\frac{3\xi_2^2\xi_{2k}}{\xi_3^2}-\frac{2\xi_2^3\xi_{3k}}{\xi_3^3}-\xi_{0k}\Big)\frac{\xi_{3l}}{1-\xi_3}\\
&-\Big(\frac{3\xi_2^2\xi_{2l}}{\xi_3^2}-\frac{2\xi_2^3\xi_{3l}}{\xi_3^3}-\xi_{0l}\Big)\frac{\xi_{3k}}{1-\xi_3}-\Big(\frac{\xi_2^3}{\xi_3^2}-\xi_0\Big)\frac{\xi_{3k}\xi_{3l}}{(1-\xi_3)^2}\Big]
\end{aligned}
\tag{2.187}
$$

$$
\begin{aligned}
A_{kl}^{\mathrm{chain}} &= -k_BT\Big[(m_k-1)\frac{g_{kkl}^{\mathrm{hs}}}{g_{kk}^{\mathrm{hs}}}+(m_l-1)\frac{g_{llk}^{\mathrm{hs}}}{g_{ll}^{\mathrm{hs}}}\\
&\quad-\sum_{i=1}^{C}\Big[N_i(m_i-1)\frac{g_{iik}^{\mathrm{hs}}g_{iil}^{\mathrm{hs}}}{(g_{ii}^{\mathrm{hs}})^2}-N_i(m_i-1)\frac{g_{iikl}^{\mathrm{hs}}}{g_{ii}^{\mathrm{hs}}}\Big]\Big]
\end{aligned}
\tag{2.188}
$$

$$
\begin{aligned}
A_{1kl} &= \Big(\frac{I_{1kl}}{I_1}-\frac{I_{1k}I_{1l}}{I_1^2}\Big)A_1+\frac{I_{1k}}{I_1}A_{1l}\\
&-\frac{4\pi k_BT}{V}\Big[I_1m_km_l\Big(\frac{\varepsilon_{kl}}{k_BT}\Big)\sigma_{kl}^3+I_{1l}\sum_{i=1}^{C}N_im_im_k\Big(\frac{\varepsilon_{ik}}{k_BT}\Big)\sigma_{ik}^3\Big]
\end{aligned}
\tag{2.189}
$$

$$
\begin{aligned}
A_{2kl} &= \Big[\frac{\bar m_{kl}}{\bar m}-\frac{\bar m_k\bar m_l}{\bar m^2}+\frac{C_{1kl}}{C_1}-\frac{C_{1k}C_{1l}}{C_1^2}+\frac{I_{2kl}}{I_2}-\frac{I_{2k}I_{2l}}{I_2^2}\\
&\quad-\Big(\frac{\bar m_k}{\bar m}+\frac{C_{1k}}{C_1}+\frac{I_{2k}}{I_2}\Big)\Big(\frac{\bar m_l}{\bar m}+\frac{C_{1l}}{C_1}+\frac{I_{2l}}{I_2}\Big)\Big]A_2\\
&\quad+\Big(\frac{\bar m_l}{\bar m}+\frac{C_{1l}}{C_1}+\frac{I_{2l}}{I_2}\Big)A_{2k}+\Big(\frac{\bar m_k}{\bar m}+\frac{C_{1k}}{C_1}+\frac{I_{2k}}{I_2}\Big)A_{2l}\\
&\quad-\frac{2\pi k_BT}{V}\bar mC_1I_2m_km_l\Big(\frac{\varepsilon_{kl}}{k_BT}\Big)^2\sigma_{kl}^3
\end{aligned}
\tag{2.190}
$$

Furthermore, the derivatives concerning N_k, N_l of the additional relations are:

$$
\bar m_{kl} = -\frac{\bar m_k+\bar m_l}{N} \tag{2.191}
$$

$$\xi_{nkl} = 0 \tag{2.192}$$

$$\begin{aligned} g^{\rm hs}_{ijkl} = {} & \frac{2\xi_{3l}}{1-\xi_3} g^{\rm hs}_{ijk} + \frac{2\xi_{3k}}{1-\xi_3} g^{\rm hs}_{ijl} - \frac{2\xi_{3k}\xi_{3l}}{(1-\xi_3)^2} g^{\rm hs}_{ij} \\ & + \Big(\frac{d_i d_j}{d_i + d_j}\Big)^2 \Big[\frac{4\xi_{2k}\xi_{2l}}{(1-\xi_3)^3} + \frac{4\xi_2\xi_{2k}\xi_{3l}}{(1-\xi_3)^4} + \frac{4\xi_2\xi_{2l}\xi_{3k}}{(1-\xi_3)^4} + \frac{4\xi_2^2\xi_{3k}\xi_{3l}}{(1-\xi_3)^5} \Big] \end{aligned} \tag{2.193}$$

$$\begin{aligned} C_{1kl} = {} & \frac{2C_{1k}C_{1l}}{C_1} - C_1^2 \Big[4\xi_{3k}\bar{m}_l \Big(\frac{2-\xi_3}{(1-\xi_3)^4} + \frac{8\xi_3 - 2\xi_3^2}{(1-\xi_3)^5} \Big) \\ & + 4\xi_{3k}\xi_{3l}\bar{m} \Big(- \frac{1}{(1-\xi_3)^4} + 8\frac{2-\xi_3}{(1-\xi_3)^5} + 5\frac{8\xi_3 - 2\xi_3^2}{(1-\xi_3)^6} \Big) \\ & - 2\xi_{3k}\bar{m}_l \Big(\frac{10 - 27\xi_3 + 18\xi_3^2 - 4\xi_3^3}{(1-\xi_3)^2(2-\xi_3)^2} + \frac{20\xi_3 - 27\xi_3^2 + 12\xi_3^3 - 2\xi_3^4}{(1-\xi_3)^3(2-\xi_3)^2} \\ & + \frac{20\xi_3 - 27\xi_3^2 + 12\xi_3^3 - 2\xi_3^4}{(1-\xi_3)^2(2-\xi_3)^3} \Big) \\ & + 2\xi_{3k}\xi_{3l}(1-\bar{m}) \Big(\frac{-27 + 36\xi_3 - 12\xi_3^2}{(1-\xi_3)^2(2-\xi_3)^2} + 4\frac{10 - 27\xi_3 + 18\xi_3^2 - 4\xi_3^3}{(1-\xi_3)^3(2-\xi_3)^2} \\ & + 4\frac{10 - 27\xi_3 + 18\xi_3^2 - 4\xi_3^3}{(1-\xi_3)^2(2-\xi_3)^3} + 3\frac{20\xi_3 - 27\xi_3^2 + 12\xi_3^3 - 2\xi_3^4}{(1-\xi_3)^4(2-\xi_3)^2} \\ & + 3\frac{20\xi_3 - 27\xi_3^2 + 12\xi_3^3 - 2\xi_3^4}{(1-\xi_3)^2(2-\xi_3)^4} + 4\frac{20\xi_3 - 27\xi_3^2 + 12\xi_3^3 - 2\xi_3^4}{(1-\xi_3)^3(2-\xi_3)^3} \Big) \\ & + 2\bar{m}_k\xi_{3l} \Big(\frac{4-2\xi_3}{(1-\xi_3)^4} + 4\frac{4\xi_3 - \xi_3^2}{(1-\xi_3)^5} - \frac{10 - 27\xi_3 + 18\xi_3^2 - 4\xi_3^3}{(1-\xi_3)^2(2-\xi_3)^2} \\ & - \frac{20\xi_3 - 27\xi_3^2 + 12\xi_3^3 - 2\xi_3^4}{(1-\xi_3)^3(2-\xi_3)^2} - \frac{20\xi_3 - 27\xi_3^2 + 12\xi_3^3 - 2\xi_3^4}{(1-\xi_3)^2(2-\xi_3)^3} \Big) \\ & + \bar{m}_{kl} \Big(\frac{8\xi_3 - 2\xi_3^2}{(1-\xi_3)^4} - \frac{20\xi_3 - 27\xi_3^2 + 12\xi_3^3 - 2\xi_3^4}{(1-\xi_3)^2(2-\xi_3)^2} \Big) \Big] \end{aligned} \tag{2.194}$$

$$I_{1kl} = \sum_{i=0}^{6} [a_{ikl}\xi_3^i + i a_{ik}\xi_3^{i-1}\xi_{3l} + i\xi_{3k}[(i-1)a_i\xi_3^{i-2}\xi_{3l} + a_{il}\xi_3^{i-1}]] \tag{2.195}$$

$$I_{2kl} = \sum_{i=0}^{6} [b_{ikl}\xi_3^i + i b_{ik}\xi_3^{i-1}\xi_{3l} + i\xi_{3k}[(i-1)b_i\xi_3^{i-2}\xi_{3l} + b_{il}\xi_3^{i-1}]] \tag{2.196}$$

$$a_{ikl} = \frac{\bar{m}_{kl}}{\bar{m}^2} a_{1i} + \Big(\frac{3\bar{m}_{kl}}{\bar{m}^2} - \frac{4\bar{m}_{kl}}{\bar{m}^3} + \frac{4\bar{m}_k\bar{m}_l}{\bar{m}^4} \Big) a_{2i} - \frac{2\bar{m}_l}{\bar{m}} a_{ik} \tag{2.197}$$

$$b_{ikl} = \frac{\bar{m}_{kl}}{\bar{m}^2} b_{1i} + \Big(\frac{3\bar{m}_{kl}}{\bar{m}^2} - \frac{4\bar{m}_{kl}}{\bar{m}^3} + \frac{4\bar{m}_k\bar{m}_l}{\bar{m}^4} \Big) b_{2i} - \frac{2\bar{m}_l}{\bar{m}} b_{ik} \tag{2.198}$$

$T, p, \boldsymbol{n}$

The PC-SAFT EoS is also explicit in $T, V, \boldsymbol{N}$, which yields a single value for a specified coordinate set $T, V, \boldsymbol{N}$. Thus, the implementation above for $A^{\mathrm{r,v}}$ is explicit. Alternatively, the coordinate set $T, p, \boldsymbol{N}$ may be employed. In that coordinate set, the $T, V, \boldsymbol{N}$ relation must be inverted. For the PC-SAFT EoS, five values for V exist when the coordinate set $T, p, \boldsymbol{N}$ is employed [Privat et al., 2010]. Similar to the cubic EoS implementation, Newton–Raphson iteration can be performed for the PC-SAFT EoS to obtain the volume. A discussion on initializing the iteration procedure to find the appropriate volume roots and further recommendations on the PC-SAFT EoS were given by Gross and Sadowski [2001].

2.3 Thermodynamic Consistency and Testing

Thermodynamics is a highly consistent field within science. There are multiple relations that must hold at all times, and therefore there are strict rules for what can and what cannot be valid within thermodynamics. For instance, Euler's theorem for homogeneous functions must always hold. Therefore, the chemical potential, for instance, cannot have an arbitrary definition, but must satisfy the relations in eqs. (2.17a) and (2.21).

As previously mentioned, Euler's theorem for homogeneous functions and its derivative (see eq. (2.17a) and eq. (2.21), respectively) provide consistency checks for Helmholtz and Gibbs energy. For Helmholtz energy, $\boldsymbol{X} = (V, \boldsymbol{n})$ and $\xi = T$. By inserting this into eq. (2.17a) and eq. (2.21a) the result is

$$\left(\frac{\partial A^{\mathrm{r,v}}}{\partial V}\right)_{T,\boldsymbol{n}} V + \left(\frac{\partial A^{\mathrm{r,v}}}{\partial \boldsymbol{n}}\right)_{T,V}^{\top} \boldsymbol{n} = A^{\mathrm{r,v}} \tag{2.199a}$$

$$\left(\frac{\partial^2 A}{\partial V^2}\right)_{T,\boldsymbol{n}} V + \left(\frac{\partial^2 A}{\partial V \partial \boldsymbol{n}}\right)_{T}^{\top} \boldsymbol{n} = 0 \tag{2.199b}$$

$$\left(\frac{\partial^2 A}{\partial \boldsymbol{n} \partial V}\right)_{T} V + \left(\frac{\partial^2 A}{\partial \boldsymbol{n} \partial \boldsymbol{n}^{\top}}\right)_{T,V} \boldsymbol{n} = \boldsymbol{0}. \tag{2.199c}$$

For Gibbs energy, $\boldsymbol{X} = \boldsymbol{n}$ and $\boldsymbol{\xi} = (T, p)$. This results in two equalities:

$$\left(\frac{\partial G^{\mathrm{r,p}}}{\partial \boldsymbol{n}}\right)_{T,p}^{\top} \boldsymbol{n} = G^{\mathrm{r,p}} \tag{2.200a}$$

$$\left(\frac{\partial^2 G^{\mathrm{r,p}}}{\partial \boldsymbol{n} \partial \boldsymbol{n}^{\top}}\right)_{T,p} \boldsymbol{n} = \boldsymbol{0}. \tag{2.200b}$$

Taking the compositional derivative of eq. (2.200a) yields

$$\frac{\partial}{\partial \boldsymbol{n}}\left(RT\boldsymbol{n}^\top \ln \boldsymbol{\varphi}\right)_{T,p} = RT\left(\frac{\partial \ln \boldsymbol{\varphi}}{\partial \boldsymbol{n}}\right)_{T,p}\boldsymbol{n} + RT\ln \boldsymbol{\varphi} = RT\ln \boldsymbol{\varphi}. \quad (2.201)$$

Equally important is the symmetry check. This involves checking the second derivative with respect to composition

$$\left(\frac{\partial^2 A^{\mathrm{r,v}}}{\partial \boldsymbol{n}\partial \boldsymbol{n}^\top}\right)_{T,V} = \left(\frac{\partial^2 A^{\mathrm{r,v}}}{\partial \boldsymbol{n}\partial \boldsymbol{n}^\top}\right)^\top_{T,V} \quad (2.202a)$$

$$\left(\frac{\partial^2 G^{\mathrm{r,p}}}{\partial \boldsymbol{n}\partial \boldsymbol{n}^\top}\right)_{T,p} = \left(\frac{\partial^2 G^{\mathrm{r,p}}}{\partial \boldsymbol{n}\partial \boldsymbol{n}^\top}\right)^\top_{T,p}, \quad (2.202b)$$

or as commonly written

$$\left(\frac{\partial \mu_i^{\mathrm{r,v}}}{\partial n_j}\right)_{T,V} = \left(\frac{\partial \mu_j^{\mathrm{r,v}}}{\partial n_i}\right)_{T,V}, \quad \forall i,j \in \{1,\dots,C\} \quad (2.203a)$$

$$\left(\frac{\partial \mu_i^{\mathrm{r,p}}}{\partial n_j}\right)_{T,p} = \left(\frac{\partial \mu_j^{\mathrm{r,p}}}{\partial n_i}\right)_{T,p}, \quad \forall i,j \in \{1,\dots,C\}. \quad (2.203b)$$

Furthermore, an analytical test can be done with respect to the temperature derivative of the fugacity coefficient. By using eq. (2.21b):

$$\begin{bmatrix}\left(\frac{\partial^2 G^{\mathrm{r,p}}}{\partial T\partial \boldsymbol{n}^\top}\right)_p \\ \left(\frac{\partial^2 G^{\mathrm{r,p}}}{\partial p\partial \boldsymbol{n}^\top}\right)_T\end{bmatrix}\boldsymbol{n} = \begin{bmatrix}\left(\frac{\partial \boldsymbol{\mu}^{\mathrm{r,p}}}{\partial T}\right)_{p,\boldsymbol{n}} \\ \left(\frac{\partial \boldsymbol{\mu}^{\mathrm{r,p}}}{\partial p}\right)_{T,\boldsymbol{n}}\end{bmatrix}^\top \boldsymbol{n} = \begin{bmatrix}\left(\frac{\partial G^{\mathrm{r,p}}}{\partial T}\right)_{p,\boldsymbol{n}} \\ \left(\frac{\partial G^{\mathrm{r,p}}}{\partial p}\right)_{T,\boldsymbol{n}}\end{bmatrix} = \begin{bmatrix}-S^{\mathrm{r,p}} \\ V^{\mathrm{r,p}}\end{bmatrix}. \quad (2.204)$$

The upper equation along with the temperature derivative of the fugacity coefficient yields

$$\begin{aligned}\left(\frac{\partial \ln \boldsymbol{\varphi}}{\partial T}\right)^\top_{p,\boldsymbol{n}}\boldsymbol{n} &= \frac{1}{RT^2}\left(T\left(\frac{\partial \boldsymbol{\mu}^{\mathrm{r,p}}}{\partial T}\right)^\top_{p,\boldsymbol{n}}\boldsymbol{n} - (\boldsymbol{\mu}^{\mathrm{r,p}})^\top\boldsymbol{n}\right) \\ &= \frac{1}{RT^2}\left(-TS^{\mathrm{r,p}} - G^{\mathrm{r,p}}\right) \\ &= -\frac{H^{\mathrm{r,p}}}{RT^2}.\end{aligned} \quad (2.205)$$

Other tests include numerical tests. That is, the tests are done with numerical derivatives, typically finite, central differences. Thus,

$$\left|\frac{f(x_0+\theta)-f(x_0-\theta)}{2\theta} - \left.\frac{df(x)}{\mathrm{d}x}\right|_{x_0}\right| < \epsilon, \quad (2.206)$$

where θ is a small perturbation, and ϵ is the numerical error introduced from inaccuracies in the central differencing scheme. The order of the error of central differences is $O(\theta^2)$.

From the differential form of Gibbs energy in Table 2.1, the pressure derivative of Gibbs energy is

$$\left(\frac{\partial G^{\mathrm{r,p}}}{\partial p}\right)_{T,\boldsymbol{n}} = V^{\mathrm{r,p}} = V - V^{\mathrm{ig}}. \tag{2.207}$$

Thus,

$$\left(\frac{\partial \ln \boldsymbol{\varphi}}{\partial p}\right)^{\top}_{T,\boldsymbol{n}} \boldsymbol{n} = \frac{Z-1}{p} N. \tag{2.208}$$

In a Helmholtz implementation, a numerical derivative (denoted by a δ)

$$\frac{\delta}{\delta p}\left(\boldsymbol{n}^{\top} \ln \boldsymbol{\varphi}\right)_{T,\boldsymbol{n}} = \frac{Z-1}{p} N \tag{2.209}$$

will rule out any pressure dependent binary interaction parameters, k_{ij} and l_{ij}. The expression for the fugacity coefficient in eq. (2.97) is based on the integration of a pressure-explicit EoS. Pressure dependent forms of the binary interaction parameters will disturb the form of the EoS and therefore also invalidate eq. (2.97). When the numerical derivative above is calculated, the invalid expression for the fugacity coefficient is used, and the result will not equate to the right-hand side.

Chapter 3

Mass Transfer Phenomena

Mass transfer is a phenomenon in which a component i is transferred from one phase and into another over a shared phase boundary called the interface. For instance, a gas phase in contact with a liquid phase is visualized in Figure 3.1. Here, the driving force for component i is given by the difference in an appropriate quantity ψ (discussed in detail in Sections 3.1.1 to 3.1.4):

$$d_i := \Delta\psi_i = \psi_{G,i} - \psi_{L,i}. \tag{3.1}$$

The driving force in eq. (3.1) governs the qualitative and quantitative nature of the mass transfer of component i. In Figure 3.1, $\psi_{G,i} > \psi_{L,i}$, and mass is transferred out of the gas phase and into the liquid phase with the mass transfer flux N_i.

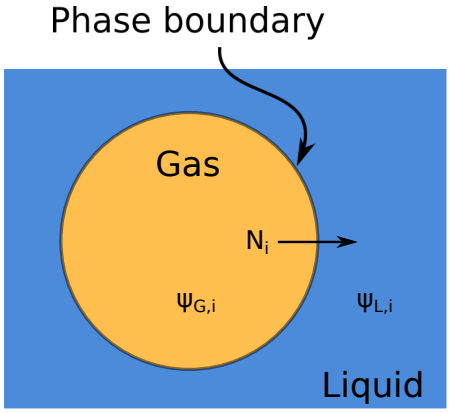

Figure 3.1: A visual representation of the nature of the mass transfer phenomenon.

In general, mass transfer can be broken down into two principal com-

ponents. The first discussion revolves around the transport phenomena involved in carrying the components to the interface and quantifying these phenomena. This discussion bases on the foundation for the mass transfer coefficient, k_i, where i denotes the considered component. The second discussion revolves around determining which physical properties are responsible for mass transfer. This discussion makes the foundation for the driving force, d_i. Together, k_i and d_i determine the mass transfer flux of component i as:

$$N_i = k_i \rho d_i \approx k_i \rho (\psi_i - \psi_{i,I}), \tag{3.2}$$

where ρ denotes a measure of the density of the fluid phase and I denotes the interface. It is common to use the species mass fraction of species i as the driving force, and in such case, $d_i = \Delta\omega_i$ is the difference in the species mass fractions and ρ is the mass density.

The complexity of determining proper expressions to evaluate k_i is stressed in the following. Suggestions in the literature are primarily based on the one and two-film models [Brunner, 1903, 2017, Whitman and Keats, 1922], the penetration theory [Higbie, 1935], the surface renewal theory [Danckwerts, 1951], and the laminar and turbulent boundary layer theories (see e.g. Bird et al. [2002] for the boundary layer theories). These theories are based on different hydrodynamical phenomena and vary in complexity. For instance, in the film models, it is assumed that a thin film of thickness δ forms next to the interface, and that this film represents a resistance to mass transfer. Furthermore, in the two-film model, one film forms on each side of the interface, and two mass transfer resistances exist. The resistance originating from the gas film with thickness δ_G is commonly termed $k_{G,i}$, and the resistance originating from the liquid film with thickness δ_L is commonly termed $k_{L,i}$. The two-film model is illustrated visually in Figure 3.2. As seen, the driving force does not need to be continuous over the interface. Examples of driving forces that are *discontinuous* through the interface include the concentration, the mole fraction, and the mass fraction.

The penetration theory was developed by Higbie [1935] to improve the film models by incorporating the turbulent nature of the fluids on each side of the interface. Here, mass is considered to be transported to the interface by turbulent fluid elements referred to as vortices or eddies (see e.g. Versteeg and Malalasekera [2007], Ferziger and Perić [2002]). The fluid elements reach the interface, and for a fixed exposure time, the fluid elements exchange mass with the neighboring phase. Subsequently, the fluid elements are replaced by new fluid elements and return to the bulk fluid, which is considered well mixed. The mass transfer is considered time-dependent, and the total mass transfer in each cycle is obtained by integrating over the exposure time.

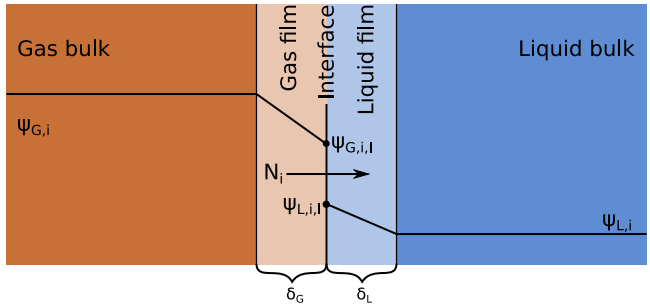

Figure 3.2: A visual representation of the two-film model.

Further improvements were made to the penetration theory by Danckwerts [1951] by replacing the constant exposure time with a mean exposure time obtained from an exposure time distribution model. The improved model was termed the Danckwerts surface renewal theory. Other rigorous attempts to improve on the hydrodynamic characteristics of the mass transfer phenomena were formulated with the laminar and turbulent boundary layer theories.

The previous modeling approaches allow for investigations related to the mass transfer coefficient k_i. For instance, for purely diffusive mass transfer, the mass based governing equation for species mass is:

$$0 = -\frac{\mathrm{d}j_i}{\mathrm{d}z}, \tag{3.3}$$

where j_i is the mass transplaced due to diffusion. Fick's first law [Fick, 1855] for binary diffusion (with mass fraction as the driving force) is given by

$$j_i = -\rho D_i \frac{\mathrm{d}\omega_i}{\mathrm{d}z}, \tag{3.4}$$

where D_i is the diffusion coefficient of species i. Equations (3.3) and (3.4) can be combined to obtain

$$0 = \rho D_i \frac{\mathrm{d}^2\omega_i}{\mathrm{d}z^2}. \tag{3.5}$$

The boundary conditions are given by

$$\omega_i = \omega_{i,b}, \quad z = 0 \tag{3.6}$$

$$\omega_i = \omega_{i,I}, \quad z = \delta, \tag{3.7}$$

where b denotes the bulk phase. Integration of eq. (3.5) with the boundary conditions in eqs. (3.6) and (3.7) leads to

$$\omega_i = \omega_{i,b} + \frac{1}{\delta}(\omega_{i,I} - \omega_{i,b})z. \tag{3.8}$$

Furthermore, by inserting the solution in eq. (3.8) into eq. (3.4), we obtain

$$j_i = \frac{D_i}{\delta}\rho(\omega_{i,b} - \omega_{i,I}). \tag{3.9}$$

The result in eq. (3.9) can be compared with eq. (3.2) to get a proper expression for the mass transfer coefficient. By employing $\psi_i = \omega_i$ in eq. (3.2), the expression in the parenthesis is cancelled, and we obtain

$$k_i = \frac{D_i}{\delta}. \tag{3.10}$$

The result in eq. (3.10) is highly significant, and through its rearrangement, the Sherwood number is defined as:

$$\mathrm{Sh} = \frac{k_i \delta}{D_i}. \tag{3.11}$$

By comparing eq. (3.11) with eq. (3.10), it is evident that $\mathrm{Sh} = 1$ for purely diffusive mass transfer. Any other contributions than diffusion will influence the Sherwood number, possibly perturbing it so that $\mathrm{Sh} \neq 1$.

There is largely consensus in the scientific community that both diffusive and convective phenomena contribute to the transportation of components to the interface. This generally means that $\mathrm{Sh} \neq 1$, and eq. (3.10) cannot be used to find the mass transfer coefficient. On the other hand, experimental data and parametrizations of Sh, either directly or in terms of other dimensionless numbers such as the Reynolds number, Re, and the Schmidt number, Sc, are readily available in the literature. See e.g., Vik et al. [2018] for a selection of direct parametrizations of k_i and indirect parametrizations of k_i through Sh.

The discussion of k_i is relevant on both the liquid side and the gas side of the interface, as resistance to mass transfer exists on both sides of the phase boundary. However, the diffusion coefficient is typically several orders of magnitude larger in gas than in liquid (commonly on the order of 10^{-2} $\mathrm{cm^2\,s^{-1}}$ for gases, and on the order of 10^{-5} $\mathrm{cm^2\,s^{-1}}$ for liquids, see e.g., Reid et al. [1987]). Thus, to obtain a closed expression for the mass transfer flux, some assumptions are usually made in combination with some arithmetic operations to eliminate one of them. The manipulations typically result in the elimination of the gas side resistance, due to the relatively small diffusivity on the liquid side compared to the diffusivity on the gas side of the interface. This topic is explored further in Section 3.1.

3.1 Deriving Expressions for Mass Transfer

The driving force for mass transfer is less discussed in the literature. For a two-film modeling approach, mass transfer flux equations are formulated on both sides of the interface. With reference to Figure 3.2, the gas side mass transfer flux equation is formulated as

$$N_i^{G-I} = k_{G,i}\rho_G d_{G,i} \approx k_{G,i}\rho_G(\psi_{G,i} - \psi_{G,i,I}). \tag{3.12}$$

Similarly, the liquid phase mass transfer flux is

$$N_i^{I-L} = k_{L,i}\rho_L d_{L,i} \approx k_{L,i}\rho_L(\psi_{L,i,I} - \psi_{L,i}). \tag{3.13}$$

Equations (3.12) and (3.13) represent two equations with six unknowns; N_i^{G-I}, N_i^{I-L}, $k_{G,i}$, $k_{L,i}$, $\psi_{G,i,I}$, and $\psi_{L,i,I}$. The film is assumed not to accumulate mass, and hence, the mass transferred out of the gas phase is subsequently received in the liquid phase:

$$N_i = N_i^{G-I} = N_i^{I-L}. \tag{3.14}$$

To close the mass transfer problem, relations for $\psi_{G,i,I}$ and $\psi_{L,i,I}$ are required. An assumption is that there is no net mass transfer when the phases are in phase equilibrium. Therefore, it is natural to assume $\psi_{i,I} = \psi_i^*$, i.e., phase equilibrium is assumed to prevail at the interface. This assumption implies that $N_i = 0$ when $\psi_i = \psi_i^*$.

The difference in the concentration, the mole fraction, or the mass fraction is usually employed as the driving force. In this work, four different driving forces were formulated, all of which were based on the assumption that phase equilibrium prevails at the interface. After careful evaluation, only one of them was deemed appropriate, while the remaining formulations were discarded for various reasons. The four formulations are presented in the following sections 3.1.1 to 3.1.4.

The mass transfer expression in eq. (3.46) to be derived in Section 3.1.3 was the only expression employed in Paper II and Paper III of Chapter 4 due to several limitations with the other derived expressions. A rigorous comparison was made between eq. (3.46) and similar mass transfer expressions based on Henry's law. Furthermore, the strengths and weaknesses of both eq. (3.46) and similar mass transfer expressions based on Henry's law were discussed.

3.1.1 Chemical Potential as the Driving Force

Commonly, phase equilibrium is assumed to prevail at the phase boundary separating the two adjoining phases. The criteria for phase equilibrium are

$$T_G = T_L, \tag{3.15}$$

$$p_G = p_L, \tag{3.16}$$

$$\mu^*_{G,i} = \mu^*_{L,i}, \tag{3.17}$$

where T is the temperature, p is the pressure, $\mu_i(T, p, \boldsymbol{n})$ is the chemical potential, and $\boldsymbol{n}$ is the vector of mole numbers in the mixture. As seen in eq. (3.17), the chemical potential emerges as a natural variable of interest. The chemical potential was therefore suggested in this work as an interesting driving force for mass transfer.

By inserting $\psi_i = \mu_i$ into eqs. (3.12) and (3.13), we obtain respectively

$$N_i = k_{G,i}\rho_G(\mu_{G,i} - \mu^*_{G,i}), \tag{3.18}$$

$$N_i = k_{L,i}\rho_L(\mu^*_{L,i} - \mu_{L,i}). \tag{3.19}$$

Furthermore, from eq. (3.17), the chemical potential is the same on both sides of the interface, and a condensed form of eqs. (3.18) and (3.19) is written as:

$$N_i = k_{G,i}\rho_G(\mu_{G,i} - \mu^*_i), \tag{3.20}$$

$$N_i = k_{L,i}\rho_L(\mu^*_i - \mu_{L,i}). \tag{3.21}$$

For a qualitative visual representation of the profiles with chemical potential as the driving force, see Figure 3.3. As seen, the driving force profile is *continuous* through the interface, which is considered a conceptual strength due to its close resemblance to the driving force profile in heat transfer phenomena.

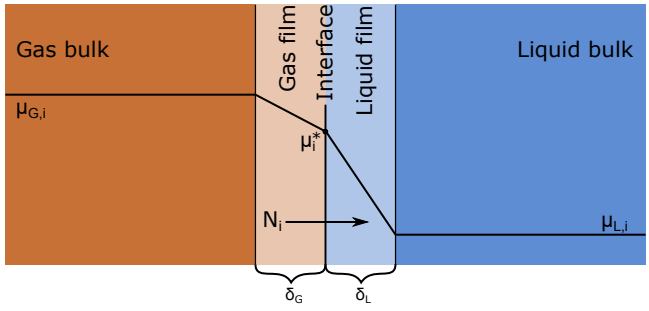

Figure 3.3: Mass transfer from a gas phase to a liquid phase. Here, the chemical potential is used as the driving force, and the profile is continuous through the interface.

An expression for mass transfer can be obtained by combining eqs. (3.20) and (3.21) by first dividing eq. (3.20) by $k_{G,i}\rho_G$, and dividing eq. (3.21) by $k_{L,i}\rho_L$:

$$\frac{N_i}{k_{G,i}\rho_G} = \mu_{G,i} - \mu^*_i \tag{3.22}$$

$$\frac{N_i}{k_{L,i}\rho_L} = \mu_i^* - \mu_{L,i}. \tag{3.23}$$

Subsequently, eqs. (3.22) and (3.23) are added to obtain

$$N_i\left(\frac{1}{k_{G,i}\rho_G} + \frac{1}{k_{L,i}\rho_L}\right) = \mu_{G,i} - \mu_{L,i}, \tag{3.24}$$

in which the chemical potential at the phase boundary has been eliminated. Hence, knowledge about the temperature, pressure, and composition *at* the interface is no longer required. The expression for the mass transfer flux becomes

$$N_i = \frac{1}{\frac{1}{k_{G,i}\rho_G} + \frac{1}{k_{L,i}\rho_L}}(\mu_{G,i} - \mu_{L,i}). \tag{3.25}$$

The diffusion coefficient on the gas side is typically many orders of magnitude larger than the diffusion coefficient on the liquid side. Since the mass transfer coefficient is proportional to the diffusion coefficient, see eq. (3.11), then $k_{G,i} \gg k_{L,i}$. However, at the same time, $\rho_G \ll \rho_L$; typically, ρ_L is two to three orders of magnitude larger than ρ_G. Thus, each contribution to the prefactor in eq. (3.25) consists of one large and one small number. As a result, it is impossible to a priori determine whether $1/(k_{G,i}\rho_G) > 1/(k_{L,i}\rho_L)$ or $1/(k_{G,i}\rho_G) < 1/(k_{L,i}\rho_L)$, and hence, both contributions must be included in the final expression for the mass transfer flux.

The major benefits of eq. (3.25) are that i) the driving force only requires knowledge about quantities in the bulk of each of the phases, ii) the driving force is continuous through the interface, which is conceptually appealing, iii) the phase equilibrium assumption is respected and incorporated without computing the phase equilibrium state, and iv) the net mass transfer is zero when phase equilibrium is established, that is when $\mu_{G,i} = \mu_{L,i}$.

On the other hand, the downsides of eq. (3.25) are notable. The primary issue is concerned with how the mass transfer coefficient is found experimentally. In the literature, the liquid side mass transfer coefficient, $k_{L,i}$, is fitted to experimental data. In eq. (3.25), the overall mass transfer coefficient consists of $k_{L,i}$, $k_{G,i}$, ρ_L, and ρ_G. This yields a complicated function of the mixture, which is undesirable.

Furthermore, the overall mass transfer coefficient must cancel the unit in the driving force so that the unit of the mass transfer flux remains $\mathrm{kg\,m^{-2}\,s^{-1}}$. Hence, the overall mass transfer coefficient in eq. (3.25) must have unit $\mathrm{m^2\,kg\,s^{-1}\,J^{-1}}$, which does not agree well with the definition of the Sherwood number in eq. (3.11), where the mass transfer coefficient is required to have unit $\mathrm{m^2\,s^{-1}}$.

Additionally, the fitting process of the mass transfer coefficient is dependent on the driving force. Using a driving force that is typically larger than

10^5 would inevitably yield different results from using a driving force on the order of magnitude of 10^{-1}, which is the case for $\psi_i = \omega_i$. Thus, using the chemical potential as the driving force, the mass transfer coefficients would have to be re-parametrized for different systems or new experiments would have to be conducted.

Moreover, by using $\psi_i = \mu_i$, the driving force cannot be measured, but instead, the mass transfer flux becomes dependent on the thermodynamic modeling of μ_i. Mixtures can be classified as ideal or non-ideal, in which mixtures can be modeled with EoSs or activity coefficient-based models. Hence, μ_i can be classified through a wide variety of models.

Some problems were eliminated through reducing the driving force by RT, that is, $\psi_i = \mu_i/(RT)$. This makes the driving force dimensionless, and it reduces its magnitude by more than a factor of 1,000. Still, the overall mass transfer coefficient cannot be reduced so that it is only a function of $k_{L,i}$, and hence, the model requires experimental fits for a mass transfer coefficient that is a complicated function of both phases and their densities. In conclusion, the drawbacks were considered to outweigh the benefits of using the chemical potential as the driving force for mass transfer. Hence, this approach was not implemented nor quantitatively validated or verified in this work. Further development was therefore discontinued, and the approach was abandoned.

3.1.2 Mass Fraction as the Driving Force – Direct Use of the Liquid Side Flux Equation

Taylor and Krishna [1993] defined the driving force for diffusion as

$$d_i := \frac{x_i}{RT} \nabla_{T,p} \mu_i, \tag{3.26}$$

where x_i is the species mole fraction and $\nabla_{T,p}$ is interpreted as the spatial gradient while holding T and p fixed. Ignoring T and p in the spatial gradient prevents diffusion due to local temperature and pressure variations. Diffusion due to temperature variations is denoted thermal diffusion, or the Soret effect, and is generally much smaller than the contribution from $\nabla_{p,\boldsymbol{n}} \mu_i$. Hence, the contribution from $\nabla_{p,\boldsymbol{n}} \mu_i$ is omitted from the driving force. Furthermore, the local pressure variations yield convective flow, and its inclusion is inappropriate for an expression used for computing diffusion fluxes. Hence, the contribution from $\nabla_{T,\boldsymbol{n}} \mu_i$ is also omitted from the driving force. For ideal mixtures, eq. (3.26) reduces to (see Taylor and Krishna [1993] for the derivation):

$$d_i = \nabla x_i \tag{3.27}$$

In an endeavor to obtain a simple expression for mass transfer, the (mass based) results of Taylor and Krishna [1993] in eq. (3.27) were employed here; that is $\psi_i = \omega_i$. Inserting mass fraction as the driving force into eq. (3.13) yields

$$N_i^{I-L} = k_{L,i}\rho_L(\omega_{L,i}^* - \omega_{L,i}), \tag{3.28}$$

where $\omega_{L,i}^*$ is used to denote the mass fraction in the liquid at phase equilibrium.

The phase equilibrium criteria in eqs. (3.15) to (3.17) yield $C + 2$ equations with $2C + 2$ unknowns, where C denotes the number of components. A mass balance on the two phases yields an additional C equations, and by specifying (or with knowledge of) the temperature and pressure, we have $2C + 2$ equations for $2C + 2$ unknowns. The mass balances are given as

$$n_{G,i} + n_{L,i} = \beta_i, \tag{3.29}$$

where β_i is the total amount of moles of component i present. With this knowledge, $\omega_{L,i}^*$ can be computed; however, it is emphasized that $\omega_{L,i}^*$ is a function of the temperature, pressure, and the composition of *both* phases, that is $\omega_{L,i}^* = f(T, p, \boldsymbol{n}_G, \boldsymbol{n}_L)$. Nevertheless, the composition dependency is only partially true due to the constraints placed by Gibbs' phase rule for equilibrium systems:

$$F = C - P + 2. \tag{3.30}$$

Here, F is the degree of freedom, and P is the number of phases. For a binary system consisting of a gas and a liquid phase, $C = P = 2$, meaning there are two degrees of freedom. The equilibrium state is unambiguously determined by specifying the temperature and pressure as the last two degrees of freedom, and eq. (3.29) is obsolete. In that case, $\omega_{L,i}^* = f(T, p)$ is only a function of temperature and pressure, and knowledge of $\omega_{G,i}$ or $\omega_{L,i}$ is not required to solve the equilibrium problem. Thus, with $C = P = 2$, mass transfer computed with eq. (3.28) is solely a function of T, p, $\omega_{L,i}(T, p)$, and $\rho_L(T, p, \boldsymbol{\omega}_L)$. The mass transfer flux expression in eq. (3.28) thus allows mass to be transferred out of the gas phase without considering any of the conditions in the gas phase. Hence, eq. (3.28) may predict a non-zero mass transfer of a component that is absent in the gas phase. As a result, $\omega_{G,i}$ decreases, and potentially becomes negative, while $\omega_{L,i}$ approaches its equilibrium value, $\omega_{L,i}^*$. This property is undesirable.

Table 3.1: Governing equations describing the bubble column.[1]

Transport of total mass

$$\frac{\mathrm{d}}{\mathrm{d}z}(\alpha_L \rho_L v_L) = \sum_{j=1}^{C} N_j a \tag{3.31}$$

$$\frac{\mathrm{d}}{\mathrm{d}z}(\alpha_G \rho_G v_G) = -\sum_{j=1}^{C} N_j a \tag{3.32}$$

Transport of species mass

$$\frac{\mathrm{d}}{\mathrm{d}z}(\alpha_L \rho_L v_L \omega_{L,i}) = \frac{\mathrm{d}}{\mathrm{d}z}\left(\alpha_L \rho_L D_{L,\mathrm{eff},z} \frac{\mathrm{d}\omega_{L,i}}{\mathrm{d}z}\right) + N_i a \tag{3.33}$$

$$\frac{\mathrm{d}}{\mathrm{d}z}(\alpha_G \rho_G v_G \omega_{G,i}) = \frac{\mathrm{d}}{\mathrm{d}z}\left(\alpha_G \rho_G D_{G,\mathrm{eff},z} \frac{\mathrm{d}\omega_{G,i}}{\mathrm{d}z}\right) - N_i a \tag{3.34}$$

Transport of momentum

$$\begin{aligned}\frac{\mathrm{d}}{\mathrm{d}z}(\alpha_L \rho_L v_L v_L) = \frac{\mathrm{d}}{\mathrm{d}z}\left(\alpha_L \mu_{L,\mathrm{eff},z} \frac{\mathrm{d}v_L}{\mathrm{d}z}\right) - \alpha_L \frac{\mathrm{d}p}{\mathrm{d}z} - \alpha_L \rho_L g \\ + f_{\mathrm{drag}}^{G-L} + f_{\mathrm{fric}}^{W-L}\end{aligned} \tag{3.35}$$

$$\frac{\mathrm{d}}{\mathrm{d}z}(\alpha_G \rho_G v_G v_G) = \frac{\mathrm{d}}{\mathrm{d}z}\left(\alpha_G \mu_{G,\mathrm{eff},z} \frac{\mathrm{d}v_G}{\mathrm{d}z}\right) - \alpha_G \frac{\mathrm{d}p}{\mathrm{d}z} - \alpha_G \rho_G g - f_{\mathrm{drag}}^{G-L} \tag{3.36}$$

Transport of energy

$$\begin{aligned}\alpha_L \rho_L v_L c_{p,L} \frac{\mathrm{d}T_L}{\mathrm{d}z} = \frac{\mathrm{d}}{\mathrm{d}z}\left(\alpha_L \lambda_{L,\mathrm{eff},z} \frac{\mathrm{d}T_L}{\mathrm{d}z}\right) + \frac{S_I}{A} U (T_a - T_L) \\ + h_L a (T_G - T_L)\end{aligned} \tag{3.37}$$

$$\alpha_G \rho_G v_G c_{p,G} \frac{\mathrm{d}T_G}{\mathrm{d}z} = \frac{\mathrm{d}}{\mathrm{d}z}\left(\alpha_G \lambda_{G,\mathrm{eff},z} \frac{\mathrm{d}T_G}{\mathrm{d}z}\right) - h_L a (T_G - T_L) \tag{3.38}$$

An initial test was performed to verify the hypothesis above. Hence, a bubble column consisting of a binary mixture of N_2 and H_2O was simulated. The governing equations employed are listed in Table 3.1. The mass transfer terms N_j in eqs. (3.33) and (3.34) can be computed from eq. (3.28) in combination with eq. (3.14).

The numerical solution of the mass fraction is shown for both the gas and the liquid phases in Figure 3.4. As seen, both phases are initially in their stable phase region, that is $\omega_{G,\mathrm{N_2}} > \omega^*_{G,\mathrm{N_2}}$, and $\omega_{L,\mathrm{H_2O}} > \omega^*_{L,\mathrm{H_2O}}$ at $z = 0$. As the reactor height increases, N_2 is transferred out of the bubbles and into the liquid without considering the gas phase conditions. Consequently, $N_i > 0$ until $\omega_{L,\mathrm{N_2}} = \omega^*_{L,\mathrm{N_2}}$. At this point, N_2 has reached its equilibrium value in the liquid; however, simultaneously, the gas phase is well within the two-phase unstable region due to N_2 being transferred without being limited by $\omega^*_{G,\mathrm{N_2}}$. This experiment verifies the hypothesis above, and eq. (3.28) is unsuitable for mass transfer computations.

3.1.3 Mass Fraction as the Driving Force – The Equilibrium Ratio Method

The approach proposed here is inspired by a combination of the classical approach using Henry's law, and the discarded approach in Section 3.1.2. The mass fraction is used as driving force, that is $\psi_i = \omega_i$, resulting in an interface-to-liquid equation similar to eq. (3.28). Additionally, a gas-to-interface equation is given. The two flux equations are given as

$$N_i^{G-I} = k_{G,i}\rho_G(\omega_{G,i} - \omega^*_{G,i}), \tag{3.39}$$

$$N_i^{I-L} = k_{L,i}\rho_L(\omega^*_{L,i} - \omega_{L,i}), \tag{3.40}$$

and the phase equilibrium ratio is introduced as

$$K_i := \frac{\omega^*_{G,i}}{\omega^*_{L,i}}. \tag{3.41}$$

[1] In Table 3.1, z is the axial direction, α is the area fraction, v is the axial velocity, a is the interfacial area of the adjoining phases, eff denotes effective, g is the gravitational acceleration, f denotes a frictional or drag force, μ is the dynamic viscosity, λ is the thermal conductivity, S_I and A is the perimeter and the area of the surface shared with the heat exchanging medium, U is the overall heat transfer coefficient indicating the resistance of heat transfer from bulk liquid to heating/cooling medium, and h_L is the heat transfer coefficient.

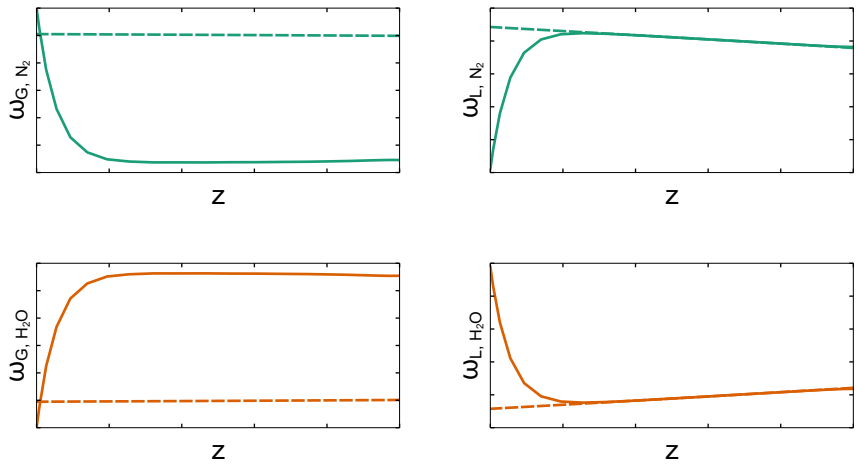

Figure 3.4: Mass fraction profiles in the bubble column. The mass transfer flux was computed with eq. (3.28). Full lines denote ω_i, and dashed lines denote the corresponding equilibrium mass fraction, ω_i^*. Moreover, N_2 is shown in the first row, (■), and H_2O is shown in the second row (■).

Equation (3.39) is divided by $k_{G,i}\rho_G K_i$, and eq. (3.40) is divided by $k_{L,i}\rho_L$:

$$\frac{N_i^{G-I}}{k_{G,i}\rho_G K_i} = \frac{\omega_{G,i}}{K_i} - \frac{\omega_{G,i}^*}{K_i}, \tag{3.42}$$

$$\frac{N_i^{I-L}}{k_{L,i}\rho_L} = \omega_{L,i}^* - \omega_{L,i}. \tag{3.43}$$

Rearranging eq. (3.41), and inserting into eq. (3.42) yields:

$$\frac{N_i^{G-I}}{k_{G,i}\rho_G K_i} = \frac{\omega_{G,i}}{K_i} - \omega_{L,i}^*. \tag{3.44}$$

The mass transfer flux is continuous through the interface, see eq. (3.14). Thus, $N_i^{G-I} = N_i^{I-L}$, and we may therefore add eqs. (3.43) and (3.44) to obtain

$$N_i\left(\frac{1}{k_{G,i}\rho_G K_i} + \frac{1}{k_{L,i}\rho_L}\right) = \frac{\omega_{G,i}}{K_i} - \omega_{L,i}. \tag{3.45}$$

Previously with the approach based on the chemical potential, see e.g., eq. (3.25), no conclusions could be drawn on whether $1/(k_{G,i}\rho_G) > 1/(k_{L,i}\rho_L)$ or $1/(k_{G,i}\rho_G) < 1/(k_{L,i}\rho_L)$. Here, however, there is also an equilibrium ratio on the gas side resistance. Typically, for volatile gases, $K_i \gg 1$, meaning a

relatively large quantity is in the denominator. Thus, the gas side contribution to the overall mass transfer resistance becomes small in comparison to the liquid side resistance, and we may conclude that $\frac{1}{k_{G,i}\rho_G K_i} \ll \frac{1}{k_{L,i}\rho_L}$. As a result, eq. (3.45) becomes

$$N_i = k_{L,i}\rho_L\left(\frac{\omega_{G,i}}{K_i} - \omega_{L,i}\right). \tag{3.46}$$

The proposed expression for the mass transfer flux in eq. (3.46) possesses the advantage of i) simplicity, ii) only employs the liquid side mass transfer coefficient, $k_{L,i}$, iii) the driving force is measurable (disregarding K_i which is model dependent), and iv) the driving force is dimensionless yielding the proper units for $k_{L,i}$. Furthermore, while common approaches based on Henry's law cannot predict mass transfer of the solvent, eq. (3.46) does not suffer from this weakness.

On the other hand, the most notable drawback of eq. (3.46) is the computation of K_i, which relies on converging a complete phase equilibrium problem. Moreover, the equilibrium ratio is in the denominator, and volatile components typically have large values (10^2–10^3), whereas non-volatile compounds typically have small values (< 1). Hence, the non-volatile compounds are quickly taken to equilibrium due to division by a small number, while volatile compounds take longer to approach equilibrium.

The same initial test as in Section 3.1.2 was performed to evaluate the qualitative performance of eq. (3.46). The results are shown in Figure 3.5, and as seen, all components in both phases are forced to their equilibrium value as the bubbles rise through the bubble column. This indicates that the mass transfer computed with eq. (3.46) terminates when the component of interest reaches its equilibrium value in both phases. Hence, eq. (3.46) is appropriate for computing mass transfer fluxes, and the terminal state is the equilibrium state that is assumed to prevail at the phase boundary.

The mass transfer expression in eq. (3.46) is subject to the constraints imposed by the phase equilibrium criteria. From eqs. (3.15) and (3.16), this means that both phases share the same temperature and pressure at the interface. Commonly in transport phenomena, the computation of temperature and pressure at the interface is avoided, as this computation is quite expensive. When the temperature and the pressure in the bulk of both phases coincide, then the bulk temperature and pressure can be used for the phase equilibrium computation, and K_i is extracted from the equilibrium composition.

When the temperature and pressure in the bulk of the two phases differ significantly, it is not straightforward to determine which temperature and pressure to use for the phase equilibrium computation. One alternative

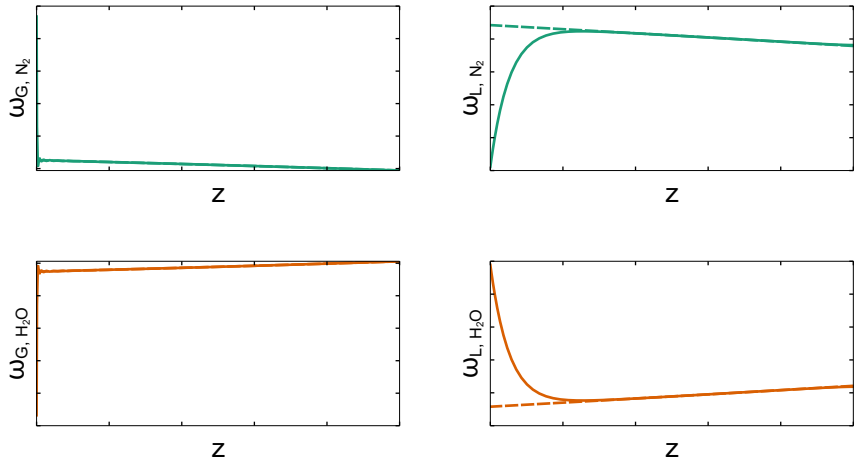

Figure 3.5: Mass fraction profiles in the bubble column. The mass transfer flux was computed with eq. (3.46). Full lines denote ω_i, and dashed lines denote the corresponding equilibrium mass fraction, ω_i^*. Moreover, N_2 is shown in the first row, (■), and H_2O is shown in the second row (■).

is to formulate an energy and momentum balance around the interface to determine the common interface temperature and pressure to use for the phase equilibrium computation.

A second alternative is to combine the hypothetical equilibrium lines in Figure 3.6. Here, the horizontal lines indicate the tie line if both phases should have the same temperature. For instance, if both phases should have the temperature T_G, then the equilibrium mass fraction in the liquid would be $\omega^*_{G,2}$, and the equilibrium mass fraction in the gas would be $\omega^*_{G,1}$. Conversely, if both phases should have the temperature T_L, then the equilibrium mass fraction in the liquid would be $\omega^*_{L,2}$, and the equilibrium mass fraction in the gas would be $\omega^*_{L,1}$.

Since the interface temperature is somewhere in between T_L and T_G, that is $T_L \leq T_I \leq T_G$, then at T_I, the equilibrium mass fraction of the liquid would be somewhere along the bubble point line between $\omega^*_{L,2}$ and $\omega^*_{G,2}$ (blue line fragment), and the true equilibrium mass fraction of the vapor would be somewhere along the dew point line between $\omega^*_{L,1}$ and $\omega^*_{G,1}$ (red line fragment).

A third alternative is to make the rough assumption that the liquid phase temperature largely governs the interface temperature and that $T_I \approx T_L$. This assumption is based on the fact that the density and heat capacity

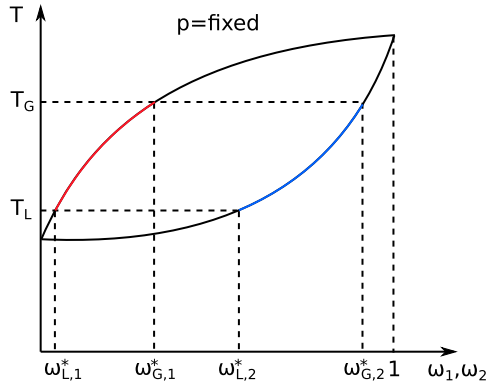

Figure 3.6: Binary phase diagram at a fixed pressure. A gas and a liquid phase in contact have different temperatures, and the two horizontal dashed lines indicate the equilibrium line if both phases were to have the temperature indicated. For the two phase equilibria shown at the temperatures T_L and T_G, the equilibrium vapor compositions are denoted $\omega^*_{L,1}$ and $\omega^*_{G,1}$, respectively, whereas the equilibrium liquid compositions are denoted $\omega^*_{L,2}$ and $\omega^*_{G,2}$, respectively.

of the liquid phase is generally much higher than those for the gas phase. Therefore, more energy is required to perturb T_L than what is required to perturb T_G. In turn, the temperature profile from the liquid phase to the interface is expected to exhibit smaller gradients than the temperature profile from the gas phase to the interface. This is visually displayed in Figure 3.7. As a result, $T_I \approx T_L$.

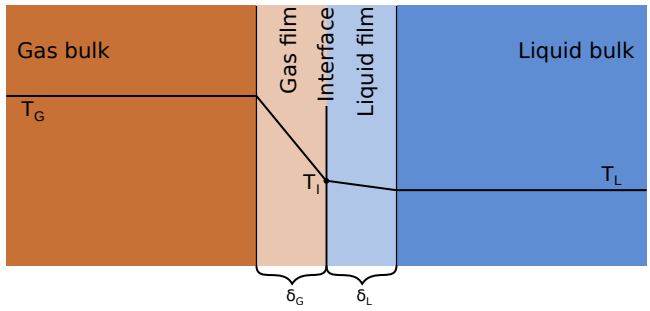

Figure 3.7: The temperature profiles from the bulk phases to the interface. Here, the interface temperature is largely governed by the bulk liquid phase temperature.

3.1.4 Mass Fraction as the Driving Force – Manipulating the Mass Transfer Coefficients

Previously in Section 3.1.3, comments were made regarding the use of the equilibrium ratio in the denominator since this creates large driving forces for non-volatile compounds and smaller driving forces for volatile compounds. While this is expected for a $1/x$ functional, it can be challenging numerically, as it may produce a stiff system of equations.

Here, a straight-forward approach is suggested with $\psi_i = \omega_i$. Similar to the approach in Section 3.1.3, the outset is eqs. (3.39) and (3.40). Then, the two equations are divided by their respective mass transfer coefficient. That is, eq. (3.39) is divided by $k_{G,i}$ and eq. (3.40) is divided by $k_{L,i}$. Hence,

$$\frac{N_i^{G-I}}{k_{G,i}} = \rho_G(\omega_{G,i} - \omega_{G,i}^*), \tag{3.47}$$

$$\frac{N_i^{I-L}}{k_{L,i}} = \rho_L(\omega_{L,i} - \omega_{L,i}^*). \tag{3.48}$$

The two equations are subsequently added to obtain

$$N_i\left(\frac{1}{k_{G,i}} + \frac{1}{k_{L,i}}\right) = \rho_G(\omega_{G,i} - \omega_{G,i}^*) + \rho_L(\omega_{L,i} - \omega_{L,i}^*). \tag{3.49}$$

Since $k_{G,i}$ is typically many orders of magnitude larger than $k_{L,i}$, then $1/k_{G,i} \ll 1/k_{L,i}$. As a result, the terms in the parenthesis on the left-hand side of the equality can be approximated as $1/k_{L,i}$, and the resulting expression for the mass transfer flux reads

$$N_i = k_{L,i}\rho_L(\omega_{L,i} - \omega_{L,i}^* + \frac{\rho_G}{\rho_L}(\omega_{G,i} - \omega_{G,i}^*)). \tag{3.50}$$

The results of eq. (3.50) have no rough approximations, and we expect no large variations in the driving force since there are no species-specific variables in the denominator that could vary by multiple orders of magnitude, as is the case for the K-value in eq. (3.46). Although it is appealing to utilize eq. (3.50) for computing the mass transfer, the prefactor ρ_G/ρ_L, which is typically in the order of 10^{-2}–10^{-3}, make the gas phase variables contribute far less to the mass transfer flux than the liquid phase variables. For instance, $\omega_{G,i} - \omega_{G,i}^*$ is weighted 100–1,000 times less than $\omega_{L,i} - \omega_{L,i}^*$, making the offset from equilibrium on the liquid side far more contributing to the overall mass transfer flux. If the gas phase contribution at any point becomes negligible compared to the liquid phase contribution, eq. (3.50) reduces to

eq. (3.28), which was discarded for the reasons discussed in Section 3.1.2. In those cases, eq. (3.50) is also inappropriate.

The mass transfer flux expression in eq. (3.50) was subjected to the same test as the one performed for the mass transfer flux expressions in eqs. (3.28) and (3.46) of Sections 3.1.2 and 3.1.3, respectively. The results are shown in Figure 3.8. As seen, the mass transfer flux computed with eq. (3.50) terminates before the one obtained with eq. (3.28) in Figure 3.4. However, also here, the gas phase enters the unstable two-phase region. Hence, the mass transfer expression in eq. (3.50) was also deemed inappropriate for computing the mass transfer flux.

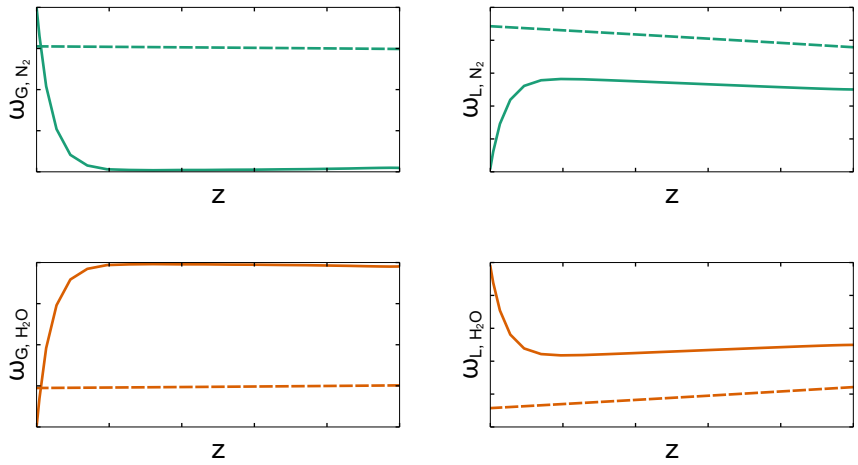

Figure 3.8: Mass fraction profiles in the bubble column. The mass transfer flux was computed with eq. (3.50). Full lines denote ω_i, and dashed lines denote the corresponding equilibrium mass fraction, ω_i^*. Moreover, N_2 is shown in the first row, (■), and H_2O is shown in the second row (■).

3.2 Remarks on Heat and Momentum Transfer Induced by Mass Transfer

When mass is transferred from one phase to another, that mass carries a certain amount of heat and momentum. The momentum transfer was beyond the scope of this study, and it was thus neglected throughout the entirety of this work. The interphase heat transfer can be in terms of i) heat of vaporization/condensation (due to latent heat), $\Delta_{\text{vap}}h$, ii) heat of

mixing (due to differences in composition), $\Delta_{\text{mix}}h$, and iii) sensible heat due to temperature differences between the two phases.

The heat of vaporization in i) is subject to debate. While the enthalpy, h, for single component systems only varies with temperature and pressure, h additionally varies with composition for multicomponent systems. This is not trivial, as this means that when mass is transferred, h changes, and the amount of heat transferred is a function of the mass transferred. For instance, $\Delta_{\text{vap}}h$ is defined as

$$\Delta_{\text{vap}}h := h_G - h_L. \tag{3.51}$$

The enthalpy is a function of T, p, and $\boldsymbol{\omega}$, and inserting the respective variables for each phase yields

$$h_G = f_1(T_G, p_G, \boldsymbol{\omega}_G), \tag{3.52}$$

$$h_L = f_2(T_L, p_L, \boldsymbol{\omega}_L), \tag{3.53}$$

$$\Delta_{\text{vap}}h = f_3(T_G, T_L, p_G, p_L, \boldsymbol{\omega}_G, \boldsymbol{\omega}_L). \tag{3.54}$$

Since $\boldsymbol{\omega}$ in both phases change with mass transfer, it is clear from eq. (3.54) that $\Delta_{\text{vap}}h$ also changes with mass transfer. However, $\Delta_{\text{vap}}h$ also changes as the temperatures of the two phases change, e.g., due to heat transfer in the form of vaporization/condensation, mixing, heat exchange between the two phases, or heat exchange between one or both of the phases with an external cooling/heating medium.

Although $\Delta_{\text{vap}}h$ is a complex function of the intensive variables in both phases, it should in general not be disregarded, as its contribution could be significant. In the mass transfer studies in this work, the components considered include CH_4, O_2, NH_3, CO, CO_2, H_2O, H_2, and linear alkanes. For pure component, $\Delta_{\text{vap}}h$ was computed by the Peng–Robinson EoS at $T = 0.7T_c$ for the compounds studied here. The results are given along with the heat of formation of gas, $\Delta_f h^\circ$ (gas), in Table 3.2. Without considering the sensible heat obtained from $\int_{T_\circ}^{T} c_p \mathrm{d}T$, the most significant contribution to the total heat content of a particular phase originates from the $\Delta_f h^\circ$. Moreover, the heat of reaction, $\Delta_{\text{rx}}h$, in the two bubble columns studied in this work is listed in Table 3.3. As seen, the heat of reaction is several times larger than the $\Delta_{\text{vap}}h$.

The previous comparison of enthalpy contributions was on a purely thermodynamic basis. That is, no transport phenomena were taken into consideration. This includes the reaction kinetics, the rate at which mass is transferred between the two phases, the heat exchange between the two phases,

Table 3.2: Heat of vaporization and the heat of formation for the studied compounds. The heat of vaporization was computed with the Peng–Robinson EoS at $T = 0.7T_c$. Here, $T_\circ = 298\,\mathrm{K}$ is used to denote the reducing temperature.

Compound	$\Delta_{\mathrm{vap}}h/(RT_\circ)$ [-]	$\Delta_f h^\circ/(RT_\circ)$ (gas) [-]
O_2	2.6	0.0
NH_3	8.8	-18.6
CO	2.3	-44.8
CO_2	6.4	-158.9
H_2O	15.3	-97.6
H_2	0.4	0.0
CH_4	3.1	-29.9
C_2H_6	5.6	-33.9
C_3H_8	7.2	-42.4
n-butane	8.7	-50.8
n-pentane	10.1	-59.3
n-hexane	11.4	-67.4
n-heptane	12.7	-75.8
n-octane	14.0	-84.3
n-nonane	15.2	-92.0
n-decane	16.4	-100.8
n-undecane	17.6	-109.3
n-dodecane	18.6	-117.0
n-tridecane	19.7	-125.5
n-tetradecane	20.6	-133.9
n-pentadecane	21.6	-143.2
n-hexadecane	22.5	-151.3
n-heptadecane	23.4	-158.9
n-octadecane	24.5	-167.4
n-nonadecane	25.4	-175.5
n-eicosane	26.1	-183.9

Table 3.3: Heat of reaction in the two bubble columns studied in this work. Here, $T_\circ = 298.15\,\mathrm{K}$ is used to denote the reducing temperature.

Enthalpy contribution	Single cell protein	Fischer–Tropsch synthesis
$\Delta_{\mathrm{rx}}h/(RT_\circ)$	518.9	67.4

and the heat exchange with the cooling/heating medium. For instance, the rate at which heat evolves through a reaction taking place is

$$\hat{h}_{\mathrm{rx}} = r_{\mathrm{rx}} \Delta_{\mathrm{rx}} h. \tag{3.55}$$

Here, r_{rx} denotes the reaction rate, a quantity that depends on the conditions in the column. Similarly, the heat transferred between the two adjoining phases relies on the heat transfer coefficient, h_L, and the temperature difference between the phases. Furthermore, heat transferred between one of the phases and the cooling/heating medium relies on the heat transfer coefficient, h_{cooling}, and the temperature difference between the phase and the cooling/heating medium.

Moreover, the heat transfer due to mass transfer between the two adjoining phases relies on the magnitude of the mass transfer flux, N_i. For instance, the light hydrocarbons have high vapor pressures, and thus they have a high tendency to evaporate when they are produced in the Fischer–Tropsch synthesis at temperature (240 °C) and pressure (30 bar) conditions commonly found in a Fischer–Tropsch slurry bubble column reactor. On the other hand, the heavier hydrocarbons have low vapor pressures, and thus they have a low tendency to evaporate when they are produced in the Fischer–Tropsch synthesis at temperature and pressure conditions commonly found in a Fischer–Tropsch slurry bubble column reactor. Hence, light hydrocarbons will have a higher mass transfer flux, while heavier hydrocarbons will have a smaller mass transfer flux. The combination of N_i and the associated $\Delta_{\mathrm{vap}} h_i$ over all components i will determine the total contribution of the heat of vaporization/condensation.

The quantities discussed in the previous paragraph are system specific due to the implicit dependency on the flow conditions in N_i, r_{rx}, h_L and h_{cooling}. Therefore, the impact of r_{rx}, N_i, and heat transfer on the total heat equation *cannot* be determined on a general basis. Based on the quantities that *could* be described on a general basis ($\Delta_{\mathrm{vap}} h$, $\Delta_f h^\circ$, $\int_{T_\circ}^{T} c_p \mathrm{d}T$, and $\Delta_{\mathrm{rx}} h$) the authors have chosen to neglect the impact of $\Delta_{\mathrm{vap}} h$ in all applications throughout the entirety of this work. The rationale for this decision bases on the magnitude of the different contributions; the magnitude of $\Delta_{\mathrm{vap}} h$ is several times less (for all compounds studied) than the magnitude of the other mentioned quantities.

Chapter 4

Journal Publications

The work within this dissertation is published in three journal articles given in the following sections as Paper I, Paper II, and Paper III. Paper I contains work on the differential Gibbs and Helmholtz reactor models, which are reactor models that are based on chemical equilibrium rather than reaction kinetics. Here, non-ideal gas descriptions are employed and tested for two chemical processes (steam methane reforming and the methanol synthesis). Furthermore, the reactor models are solved with two different numerical approaches; the finite volume method and the orthogonal collocation method. For the differential Helmholtz reactor model, the finite volume method was particularly interesting due to providing a numerical grid volume that can be utilized while minimizing the Helmholtz energy function. As the pressure is readily available from the continuity/momentum equations, it is natural to choose this pressure as the pressure to be held constant while minimizing the Gibbs energy function.

In Paper II (single cell protein production) and Paper III (Fischer–Tropsch synthesis), emphasis was placed on mass transfer phenomena, and in particular the equilibrium that is believed to prevail at the interface separating the two adjoining phases. The approaches discussed in Chapter 3 were presented, and in particular the approach discussed in section 3.1.3 was implemented and demonstrated for three different EoSs: the Soave–Redlich–Kwong, the Peng–Robinson, and the PC-SAFT EoSs. In all cases, the results were compared to classical mass transfer expressions based on Henry's law. Furthermore, perturbation studies were performed to explore the sensitivity of the numerical solution of the governing equations. Especially temperature and pressure perturbation studies were performed, however, the simulation time to achieve converged governing equations was also shown to be decisive in the mass transfer modeling. The novel mass transfer

expressions developed here are inevitably more computationally expensive than the expressions based on Henry's law due to the need of converging an optimization problem for the mass transfer.

The qualitative differences between eq. (3.46) and mass transfer expressions based on Henry's law were presented, e.g., the evaporation or condensation of the solvent. It is advisable to perform careful evaluations when choosing which mass transfer expression to employ for the reasons discussed in Paper II and Paper III. For instance, if the evaporation or condensation of the solvent is important, then the novel mass transfer expressions in eq. (3.46) are superior to the expressions based on Henry's law. Conversely, if numerical efficiency is important, then the mass transfer expressions based on Henry's law are favored due to being computationally cheaper than the mass transfer expression proposed in eq. (3.46).

4.1 Paper I: The Differential Gibbs and Helmholtz Reactor Models

Chemical Engineering Science 234 (2021) 116257

Contents lists available at ScienceDirect

Chemical Engineering Science

journal homepage: www.elsevier.com/locate/ces

Differential Gibbs and Helmholtz reactor models for ideal and non-ideal gases: Applications to the SMR and methanol processes

S.B. Øyen *, H.A. Jakobsen, T. Haug-Warberg, J. Solsvik

Department of Chemical Engineering, Norwegian University of Science and Technology (NTNU), N-7491 Trondheim, Norway

HIGHLIGHTS

- Chemical equilibrium and fluid dynamics are combined for non-ideal gas mixtures.
- Minimum Gibbs and Helmholtz energy analyzes performed.
- Collocation method preferred over finite volume method.

ARTICLE INFO

Article history:
Received 13 July 2020
Received in revised form 23 September 2020
Accepted 28 October 2020
Available online 7 November 2020

Keywords:
Thermodynamics
Gibbs energy
Helmholtz energy
Chemical equilibrium
Equation of state
Packed bed reactor

ABSTRACT

This work unifies the concepts of chemical reaction equilibrium and transport phenomena applied to fluid flow of reactive gas mixtures over solid catalysts. Different from accurate modeling of reactions, which in the outset relies on reaction kinetics, the current approach is rather based on calculation of thermodynamic equilibrium thus requiring far fewer model parameters. Here, minimization of Gibbs or Helmholtz energy is solved in an inner loop inside the transport equations for heat, mass, and momentum. In addition to ideal gas, the non-ideal virial expansion and Soave-Redlich-Kwong equations of state have been used to model the gas mixture. The use of thermodynamic energy potentials ensures that all the derived properties like e.g. heat capacity, density, reaction enthalpy and equilibrium composition are derived from one fundamental relation only. The complete model framework is exemplified using the steam methane reforming and methanol synthesis processes. Herein, different combinations of energy potential (Gibbs versus Helmholtz) and numerical solution method for solving the transport equations (finite volume versus orthogonal collocation) have been studied with focus on model complexity, and efficiency and robustness of the solver. Orthogonal collocation is shown to be more efficient than finite volume, and Gibbs energy is shown to be more efficient than Helmholtz energy. The last statement depends on both flow conditions and implementation details and is therefore not a general result. The proposed model framework is a novel tool for calculating industrial reactors which operate quite close to equilibrium and might as such be useful for process design studies, albeit not for accurate simulation.

1. Introduction

In transport phenomena, chemical reactions are characterized and quantified by kinetic expressions of two types: 1) irreversible reactions, where the reaction proceeds unidirectionally until one of the reactants is exhausted and 2) reversible reactions, where forward and backward reactions compete. Reversible reactions asymptotically approach chemical equilibrium, which is mathematically enforced by including the equilibrium constant in the reaction rate expressions.

Many studies have been conducted in order to shift the equilibrium limitation imposed on the reversible reaction kinetics. The steam methane reforming (SMR) process (see e.g. Tran et al. (2017) and Dixon (2017)), where CH_4 and H_2O are converted into CO, CO_2 and H_2, is the largest industrial source of hydrogen and accounts for $\approx 50\%$ of its production (Wismann et al., 2019). Sánchez et al. (2017), Chao et al. (2017), Wang et al. (2010) and Fernández and Abanades (2017) investigated the possibility of overcoming equilibrium limited reaction kinetics in the SMR process by removing the CO_2 product with the adsorbing agent CaO. The gaseous CO_2 was adsorbed on CaO to form $CaCO_3$, and in the studies of Sánchez et al. (2017) and Fernández and Abanades

* Corresponding author.
E-mail addresses: sindre.b.oyen@ntnu.no (S.B. Øyen), hugo.a.jakobsen@ntnu.no (H.A. Jakobsen), tore.haug-warberg@ntnu.no (T. Haug-Warberg), jannike.solsvik@ntnu.no (J. Solsvik).

https://doi.org/10.1016/j.ces.2020.116257
0009-2509/

Nomenclature

Latin Letters

$\boldsymbol{A}$	Formula matrix –
A	Area m^2
A	Helmholtz energy function J
a	Molar attractive term SRK Pa m^6/mol^2
$\boldsymbol{b}$	Formula vector –
$\mathcal{B}$	Mixture excluded volume SRK m^3
B	Mixture second virial coefficient m^3
b	Molar excluded volume SRK m^3 mol^{-1}
b	Molar second virial coefficient cm^3 mol^{-1}
C	Number of components –
c	Component –
c	Constraint optimization problem –
C_p	Isobaric heat capacity J K^{-1}
c_p	Specific isobaric heat capacity J K^{-1} kg^{-1}
C_v	Isochoric heat capacity J K^{-1}
$\boldsymbol{D}$	Diagonal matrix mol^{-1}
D	Mixture attractive term SRK Pa m^6
d	Diameter m
$\boldsymbol{E}$	Auxiliary matrix –
$\boldsymbol{e}$	Vector of only ones –
$\mathcal{E}$	Set of equality constraints –
F	Mass flow kg s^{-1}
f	Friction factor –
f	function varying
G	Gibbs energy function J
$\boldsymbol{H}$	Hessian matrix varying
H	Enthalpy J
h	Molar enthalpy J mol^{-1}
$\boldsymbol{I}$	Identity matrix –
$\mathcal{I}$	Set of inequality constraints –
I	Ionization energy eV
$\boldsymbol{J}$	Jacobian vector varying
k	Binary interaction parameter –
k	Boltzmann's constant J K^{-1}
$\mathcal{L}$	Lagrangian function J
m	Parameter –
M_m	Molar mass kg $kmol^{-1}$
$\boldsymbol{N}$	Stoichiometric matrix –
N	Total number of moles mol
N	Total number –
n	Number of moles mol
N_A	Avogadro's number particles/mol
p	Newton step in search direction varying
p	Pressure Pa
R	Rate of generation of a component kg s^{-1} m^{-3}
R	Universal gas constant J K^{-1} mol^{-1}
r	Spatial separation cm
r	Radius m
Re	Reynolds number –
S	Entropy J K^{-1}
s	Molar entropy J K^{-1} mol^{-1}
T	Temperature K
U	Internal energy function J
U	Overall heat transfer coefficient W m^{-2} K^{-1}
V	Volume m^3
v	Velocity m s^{-1}
$\boldsymbol{x}$	Vector of decision variables varying
X	Generic extensive property varying
$\overline{x}_i$	Partial molar X varying/mol
y	Molar fraction –
Z	Compressibility factor –
z	z-coordinate in physical space m

Greek Letters

α	Step length in search direction –
α	Trial coefficient varying
Δ	Change –
δ	Kronecker delta –
ε	Minimum of potential well J
ε	Void fraction of catalyst –
λ	Lagrangian multiplier varying
λ	Well width –
λ	Thermal conductivity W m^{-1} K^{-1}
μ	Chemical potential J mol^{-1}
μ	Dynamic viscosity Pa s
∇	Gradient operator in optimization varying
ν	Iteration count –
ν	Variable of integration m^3
ν	Stoichiometric coefficient –
ξ	Pressure equation on residual form Pa
π	Variable of integration Pa
ρ	Mass density of mixture kg m^{-3}
σ	Separation distance Å
ϕ	Pair-potential J
ϕ	Trial function varying
φ	Fugacity coefficient –
ω	Acentric factor –
ω	Mass fraction –

Superscripts

HS	Hard sphere –
ig	Ideal gas –
o	Standard state –
r, p	Residual at the same pressure –
r, v	Residual at the same volume –
$*$	Optimal value –
s	Superficial –

Subscripts

0	Start estimate –
a	Ambient –
c	Value at critical point –
el	Element –
eq	At chemical equilibrium –
f	Formation –
i	Component number –
i	Inner –
ii	Pair like-like molecules –
ij	Pair unlike molecules –
in	At reactor inlet –
N	Order of approximation –
o	Outer –
p	Catalyst pellet –
r	Reduced –
rx	Reaction –
t	Tube –

(2017), the $CaCO_3$ was stripped for CO_2 in a regenerator unit and CaO was sent back to the reactor to repeat the cycle. Among others, Solsvik and Jakobsen (2011) and Phuakpunk et al. (2018) explored the possibility to combine the catalyst and adsorbing agent into the same pellet. The product yield was higher in this so-called sorption-enhanced SMR process than the conventional SMR

process. Wu et al. (2016) provide more details in an excellent review of the sorption-enhanced SMR process. The principle of shifting the equilibrium condition of the SMR by removing a product component from the chemical mixture has also been analyzed in a membrane reactor by multiple investigators (e.g. Jordal et al. (2004, 2005) and Pedernera et al. (2007) for H_2 removal).

In chemically reactive non-equilibrium systems, reaction kinetic models determine the reactivity of species. These models are typically empirical (Fogler, 2014), and in cases where models do not exist, the change in composition due to chemical reaction cannot be computed. In many process design studies, the reaction kinetics is unknown or is not well developed, and chemical reactors are therefore traditionally computed solely by chemical equilibrium, corresponding to infinitely fast kinetics. Chemical equilibrium is equivalent to a minimum energy principle. Specifically, this could involve a) minimizing the Helmholtz energy function at given temperature, or b) minimizing the Gibbs energy function at given temperature and pressure.

As a compromise between the fluid mechanical framework and the chemical equilibrium concept, Solsvik et al. (2016) proposed the "Differential Gibbs and Helmholtz reactor models". The combined framework employs the fluid mechanical transport equations for mass, species mass, momentum, and energy. In particular, the source term of species mass is computed algebraically assuming instantaneous chemical reactions limited by thermodynamic equilibrium only. This forces the transport equations to be DAE rather than ODE. The notation of "Differential Gibbs and Helmholtz reactor models" solely reflect this transition. From the DAE description, chemical equilibrium prevails at all points in space and time (unsteady flow). Here, the temperature field (and for Gibbs energy also the pressure field) is controlled by the fluid flow solver. One practical consequence of the transition to DAE is that all thermodynamic properties of the reacting system, like e.g. heat capacity, will require iterations inside a nested loop in the fluid flow solver. The differential Gibbs and Helmholtz reactor models are to be used in the absence of reaction rate kinetic models, or in order to investigate the equilibrium limits of a reversible reaction. They also arguably improve the much simplified "chemical reactors" used in process design software.

In the work of Solsvik et al. (2016), the chemical composition was first found by minimizing Gibbs or Helmholtz energy. This composition was afterwards used to calculate the reaction rate source terms, which finally were used to determine the rate of energy production due to chemical reaction. Subsequently, the velocity and pressure fields were obtained from the continuity and momentum equations. This procedure was repeated until convergence was achieved.

The authors employed a one-dimensional plug flow packed bed reactor model assuming ideal gas, see Froment and Bischoff (1990). The reactor model was applied to the SMR process and solved with the orthogonal collocation method (OCM, see e.g. Villadsen and Stewart, 1995; Shen et al., 2011; Solsvik et al., 2013; Jakobsen, 2014). The result was compared to the reaction rate kinetics of Xu and Froment (1989a), Xu and Froment (1989b), which for a reaction kinetic based reactor model obtained conditions close to equilibrium at the reactor outlet (Froment and Bischoff, 1990).

In many industrial situations, however, deviations from ideal gas are significant. Examples include synthesis of ammonia (Bell et al., 2010, Chap. 11), urea (Chinda et al., 2019), Fischer–Tropsch fuels (Mikhailova et al., 2003), and as in this work: methanol (Miroshnichenko and Vrabec, 2015).

Recently Marino et al. (2019) coupled ANSYS FLUENT (ANSYS Inc, 2013) to the thermodynamic software HSC (Roine, 2019) for performing fluid flow calculations with local chemical equilibrium at each point in space and time. Solid and gas phases were assumed ideal whereas liquid phases were non-ideal utilizing the activity coefficient method. The steady state flow problem is solved in two stages. Species mass balances were solved by first ignoring the reaction term to calculate an estimated molar concentration field. In the second stage, the concentration field was input to HSC as an initial estimate, and the optimum solution from the Gibbs energy minimization was taken as the true molar concentration field at that iteration step. This two-stage procedure was repeated until convergence was achieved.

Here, the focus is to relax the ideal gas assumption used in the work of Solsvik et al. (2016), by incorporating non-ideal equations of state (EOSs) for a more accurate thermodynamic state description. Consequently, the equilibrium composition, density and temperature fields are all different from those computed by Solsvik et al. (2016). As known from the continuity equation, velocity is inversely proportional to density, and from the momentum equation, the pressure is strongly coupled to the velocity field. Hence, it is expected that the velocity and pressure fields will also change by going from ideal to non-ideal gases. The extended model framework will be applied to the SMR process also considered by Solsvik et al. (2016) and the methanol synthesis which is an example of a nearly equilibrated process (Dadgar et al., 2018). Both the assumption of ideal gas and non-ideal EOSs will be studied.

The numerical properties of the differential Gibbs and Helmholtz reactor models are investigated with respect to speed and number of iterations in two well-established numerical solution approaches: the OCM and the finite volume method (FVM, see e.g. Versteeg and Malalasekera, 2007; Ferziger et al., 2020; Roache, 1998; Jakobsen, 2014).

The first part of this paper encompasses the transport phenomena, i.e. reactor model, constitutive equations, and numerical solution approach. The second part contains results and discussion, and the last part contains conclusions. An outline of the required thermodynamic theory, including EOSs, chemical reaction equilibrium along with optimization theory, and finally the framework of residual functions can be found in Appendix A.

2. Differential reactor model equations

In the present study, we employ a one-dimensional pseudo-homogeneous plug flow packed bed reactor model (Froment and Bischoff, 1990). The model equations consist of the continuity equation, species mass balance, momentum equation, and enthalpy equation. The continuity equation is given by

$$\frac{d(\rho v^s)}{dz} = 0, \tag{1}$$

where ρ and v^s denote the mass density and superficial velocity. The latter is the cross-sectionally average of the velocity vector, that is $v^s = \langle \boldsymbol{v} \rangle_A$. Furthermore, z denotes the spatial coordinate considered.

The species mass balance is given by

$$\frac{d(\rho v^s \omega_c)}{dz} = R_c, \tag{2}$$

where ω_c and R_c denote the mass fraction and reaction rate of component c, respectively. The mass fractions, ω_c, are determined from the chemical equilibrium calculation by minimizing the Helmholtz or Gibbs energy functions using the iterative numerical schemes of (7) or (8), respectively. The reaction rates, R_c, are determined from the species mass balances (2).

The momentum equation is given by

$$\frac{d}{dz}\left(\frac{\rho v^s v^s}{\varepsilon^2}\right) = -\frac{dp}{dz} - f\frac{\rho v^s \mid v^s \mid}{d_p}, \tag{3}$$

where ε, p, f, and d_p represent the void fraction, pressure, friction factor, and diameter of the catalyst pellets, respectively. Here the void fraction is assumed uniform.

The enthalpy equation is given in terms of temperature as

$$\rho v^s c_p \frac{dT}{dz} = \sum_{r=1}^{N_{rx}} (-\Delta_{rx} H_r R_r) + \frac{4U}{d_t}(T_a - T), \tag{4}$$

and will henceforth be referred to as the temperature equation. In (4), c_p is the specific isobaric heat capacity, T is the temperature, N_{rx} is the number of reactions taking place, $\Delta_{rx}H_r$ is the specific reaction enthalpy for reaction r, T_a is the ambient temperature (temperature of the heating/cooling medium), d_t is the diameter of the tube, and U is the heat transfer coefficient parametrized in detail by Yagi and Kunii (1957, 1960), de Wasch and Froment (1972) and Froment and Bischoff (1990). Pure component gas conductivities are required in order to compute the heat transfer coefficient and were obtained from Reid et al. (1987). The temperature Eq. (4) is solved for temperature, T.

2.1. Closure equations

2.1.1. Species mass

In the proposed reactor model concept, the species mass transport equations are solved for the rate of production/consumption, i.e. (2) is solved for R_c. Hence, the mass fractions must be computed from another relation. In this work, the mass fractions are taken as the equilibrium composition computed by minimizing the thermodynamic functions Gibbs (G) or Helmholtz energy (A). The procedure is performed at all nodal points. Thus, there are as many minimization problems as there are discretized nodal points in the reactor.

The optimization problem in terms of the Helmholtz energy function reads

$$\begin{aligned} \min_{V,n_1,n_2,\ldots,n_C} \quad & (A)_T \\ \text{s.t.} \quad V &= V_o \\ \sum_{j=1}^{C} A_{ij} n_j &= b_i, \quad i = 1,2,\ldots,N_{el} \\ n_i &\geq 0, \quad i = 1,2,\ldots,C, \end{aligned} \tag{5}$$

and in terms of the Gibbs energy function, the optimization problem reads

$$\begin{aligned} \min_{n_1,n_2,\ldots,n_C} \quad & (G)_{T,p} \\ \text{s.t.} \quad \sum_{j=1}^{C} A_{ij} n_j &= b_i, \quad i = 1,2,\ldots,N_{el} \\ n_i &\geq 0, \quad i = 1,2,\ldots,C. \end{aligned} \tag{6}$$

In (5) and (6), V is the volume, n_i are mole numbers, A_{ij} represents the number of element i present in one unit of species j, and b_i represents the number of element i present in total. The product $\sum_{j=1}^{C} A_{ij} n_j = b_i$ is therefore a mass balance over element i (Michelsen and Mollerup, 2007). There are N_{el} number of distinct elements, and thus, there are N_{el} balance equations of the form $\sum_{j=1}^{C} A_{ij} n_j = b_i$.

By formulating a Lagrangian function and linearizing (see Appendix A.2 Eqs. (A.27)–(A.39b)), the iterative numerical scheme for minimizing the Helmholtz energy function is formulated as

$$\begin{pmatrix} \boldsymbol{H}_A & \begin{pmatrix} 1 & \boldsymbol{0} \\ \boldsymbol{0} & \boldsymbol{A} \end{pmatrix}^\top \\ \begin{pmatrix} 1 & \boldsymbol{0} \\ \boldsymbol{0} & \boldsymbol{A} \end{pmatrix} & \begin{pmatrix} 0 & \boldsymbol{0} \\ \boldsymbol{0} & \boldsymbol{0} \end{pmatrix} \end{pmatrix}^{\nu} \begin{pmatrix} -\begin{pmatrix} p_V \\ \boldsymbol{p_n} \end{pmatrix} \\ \begin{matrix} \lambda_1 \\ \lambda_{i\neq 1} \end{matrix} \end{pmatrix}^{\nu+1} = \begin{pmatrix} \boldsymbol{J}_A \\ V - V_0 \\ \boldsymbol{An} - \boldsymbol{b} \end{pmatrix}^{\nu}, \tag{7}$$

and the iterative numerical scheme for minimizing the Gibbs energy function is formulated as

$$\begin{pmatrix} \boldsymbol{H}_G & \boldsymbol{A}^\top \\ \boldsymbol{A} & \boldsymbol{0} \end{pmatrix}^{\nu} \begin{pmatrix} -\boldsymbol{p_n} \\ \boldsymbol{\lambda} \end{pmatrix}^{\nu+1} = \begin{pmatrix} \boldsymbol{J}_G \\ \boldsymbol{An} - \boldsymbol{b} \end{pmatrix}^{\nu}. \tag{8}$$

Here $\boldsymbol{H}$ and $\boldsymbol{J}$ denote the Hessian matrix and Jacobian vector of the thermodynamic function indicated in the subscript. For instance, $\boldsymbol{H}_A$ is the Hessian matrix of the Helmholtz energy function. Furthermore, $\boldsymbol{p_n} = \boldsymbol{n}^{\nu+1} - \boldsymbol{n}^{\nu}$ are the steps in mole number, $p_V = V^{\nu+1} - V^{\nu}$ is the step in volume, $\boldsymbol{\lambda}$ are the Lagrangian multipliers, ν is the iteration counter, $\boldsymbol{A}$ is the formula matrix and $\boldsymbol{b}$ is the formula vector.

The iterative schemes in (7) and (8) require initialization. The routine is initialized by the current mole numbers. To start off with, the mole number vector, $\boldsymbol{n}$, at each nodal point in the reactor is specified as the mole fraction vector at the reactor inlet. After converging the minimization problem, $\boldsymbol{n}$ is updated according to the converged equilibrium mole numbers. Furthermore, the mole fractions are updated as $\boldsymbol{y} = \boldsymbol{n}/N$, where N is the total mole number, that is $N = \sum n_i$.

Every iteration in (7) and (8) require evaluating the Hessian and Jacobian. For the Helmholtz energy function, the Jacobian and Hessian are given by

$$\boldsymbol{J}_A = \begin{pmatrix} \left(\frac{\partial A}{\partial V}\right)_{T,\boldsymbol{n}} \\ \left(\frac{\partial A}{\partial \boldsymbol{n}}\right)_{T,V} \end{pmatrix} = \begin{pmatrix} -p \\ \boldsymbol{\mu} \end{pmatrix} \tag{9a}$$

$$\begin{aligned} \boldsymbol{H}_A &= \begin{pmatrix} \left(\frac{\partial^2 A}{\partial V^2}\right)_{T,\boldsymbol{n}} & \left(\frac{\partial^2 A}{\partial V \partial \boldsymbol{n}^\top}\right)_{T} \\ \left(\frac{\partial^2 A}{\partial \boldsymbol{n} \partial V}\right)_{T} & \left(\frac{\partial^2 A}{\partial \boldsymbol{n} \partial \boldsymbol{n}^\top}\right)_{T,V} \end{pmatrix} \\ &= \begin{pmatrix} -\left(\frac{\partial p}{\partial V}\right)_{T,\boldsymbol{n}} & -\left(\frac{\partial p}{\partial \boldsymbol{n}^\top}\right)_{T,V} \\ \left(\frac{\partial \boldsymbol{\mu}}{\partial V}\right)_{T,\boldsymbol{n}} & \left(\frac{\partial \boldsymbol{\mu}}{\partial \boldsymbol{n}^\top}\right)_{T,V} \end{pmatrix}, \end{aligned} \tag{9b}$$

and for the Gibbs energy function, the Jacobian and Hessian are given by

$$\boldsymbol{J}_G = \left(\frac{\partial G}{\partial \boldsymbol{n}}\right)_{T,p} = \boldsymbol{\mu} \tag{10a}$$

$$\boldsymbol{H}_G = \left(\frac{\partial^2 G}{\partial \boldsymbol{n} \partial \boldsymbol{n}^\top}\right)_{T,p} = \left(\frac{\partial \boldsymbol{\mu}}{\partial \boldsymbol{n}^\top}\right)_{T,p}. \tag{10b}$$

Here $\boldsymbol{\mu}$ is the vector of chemical potentials. The Jacobian and Hessian in (9) and (10) are valid for any utilized EOS. For instance, the ideal gas Jacobian and Hessian of the Helmholtz energy function are written

$$\boldsymbol{J}_A^{\text{ig}} = \begin{pmatrix} -NRT/V \\ \boldsymbol{\mu}^o(T) + RT \ln \frac{\boldsymbol{n}RT}{Vp_o} \end{pmatrix} \tag{11a}$$

$$\boldsymbol{H}_A^{\text{ig}} = RT \begin{pmatrix} N/V^2 & -V^{-1}\boldsymbol{e}^\top \\ -V^{-1}\boldsymbol{e} & \boldsymbol{D} \end{pmatrix}, \tag{11b}$$

while for the Gibbs energy function, they are written

$$\boldsymbol{J}_G^{\text{ig}} = \boldsymbol{\mu}^o(T) + RT \ln \frac{\boldsymbol{n}p}{Np_o} \tag{12a}$$

$$\boldsymbol{H}_G^{\text{ig}} = RT\left(\boldsymbol{D} - \frac{1}{N}\boldsymbol{e}\boldsymbol{e}^\top\right). \tag{12b}$$

Here R is the universal gas constant, p_o is the standard pressure of 1 bar, and $D_{ij} = \delta_{ij}/n_i$ is the diagonal matrix with δ_{ij} representing the Kronecker delta which is 1 for $i = j$ and 0 otherwise. The standard chemical potential, $\boldsymbol{\mu}^o(T)$, is given by (Winterbone and Turan, 1997, p. 268; Haug-Warberg, 2006, p. 134)

$$\mu_i^o(T,p_o) = \overline{h}_i^{ig}(T,p_o) - T\overline{s}_i^{ig}(T,p_o) = \left[\Delta_f h_i^o(T_o) + \int_{T_o}^{T} c_{p,i}^o(T)dT\right] - T\left[s_i^o(T_o) + \int_{T_o}^{T} \frac{c_{p,i}^o}{T}dT\right], \tag{13}$$

where $\overline{h}_i^{ig}$ and $\overline{s}_i^{ig}$ are the ideal gas partial molar enthalpy and entropy, respectively, $\Delta_f h_i^o$ is the standard heat of formation, $c_{p,i}^o$ is the standard, ideal gas heat capacity and s_i^o is the standard entropy of component i. The standard heat of formation and the standard entropy are tabulated at the reference temperature, T_o, at NIST JANAF[1]. The standard heat capacities were determined from the polynomial expression (for flexibility over a small temperature range)

$$c_{p,i}^o(T) = A_i + B_i T + C_i T^2 + D_i T^3. \tag{14}$$

Here A_i, B_i, C_i and D_i are constants specific to species i. The constants are taken from Lydersen (1983).

Due to non-trivial technicalities of the considered state ($T, V, \boldsymbol{n}$ or $T, p, \boldsymbol{n}$), details on the evaluation of the non-ideal gas Jacobian and Hessian functions in (9) and (10) are given in A.3. It is emphasized that the residual Gibbs energy function is not derived in a straight forward manner for pressure explicit EOSs, such as the SRK-EOS. In this case, the residual Gibbs energy function is evaluated through the residual Helmholtz energy function.

2.1.2. Density

The density for any EOS at any spatial point in the reactor is given by

$$\rho(T,p,\boldsymbol{n}) = \frac{N}{V}\sum_{i=1}^{C} y_i M_{m,i}, \tag{15}$$

where V is dependent on the EOS and computed iteratively by a Newton–Raphson search at the $T, p, \boldsymbol{n}$ of the nodal point considered. The relations are taken from Michelsen and Mollerup (2007, p. 94):

$$V^{v+1} = V^v - \frac{\xi(T,p,V,\boldsymbol{n})}{\left(\frac{\partial \xi(T,p,V,\boldsymbol{n})}{\partial V}\right)_{T,p,\boldsymbol{n}}}, \tag{16}$$

where ξ is the pressure Eq. (C.1) on residual form given in Appendix C. The required derivative is given by (C.2b).

For ideal gas (see Appendix A.1.1), no iterations are needed in order to compute the volume, and (15) reduces to

$$\rho = \frac{p}{RT}\sum_{i=1}^{C} y_i M_{m,i}. \tag{17}$$

2.1.3. Momentum

The friction factor in (3) is parameterized by Ergun (1952) but was later modified by Tallmadge (1970) to higher Reynolds numbers (Coker, 2001). In this work, the Tallmadge (1970) modification is used

$$f = \frac{1-\varepsilon}{\varepsilon^3}\left(1.75 + 4.2\frac{1-\varepsilon}{\mathrm{Re}^{1/6}}\right). \tag{18}$$

The Reynolds number is given by

$$\mathrm{Re} = \frac{\rho v^s d_p}{\mu}, \tag{19}$$

where μ denotes the mixture dynamic viscosity and is given by

$$\mu = \sum_{i=1}^{C} y_i \mu_i. \tag{20}$$

The individual contribution of each species, μ_i, is given by the Sutherland et al. (1893) expression

$$\mu_i = \frac{B_i T^{3/2}}{S_i + T}, \tag{21}$$

where B_i and S_i denote species specific constants taken from Lydersen (1983).

2.1.4. Temperature

Heat capacity: The extensive[2] isobaric heat capacity is defined as

$$C_p \equiv T\left(\frac{\partial S}{\partial T}\right)_{p,\boldsymbol{n}} = -T\left(\frac{\partial^2 G}{\partial T^2}\right)_{p,\boldsymbol{n}}. \tag{22}$$

However, for pressure explicit EOSs, an alternative relation exists

$$C_p = C_V - T\frac{\left(\frac{\partial p}{\partial T}\right)^2_{V,\boldsymbol{n}}}{\left(\frac{\partial p}{\partial V}\right)_{T,\boldsymbol{n}}}, \tag{23}$$

where the extensive isochoric heat capacity is defined as

$$C_V \equiv T\left(\frac{\partial S}{\partial T}\right)_{V,\boldsymbol{n}} = -T\left(\frac{\partial^2 A}{\partial T^2}\right)_{V,\boldsymbol{n}}. \tag{24}$$

For the virial expansion, evaluating (22) is possible, and when using the Gibbs energy function, (22) is obviously preferred over (23). However, for pressure explicit EOSs, such as the SRK-EOS, (23) must be used in combination with (24), both for the Gibbs and the Helmholtz energy function. The volume required for evaluating the pressure derivatives in (23) and the Helmholtz energy function derivatives in (24) is computed through (16). The auxiliary pressure derivatives are given in (C.2), and the second-order derivatives of the Helmholtz energy function are given in Appendix B. Further details on evaluating the heat capacity are given in Appendix A.3.

The specific heat capacity required in the temperature Eq. (4) is obtained by the appropriate conversion

$$c_p^{\text{specific}} = \frac{C_p^{\text{extensive}}}{N\sum_{i=1}^{C} y_i M_{m,i}}, \tag{25}$$

where $M_{m,i}$ is the molar mass of component i and the superscripts "specific" and "extensive" are applied for clarity.

Reaction enthalpy: The reaction enthalpy is computed from

$$\Delta_{rx}H_r = \sum_{i=1}^{C} \nu_{i,r}\overline{h}_i, \tag{26}$$

where $\nu_{i,r}$ denotes the stoichiometric coefficient of component i in reaction r, and $\overline{h}_i$ is the partial molar enthalpy. The independent reactions, and thus also the stoichiometric coefficients, are found from the null space of the formula matrix, $\boldsymbol{A}$. The formula matrix described in the optimization problems (5) and (6) is first put on row reduced echelon form, that is $\boldsymbol{A} \sim (\boldsymbol{I} \quad \boldsymbol{E})$. The stoichiometric matrix is then recovered as

$$\boldsymbol{N} = \begin{pmatrix} -\boldsymbol{E} \\ \boldsymbol{I} \end{pmatrix}, \tag{27}$$

where $\boldsymbol{I}$ is the identity matrix. The stoichiometric matrix has dimensions $N_C \times N_{rx}$. For the SMR and the methanol processes, the stoichiometric matrices are given as

[1] The values are tabulated at https://janaf.nist.gov/ (last accessed 26.06.2020), except for methanol which is found in Green (1961).

[2] Property that depends on the physical size of the system considered.

$$\boldsymbol{N}_{SMR} = \begin{array}{c} \begin{matrix} \text{Rx 1} & \text{Rx 2} \end{matrix} \\ \begin{pmatrix} -1/2 & -1/2 \\ 1 & 2 \\ -1/2 & -3/2 \\ 1 & 0 \\ 0 & 1 \end{pmatrix} \end{array} \begin{matrix} \text{CH}_4 \\ \text{CO} \\ \text{CO}_2 \\ \text{H}_2 \\ \text{H}_2\text{O} \end{matrix}, \quad \boldsymbol{N}_{MeOH} = \begin{array}{c} \begin{matrix} \text{Rx 1} & \text{Rx 2} \end{matrix} \\ \begin{pmatrix} 1 & -1 \\ -1 & 0 \\ -1 & -2 \\ 1 & 0 \\ 0 & 1 \end{pmatrix} \end{array} \begin{matrix} \text{CO} \\ \text{CO}_2 \\ \text{H}_2 \\ \text{H}_2\text{O} \\ \text{CH}_3\text{OH} \end{matrix} \tag{28}$$

Hence there are two independent reactions in both the SMR process and the methanol process. The reactions may be read from the stoichiometric matrices in (28). For the SMR process, the reactions are

$$\tfrac{1}{2}\text{CH}_4 + \tfrac{1}{2}\text{CO}_2 = \text{CO} + \text{H}_2$$
$$\tfrac{1}{2}\text{CH}_4 + \tfrac{3}{2}\text{CO}_2 = 2\text{CO} + \text{H}_2\text{O},$$

and for the methanol process, the reactions are

$$\text{CO}_2 + \text{H}_2 = \text{CO} + \text{H}_2\text{O}$$
$$\text{CO} + 2\text{H}_2 = \text{CH}_3\text{OH}.$$

Furthermore, the required partial molar enthalpies are given by (see also definitions (A.26) and (A.52a))

$$\overline{h}_i = \mu_i + T\overline{s}_i = \left(\frac{\partial G}{\partial n_i}\right)_{p,\boldsymbol{n}} - T\left(\frac{\partial^2 G}{\partial T \partial n_i}\right)_p. \tag{29}$$

For the virial expansion, evaluating (29) is possible, and when using the Gibbs energy function, it is obviously preferred. However, for pressure explicit EOSs, the derivation is more involved. This is primarily due to the implicit form obtained when mixing T, p and T, V as free variables. The reader is referred to Appendix A.3 for a detailed description on evaluating the partial molar enthalpies, or to Michelsen and Mollerup (2007) for general details on the subject.

2.2. Numerical solution approaches

Two numerical solution methods have been studied in this work: the OCM (Villadsen and Stewart, 1995; Shen et al., 2011; Solsvik et al., 2013; Jakobsen, 2014) and the FVM (Versteeg and Malalasekera, 2007; Ferziger et al., 2020; Roache, 1998; Jakobsen, 2014). In the former of the two methods, the quantity of interest is found by forcing the residual of the equations to zero at a set of points called *collocation points*. The collocation points have no spatial extent, and correspondingly no volume is associated with these discrete points. Therefore, in this numerical solution method, intensive[3] variables are the most accessible. In finding the equilibrium composition, the most natural choice of thermodynamic energy function is the Gibbs energy as it is formulated in the T and p variables, which are both intensive quantities. The minimization problem presented by (6) in Section 2.1.1 is then solved for all collocation points, and each minimization problem has the constraints of keeping the temperature and pressure constant at the considered collocation point.

The FVM, on the other hand, is based on balancing quantities, such as mass, momentum, and energy, over grid cell volumes that do have spatial extent, contrary to the collocation points in the OCM. In terms of the Gibbs energy function, the calculation routine is similar (but not identical) to the one for the OCM. On the other hand, the Helmholtz energy function is a function of T and V. The volume to be held constant in optimization problem (5) is then computed from the EOS with (16). However, a second alternative for the volume may be proposed for the Helmholtz energy function with the FVM; that is, the volume is *not* computed from the EOS, but taken from the computational grid.

The discrete points at which the velocity field is computed is indicated by arrows, while the scalar quantities are computed at the bullet points. In the OCM, the velocity and scalar points coincide, while the FVM uses a staggered grid. This is illustrated in Fig. 1.

2.2.1. Orthogonal collocation method

In the OCM, the unknown function, $f(x)$, is approximated as a truncated series expansion of interpolating polynomials, i.e.

$$f(x) \approx f^N(x) = \sum_{i=0}^{N} \alpha_i \phi_i^N(x), \tag{30}$$

where α_i is a basis coefficient and $\phi_i^N(x)$ is an N'th order polynomial. By choosing $\phi_i^N(x)$ as Lagrange interpolating polynomials, α_i can be chosen as $f(x_i)$ (Kreyszig, 2011). Thus, the problem of finding a function, $f(x)$, reduces to finding a set of coefficients, $f(x_i)$, at a set of abscissas, x_i, called *collocation points*. This problem takes a linearized form of $\boldsymbol{Af} = \boldsymbol{b}$, where the $\boldsymbol{A}$-matrix contains linear operators such as derivatives and integrals. These are dependent on the location of the collocation points.

The collocation points are usually taken as the roots of orthogonal polynomials, hence the name *orthogonal* collocation. Depending on whether collocation points are placed on the boundary or not, three different types of grids exist: Gauss (no boundary nodes), Gauss–Lobatto (both boundary nodes), and Gauss-Radau (one boundary node). In this work, the collocation points were taken as the roots of Legendre polynomials and placed in a Gauss–Lobatto type of grid. Information on how to find the collocation points and construct $\boldsymbol{A}$ and $\boldsymbol{b}$ is studied extensively in literature and can be found elsewhere (Villadsen and Michelsen, 1978; Press et al., 1992; Solsvik and Jakobsen, 2012; Solsvik et al., 2013; Solsvik and Jakobsen, 2013a; Shen et al., 2011; Golub and Welsch, 1969; Golub, 1973; Jakobsen, 2014).

With the OCM approach, the continuity Eq. (1) is solved for the velocity, v^s, the species mass balance (2) is solved for the reaction rate, R_c, the momentum Eq. (3) is solved for pressure, p, and the temperature Eq. (4) is solved for temperature, T. The density, ρ, is obtained from a thermodynamic computation on the volume, as discussed in Section 2.1.2.

2.2.2. Finite volume method

In the FVM the transport equations are written as balances over a set of grid cell volumes (Versteeg and Malalasekera, 2007; Ferziger et al., 2020; Roache, 1998; Jakobsen, 2014). The unknown quantities are then approximated as an average assumed representative for the entire grid cell volume. In the present study, two solution strategies are considered for the pressure–velocity field. In the first approach, the SIMPLE algorithm of Patankar and Spalding (1972) (see also e.g. Patankar, 1980) along with the upwind scheme is employed for pressure velocity coupling, and a staggered grid is considered. In this methodology, the pressure is corrected by a constructed pressure correction equation generated from the momentum and continuity equations, whereas the velocity is determined from the momentum equation. This solution approach differs from the OCM approach. In the latter, the velocity is determined from the continuity equation and the pressure is determined from the momentum equation.

In the second approach, the Ergun equation – which represents a simplified form of the momentum equation – is used to compute the pressure whereas the velocity is obtained from the continuity equation. The transport equations are thus solved for the same variables in this approach as in the OCM approach.

[3] Property that is independent of the physical size of the system considered.

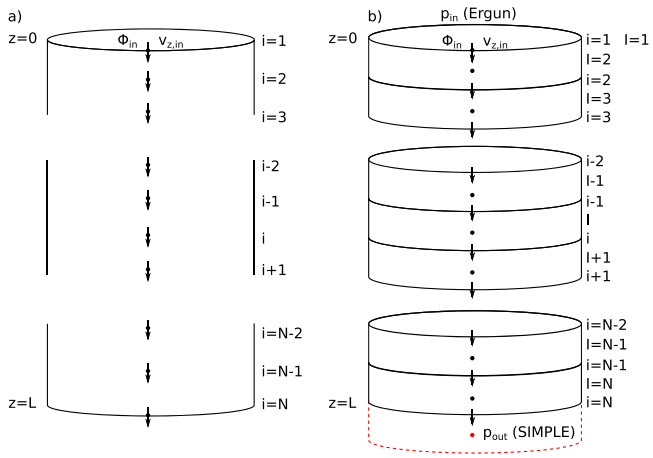

Fig. 1. The numerical grids used in (a) the OCM and (b) the FVM. A uniform staggered grid is used in the FVM and Gauss–Lobatto points are used in the OCM.

Both solution strategies in the FVM framework utilize the staggered grid in Fig. 1b) with the upwind scheme. The two strategies utilizing the FVM will be referred to as FVM-SIMPLE and FVM-Ergun.

2.2.3. Program flow

The combination of numerical schemes, chemical processes and EOSs considered in this study is presented in Fig. 2. For the OCM, the SMR and methanol (MeOH) processes were simulated for ideal gas, second virial expansion, and SRK-EOSs. For the FVM, both FVM-Ergun and FVM-SIMPLE were employed. For the FVM-Ergun, two options were analyzed for the volume to be utilized in minimizing the Helmholtz energy function: (i) computing the volume from the EOS with (16) (V_{EOS}) and (ii) using the volume of the grid cell (V_{cell}). This volume analysis was applied to the SMR process with the SRK-EOS. The two solutions were compared. It was assumed that the volume analysis was purely of numerical character (independent of the chemical process and EOS), and consequently, no other cases than the SMR process with the SRK-EOS were analyzed.

For the FVM-SIMPLE, the methanol and SMR processes were solved with the second virial expansion and calculating the volume from the EOS with (16). The solution profiles obtained with the FVM-Ergun employing the second virial expansion and calculating the volume from the EOS with (16) were compared to the solution profiles obtained with the FVM-SIMPLE for both chemical processes. The differences in the solution profiles in the FVM-SIMPLE and the FVM-Ergun were only investigated employing the second virial expansion in the present work.

In Fig. 3, the general program structure algorithm is illustrated for both the differential Gibbs (left-hand side) and Helmholtz (right-hand side) reactor models. The shaded background highlights the novelty of this work compared to the ideal gas algorithm by Solsvik et al. (2016), and furthermore its differences compared to a reaction rate based reactor model. This involves the equilibrium computations, as well as the non-ideal blocks computing the density and residual properties. Moreover, the Helmholtz energy function is evaluated at the volume of the system, and it is proposed that two different volumes exist, namely the V_{EOS} or the V_{cell}. As such, the equilibrium computation can be carried out at two different volumes. The Gibbs energy function, on the other hand, utilizes pressure and not volume. As a result, no choice of volume is associated with the differential Gibbs reactor model. The Gibbs energy function is evaluated at the pressure obtained from the continuity/momentum equations and the equilibrium computation is subsequently carried out at that pressure.

Before entering the equilibrium computation, the differential Helmholtz reactor model must compute an initial composition or volume by Newton–Raphson iteration depending on the choice of volume: if EOS is chosen (V_{EOS}), the initial composition, $\boldsymbol{n}$, is known and the initial volume, V, is calculated by (16). If the grid cell is chosen (V_{cell}, only for the SRK-EOS), the initial volume, V, is known

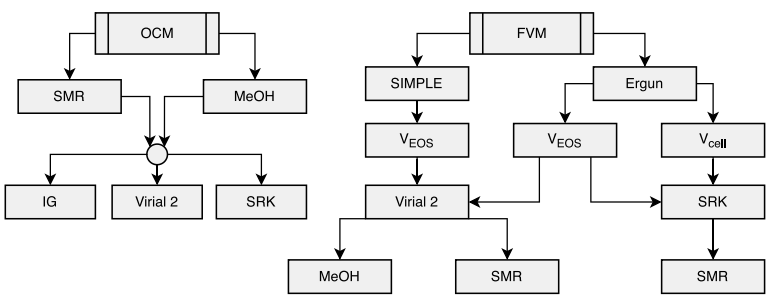

Fig. 2. Flow chart of the different combinations of numerical schemes, processes, and EOSs analyzed in the present work. Here IG denotes ideal gas.

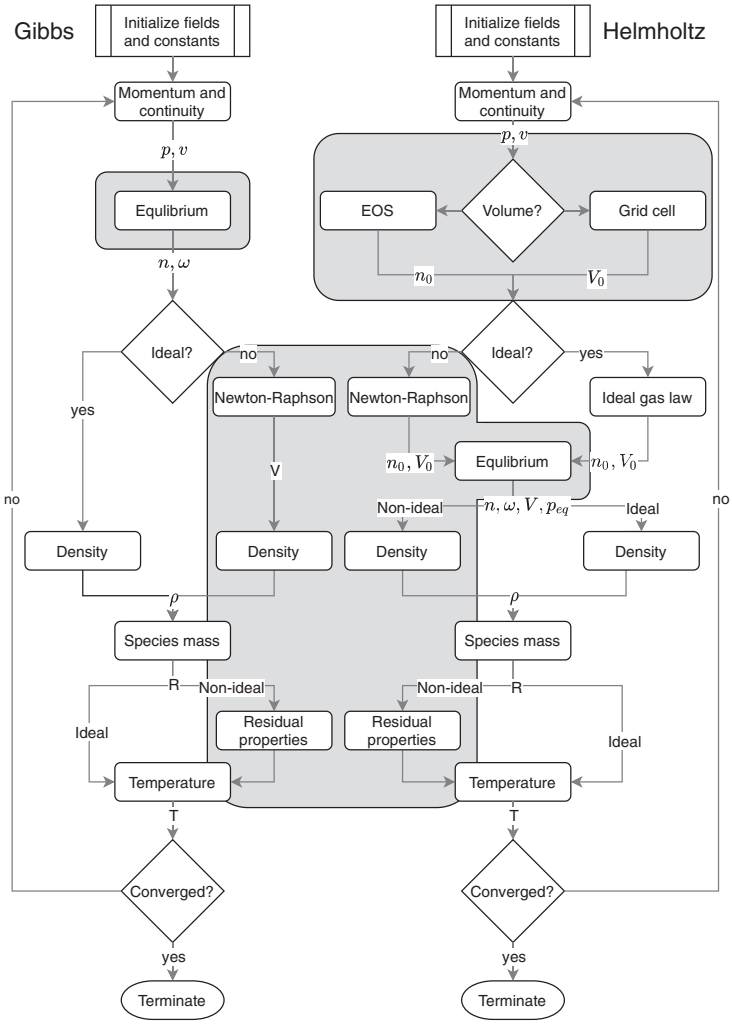

Fig. 3. General algorithm for the differential Gibbs and Helmholtz reactors. The choice of approach to compute the volume and the choice of EOS are indicated by decision blocks. The arrows indicate which variable the equations are solved for.

and the composition, $\boldsymbol{n}$ is computed by the real root of the SRK pressure Eq. (A.10). The equation is rearranged in terms of the total mole numbers and given as

$$[ab]N^3 + \left[V\left(RTb + b^2p - a\right)\right]N^2 + \left[V^2RT\right]N - pV^3 = 0, \tag{31}$$

and the composition is given as $\boldsymbol{n} = \boldsymbol{y}N$. In (31), $b(\boldsymbol{y}) = \mathcal{B}/N$ is the excluded volume per mole and $a(T, \boldsymbol{y}) = D/N^2$ represents the attractive term per square mole. $\mathcal{B}$ and D are computed by (A.11a) and (A.11b), respectively. In both the case of choosing V_{EOS} and the case of choosing V_{cell}, the volume is held constant under minimization, and as a result, the pressure changes.

In the Gibbs reactor model, the pressure is held constant under minimization, and the volume consequently changes. Thus, in order to find the density for the differential Gibbs reactor model, the volume is found by Newton–Raphson iteration with (16) *after* the minimization, in contrast to the Helmholtz reactor model where the Newton–Raphson iteration with (16) is done *before* the minimization. In both the differential Gibbs and Helmholtz reactor models, the density at any location in the reactor is computed by (15).

In the Helmholtz reactor, there is an additional convergence criterion compared to the Gibbs reactor. Since the equilibrium problem is solved by changing the composition while holding temperature and volume constant, the pressure consequently changes during optimization. The pressure at minimum Helmholtz energy is indicated by p_{eq} in Fig. 3. However, the solution of the transport equations provides another pressure indicated by p in the top right of Fig. 3, which does not necessarily coincide with p_{eq}. Thus, the two pressures must be iterated until they converge to the same value.

By specifying the composition vector at the reactor inlet, $\boldsymbol{n}_{\text{in}}$, the composition vector can be updated throughout the reactor according to the minimum of (5) or (6). In order to update the density in the reactor model, the volume is calculated by (16) in each discretization node utilizing the computed $T, p, \boldsymbol{n}$ of that node. In

terms of the Helmholtz reactor model, $T, p_{eq}, \boldsymbol{n}$ is used to update the volume, resulting in a Gauss–Seidel iteration scheme for the density update.

2.3. Initial values, boundary conditions and parameter values

All the transport Eqs. (1)–(4) are ordinary differential equations, and with the computational grids in Fig. 1, there are three cases. In the case of the OCM, all variables share the same collocated grid. That is, the spatial coordinate, z, is discretized in a set of collocation points $\{z_i\}_{i=1}^{N}$, and the dependent variables are evaluated at this set. By using the Gauss–Lobatto grid, all variables were specified at the reactor inlet. The problem is an initial value problem, and the initial values are given as

$$\left.\begin{aligned} p &= p_{\text{in}} \\ v^s &= v^s_{\text{in}} \\ T &= T_{\text{in}} \\ \omega_c &= \omega_{c,\text{in}}, \forall c \\ \rho &= \rho(T_{\text{in}}, p_{\text{in}}, \boldsymbol{\omega}_{\text{in}}) \end{aligned}\right\} \text{ at } z = 0, \tag{32}$$

where the density was computed by the EOS with (15).

In the case of the FVM, there are two alternative approaches: the FVM-Ergun and the FVM-SIMPLE. In both cases, the values for v^s, T, and ω_c were specified at the reactor inlet. The pressure was, however, specified at two different boundaries for the two numerical approaches. With FVM-Ergun, the pressure was specified at the reactor inlet and thus all variables were specified identically to the OCM. Hence, FVM-Ergun is also an initial value problem and the initial values are given by (32). In the FVM-SIMPLE methodology, p was specified at a ghost node at the reactor outlet as indicated in Fig. 1b). As a result, p_{in} was unknown and extrapolated from the interior part of the grid. Consequently, ρ_{in} was recalculated as a function of the changing p_{in} in each iteration. The FVM-SIMPLE problem is thus a boundary value problem.

In both FVM-Ergun and FVM-SIMPLE, the last velocity node was calculated by assuming the mass flow at the reactor outlet was constant, i.e. $F_{i=N+1} = F_{i=N} = (\rho v^s A)_{i=N}$. The density at the reactor outlet was extrapolated as $\rho_{i=N} = \rho_{i=N}$ (see Fig. 1). In the interior part of the domain, the density at the velocity nodes, ρ_i, was interpolated from the density at the scalar nodes, ρ_I, to evaluate the mass flow at the velocity nodes, F_i. The mass flow at the scalar nodes, F_I, was subsequently interpolated from F_i.

The numerical values of the initial values are given in Table 1 and were the same as those in Solsvik et al. (2016) for the SMR process, and the same as those in Solsvik and Jakobsen (2013b) for the methanol process.

Table 1
Initial values and parameters to initialize the Differential Gibbs and Helmholtz reactors.

Variable	SMR	Methanol	Unit
Reactor length	7	7	m
d_p	0.0173	0.0042	m
ε	0.5	0.5	–
r_i	0.051	0.051	m
r_o	0.066	0.066	m
λ_{steel}	52	52	W m^{-1} K^{-1}
T_a	1050	520	K
T_{in}	700	500	K
p_{in}	29	50	bar
v^s_{in}	1.5	1.5	m s^{-1}
$y_{CH_4,\text{in}}$	0.22	–	–
$y_{MeOH,\text{in}}$	–	0.0022	–
$y_{CO,\text{in}}$	0.00007	0.0580	–
$y_{CO_2,\text{in}}$	0.008	0.0220	–
$y_{H_2O,\text{in}}$	0.73	0.0005	–
$y_{H_2,\text{in}}$	0.04193	0.8900	–

3. Results and discussion

The plug flow reactor model in which the composition is provided from thermodynamic equilibrium was utilized. The effect of the EOS and numerical solution approach was analyzed for the SMR and methanol processes. For the SMR process with the ideal gas EOS, the pressure, velocity, temperature, and density profiles are shown in Fig. 4, while the composition profiles are shown in Fig. 5. The Gibbs and Helmholtz function formulations provide two identical equilibrium problem formulations, and consequently, the compositions resulting from the optimization routines are equivalent. This should be expected since the two energy functions contain the same information, and their optima correspond to the same state. As a result, it is immaterial whether the Gibbs energy function or the Helmholtz energy function is used with respect to the result.

There is, however, a difference regarding calculation routine and efficiency. The chemical equilibrium reactor models are more complicated to implement compared to that of a standard reactor model based on reaction rate kinetics because an optimization problem needs to be solved. This is easily seen in Fig. 3. Additionally, as pointed out in Section 2.2.3, the differential Helmholtz reactor model is more complicated than the Gibbs reactor model due to the two pressures, p and p_{eq}, computed before and after the minimization, respectively. This imposes an additional convergence criterion on the Helmholtz reactor, making it slightly more demanding to implement than the Gibbs reactor. However, computing the equilibrium pressure, p_{eq}, allows the density to be updated with the current iteration's pressure estimate, which decreases the total number of iterations spent before convergence is obtained compared to the Gibbs reactor where the pressure of the previous iteration is used.

By choosing the Helmholtz reactor, the optimization problem to be solved increases in dimensionality due to the additional constraints and decision variables, as seen by comparing (5) and (6). This makes the optimization problem slower for the Helmholtz energy function formulation, and even though the Helmholtz reactor model converges in fewer iterations, it spends more time at each iteration than the Gibbs reactor model. Overall, the Gibbs reactor model converges approximately 30%, 140%, and 14% faster than the Helmholtz reactor model for ideal gas, the virial expansion, and the SRK-EOS, respectively. The virial expansion can be implemented both as a volume-explicit as well as a pressure-explicit EOS, allowing both the residual Gibbs and the residual Helmholtz energy functions to be computed from their defining Eqs. (A.47) and (A.59), respectively. The residual Helmholtz energy function is, however, more demanding to compute as seen in Appendix B.1. In terms of the SRK-EOS, both the Gibbs and Helmholtz reactors were implemented through the residual Helmholtz energy function, as indicated by (A.50) and (A.61), respectively. Thus, the mathematical complexity between the residual Gibbs and Helmholtz energy functions are similar. Due to the larger dimensionality in the Helmholtz energy function optimization problem, the Helmholtz reactor spends more time in each iteration than the Gibbs reactor. The Gibbs and Helmholtz reactor models with the SRK-EOS spend similar times overall.

In terms of numerical solution strategy, the OCM was more efficient than both the FVM-Ergun and the FVM-SIMPLE for all cases analyzed. A total number of 40 points were utilized in both the OCM and the FVM numerical approaches.

For any EOS different from ideal gas, the density cannot be directly computed at a given temperature, pressure and composi-

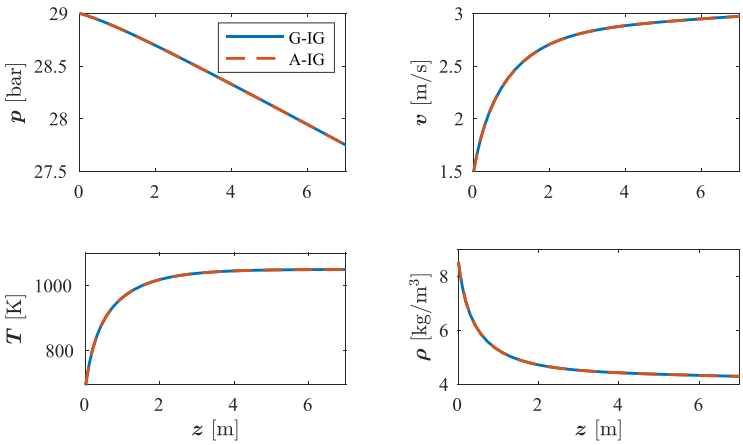

Fig. 4. Pressure, velocity, temperature, and density along the axial direction, z (m), for the Gibbs (G) and Helmholtz (A) differential reactors assuming ideal gas (IG) for the SMR process.

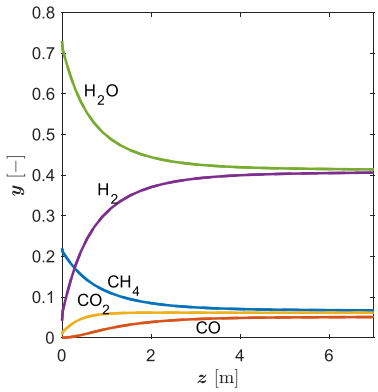

Fig. 5. Mole fractions along the axial direction, z (m), for the Gibbs and Helmholtz differential reactors assuming ideal gas for the SMR process.

tion. This is indicated by the Newton–Raphson block before the density block near the middle of Fig. 3. To find the density, the volume is first found by iteration on (16), and as such, the calculation time is significantly increased. This is true also for the differential Gibbs reactor model, which for ideal gas had no extra calculation loop other than the equilibrium calculation.

All subsequent results are obtained by using the Ergun's equation to compute the pressure and the continuity equation to compute the velocity unless explicitly stated that the FVM-SIMPLE is used.

3.1. Steam-methane reforming

To assess the assumption of ideal gas at the simulated conditions, other EOSs were attempted, namely the virial EOS and the SRK-EOS. The relative deviation from ideal gas is shown in Fig. 6 and Fig. 7 and were obtained by using the OCM on the differential Gibbs reactor. At the specified conditions, the relative deviations from ideal gas are all below 5%. As seen in Fig. 8, CO_2 is favored by high temperatures, and whenever the temperature is lower than that of ideal gas, a negative deviation in CO_2 is observed. Similar arguments hold for the other products (CO, H_2), while the converse is true for the reactants (CH_4, H_2O). The deviation in density at the reactor inlet is caused by its initial value. The reactor inlet temperature, pressure and composition are specified and constant. The density is calculated from either the ideal gas EOS, virial expansion EOS or the SRK-EOS. Utilizing an EOS other than the ideal gas EOS will cause a deviation in the density computed at the reactor inlet.

In the Helmholtz energy function approach, the volume chosen is either calculated from the EOS with (16), or if the FVM is employed, the grid cell volume could be chosen. This is shown near the top of the Helmholtz approach in Fig. 3. The relative deviations between the two approaches are at the number representation in MATLAB. Whether the volume is calculated from the EOS or mixed with the numerics by using the grid cell volume, the solution is unaltered. It is therefore a matter of preference which method is used.

Furthermore, the differences between the FVM-SIMPLE and the FVM-Ergun were investigated. The results are obtained with the virial EOS on the differential Helmholtz reactor and are shown in Fig. 9 and Fig. 10. With FVM-Ergun, the pressure was given at the reactor inlet, however, with the FVM-SIMPLE algorithm, the pressure was given at the reactor outlet. The specified reactor outlet pressure was the solution to the FVM-Ergun simulation, and therefore the deviations are zero at the reactor outlet. However, at the reactor inlet, there is a slight mismatch which also causes the other variables to deviate from the solution to FVM-Ergun. The deviations approach zero as the pressure differences vanish. The deviation in mole fraction of CO seems higher than the others due to its initially low value. Small errors are amplified due to being relative deviations, not absolute. Altogether, the deviations are small and negligible, showing that the differential Gibbs and Helmholtz reactors are suitable for existing pressure-based solution strategies, even for more rigorous EOSs.

A parameter sensitivity study was performed to investigate the sensitivity of the solution. Therefore, the temperature initial value was decreased from 700 K to 400 K while keeping everything else constant. The results are obtained with the OCM on the differential Gibbs reactor and are shown in Fig. 11 and Fig. 12. The results display relative deviations in the variables at the reactor outlet as a function of the reactor inlet temperature. As the reactor inlet temperature is decreased, a stronger deviation is observed for density, and therefore also in velocity. In turn, the pressure drops due to the coupling between pressure and velocity. At 400 K a relative devia-

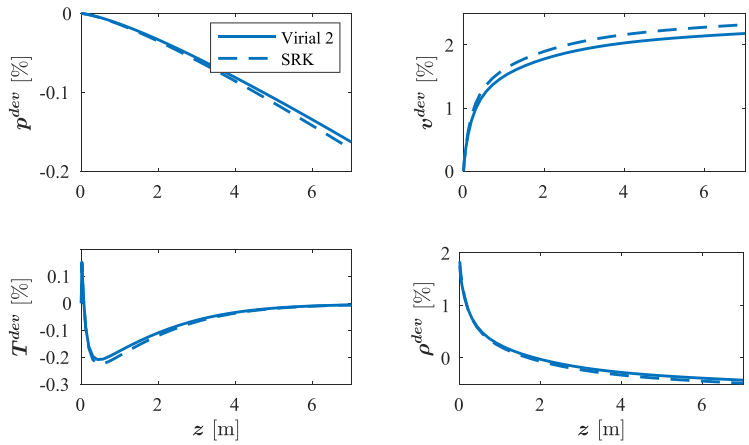

Fig. 6. Pressure, velocity, temperature, and density relative percent deviation from ideal gas along the axial direction, z (m), for the SMR process. Full lines (——) are the virial EOS, and the dashed lines (– – –) are SRK.

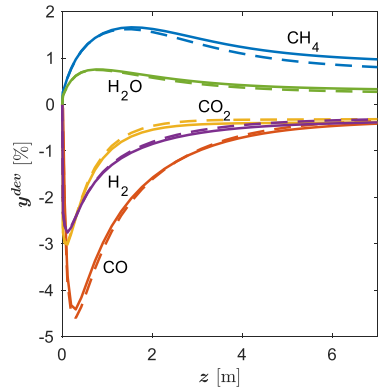

Fig. 7. Mole fraction relative percent deviation from ideal gas along the axial direction, z (m), for the SMR process. Full lines (——) are the virial EOS, and the dashed lines (– – –) are SRK.

tion as high as 30% is observed in the velocity for the virial EOS. The deviations are more modest for the SRK-EOS; however, the deviations are still large. The trends for the SRK-EOS agree with the virial expansion for all variables: there are positive deviations in velocity and negative deviations in pressure, temperature, and density. As for the mole fractions in Fig. 12, the deviations are small. Even for a pressure deviation of 7% less, the greatest deviation observed is 1.2% less for CO. This is due to chemical reaction equilibrium being mainly governed by the temperature as is showcased in Fig. 8. The trends apply for the other components as well; mole fractions of reactants drop, and mole fractions of products rise as the temperature increases. The temperature at the reactor outlet only deviates from ideal gas by a maximum of 0.6% less, and at this temperature, the ideal gas assumption was shown to be satisfactory. Therefore, the observed deviations in mole fractions are minor.

3.2. Methanol synthesis

The methanol synthesis was also first simulated for ideal gas using the OCM, and the results are displayed in Fig. 13 and

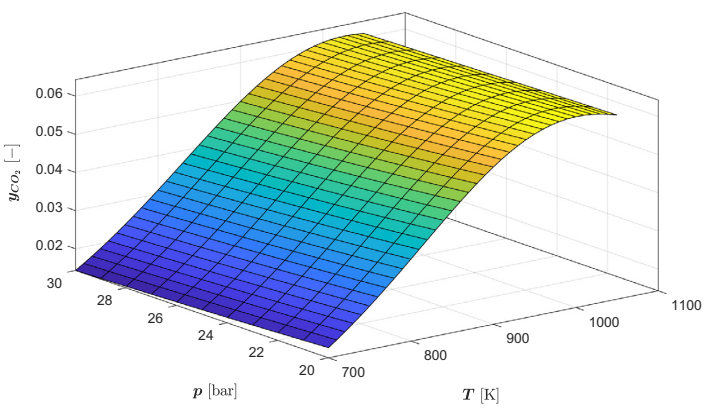

Fig. 8. Mole fraction of CO_2 at equilibrium as a function of temperature and pressure. The figure is generated based on ideal gas assumption. The virial EOS and the SRK-EOS display the same trend values to within 2% relative error.

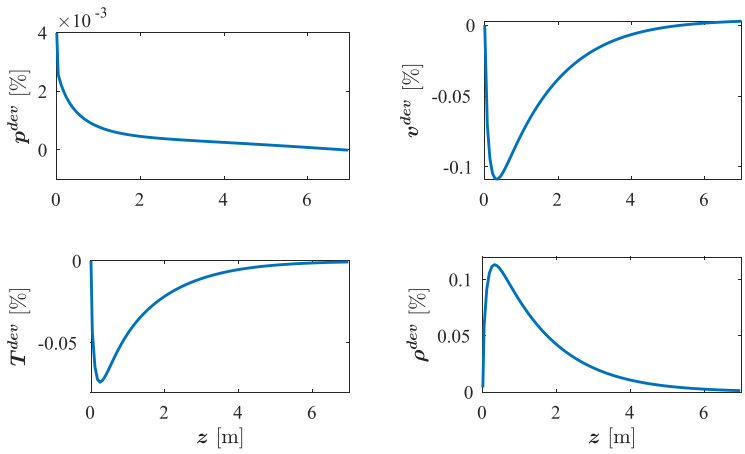

Fig. 9. Pressure, velocity, temperature and density relative percent deviation between the FVM-SIMPLE pressure correction approach and FVM-Ergun along the axial direction, z (m), for the SMR process. The profiles are obtained with the virial EOS.

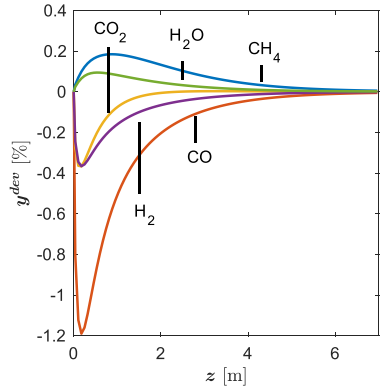

Fig. 10. Mole fraction relative percent deviation between the FVM-SIMPLE pressure correction approach and FVM-Ergun along the axial direction, z (m), for the SMR process. The profiles are obtained with the virial EOS.

Fig. 14. In line with the SMR results, the differential Gibbs and Helmholtz reactors for the methanol synthesis also produce equivalent results. Since the reactions in this process are overall exothermic, the temperature rises for a positive reaction term. As the reactors establish instantaneous equilibrium, this exothermic part yields a strong contribution to the temperature equation. It is seen that the reaction term dominates over the heat exchange term from the ambient cooling medium.

It is observed from Fig. 14 that the inlet temperature of 500 K gives a large change in composition. As a result of the exothermic reaction, the temperature spikes as seen in Fig. 13. As the cooling from the heat exchange with the cooling medium starts to dominate the temperature equation, the reaction slowly proceeds. The reactor stabilizes at the temperature of the cooling medium (520 K), and the profiles are constant thereafter. From the compositional profiles, it is seen that the mole fraction of the products increases as the temperature decreases from 570 – 520 K. Hence, it can be concluded that the equilibrium in the range 500 – 570 K is best favored somewhere between 500 K and 520 K.

Immediately after the temperature rises, the density also drops. However, as the cooling takes place, the density slowly rises again up until $z = 4$ m. At this point, the temperature is unaltered, and the reaction has died out. Hence, the density is governed by the pressure drop from the flow conditions. As the pressure declines, so does the density. To satisfy the continuity equation, the velocity inversely follows the density profile. However, the changes in density and velocity after $z = 4$ m are minor.

The relative deviations between the virial expansion and ideal gas as well as the relative deviations between the SRK-EOS and ideal gas are given in Fig. 15 and Fig. 16. The results were obtained by using the OCM on the differential Gibbs reactor. Even though the temperature range is significantly lower than that for the SMR process, the deviations observed are still minor for all flow variables. For the composition profiles, the highest deviation in the mole fractions obtained by the different EOSs is observed as the temperature gradient approaches zero, i.e. $z = 3$ m. At this point, the heat exchange from the cooling medium dominates in the temperature equation, and the reactor temperature approaches the ambient temperature for all EOSs. Hence, the compositions are computed at the same temperature for the different EOSs, and the deviations are therefore a result of the EOS itself, not the flow conditions. The highest deviation observed is around 8%, indicating that ideal gas should be used with caution.

The results in Fig. 17 and Fig. 18 are relative deviations between the solution obtained by the FVM-SIMPLE approach and the FVM-Ergun. The same procedure was applied here as for the SMR process; hence the pressure deviation is zero at the reactor outlet. However, as the deviations are smaller at the reactor inlet for this process, the velocity deviations throughout the whole reactor are also smaller. Once again, the deviations are negligible for all variables, including the composition. Thus, the differential Gibbs and Helmholtz reactor models fit well into the SIMPLE methodology, even with the sharp gradients illustrated by the methanol process.

To investigate how the variables respond to perturbed initial values, the reactor inlet temperature was once again decreased, this time from 500 K to 300 K. The deviations at the reactor outlet were plotted as a function of the perturbed inlet temperature. The results were obtained by the OCM on the differential Gibbs reactor and are shown in Fig. 19 and Fig. 20. As seen in Fig. 20, the compositional deviations are approximately equal for all inlet temperatures investigated. This is due to the low deviations in the flow variables shown in Fig. 19. For small deviations in temperature and pressure, the resulting deviation in composition remains con-

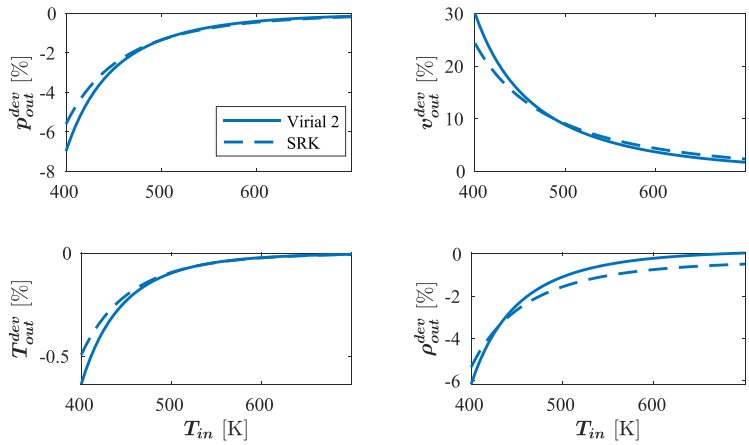

Fig. 11. Pressure, velocity, temperature and density relative deviation from ideal gas at lowered inlet temperatures for the SMR process. Full lines (——) are the virial EOS, and the dashed lines (– – –) are SRK.

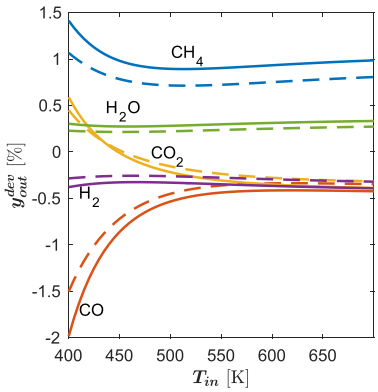

Fig. 12. Mole fraction relative deviation from ideal gas at lowered inlet temperatures for the SMR process. Full lines (——) are the virial EOS, and the dashed lines (– – –) are SRK.

stant. Hence, the deviations observed in Fig. 20 are caused by the EOS, and not the decreased inlet temperatures.

4. Conclusion

Chemical equilibrium computations play an important role due to the limitations the state of equilibrium imposes on reversible reaction kinetics. However, by solely performing a chemical equilibrium computation the temperature (and pressure) are assumed constant. For transport phenomena, the constant temperature (and pressure) are not necessarily physically realistic and restrict e.g. density variations and fluid acceleration due to temperature and pressure gradients, respectively.

In transport phenomena, reaction rate kinetic models are frequently employed in order to compute compositional change due to chemical reaction. These models are correlated empirically, and if they are unknown, the production and consumption of species due to chemical reaction cannot be computed. Hence, at the expense of transient information of the reaction rates, Solsvik

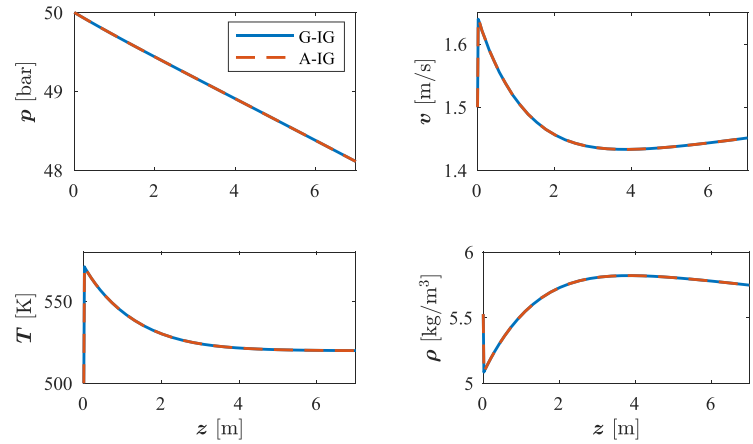

Fig. 13. Pressure, velocity, temperature and density along the axial direction, z (m), for the Gibbs and Helmholtz differential reactors assuming ideal gas for the methanol process.

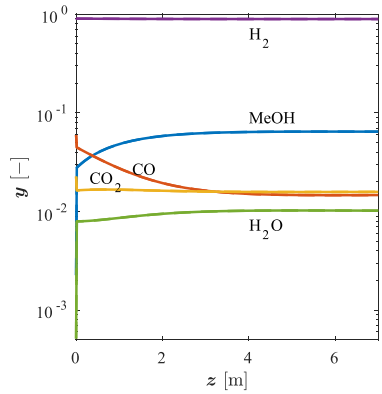

Fig. 14. Mole fractions along the axial direction, z (m), for the Gibbs and Helmholtz differential reactors assuming ideal gas for the methanol process.

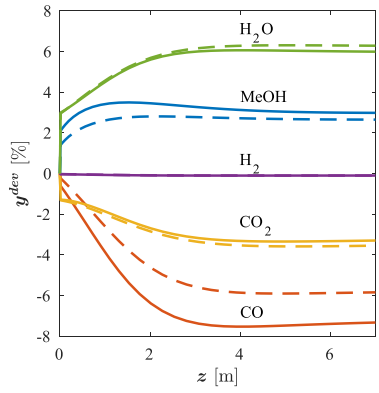

Fig. 16. Mole fraction relative percent deviation from ideal gas along the axial direction, z (m), for the methanol process. Full lines (——) are the virial EOS, and the dashed lines (– – –) are SRK.

et al. (2016) replaced the reaction rate kinetic framework by the chemical equilibrium framework. The result was coined the differential Gibbs and Helmholtz reactor models and represents an alternative to classical reactor computations in the absence of reaction rate kinetics. The reactor models were implemented for ideal gas using the OCM and demonstrated for the SMR process.

In this work, the efforts of Solsvik et al. (2016) were extended to incorporate EOSs for real fluid mixtures, namely the virial EOS and the SRK-EOS. The proposed formalism provides coherency and internal consistency between the chemical equilibrium composition, reaction enthalpy, density, and heat capacity as they are all derived and computed from the same energy function, i.e. the Helmholtz or Gibbs energy functions. The new approach for computing chemical reaction in a transportive, reactive system does, however, introduce an iterative approach for computing the density due to the possible existence of multiple density roots at the temperature and pressure of the discretization point.

The assumption that the gas mixture behaves ideally for the SMR process was verified by the two alternative EOSs utilized for real gases, with all deviations from ideal gas being below 2% for the specified operating conditions. When the inlet temperature was decreased from 700 K to 400 K, on the other hand, the deviations ranged as high as 30% at most for the velocity. For the methanol synthesis, the deviations in flow variables, i.e. velocity, pressure, density and temperature, were minor between ideal gas and the virial EOS and the SRK-EOS. However, the equilibrium computation was affected more with deviations in mole fraction from ideal gas ranging up to approximately 8%. Thus, at the investigated operating conditions, the common assumption of ideal gas is reasonable for the SMR process. On the other hand, the deviations in chemical composition observed for the methanol synthesis suggest that ideal gas should be used with caution.

A numerical study was carried out in order to investigate how the differential Gibbs and Helmholtz reactor models perform in well-established numerical routines such as the OCM and the FVM. For the FVM, the pressure-based solution strategy SIMPLE was attempted. The differential Gibbs and Helmholtz reactor models both converged to within an error of 10^{-6} for all variables and are therefore suitable in the OCM and the FVM frameworks, even for the methanol process which displayed sharp gradients at the reactor inlet. In all cases investigated, the OCM was more efficient, and converged faster, than both the FVM-Ergun and the FVM-SIMPLE.

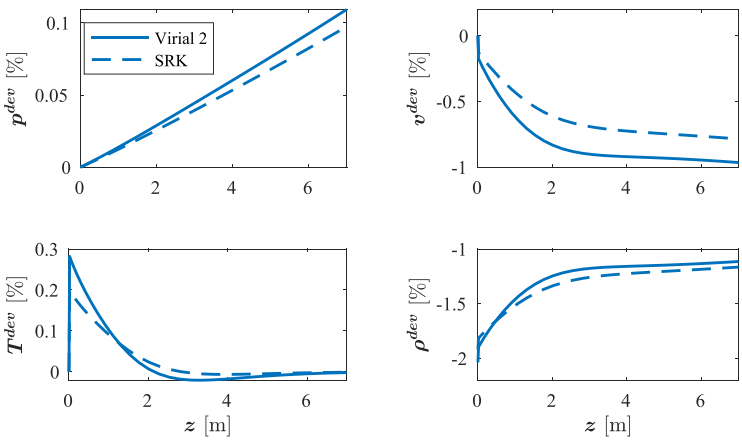

Fig. 15. Pressure, velocity, temperature and density relative percent deviation from ideal gas along the axial direction, z (m), for the methanol process. Full lines (——) are the virial EOS, and the dashed lines (– – –) are SRK.

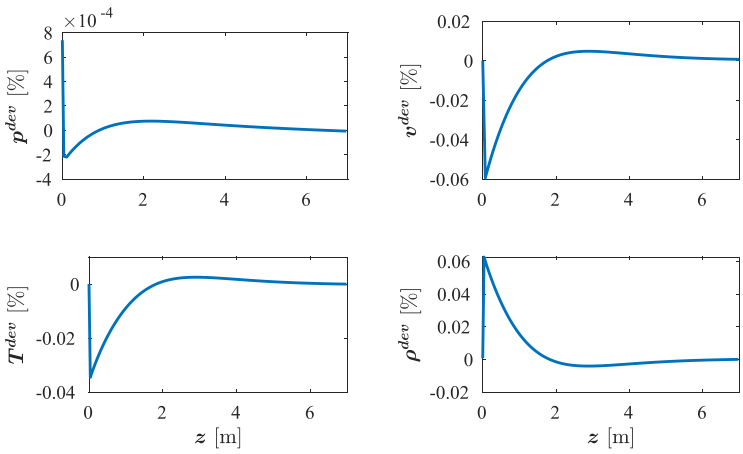

Fig. 17. Pressure, velocity, temperature, and density relative percent deviation between the FVM-SIMPLE pressure correction approach and FVM-Ergun along the axial direction, z (m), for the methanol process. The profiles are obtained with the virial EOS.

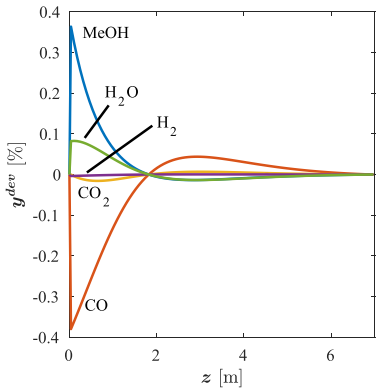

Fig. 18. Mole fraction relative percent deviation between the FVM-SIMPLE pressure correction approach and FVM-Ergun along the axial direction, z (m), for the methanol process. The profiles are obtained with the virial EOS.

The differential Gibbs and Helmholtz reactor models have different numerical properties. In the Helmholtz reactor, computing the equilibrium pressure, p_{eq}, allows the density to be updated with the current iteration's pressure estimate, which decreases the total number of iterations spent before convergence is obtained compared to the Gibbs reactor where the pressure of the previous iteration is used to update the density. However, the optimization problem to be solved is larger in dimensionality for the Helmholtz reactor model than the Gibbs reactor model. The increased computational burden due to the larger dimensionality outweighs the decreased computational burden due to the fewer number of iterations from the rapid density updates. Overall, the Gibbs reactor model converges approximately 30%, 140%, and 14% faster than the Helmholtz reactor model for ideal gas, the virial expansion, and the SRK-EOS, respectively.

The equilibrium solutions are minima to the Gibbs or Helmholtz energy functions, and for other EOSs than the ideal gas law, the existence of multiple minima may occur. Further work includes investigating the probability and consequences related to the exis-

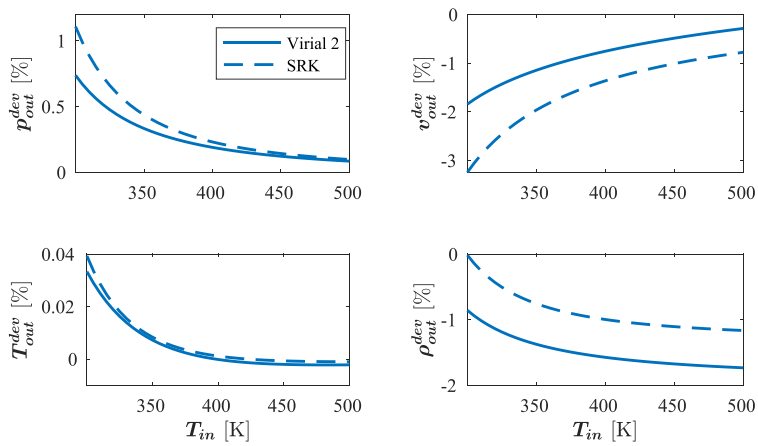

Fig. 19. Pressure, velocity, temperature and density relative deviation from ideal gas at lowered inlet temperatures for the methanol process. Full lines are from the virial EOS and dashed lines are from SRK.

tence of multiple minima, as well as investigating the multiphase behavior of the reactor concepts. It is not foreseen any conceptual problems with extending the present framework for the Gibbs and Helmholtz equilibrium calculations to more complex reactor models than the present tubular ones.

Declaration of Competing Interest

The authors declare that they have no known competing financial interests or personal relationships that could have appeared to influence the work reported in this paper.

Acknowledgments

Funding: This project was supported by the Department of Chemical Engineering at NTNU.

Appendix A. Thermodynamic theory

In this section, a description of three different EOSs is presented: the ideal gas law, the virial expansion, and the SRK-EOS. Next, a general description of chemical reaction equilibrium will be formulated as a minimization problem in terms of the Gibbs and Helmholtz energy functions. Thus, an outline of the optimization theory follows. In order to compute the behavior of real fluid mixtures, residual functions are introduced. The EOSs first presented will then be utilized in the residual functions, and the behavior of the non-ideal gas mixtures are quantified.

A.1. Equations of State

A.1.1. Ideal gas

The ideal gas law is the simplest EOS in terms of model complexity and it often gives a good approximation. For these reasons, it is frequently employed in transport phenomena. Additionally, real gas behavior is defined in the residual framework as the deviation from ideal gas behavior, as discussed in Appendix A.3. The ideal gas law has the following form:

$$p(T,V,\boldsymbol{n}) = \frac{NRT}{V}. \tag{A.1}$$

An ideal gas consists of particles (atoms or molecules) moving freely and independently in space without any inter-particle interactions (Elliott and Lira, 2012, Chap. 1). Furthermore, the particles occupy no volume, and hence, there are no attractive nor repulsive interactions for an ideal gas. These assumptions are generally better at high temperatures, where the kinetic energy is far greater than the inter-particle potential energy, as well as low pressure, where the particles have greater separation distances. For large separation distances, the volume occupied by the particles themselves is less relevant compared to the total volume of the system considered. The low pressure and large separation distances can also be viewed as low density.

The chemical potential of component i in an ideal gas mixture can be shown to be (Elliott and Lira, 2012, Chap. 10)

$$\mu_i^{\text{ig}}(T,p,\boldsymbol{n}) = \mu_i^o(T) + RT\ln\frac{n_i p}{Np_o}, \tag{A.2}$$

where the standard chemical potential is given by (13).

A.1.2. Virial equation of state

In order to quantify real gases with modest deviations from the ideal gas behavior, the virial EOS was chosen. The virial EOS represents a power series expansion in which the virial coefficients are systematically incorporated to correct for the deviations from the ideal gas state. The n-th virial coefficient accounts for interactions between n molecules. For instance, the second virial coefficient accounts for interactions between two colliding molecules. The virial expansion is applicable from low to moderate densities or pressures (Prausnitz et al., 1999, Chap. 5), and as the ideal gas state is characterized by the zero density or pressure limit, the virial expansion is suitable at slight deviations from the ideal gas state.

The virial EOS is primarily a power series in molar density; however, it can readily be recast into a pressure expansion. The virial expansion in terms of pressure reads (truncated after the second term) (Elliott and Lira, 2012, Chap. 7)

$$\frac{pV}{NRT} = 1 + \frac{b(T)}{RT}p, \tag{A.3}$$

where b is the same temperature-dependent virial coefficient as that for the density expansion. For charge-symmetric particles, this (pure component) coefficient is related to the intermolecular pair-potential, $\phi(r)$, through (Hirschfelder et al., 1964)

$$b(T) = 2\pi N_A \int_0^\infty \left(1 - \exp\left(-\frac{\phi(r)}{kT}\right)\right) r^2 dr. \tag{A.4}$$

Here Avogadro's number, Boltzmann's constant and the radial separation are denoted N_A, k, and r, respectively.

In this work, the square well pair-potential was chosen. This has the following mathematical form

$$\phi(r) = \begin{cases} \infty, & r \leqslant \sigma \\ -\varepsilon, & \sigma < r \leqslant \lambda\sigma \\ 0 & r > \lambda\sigma, \end{cases} \tag{A.5}$$

where σ is the radial separation distance where the particles cannot get closer due to their hard sphere volumes, ε is the well depth and $\lambda > 1$ is a parameter used to choose the width of the well. Here all three parameters are fitted to the experimental data of Dymond et al. (2002) for the second virial coefficient. The computed virial coefficients are obtained by inserting (A.5) into (A.4) and performing the integration

$$\begin{aligned} b(T) &= \tfrac{2}{3}\pi N_A \sigma^3 \left[1 + \left(1-\lambda^3\right)\left(\exp\left(\tfrac{\varepsilon}{kT}\right) - 1\right)\right] \\ &= b^{\text{HS}}\left[1 + \left(1-\lambda^3\right)\left(\exp\left(\tfrac{\varepsilon}{kT}\right) - 1\right)\right]. \end{aligned} \tag{A.6}$$

Here b^{HS} denotes the virial coefficient of a corresponding hard sphere pair-potential. The optimized parameter values are given in Table 2.

Combining rules are required for ϕ_{ij} to account for the interactions of unlike molecules. The combining rules used in this study are the Lorentz (1881) combining rule, and those derived from London dispersion forces (Haslam et al., 2008):

$$\sigma_{ij} = \frac{1}{2}\left(\sigma_{ii} + \sigma_{jj}\right) \tag{A.7a}$$

$$\lambda_{ij} = \frac{\sigma_{ii}\lambda_{ii} + \sigma_{jj}\lambda_{jj}}{\sigma_{ii} + \sigma_{jj}} \tag{A.7b}$$

$$\varepsilon_{ij} = 2\frac{\sigma_{ii}^3\sigma_{jj}^3}{\sigma_{ij}^6}\left(\frac{\left(\lambda_{ii}^3 - 1\right)^{1/2}\left(\lambda_{jj}^3 - 1\right)^{1/2}}{\lambda_{ij}^3 - 1}\right)\left(\frac{\left(I_i I_j\right)^{1/2}}{I_i + I_j}\right)\left(\varepsilon_{ii}\varepsilon_{jj}\right)^{1/2}, \tag{A.7c}$$

where I_i is the ionization energy of molecule i taken from Lide (2005). Furthermore, the virial coefficient of the mixture is theoretically derived as

$$NB(T,\boldsymbol{n}) = \sum_{i=1}^{C} n_i \sum_{j=1}^{C} n_j b_{ij}(T), \tag{A.8}$$

where b_{ij} are cross-terms. The cross-terms are determined by inserting (A.7) into (A.6). The resulting EOS reads

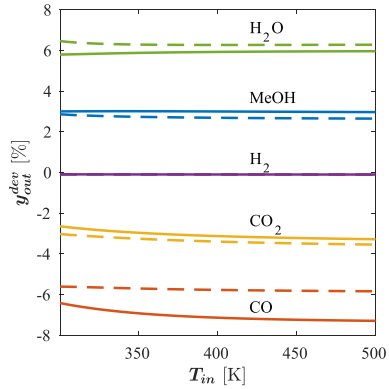

Fig. 20. Mole fraction relative deviation from ideal gas at lowered inlet temperatures for the methanol process. Full lines are from the virial EOS and dashed lines are from SRK.

$$\frac{pV}{NRT} = 1 + \frac{B(T,\boldsymbol{n})}{NRT}p. \tag{A.9}$$

A.1.3. Soave-Redlich-Kwong

For the compounds CO, CO_2, CH_4 in the SMR and methanol processes the SRK-EOS (Soave, 1972) describes the gas behavior satisfactorily (Elliott and Lira, 2012, Chap. D.2). The SRK-EOS is, however, not primarily intended for associating (polar) compounds, such as H_2, H_2O and methanol found in the SMR and the methanol processes. Alternatives such as cubic plus association exist, however in this study no association term is employed. A desirable feature of the SRK-EOS is its ability to predict thermodynamic properties at any conditions of temperature and pressure, although inaccurate results may be obtained far from the region where it was fitted. As the SRK-EOS can handle a broad range of conditions, this EOS is a suitable choice in the transport phenomena framework, where temperature and pressure vary in space and time.

The cubic SRK-EOS represents a further development of the pioneering cubic EOS of van der Waals (1873, chap. 8). The pressure equation for SRK reads

$$p(T,V,\boldsymbol{n}) = \frac{NRT}{V - \mathcal{B}(\boldsymbol{n})} - \frac{D(T,\boldsymbol{n})}{V(V+\mathcal{B})}. \tag{A.10}$$

Here $\mathcal{B}$ denotes an excluded volume and D denotes an attractive term, both of which are functions of the composition of the mixture. The parameters are determined by quadratic mixing rules

$$N\mathcal{B}(\boldsymbol{n}) = \sum_{i=1}^{C} n_i \sum_{j=1}^{C} n_j b_{ij} \tag{A.11a}$$

$$D(T,\boldsymbol{n}) = \sum_{i=1}^{C} n_i \sum_{j=1}^{C} n_j a_{ij}(T), \tag{A.11b}$$

where the cross coefficients b_{ij} and a_{ij} are determined by a set of combining rules. The cross coefficients are functions of their pure component counterpart, b_{ii} and a_{ii}. In this study, the arithmetic mean combining rule was used for b_{ij} and the geometric mean was used for a_{ij}:

$$b_{ij} = \frac{1}{2}(b_{ii} + b_{jj}) \tag{A.12a}$$

$$a_{ij} = \sqrt{a_{ii}a_{jj}}(1 - k_{ij}). \tag{A.12b}$$

Here k_{ij} represents adjustable binary interaction parameters. In the present work, all k_{ij} were set to zero. For the SRK-EOS, the pure component b_{ii} and a_{ii} are computed from (Soave, 1972)

$$b_{ii} = 0.08664\frac{RT_c}{p_c} \tag{A.13a}$$

$$a_{ii} = 0.42747\frac{(RT_c)^2}{p_c}\left(1 + m\left(1 - \sqrt{T/T_c}\right)\right)^2 \tag{A.13b}$$

$$m = 0.480 + 1.574\omega - 0.176\omega^2, \tag{A.13c}$$

where T_c and p_c are the critical temperature and pressure and ω is the acentric factor. Critical parameters and acentric factors were taken from NIST Chemistry WebBook (Lemmon et al., 2019) and are given in Table 3. Further information on the SRK-EOS can be found elsewhere, such as Michelsen and Mollerup (2007, Chap. 3) or the original work of Soave (1972).

A.2. Chemical reaction equilibrium

The total differential of the internal energy function is written

$$dU(S,V,\boldsymbol{n}) = \left(\frac{\partial U}{\partial S}\right)_{V,\boldsymbol{n}} dS + \left(\frac{\partial U}{\partial V}\right)_{S,\boldsymbol{n}} dV + \sum_{i=1}^{C}\left(\frac{\partial U}{\partial n_i}\right)_{S,V,n_{j\neq i}} dn_i, \tag{A.14}$$

where S is the entropy. From the first law of thermodynamics, (A.14) may be rewritten as

$$dU(S,V,\boldsymbol{n}) = TdS - pdV + \sum_{i=1}^{C}\mu_i dn_i. \tag{A.15}$$

By a Legendre transformation, the Helmholtz and Gibbs energy functions are *defined* as (Callen, 1985; Hołyst and Poniewierski, 2012)

$$A(T,V,\boldsymbol{n}) \equiv U - \left(\frac{\partial U}{\partial S}\right)_{V,\boldsymbol{n}} S = U - TS \tag{A.16a}$$

$$G(T,p,\boldsymbol{n}) \equiv U - \left(\frac{\partial U}{\partial S}\right)_{V,\boldsymbol{n}} S - \left(\frac{\partial U}{\partial V}\right)_{S,\boldsymbol{n}} V = U - TS + pV. \tag{A.16b}$$

By virtue of being an Euler-homogeneous function of degree one, the internal energy function in (A.15) can be integrated to

$$U(S,V,\boldsymbol{n}) = TS - pV + \sum_{i=1}^{C}\mu_i n_i, \tag{A.17}$$

which is used in combination with (A.16) to obtain the more frequently encountered form of the Helmholtz and Gibbs energy functions

$$A(T,V,\boldsymbol{n}) = -pV + \sum_{i=1}^{C}\mu_i n_i \tag{A.18a}$$

$$G(T,p,\boldsymbol{n}) = \sum_{i=1}^{C}\mu_i n_i. \tag{A.18b}$$

Table 2
Fitted parameters for a square well potential.

Property	CH_4	CO	CO_2	H_2	H_2O	MeOH
σ [Å]	3.3515	3.3437	3.4155	2.5362	2.7905	0.3790
ε $\left[10^{-20}\ \mathrm{J}\right]$	0.1873	0.1215	0.4527	0.0680	1.5900	2.3036
λ [–]	1.6252	1.6419	1.3968	1.3994	1.2185	4.5757

Table 3
Fluid properties for the components.

Property	CH_4	CO	CO_2	H_2	H_2O	MeOH
T_c [K]	190.56	132.86	304.13	33.145	647.096	512.6
p_c [MPa]	4.5992	3.4935	7.3773	1.2964	22.0640	8.1035
ω [–]	0.01142	0.050	0.22394	−0.219	0.3443	0.5625

The total differential of the Helmholtz and Gibbs energy functions are

$$dA(T,V,\boldsymbol{n}) = \left(\frac{\partial A}{\partial T}\right)_{V,\boldsymbol{n}} dT + \left(\frac{\partial A}{\partial V}\right)_{T,\boldsymbol{n}} dV + \sum_{i=1}^{C}\left(\frac{\partial A}{\partial n_i}\right)_{T,V,n_{j\neq i}} dn_i \quad \text{(A.19a)}$$

$$dG(T,p,\boldsymbol{n}) = \left(\frac{\partial G}{\partial T}\right)_{p,\boldsymbol{n}} dT + \left(\frac{\partial G}{\partial p}\right)_{T,\boldsymbol{n}} dp + \sum_{i=1}^{C}\left(\frac{\partial G}{\partial n_i}\right)_{T,p,n_{j\neq i}} dn_i. \quad \text{(A.19b)}$$

However, they can equivalently be obtained by differentiating (A.16) and inserting the total differential for the internal energy function in (A.15):

$$\begin{aligned} dA(T,V,\boldsymbol{n}) &= dU - TdS - SdT \\ &= -SdT - pdV + \sum_{i=1}^{C}\mu_i dn_i \end{aligned} \quad \text{(A.20a)}$$

$$\begin{aligned} dG(T,p,\boldsymbol{n}) &= dU - TdS - SdT + pdV + Vdp \\ &= -SdT + Vdp + \sum_{i=1}^{C}\mu_i dn_i. \end{aligned} \quad \text{(A.20b)}$$

By comparing (A.19) and (A.20), six identities are obtained. The result is presented in Table 4.

The equilibrium state is the set of variables that minimizes the energy function chosen. That is, the set $\{T,V,\boldsymbol{n}\}$ that minimizes A at a fixed temperature, or the set $\{T,p,\boldsymbol{n}\}$ that minimizes G at fixed temperature and pressure. For both the Helmholtz and the Gibbs energy functions, the vector of mole numbers, $\boldsymbol{n}$, must be determined in the respective optimization problem formulation. If multiple phases are present, the volume root of the EOS utilized must be identified for each phase subject to an additional constraint (Pereira et al., 2010). In the Helmholtz energy function formulation, the phase volumes are constrained by the specified total volume, V_0, of the system considered, i.e. the total volume of the nodal discretization point. Thus, it is sufficient to specify the temperature and total volume in order to solve the minimum Helmholtz energy problem. On the other hand, if the Gibbs energy function is chosen, the phase volumes are constrained by the specified pressure, i.e. the pressure at the nodal discretization point. Thus, it is sufficient to specify temperature and pressure in order to solve the minimum Gibbs energy problem. Although only one phase is considered in this work, the volume is included in the Helmholtz energy function formulation in order to construct a routine that only needs minor modifications to handle multiphase systems.

Table 4
Thermodynamic identities for the Helmholtz and Gibbs energy functions.

Helmholtz		Gibbs	
$S = -\left(\frac{\partial A}{\partial T}\right)_{V,\boldsymbol{n}}$	(A.21)	$S = -\left(\frac{\partial G}{\partial T}\right)_{p,\boldsymbol{n}}$	(A.22)
$p = -\left(\frac{\partial A}{\partial V}\right)_{T,\boldsymbol{n}}$	(A.23)	$V = \left(\frac{\partial G}{\partial p}\right)_{T,\boldsymbol{n}}$	(A.24)
$\mu_i = \left(\frac{\partial A}{\partial n_i}\right)_{T,V,n_{j\neq i}}$	(A.25)	$\mu_i = \left(\frac{\partial G}{\partial n_i}\right)_{T,p,n_{j\neq i}}$	(A.26)

The state of equilibrium is found by formulating and solving an optimization problem, either for the Helmholtz energy function as

$$\begin{aligned} &\min_{V,n_1,n_2,\ldots,n_C} (A)_T \\ &V = V_o \text{ s.t.} \sum_{j=1}^{C} A_{ij} n_j = b_i, \quad i = 1,2,\ldots,N_{el} \\ &\qquad\qquad n_i \geqslant 0, \quad i = 1,2,\ldots,C, \end{aligned} \quad \text{(A.27)}$$

or the Gibbs energy function as

$$\begin{aligned} &\min_{n_1,n_2,\ldots,n_C} (G)_{T,p} \\ &\text{s.t.} \sum_{j=1}^{C} A_{ij} n_j \;= b_i, \quad i = 1,2,\ldots,N_{el} \\ &\qquad n_i \qquad\quad \geqslant 0, \quad i = 1,2,\ldots,C. \end{aligned} \quad \text{(A.28)}$$

As there is only one phase present in the systems considered in this work, there is only one phase volume present in the Helmholtz problem in (A.27). Hence, the volume constraint is reduced, and the phase considered occupies the entire total volume.

The equilibrium problems can be solved by the method of Lagrangian multipliers as described in Taylor (2010) and Nocedal and Wright (2006). First, the minimization problem in terms of the Helmholtz energy function is discussed, and subsequently, minimizing the Gibbs energy function is treated. In order to minimize the Helmholtz energy function subject to the constraints written on residual form, $\sum_{j=1}^{C} A_{ij} n_j - b_i$ and $V - V_0$, the Lagrangian function is defined:

$$\mathcal{L}(V,\boldsymbol{n},\boldsymbol{\lambda}) = A(T,V,\boldsymbol{n}) - \lambda_1(V - V_0) - \sum_{i=1}^{N_{el}}\sum_{j=1}^{C}\lambda_{i+1}\left(A_{ij}n_j - b_i\right). \quad \text{(A.29)}$$

By using the Lagrangian function instead of the Helmholtz energy function directly, we can ensure that the constraints are satisfied at the minimum. Here $(V,\boldsymbol{n})$ represents the vector of decision variables (the variables to find in the optimization problem) and λ_i represents the Lagrangian multipliers.

To iterate towards a minimum, a search direction is to be specified. Newton's method is chosen in this study due to its quadratic convergence property. The resulting step, called the Newton step, is obtained from a second-order Taylor expansion on (A.29) around $(V,\boldsymbol{n},\boldsymbol{\lambda})$:

$$\begin{aligned} \mathcal{L}'(V + p_V, \boldsymbol{n} + \boldsymbol{p}_{\boldsymbol{n}}, \boldsymbol{\lambda} + \boldsymbol{p}_{\lambda}) \approx\; & \mathcal{L}(V,\boldsymbol{n},\boldsymbol{\lambda}) \\ & + \left[\mathcal{L}_V p_V + \sum_{j=1}^{C}\mathcal{L}_{n_j} p_{n_j} + \sum_{j=1}^{N_{el}+1}\mathcal{L}_{\lambda_j} p_{\lambda_j}\right] \\ & + \frac{1}{2}\left[\left[\mathcal{L}_{VV} p_V^2 + \sum_{j=1}^{C}\mathcal{L}_{Vn_j} p_V p_{n_j} + \sum_{j=1}^{N_{el}+1}\mathcal{L}_{V\lambda_j} p_V p_{\lambda_j}\right]\right. \\ & + \sum_{i=1}^{C}\left[\mathcal{L}_{n_i V} p_{n_i} p_V + \sum_{j=1}^{C}\mathcal{L}_{n_i n_j} p_{n_i} p_{n_j} + \sum_{j=1}^{N_{el}+1}\mathcal{L}_{n_i\lambda_j} p_{n_i} p_{\lambda_j}\right] \\ & \left. + \sum_{i=1}^{N_{el}+1}\left[\mathcal{L}_{\lambda_i V} p_{\lambda_i} p_V + \sum_{j=1}^{C}\mathcal{L}_{\lambda_i n_j} p_{\lambda_i} p_{n_j} + \sum_{j=1}^{N_{el}+1}\mathcal{L}_{\lambda_i\lambda_j} p_{\lambda_i} p_{\lambda_j}\right]\right], \end{aligned} \quad \text{(A.30)}$$

where $\boldsymbol{p} = (p_V, \boldsymbol{p_n}, \boldsymbol{p_\lambda})^\top$ is the Newton step vector, and a short-hand notation is used to denote partial derivatives with respect to the independent variables. For instance, $\mathcal{L}_{Vn_j} = \left(\frac{\partial^2 \mathcal{L}}{\partial V \partial n_j}\right)_{n_{k\neq j}, \boldsymbol{\lambda}}$ denotes the partial derivative with respect to V and n_j while keeping all other mole numbers, n_k, and Lagrangian multipliers, $\boldsymbol{\lambda}$, constant. In (A.30), the first bracket represents all first derivatives, and the second bracket containing all remaining elements represents the second derivatives. The Lagrangian function evaluated at the new location $(V + p_V, \boldsymbol{n} + \boldsymbol{p_n}, \boldsymbol{\lambda} + \boldsymbol{p_\lambda})$ is indicated by $\mathcal{L}\prime$.

At the minimum, the gradient of (A.30) is zero. By differentiating (A.30) with respect to p_V, p_{n_i} and p_{λ_i}, we obtain $2 + C + N_{el}$ equations:

$$\mathcal{L}'_{p_V} = \mathcal{L}_V + \mathcal{L}_{VV} p_V + \sum_{j=1}^{C} \mathcal{L}_{Vn_j} p_{n_j} + \sum_{j=1}^{N_{el}+1} \mathcal{L}_{V\lambda_j} p_{\lambda_j} \tag{A.31a}$$

$$\mathcal{L}'_{p_{n_i}} = \mathcal{L}_{n_i} + \mathcal{L}_{n_i V} p_V + \sum_{j=1}^{C} \mathcal{L}_{n_i n_j} p_{n_j} + \sum_{j=1}^{N_{el}+1} \mathcal{L}_{n_i \lambda_j} p_{\lambda_j} \tag{A.31b}$$

$$\mathcal{L}'_{p_{\lambda_i}} = \mathcal{L}_{\lambda_i} + \mathcal{L}_{\lambda_i V} p_V + \sum_{j=1}^{C} \mathcal{L}_{\lambda_i n_j} p_{n_j} + \sum_{j=1}^{N_{el}+1} \mathcal{L}_{\lambda_i \lambda_j} p_{\lambda_j}, \tag{A.31c}$$

where $i = 1, 2, \ldots C$ in (A.31b) and $i = 1, 2, \ldots N_{el} + 1$ in (A.31c). In all the equations in (A.31), the first term on the right-hand side represents the first derivative and the following terms represent the second derivatives of the Lagrangian function in (A.29). Differentiation of (A.29) with respect to V, n_i and λ_i yields

$$\begin{pmatrix} \mathcal{L}_V \\ \mathcal{L}_{n_i} \\ \mathcal{L}_{\lambda_1} \\ \mathcal{L}_{\lambda_{i\neq 1}} \end{pmatrix} = \begin{pmatrix} \left(\frac{\partial A}{\partial V}\right)_{T,\boldsymbol{n}} - \lambda_1 \\ \left(\frac{\partial A}{\partial n_i}\right)_{T,V,n_{j\neq i}} - \sum_{j=1}^{N_{el}} A_{ji}\lambda_{j+1} \\ V_0 - V \\ b_i - \sum_{j=1}^{C} A_{ij} n_j \end{pmatrix} \tag{A.32}$$

The notation $\lambda_{i\neq 1}$ with $i = 2, 3, \ldots, N_{el} + 1$ has been used to represent the Lagrangian multipliers related to the elemental balance constraints. By further differentiating (A.32), the second derivatives are obtained:

$$\begin{pmatrix} \mathcal{L}_{VV} & \mathcal{L}_{Vn_i} & \mathcal{L}_{V\lambda_1} & \mathcal{L}_{V\lambda_{i\neq 1}} \\ \mathcal{L}_{n_i V} & \mathcal{L}_{n_i n_j} & \mathcal{L}_{n_i \lambda_1} & \mathcal{L}_{n_i \lambda_{j\neq 1}} \\ \mathcal{L}_{\lambda_1 V} & \mathcal{L}_{\lambda_1 n_i} & \mathcal{L}_{\lambda_1 \lambda_1} & \mathcal{L}_{\lambda_1 \lambda_{j\neq 1}} \\ \mathcal{L}_{\lambda_{i\neq 1} V} & \mathcal{L}_{\lambda_{i\neq 1} n_j} & \mathcal{L}_{\lambda_{i\neq 1}\lambda_1} & \mathcal{L}_{\lambda_{i\neq 1}\lambda_{j\neq 1}} \end{pmatrix} = \begin{pmatrix} \left(\frac{\partial^2 A}{\partial V^2}\right)_{T,\boldsymbol{n}} & \left(\frac{\partial^2 A}{\partial V \partial n_i}\right)_{T,n_{j\neq i}} & -1 & 0 \\ \left(\frac{\partial^2 A}{\partial n_i \partial V}\right)_{T,n_{j\neq i}} & \left(\frac{\partial^2 A}{\partial n_i \partial n_j}\right)_{T,V,n_{k\neq ij}} & 0 & -A_{ji} \\ -1 & 0 & 0 & 0 \\ 0 & -A_{ij} & 0 & 0 \end{pmatrix}. \tag{A.33}$$

By inspecting the first and second derivatives in (A.32) and (A.33), respectively, some simplifications can be made to the gradient of the Lagrangian in (A.31). In (A.31a) and (A.31b), the first and last terms on the right-hand side have cancelling terms. The definition of the step in the Lagrangian multipliers are $p_\lambda^{\nu+1} = \lambda^{\nu+1} - \lambda^\nu$, where ν denotes the iteration number. By employing this definition along with the first and second derivatives of (A.32) and (A.33), the first and fourth terms of the right-hand side of (A.31a) and (A.31b) are expanded as:

$$\left[\left(\frac{\partial A}{\partial V}\right)^\nu_{T,\boldsymbol{n}} - \cancel{\lambda_1^\nu}\right] + \left[-(\lambda_1^{\nu+1} - \cancel{\lambda_1^\nu})\right] = \left(\frac{\partial A}{\partial V}\right)^\nu_{T,\boldsymbol{n}} - \lambda_1^{\nu+1} \tag{A.34a}$$

$$\left[\left(\frac{\partial A}{\partial n_i}\right)^\nu_{T,V,n_{j\neq i}} - \cancel{\sum_{j=1}^{N_{el}} A_{ji}\lambda_{j+1}^\nu}\right] + \left[\sum_{j=1}^{N_{el}} -A_{ji}(\lambda_{j+1}^{\nu+1} - \cancel{\lambda_{j+1}^\nu})\right] = \left(\frac{\partial A}{\partial n_i}\right)^\nu_{T,V,n_{j\neq i}} - \sum_{j=1}^{N_{el}} A_{ji}\lambda_{j+1}^{\nu+1}. \tag{A.34b}$$

In (A.34a), the first and second brackets denote the first and fourth term of (A.31a), respectively. Similarly, the first and second brackets of (A.34a) denote the first and fourth term of (A.31b), respectively.

From the lower right quadrant of (A.33), it is seen that all derivatives in the last summation of (A.31c) are zero. Hence, (A.31c) is independent of p_λ. The remaining equations, (A.31a) and (A.31b), eliminated λ^ν by (A.34), and as a result, λ^ν is not required in order to solve the system of equations. Thus, no initial guess of λ is required, and the new Lagrangian multipliers, $\lambda^{\nu+1}$, are obtained independently of the previous values by solving the system of Eqs. (A.31).

The derivatives in (A.32) and (A.33) along with the simplifications in (A.34) are inserted into (A.31). For optimal steps, the left-hand side is set to zero, yielding:

$$0 = \left[\left(\frac{\partial A}{\partial V}\right)^\nu_{T,\boldsymbol{n}}\right] + \left[\left(\frac{\partial^2 A}{\partial V^2}\right)^\nu_{T,\boldsymbol{n}}\right] p_V^{\nu+1} + \sum_{j=1}^{C}\left[\left(\frac{\partial^2 A}{\partial V \partial n_j}\right)^\nu_{T,n_{k\neq j}}\right] p_{n_j}^{\nu+1} + [-1]\lambda_1^{\nu+1} \tag{A.35a}$$

$$0 = \left[\left(\frac{\partial A}{\partial n_i}\right)^\nu_{T,V,n_{j\neq i}}\right] + \left[\left(\frac{\partial^2 A}{\partial n_i \partial V}\right)^\nu_{T,n_{j\neq i}}\right] p_V^{\nu+1} + \sum_{j=1}^{C}\left[\left(\frac{\partial^2 A}{\partial n_i \partial n_j}\right)^\nu_{T,n_{k\neq ij}}\right] p_{n_j}^{\nu+1} + \sum_{j=1}^{N_{el}}[-A_{ji}]\lambda_{j+1}^{\nu+1} \tag{A.35b}$$

$$0 = [V_0 - V^\nu] + [-1]p_V^{\nu+1} \tag{A.35c}$$

$$0 = \left[b_i - \sum_{j=1}^{C} A_{ij} n_j^\nu\right] + \sum_{j=1}^{C}[-A_{ij}]p_{n_j}^{\nu+1}. \tag{A.35d}$$

Here the inserted derivatives are indicated by brackets. Solving (A.35) for the first derivatives and multiplying the results by -1 yield the Newton iteration scheme:

$$\left(\frac{\partial A}{\partial V}\right)^\nu_{T,\boldsymbol{n}} = \left(\frac{\partial^2 A}{\partial V^2}\right)^\nu_{T,\boldsymbol{n}} (-p_V^{\nu+1}) + \sum_{j=1}^{C}\left(\frac{\partial^2 A}{\partial V \partial n_j}\right)^\nu_{T,n_{k\neq j}} \left(-p_{n_j}^{\nu+1}\right) + \lambda_1^{\nu+1} \tag{A.36a}$$

$$\left(\frac{\partial A}{\partial n_i}\right)^\nu_{T,V,n_{j\neq i}} = \left(\frac{\partial^2 A}{\partial n_i \partial V}\right)^\nu_{T,n_{j\neq i}} (-p_V^{\nu+1}) + \sum_{j=1}^{C}\left(\frac{\partial^2 A}{\partial n_i \partial n_j}\right)^\nu_{T,V,n_{k\neq ij}} \left(-p_{n_j}^{\nu+1}\right) + \sum_{j=1}^{N_{el}} A_{ji}\lambda_{j+1}^{\nu+1} \tag{A.36b}$$

$$V^\nu - V_0 = \left(-p_V^{\nu+1}\right) \tag{A.36c}$$

$$\sum_{j=1}^{C} A_{ij} n_j^\nu - b_i = \sum_{j=1}^{C} A_{ij}\left(-p_{n_j}^{\nu+1}\right). \tag{A.36d}$$

The first and second derivatives of the Helmholtz energy function in (A.36) are gathered in matrix notation as:

$$\boldsymbol{J}_A = \begin{pmatrix} \left(\frac{\partial A}{\partial V}\right)_{T,\boldsymbol{n}} \\ \left(\frac{\partial A}{\partial \boldsymbol{n}}\right)_{T,V} \end{pmatrix} = \begin{pmatrix} -p \\ \boldsymbol{\mu} \end{pmatrix} \tag{A.37a}$$

$$\begin{aligned} \boldsymbol{H}_A &= \begin{pmatrix} \left(\frac{\partial^2 A}{\partial V^2}\right)_{V,\boldsymbol{n}} & \left(\frac{\partial^2 A}{\partial V \partial \boldsymbol{n}^\top}\right)_T \\ \left(\frac{\partial^2 A}{\partial \boldsymbol{n} \partial V}\right)_T & \left(\frac{\partial^2 A}{\partial \boldsymbol{n} \partial \boldsymbol{n}^\top}\right)_{T,V} \end{pmatrix} \\ &= \begin{pmatrix} -\left(\frac{\partial p}{\partial V}\right)_{T,\boldsymbol{n}} & -\left(\frac{\partial p}{\partial \boldsymbol{n}^\top}\right)_{T,V} \\ \left(\frac{\partial \boldsymbol{\mu}}{\partial V}\right)_{T,\boldsymbol{n}} & \left(\frac{\partial \boldsymbol{\mu}}{\partial \boldsymbol{n}^\top}\right)_{T,V} \end{pmatrix}, \end{aligned} \tag{A.37b}$$

and are referred to as the Jacobian and Hessian functions, respectively. The last equalities in (A.37a) and (A.37b) were obtained by employing (A.23) and (A.25) in Table 4. Utilizing the short-hand notation of (A.37), the system of equations in (A.36) is rewritten on matrix form as

$$\begin{pmatrix} \boldsymbol{H}_A & \begin{pmatrix} 1 & \boldsymbol{0} \\ \boldsymbol{0} & \boldsymbol{A} \end{pmatrix}^\top \\ \begin{pmatrix} 1 & \boldsymbol{0} \\ \boldsymbol{0} & \boldsymbol{A} \end{pmatrix} & \begin{pmatrix} 0 & \boldsymbol{0} \\ \boldsymbol{0} & \boldsymbol{0} \end{pmatrix} \end{pmatrix}^{\nu} \begin{pmatrix} -\begin{pmatrix} p_V \\ \boldsymbol{p_n} \end{pmatrix} \\ \lambda_1 \\ \lambda_{i\neq 1} \end{pmatrix}^{\nu+1} = \begin{pmatrix} \boldsymbol{J}_A \\ V - V_0 \\ \boldsymbol{An} - \boldsymbol{b} \end{pmatrix}^{\nu}. \tag{7}$$

The system of equations in (7) along with the Jacobian and Hessian functions in (A.37) represent an iterative scheme for minimizing the Helmholtz energy function.

The Gibbs energy function is approached in the same manner as the Helmholtz energy function by forming a Lagrangian function:

$$\mathcal{L}(\boldsymbol{n}, \boldsymbol{\lambda}) = G(T, p, \boldsymbol{n}) - \sum_{i=1}^{N_{el}} \sum_{j=1}^{C} \lambda_i (A_{ij} n_j - b_i). \tag{A.38}$$

Following the systematic procedure in (A.30)–(A.36) employed for the Helmholtz energy function, the system of equations on matrix form now reads

$$\begin{pmatrix} \boldsymbol{H}_G & \boldsymbol{A}^\top \\ \boldsymbol{A} & \boldsymbol{0} \end{pmatrix}^{\nu} \begin{pmatrix} -\boldsymbol{p_n} \\ \boldsymbol{\lambda} \end{pmatrix}^{\nu+1} = \begin{pmatrix} \boldsymbol{J}_G \\ \boldsymbol{An} - \boldsymbol{b} \end{pmatrix}^{\nu} \tag{8}$$

instead of (7). With identity (A.26) in Table 4, the Jacobian and Hessian functions of the Gibbs energy function in the system of Eqs. (8) are written as

$$\boldsymbol{J}_G = \left(\frac{\partial G}{\partial \boldsymbol{n}}\right)_{T,p} = \boldsymbol{\mu} \tag{A.39a}$$

$$\boldsymbol{H}_G = \left(\frac{\partial^2 G}{\partial \boldsymbol{n} \partial \boldsymbol{n}^\top}\right)_{T,p} = \left(\frac{\partial \boldsymbol{\mu}}{\partial \boldsymbol{n}^\top}\right)_{T,p}. \tag{A.39b}$$

The system of equations in (8) along with the Jacobian and Hessian functions in (A.39) represent an iterative scheme for minimizing the Gibbs energy function.

In both the Gibbs and Helmholtz energy function formulations, it is necessary to ensure that the mole numbers are positive at all iterations, since the chemical potential is undefined for any $n_i < 0$, as seen for ideal gas in (A.2). To accept the step $\boldsymbol{p}_{\boldsymbol{n}}^{\nu+1}$, it is required that n_i remains positive. This is implemented as $n_i^{\nu+1} = n_i^{\nu} + \alpha^{\nu} p_{n_i}^{\nu+1} \geqslant 0, \forall i$, where α represents a scaling factor. This equation is rearranged so that $\alpha^{\nu} \leqslant -\frac{n_i^{\nu}}{p_{n_i}^{\nu+1}}, \forall i$. Hence,

$$\alpha^{\nu} = \min\left(1, \min_{p_{n_i}<0} \frac{-n_i^{\nu}}{p_{n_i}^{\nu+1}}\right). \tag{A.40}$$

In (A.40), the most violating step $p_{n_i}^{\nu+1}$ determines α^{ν}. If no constraints are violated, $\alpha^{\nu} = 1$. For the Helmholtz energy function, the step in V and $\boldsymbol{\lambda}$ must be shortened by the same α^{ν}, so that (7) is satisfied. In terms of the Gibbs energy function, the scaling affects $\boldsymbol{n}$ and $\boldsymbol{\lambda}$ only.

At the optimal solution, the first-order conditions known as the Karush–Kuhn–Tucker (KKT) conditions must be satisfied (Nocedal and Wright, 2006, p. 321)(Kuhn and Tucker, 1951)

$$\nabla_{\boldsymbol{x}} \mathcal{L}(\boldsymbol{x}^*, \boldsymbol{\lambda}^*) = 0 \tag{A.41a}$$

$$c_i(\boldsymbol{x}^*) = 0, \quad \text{for all } i \in \mathcal{E} \tag{A.41b}$$

$$c_i(\boldsymbol{x}^*) \geqslant 0, \quad \text{for all } i \in \mathcal{I} \tag{A.41c}$$

$$\lambda_i^* \geqslant 0, \quad \text{for all } i \in \mathcal{I} \tag{A.41d}$$

$$\lambda_i^* c_i(\boldsymbol{x}^*) = 0, \quad \text{for all } i \in \mathcal{E} \cup \mathcal{I}, \tag{A.41e}$$

where $\boldsymbol{x}$ represents the vector of decision variables, $(V, \boldsymbol{n})$ or $\boldsymbol{n}$, c_i is constraint i, $*$ indicates the trial solution (which is optimal when (A.41) is satisfied) and $\mathcal{E}$ and $\mathcal{I}$ represent the set of equality ($\boldsymbol{An} - \boldsymbol{b}$ and $V - V_0$) and inequality constraints ($\boldsymbol{n} \geqslant \boldsymbol{0}$), respectively. Since α limits the step to never break any inequalities, (A.41c) and (A.41d) are automatically satisfied. Solving the system (7) or (8) ensures that (A.41b) is satisfied and therefore also (A.41e). Satisfying (A.41a) is an iterative process, however when this condition is fulfilled, the KKT conditions are satisfied.

A.3. Residual properties

Residual functions are defined as the deviation between a real fluid from the ideal gas behavior in the same state. Hence, incorporating the framework of residual functions in the solution of the energy minimization problems (5) and (6) allow us to consider chemical equilibrium compositions of real fluids. It is emphasized that all residual functions are zero if the ideal gas law in (A.1) is employed.

Gibbs energy: For the Gibbs energy function, the residual is defined as

$$G^{r,p}(T, p, \boldsymbol{n}) \equiv G(T, p, \boldsymbol{n}) - G^{\text{ig}}(T, p, \boldsymbol{n}), \tag{A.42}$$

where the superscript ig is used to denote ideal gas and r, p is used to denote the residual with respect to pressure. Hence, in order to determine the Gibbs energy function of the real fluid mixture:

$$G(T, p, \boldsymbol{n}) = G^{\text{ig}}(T, p, \boldsymbol{n}) + G^{r,p}(T, p, \boldsymbol{n}). \tag{A.43}$$

Furthermore, we need expressions for the ideal gas- and residual Gibbs energy functions. By the linearity of the differentiation operators, the Jacobian and Hessian functions required in (A.39) are determined by the ideal gas and residual Jacobian and Hessian:

$$\mathbf{J}_G = \mathbf{J}_G^{\text{ig}} + \mathbf{J}_G^{r,p} \tag{A.44a}$$

$$\mathbf{H}_G = \mathbf{H}_G^{\text{ig}} + \mathbf{H}_G^{r,p}. \tag{A.44b}$$

The ideal gas Gibbs energy function is found from (A.18b):

$$G^{\text{ig}} = \sum_{i=1}^{C} \mu_i^{\text{ig}} n_i, \tag{A.45}$$

where the chemical potential of component i for an ideal gas was given in (A.2). The required Jacobian and Hessian functions of the ideal gas Gibbs energy function is found by differentiating (A.45) with respect to n_i. The result is given by (A.39) written out for ideal gas

$$\boldsymbol{J}_G^{\text{ig}} = \boldsymbol{\mu}^o(T) + RT \ln \frac{\boldsymbol{n}p}{Np_o} \tag{12a}$$

$$\boldsymbol{H}_G^{\text{ig}} = RT\left(\boldsymbol{D} - \frac{1}{N}\boldsymbol{e}\boldsymbol{e}^\top\right). \tag{12b}$$

The residual Gibbs energy function is written as (Haug-Warberg, 2006)

$$G^{r,p} = \int_0^p \left(\left(\frac{\partial G}{\partial \pi} \right)_{T,\boldsymbol{n}} - \left(\frac{\partial G^{\mathrm{ig}}}{\partial \pi} \right)_{T,\boldsymbol{n}} \right) d\pi, \tag{A.47}$$

where π indicates a variable of integration. The equation above is rewritten by inserting the identity (A.24) of the partial derivative of G and substituting the ideal gas law (A.1) for V^{ig}:

$$G^{r,p} = \int_0^p \left(V(\pi) - \frac{NRT}{\pi} \right) d\pi. \tag{A.48}$$

The residual function in (A.48) can be computed without any further manipulations of the integral for EOSs that are explicit in volume, like the virial EOS in (A.9) (Elliott and Lira, 2012). Subsequently, residual functions such as the residual chemical potential and entropy can readily be obtained by differentiation using Table 4, see (A.52).

The required residual Jacobian and Hessian functions are given, respectively, as

$$\boldsymbol{J}_G^{r,p} = RT \ln \boldsymbol{\varphi} \equiv \boldsymbol{\mu}^{r,p} = \left(\frac{\partial G^{r,p}}{\partial \boldsymbol{n}} \right)_{T,p} \tag{A.49a}$$

$$\boldsymbol{H}_G^{r,p} = RT \left(\frac{\partial \ln \boldsymbol{\varphi}}{\partial \boldsymbol{n}} \right)_{T,p} = \left(\frac{\partial \boldsymbol{\mu}^{r,p}}{\partial \boldsymbol{n}^\top} \right)_{T,p} = \left(\frac{\partial^2 G^{r,p}}{\partial \boldsymbol{n} \partial \boldsymbol{n}^\top} \right)_{T,p}, \tag{A.49b}$$

where the fugacity coefficient, φ_i, has been defined as the residual chemical potential at specified temperature and pressure. In terms of the virial expansion, the first and second-order derivatives of the far right-hand side of (A.49) are calculated from (B.10) and (B.11), respectively. In terms of the SRK-EOS, the fugacity coefficient and its derivative with respect to mole numbers are implicitly computed through the Helmholtz energy function, that is (Michelsen and Mollerup, 2007, p. 64)

$$\ln \varphi_i = \frac{1}{RT} \left(\frac{\partial A^{r,v}}{\partial n_i} \right)_{T,V,n_{j\neq i}} - \ln Z \tag{A.50a}$$

$$\begin{aligned} \left(\frac{\partial \ln \varphi_i}{\partial n_j} \right)_{T,p,n_{k\neq j}} &= \frac{1}{RT} \left(\frac{\partial^2 A^{r,v}}{\partial n_i \partial n_j} \right)_{T,V,n_{k\neq j}} + \frac{1}{N} \\ &\quad + \frac{1}{RT} \frac{\left(\frac{\partial p}{\partial n_i} \right)_{T,V,n_{k\neq i}} \left(\frac{\partial p}{\partial n_j} \right)_{T,V,n_{k\neq j}}}{\left(\frac{\partial p}{\partial V} \right)_{T,\boldsymbol{n}}}, \end{aligned} \tag{A.50b}$$

where the compressibility factor is $Z = pV/NRT$, and V is computed at given $T, p, \boldsymbol{n}$ by (16).

In transport phenomena, the most common is to utilize the temperature and pressure fields computed from the temperature and momentum/continuity equations to perform thermodynamic computations. Thus, heat capacities and derivatives with respect to mole numbers are evaluated at constant pressure, and the variables of interest include the specific isobaric heat capacity, c_p, and the partial molar enthalpy, $\overline{h}_i \equiv (\partial H/\partial n_i)_{T,p}$, for the temperature equation. The extensive heat capacity is defined as

$$C_p \equiv T \left(\frac{\partial S}{\partial T} \right)_{p,\boldsymbol{n}} = -T \left(\frac{\partial^2 G}{\partial T^2} \right)_{p,\boldsymbol{n}}, \tag{22}$$

where identity (A.22) is used for entropy. Hence, the residual heat capacity is given by

$$C_p^{r,p} = -T \left(\frac{\partial^2 G^{r,p}}{\partial T^2} \right)_{p,\boldsymbol{n}}. \tag{A.51}$$

For the virial expansion, (A.51) may be used in combination with the derivatives in (B.11). However, for the SRK-EOS, which is explicit in pressure, the residual isobaric heat capacity is evaluated through the Helmholtz energy function, see (A.62d).

The heat capacity of the real fluid mixture is obtained by summing the ideal gas contribution shown in (14) and the residual contribution discussed above. The resulting heat capacity is divided by the total mass with (25) to obtain the specific heat capacity required for the temperature equation in Section 2.

The partial molar property of a generic extensive quantity $X(T, p, \boldsymbol{n})$ is defined as $\overline{x}_i \equiv \left(\frac{\partial X}{\partial n_i} \right)_{T,p}$. This definition along with the identities for entropy (A.22) and chemical potential (A.26) yield the following partial molar properties:

$$\overline{g}_i^{r,p} \equiv \mu_i^{r,p} = \left(\frac{\partial G^{r,p}}{\partial n_i} \right)_{T,p,n_{j\neq i}} \tag{A.52a}$$

$$\overline{s}_i^{r,p} = -\left(\frac{\partial^2 G^{r,p}}{\partial T \partial n_i} \right)_{p,n_{j\neq i}}, \tag{A.52b}$$

where the partial derivatives of the Gibbs energy function depend on the choice of EOS and are given for the virial expansion in Appendix B. For the SRK-EOS, they are given through the Helmholtz energy function, see e.g. (A.50a) for $\overline{g}_i^{r,p}$.

The partial molar enthalpy required for the temperature equation in Section 2 is given by its relation to the Gibbs energy function: $H = G + TS$. By the linearity of the differentiation operator, the derivative of enthalpy with respect to mole numbers at constant temperature and pressure yields

$$\overline{h}_i^{r,p} = \overline{g}_i^{r,p} + T\overline{s}_i^{r,p}. \tag{A.53}$$

For the virial expansion, (A.53) is used in combination with (A.52). However, for the SRK-EOS, which is explicit in pressure, the residual partial molar enthalpy is evaluated through the Helmholtz energy function, see (A.62b). The partial molar enthalpy of the real gas mixture is obtained by adding the ideal gas partial molar enthalpy shown in (13) to the residual contribution.

Helmholtz energy: For the Helmholtz energy function, the residual function is defined as

$$A^{r,v}(T, V, \boldsymbol{n}) \equiv A(T, V, \boldsymbol{n}) - A^{\mathrm{ig}}(T, V, \boldsymbol{n}), \tag{A.54}$$

where the superscript r, v is used to denote residual with respect to volume. That is, the real fluid and the ideal gas fluid are evaluated at the same temperature and volume. Hence, in order to determine the Helmholtz energy function of the real fluid mixture:

$$A(T, V, \boldsymbol{n}) = A^{\mathrm{ig}}(T, V, \boldsymbol{n}) + A^{r,v}(T, V, \boldsymbol{n}). \tag{A.55}$$

Furthermore, we need expressions for the ideal- and residual Helmholtz energy functions. Following the derivation of the Gibbs energy function, the required properties for the chemical equilibrium problem consist of the Jacobian and Hessian functions of the real fluid mixture.

The ideal gas Helmholtz energy function is found from (A.18a)

$$A^{\mathrm{ig}} = -NRT + \sum_{i=1}^{C} \mu_i^{\mathrm{ig}} n_i, \tag{A.56}$$

where the chemical potential is expressed in volume by rewriting (A.2) using the ideal gas law in (A.1):

$$\mu_i^{\mathrm{ig}}(T, V, \boldsymbol{n}) = \mu_i^o(T) + RT \ln \frac{n_i RT}{V p_o}. \tag{A.57}$$

The required Jacobian and Hessian functions of the ideal gas Helmholtz energy function are found by differentiating (A.56) with respect to V and n_i. The result is given by (A.37) written out for ideal gas

$$\boldsymbol{J}_A^{\mathrm{ig}} = \begin{pmatrix} -NRT/V \\ \boldsymbol{\mu}^o(T) + RT \ln \frac{\boldsymbol{n}RT}{V p_o} \end{pmatrix} \tag{11a}$$

$$\boldsymbol{H}_A^{\mathrm{ig}} = RT \begin{pmatrix} N/V^2 & -V^{-1}\boldsymbol{e}^\top \\ -V^{-1}\boldsymbol{e} & \boldsymbol{D} \end{pmatrix}. \tag{11b}$$

The residual Helmholtz energy is written as (Haug-Warberg, 2006)

$$A^{r,v} = \int_{\infty}^{V} \left(\left(\frac{\partial A}{\partial v} \right)_{T,\boldsymbol{n}} - \left(\frac{\partial A^{\mathrm{ig}}}{\partial v} \right)_{T,\boldsymbol{n}} \right) dv, \tag{A.59}$$

where v is a variable of integration. The equation above is rewritten by inserting the identity (A.23) of the partial derivative of A and substituting the ideal gas law (A.1) for p^{ig}:

$$A^{r,v} = \int_{\infty}^{V} \left(\frac{NRT}{v} - p(v) \right) dv. \tag{A.60}$$

The residual in (A.60) can be computed without any further manipulations of the integral for EOSs that are explicit in pressure, like the SRK-EOS. Subsequently, residual functions such as the residual entropy, pressure and chemical potential may readily be obtained by differentiation using Table 4. That is, $S^{r,v} = -\left(\frac{\partial A^{r,v}}{\partial T}\right)_{V,\boldsymbol{n}}$, $p^{r,v} = -\left(\frac{\partial A^{r,v}}{\partial V}\right)_{T,\boldsymbol{n}}$ and $\mu_i^{r,v} = \left(\frac{\partial A^{r,v}}{\partial n_i}\right)_{T,V,n_{j\neq i}}$.

The required residual Jacobian and Hessian functions are given, respectively, as

$$\boldsymbol{J}_A^{r,v} = \begin{pmatrix} \left(\frac{\partial A^{r,v}}{\partial V} \right)_{T,\boldsymbol{n}} \\ \left(\frac{\partial A^{r,v}}{\partial \boldsymbol{n}} \right)_{T,V} \end{pmatrix} \tag{A.61a}$$

$$\boldsymbol{H}_A^{r,v} = \begin{pmatrix} \left(\frac{\partial^2 A^{r,v}}{\partial V^2} \right)_{T,\boldsymbol{n}} & \left(\frac{\partial^2 A^{r,v}}{\partial V \partial \boldsymbol{n}^{\top}} \right)_{T} \\ \left(\frac{\partial^2 A^{r,v}}{\partial \boldsymbol{n} \partial V} \right)_{T} & \left(\frac{\partial^2 A^{r,v}}{\partial \boldsymbol{n} \partial \boldsymbol{n}^{\top}} \right)_{T,V} \end{pmatrix}. \tag{A.61b}$$

The derivatives of the residual Helmholtz energy function depend on the choice of EOS and are given for the virial expansion and the SRK-EOS in Appendix B.

Useful quantities such as c_p and $\overline{h}_i$ are not obtained by straight forward differentiation of the Helmholtz energy function as is the case with the Gibbs energy function. This invites to mixed use of T, V- and T, p-variables. The relations are given by Michelsen and Mollerup (2007, p. 64-65):

$$\left(\frac{\partial \ln \varphi_i}{\partial T} \right)_{p,\boldsymbol{n}} = \frac{1}{RT^2} \left[T \left(\frac{\partial^2 A^{r,v}}{\partial T \partial n_i} \right)_{V,n_{j\neq i}} - \left(\frac{\partial A^{r,v}}{\partial n_i} \right)_{T,V,n_{j\neq i}} \right] + \frac{1}{T} - \frac{\overline{v}_i}{RT} \left(\frac{\partial p}{\partial T} \right)_{V,\boldsymbol{n}} \tag{A.62a}$$

$$\overline{h}_i^{r,p} = -RT^2 \left(\frac{\partial \ln \varphi_i}{\partial T} \right)_{p,\boldsymbol{n}} \tag{A.62b}$$

$$C_V^{r,v} = -T \left(\frac{\partial^2 A^{r,v}}{\partial T^2} \right)_{V,\boldsymbol{n}} \tag{A.62c}$$

$$C_p^{r,p} = C_V^{r,v} - T \frac{\left(\frac{\partial p}{\partial T} \right)_{V,\boldsymbol{n}}^2}{\left(\frac{\partial p}{\partial V} \right)_{T,\boldsymbol{n}}} - NR, \tag{A.62d}$$

where $C_V^{r,v}$ denotes residual isochoric heat capacity, and the partial molar volume, $\overline{v}_i$, is obtained by a cyclic relation at constant temperature (Michelsen and Mollerup, 2007, p. 55):

$$\left(\frac{\partial p}{\partial n_i} \right)_{T,V,n_{j\neq i}} \left(\frac{\partial n_i}{\partial V} \right)_{T,p} \left(\frac{\partial V}{\partial p} \right)_{T,\boldsymbol{n}} = -1. \tag{A.63}$$

Rearranging this relation leads to the expression (Michelsen and Mollerup, 2007, p. 57)

$$\overline{v}_i = \left(\frac{\partial V}{\partial n_i} \right)_{T,p,n_{j\neq i}} = -\left(\frac{\partial p}{\partial n_i} \right)_{T,V,n_{j\neq i}} \Bigg/ \left(\frac{\partial p}{\partial V} \right)_{T,\boldsymbol{n}}. \tag{A.64}$$

The partial derivatives of the residual Helmholtz energy function in (A.62) as well as the pressure derivatives in (A.64) are given in Appendices B and C, respectively.

The heat capacity of the real gas mixture is obtained by adding the ideal gas contribution shown in (14) to the residual contribution in (A.62d). Equivalently, the partial molar enthalpies of the real gas mixture is obtained by adding the ideal gas contribution shown in (13) to the residual contribution in (A.62b).

Appendix B. Derivatives of residual functions

B.1. Virial equation of state

B.1.1. The helmholtz energy function

The virial EOS on pressure explicit form is given as

$$p(T, V, \boldsymbol{n}) = \frac{NRT}{V - B(T, \boldsymbol{n})}. \tag{B.1}$$

The residual Helmholtz energy function is obtained by employing its defining Eq. (A.60) and inserting (B.1). The result is:

$$A^{r,v}(T, V, \boldsymbol{n}) = -NRT \ln \frac{V - B(T, \boldsymbol{n})}{V}. \tag{B.2}$$

Differentiating (B.2) yields the first-order derivatives of the residual Helmholtz energy function:

$$\left(\frac{\partial A^{r,v}}{\partial T} \right)_{V,\boldsymbol{n}} = -NR \left[\ln \frac{V - B}{V} - \frac{T}{V - B} \left(\frac{\partial B}{\partial T} \right)_{\boldsymbol{n}} \right] \tag{B.3a}$$

$$\left(\frac{\partial A^{r,v}}{\partial V} \right)_{T,\boldsymbol{n}} = -NRT \frac{B}{V(V - B)} \tag{B.3b}$$

$$\left(\frac{\partial A^{r,v}}{\partial n_i} \right)_{T,V,n_{j\neq i}} = -RT \left[\ln \frac{V - B}{V} - \frac{N}{V - B} \left(\frac{\partial B}{\partial n_i} \right)_{T,n_{j\neq i}} \right]. \tag{B.3c}$$

The second-order derivatives are obtained by differentiating (B.3):

$$\left(\frac{\partial^2 A^{r,v}}{\partial T^2} \right)_{V,\boldsymbol{n}} = \frac{NR}{V - B} \left[2 \left(\frac{\partial B}{\partial T} \right)_{\boldsymbol{n}} + \frac{T}{V - B} \left(\frac{\partial B}{\partial T} \right)_{\boldsymbol{n}}^2 + T \left(\frac{\partial^2 B}{\partial T^2} \right)_{\boldsymbol{n}} \right] \tag{B.4a}$$

$$\left(\frac{\partial^2 A^{r,v}}{\partial V^2} \right)_{T,\boldsymbol{n}} = \frac{NRTB}{V(V - B)} \left[\frac{1}{V} + \frac{1}{V - B} \right] \tag{B.4b}$$

$$\left(\frac{\partial^2 A^{r,v}}{\partial n_i \partial n_j} \right)_{T,V,n_{k\neq ij}} = \frac{RT}{V - B} \left[\left(\frac{\partial B}{\partial n_i} \right)_{T,n_{j\neq i}} + \left(\frac{\partial B}{\partial n_j} \right)_{T,n_{k\neq j}} + \frac{N}{V - B} \left(\frac{\partial B}{\partial n_i} \right)_{T,n_{j\neq i}} \left(\frac{\partial B}{\partial n_j} \right)_{T,n_{k\neq j}} + N \left(\frac{\partial^2 B}{\partial n_i \partial n_j} \right)_{T,n_{k\neq ij}} \right] \tag{B.4c}$$

$$\left(\frac{\partial^2 A^{r,v}}{\partial T \partial V} \right)_{\boldsymbol{n}} = -\frac{NR}{V - B} \left[\frac{B}{V} + \frac{T}{V - B} \left(\frac{\partial B}{\partial T} \right)_{\boldsymbol{n}} \right] \tag{B.4d}$$

$$\left(\frac{\partial^2 A^{r,v}}{\partial T \partial n_i} \right)_{V,n_{j\neq i}} = -R \left[\ln \frac{V - B}{V} - \frac{N}{V - B} \left(\frac{\partial B}{\partial n_i} \right)_{T,n_{j\neq i}} - \frac{T}{V - B} \left[\left(\frac{\partial B}{\partial T} \right)_{\boldsymbol{n}} + N \left[\left(\frac{\partial^2 B}{\partial n_i \partial T} \right)_{T,n_{j\neq i}} + \frac{\left(\frac{\partial B}{\partial n_i} \right)_{T,n_{j\neq i}} \left(\frac{\partial B}{\partial T} \right)_{\boldsymbol{n}}}{V - B} \right] \right] \right] \tag{B.4e}$$

$$\left(\frac{\partial^2 A^{r,v}}{\partial V \partial n_i} \right)_{T,n_{j\neq i}} = -\frac{RT}{V - B} \left[\frac{B}{V} + \frac{N}{V - B} \left(\frac{\partial B}{\partial n_i} \right)_{T,n_{j\neq i}} \right]. \tag{B.4f}$$

The derivatives of the mixture virial coefficient are obtained by differentiating (A.8) twice. The first-order derivatives are given as

$$\left(\frac{\partial B}{\partial T}\right)_{\boldsymbol{n}} = \frac{1}{N}\sum_{i=1}^{C} n_i \sum_{j=1}^{C} n_j \frac{db_{ij}}{dT} \tag{B.5a}$$

$$\left(\frac{\partial B}{\partial n_i}\right)_{T} = \frac{2\sum_{j=1}^{C} n_j b_{ij} - B}{N}, \tag{B.5b}$$

and the second-order derivatives are given as

$$\left(\frac{\partial^2 B}{\partial T^2}\right)_{\boldsymbol{n}} = \frac{1}{N}\sum_{i=1}^{C} n_i \sum_{j=1}^{C} n_j \frac{d^2 b_{ij}}{dT^2} \tag{B.6a}$$

$$\left(\frac{\partial^2 B}{\partial n_i \partial n_j}\right)_{T} = \frac{2b_{ij} - \left(\frac{\partial B}{\partial n_i}\right)_T - \left(\frac{\partial B}{\partial n_j}\right)_T}{N} \tag{B.6b}$$

$$\left(\frac{\partial^2 B}{\partial T \partial n_i}\right) = \frac{2\sum_{j=1}^{C} n_j \frac{db_{ij}}{dT} - \left(\frac{\partial B}{\partial T}\right)_{\boldsymbol{n}}}{N}. \tag{B.6c}$$

The integrated pair-potential of components i and j results in the cross coefficients $b_{ij}(T)$. The temperature derivatives of these are obtained by differentiating (A.6)

$$\frac{db_{ij}}{dT} = -b_{ij}^{HS}\varepsilon_{ij}\frac{\left(1-\lambda_{ij}^3\right)}{kT^2}\exp\left(\frac{\varepsilon_{ij}}{kT}\right) \tag{B.7a}$$

$$\frac{d^2 b_{ij}}{dT^2} = -b_{ij}^{HS}\varepsilon_{ij}\left(1-\lambda_{ij}^3\right)\left(\frac{-\frac{\varepsilon_{ij}}{kT^2}\exp\left(\frac{\varepsilon_{ij}}{kT}\right)kT^2 - 2kT\exp\left(\frac{\varepsilon_{ij}}{kT}\right)}{\left(kT^2\right)^2}\right) = -\frac{db_{ij}}{dT}\frac{\varepsilon_{ij}+2kT}{kT^2}. \tag{B.7b}$$

B.1.2. The Gibbs Energy Function

The virial EOS on volume explicit form is given as

$$V(T,p,\boldsymbol{n}) = \frac{NRT}{p} + B(T,\boldsymbol{n}). \tag{B.8}$$

The residual Gibbs energy function is obtained by employing its defining Eq. (A.48) and inserting (B.8). The result is:

$$G^{r,p}(T,p,\boldsymbol{n}) = B(T,\boldsymbol{n})p. \tag{B.9}$$

Differentiating (B.9) yields the first-order derivatives of the residual Gibbs energy function:

$$\left(\frac{\partial G^{r,p}}{\partial T}\right)_{p,\boldsymbol{n}} = p\left(\frac{\partial B}{\partial T}\right)_{\boldsymbol{n}} \tag{B.10a}$$

$$\left(\frac{\partial G^{r,p}}{\partial p}\right)_{T,\boldsymbol{n}} = B \tag{B.10b}$$

$$\left(\frac{\partial G^{r,p}}{\partial n_i}\right)_{T,p} = p\left(\frac{\partial B}{\partial n_i}\right)_{T}, \tag{B.10c}$$

The second-order derivatives are obtained by differentiating (B.10):

$$\left(\frac{\partial^2 G^{r,p}}{\partial T^2}\right)_{p,\boldsymbol{n}} = p\left(\frac{\partial^2 B}{\partial T^2}\right)_{\boldsymbol{n}} \tag{B.11a}$$

$$\left(\frac{\partial^2 G^{r,p}}{\partial p^2}\right)_{T,\boldsymbol{n}} = 0 \tag{B.11b}$$

$$\left(\frac{\partial^2 G^{r,p}}{\partial n_i \partial n_j}\right)_{T,p} = p\left(\frac{\partial^2 B}{\partial n_i \partial n_j}\right)_{T} \tag{B.11c}$$

$$\left(\frac{\partial^2 G^{r,p}}{\partial T \partial p}\right)_{\boldsymbol{n}} = \left(\frac{\partial B}{\partial T}\right)_{\boldsymbol{n}} \tag{B.11d}$$

$$\left(\frac{\partial^2 G^{r,p}}{\partial T \partial n_i}\right)_{p} = p\left(\frac{\partial^2 B}{\partial T \partial n_i}\right) \tag{B.11e}$$

$$\left(\frac{\partial^2 G^{r,p}}{\partial p \partial n_i}\right)_{T} = \left(\frac{\partial B}{\partial n_i}\right)_{T}. \tag{B.11f}$$

The derivatives of the mixture virial coefficient and the cross coefficients are the same as for the residual Helmholtz energy function and are given by (B.5), (B.6) and (B.7).

B.2. Soave-Redlich-Kwong

The derivatives for the SRK-EOS are given in terms of the residual Helmholtz energy function in Michelsen and Mollerup (2007, Chap. 3), except for the temperature derivatives of the attractive terms, a. The mixture attractive terms are given by (A.11b), and the cross-terms are determined by (A.12b). The pure component a_{ii} is given by (A.13b).

The temperature derivative of any of the a_{ij} are obtained by differentiating (A.12b):

$$\frac{da_{ij}}{dT} = \frac{1}{2\sqrt{a_{ii}a_{jj}}}\left(a_{jj}\frac{da_{ii}}{dT} + a_{ii}\frac{da_{jj}}{dT}\right)\left(1-k_{ij}\right) \tag{B.12a}$$

$$\frac{d^2 a_{ij}}{dT^2} = \left[\frac{a_{jj}\frac{d^2 a_{ii}}{dT^2} + 2\frac{da_{ii}}{dT}\frac{da_{jj}}{dT} + a_{ii}\frac{d^2 a_{jj}}{dT^2}}{2\sqrt{a_{ii}a_{jj}}} - \frac{\left(a_{jj}\frac{da_{ii}}{dT} + a_{ii}\frac{da_{jj}}{dT}\right)^2}{4\left(a_{ii}a_{jj}\right)^{3/2}}\right]\left(1-k_{ij}\right). \tag{B.12b}$$

Differentiating (A.13b) yields the pure component temperature derivatives:

$$\frac{da_{ii}}{dT} = -0.42747\frac{(RT_c)^2}{p_c}\frac{m\left(1+m\left(1-\sqrt{T_r}\right)\right)}{T_c\sqrt{T_r}} \tag{B.13a}$$

$$\frac{d^2 a_{ii}}{dT^2} = 0.42747\frac{(RT_c)^2}{p_c}\frac{m(1+m)}{2TT_c\sqrt{T_r}}. \tag{B.13b}$$

The reduced temperature has been introduced as $T_r = T/T_c$.

The fugacity coefficient and its derivative required for the Gibbs energy function minimization problem were previously expressed in terms of the residual Helmholtz energy function. The relations were given by (A.50). The isobaric heat capacity and partial molar enthalpy required for the temperature Eq. (4) were also expressed in terms of the residual Helmholtz energy function and were given by (A.62d) and (A.62b), respectively.

The interested reader is referenced to Michelsen and Mollerup (2007) for further information on the SRK-EOS.

Appendix C. Pressure and its derivatives

From (A.23), the pressure is given by $p = -\left(\frac{\partial A}{\partial V}\right)_{T,\boldsymbol{n}}$. Due to (A.55), the pressure of the real gas mixtures may be split into the residual and ideal gas contribution

$$p = -\left(\frac{\partial A^{r,v}}{\partial V}\right)_{T,\boldsymbol{n}} + \frac{NRT}{V}. \tag{C.1}$$

Thus, the required pressure derivatives are given in terms of the residual Helmholtz energy function and an ideal gas contribution:

$$\left(\frac{\partial p}{\partial T}\right)_{V,\boldsymbol{n}} = -\left(\frac{\partial^2 A^{r,v}}{\partial T \partial V}\right)_{\boldsymbol{n}} + \frac{NR}{V} \tag{C.2a}$$

$$\left(\frac{\partial p}{\partial V}\right)_{T,\boldsymbol{n}} = -\left(\frac{\partial^2 A^{r,v}}{\partial V^2}\right)_{T,\boldsymbol{n}} - \frac{NRT}{V^2} \tag{C.2b}$$

$$\left(\frac{\partial p}{\partial n_i}\right)_{T,V,n_{j\neq i}} = -\left(\frac{\partial^2 A^{r,v}}{\partial V \partial n_i}\right)_{T,n_{j\neq i}} + \frac{RT}{V}. \tag{C.2c}$$

References

ANSYS Inc, ANSYS® Fluent Theory Guide, Release 15.0, 2013.

Bell, D.A., Towler, B.F., Fan, M., 2010. Coal Gasification and Its Applications, Binghamton: Elsevier Science & Technology Books, Binghamton, 1st ed. edn., ISBN 9780815520498, 2010.

Callen, H.B., 1985. Thermodynamics and an Introduction to Thermostatics, Wiley, New York, 2nd edn., ISBN 0471862568, 1985.
Chao, Z., Zhang, Y., Wang, Y., Jakobsen, J.P., Jakobsen, H.A., 2017. Modelling of binary fluidized bed reactors for the sorption-enhanced steam methane reforming process. Canad. J. Chem. Eng. 95 (1), 157–169. https://doi.org/10.1002/cjce.22602. ISSN 00084034.
Chinda, R., Yamamoto, C., Lima, D., Pessoa, F., 2019. Industrial Urea Process – Simulation and Validation. Int. J. Adv. Eng. Res. Sci. 6 (8), 324–330. https://doi.org/10.22161/ijaers.68.40. ISSN 23496495.
Coker, A.K., 2001. Modeling of chemical kinetics and reactor design, Gulf Professional Pub., Boston, MA, 1st edn., ISBN 1-281-00696-3, 2001.
Dadgar, F., Venvik, H.J., Pfeifer, P., 2018. Application of hot-wire anemometry for experimental investigation of flow distribution in micro-packed bed reactors for synthesis gas conversion. Chem. Eng. Sci. 177, 110–121. https://doi.org/10.1016/j.ces.2017.10.039. ISSN 00092509.
de Wasch, A., Froment, G., 1972. Heat transfer in packed beds. Chem. Eng. Sci. 27 (3), 567–576. https://doi.org/10.1016/0009-2509(72)87012-X. ISSN 00092509.
Dixon, A.G., 2017. Local transport and reaction rates in a fixed bed reactor tube: Endothermic steam methane reforming. Chem. Eng. Sci. 168, 156–177. https://doi.org/10.1016/j.ces.2017.04.039. ISSN 00092509.
Dymond, J.H., Frenkel, M., Marsh, K.N., Börnstein, R., Landolt, H., Hellwege, K.-H., 2002. Virial Coefficients of Pure Gases, vol. 21A of Landolt-Börnstein - Group IV Physical Chemistry, Springer-Verlag, Berlin/Heidelberg, ISBN 3-540-43345-7, 2002, doi:10.1007/b71692.
Elliott, J.R., Lira, C.T., 2012. Introductory Chemical Engineering Thermodynamics, Prentice Hall, Upper Saddle River, NJ, 2nd edn., ISBN 0136068545, 2012.
Ergun, S., 1952. Fluid Flow through Packed Columns. J. Chem. Eng. Prog. 48 (2), 89–94.
Fernández, J., Abanades, J., 2017. Optimized design and operation strategy of a Ca Cu chemical looping process for hydrogen production. Chem. Eng. Sci. 166, 144–160. https://doi.org/10.1016/j.ces.2017.03.039. ISSN 00092509.
Ferziger, J.H., Perić, M., Street, R.L., 2020. Computational Methods for Fluid Dynamics, Springer International Publishing, Cham, 4th edn., ISBN 978-3-319-99691-2, 2020, doi:10.1007/978-3-319-99693-6.
Fogler, H.S., 2014. Elements of chemical reaction engineering, Prentice Hall, Boston, 4th edn., ISBN 978-0-13-388751-8, 2014.
Froment, G.F., Bischoff, K.B., 1990. Chemical reactor analysis and design, Wiley, New York, 2nd edn., ISBN 0471510440, 1990.
Golub, G.H., 1973. Some Modified Matrix Eigenvalue Problems. SIAM Rev. 15 (2), 318–334. https://doi.org/10.1137/1015032. ISSN 0036-1445.
Golub, G.H., Welsch, J.H., 1969. Calculation of Gauss quadrature rules. Math. Comput. 23 (106), 221. https://doi.org/10.1090/S0025-5718-69-99647-1. ISSN 0025-5718.
Green, J.H.S., 1961. Thermodynamic properties of the normal alcohols, C1 C12. J. Appl. Chem. 11 (10), 397–404. https://doi.org/10.1002/jctb.5010111007. ISSN 00218871.
Haslam, A.J., Galindo, A., Jackson, G., 2008. Prediction of binary intermolecular potential parameters for use in modelling fluid mixtures. Fluid Phase Equilib. 266 (1–2), 105–128. https://doi.org/10.1016/j.fluid.2008.02.004. ISSN 03783812.
Haug-Warberg, T., 2006. Den termodynamiske arbeidsboken, Kolofon, Forlag AS, Fornebu, 1st edn., ISBN 978-82-300-0205-6, 2006.
Hirschfelder, J.O., Curtiss, C.F., Bird, R.B., 1964. Molecular Theory of Gases and Liquids, Wiley, New York, corrected edn., ISBN 0471400653, 1964.
Hołyst, R., Poniewierski, A., 2012. Thermodynamics for Chemists, Physicists and Engineers, Springer, Netherlands, Dordrecht, 1st edn., ISBN 978-94-007-2998-8, 2012, doi:10.1007/978-94-007-2999-5.
Jakobsen, H.A., 2014. Chemical Reactor Modeling, Springer International Publishing, Cham, 2nd edn., ISBN 978-3-319-05091-1, 2014, doi:10.1007/978-3-319-05092-8.
Jordal, K., Bredesen, R., Kvamsdal, H., Bolland, O., 2004. Integration of H2-separating membrane technology in gas turbine processes for CO2 capture. Energy 29 (9–10), 1269–1278. https://doi.org/10.1016/j.energy.2004.03.086. ISSN 03605442.
Jordal, K., Bolland, O., Möller, B.F., Torisson, T., 2005. Optimization with Genetic Algorithms of a Gas Turbine Cycle with H 2 -Separating Membrane Reactor for CO 2 Capture. Int. J. Green Energy 2 (2), 167–180. https://doi.org/10.1081/GE-200058975. ISSN 1543-5075.
Kreyszig, E., 2011. Advanced engineering mathematics, Wiley, Hoboken, NJ, 10th edn., ISBN 9780470646137, 2011.
Kuhn, H.W., Tucker, A.W., 1951. Nonlinear Programming. In: Proceedings of the Second Berkeley Symposium on Mathematical Statistics and Probability, Second Berkeley Symposium on Mathematical Statistics and Probability, University of California Press, Berkeley, Calif., 481–492, ISBN 0097-0433, 1951.
Lemmon, E.W., McLinden, M.O., Friend, D.G., 2019. Thermophysical Properties of Fluid Systems. In: Linstrom, P.J., Mallard, W.G. (Eds.), NIST Chemistry WebBook, NIST Standard Reference Database Number 69. National Institute of Standards and Technology, Gaithersburg MD, 20899, USA.
Lide, D.R., 2005. CRC handbook of chemistry and physics, Taylor & Francis, Boca Raton, FL, 86th edn., ISBN 0849304865, 2005.
Lorentz, H.A., 1881. Ueber die Anwendung des Satzes vom Virial in der kinetischen Theorie der Gase, Annalen der Physik 248 (1) (1881) 127–136, ISSN 0003–3804.
Lydersen, A.L., 1983. Mass transfer in engineering practice, Wiley, Chichester, ISBN 047110437X, 1983.
Marino, A., . Peltomäki, A., Lim, J., Aerts, A., 2019. A multi-physics computational tool based on CFD and GEM chemical equilibrium solver for modeling coolant chemistry in nuclear reactors, Prog. Nucl. Energy 120 (November 2019) (2020) 103190, doi:10.1016/j.pnucene.2019.103190, ISSN 01491970.
Michelsen, M.L., Mollerup, J.M., 2007. Thermodynamic models: fundamentals & computational aspects, Tie-Line Publications, Holte, 2nd edn., ISBN 8798996134, 2007.
Mikhailova, I.A., Fadeev, S.I., Khasin, A.A., Chermashentseva, G.K., Kirillov, V.A., 2003. Calculating the Liquid – Gas Equilibrium in the Fischer – Tropsch. Synthesis 37 (2), 184–188.
Miroshnichenko, S., Vrabec, J., 2015. Excess properties of non-ideal binary mixtures containing water, methanol and ethanol by molecular simulation. J. Mol. Liq. 212, 90–95. https://doi.org/10.1016/j.molliq.2015.08.058. ISSN 01677322.
Nocedal, J., Wright, S., 2006. Numerical Optimization, Springer Series in Operations Research and Financial Engineering, Springer, New York, New York, 2nd ed. edn., ISBN 978-0-387-30303-1, 2006, doi:10.1007/978-0-387-40065-5.
Patankar, S.V., 1980. Numerical Heat Transfer and Fluid Flow, Series in computational methods in mechanics and thermal sciences. CRC Press, Boca Raton, FL, ISBN 9781315275130. https://doi.org/10.1201/9781482234213.
Patankar, S.V., Spalding, D.B., 1972. A calculation procedure for heat, mass and momentum transfer in three-dimensional parabolic flows. Int. J. Heat Mass Transf. 15 (10), 1787–1806. https://doi.org/10.1016/0017-9310(72)90054-3. ISSN 00179310.
Pedernera, M.N., Piña, J., Borio, D.O., 2007. Kinetic evaluation of carbon formation in a membrane reactor for methane reforming. Chem. Eng. J. 134 (1–3), 138–144. https://doi.org/10.1016/j.cej.2007.03.051. ISSN 13858947.
Pereira, F.E., Jackson, G., Galindo, A., Adjiman, C.S., 2010. A duality-based optimisation approach for the reliable solution of (P, T) phase equilibrium in volume-composition space. Fluid Phase Equilib. 299 (1), 1–23. https://doi.org/10.1016/j.fluid.2010.08.001. https://linkinghub.elsevier.com/retrieve/pii/S0378381210004048, ISSN 03783812.
Phuakpunk, K., Chalermsinsuwan, B., Putivisutisak, S., Assabumrungrat, S., 2018. Parametric study of hydrogen production via sorption enhanced steam methane reforming in a circulating fluidized bed riser. Chem. Eng. Sci. 192, 1041–1057. https://doi.org/10.1016/j.ces.2018.08.042. ISSN 00092509.
Prausnitz, J.M., Lichtenthaler, N.R., Gomes de Azevedo, E., 1999. Molecular thermodynamics of fluid-phase equilibria, Prentice-Hall, Upper Saddle River, N.J., 3rd edn., ISBN 0139777458, 1999.
Press, W.H., Teukolsky, S.A., Vetterling, W.T., Flannery, B.P., 1992. Numerical Recipes in Fortran 77: The Art of Scientific Computing. Cambridge University Press, Cambridge, UK.
Reid, R.C., Prausnitz, J.M., Poling, B.E., 1987. The properties of gases and liquids. McGraw-Hill, New York.
Roache, P.J., 1998. Fundamentals of computational fluid dynamics, Hermosa Publishers, Albuquerque, N.M., ISBN 0913478091, 1998.
Roine, A., 2019. HSC-Chemistry [Software]. Outotec, Pori.
Sánchez, R.A., Riboldi, L., Jakobsen, H.A., 2017. Numerical modelling and simulation of hydrogen production via four different chemical reforming processes: Process performance and energy requirements. Canad. J. Chem. Eng. 95 (5), 880–901. https://doi.org/10.1002/cjce.22758. ISSN 00084034.
Shen, J., Tang, T., Wang, L.-L., 2011. Spectral Methods, vol. 41 of Springer Series in Computational Mathematics, Springer, Berlin Heidelberg, Berlin, Heidelberg, 1st edn., ISBN 978-3-540-71040-0, 2011, doi:10.1007/978-3-540-71041-7.
Soave, G., 1972. Equilibrium constants from a modified Redlich-Kwong equation of state. Chem. Eng. Sci. 27 (6), 1197–1203. https://doi.org/10.1016/0009-2509(72)80096-4. ISSN 00092509.
Solsvik, J., Jakobsen, H.A., 2011. A numerical study of a two property catalyst/sorbent pellet design for the sorption-enhanced steam–methane reforming process: Modeling complexity and parameter sensitivity study. Chem. Eng. J. 178, 407–422. https://doi.org/10.1016/j.cej.2011.10.045. ISSN 13858947.
Solsvik, J., Jakobsen, H., 2012. Solution of the Pellet Equation by use of the Orthogonal Collocation and Least Squares Methods: Effects of Different Orthogonal Jacobi Polynomials. Int. J. Chem. React. Eng. 10 (1), ISSN 1542–6580, doi:10.1515/1542-6580.2702.
Solsvik, J., Jakobsen, H.A., 2013a. On the solution of the population balance equation for bubbly flows using the high-order least squares method: implementation issues. Rev. Chem. Eng. 29 (2), 63–98. https://doi.org/10.1515/revce-2012-0018. ISSN 2191-0235.
Solsvik, J., Jakobsen, H.A., 2013b. Multicomponent mass diffusion in porous pellets: Effects of flux models on the pellet level and impacts on the reactor level. Application to methanol synthesis. Canad. J. Chem. Eng. 91 (1), 66–76. https://doi.org/10.1002/cjce.20680. ISSN 00084034.
Solsvik, J., Tangen, S., Jakobsen, H.A., 2013. Evaluation of weighted residual methods for the solution of the pellet equations: The orthogonal collocation, Galerkin, tau and least-squares methods. Comput. Chem. Eng. 58, 223. https://doi.org/10.1016/j.compchemeng.2013.07.002, ISSN 0098-1354.
Solsvik, J., Haug-Warberg, T., Jakobsen, H.A., 2016. Implementation of chemical reaction equilibrium by Gibbs and Helmholtz energies in tubular reactor models: Application to the steam–methane reforming process. Chem. Eng. Sci. 140, 261–278. https://doi.org/10.1016/j.ces.2015.10.011. ISSN 00092509.
. Sutherland, H. LII., 1893. The viscosity of gases and molecular force. The London, Edinburgh, and Dublin Philos. Magaz. J. Sci. 36 (223) (1893) 507–531, doi:10.1080/14786449308620508, ISSN 1941-5982.
Tallmadge, J.A., 1970. Packed bed pressure drop—an extension to higher Reynolds numbers. AIChE J. 16 (6), 1092–1093. https://doi.org/10.1002/aic.690160639. ISSN 0001-1541.

B.W. Taylor, Introduction to management science, Pearson, Boston, 10th edn., ISBN 9780132457576, 2010.
Tran, A., Aguirre, A., Durand, H., Crose, M., Christofides, P.D., 2017. CFD modeling of a industrial-scale steam methane reforming furnace. Chem. Eng. Sci. 171, 576–598. https://doi.org/10.1016/j.ces.2017.06.001. ISSN 00092509.
van der Waals, J.D., 1873. De continuiteit van den gasen Vloeistoftoestand, Ph.D. thesis.
Versteeg, H.K., Malalasekera, W., 2007. An introduction to computational fluid dynamics: the finite volume method, Pearson/Prentice Hall, Harlow, 2nd ed.
Villadsen, J., Michelsen, M.L.,1978. Solution of Differential Equation Models by Polynomial Approximation, Prentice-Hall International, Prentice-Hall, Englewood Cliffs, NJ, ISBN 0138222053, 1978.
Villadsen, J., Stewart, W., 1995. Solution of boundary-value problems by orthogonal collocation. Chem. Eng. Sci. 50 (24), 1483–1501. https://doi.org/10.1016/0009-2509(96)81831-8. ISSN 00092509.
Wang, X., Wang, N., Zhao, J., Wang, L., 2010. Thermodynamic analysis of propane dry and steam reforming for synthesis gas or hydrogen production. Int. J. Hydrogen Energy 35 (23), 12800–12807. https://doi.org/10.1016/j.ijhydene.2010.08.132. ISSN 03603199.
Winterbone, D.E., Turan, A., 1997. Advanced Thermodynamics for Engineers, Elsevier, Kidlington, 2nd edn., ISBN 9780340676998, 1997, doi:10.1016/B978-0-340-67699-8.X5000-5.
Wismann, S.T., Engbæk, J.S., Vendelbo, S.B., Bendixen, F.B., Eriksen, W.L., Aasberg-Petersen, K., Frandsen, C., Chorkendorff, I., Mortensen, P.M., 2019. Electrified methane reforming: A compact approach to greener industrial hydrogen production. Science 364 (6442), 756–759. https://doi.org/10.1126/science.aaw8775. ISSN 0036-8075.
Wu, Y.J., Li, P., Yu, J.G., Cunha, A.F., Rodrigues, A.E., 2016. Progress on sorption-enhanced reaction process for hydrogen production. Rev. Chem. Eng. 32 (3), 271–303. https://doi.org/10.1515/revce-2015-0043. ISSN 01678299.
Xu, J., Froment, G.F., 1989a. Methane steam reforming: II. Diffusional limitations and reactor simulation. AIChE J. 35 (1), 97–103. https://doi.org/10.1002/aic.690350110. ISSN 15475905.
Xu, J., Froment, G.F., 1989b. Methane steam reforming, methanation and water-gas shift: I. Intrinsic kinetics. AIChE J. 35 (1), 88–96. https://doi.org/10.1002/aic.690350109. ISSN 0001-1541.
Yagi, S., Kunii, D., 1957. Studies on effective thermal conductivities in packed beds. AIChE J. 3 (3), 373–381. https://doi.org/10.1002/aic.690030317. ISSN 0001-1541.
Yagi, S., Kunii, D., 1960. Studies on heat transfer near wall surface in packed beds. AIChE J. 6 (1), 97–104. https://doi.org/10.1002/aic.690060119. ISSN 0001-1541.

4.2 Paper II: Mass Transfer Modeling in a Biochemical Process

I&EC research
Industrial & Engineering Chemistry Research

pubs.acs.org/IECR

Article

Interface Mass Transfer in Reactive Bubbly Flow: A Rigorous Phase Equilibrium-Based Approach

S. B. Øyen,* H. A. Jakobsen, T. Haug-Warberg, and J. Solsvik

Cite This: https://doi.org/10.1021/acs.iecr.1c03131

Read Online

ACCESS | Metrics & More | Article Recommendations | Supporting Information

ABSTRACT: In this work, the driving force of interfacial mass transfer is modeled as deviation from the gas−liquid equilibrium, which by assumption is thought to exist at the interface separating the gas and liquid phases. The proposed mass transfer model provides a flexible framework where the phase equilibrium description in the driving force can be substituted without difficulties, allowing the mass transfer modeling of distillation, absorption/stripping, extraction, evaporation, and condensation to be based on a thermodynamically consistent phase equilibrium formulation. Phase equilibrium by the Soave−Redlich−Kwong equation of state (SRK-EoS) is in this work compared to the results of the classical Henry's law approach. The new model formulation can predict mass transfer of the solvent, which Henry's law cannot. The mass transfer models were evaluated by simulating a single-cell protein process operated in a bubble column bioreactor, and the solubilities computed from the SRK-EoS and Henry's law were in qualitative agreement, albeit in quantitative disagreement. At the reactor inlet, the solubility of O_2 and CH_4 was 150% higher with the SRK-EoS than with Henry's law. Furthermore, the SRK-EoS was computationally more expensive and spent 10% more time than Henry's law.

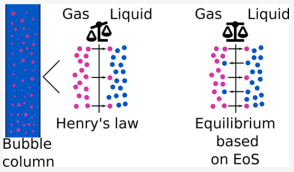

INTRODUCTION

Mass transfer is crucial in many chemical engineering applications. For instance, mathematical modeling of separation processes such as distillation, absorption/stripping, extraction, evaporation, and condensation depends on a physical description of mass transfer between a liquid and a gas phase. In biochemical engineering, on the other hand, bacteria rely on substrates and also possibly O_2 to sustain their metabolism. For instance, a particular bacterium, *Methylococcus capsulatus* (Bath), is an aerobic, methanotrophic bacterium that has received much attention due to its high protein content (≈70−80% on a dry mass basis, see, e.g., Olsen et al.,[1] Øverland et al.,[2] and Anupama and Ravindra[3]). The accumulated biomass is termed single-cell protein (SCP) and could serve as a potential food or animal feed.[2−5] In Norway, fish farming is a significant source of income, and the high cost of fishmeal[6] makes SCP production an attractive alternative to existing protein sources. *M. capsulatus* (Bath) consumes CH_4 and O_2 to grow.[7] Both CH_4 and O_2 are highly volatile compounds, and consequently, they are conveniently supplied to the broth from a gaseous phase. Hence, the liquid phase, where the bacteria grow, receives CH_4 and O_2 through mass transfer with the gaseous phase. According to several investigators, the gas fermentation of SCP is mass transfer limited,[1,8−11] and hence, the modeling of this process relies on accurate mass transfer models.

Mass transfer coefficients are based on a diverse set of theories addressing different physical phenomena such as the surface renewal,[12] the laminar and turbulent boundary layers, one-film[13,14] and two-film,[15] and the penetration concept of Higbie.[16] Mass transfer models of this kind served as a foundation for studying the mass transfer coefficient, k_L, which governs the resistance to mass transfer on the liquid side of the phase boundary. For instance, Weber[17] investigated the mass transfer coefficient for spherical cap bubbles and derived an expression for k_L based on the penetration theory. On the other hand, Rzehak[18] derived an expression for k_L based on the surface renewal theory. Other investigators, such as Frössling[19] and Hughmark,[20] based their work on the boundary layer theory. Furthermore, some investigators have suggested empirical relations for the mass transfer coefficient, see, for example, Calderbank and Moo-Young.[21]

The driving force for mass transfer is commonly regarded as a difference in concentration between the bulk phase and the interface.[22] All the theories above for mass transfer require a relation for the interface concentration, and most commonly, phase equilibrium is assumed to prevail at the interface separating the two phases. Hence, the driving force for mass transfer is the deviation from phase equilibrium. Highly volatile gases, such as CH_4 and O_2, have low solubility in H_2O, and consequently, Henry's law and the Henry's law constant are frequently employed to describe the gas−liquid equilibrium.[23−28] However, the Henry's law constant is not truly constant but depends on temperature and weakly on pressure. Neglecting this dependency may lead to erroneous predictions,

Received: August 4, 2021
Revised: October 25, 2021
Accepted: November 4, 2021

depending on the compounds present and the temperature variation.[29] For instance, the solubility of CO_2 in H_2O doubles over a temperature interval of 20 K.[30]

Furthermore, the Henry's law constant is extensively studied for solutes in H_2O, see, for example, the compiled database of Sander.[31] On the other hand, data are scarce for solvents other than H_2O. This limits the applicability of mass transfer models relying on Henry's law and Henry's law constants. Moreover, the experimental data on the Henry's law constant are mainly limited to one solute−solvent pair at a time. Thus, the Henry's law constants are meant for binary gas−liquid equilibria computations. In the presence of multiple, poorly soluble compounds, a set of Henry's law constants are frequently employed. This is equivalent to approximating the multicomponent phase equilibrium as a set of pseudo-binary phase equilibria.

Henry's law is valid at the infinite dilution limit for solute i in solvent j. Hence, it is an appropriate choice for approximating poor solubilities in a solvent. For the slightly soluble gas NH_3, the solubility is not poor, and Henry's law is not appropriate.[32] Hence, mass transfer models employing Henry's law are inappropriate for predicting mass transfer of slightly soluble gases. Additionally, the mass transfer of the solvent cannot be computed in the Henry's law model approach since the Henry's law constant is not available for the solvent. The mass transfer of the solvent is thus commonly neglected or ignored.

The mass transfer flux from gas to liquid is mainly modeled by the mass transfer coefficient and a suitable equilibrium relation. The mass transfer coefficient is extensively studied; however, limited studies exist on the equilibrium relations. In this study, we focus on the equilibrium condition that is assumed to prevail at the interface. In common practice, Henry's law is assumed to be a suitable equilibrium relation and is used to close the gas−liquid mass transfer problem. However, due to the limitations of Henry's law discussed above, we aim to (a) extend the concentration range where the mass transfer models are valid and (b) predict mass transfer of the solvent. By utilizing an equation of state (EoS), the equilibrium composition at the gas−liquid interface is computed rigorously without assumptions of the solute concentrations or which solvent is present.

This study employs the one- and two-film model and suggests a general phase equilibrium approach to relate the interface concentrations. In particular, we suggest a rigorous EoS-based phase equilibrium approach capable of predicting multicomponent mass transfer of all components. This methodology allows for predicting the mass transfer of poorly soluble and slightly soluble gases and the solvent. The novel mass transfer model handles evaporation and condensation processes equally well, as no assumptions are made for the concentrations in each phase. This allows for mass transfer processes where Henry's law is inappropriate, such as processes where the solutes are not infinitely diluted or when mass transfer of the solvent is critical. The suggested mass transfer concept is evaluated by simulating the biochemical production of SCP with the bacteria *M. capsulatus* (Bath) operated in a bubble column bioreactor.

The contribution of this work lies in the treatment of the gas−liquid interface in the context of mass transfer. Although phase equilibrium is commonly assumed to prevail at the interface, the phase equilibrium has, to the authors' knowledge, not been computed to date in the literature. Rather, Henry's law is employed to relate the gas- and liquid-side concentrations through a constant or a correlation at best. This study will endeavor to treat the driving force for mass transfer in agreement with the underlying assumptions. Hence, to determine the driving force, a full phase equilibrium computation is performed at the gas−liquid interface.

This paper is divided into five parts. First, a thorough introduction to thermodynamic theory and phase equilibrium is provided. Second, the mass transfer models are derived and discussed. The third part contains transport phenomena, reactor model, constitutive equations, and numerical solution approach. In the fourth part, results and discussion are provided, and in the fifth part, concluding remarks are given.

THERMODYNAMIC MODELING

A common assumption in the gas−liquid mass transfer modeling is that phase equilibrium prevails at the interface separating the two phases. We thus provide a thorough introduction to thermodynamics and phase equilibrium in the following.

The criteria for gas−liquid phase equilibrium are

$$T_G = T_L \tag{1a}$$

$$p_G = p_L \tag{1b}$$

$$\mu_{G,i} = \mu_{L,i}, \qquad i = 1,2, ..., N_C \tag{1c}$$

where T is the temperature, p is the pressure, μ_i is the chemical potential of component i, and N_C is the number of components. The gas and liquid phases are denoted G and L, respectively. Equation 1c constitutes N_C equations in $2N_C$ unknown chemical potentials. Hence, additional N_C relations are required to determine the chemical potentials and the equilibrium composition in both phases. The additional mass balances required to close the equilibrium problem is formulated as

$$n_{L,i} + n_{G,i} = \beta^0_{L,i} + \beta^0_{G,i} \tag{2}$$

where n_i is the number of moles of component i and β^0_i is the initial number of moles of component i. Thus, eq 2 is a constraint to ensure that mass is conserved through the process of finding the equilibrium composition. Further treatment of $\beta^0_{L,i}$ and $\beta^0_{G,i}$ is deferred to the section Rigorous Phase Equilibrium: Consistent Fluxes.

There are primarily three different concepts for modeling the chemical potentials in the liquid and gas phases: the assumption of ideality, the methods of nonideal EoS, and activity coefficients. For instance, the ideal gas law

$$p^{ig}V = NRT \tag{3}$$

can be used to model the chemical potential in the gas phase as

$$\mu_i^{ig}(T, p, \mathbf{n}) = \mu_i^\circ(T, p_\circ) + RT \ln \frac{n_i p}{N p_\circ} \tag{4}$$

In Eq. 3, V is the volume, N is the total number of moles in the gas mixture, and R is the gas constant. The superscript "ig" denotes ideal gas. In eq 4, $\mathbf{n}$ is the vector of mole numbers, $p_\circ$ is the standard state pressure, and μ_i° is the standard state chemical potential given by[33,34]

$$\begin{aligned}\mu_i^\circ(T, p_\circ) &= \bar{h}_i^{ig}(T, p_\circ) - T\bar{s}_i^{ig}(T, p_\circ) \\ &= \left[\Delta_f h_i^\circ(T_\circ) + \int_{T_\circ}^{T} c_{p,i}^\circ(T)\mathrm{d}T\right] \\ &\quad - T\left[s_i^\circ(T_\circ) + \int_{T_\circ}^{T} \frac{c_{p,i}^\circ}{T}\,\mathrm{d}T\right]\end{aligned} \tag{5}$$

https://doi.org/10.1021/acs.iecr.1c03131
Ind. Eng. Chem. Res. XXXX, XXX, XXX−XXX

where the ideal gas partial molar enthalpy and entropy at the reference pressure are denoted as $\overline{h}_i^{ig}(T,p_\circ)$ and $\overline{s}_i^{ig}(T,p_\circ)$, respectively. The standard heat of formation is denoted as $\Delta_f h_i^\circ(T_\circ)$, the standard ideal gas heat capacity is denoted as $c_{p,i}^\circ$, and the standard entropy is denoted as s_i°. The standard heat of formation and entropy are tabulated at the reference temperature $T_\circ$ by Aylward and Findlay.[35]

Equations of State. Fluids may be described by an EoS. For instance, ideal gases are described by the ideal gas EoS in eq 3. On the other hand, real fluids require a nonideal EoS to be characterized. Thus, to characterize the real fluid μ_i in eq 1c, we require a nonideal EoS. Details on a specific EoS are therefore given in the following.

A particular class of EoSs is cubic in volume. This permits the EoS to model the behavior of both gases and liquids with the same, relatively simple model description. Here, the cubic Soave−Redlich−Kwong EoS (SRK-EoS) was used, see, for example, Soave[36]

$$p(T, V, \mathbf{n}) = \frac{NRT}{V - B(\mathbf{n})} - \frac{D(T, \mathbf{n})}{V(V + B(\mathbf{n}))}. \tag{6}$$

In eq 6, B denotes an excluded volume and D denotes an attractive term, both of which are functions of the composition of the mixture. Additionally, D is a function of the system temperature. The mixture B and D were modeled by the quadratic mixing rules

$$NB(\mathbf{n}) = \sum_{i=1}^{N_C} n_i \sum_{j=1}^{N_C} n_j b_{ij} \tag{7a}$$

$$D(T, \mathbf{n}) = \sum_{i=1}^{N_C} n_i \sum_{j=1}^{N_C} n_j a_{ij}(T) \tag{7b}$$

The cross coefficients b_{ij} and a_{ij} in eqs 7a and 7b were determined by combining rules, which are functions of their pure component contributions, b_{ii} and a_{ii}. In this study, the arithmetic and geometric mean combining rules for b_{ij} and a_{ij} were employed[37]

$$b_{ij} = \frac{1}{2}(b_{ii} + b_{jj}) \tag{8a}$$

$$a_{ij} = \sqrt{a_{ii}a_{jj}}(1 - k_{ij}) \tag{8b}$$

The binary interaction parameter, k_{ij}, is an adjustable parameter used to fit experimental data. Soave[36] modeled pure component a_{ii} and b_{ii} in eqs 8a and 8b as

$$b_{ii} = 0.08664\frac{RT_c}{p_c} \tag{9a}$$

$$a_{ii} = 0.42747\frac{(RT_c)^2}{p_c}(1 + m(1 - \sqrt{T/T_c}))^2 \tag{9b}$$

$$m = 0.480 + 1.574\omega - 0.176\omega^2 \tag{9c}$$

In eqs 9a, 9b, and 9c, the critical temperature and pressure are denoted as T_c and p_c, respectively, and the acentric factor is denoted as ω. Critical constants and acentric factors were taken from NIST Chemistry WebBook.[38]

Chemical Potential. As illustrated in Figure 1, the chemical potential following the SRK-EoS was obtained from the ideal gas chemical potential and the residual chemical potential. The sum of the two gives the chemical potential of the real fluid

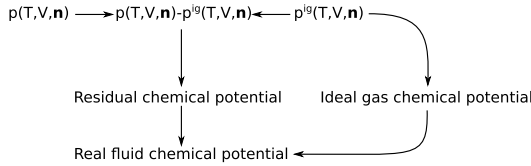

Figure 1. Nonideal EoS is used in combination with the ideal gas EoS to characterize the real fluid chemical potential. Here, p and p^{ig} are independent models.

$$\mu_i(T, p, \mathbf{n}) = \mu_i^{r,p}(T, p, \mathbf{n}) + \mu_i^{ig}(T, p, \mathbf{n}) \tag{10}$$

Here $\mu_i^{r,p}$ denotes the residual chemical potential at specified T and p. Michelsen and Mollerup[39] derived the residual chemical potential as

$$\mu_i^{r,p} \equiv RT \ln \varphi_i = \frac{\partial}{\partial n_i}\left(\int_\infty^V (p^{ig} - p)\mathrm{d}\nu\right)_{T,V,n_{k\neq j}} - RT \ln Z \tag{11}$$

where both the ideal gas EoS in eq 3 and the nonideal gas EoS in eq 6 have been used in the integral. Here, φ_i has been introduced as the fugacity coefficient of component i, and $Z = pV/(NRT)$ is the compressibility factor. Michelsen and Mollerup[39] gave the solution to the integral in eq 11 and its compositional derivative. The required temperature derivatives of the attractive term, a, can be found in Øyen et al.[40]

Due to the SRK-EoS being cubic in volume, three possible volumes satisfy eq 6 at a given temperature, pressure, and composition. Thus, eq 11 is an implicit relation in volume, and the appropriate compressibility factor must be chosen for the corresponding phase. In this study, the three volumes satisfying eq 6 were obtained by the built-in function roots in Matlab. The smallest of these roots corresponded to the liquid phase, while the largest root corresponded to the gas phase.

By definition, fugacity is defined as

$$RT \ln \frac{f_i}{p_\circ} \equiv \mu_i(T, p, \mathbf{n}) - \mu_i^\circ(T, p_\circ) \tag{12}$$

and the criterion for phase equilibrium in eq 1c can alternatively be stated as

$$f_{G,i} = f_{L,i} \tag{13}$$

The chemical potential in eq 10 is combined with eqs 4, 11, and 12, and the result is inserted into eq 13 to obtain

$$\ln \frac{n_{G,i}}{N_G} + \ln \varphi_{G,i} = \ln \frac{n_{L,i}}{N_L} + \ln \varphi_{L,i} \tag{14}$$

In eq 14, the first term on the left-hand side is the ideal gas contribution, and the second term on the left-hand side is the residual (departure from ideal gas) contribution to the gas-phase chemical potential of component i. Similarly, on the right-hand side, the first term is the ideal gas contribution and the second term is the residual contribution to the liquid-phase chemical potential of component i.

Negative Flash Algorithm. The combination of eqs 2 and 14 is sufficient to identify the equilibrium composition in both phases; however, since the problem is nonlinear, an iterative

https://doi.org/10.1021/acs.iecr.1c03131
Ind. Eng. Chem. Res. XXXX, XXX, XXX−XXX

procedure is required. The procedure used here is based on Newton−Raphson iteration on the chemical potential. Thus, a Taylor expansion is performed on eq 14. The left-hand side is expanded in all $n_{G,j}$, and the right-hand side is expanded in all $n_{L,j}$

$$\ln \frac{n_{G,i}}{N_G} + \ln \varphi_{G,i} + \sum_{j=1}^{N_C} \left(\left[\frac{\delta_{ij}}{n_{G,i}} - \frac{1}{N_G} + \left(\frac{\partial \ln \varphi_{G,i}}{\partial n_{G,j}} \right)_{T,p,n_k \neq j} \right] \Delta n_{G,j} \right) = \ln \frac{n_{L,i}}{N_L} + \ln \varphi_{L,i} + \sum_{j=1}^{N_C} \left(\left[\frac{\delta_{ij}}{n_{L,i}} - \frac{1}{N_L} + \left(\frac{\partial \ln \varphi_{L,i}}{\partial n_{L,j}} \right)_{T,p,n_k \neq j} \right] \Delta n_{L,j} \right) \tag{15}$$

Here δ_{ij} denotes the Kronecker delta, which is 1 whenever $i = j$ and 0 otherwise, and Δn_j is used to denote the step taken in mole numbers of component j. The terms inside the summation will be denoted as the Jacobian, J_{ij}, of eq 14.

We assume that the phases establish equilibrium without any reaction, implying that the species mole numbers are conserved. Thus, any moles removed from one phase are received in the other phase, that is, $\Delta n_{G,i} = -\Delta n_{L,i}$. For brevity of notation, the subscripts describing the variables held constant under the partial differentiation are omitted. The Taylor expansion in eq 15 is thus rewritten as

$$\sum_{j=1}^{N_C} \left(\left[\frac{\delta_{ij}}{n_{L,i}} - \frac{1}{N_L} + \left(\frac{\partial \ln \varphi_{L,i}}{\partial n_{L,j}} \right) + \frac{\delta_{ij}}{n_{G,i}} - \frac{1}{N_G} + \left(\frac{\partial \ln \varphi_{G,i}}{\partial n_{G,j}} \right) \right] \Delta n_{L,j} \right) = -\left(\ln \frac{n_{L,i}}{N_L} + \ln \varphi_{L,i} - \left(\ln \frac{n_{G,i}}{N_G} + \ln \varphi_{G,i} \right) \right) \tag{16}$$

For convenience, we introduce two new variables to denote the modified chemical potentials in eq 14

$$\eta_{G,i} = \ln \frac{n_{G,i}}{N_G} + \ln \varphi_{G,i} \tag{17a}$$

$$\eta_{L,i} = \ln \frac{n_{L,i}}{N_L} + \ln \varphi_{L,i} \tag{17b}$$

It is noted that the fugacity of component i in the gas phase is $\ln f_{G,i} = \eta_{G,i} + \ln p$ and the fugacity of component i in the liquid phase is $\ln f_{L,i} = \eta_{L,i} + \ln p$. With the Jacobian of eqs 17a and 17b being

$$J_{G,ij} = \frac{\delta_{ij}}{n_{G,i}} - \frac{1}{N_G} + \left(\frac{\partial \ln \varphi_{G,i}}{\partial n_{G,j}} \right) \tag{18a}$$

$$J_{L,ij} = \frac{\delta_{ij}}{n_{L,i}} - \frac{1}{N_L} + \left(\frac{\partial \ln \varphi_{L,i}}{\partial n_{L,j}} \right) \tag{18b}$$

Equation 16 can be written in the matrix form as

$$[\mathbf{J}_L^\nu + \mathbf{J}_G^\nu] \Delta \mathbf{n}_L^{\nu+1} = -(\eta_L^\nu - \eta_G^\nu) \tag{19}$$

where the iteration count is denoted as ν. The mole numbers are updated as

$$\mathbf{n}_L^{\nu+1} = \mathbf{n}_L^\nu + \Delta \mathbf{n}_L^{\nu+1} \tag{20a}$$

$$\mathbf{n}_G^{\nu+1} = \mathbf{n}_G^\nu - \Delta \mathbf{n}_L^{\nu+1} \tag{20b}$$

With eqs 11, 17a, 17b, 18a, 18b, 19, 20a, and 20b along with the initialization in eq 2, it is possible to solve the phase equilibrium problem by a sequence of successive iterations.

There are potential pitfalls where the algorithm above might not converge. In Figure 2, a cross is used to denote a mixture

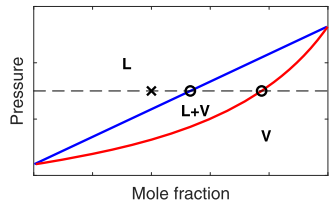

Figure 2. Simplistic binary gas−liquid phase diagram. The blue line denotes the bubble point line, and the red line denotes the dew point line.

with an overall composition, $\beta_{L,i}^0 + \beta_{G,i}^0$, inside a one-phase, stable-phase region. If the algorithm is initiated within a stable phase, the iterative procedure may not converge. If the overall composition, $\beta_{L,i}^0 + \beta_{G,i}^0$, decomposes into two phases (marked with circles in Figure 2), then the mass balance in eq 2 requires that the gas phase is present in negative amounts. This situation was discussed by Whitson and Michelsen,[41] and the proposed flash algorithm was coined "the negative flash." With this procedure, it is possible to perform equilibrium computations on stable phases to compute the equilibrium concentrations of both phases.

Our proposal to a stable convergence of the equilibrium problem with Newton−Raphson iteration, see eq 19, was inspired by the procedure of Whitson and Michelsen.[41] The algorithm allows for negative amounts of a particular phase in order to converge to two stable equilibrium phases. To prevent divergence, the iteration procedure requires careful control of the steps taken, $\Delta n_{L,i}$. As seen in eqs 17a and 17b, the mole fraction, $x_i = n_i/N$, is not allowed to become negative since the logarithm of negative numbers does not exist. Allowing negative mole numbers but not negative mole fractions implies that the mole numbers of all components in a particular phase must have the same sign, that is

$$\frac{n_1}{n_j} > 0, \qquad j = 2,3, \ldots, N_C \tag{21}$$

For a binary mixture, this is illustrated in Figure 3, where the mole number of components 1 and 2 is along the x- and y-axis, respectively. Hatched areas are illegal quadrants, meaning the second and fourth quadrants, Q_2 and Q_4, are thermodynamically illegal. On the other hand, the first and third quadrants, Q_1 and Q_3, are legal. If the equilibrium solver is initialized with both $\boldsymbol{\beta}_L^0$ and $\boldsymbol{\beta}_G^0$ in Q_1, and the converged $\mathbf{n}_L$ and $\mathbf{n}_G$ both also lie in Q_1, the problem is commonly termed a "flash" problem. If $\boldsymbol{\beta}_L^0$ and $\boldsymbol{\beta}_G^0$ lie in Q_1 and the converged $\mathbf{n}_L$ or $\mathbf{n}_G$ lie in Q_3, the problem is termed a "negative flash" problem. Note that if $\mathbf{n}_L$ or $\mathbf{n}_G$ lies in Q_3, then the volume of that phase is also negative.

With Figure 3 in mind, the step, $\Delta \mathbf{n}_L$, was controlled carefully. This process was done by scaling the step with $\tau \in (0, 1]$

$$\Delta \mathbf{n}_L = \tau \Delta \mathbf{n}_L' \tag{22}$$

https://doi.org/10.1021/acs.iecr.1c03131
Ind. Eng. Chem. Res. XXXX, XXX, XXX−XXX

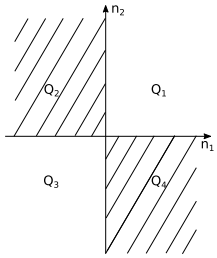

Figure 3. Allowed thermodynamic quadrants Q_1 and Q_3. The mole numbers of components 1 and 2 are along the *x*- and *y*-axis, respectively. The volume of Q_3 must be negative.

where $\Delta\mathbf{n}_L'$ is the original vector of steps in mole numbers computed from eq 19. If an update in mole numbers with eqs 20a and 20b attempted to change quadrants, the step length was reduced. A change in quadrants was detected if

$$\frac{n_j^{\nu+1}}{n_j^{\nu}} < 0 \tag{23}$$

To preserve the sign of n_j, we set the right-hand side of eqs 20a and 20b greater than 0 and utilize eq 22

$$\tau_j < -\frac{n_j}{\Delta n_j} \tag{24}$$

With eq 23 we found the j components attempting to change the quadrant, and with eq 24, we found the component determining the maximum allowable step length that preserves quadrants for all components. A condensed form of eqs 23 and 24 is given as

$$\tau = 0.8 \min_{n_j^{\nu+1}/n_j^{\nu}<0} \left(-\frac{n_j^{\nu}}{\Delta n_j^{\nu+1}} \right) \tag{25}$$

This procedure ensured that the new iterate $\mathbf{n}^{\nu+1}$ stayed inside the same legal quadrant.

If the current iterate $\mathbf{n}^{\nu}$ was sufficiently close to the origin and the step $\Delta\mathbf{n}^{\nu+1}$ would cross the origin and into another legal quadrant, then that step was accepted, and the vector of mole numbers was allowed through the origin. The step length was then obtained from the largest $-n_j^{\nu}/\Delta n_j^{\nu+1}$ out of all j

$$\tau = 1.1 \max \left(-\frac{n_j^{\nu}}{\Delta n_j^{\nu+1}} \right) \tag{26}$$

and all mole numbers were barely allowed through the origin to stabilize the algorithm and reject unreasonably large steps. If the iterate $\mathbf{n}^{\nu}$ was not sufficiently close to the origin, and the step $\Delta\mathbf{n}^{\nu+1}$ would cross the origin and into another legal quadrant, caution was exercised. If the origin is crossed and the solution to the phase equilibrium problem in eq 14 does not lie on the other side of the origin, this will most likely cause divergence. The step length was then computed by eq 25 until $\mathbf{n}^{\nu}$ was sufficiently close to the origin, where eq 26 was appropriate, and $\mathbf{n}^{\nu}$ was allowed through the origin.

Steps that stayed inside the current quadrant were also shortened to prevent aggressive steps from being taken, as these may lead to rapid divergence. When τ was computed, aggressive steps were prevented by choosing the smallest $|n_j^{\nu}/\Delta n_j^{\nu+1}|$ out of the j components with $n_j^{\nu}/\Delta n_j^{\nu+1} < 1$

$$\tau = \min_{n_j^{\nu}/\Delta n_j^{\nu+1}<1} \left(\left| \frac{n_j^{\nu}}{\Delta n_j^{\nu+1}} \right| \right) \tag{27}$$

Whenever the step, $\Delta n_j^{\nu+1}$, was larger than the current iterate, n_j^{ν}, the step length was reduced. If more than one component met this condition, the component j having the most aggressive step (smallest fraction in eq 27) was chosen for computing τ. This corresponds to the most significant reduction in step length.

Full steps, that is, $\tau = 1$, were allowed for steps inside the same quadrant if the phase equilibrium criterion was close to satisfied. This is equivalent to the right-hand side of eq 19 being close to zero. All other steps inside the same quadrant were shortened by $\tau = 0.5$ to prevent aggressive steps.

The previous discussion was applied to both the liquid-phase mole numbers, $\mathbf{n}_L^{\nu}$, and the gas-phase mole numbers, $\mathbf{n}_G^{\nu}$. If the step length was reduced considering one of the phases, this must not lead to the violation of eq 21 for the other phase, as this will cause the algorithm to fail.

Mass Transfer. For a gas in contact with a liquid, the mass transfer occurs over the interface that separates the two phases. In the two-film model, a thin film is formed on each side of the interface that separates the phases, that is, a film of thickness δ_G is formed on the gas side and a film of thickness δ_L is formed on the liquid side of the interface (see Figure 4).

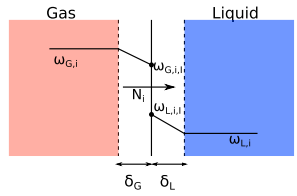

Figure 4. Two-film mass transfer model.

The mass transfer flux is assumed to be proportional to the difference in mass fraction, analogous to Fick's law. Furthermore, the flux is steady state, as the interface is assumed not to accumulate mass. Hence, the mass transfer flux from the gas phase to the interface is given by

$$N_i^{G-I} = k_{G,i}\rho_G(\omega_{G,i,I} - \omega_{G,i}) \tag{28}$$

where $k_{G,i}$ is the mass transfer coefficient of component i on the gas side of the interface, ρ_G is the mass density of the gas mixture, $\omega_{G,i,I}$ is the mass fraction of component i at the interface on the gas side, and $\omega_{G,i}$ is the mass fraction of component i in the bulk of the gas phase. For a purely diffusive flux, $k_{G,i} = D_{G,i}/\delta_G$ where $D_{G,i}$ is the diffusion coefficient of the gaseous component i. However, for combined convective and diffusive contributions, $k_{G,i}$ is parametrized by the Reynolds and Schmidt numbers[42].

The mass transfer flux from the interface and into the liquid is given by

$$N_i^{I-L} = k_{L,i}\rho_L(\omega_{L,i,I} - \omega_{L,i}) \tag{29}$$

Here $k_{L,i}$ is the mass transfer coefficient of component i on the liquid side, ρ_L is the mass density of the liquid mixture, $\omega_{L,i,I}$ is the mass fraction of component i at the interface on the liquid side, and $\omega_{L,i}$ is the mass fraction of component i in the bulk of the liquid phase. For a purely diffusive flux, $k_{L,i} = D_{L,i}/\delta_L$ where $D_{L,i}$ is the diffusion coefficient of the liquid component i.

https://doi.org/10.1021/acs.iecr.1c03131
Ind. Eng. Chem. Res. XXXX, XXX, XXX−XXX

However, for combined convective and diffusive contributions, $k_{L,i}$ is parametrized by the Reynolds and Schmidt numbers[42].

Generally accepted, gas−liquid equilibrium prevails at the interface, implying $\omega_{L,i,I} = \omega^*_{L,i}$ and $\omega_{G,i,I} = \omega^*_{G,i}$, where the asterisk (*) denotes the thermodynamic phase equilibrium state. In general, $\omega^*_{L,i} = f(T,p,\boldsymbol{\omega}_L,\boldsymbol{\omega}_G)$ and $\omega^*_{G,i} = f(T,p,\boldsymbol{\omega}_L,\boldsymbol{\omega}_G)$, where the boldface $\boldsymbol{\omega}$ indicates the vector of species mass fractions. Thus, the equilibrium state depends on a common and equal temperature, T, a common and equal pressure, p, and the composition of both phases. This dependency is clear from the phase equilibrium criteria in eqs 1a, 1b, and 1c and the mass balance closures in eq 2. However, this dependency reduces to temperature and pressure for a binary mixture with two phases, as seen from the Gibbs phase rule

$$F = N_C - N_P + 2 \tag{30}$$

Here, F is the degree of freedom, N_C is the number of components, N_P is the number of phases, and the number 2 denotes that two intensive variables may be specified. For a binary mixture with two phases, $F = 2$; however, if the intensive variables T and p are specified, then $F = 0$. Thus, varying the composition at constant T and p within any two-phase region of a binary mixture does not alter the equilibrium composition.

From eqs 28 and 29, we propose three different formulations for mass transfer. The first and second formulations are based on the continuity of fluxes through the interface, meaning the mass leaving the gas phase with eq 28 is received in the liquid phase with eq 29. Utilizing this equality, eqs 28 and 29 are gathered into a single expression for mass transfer. The third formulation employs eq 29 solely and thus assumes that the conditions in the liquid phase govern mass transfer. The first and second formulations are equivalent to the two-film model, and the third formulation is equivalent to the one-film model.

In the first approach, which is the most common in transport phenomena involving mass transfer (see, e.g., refs 43−49), Henry's law is employed in order to relate the two interface concentrations, $\omega_{G,i,I}$ and $\omega_{L,i,I}$. This relation closes the mass transfer problem and allows the mass transfer flux to be computed. Details on the first approach are given in the section Approach Based on Henry's Law.

The second approach employs the multicomponent gas−liquid equilibrium algorithm in the section Negative Flash Algorithm to compute the interface concentrations, $\omega_{G,i,I}$ and $\omega_{L,i,I}$, directly. Thus, the mass transfer flux can readily be computed through unifying eqs 28 and 29. The second approach is discussed in the section Rigorous Phase Equilibrium: Consistent Fluxes.

The third approach, see eq 29, is similar to the second approach because the multicomponent gas−liquid equilibrium algorithm in the section Negative Flash Algorithm is employed. However, no further manipulations are exercised on the mass transfer equations. In all formulations, no net mass transfer takes place when the bulk gas is in phase equilibrium with the bulk liquid.

Approach Based on Henry's Law. With eqs 28 and 29 being equal, their expressions may be combined into a single equation. For poorly soluble gases in the liquid solvent, the infinite dilution limit known as Henry's law is an appropriate relation for the interface concentrations. The definition of the Henry's law constant of solute i in solvent j is[50]

$$H_{ij} \equiv \lim_{x_i^* \to 0} \frac{f_{L,i}}{x_i^*} \tag{31}$$

where x_i^* is the mole fraction of component i in the liquid at equilibrium. With the definition in eq 31 along with eqs 4, 11, and 12, eq 13 is written as

$$p y_i^* \varphi_i = H_{ij} x_i^* \tag{32}$$

Here, y_i^* is the mole fraction of component i in the gas at equilibrium. In the Henry's law implementation, the gas phase was assumed ideal, and thus, $\varphi_i = 1$. The conversion from mole fractions to mass fractions is given as

$$x_i = \frac{\omega_i / M_{w,i}}{\sum_{j=1}^{N_C} \omega_j / M_{w,j}} \tag{33}$$

where $M_{w,i}$ is the molar weight of component i. Thus, eq 32 is written as

$$p \frac{\omega^*_{G,i}}{\sum_j \omega^*_{G,j}/M_{w,j}} = H_{ij} \frac{\omega^*_{L,i}}{\sum_j \omega^*_{L,j}/M_{w,j}} \tag{34}$$

and by introducing the average molar weight of the mixture as

$$\bar{M}_w = \frac{1}{\sum_j \omega_j / M_{w,j}} \tag{35}$$

Equation 34 is rewritten as

$$\omega^*_{L,i} = \frac{p}{H_{ij}} \frac{\bar{M}^*_{w,G}}{\bar{M}^*_{w,L}} \omega^*_{G,i} \tag{36}$$

Equation 29 is divided by $k_{L,i}\rho_L$, and since $\omega_{L,i,I} = \omega^*_{L,i}$, the expression in eq 36 is inserted

$$\frac{N_i^{I-L}}{k_{L,i}\rho_L} = \frac{p}{H_{ij}} \frac{\bar{M}^*_{w,G}}{\bar{M}^*_{w,L}} \omega^*_{G,i} - \omega_{L,i} \tag{37}$$

Furthermore, we divide eq 28 by $k_{G,i}\rho_G \frac{H_{ij}}{p} \frac{\bar{M}^*_{w,L}}{\bar{M}^*_{w,G}}$ and insert $\omega_{G,i,I} = \omega^*_{G,i}$

$$\frac{N_i^{G-I}}{k_{G,i}\rho_G \frac{H_{ij}}{p} \frac{\bar{M}^*_{w,L}}{\bar{M}^*_{w,G}}} = \frac{p}{H_{ij}} \frac{\bar{M}^*_{w,G}}{\bar{M}^*_{w,L}} (\omega^*_{G,i} - \omega_{G,i}) \tag{38}$$

Equation 38 is subtracted from eq 37, and the equality of fluxes $N_i^{G-I} = -N_i^{I-L} = -N_i$ is employed in order to eliminate the dependency on $\omega^*_{G,i}$

$$N_i \left(\frac{1}{k_{L,i}\rho_L} + \frac{1}{k_{G,i}\rho_G \frac{H_{ij}}{p} \frac{\bar{M}^*_{w,L}}{\bar{M}^*_{w,G}}} \right) = \frac{p}{H_{ij}} \frac{\bar{M}^*_{w,G}}{\bar{M}^*_{w,L}} \omega_{G,i} - \omega_{L,i} \tag{39}$$

It is commonly accepted that most of the resistance to mass transfer lies on the liquid side and that this assumption implies that $1/(k_{L,i}\rho_L) \gg 1/\left(k_{G,i}\rho_G \frac{H_{ij}}{p} \frac{\bar{M}^*_{w,L}}{\bar{M}^*_{w,G}}\right)$. By implementing this inequality into eq 39, the resulting mass-based mass transfer flux reads

$$N_i = k_{L,i}\rho_L \left(\frac{p}{H_{ij}} \frac{\bar{M}^*_{w,G}}{\bar{M}^*_{w,L}} \omega_{G,i} - \omega_{L,i} \right) \tag{40}$$

https://doi.org/10.1021/acs.iecr.1c03131
Ind. Eng. Chem. Res. XXXX, XXX, XXX−XXX

The evaluation of eq 40 requires knowledge of $\bar{M}^*_{w,L}$ and $\bar{M}^*_{w,G}$. For the liquid, eq 32 is rewritten as

$$x_i^* = \frac{p}{H_{ij}} y_i \tag{41}$$

to obtain

$$\bar{M}^*_{w,L} = \sum_{j=1}^{N_C} x_j^* M_{w,j} \tag{42}$$

For the gas, we assume $\omega^*_{G,i} = \omega_{G,i}$ to evaluate $\bar{M}^*_{w,G} = \bar{M}_{w,G}$ with eq 35. Thus, with $\bar{M}^*_{w,G} = \bar{M}_{w,G}$, eq 40 is simplified, and we obtain the expression for mass transfer assuming Henry's law

$$N_i = k_{L,i}\rho_L \left(\frac{p}{H_{ij}} \frac{\bar{M}_{w,G}}{\bar{M}^*_{w,L}} \omega_{G,i} - \omega_{L,i} \right) \tag{43}$$

As expected, eq 43 reduces to zero when the gas and liquid phases are in phase equilibrium.

To show the similarities between eq 43 and the next mass transfer models, we introduce the equilibrium constant (K-value). The mole-based K-value is defined as

$$K_i^m \equiv \frac{y_i^*}{x_i^*} \tag{44}$$

and the mass-based K-value is defined as

$$K_i \equiv \frac{\omega^*_{G,i}}{\omega^*_{L,i}} \tag{45}$$

By employing eqs 44 and 45 in combination with eqs 33 and 35, we obtain

$$K_i = \frac{\bar{M}^*_{w,L}}{\bar{M}^*_{w,G}} K_i^m \tag{46}$$

Furthermore, eq 32 is inserted for K_i^m in eq 46 to obtain

$$K_{ij}^\infty = \frac{H_{ij}}{p} \frac{\bar{M}^*_{w,L}}{\bar{M}^*_{w,G}} \tag{47}$$

Here, K_{ij}^∞ denotes the mass-based K-value as solute i is infinitely diluted in solvent j. Thus, K_{ij}^∞ is restricted to Henry's law, whereas K_i is not. Equation 43 may be rewritten with eq 47

$$N_i = k_{L,i}\rho_L \left(\frac{\omega_{G,i}}{K_{ij}^\infty} - \omega_{L,i} \right) \tag{48}$$

We emphasize that, in general, eq 31 is valid for both binary and multicomponent systems. However, in practice, the Henry's law constants are taken from binary gas−liquid equilibrium experiments. Hence, by employing a set of binary Henry's law constants in a multicomponent mixture, the multicomponent phase equilibrium is approximated as a set of pseudo-binary phase equilibria. This approximation has four significant consequences. First and foremost, the solubility of each gaseous component is entirely independent of all other gaseous components. Thus, the pseudo-binary phase equilibria are only functions of T and p, as previously mentioned with the Gibbs phase rule in eq 30. This approximation is the major strength of Henry's law as it simplifies the phase equilibrium computations substantially. However, for complicated systems where the mass transfer fluxes depend on each other, the pseudo-binary equilibrium approximation may not be accurate.

Second, Henry's law assumes that one solvent is in excess in the liquid phase and that the gaseous components exist as solutes in trace amounts in this solvent. Liquid mixtures containing substantial amounts of dissolved gas solutes violate the assumption of infinite dilution in eq 31 where Henry's law is valid.

Third, it is impossible to compute the mass transfer of the solvent directly with eq 43 since H_{ij} is neither available nor a meaningful quantity. However, this mass transfer flux is not directly required since the amount of solvent can be computed as

$$\omega_{N_C} = 1 - \sum_{i=1}^{N_C - 1} \omega_i \tag{49}$$

On the other hand, this does not provide any guarantee that gas−liquid equilibrium prevails at the interface for the solvent, since phase equilibrium is governed by the equality of chemical potentials in eq 1c and not eq 49. Furthermore, using eq 49, the errors in the species mass balances of component $j = 1, 2, ..., N_C - 1$ are accumulated into ω_{N_C}. Hence, it is unwise to employ eq 49 for the solvent in the gas phase as it is likely to exist in trace amounts in the gas phase. The numerical errors propagating from the species mass balances of component $j = 1, 2, ..., N_C - 1$ may therefore be large compared to the small ω_{G,N_C}, and the use of eq 49 may in the worst case yield a negative mass fraction of solvent, that is, $\omega_{G,N_C} < 0$. Hence, the mass transfer of the solvent is commonly neglected or ignored and $N_{N_C} = 0$. Consequently, the mass fraction of the solvent in the gas phase is likely erroneous.

Fourth, the simplicity and applicability of eq 43 rest on the availability of experimental or correlated values for the Henry's law constant for solute i in solvent j. Most experimental work on the Henry's law constant is for poorly soluble gases in H_2O. This limits the practicality of eq 43, and for studies where H_{ij} is not available, the mass transfer flux, N_i, cannot be computed.

Rigorous Phase Equilibrium: Consistent Fluxes. This approach aims to remedy the four shortcomings of the Henry's law approach mentioned in the section Approach Based on Henry's Law. Therefore, we model the solubilities as a coupled set of equations using the rigorous phase equilibrium approach discussed in the section Negative Flash Algorithm. The K-values in eq 45 are thus functions of the temperature, pressure, and composition of both phases, in contrast to the pseudo-binary phase equilibria employed with Henry's law, where K_{ij}^∞ was a function of temperature and pressure only (see eq 30).

The mass transfer flux expression is derived by assuring that the gas-to-interface flux is consistent with the interface-to-liquid flux. By dividing eq 28 by $k_{G,i}\rho_G K_i$ and noting that $\omega_{G,i,I} = \omega^*_{G,i}$, we obtain

$$\frac{N_i^{G-I}}{k_{G,i}\rho_G K_i} = \frac{\omega^*_{G,i}}{K_i} - \frac{\omega_{G,i}}{K_i} \tag{50}$$

Furthermore, division of eq 29 by $k_{L,i}\rho_L$ and inserting eq 45 for $\omega^*_{L,i}$ yields

$$\frac{N_i^{I-L}}{k_{L,i}\rho_L} = \frac{\omega^*_{G,i}}{K_i} - \omega_{L,i} \tag{51}$$

https://doi.org/10.1021/acs.iecr.1c03131
Ind. Eng. Chem. Res. XXXX, XXX, XXX−XXX

Equation 50 is subtracted from eq 51 and $N_i^{G-I} = -N_i^{I-L} = -N_i$

$$N_i\left(\frac{1}{k_{L,i}\rho_L} + \frac{1}{k_{G,i}\rho_G K_i}\right) = \frac{\omega_{G,i}}{K_i} - \omega_{L,i} \tag{52}$$

It is commonly accepted that most of the resistance to mass transfer lies on the liquid side and that this assumption implies that $1/(k_{L,i}\rho_L) \gg 1/(k_{G,i}\rho_G K_i)$. By implementing this inequality into eq 52, the resulting mass-based mass transfer flux reads

$$N_i = k_{L,i}\rho_L\left(\frac{\omega_{G,i}}{K_i} - \omega_{L,i}\right) \tag{53}$$

We emphasize the similarities in eqs 48 and 53. The similarities originate from the assumption that phase equilibrium prevails at the interface; however, eq 48 is restricted to the infinite dilution limit. Furthermore, the mass transfer of the solvent cannot be predicted with eq 48. These two limitations do not apply to eq 53 as the assumptions limiting Henry's law were not made in the derivation of eq 53.

The K-values in eq 53 were obtained by solving the phase equilibrium problem with eqs 11 and 17−20 along with the initialization in eq 2. We assumed that the equilibrium prevailing at the interface is the state obtained if the bulk gas and liquid phases were in phase equilibrium. Thus, the initializations in eq 2 were determined by the reactor's local bulk gas and liquid fluxes. The liquid, gas, and total molar fluxes are given, respectively, by

$$G_L = \frac{\rho_L|\boldsymbol{v}_L|\alpha_L}{\sum_{j=1}^{N_C} M_{w,j}x_j} \tag{54a}$$

$$G_G = \frac{\rho_G|\boldsymbol{v}_G|\alpha_G}{\sum_{j=1}^{N_C} M_{w,j}y_j} \tag{54b}$$

$$G_T = G_L + G_T \tag{54c}$$

Here, $|\mathbf{v}_L|$ and $|\mathbf{v}_G|$ are the Euclidean lengths of the local instantaneous velocities of the liquid and gas phases, respectively. Moreover, the volume fraction of the liquid is denoted as $\alpha_L = V_L/V$, representing the fractional volume of the averaging volume occupied by the liquid. Similarly, the volume fraction of gas is denoted as $\alpha_G = V_G/V$, representing the fractional volume of the averaging volume occupied by gas—the volume fractions sum to unity for a two-phase flow.

The normalized mole number fluxes at each cross section were obtained from eqs 54a, 54b, and 54c and describe the required mass balances in eq 2

$$\beta_{L,i}^0 = \frac{G_L}{G_T}x_i \tag{55a}$$

$$\beta_{G,i}^0 = \left(1 - \frac{G_L}{G_T}\right)y_i \tag{55b}$$

The phase equilibrium computation is visualized in Figure 5. In order to obtain the mass balances required for the equilibrium computation, the gas and liquid molar fluxes, G_G and G_L, are hypothetically mixed in the first tank. The resulting stream G_T contains both gas and liquid. This mixing process corresponds to eqs 54a, 54b, 54c, 55a, and 55b. In the second tank, the negative flash computation described in the section Negative Flash Algorithm is performed, and eq 19 is solved with the initialization obtained from the first tank with eqs 54a, 54b, 54c, 55a, and 55b.

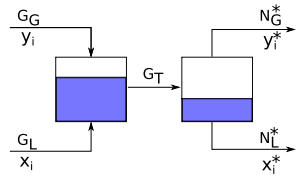

Figure 5. Bulk phases are hypothetically mixed according to the molar fluxes, and the total mixture is flashed according to the SRK-EoS and the negative flash algorithm.

It is emphasized that we use the mixing and flash process visualized in Figure 5 exclusively to find the equilibrium concentrations that would exist *if* the bulk phases were to establish phase equilibrium. Hence, the bulk gas and liquid phases are not necessarily in phase equilibrium as demonstrated in Figure 5.

The equilibrium mole fractions were retrieved as

$$y_i^* = \frac{n_{G,i}^*}{N_G^*} \tag{56a}$$

$$x_i^* = \frac{n_{L,i}^*}{N_L^*} \tag{56b}$$

and converted to equilibrium mass fractions with

$$\omega_i^* = \frac{x_i^* M_{w,i}}{\bar{M}_w^*} \tag{57}$$

where $\bar{M}_w^*$ was computed with eq 42. The K-values on mass basis were thus directly computed with eq 45 and the mass transfer flux of component i was computed with eq 53.

Rigorous Phase Equilibrium: Liquid-Side Flux Equations. The third approach was similar to the one discussed in the section Rigorous Phase Equilibrium: Consistent Fluxes: the equilibrium composition was rigorously determined from eqs 11 and 17−20 along with the initialization in eqs 54a, 54b, 54c, 55a, and 55b. However, here, the mass transfer flux was determined from eq 29, and thus, it did not directly depend on neither ω_G nor ω_G^*. However, ω_L^* depends on ω_G through eqs 54a, 54b, 54c, 55a, and 55b, and hence, the mass transfer fluxes still depend on the conditions of both phases.

As seen from the Gibbs phase rule in eq 30, ω_L^* and ω_G^* depend exclusively on temperature and pressure for binary mixtures. As the mass transfer expression in eq 29 depends only on $\omega_L^*(T,p)$ and ω_L, mass transfer is allowed without considering the gas-phase concentrations. A possible, unphysical scenario is a nonzero driving force, $\omega_{L,i}^* - \omega_{L,i} \neq 0$, in combination with a gaseous absence of the same component, $\omega_{G,i} = 0$. The driving force in eq 29 thus allows mass to be transferred from the gas phase and into the liquid phase, although this mass does not exist in the gas phase. This is unacceptable. As a result, this method was abandoned and not explored further.

REACTOR MODEL

In SCP production, mass transfer is crucial to sustain a healthy microbiological culture and maintain high production. A reactor design that facilitates mass transfer is the vertical U-loop reactor pilot situated at the Technical University of Denmark (DTU).

https://doi.org/10.1021/acs.iecr.1c03131
Ind. Eng. Chem. Res. XXXX, XXX, XXX−XXX

Table 1. Governing Equations Describing the Bubble Column

Transport of Total Mass

$$\frac{\mathrm{d}}{\mathrm{d}z}(\alpha_\mathrm{L}\rho_\mathrm{L}v_\mathrm{L}) = \sum_{j=1}^{N_\mathrm{C}} N_j a \tag{59}$$

$$\frac{\mathrm{d}}{\mathrm{d}z}(\alpha_\mathrm{G}\rho_\mathrm{G}v_\mathrm{G}) = -\sum_{j=1}^{N_\mathrm{C}} N_j a \tag{60}$$

Transport of Species Mass

$$\frac{\mathrm{d}}{\mathrm{d}z}(\alpha_\mathrm{L}\rho_\mathrm{L}v_\mathrm{L}\omega_{\mathrm{L},i}) = \frac{\mathrm{d}}{\mathrm{d}z}\left(\alpha_\mathrm{L}\rho_\mathrm{L}D_{\mathrm{L,eff},z}\frac{\mathrm{d}\omega_{\mathrm{L},i}}{\mathrm{d}z}\right) + N_i a + \alpha_\mathrm{L}R_i \tag{61}$$

$$\frac{\mathrm{d}}{\mathrm{d}z}(\alpha_\mathrm{G}\rho_\mathrm{G}v_\mathrm{G}\omega_{\mathrm{G},i}) = \frac{\mathrm{d}}{\mathrm{d}z}\left(\alpha_\mathrm{G}\rho_\mathrm{G}D_{\mathrm{G,eff},z}\frac{\mathrm{d}\omega_{\mathrm{G},i}}{\mathrm{d}z}\right) - N_i a \tag{62}$$

Transport of Momentum

$$\frac{\mathrm{d}}{\mathrm{d}z}(\alpha_\mathrm{L}\rho_\mathrm{L}v_\mathrm{L}v_\mathrm{L}) = \frac{\mathrm{d}}{\mathrm{d}z}\left(\alpha_\mathrm{L}\mu_{\mathrm{L,eff},z}\frac{\mathrm{d}v_\mathrm{L}}{\mathrm{d}z}\right) - \alpha_\mathrm{L}\frac{\mathrm{d}p}{\mathrm{d}z} - \alpha_\mathrm{L}\rho_\mathrm{L}g + f_\mathrm{drag}^{\mathrm{G-L}} + f_\mathrm{fric}^{\mathrm{W-L}} \tag{63}$$

$$\frac{\mathrm{d}}{\mathrm{d}z}(\alpha_\mathrm{G}\rho_\mathrm{G}v_\mathrm{G}v_\mathrm{G}) = \frac{\mathrm{d}}{\mathrm{d}z}\left(\alpha_\mathrm{G}\mu_{\mathrm{G,eff},z}\frac{\mathrm{d}v_\mathrm{G}}{\mathrm{d}z}\right) - \alpha_\mathrm{G}\frac{\mathrm{d}p}{\mathrm{d}z} - \alpha_\mathrm{G}\rho_\mathrm{G}g - f_\mathrm{drag}^{\mathrm{G-L}} \tag{64}$$

Transport of Energy

$$\alpha_\mathrm{L}\rho_\mathrm{L}v_\mathrm{L}c_{p,\mathrm{L}}\frac{\mathrm{d}T_\mathrm{L}}{\mathrm{d}z} = \frac{\mathrm{d}}{\mathrm{d}z}\left(\alpha_\mathrm{L}\lambda_{\mathrm{L,eff},z}\frac{\mathrm{d}T_\mathrm{L}}{\mathrm{d}z}\right) + \frac{4U}{d_\mathrm{col}}(T_\mathrm{a} - T_\mathrm{L}) + h_\mathrm{L}a(T_\mathrm{G} - T_\mathrm{L}) + \alpha_\mathrm{L}R_{\mathrm{O}_2}\Delta_{rx}h \tag{65}$$

$$\alpha_\mathrm{G}\rho_\mathrm{G}v_\mathrm{G}c_{p,\mathrm{G}}\frac{\mathrm{d}T_\mathrm{G}}{\mathrm{d}z} = \frac{\mathrm{d}}{\mathrm{d}z}\left(\alpha_\mathrm{G}\lambda_{\mathrm{G,eff},z}\frac{\mathrm{d}T_\mathrm{G}}{\mathrm{d}z}\right) - h_\mathrm{L}a(T_\mathrm{G} - T_\mathrm{L}) \tag{66}$$

At Tjeldbergodden in Norway, an industrial horizontal U-loop reactor was also operated by Norferm for several years before being shut down in 2006, possibly due to restructuring of Norferm's available resources. At both DTU and Tjeldbergodden, the U-loop tube is equipped with static mixers and a heat exchanger for heat removal. A degassing tank is connected to the U-loop to remove the CO_2 produced.

The methanotrophic bacteria *M. capsulatus* (Bath) were used to produce SCP by consuming CH_4. A black box model was used to lump all metabolic reactions into one representative reaction[9,S1]

$$\mathrm{CH_4} + 1.454\mathrm{O_2} + 0.104\mathrm{NH_3} = 0.52\mathrm{X} + 0.48\mathrm{CO_2} + 1.688\mathrm{H_2O} \tag{58}$$

Here, X represents a lump of representative biomass, which is assumed to have the chemical formula $CH_{1.8}O_{0.5}N_{0.2}$. The reaction kinetics of eq 58 was studied by Joergensen and Degn,[52] and the bacteria were found to metabolize optimally at 45 °C. Hence, Joergensen and Degn[52] parametrized the reaction rate at 45 °C. Their correlation is given in the Supporting Information.

The U-loop tube is commonly regarded as a plug flow reactor, and the degassing tank is commonly regarded as a combination of a separator unit and a continuously stirred tank reactor.[1,9,11,53] In this work, we modeled the U-loop tube as a bubble column reactor described by two phases: one gas phase and one liquid phase. The gas phase was assumed to consist of bubbles of constant diameter and contain a mixture of O_2 and CH_4. On the other hand, the liquid phase was a broth consisting of H_2O, NH_3, and bacteria. Moreover, the reaction was assumed to take place in the liquid broth exclusively. We modeled each phase by a set of continuity, species mass, momentum, and energy equations, referred to as the governing equations. In this work, the governing equations were cross-sectionally averaged and assumed time-independent. Mass transfer between the gas and liquid phases was accounted for by the methods described in the section Mass Transfer.

The one-dimensional governing equations are shown in Table 1. Further closure equations required to solve the set of governing equations are given in the section Closure Equations to Reactor Model in the Supporting Information. In the following, we present the gas- and liquid-phase density, the numerical solution method, the program flow, a set of parameters, and reactor dimensions.

Density. The liquid-phase density was assumed constant and equal to the pure liquid H_2O density at $T = 298.15$ K, that is, $\rho_\mathrm{L} = \rho_{\mathrm{L,H_2O}}(298.15\ \mathrm{K})$. The value is tabulated by Aylward and Findlay.[35] For mass transfer governed by Henry's law, see eq 43, the gas-phase density was obtained by the ideal gas law, as this is consistent with the assumptions made in eq 32. The density was thus obtained by rewriting eq 3

$$\rho_\mathrm{G} = \frac{p\bar{M}_{\mathrm{w,G}}}{RT} \tag{67}$$

On the other hand, for mass transfer governed by rigorous phase equilibrium as in the section Rigorous Phase Equilibrium: Consistent Fluxes, the gas-phase volume was obtained from the SRK-EoS (see eq 6). Subsequently, the density was obtained by

$$\rho_\mathrm{G} = \frac{N}{V}\bar{M}_{\mathrm{w,G}} \tag{68}$$

In eq 68, V was chosen as the largest of the three solutions to eq 6.

Numerical Solution Method. The governing equations in Table 1 were solved with the orthogonal collocation method, which is a spectral method of weighted residuals. Here, the function is approximated at a set of nodal points termed collocation points

https://doi.org/10.1021/acs.iecr.1c03131
Ind. Eng. Chem. Res. XXXX, XXX, XXX−XXX

$$f(z) \approx \sum_{j=0}^{N} \gamma_j \phi_j^N(z) \tag{69}$$

In eq 69, $f(z)$ is the function of interest, γ_j are the basis coefficients independent of z, and $\phi_j^N(z)$ are Nth-order trial polynomials. If $\phi_j^N(z)$ are chosen as Lagrange interpolating polynomials, then $\gamma_j = f(z_j)$ is the function value itself.[54] Here, $\{z_j\}$ is the set of collocation points and $j = 0, 1, ..., N$. With this approach, the problem can be written on a linearized form, $\mathbf{Af} = \mathbf{b}$, where $\mathbf{A}$ contains linear terms in $\mathbf{f}$, such as derivatives and integrals.

The collocation points were computed from the roots of Legendre polynomials, as they yield low condition numbers and low error.[55] Furthermore, both endpoints of the physical domain were included. Hence, both the reactor inlet and the reactor outlet were included in the computational domain, resulting in a Gauss Lobatto type of grid. Obtaining the collocation points has been studied extensively, and the reader is referred elsewhere for details.[42,56−62] In total, 30 grid points were placed in the z-direction. A summary of the numerical solution strategy is given in Table 2.

Table 2. Numerical Properties

property	value
solution method	orthogonal collocation method
collocation points	roots of Legendre polynomials
grid size	30 grid points
error	10^{-9}−10^{-16}, see Figure 16 in results
run time	8−10 h, see Figure 16 in results

With the orthogonal collocation method, eq 59 was solved for v_L, eq 60 was solved for α_G, eqs 61 and 62 were solved for $\omega_{L,i}$ and $\omega_{G,i}$, respectively, eq 63 was solved for p, eq 64 was solved for v_G, and eqs 65 and 66 were solved simultaneously for T_L and T_G, respectively.

Program Flow. A schematic representation of the program is given in Figure 6. The program was initialized before attempting to solve all of the governing equations in Table 1. The initialization was performed by converging the species mass balances and holding all other variables constant. This reduces the initially high mass transfer, which reduces the likelihood of divergence once all the governing equations are solved.

After initialization, all governing equations were solved sequentially, except for the energy equations, which were solved simultaneously. Furthermore, the K-values were updated once every *outer iteration* to reduce the computational expense associated with this update. The *inner loop* on the species mass balances was crucial to ensure that the mass transfer did not cause divergence in the continuity equations, as the continuity equations are sensitive to mass transfer.

In Figure 6, the approach for modeling the K-values (Henry's law or rigorous phase equilibrium) and the mass transfer may easily be changed without altering the main structure significantly. Thus, the mass transfer model for Henry's law in the section Approach Based on Henry's Law and the mass transfer model for rigorous phase equilibrium in the section Rigorous Phase Equilibrium: Consistent Fluxes share the same flow chart in Figure 6. The differences between the Henry's law and SRK-EoS approach reside in the phase equilibrium computation and are displayed in Figure 7. The mass transfer model in the section Rigorous Phase Equilibrium: Liquid-Side Flux Equations was deemed inappropriate and, hence, not implemented.

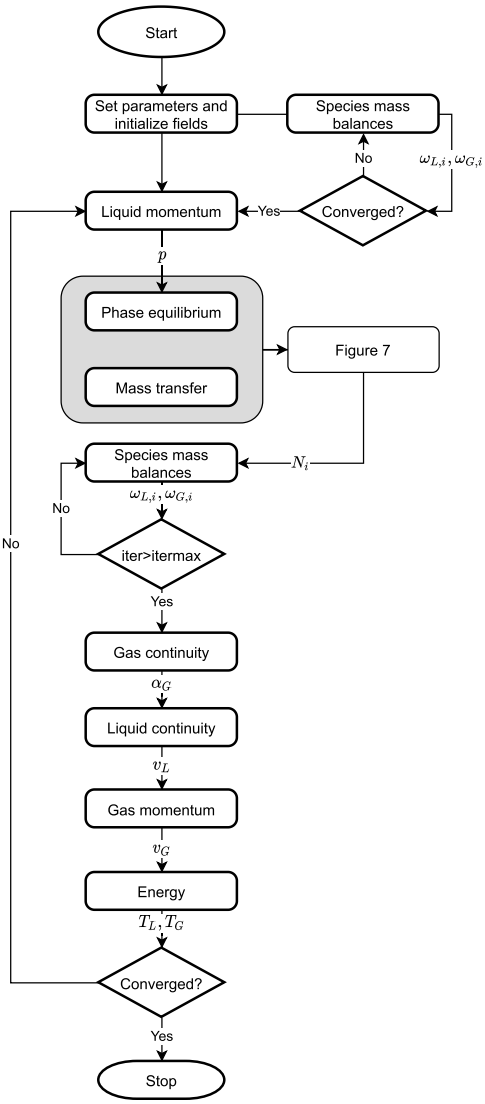

Figure 6. Program flow of the bubble column bioreactor. The program utilizes an outer loop and an inner loop in order to converge all governing equations.

Parameters and Initial Conditions. The parameters and reactor dimensions used for the simulations are shown in Table S1 in the Supporting Information. The binary interaction parameters, k_{ij}, were fitted to the literature data[50,63−90] by the authors for the species pairs O_2−H_2O, CH_4−H_2O, and CO_2−H_2O. The other species pairs were found in the literature.[91−93] All binary interaction parameters are given in Table 3. Furthermore, the critical constants required for the SRK-EoS were obtained from Lemmon et al.[38] and are summarized in Table S2 in the Supporting Information.

https://doi.org/10.1021/acs.iecr.1c03131
Ind. Eng. Chem. Res. XXXX, XXX, XXX−XXX

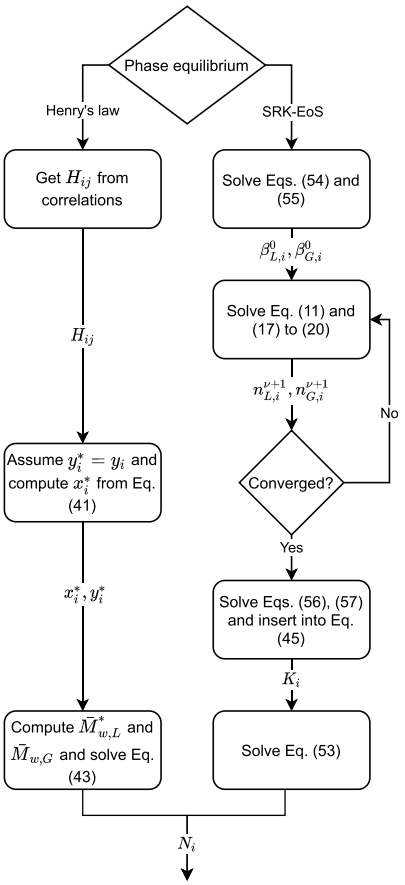

Figure 7. Differences in phase equilibrium computations between the Henry's law and the SRK-EoS approaches.

Table 3. Binary Interaction Parameters Used with the SRK-EoS

k_{ij}	O_2	CH_4	CO_2	NH_3	H_2O
O_2	0	0	0.106	0	−0.365
CH_4	0	0	0.118	0	−0.37
CO_2	0.106	0.118	0	0	−0.138
NH_3	0	0	0	0	−0.28
H_2O	−0.365	−0.37	−0.138	−0.28	0

Furthermore, the inlet values are shown in Table 4, where the superficial velocity is denoted as $v^s = v\alpha$. The superficial liquid velocity was based on the dilution rates

$$D_L = \frac{\dot{V}_L}{V_{reactor}} \tag{70}$$

where $\dot{V}_L = v^s_L A_{reactor}$ is the volumetric flow rate and $V_{reactor}$ is the reactor volume. Dilution rates relevant for the SCP fermentation process are given in Table 5, and the superficial liquid velocity was obtained by rearranging eq 70

$$v^s_L = D_L L \tag{71}$$

Table 4. Initial Conditions Used in Simulation of the Bubble Column Bioreactor

variable	liquid	gas	unit
v^s_{in}	6.34×10^{-4}	0.05	$m^3\ m^{-2}\ s^{-1}$
$x_{O_2,in}$	10^{-9}	0.430	
$x_{CH_4,in}$	10^{-9}	0.567	
$x_{CO_2,in}$	10^{-9}	0.001	
$x_{NH_3,in}$	0.01	0.001	
$x_{H_2O,in}$	0.975319997	0.001	
$x_{X,in}$	0.01468	0	
p_{out}	3	3	bar
T_{in}	45	45	°C

Table 5. Dilution Rates in the Literature

dilution rate	reference
0.0697−0.2231 h^{-1}	Olsen et al.[1]
0.0463−0.0940 h^{-1}	Petersen et al.[10]
0.19−0.2 h^{-1}	Villadsen[8]
0−0.035 h^{-1}	Prado-Rubio et al.[11]
120 h^{-1}	Al Taweel et al.[9]

where L is the length of the reactor. Moreover, v^s_G was based on values similar to the experimental study of Petersen et al.[10] and the theoretical study of Al Taweel et al.[9] The reactor temperature was chosen to match the optimal growth temperature found by Joergensen and Degn.[52] Increasing the pressure increases the solubility of O_2 and CH_4, but it simultaneously increases the operating costs of the plant. The nominal operating pressure was set by considering a trade-off between solubility and operating costs.

The initial composition of the liquid phase was based on an SCP plant operated at Tjeldbergodden Norway by Norferm from the late 1990s to 2006.[94] On the other hand, the initial composition of the gas phase was based on two considerations: (i) the stoichiometry of the biological reaction in eq 58 requires an O_2/CH_4 ratio of 1.454 (we have chosen 0.76) and (ii) the combustibility of the O_2-CH_4 mixture.[95−99]

The initial conditions used in the continuity eqs 59 and 60 were set to

$$v^{\nu+1}_{L,in} = \frac{v^s_{L,in}}{1 - \alpha^{\nu+1}_{G,in}} \tag{72}$$

and

$$\alpha^{\nu+1}_{G,in} = \alpha^{\nu}_{G,in} \tag{73}$$

Since only the superficial velocities were specified, the inlet gas area fraction in eq 73 must be recomputed at each iteration by

$$\alpha^{\nu}_{G,in} = \frac{v^s_{G,in}}{v^{\nu+1}_{G,in}} \tag{74}$$

In eq 74, the inlet local instantaneous velocity was computed from the algebraic slip model

https://doi.org/10.1021/acs.iecr.1c03131
Ind. Eng. Chem. Res. XXXX, XXX, XXX−XXX

$$v_{G,in}^{\nu+1} = v_{L,in}^{\nu} - \frac{1}{\frac{3}{4d_b}\rho_L C_{D,z=0}|v_{L,in}^{\nu} - v_{G,in}^{\nu}|} \left(\left.\frac{dp}{dz}\right|_{z=0} + g\rho_{G,z=0} \right) \quad (75)$$

which was directly obtained by neglecting the convective and viscous terms in eq 64. The expression in eq 75 is implicit in $v_{G,in}$, and the iteration count is denoted as ν. At the reactor outlet, the boundary condition was specified as

$$\frac{dv_G}{dz} = 0 \quad (76)$$

For the liquid-phase momentum equation, the pressure was specified at the outlet, $p_{z=L} = p_{out}$.

The species mass balances employed Danckwerts boundary conditions.[100] For the inlet, the boundary condition for the liquid phase was

$$(\alpha_L \rho_L v_L \omega_{L,i})_{z=0^+} - \left(\alpha_L \rho_L D_{L,eff,z} \frac{d\omega_{L,i}}{dz} \right)_{z=0^+} = (\rho_L v_L^s \omega_{L,i})_{z=0^-} \quad (77)$$

and for the gas phase

$$(\alpha_G \rho_G v_G \omega_{G,i})_{z=0^+} - \left(\alpha_G \rho_G D_{G,eff,z} \frac{d\omega_{G,i}}{dz} \right)_{z=0^+} = (\rho_G v_G^s \omega_{G,i})_{z=0^-} \quad (78)$$

Here, the symbol 0^- denotes the inlet values as specified in Table 4 and 0^+ denotes the inlet values on the inside of the reactor, which is part of the computational grid. The outlet boundary conditions were

$$\left.\frac{d\omega_{L,i}}{dz}\right|_{z=L} = 0 \quad (79)$$

$$\left.\frac{d\omega_{G,i}}{dz}\right|_{z=L} = 0 \quad (80)$$

For the energy equations, the Danckwerts boundary conditions were also employed. Thus, the inlet boundary conditions were

$$(\alpha_L \rho_L v_L c_{p,L} T_L)_{z=0^+} - \left(\alpha_L \lambda_{L,eff,z} \frac{dT_L}{dz} \right)_{z=0^+} = (\rho_L v_L^s c_{p,L} T_L)_{z=0^-} \quad (81)$$

$$(\alpha_G \rho_G v_G c_{p,G} T_G)_{z=0^+} - \left(\alpha_G \lambda_{G,eff,z} \frac{dT_G}{dz} \right)_{z=0^+} = (\rho_G v_G^s c_{p,G} T_G)_{z=0^-} \quad (82)$$

and the outlet boundary conditions were

$$\left.\frac{dT_L}{dz}\right|_{z=L} = 0 \quad (83)$$

$$\left.\frac{dT_G}{dz}\right|_{z=L} = 0 \quad (84)$$

The reactor model is described through eqs 59−66 with initial and boundary conditions given by eqs 72−84. A graphical representation of the reactor model and the initial and boundary conditions are given in Figure 8.

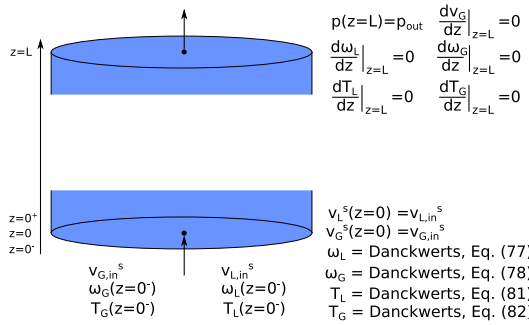

Figure 8. Graphical representation of the reactor model and its initial and boundary conditions.

Additional closure relations for eqs 61−66 in the Supporting Information. The closure relations include, but are not limited to, the reaction rate, drag forces, and heat capacities.

RESULTS AND DISCUSSION

A novel mass transfer model based on thermodynamic phase equilibrium at the gas−liquid interface was derived for the bubble column in the section Mass Transfer. The new and the conventional mass transfer formulations were here analyzed for a bioreactor producing SCP. That is, gas−liquid equilibrium relations based on (i) Henry's law and (ii) the SRK-EoS were used to relate the interface concentrations and close the mass transfer problem. The two solutions were compared in terms of differences in flow fields, phase fraction, pressure, density, species composition, temperature, and numerical properties including convergence time and residual.

This section is organized into five parts. The first part gives the limitations and considerations regarding verification and validation of the novel mass transfer expression. The second part, Nonreactive System: Three Components, presents the results of a simplified test case of mass transfer in a ternary mixture without reaction to verify that the novel mass transfer model described in the section Rigorous Phase Equilibrium: Consistent Fluxes yields physical results. It is noted that a study of a binary system would suffice for an analysis of the proposed mass transfer models. However, binary phase equilibria depend exclusively on T and p, and in this study, we intend to explore how the dependency on $\boldsymbol{\omega}$ affects the equilibrium and hence the mass transfer flux. In the third part, Reactive System: The SCP Bioreactor, the SCP bioreactor exemplifies a reactive six-component system with mass transfer. The fourth part presents a sensitivity study in pressure for the SCP bioreactor, and the fifth part presents a sensitivity study in k_{ij}, k_L, and d_b for the SCP bioreactor.

Limitations, Verification, and Validation of the Mass Transfer Expressions. It is noted that the density of the gas mixture in this work may exhibit nonideal behavior. However, from the experimental compressibility charts obtained by Viswanath and Su,[101] pure O_2, CH_4, CO_2, and H_2O behave ideally at the temperature and pressure considered for the SCP process. On the other hand, for pure NH_3, the reduced

https://doi.org/10.1021/acs.iecr.1c03131
Ind. Eng. Chem. Res. XXXX, XXX, XXX−XXX

temperature is 0.785 and the reduced pressure is 0.0265. For low reduced temperatures, such as that for NH_3 in this work, nonideal behavior is commonly observed. However, since the reduced pressure is very low, pure NH_3 behaves approximately ideally. Hence, all compounds present in the SCP process would behave ideally as pure components at the T and p investigated in this study. Since most of the gas phase consists of O_2, CH_4, and CO_2, which are all supercritical with high reduced temperature and low reduced pressures, an ideal gas assumption is considered reasonable.

In the mass transfer model formulation in eq 53, we assumed that the temperature and pressure profiles through the gas−liquid interface have no gradient, that is, $T_L = T_I = T_G$ and $p_L = p_I = p_G$. High heat transfer coefficients have been observed for the bubble column reactor,[102] and thus, the equality of temperatures in eq 1a is, in this work, justified. Furthermore, the equality of pressures in eq 1b is not believed to be the weakest link, as the pressure difference $p_G - p_L$ is balanced by the interfacial tension.[103] Here, the interfacial tension effects are assumed to be small compared to the operating pressure. However, for other cases where $T_G \neq T_L$ or $p_G \neq p_L$, the proposed mass transfer model breaks down as the conditions of phase equilibrium are violated. Thus, the proposed mass transfer model requires sufficiently high heat transfer coefficients and negligible pressure differences between the gas and liquid phases in the reactor/separator considered. Alternatively, two additional equations stating the balance of momentum and energy over the interface (jump conditions) must be formulated to find the interface temperature, T_I, and the interface pressure, p_I. In that case, the novel mass transfer concept is generic, and the K-values required in the mass transfer expression in eq 53 can be computed at T_I and p_I by converging the phase equilibrium problem.

The derived expression for mass transfer in eq 53 requires convergence of the phase equilibrium problem. The solution strategy employed here assumes that the converged solution consists of two stable phases; however, in general, P phases can coexist. A fundamental problem with the phase equilibrium formulation is that in order to solve the phase equilibrium problem, P must be specified. However, P is not known until the problem is solved. The common strategy is to solve the two-phase equilibrium problem and check for stability. If the converged phases are unstable, new phases are added successively until stability is obtained.[39] This procedure was not adopted here due to the coupling to the transport phenomena. It is generally difficult to handle phases appearing or disappearing in transport phenomena. Thus, to ensure that the number of phases was consistent with the transport phenomena solver, we required two phases from the phase equilibrium problem. No test was performed on phase stability; however, most of the liquid phase considered in this work consists of H_2O with approximately 1% NH_3 by weight. Since NH_3 is soluble in H_2O, the liquid phase is unlikely to separate into two liquid phases. Furthermore, the gas phase consists primarily of O_2, CH_4, and CO_2. The mixture of these compounds do not form two gaseous phases at the temperature and pressure studied in this work. Hence, the assumption that the phase equilibrium problem yields two phases is reasonable in this study.

The driving force for species mass transfer in eq 53 employs the K-value in the denominator. This has the advantage of reducing the driving force to zero when $\omega_{G_i}/\omega_{L,i} = \omega^*_{G_i}/\omega^*_{L,i}$. However, volatile compounds have high K-values and nonvolatile compounds have low K-values. Thus, the driving force for the different compounds may be separated by several orders of magnitude. Typically, nonvolatile compounds with low K-values tend to exhibit very high driving forces, which quickly forces ω_i to ω_i^* for that compound i. Furthermore, the nonvolatile compounds exhibit high mass transfer compared to the nonvolatile compounds. Hence, the sum of mass transfer of all components in the continuity eqs 59 and 60 is essentially determined by the nonvolatile compounds with high mass transfer. Resultingly, the continuity equations are particularly sensitive to mass transfer of nonvolatile compounds when mass transfer is computed with eq 53. Iterating on the continuity equations therefore required small under-relaxation factors. It is worth mentioning that H_{ij} is also in the denominator, and the discussion above also applies for the classical mass transfer expression based on Henry's law, except for the nonvolatile solvent, which is neglected with Henry's law.

The implementation of the thermodynamic code for the SRK-EoS has been thoroughly verified by multiple internal consistency tests. Since the SRK-EoS is explicit in pressure, the full library was implemented as a Helmholtz energy library. Furthermore, Gibbs energy is related to Helmholtz energy through $G = A + pV$. Both Helmholtz and Gibbs energy are Euler homogeneous functions of degree one, and hence, Euler's theorem for homogeneous functions applies. This yields $2 + N_C$ tests for Helmholtz energy and $1 + N_C$ tests for Gibbs energy. Further tests include the Gibbs−Duhem relation, the symmetry of the second derivative matrix, and tests on the first derivatives of Gibbs energy. The interested reader is encouraged to see Michelsen and Mollerup[39] for a full list of the performed tests.

To the authors' knowledge, there is no experimental data for bubble columns to validate the novel mass transfer concept: it is experimentally challenging to measure the composition of both phases at different positions in the reactor. This is also the case for the SCP process, where experimental data scarcity is a considerable concern in the first place. Kashid et al.[24] employed a logarithmic mean concentration difference to experimentally study k_La. The equilibrium concentration was experimentally determined; however, only inlet and outlet effects were studied, and conditions inside the microreactor were ignored. On the other hand, Darmana et al.[25] set the mass transfer to a constant term and integrated in time in an attempt to obtain an analytical solution to the single bubble trajectory. This approach had several flaws: (i) the gas-phase density change as the bubble rose through the column was neglected, (ii) the change in k_L was neglected, (iii) the concentration change was neglected, (iv) the equilibrium concentration change was neglected, and (v) the liquid was quiescent. These assumptions are questionable; for instance, the gas-phase density would change by a factor of 2 in the system studied. In another study, Mohamadi-Baghmolaei et al.[104] endeavored to obtain an analytical solution to the species mass balance equation. Here, all variables were fixed except a normalized concentration of the studied species. The normalized concentration contained both the bulk and the equilibrium concentration, and thus, their analytical solution could not predict them both. In this study, we aim to predict the bulk concentration by employing mass transfer expressions based on the equilibrium concentration. We therefore require individual knowledge of both ω_i and ω_i^*. Current experimental studies measure ω_i and ω_i^* at reactor inlets and/or outlets, such as in the study of Kashid,[105] whereas a validation of mass transfer models requires knowledge of the composition locally through the reactor. The novel mass transfer concept presented in this

https://doi.org/10.1021/acs.iecr.1c03131
Ind. Eng. Chem. Res. XXXX, XXX, XXX−XXX

study proposes a conceptual improvement to mass transfer with less restrictions and assumptions.

Nonreactive System: Three Components. In a nonreactive system, a mixture of O_2, CH_4, and H_2O is considered. From Figure 9, we observe that $\omega_{L,i}$ obtained from the Henry's law and the SRK-EoS approaches are in qualitative agreement. As the liquid is almost stagnant, the mixture establishes phase equilibrium at a bubble column height of 1 m, and the equilibrium prevails for the remaining height of the bubble column. However, the two mass transfer approaches do give quantitatively different results, and the solubility of O_2 and CH_4 is 50% higher for the SRK-EoS approach than the Henry's law approach.

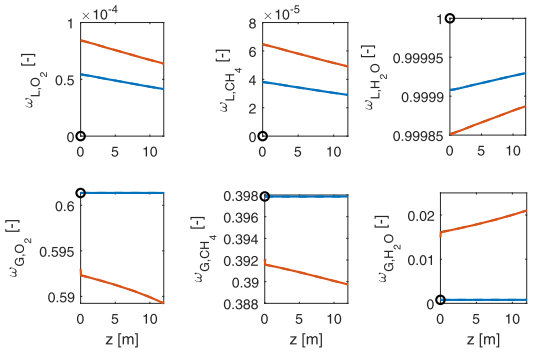

Figure 9. Mass fractions in the gas- and liquid-phase in the nonreactive system. Blue lines denote results utilizing Henry's law, and red lines denote results utilizing the SRK-EoS. Full lines (—) denote the converged values, and dashed lines (– –) denote the equilibrium state. The solid and dashed lines overlap. Black circles denote the inlet values specified in Table 4.

On the other hand, in Figure 9, the trends in the profiles for $\omega_{G,i}$ are in qualitative disagreement for all components. In the SRK-EoS approach, ω_{G,O_2} and ω_{G,CH_4} decrease, while ω_{G,H_2O} increase with height. However, in the Henry's law approach, all profiles are constant over the reactor height. With the Henry's law approach, $\omega^*_{G,i}$ cannot be obtained from the Henry's law constants; hence, we assumed $\omega^*_{G,i} = \omega_{G,i}$. This assumption reduces the driving force in eq 53 from $\omega_{G,i}/K_i - \omega_{L,i}$ to $\omega^*_{L,i} - \omega_{L,i}$. The $\omega_{L,i}$ are thus forced to $\omega^*_{L,i}$, which depend on pressure. At convergence, the pressure drop yields an oblique $\omega_{L,i}$ profile; however, $\omega_{G,i}$ are horizontal due to the assumption $\omega^*_{G,i} = \omega_{G,i}$. On the other hand, the SRK-EoS approach is not restricted to $\omega^*_{G,i} = \omega_{G,i}$, and resultingly, the $\omega_{G,i}$ are oblique.

There are limitations in the Henry's law approach with respect to the modeling of the solvent, that is, H_2O. In the Henry's law approach, the coefficient H_{jj} does not exist. Furthermore, ω_{G,H_2O} cannot be computed by $1 - \sum_{i \neq H_2O} \omega_i$ due to $\omega_{G,H_2O} \ll 1$. Hence, the mass transfer flux $N_{H_2O} = 0$ was used in the gas-phase species mass balance to obtain ω_{G,H_2O}, see eq 62. The SRK-EoS approach is not restricted to any assumption about the solvent, and consequently, $N_{H_2O} = 0$ was obtained from eq 53, which was used in the gas-phase species mass balance to obtain ω_{G,H_2O}. Thus, we observe significant differences in the ω_{G,H_2O} obtained with the Henry's law and the SRK-EoS approaches.

The α_G profiles obtained with the Henry's law and the SRK-EoS approaches are presented in Figure 10. The two approaches are in qualitative agreement, and the α_G profiles increase with the dispersion height in both approaches. As observed in Figure 9, ω_{L,O_2} and ω_{L,CH_4} decrease as the liquid rises through the column and the pressure drops (see Figure S2). This re-evaporation causes α_G to increase.

Although the Henry's law and the SRK-EoS approaches yield significantly different liquid compositions, the differences in α_G are moderate. While the maximum difference in liquid composition was found to be approximately 50%, the maximum difference in α_G is merely 2.2%. Furthermore, the SRK-EoS approach yields slightly higher α_G, presumably due to the evaporation of H_2O.

For completeness of the case study, the simulation results of v_L, v_G, ρ, and p are given in the section Supporting Figures in the Supporting Information.

Reactive System: The SCP Bioreactor. The species mass fraction profiles of the liquid and gas phases are shown in Figures 11 and 12, respectively. O_2 and CH_4 are transferred from the gas phase to the liquid phase, where the bacteria consume these species and produce biomass. As the phase equilibrium governs

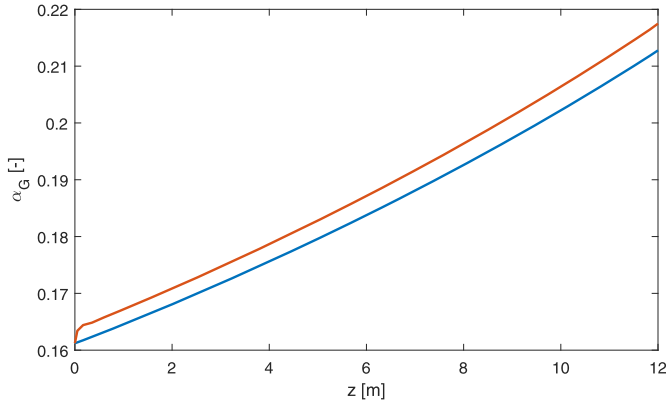

Figure 10. Area fraction of the gas-phase in the nonreactive ternary system. Blue lines denote results utilizing Henry's law, and red lines denote results utilizing the SRK-EoS.

https://doi.org/10.1021/acs.iecr.1c03131
Ind. Eng. Chem. Res. XXXX, XXX, XXX−XXX

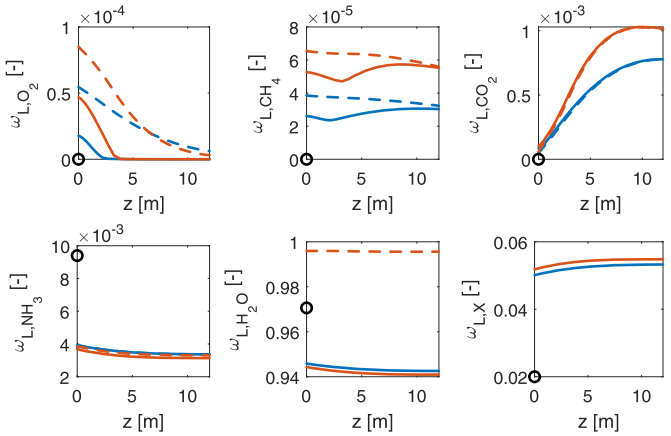

Figure 11. Mass fractions in the liquid phase in the reactive SCP system. Blue lines denote results utilizing Henry's law, and red lines denote results utilizing the SRK-EoS. Full lines (—) denote the converged values, and dashed lines (– –) denote the equilibrium state. Black circles denote the inlet values specified in Table 4.

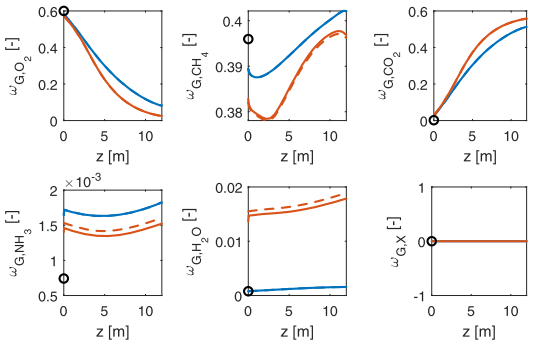

Figure 12. Mass fractions in the gas phase in the reactive SCP system. Blue lines denote results utilizing Henry's law, and red lines denote results utilizing the SRK-EoS. Full lines (—) denote the converged values, and dashed lines (– –) denote the equilibrium state. Black circles denote the inlet values specified in Table 4.

mass transfer, the trends are realistic; for reactants in the liquid phase, $\omega_L < \omega_L^*$ as they are consumed, and for products in the liquid phase, $\omega_L > \omega_L^*$ as they are produced. Since $\omega_L < \omega_L^*$ for the reactants, the driving force for mass transfer increases. Consequently, we observe a net mass transfer from the gas to the liquid phase in the reactive system, and as a result, α_G decreases (see Figure 13). The reactive system thus differs qualitatively from the nonreactive system, where $\omega_L = \omega_L^*$ and $\omega_G = \omega_G^*$ for the entire dispersion height of the bubble column, and α_G increases as the pressure declines (see Figure 10). Furthermore, the ω_L^* and ω_G^* profiles in Figures 11 and 12 are different from those in the section Nonreactive System: Three Components.

In the nonreactive system, O_2 and CH_4 condensate initially. At a column height of 1 m, they have reached equilibrium, and as the pressure declines, the solubility of O_2 and CH_4 proportionally follows. Hence, O_2 and CH_4 re-evaporate at column heights greater than 1 m in the nonreactive system. In the reactive system, O_2 and CH_4 are continuously consumed in the liquid phase, preventing them from reaching phase equilibrium. As the offset from liquid-phase equilibrium prevails, $N_{O_2} > 0$, and O_2 is

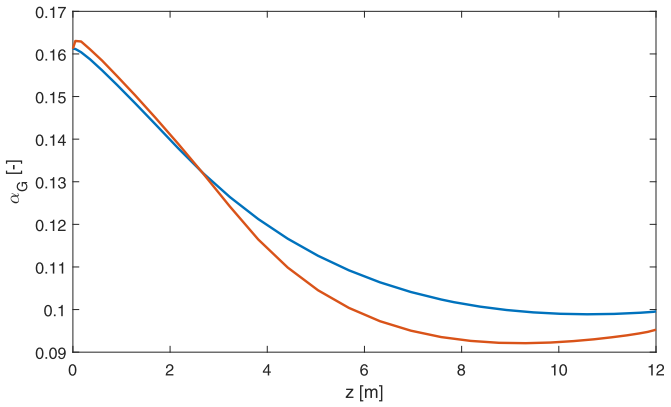

Figure 13. Area fraction of the gas phase in the reactive SCP system. Blue lines denote results utilizing Henry's law, and red lines denote results utilizing the SRK-EoS.

https://doi.org/10.1021/acs.iecr.1c03131
Ind. Eng. Chem. Res. XXXX, XXX, XXX−XXX

transferred from the gas phase into the liquid phase. Thus, the ω_{G,O_2} profile declines for both the Henry's law and the SRK-EoS approaches in the reactive system. In the nonreactive system, ω_{G,O_2} remained approximately constant with the Henry's law approach due to $\omega_{L,O_2} = \omega^*_{L,O_2}$. We conclude that with the Henry's law approach, the gradients in the ω_{G,O_2} profile are produced by the offset from liquid-phase equilibrium resulting from the reaction. Furthermore, the decrease in the α_G profile originates from $N_{O_2,CH_4} > 0$, and this mass transfer is caused by the offset from liquid-phase equilibrium induced by the reaction.

We emphasize that biomass is not included as a component in the phase equilibrium computations, and hence, the ω^*_{L,H_2O} computed based on the SRK-EoS approach is significantly higher than ω_{L,H_2O} (approximately 0.999 vs 0.94). Moreover, as previously mentioned for the nonreactive case, the mass transfer of H_2O cannot be modeled in the Henry's law approach, as the H_{jj} coefficient does not exist. Furthermore, ω_{G,H_2O} cannot be computed with $1 - \sum_{i\neq H_2O}\omega_i$, as the errors from the other species mass balances would propagate into ω_{G,H_2O}. Since ω_{G,H_2O} is small, the numerical errors would be relatively large, possibly allowing ω_{G,H_2O} to become negative. Ultimately, the mass transfer (evaporation) of H_2O cannot be predicted with the Henry's law approach, and N_{H_2O} must be neglected. As seen in Figure 12, this can amount to 2% by weight under the current operating conditions.

The volumetric mass transfer coefficient, k_La, used was based on the parametrizations of Calderbank and Moo-Young.[21] In this study, the values of k_La lay in the range 800−2000 h^{-1}. This is similar to what was experimentally found by Petersen et al.[10] However, Petersen et al.[10] placed static mixers in the reactor in order to break up bubbles and hence increase the interfacial area, while in this study, the bubble diameters were kept constant. Petersen et al.[10] claimed that the static mixers produced an exceptionally high interfacial area; however, no value for this area was given, presumably due to the experimental complexity of separating k_L and a.[106] Hence, no comparison can be made on the individual values of k_L and a.

On the other hand, Olsen et al.,[1] Villadsen,[8] Villadsen et al.,[51] and Al Taweel et al.[9] have based their computations on values in the range 0−720 h^{-1} and concluded that the process was mass transfer limited. Despite the fact that k_La was larger in this study, we still found the SCP production to be mass transfer limited (see Figure 11). At a reactor height of approximately 3−5 m, the O_2 dissolved in the liquid phase is depleted, and the reaction only proceeds as it is continuously supplied with O_2 from the gaseous phase. At a reactor height of 3−5 m, a cusp in the CH_4 profile is observed. Since the O_2 depletion has throttled the reaction, mass transfer dominates the species mass balance of CH_4, resulting in increased ω_{L,CH_4}.

Although O_2 and CH_4 have similar solubilities in the liquid phase, O_2 is the component that depletes and becomes the limiting reactant. From the bioreaction in eq 58, O_2 is consumed in larger quantities than CH_4, and consequently, the results agree with our intuitive understanding of the system studied. It should be mentioned that depleting the O_2 available to the bacteria at a height of 3−5 m will result in a lack of O_2 for heights greater than 5 m which may yield undesirable metabolic effects that are not yet well-understood.[107]

From Figure 12, the gas phase almost depletes entirely of O_2 toward the end of the reactor. Over the reactor height, ω_{G,O_2} decreases from an inlet value of 0.6 down to approximately 0.026 at the reactor outlet. On the other hand, ω_{G,CH_4} is relatively constant, although mass is transferred from gas to liquid. This results from the decrease in ρ_G and α_G, the increase in v_G, and the fact that CH_4 is a relatively light component (low molecular weight). Ultimately, the mass flux of CH_4, computed as $\rho_G v_G \alpha_G \omega_{G,CH_4}$, decreases with height. Furthermore, the mass fraction profile of CO_2 in the gas phase increases with height as it is produced in the liquid phase and transferred to the gas phase. Moreover, CO_2 is a heavy component, and on mass basis, it represents a significant part of the density of the mixture.

For the slightly soluble NH_3, the underlying assumptions of Henry's law break down. Interestingly, the differences in ω_{NH_3} between the Henry's law and the SRK-EoS approaches are less than those for O_2 and CH_4. The differences in ω_{L,NH_3} are within 8%, and the differences in ω_{G,NH_3} are within 20%. The accuracy of the Henry's law approach is possibly due to the trace amounts of NH_3 in this particular system. As seen from the definition of the Henry's law constant in eq 31, the equilibrium relation is valid as the concentration of the solute approaches zero. This is the case here, although a higher gas-phase concentration would ultimately dissolve enough NH_3 to violate eq 31. Conversely, liquid-phase concentrations of NH_3 that violate eq 31 are also prone to erroneous predictions of the evaporation rates.

Henry's law in its definition (see eq 31) is valid for multicomponent systems. However, in practice, the tabulated Henry's law constants are taken from binary experiments or as correlations based on the regression of binary experiments. By employing a set of H_{ij} meant for binary phase equilibrium, the multicomponent phase equilibrium reduces to a set of pseudo-binary phase equilibria. This does give the advantage that the solution to the phase equilibrium problem is independent of eq 2, as seen from Gibbs phase rule in eq 30, but rules out possible cross-interactions between solutes. The mass fraction profiles obtained from the SRK-EoS approach did not clearly indicate any cross-interaction effects between solutes.

Although the simple one-film model in eq 29 was considered inappropriate, an interesting similarity is noted between this approach and the two-film approach, see eq 53 in the section Rigorous Phase Equilibrium: Consistent Fluxes. If $\omega_{G,i}$ at any point takes the exact value of the equilibrium mass fraction, $\omega_{G,i} = \omega^*_{G,i}$, then $\omega_{G,i}/K_i = \omega^*_{G,i}/(\omega^*_{G,i}/\omega^*_{L,i}) = \omega^*_{L,i}$. In this particular scenario, the mass transfer expressions in eqs 29 and 53 coincide. At any iteration where this is not true, the mass transfer expressions would differ. Employing eq 29 will thus produce different results from eq 53 employed here.

In Figure 13, α_G is displayed. As α_G was solved from eq 60, it is especially sensitive to the net mass transfer on the right-hand side of the equation. Furthermore, as the bubble diameter was assumed constant, any mass transferred out of the gas phase was captured in α_G. From Figure 13, α_G is seen to decrease for the entire dispersion height with the mass transfer expression based on Henry's law. The results based on the SRK-EoS are different on two levels: (i) α_G initially increases before it starts decreasing, and (ii) at a height of 7 m, a minimum in α_G is observed before an increase takes place. The trends observed in (i) originates from the evaporation of H_2O, as this agrees with the mass fraction profile of H_2O in Figure 12. Moreover, the increase in α_G with the SRK-EoS at reactor heights greater than 7 m is also

https://doi.org/10.1021/acs.iecr.1c03131
Ind. Eng. Chem. Res. XXXX, XXX, XXX−XXX

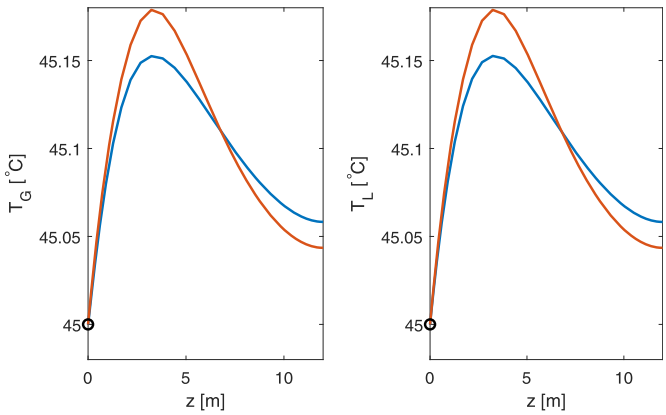

Figure 14. Temperature profiles in the gas and liquid phases in the reactive SCP system. Blue lines denote results utilizing Henry's law, and red lines denote results utilizing the SRK-EoS.

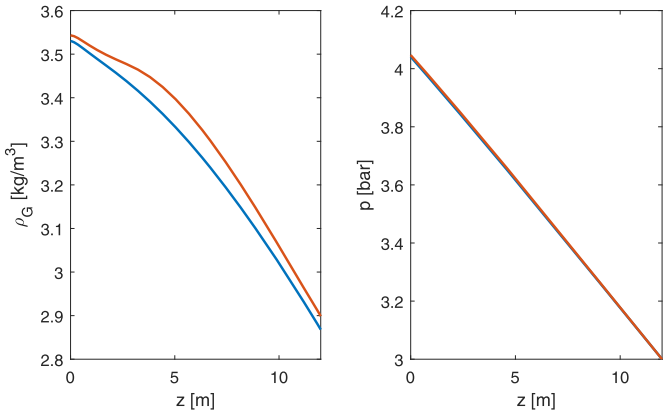

Figure 15. Density in the gas phase and the pressure common to both phases in the reactive SCP system. Blue lines denote results utilizing Henry's law, and red lines denote results utilizing the SRK-EoS.

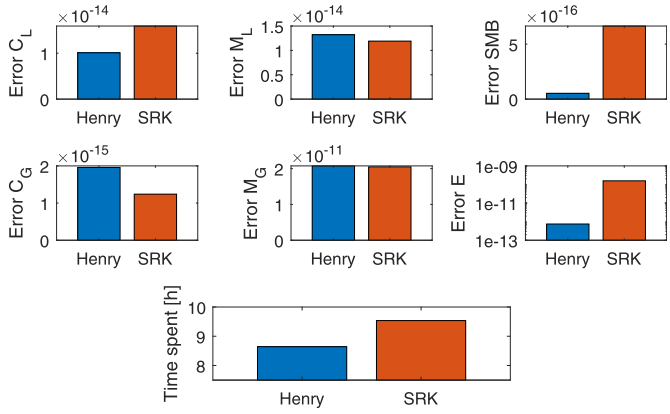

Figure 16. Errors of the governing equations in terms of the L2-norm of the residual. L is the liquid phase, G is the gas phase, C is the continuity equation, *M* is the momentum equation, SMB is species mass balance, and *E* is energy. Blue is Henry's law and red is the SRK-EoS. Note the logarithmic axis in the energy equations.

https://doi.org/10.1021/acs.iecr.1c03131
Ind. Eng. Chem. Res. XXXX, XXX, XXX−XXX

caused by the mass transfer of H_2O near the end of the reactor. Since H_2O is relatively nonvolatile, its K-value is low. From eq 53, large driving forces are expected for low K-values when the phases are not in phase equilibrium, causing the mass transfer of H_2O to have a significant impact on the continuity equations, see eqs 59 and 60. This creates a positive gradient in the gas continuity equation (see eq 60), causing the increase in α_G near the reactor outlet.

It is crucial to control the temperature, as the bacteria metabolize optimally at 45 °C.[52] In Figure 14, the temperature is seen to vary at most by 0.18 °C. Hence, the bubble column reactor is a good choice for heat removal from the reaction in eq 58. As the reaction initiates, the temperature of the liquid phase increases as heat is released from the reaction. The temperature reaches a maximum at an approximate reactor height of 4 m and decreases as the bubble column reactor is cooled by the heat exchange with the cooling medium. The gas-phase temperature follows the liquid-phase temperature closely due to the high heat transfer coefficients observed in bubble column reactors.[102]

The pressure $p_L = p_G = p$ is displayed in the right part of Figure 15. The pressure is obtained from the momentum equation for the liquid phase, which is dominated by the hydrostatic pressure of the liquid. Consequently, the pressure differences between the approaches based on Henry's law and the SRK-EoS are negligible here.

The gas-phase density is displayed in the left part of Figure 15. At the reactor inlet, the simulations based on the SRK-EoS and Henry's law share the same T, p, and composition, $\boldsymbol{\omega}$. Thus, the observed differences in ρ_G at the inlet originate from the different EoSs employed: with the SRK-EoS, ρ_G was computed from eqs 68 and 6, and with Henry's law, ρ_G was computed from eq 67. At heights above the reactor inlet, the differences in ρ_G originate from the differences in T_G and ω_G (the pressure differences are negligible). Nevertheless, the differences in ρ_G are minor, and the relative differences are at most 2%. The ideal gas law and the SRK-EoS are in agreement on the prediction of the gas density.

For completeness of the study of the SCP bioreactor, the results for v_L and v_G are given in the section Supporting Figures in the Supporting Information.

Overall, the Henry's law and the SRK-EoS approaches use similar simulation times, see Figure 16. However, the approach based on Henry's law is approximately 1 h faster. This difference is attributed to how the mass transfer fluxes are updated. The mass transfer fluxes with the Henry's law approach are updated by H_{ij} obtained from a correlation, while the update in the mass transfer fluxes with the SRK-EoS approach requires the convergence of the multicomponent phase equilibrium problem in eq 19. Hence, the update in the mass transfer fluxes with the SRK-EoS approach is expected to be more computationally expensive than the update in the mass transfer fluxes with the Henry's law approach. The computational costs are reflected in Figure 16.

The errors shown in Figure 16 were computed in terms of the L2 norm of the residual of the governing equations in Table 1

$$\epsilon_{L_2} = \sqrt{\sum_{i=1}^{N_e}\left(\sum_{j=1}^{N_e} a_{ij}x_j - b_i\right)^2} \tag{85}$$

In eq 85, a_{ij} denotes element ij of the **A**-matrix used to compute the dependent variables, **x**, and **b** is the source/sink vector of the algebraic equations for (i) the continuity equations, (ii) the momentum equations, (iii) the energy equations, and (iv) the species mass balances. The error in the energy equations was taken as the largest error of the two phases: $\epsilon_E = \max(\epsilon_{E,G}, \epsilon_{E,L})$. Similarly, the error in the species mass balance of component i was computed by $\epsilon_{SMB,i} = \max(\epsilon_{SMB,G,i}, \epsilon_{SMB,L,i})$. The component i with the largest $\epsilon_{SMB,i}$ is displayed in Figure 16.

The errors in the governing equations are all relatively low, both for the Henry's law and for the SRK-EoS approaches. The error in liquid continuity, species mass balances, and energy is lower for the Henry's law approach than that for the SRK-EoS approach. However, the error in gas continuity and liquid momentum is lower for the SRK-EoS approach than for the Henry's law approach. The errors are on the order of machine precision, except for the energy equation. The error in the energy equation is approximately 2 orders of magnitude lower with the Henry's law approach than with the SRK-EoS approach. From the error bars in Figure 16, it is concluded that the profiles in Figures 11−15 and S3 are converged profiles.

The initial composition in the gas phase used in this work consists of approximately 57 mol % CH_4 and 43 mol % O_2. As CH_4 is highly flammable, the U-loop reactor at Tjeldbergodden utilized a series of injection points where CH_4 was injected. Thus, O_2 was separated from CH_4, and the risk of explosion was severely reduced. The autoignition temperature for CH_4 in air has a lower limit of approximately 640 °C,[95] far from the operating conditions of 45 °C of the SCP reactor. On the other hand, the explosion limit does change dramatically in the presence of an ignition source. Gieras et al.[96] used an ignition source with an effect of ca. 10 W, and they found experimentally that a CH_4−air mixture has a lower and upper explosion limit of 4.65 mol % CH_4 and 15.5 mol % CH_4, respectively, at 20 °C. Their results agree with Takahashi et al.[97] and Kondo et al.,[98] where similar low-intensity sources of ignition were used. Huang et al.[99] used a tungsten wire to supply 3400 J over 6 s, and their lower and upper explosion limits agree with other investigators.[96−98]

The experimentally observed lower and upper CH_4 explosion limits correspond to O_2:CH_4 ratios of approximately 4.3 and 1.14, respectively. The stoichiometric ratio for the combustion of CH_4 is 2, and the gas mixture used in this work has a ratio of 0.76 at the reactor inlet. The ratio used here is thus well below both the stoichiometric ratio and the upper explosion limit. Hence, the gas phase will not combust even in the presence of ignition sources. There is, however, a risk of explosion if the composition should drift to 47 mol % CH_4 and 53 mol % O_2 during operation. This explains why CH_4 was injected at a series of locations at the SCP production plant at Tjeldbergodden: a gas leakage in the 57 mol % CH_4 and 43 mol % O_2 mixture employed in this work in combination with an ignition source will likely combust, while the pure O_2 stream used at Tjeldbergodden will not combust.

The bacteria assumed for this work consume more O_2 than CH_4 (see eq 58), and as a result, we expect a higher mass transfer driving force for O_2. As the bubbles rise in the reactor, the O_2:CH_4 ratio is expected to decrease. This reduction is observed in Figure 12, where the inlet ratio is 0.76 and the outlet ratio is approximately 0.03 for the gas phase. The explosion hazards thus decrease over the reactor height, and the risks are mainly attributed to gas leakages in the upstream pipeline transporting a mixture of 57 mol % CH_4 and 43 mol % O_2.

Sensitivity Study in Pressure. A sensitivity study was performed to explore how the solution responds to perturbations in the pressure. Thus, the outlet pressure boundary

https://doi.org/10.1021/acs.iecr.1c03131
Ind. Eng. Chem. Res. XXXX, XXX, XXX−XXX

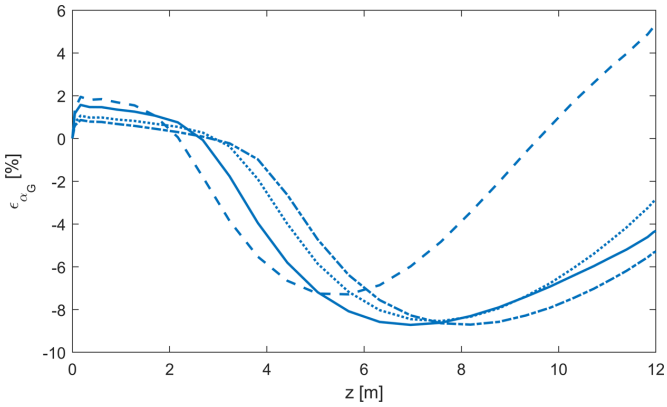

Figure 17. Relative difference in α_G for different outlet pressures. Legend: p_{out} = 2 bar (– –); p_{out} = 3 bar (—); p_{out} = 4 bar (···); and p_{out} = 5 bar (–·–).

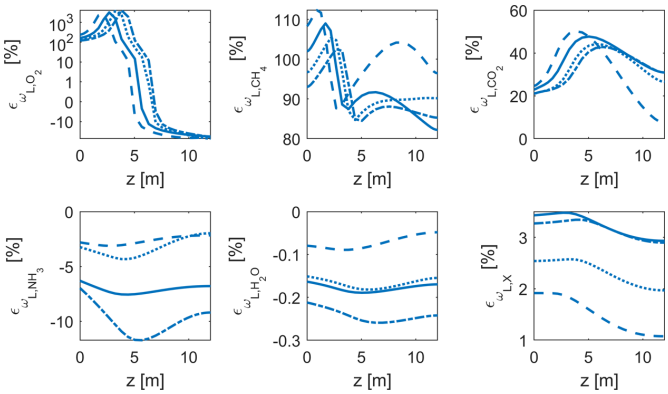

Figure 18. Relative difference in ω_L for different outlet pressures. Legend: p_{out} = 2 bar (– –); p_{out} = 3 bar (—); p_{out} = 4 bar (···); and p_{out} = 5 bar (–·–).

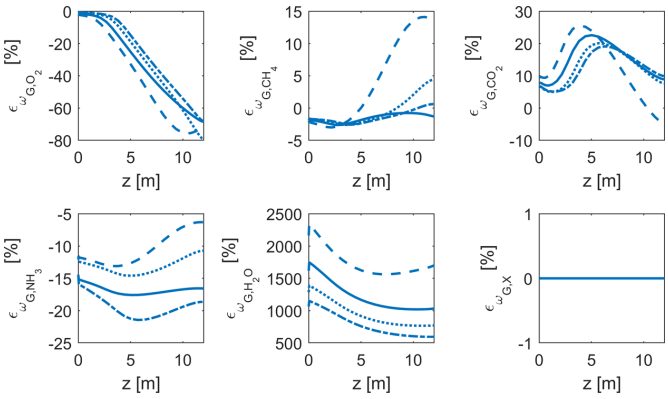

Figure 19. Relative difference in ω_G for different outlet pressures. Legend: p_{out} = 2 bar (– –); p_{out} = 3 bar (—); p_{out} = 4 bar (···); and p_{out} = 5 bar (–·–).

condition was set to four different values: p_{out} = {2, 3, 4, 5} bar, all within the recommendation of Villadsen[8] of 10 bar. Full simulations were performed for both the mass transfer based on Henry's law and the SRK-EoS for each of the different p_{out} boundary conditions. All other variables and boundary conditions were kept as specified in Tables 1, 4, 5, and S1.

The relative difference between the solution obtained by employing Henry's law and the SRK-EoS are displayed in Figures 17–21 and were computed as $\epsilon_X = 100(X_{SRK} - X_{Henry})/X_{Henry}$. Here, X represents α_G, ω_G, ω_L, T_G, T_L, ρ_G, and p.

In Figure 17, the initial evaporation of H_2O creates a positive relative difference between the SRK-EoS and the Henry's law

https://doi.org/10.1021/acs.iecr.1c03131
Ind. Eng. Chem. Res. XXXX, XXX, XXX−XXX

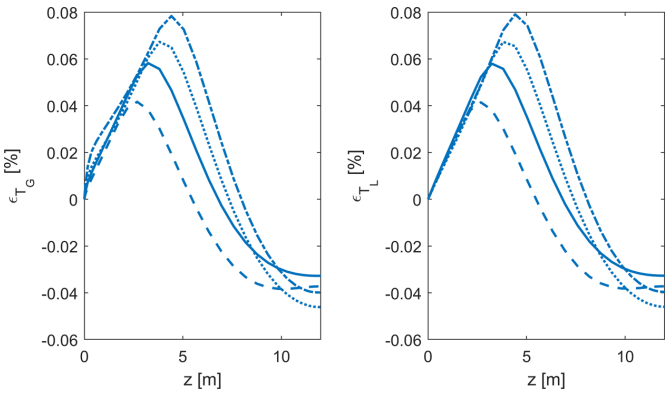

Figure 20. Relative difference in T_G and T_L for different outlet pressures. Legend: p_{out} = 2 bar (– –); p_{out} = 3 bar (—); p_{out} = 4 bar (···); and p_{out} = 5 bar (–·–).

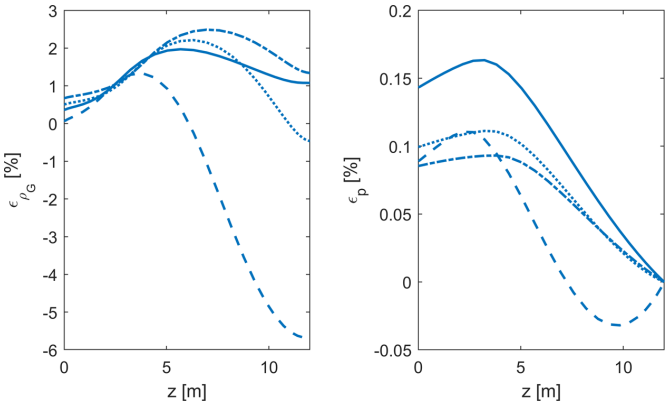

Figure 21. Relative difference in ρ_G and p for different outlet pressures. Legend: p_{out} = 2 bar (– –); p_{out} = 3 bar (—); p_{out} = 4 bar (···); and p_{out} = 5 bar (–·–).

approaches. At a reactor height of approximately 2 m, the Henry's law approach predicts a higher α_G than the SRK-EoS approach. This is true for all pressures studied and is visualized for p_{out} = 3 bar in Figure 13. A minimum is then observed at a reactor height of 5−8 m before the differences become smaller. The minimum is located at the same height as where the differences in ω_{L,O_2} level out, see Figure 18. The highest relative difference observed is approximately 8%.

In Figure 18, the differences in ω_{L,O_2} are conspicuous due to spanning 3 orders of magnitude over the reactor height. Increasing the pressure tends to delay the peak of the relative differences in ω_{L,O_2}: for p_{out} = 2 bar, the differences start increasing immediately and peak at a reactor height of 2.5 m. On the other hand, for p_{out} = 5 bar, the peak of the relative differences in ω_{L,O_2} is shifted to 4 m. For the volatile compounds CH_4 and CO_2, increasing the outlet pressure tends to decrease the highest relative difference observed. For the medium-volatile NH_3, the nonvolatile H_2O, and biomass, the opposite is true: higher outlet pressure increases the highest relative difference. High relative differences are observed for all volatile compounds, while lower differences are observed for less volatile compounds. The high relative differences observed for the volatile compounds at low pressures are in agreement with the trends observed for ρ_G in Figure 21. As $p \to 0$, the ideal gas law is increasingly accurate, especially since the gas mixture consists primarily of O_2, CH_4, and CO_2, which all exhibit ideal behavior under the conditions studied.[101] Thus, the ideal gas law is assumed to correctly predict ρ_G. The differences in ρ_G between the Henry's law and the SRK-EoS simulations are partly due to the different gas-phase compositions and partly due to the use of different EoSs (the ideal gas law vs the SRK-EoS). This was tested by computing ρ_G with the ideal gas law under the conditions otherwise obtained with the SRK-EoS, $(T,p,\boldsymbol{\omega})_{SRK}$. At $(T,p,\boldsymbol{\omega})_{SRK}$, the SRK-EoS predicted a ρ_G at most 7.59% higher than the ideal gas law at a reactor height of 5.7 m.

In Figure 19, the evaporation of H_2O produces a large relative difference due to the inability of Henry's law to predict mass transfer of the solvent. This is especially prominent at lower pressures, as this further facilitates evaporation. Except for CH_4, the relative differences in ω_G are all considerable. From the ω_{L,O_2} profiles in Figure 19, we point out that the SRK-EoS approach predicts a higher mass transfer of O_2 than what the Henry's law approach predicts. The high mass transfer of O_2 increases the reaction rate of the liquid-phase reaction, and ω_{L,NH_3} decreases while ω_{L,CO_2} increases. Thus, *less* NH_3 evaporates with the SRK-

https://doi.org/10.1021/acs.iecr.1c03131
Ind. Eng. Chem. Res. XXXX, XXX, XXX−XXX

EoS than with the Henry's law approach. Similarly, *more* CO_2 evaporates with the SRK-EoS than the Henry's law approach. This is reflected in Figure 19 for all values of p_{out}.

The relative differences between the Henry's law and the SRK-EoS approaches are modest for T_G, T_L, and p, as seen from Figures 20 and 21, respectively. Moreover, the relative differences in v_G and v_L (not shown in graphics) were also below 1%.

It is worth mentioning that the reaction rate is not a function of temperature. Joergensen and Degn[52] parametrized the reaction rate solely as a function of concentration at the optimal growth temperature T = 45 °C. Perturbing the temperature could therefore yield unrealistic growth rates, where the concentration of biomass may be erroneously estimated. Hence, a sensitivity study in temperature was not performed. Furthermore, the reaction rate expression ignored inhibiting effects due to excessive substrate (CH_4) feeding and cell poisoning due to the presence or production of toxic compounds from other metabolic pathways. One such phenomenon is the inhibitory effects of NH_3 oxidation on CH_4 uptake in the bacteria, reported by Petersen et al.[28]

Sensitivity Study in k_{ij}, k_L, and d_b. Four additional studies were performed where the solution obtained with mass transfer based on the SRK-EoS was examined for sensitivities in three different parameters: the binary interaction parameters, k_{ij}, the mass transfer coefficient, k_L, and the bubble diameter, d_b. The base case is defined by the simulations done with the k_{ij} fitted to the literature data (Table 3) and the parameters in Tables 4, 5, and S1. The sensitivity in k_{ij} was examined by performing simulations with mass transfer based on the SRK-EoS, where the K-values were computed with k_{ij} obtained from Aspen HYSYS. The k_{ij} from Aspen HYSYS are displayed in Table 6. The

Table 6. Binary Interaction Parameters from Aspen HYSYS Used with the SRK-EoS[a]

k_{ij}	O_2	CH_4	CO_2	NH_3	H_2O
O_2	0	0	0.0975	0	0
CH_4	0	0	0.0956	0	0.5
CO_2	0.0975	0.0956	0	0	0.0392
NH_3	0	0	0	0	−0.2725
H_2O	0	0.5	0.0392	−0.2725	0

[a]Conversely, the binary interaction parameters fitted to the literature by the authors are displayed in Table 3.

sensitivity in k_L was studied by setting it to 1/2 and 2 times the nominal k_L° obtained from the correlation of Calderbank and Moo-Young.[21] The sensitivity in d_b was investigated by employing d_b = 1 mm as opposed to the nominal value of d_b° = 2 mm. The results of all perturbation studies are shown in Figures 22−27.

Clearly, from Figure 25, the ω^*_{L,O_2} and ω^*_{L,CH_4} were severely underestimated when k_{ij} was obtained from Aspen HYSYS. The values at the outlet with conditions T = 45 °C and p = 3 bar were $\omega^*_{L,O_2} = 6.41 \times 10^{-6}$ and $\omega^*_{L,CH_4} = 2.07 \times 10^{-8}$. Conversely, the values observed by experimental investigators[50,63,77,108] (also see Battino and Clever[109]) at T = 40−50 °C and p = 1 bar are ω^*_{L,O_2} = [1.67, 1.87] × 10^{-5} and $\omega^*_{L,CH_4} = 3.15 \times 10^{-5}$. With the pressure in this study being higher than in the experimental studies, the solubility is expected to be even higher than those found experimentally at p = 1 bar. Hence, the equilibrium is erroneously predicted by 1 to 3 orders of magnitude with k_{ij} obtained from Aspen HYSYS. As the driving force for mass transfer relies on $\omega^*_{L,i}$, virtually no O_2 and CH_4 are transferred from the gas to the liquid phase. Thus, the bacteria are deprived of the substrates they require, and they do not metabolize. No reaction is observed in Figure 25 for the simulations based on k_{ij} from Aspen HYSYS.

The studies based on k_L are similar to the base case. For the case with $k_L = 1/2k_L^\circ$, the $\omega_{L,i}$ profiles are strikingly similar to those obtained with the Henry's law, see Figures 11 and 25. The same is not true for the $\omega_{G,i}$, mostly due to the evaporation of H_2O. On the other hand, for the case with $k_L = 2k_L^\circ$, a higher ω_{L,CO_2} and ω_{L,CH_4} than the base case are observed. This further emphasizes that the process is mass transfer limited. Interestingly, the $\omega_{L,i}$ and $\omega_{G,i}$ profiles are remarkably similar to those obtained with d_b = 1 mm; the reason for this is that the interfacial area becomes $a = 2a^\circ$ when $d_b = 1/2d_b^\circ$, as seen from eq S93. Hence, when the effects related to the driving force are neglected, $N_i a = 2(N_i a)^\circ$ for both $k_L = 2k_L^\circ$ and $d_b = 1/2d_b^\circ$. It is emphasized that the solution is quite sensitive to bubble diameter. Consequently, the model formulation would benefit from increased knowledge of the bubble size distribution through, for example, the population balance framework.[110]

Industrial Implications of the Mass Transfer Expression. Currently, efforts are made to build a competitive biological industry. In this endeavor, it is vital to acquire a proper understanding of the transport phenomena in the reactor unit. Theoretical prestudies of reactor units are reliable tools in predicting optimal operating conditions and consequently reduces the costs of equipment. Furthermore, the overall feasibility of the process based on the productivity can be predetermined before expensive investments are made. In gas fermentation, the theoretical prestudy for predicting the productivity relies on accurate mass transfer modeling. For this purpose, the novel mass transfer expression developed in this study can be a useful tool for the biological industry.

Other examples in industry include systems where the solvent is expensive, and predicting its evaporation is crucial for estimating operating costs. For instance, in CO_2 absorption plants, loss of absorbent due to evaporation is a known issue, and low vapor pressure is one of the criteria for choosing the absorbent.[111−113] Furthermore, the environmental impact of absorbent evaporation is not negligible. For instance, monoethanolamine degrades over time and—in the presence of precursor amines or oxidants—forms carcinogenic compounds that represent a risk to the aquatic ecosystem and drinking water supplies.[114] In this case, quantification of the solvent mass transfer is important, and this is not possible with mass transfer expressions based on Henry's law. With the novel mass transfer concept developed in this study, the mass transfer of the solvent can be predicted.

In the Fischer−Tropsch synthesis, many liquid products form through a chain-elongating hydrogenation reaction. Here, the solvent is not uniquely defined, and the liquid consists of a mixture of n-alkanes, n-alkenes, oxygenated compounds, H_2O, and dissolved CO, H_2, and CO_2. Moreover, the mixture represents both highly volatile and nonvolatile compounds, making Henry's law applicable for only a small portion of compounds present. In the Fischer−Tropsch synthesis, it is, therefore, reasonable to employ the novel mass transfer concepts developed in this study since it amends the two main shortcomings of Henry's law: (i) the new concept does not require identification of a single solvent to predict mass transfer,

https://doi.org/10.1021/acs.iecr.1c03131
Ind. Eng. Chem. Res. XXXX, XXX, XXX−XXX

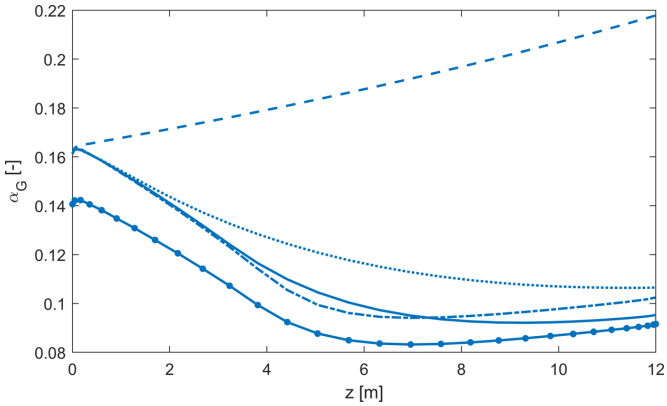

Figure 22. Sensitivity of α_G in k_{ij}, k_L, and d_b. Legend: base case (—); k_{ij} from Aspen HYSYS (− −); $k_L = 1/2k_L^\circ$ (···); $k_L = 2k_L^\circ$ (−·−); and $d_b = 1$ mm (-●-).

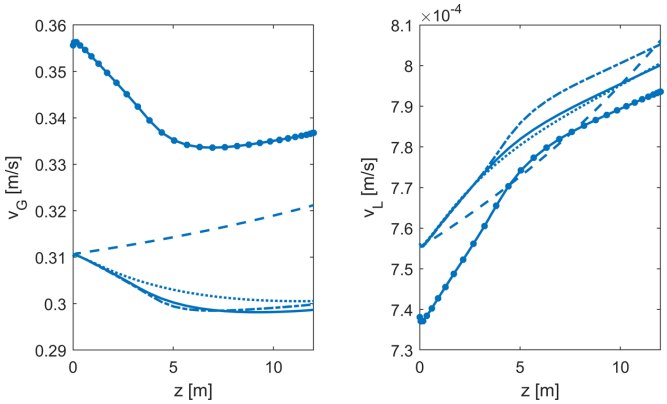

Figure 23. Sensitivity of v_G and v_L in k_{ij}, k_L, and d_b. Legend: base case (—); k_{ij} from Aspen HYSYS (− −); $k_L = 1/2k_L^\circ$ (···); $k_L = 2k_L^\circ$ (−·−); and $d_b = 1$ mm (-●-).

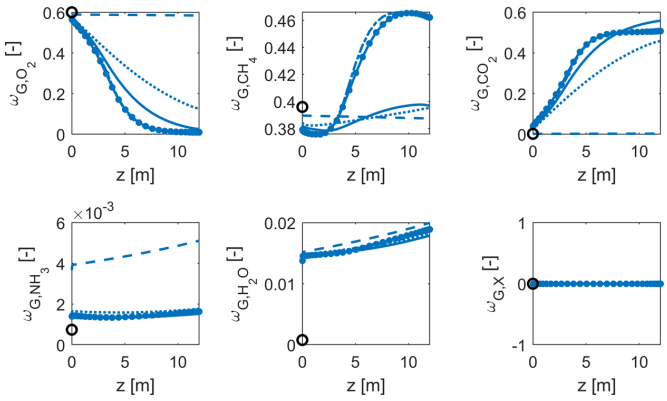

Figure 24. Sensitivity of ω_G in k_{ij}, k_L, and d_b. Legend: base case (—); k_{ij} from Aspen HYSYS (− −); $k_L = 1/2k_L^\circ$ (···); $k_L = 2k_L^\circ$ (−·−); and $d_b = 1$ mm (-●-).

and (ii) the new concept does not require the infinite dilution assumption but is also applicable for mixtures containing volatile and nonvolatile compounds.

https://doi.org/10.1021/acs.iecr.1c03131
Ind. Eng. Chem. Res. XXXX, XXX, XXX−XXX

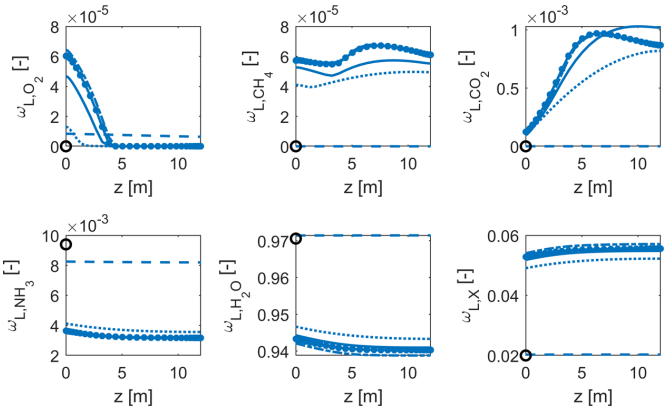

Figure 25. Sensitivity of ω_L in k_{ij}, k_L, and d_b. Legend: base case (—); k_{ij} from Aspen HYSYS (− −); $k_L = 1/2k_L^\circ$ (···); $k_L = 2k_L^\circ$ (−·−); and $d_b = 1$ mm (-●-).

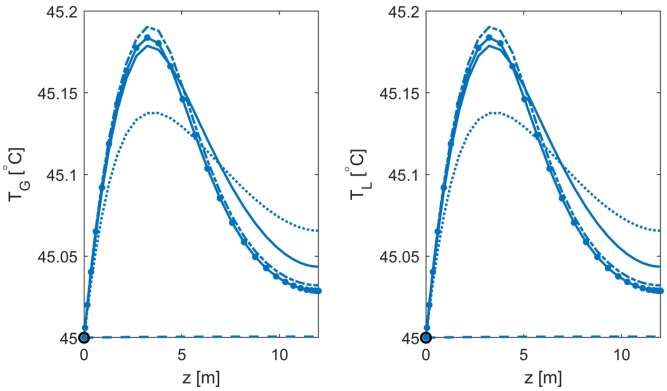

Figure 26. Sensitivity of T_G and T_L in k_{ij}, k_L, and d_b. Legend: base case (—); k_{ij} from Aspen HYSYS (− −); $k_L = 1/2k_L^\circ$ (···); $k_L = 2k_L^\circ$ (−·−); and $d_b = 1$ mm (-●-).

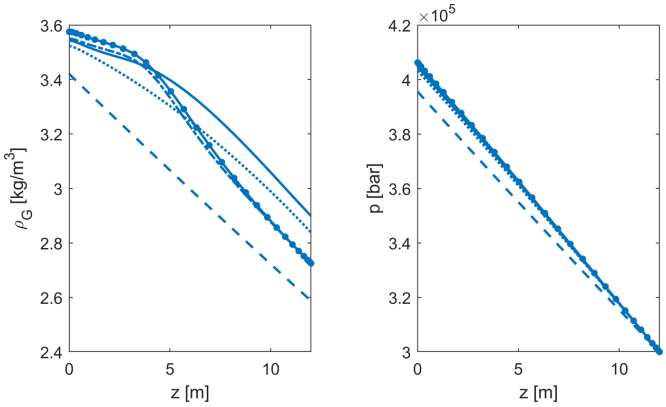

Figure 27. Sensitivity of ρ_G and p in k_{ij}, k_L, and d_b. Legend: base case (—); k_{ij} from Aspen HYSYS (− −); $k_L = 1/2k_L^\circ$ (···); $k_L = 2k_L^\circ$ (−·−); and $d_b = 1$ mm (-●-).

https://doi.org/10.1021/acs.iecr.1c03131
Ind. Eng. Chem. Res. XXXX, XXX, XXX−XXX

CONCLUSIONS

This work suggests a novel approach for modeling mass transfer and is examined by simulation of a bubble column bioreactor producing SCP. We employ the two-film model, and in contrast to the standard practice, full phase equilibrium (i.e., also including the solvent) has been assumed at the interface separating the two phases. Furthermore, we employ a thermodynamically consistent multicomponent phase equilibrium approach based on the SRK-EoS to model the interface concentrations. The results were compared to the classical approach using Henry's law, which is thermodynamically inconsistent.

The mass transfer model based on the SRK-EoS predicted solubilities for O_2, CH_4, CO_2, and NH_3 in qualitative agreement with the mass transfer model based on Henry's law. However, the standard modeling approach based on Henry's law cannot predict any mass transfer of H_2O, which is the solvent in this system. According to the modeling approach based on the SRK-EoS, the mass transfer of H_2O corresponds to evaporation, and at the reactor outlet, H_2O constitutes 2% of the gas mixture by weight. Furthermore, the quantitative differences for the solubilities in the liquid phase are considerable. At the reactor inlet, the solubility of O_2 is approximately 150% higher (relatively) for the SRK-EoS approach than for the Henry's law approach. This difference was obtained with experimentally fitted interaction parameters for the SRK-EoS.

The production of SCP in a bubble column bioreactor was mass transfer limited in accordance with other investigators.[1,8,S1] This was further supported by a sensitivity study in k_L, where the productivity of SCP biomass increased when k_L was increased, and the productivity of SCP biomass decreased when k_L was decreased. Here, k_La was comparable to experimental values,[10] and we rigorously modeled the phase equilibrium at the interface with the SRK-EoS and experimentally fitted interaction parameters. Hence, we consider the mass transfer in this work to represent the bubble column bioreactor adequately. Binary interaction parameters obtained from Aspen HYSYS were regrettably found to be unsuitable in this study.

In terms of numerical efficiency, the approach based on Henry's law is approximately 10% faster than the SRK-EoS, which corresponds to 1 h. Furthermore, the L2-norm of the residual of the governing equations is considered satisfactory for both the Henry's law and the SRK-EoS approaches, with the largest L2-norm being 10^{-11} for the gas-phase momentum with the Henry's law approach and 10^{-9} for the energy equation with the SRK-EoS approach.

Significant deviations between the Henry's law and the SRK-EoS approaches were observed. However, there are no experimental data for the SCP bioreactor to support neither the Henry's law approach nor the SRK-EoS approach. Thus, further work on the SCP bioreactor requires measurements of the composition in the gas and liquid phases. As a concluding remark, we suggest employing a thermodynamic model (Henry's law, EoS, or activity coefficient method) that accurately models the gas–liquid equilibrium of the studied compounds. If the mass transfer of the solvent is crucial, we emphasize that Henry's law is inappropriate, and the novel mass transfer concept is preferable.

Although we employed the SRK-EoS to compute the interface concentrations in the novel mass transfer model, the mass transfer concept is generic. We foresee no difficulties extending the concept to activity coefficient methods.

ASSOCIATED CONTENT

Supporting Information

The Supporting Information is available free of charge at https://pubs.acs.org/doi/10.1021/acs.iecr.1c03131.

Additional correlations required to solve the reactor model equations; velocity profiles for nonreactive ternary mixture; density, pressure, and velocity profiles for the SCP bioreactor; parameters and reactor dimensions; and critical constants and acentric factors (PDF)

AUTHOR INFORMATION

Corresponding Author

S. B. Øyen − *Department of Chemical Engineering, Norwegian University of Science and Technology (NTNU), N-7491 Trondheim, Norway;* orcid.org/0000-0003-3350-2659; Email: sindre.b.oyen@ntnu.no, jannike.solsvik@ntnu.no

Authors

H. A. Jakobsen − *Department of Chemical Engineering, Norwegian University of Science and Technology (NTNU), N-7491 Trondheim, Norway*

T. Haug-Warberg − *Department of Chemical Engineering, Norwegian University of Science and Technology (NTNU), N-7491 Trondheim, Norway*

J. Solsvik − *Department of Chemical Engineering, Norwegian University of Science and Technology (NTNU), N-7491 Trondheim, Norway*

Complete contact information is available at: https://pubs.acs.org/10.1021/acs.iecr.1c03131

Notes

The authors declare no competing financial interest.

ACKNOWLEDGMENTS

This project was supported by the Department of Chemical Engineering at NTNU. The authors are grateful for the information provided by Kurt Strand, the former leader at the Norferm plant.

LIST OF SYMBOLS

Latin Letters

A	area (m^2)
a	gas–liquid contact area ($m^2\ m^{-3}$)
a	molar attractive term SRK (Pa $m^6\ mol^{-2}$)
B	mixture excluded volume SRK (m^3)
b	molar excluded volume SRK ($m^3\ mol^{-1}$)
C	coefficient (varying)
c	concentration (mol L^{-1})
c_p	specific isobaric heat capacity (J $K^{-1}\ kg^{-1}$)
D	mixture attractive term SRK (Pa m^6)
D	dispersion coefficient ($m^2\ s^{-1}$)
D	dilution rate (h^{-1})
d	diameter (m)
$Eö$	Eötvös number (—)
F	degree of freedom (—)
f	friction factor (—)
f	function (varying)
f	fugacity (Pa)
G	molar flux (kmol $m^{-2}\ s^{-1}$)
g	gravitational acceleration (m s^{-2})
H	Henry's law constant (Pa)

https://doi.org/10.1021/acs.iecr.1c03131
Ind. Eng. Chem. Res. XXXX, XXX, XXX−XXX

h molar enthalpy (J mol^{-1})
h heat transfer coefficient (W m^{-2} K^{-1})
$\mathbf{J}$ Jacobian matrix (mol^{-1})
K equilibrium K-value (—)
K kinetic saturation constant (μ mol L^{-1})
k binary interaction parameter (—)
k mass transfer coefficient (m s^{-1})
k conductivity (W m^{-1} K^{-1})
L reactor length (m)
m parameter (—)
$\dot{m}$ mass flow (kg h^{-1})
M_w molar weight (kg $kmol^{-1}$)
N total number of moles (mol)
N total number (—)
N mass transfer flux (kg m^{-2} s^{-1})
n number of moles (mol)
P number of phases (—)
P swarm correlation parameter (—)
p pressure (Pa)
Pr Prandtl number (—)
R rate of generation of a component (kg m^{-3} s^{-1})
R gas constant (J K^{-1} mol^{-1})
Re Reynolds number (—)
s molar entropy (J K^{-1} mol^{-1})
Sc Schmidt number (—)
T temperature (K)
t thickness (m)
U overall heat transfer coefficient (W m^{-2} K^{-1})
V volume (m^3)
$\dot{V}$ volumetric flow rate (m^3 h^{-1})
v velocity (m s^{-1})
x mole fraction in liquid (—)
y mole fraction in gas (—)
Z compressibility factor (—)
z z-coordinate in physical space (m)

Greek Letters

α area fraction (—)
β initial number of moles (mol)
γ basis coefficient (varying)
Δ change (—)
δ Kronecker delta (—)
η modified chemical potential (—)
λ thermal conductivity (W m^{-1} K^{-1})
μ chemical potential (J mol^{-1})
μ dynamic viscosity (Pa s)
μ kinetic growth factor (h^{-1})
ν iteration count (—)
ν variable of integration (m^3)
ν stoichiometric coefficient (—)
ρ mass density of mixture (kg m^{-3})
σ gas−liquid surface tension (N m^{-1})
τ step size (—)
ϕ trial function (varying)
φ fugacity coefficient (—)
ω acentric factor (—)
ω mass fraction (—)

Superscripts

0 start estimate
° standard state
° base case sensitivity study
G−I gas-to-interface
G−L gas-to-liquid
I−L interface-to-liquid
ig ideal gas
m molar
r,p residual at the same pressure
s superficial
W−L wall-to-liquid
* equilibrium value

Subscripts

a ambient
b bubble
C components
c value at critical point
col bubble column
cool cooling
D drag
eff effective
f formation
fric friction
G gas
i component number
ii pair like-like molecules
ij pair unlike molecules
in at reactor inlet
L liquid
N order of approximation
out at reactor outlet
p particle
rx reaction
T total
W Wilke
X biomass

REFERENCES

(1) Olsen, D. F.; Jørgensen, J. B.; Villadsen, J.; Jørgensen, S. B. Optimal Operating Points for SCP Production in the U-Loop Reactor. *IFAC Proc.* **2010**, *43*, 499−504.
(2) Øverland, M.; Tauson, A.-H.; Shearer, K.; Skrede, A. Evaluation of methane-utilising bacteria products as feed ingredients for monogastric animals. *Arch. Anim. Nutr.* **2010**, *64*, 171−189.
(3) Anupama; Ravindra, P. Value-added food: Single cell protein. *Biotechnol. Adv.* **2000**, *18*, 459−479.
(4) Kuźniar, A.; Furtak, K.; Włodarczyk, K.; Stępniewska, Z.; Wolińska, A. Methanotrophic Bacterial Biomass as Potential Mineral Feed Ingredients for Animals. *Int. J. Environ. Res. Public Health* **2019**, *16*, 2674.
(5) Kuhad, R. C.; Singh, A.; Tripathi, K. K.; Saxena, R. K.; Eriksson, K. E. L. Microorganisms as an alternative source of protein. *Nutr. Rev.* **1997**, *55*, 65−75.
(6) Refstie, S. Evaluating soybean meal as a fish meal substitute in feeds for Atlantic salmon and rainbow trout. Ph.D. Thesis, University of Life Sciences, Ås, 2000.
(7) Whittenbury, R.; Phillips, K. C.; Wilkinson, J. F. Enrichment, Isolation and Some Properties of Methane-utilizing Bacteria. *J. Gen. Microbiol.* **1970**, *61*, 205−218.
(8) Villadsen, J. Bioprotein. *Dan. Kemi* **2002**, *83*, 20−23.
(9) Al Taweel, A. M.; Shah, Q.; Aufderheide, B. Effect of Mixing on Microorganism Growth in Loop Bioreactors. *Int. J. Chem. Eng.* **2012**, *2012*, 1−12.
(10) Petersen, L. A. H.; Villadsen, J.; Jørgensen, S. B.; Gernaey, K. V. Mixing and mass transfer in a pilot scale U-loop bioreactor. *Biotechnol. Bioeng.* **2017**, *114*, 344−354.
(11) Prado-Rubio, O. A.; Jørgensen, J. B.; Jørgensen, S. B. *Computer Aided Chemical Engineering*; Elsevier B.V., 2010; Vol. *28*, pp 319−324.
(12) Danckwerts, P. V. Significance of Liquid-Film Coefficients in Gas Absorption. *Ind. Eng. Chem.* **1951**, *43*, 1460−1467.

https://doi.org/10.1021/acs.iecr.1c03131
Ind. Eng. Chem. Res. XXXX, XXX, XXX−XXX

(13) Brunner, E. Reaktionsgeschwindigkeit in heterogenen Systemen. Ph.D. Thesis, Georg-Augusts-Universitat: Gottingen, 1904.
(14) Brunner, E. Reaktionsgeschwindigkeit in heterogenen Systemen. *Z. Phys. Chem.* **1904**, *47*, 56−102.
(15) Whitman, W. G.; Keats, J. L. Rates of Absorption and Heat Transfer between Gases and Liquids. *J. Ind. Eng. Chem.* **1922**, *14*, 186−191.
(16) Higbie, R. The Rate of Absorption of a Pure Gas into a Still Liquid during Short Periods of Exposure. *Trans. Am. Inst. Chem. Eng* **1935**, *31*, 365−389.
(17) Weber, M. E. The effect of surface active agents on mass transfer from spherical cap bubbles. *Chem. Eng. Sci.* **1975**, *30*, 1507−1510.
(18) Rzehak, R. Modeling of mass-transfer in bubbly flows encompassing different mechanisms. *Chem. Eng. Sci.* **2016**, *151*, 139−143.
(19) Frössling, N. Über die Verdunstung fallender Tropfen. *Gerlands Beitr. Geophys.* **1938**, *52*, 170−216.
(20) Hughmark, G. A. Liquid-liquid spray column drop size, holdup, and continuous phase mass transfer. *Ind. Eng. Chem. Fundam.* **1967**, *6*, 408−413.
(21) Calderbank, P. H.; Moo-Young, M. B. The continuous phase heat and mass-transfer properties of dispersions. *Chem. Eng. Sci.* **1961**, *16*, 39−54.
(22) Taylor, R.; Krishna, R. *Multicomponent Mass Transfer*; John Wiley & Sons: New York, NY, 1993.
(23) Merker, D.; Böhm, L.; Oßberger, M.; Klüfers, P.; Kraume, M. Mass Transfer in Reactive Bubbly Flows − A Single-Bubble Study. *Chem. Eng. Technol.* **2017**, *40*, 1391−1399.
(24) Kashid, M. N.; Renken, A.; Kiwi-Minsker, L. Gas-liquid and liquid-liquid mass transfer in microstructured reactors. *Chem. Eng. Sci.* **2011**, *66*, 3876−3897.
(25) Darmana, D.; Deen, N. G.; Kuipers, J. A. M. Detailed modeling of hydrodynamics, mass transfer and chemical reactions in a bubble column using a discrete bubble model. *Chem. Eng. Sci.* **2005**, *60*, 3383−3404.
(26) Deising, D.; Bothe, D.; Marschall, H. Direct numerical simulation of mass transfer in bubbly flows. *Comput. Fluids* **2018**, *172*, 524−537.
(27) DeMontigny, D.; Aboudheir, A.; Tontiwachwuthikul, P.; Chakma, A. Modelling the performance of a CO2 absorber containing structured packing. *Ind. Eng. Chem. Res.* **2006**, *45*, 2594−2600.
(28) Petersen, L. A. H.; Lieven, C.; Nandy, S. K.; Villadsen, J.; Jørgensen, S. B.; Christensen, I.; Gernaey, K. V. Dynamic investigation and modeling of the nitrogen cometabolism in Methylococcus capsulatus (Bath). *Biotechnol. Bioeng.* **2019**, *116*, 2884−2895.
(29) Harvey, A. H.; Smith, F. L. Avoid common pitfalls when using Henry's law. *Chem. Eng. Prog.* **2007**, *103*, 33−39.
(30) Fernández-Prini, R.; Alvarez, J. L.; Harvey, A. H. Henry's Constants and Vapor−Liquid Distribution Constants for Gaseous Solutes in H_2O and D_2O at High Temperatures. *J. Phys. Chem. Ref. Data* **2003**, *32*, 903−916.
(31) Sander, R. Compilation of Henry's law constants (version 4.0) for water as solvent. *Atmos. Chem. Phys.* **2015**, *15*, 4399−4981.
(32) Clifford, I. I.; Hunter, E. The System Ammonia−Water at Temperatures up to 150°C. and at Pressures up to Twenty Atmospheres. *J. Phys. Chem.* **1933**, *37*, 101−118.
(33) Winterbone, D. E.; Turan, A. *Advanced Thermodynamics for Engineers*, 2nd ed.; Elsevier: Kidlington, 1997.
(34) Haug-Warberg, T. *Den Termodynamiske Arbeidsboken*, 1st ed.; Kolofon, Forlag AS: Fornebu, 2006; p 309.
(35) Aylward, G.; Findlay, T. *SI Chemical Data*, 6th ed.; John Wiley & Sons Australia, Ltd: 42 McDougall Street, Milton, Qld 4064, 2008.
(36) Soave, G. Equilibrium constants from a modified Redlich-Kwong equation of state. *Chem. Eng. Sci.* **1972**, *27*, 1197−1203.
(37) Wei, Y. S.; Sadus, R. J. Equations of state for the calculation of fluid-phase equilibria. *AIChE J.* **2000**, *46*, 169−196.
(38) Lemmon, E. W.; McLinden, M. O.; Friend, D. G. *NIST Chem. WebBook, NIST Stand. Ref. Database Number 69*; Linstrom, P. J., Mallard, W. G., Eds.; National Institute of Standards and Technology: Gaithersburg MDUSA, 20899, 2019.
(39) Michelsen, M. L.; Mollerup, J. M. *Thermodynamic Models: Fundamentals & Computational Aspects*, 2nd ed.; Stenby, E. H., Ed.; Tie-Line Publications: Holte, 2007.
(40) Øyen, S. B.; Jakobsen, H. A.; Haug-Warberg, T.; Solsvik, J. Differential Gibbs and Helmholtz reactor models for ideal and non-ideal gases: Applications to the SMR and methanol processes. *Chem. Eng. Sci.* **2021**, *234*, 116257.
(41) Whitson, C. H.; Michelsen, M. L. The negative flash. *Fluid Phase Equilib.* **1989**, *53*, 51−71.
(42) Jakobsen, H. A. *Chemical Reactor Modeling: Multiphase Reactive Flows*, 2nd ed.; Springer International Publishing: Cham, 2014.
(43) Lu, J. H.; Lei, H. Y.; Dai, C. S. Analysis of Henry's law and a unified lattice Boltzmann equation for conjugate mass transfer problem. *Chem. Eng. Sci.* **2019**, *199*, 319−331.
(44) Bothe, D.; Koebe, M.; Wielage, K.; Warnecke, H.-J. VOF-simulations of Mass Transfer from Single Bubbles and Bubble Chains Rising in Aqueous Solutions. *Proceedings of the ASME/JSME 2003 4th Joint Fluids Summer Engineering Conference, Vol. 2 Symp. Parts A, B, C*, 2003; pp 423−429.
(45) Haroun, Y.; Legendre, D.; Raynal, L. Volume of fluid method for interfacial reactive mass transfer: Application to stable liquid film. *Chem. Eng. Sci.* **2010**, *65*, 2896−2909.
(46) Haroun, Y.; Raynal, L.; Legendre, D. Mass transfer and liquid hold-up determination in structured packing by CFD. *Chem. Eng. Sci.* **2012**, *75*, 342−348.
(47) Nieves-Remacha, M. J.; Yang, L.; Jensen, K. F. OpenFOAM Computational Fluid Dynamic Simulations of Two-Phase Flow and Mass Transfer in an Advanced-Flow Reactor. *Ind. Eng. Chem. Res.* **2015**, *54*, 6649−6659.
(48) Onea, A.; Wörner, M.; Cacuci, D. G. A qualitative computational study of mass transfer in upward bubble train flow through square and rectangular mini-channels. *Chem. Eng. Sci.* **2009**, *64*, 1416−1435.
(49) Marschall, H.; Hinterberger, K.; Schüler, C.; Habla, F.; Hinrichsen, O. Numerical simulation of species transfer across fluid interfaces in free-surface flows using OpenFOAM. *Chem. Eng. Sci.* **2012**, *78*, 111−127.
(50) Rettich, T. R.; Handa, Y. P.; Battino, R.; Wilhelm, E. Solubility of gases in liquids. 13. High-precision determination of Henry's constants for methane and ethane in liquid water at 275 to 328 K. *J. Phys. Chem.* **1981**, *85*, 3230−3237.
(51) Villadsen, J.; Nielsen, J.; Lidén, G. *Solvent Extraction in Biotechnology*; Springer US: Boston, MA, 2011; pp 2−51.
(52) Joergensen, L.; Degn, H. Growth rate and methane affinity of a turbidostatic and oxystatic continuous culture of Methylococcus capsulatus (Bath). *Biotechnol. Lett.* **1987**, *9*, 71−76.
(53) Ritschel, T. K.; Boiroux, D.; Nielsen, M. K.; Huusom, J. K.; Jorgensen, S. B.; Jorgensen, J. B. Economic Optimal Control of a U-loop Bioreactor using Simultaneous Collocation-based Approaches *CCTA 2019—3rd IEEE Conference on Control Technology and Applications*, 2019; pp 933−938.
(54) Kreyszig, E. *Advanced Engineering Mathematics*, 10th ed.; Kreyszig, H., Norminton, E. J., Eds.; Wiley: Hoboken, NJ, 2011.
(55) Solsvik, J.; Jakobsen, H. A. Effects of Jacobi polynomials on the numerical solution of the pellet equation using the orthogonal collocation, Galerkin, tau and least squares methods. *Comput. Chem. Eng.* **2012**, *39*, 1−21.
(56) Villadsen, J.; Michelsen, M. L. *Solution of Differential Equation Models by Polynomial Approximation*; Michelsen, M. L., Ed.; Prentice-Hall International, Prentice-Hall: Englewood Cliffs, NJ, 1978.
(57) Press, W. H.; Teukolsky, S. A.; Vetterling, W. T.; Flannery, B. P. *Numerical Recipes in Fortran 77: The Art of Scientific Computing*, 2nd ed.; Cambridge University Press: Cambridge, U.K., 1992.
(58) Solsvik, J.; Jakobsen, H. Solution of the Pellet Equation by use of the Orthogonal Collocation and Least Squares Methods: Effects of Different Orthogonal Jacobi Polynomials. *Int. J. Chem. React. Eng.* **2012**, *10*. Article A40. DOI: 10.1515/1542-6580.2702
(59) Shen, J.; Tang, T.; Wang, L.-L. *Spectral Methods*, 1st ed.; Springer Series in Computational Mathematics; Springer Berlin Heidelberg: Berlin, Heidelberg, 2011; Vol. *41*.

https://doi.org/10.1021/acs.iecr.1c03131
Ind. Eng. Chem. Res. XXXX, XXX, XXX−XXX

(60) Golub, G. H.; Welsch, J. H. Calculation of Gauss quadrature rules. *Math. Comput.* **1969**, *23*, 221.
(61) Solsvik, J.; Tangen, S.; Jakobsen, H. A. Evaluation of weighted residual methods for the solution of the pellet equations: The orthogonal collocation, Galerkin, tau and least-squares methods. *Comput. Chem. Eng.* **2013**, *58*, 223.
(62) Solsvik, J.; Jakobsen, H. A. On the solution of the population balance equation for bubbly flows using the high-order least squares method: implementation issues. *Rev. Chem. Eng.* **2013**, *29*, 63−98.
(63) Morrison, T. J.; Billett, F. The salting-out of non-electrolytes. Part II.* The effect of variation in non-electrolyte. *J. Chem. Soc.* **1952**, 3819−3822.
(64) Gjaldbæk, J. C.; Grahn, M.; Fex, H.; Högberg, B.; Linderot, T.; Rosenberg, T. The Solubility of Carbon Dioxide in Perfluoro-n-heptane, Normal Heptane, Cyclo-hexane, Carbon Tetrachloride, Benzene, Carbon Disulphide and Aqueous Solution of Aerosol. *Acta Chem. Scand.* **1953**, *7*, 537−544.
(65) Dodds, W. S.; Stutzman, L. F.; Sollami, B. J. Carbon Dioxide Solubility in Water. *Ind. Eng. Chem.* **1956**, *1*, 92−95.
(66) Siqueira Campos, C. E. P.; Villardi, H. G. D. A.; Pessoa, F. L. P.; Uller, A. M. C. Solubility of carbon dioxide in water and hexadecane: Experimental measurement and thermodynamic modeling. *J. Chem. Eng. Data* **2009**, *54*, 2881−2886.
(67) Dalmolin, I.; Skovroinski, E.; Biasi, A.; Corazza, M. L.; Dariva, C.; Oliveira, J. V. Solubility of carbon dioxide in binary and ternary mixtures with ethanol and water. *Fluid Phase Equilib.* **2006**, *245*, 193−200.
(68) Ellis, A. J. The solubility of carbon dioxide in water at high temperatures. *Am. J. Sci.* **1959**, *257*, 217−234.
(69) Cox, J. D.; Head, A. J. Solubility of carbon dioxide in hydrofluoric acid solutions: "standard state" correction for the combustion calorimetry of organo-fluorine compounds. *Trans. Faraday Soc.* **1962**, *58*, 1839−1845.
(70) Austin, W. H.; Lacombe, E.; Rand, P. W.; Chatterjee, M. Solubility of carbon dioxide in serum from 15 to 38 C. *J. Appl. Physiol.* **1963**, *18*, 301−304.
(71) Yeh, S.-Y.; Peterson, R. E. Solubility of Carbon Dioxide, Krypton, and Xenon in Aqueous Solution. *J. Pharm. Sci.* **1964**, *53*, 822−824.
(72) Wiebe, R.; Gaddy, V. L. The Solubility of Carbon Dioxide in Water at Various Temperatures from 12 to 40° and at Pressures to 500 Atmospheres. Critical Phenomena. *J. Am. Chem. Soc.* **1940**, *62*, 815−817.
(73) Wiebe, R. The Binary System Carbon Dioxide-Water under Pressure. *Chem. Rev.* **1941**, *29*, 475−481.
(74) Lawrence Clever, H.; Battino, R.; Miyamoto, H.; Yampolski, Y.; Young, C. L. IUPAC-NIST Solubility Data Series. 103. Oxygen and Ozone in Water, Aqueous Solutions, and Organic Liquids (Supplement to Solubility Data Series Volume 7). *J. Phys. Chem. Ref. Data* **2014**, *43*, 033102.
(75) Narita, E.; Lawson, F.; Han, K. N. Solubility of oxygen in aqueous electrolyte solutions. *Hydrometallurgy* **1983**, *10*, 21−37.
(76) Davis, R. E.; Horvath, G. L.; Tobias, C. W. The solubility and diffusion coefficient of oxygen in potassium hydroxide solutions. *Electrochim. Acta* **1967**, *12*, 287−297.
(77) Fox, C. J. J. On the coefficients of absorption of nitrogen and oxygen in distilled water and sea-water, and of atmospheric carbonic acid in sea-water. *Trans. Faraday Soc.* **1909**, *5*, 68.
(78) Morgan, J. L. R.; Richardson, A. H. Solubility Relations in Gas-Liquid Systems. IV. *J. Phys. Chem.* **1930**, *34*, 2356−2366.
(79) Steen, H. Determinations of the Solubility of Oxygen in Pure Water. *Limnol. Oceanogr.* **1958**, *3*, 423−426.
(80) Klots, C. E.; Benson, B. B. Solubilities of nitrogen, oxygen, and argon in distilled water. *J. Mar. Res.* **1963**, *21*, 48−57.
(81) Douglas, E. Solubilities of oxygen, argon, and nitrogen in distilled water. *J. Phys. Chem.* **1964**, *68*, 169−174.
(82) Carpenter, J. H. New measurements of oxygen solubility in pure and natural water. *Limnol. Oceanogr.* **1966**, *11*, 264−277.
(83) Shchukarev, S. A.; Tolmacheva, T. A. Solubility of oxygen in ethanol - Water mixtures. *J. Struct. Chem.* **1968**, *9*, 16−21.
(84) Murray, C. N.; Riley, J. P. The solubility of gases in distilled water and sea water-II. Oxygen. *Deep-Sea Res. Oceanogr. Abstr.* **1969**, *16*, 311−320.
(85) Murray, C. N.; Riley, J. P.; Wilson, T. R. S. The solubility of gases in distilled water and sea water-I. Nitrogen. *Deep-Sea Res. Oceanogr. Abstr.* **1969**, *16*, 297−310.
(86) Wise, D. L.; Houghton, G. Solubilities and Diffusivities of Oxygen in Hemolyzed Human Blood Solutions. *Biophys. J.* **1969**, *9*, 36−53.
(87) Novak, D. M.; Conway, B. E. Technique for Repetitive Gas Solubility Determinations at Various Pressures. *Instrum. Sci. Technol.* **1974**, *5*, 79−90.
(88) Benson, B. B.; Krause, D. Empirical laws for dilute aqueous solutions of nonpolar gases. *J. Chem. Phys.* **1976**, *64*, 689−709.
(89) Pray, H. A.; Schweickert, C. E.; Minnich, B. H. Solubility of Hydrogen, Oxygen, Nitrogen, and Helium in Water at Elevated Temperatures. *Ind. Eng. Chem.* **1952**, *44*, 1146−1151.
(90) Wylie, R. G.; Fisher, R. S. Molecular interaction of water vapor and oxygen. *J. Chem. Eng. Data* **1996**, *41*, 175−180.
(91) Skogestad, S. Experience in Norsk Hydro with cubic equations of state. *Fluid Phase Equilib.* **1983**, *13*, 179−188.
(92) Jaubert, J.-N.; Privat, R. Relationship between the binary interaction parameters (kij) of the Peng-Robinson and those of the Soave-Redlich-Kwong equations of state: Application to the definition of the PR2SRK model. *Fluid Phase Equilib.* **2010**, *295*, 26−37.
(93) Chapoy, A.; Nazeri, M.; Kapateh, M.; Burgass, R.; Coquelet, C.; Tohidi, B. Effect of impurities on thermophysical properties and phase behaviour of a CO_2-rich system in CCS. *Int. J. Greenhouse Gas Control* **2013**, *19*, 92−100.
(94) Strand, K. Former leader at the Norferm plant. Personal communication, **2021**.
(95) Kong, D.; Eckhoff, R. K.; Alfert, F. Auto-ignition of CH_4 air, C_3H_8 air, CH_4/C_3H_8/air and CH_4/CO_2/air using a 11 ignition bomb. *J. Hazard. Mater.* **1995**, *40*, 69−84.
(96) Gieras, M.; Klemens, R.; Rarata, G.; Wolański, P. Determination of explosion parameters of methane-air mixtures in the chamber of 40 dm3 at normal and elevated temperature. *J. Loss Prev. Process Ind.* **2006**, *19*, 263−270.
(97) Takahashi, A.; Urano, Y.; Tokuhashi, K.; Hidekazu Nagai, H.; Kaise, M.; Kondo, S. Fusing ignition of various metal wires for explosion limits measurement of methane/air mixture. *J. Loss Prev. Process Ind.* **1998**, *11*, 353−360.
(98) Kondo, S.; Takizawa, K.; Takahashi, A.; Tokuhashi, K. On the temperature dependence of flammability limits of gases. *J. Hazard. Mater.* **2011**, *187*, 585−590.
(99) Huang, L.; Pei, S.; Wang, Y.; Zhang, L.; Ren, S.; Zhang, Z.; Xiao, Y. Assessment of flammability and explosion risks of natural gas-air mixtures at high pressure and high temperature. *Fuel* **2019**, *247*, 47−56.
(100) Danckwerts, P. V. Continuous flow systems. Distribution of residence times. *Chem. Eng. Sci.* **1953**, *2*, 1−13.
(101) Viswanath, D. S.; Su, G.-J. Generalized thermodynamic properties of real gases: Part I. Generalized PVT behavior of real gases. *AIChE J.* **1965**, *11*, 202−204.
(102) Kast, W. Analyse des wärmeübergangs in blasensäulen. *Int. J. Heat Mass Transfer* **1962**, *5*, 329−336.
(103) Lin, T.-J.; Tsuchiya, K.; Fan, L.-S. Bubble Flow Characteristics in Bubble Columns at Elevated Pressure and Temperature. *AIChE J.* **1998**, *44*, 545−560.
(104) Mohamadi-Baghmolaei, M.; Azin, R.; Osfouri, S.; Zendehboudi, S.; Hajizadeh, A.; Izadpanahi, A. Mass transfer during transient condensate vaporization: Experimental and modeling study. *J. Mol. Liq.* **2021**, *325*, 114022.
(105) Kashid, M. N. *Microstructured Devices for Chemical Processing*; Wiley, 2014.
(106) Ali, H.; Solsvik, J. Axial distributions of bubble−liquid mass transfer coefficient in laboratory-scale stirred tank with viscous Newtonian and non-Newtonian fluids. *Phys. Fluids* **2020**, *32*, 123308.

https://doi.org/10.1021/acs.iecr.1c03131
Ind. Eng. Chem. Res. XXXX, XXX, XXX−XXX

(107) Kalyuzhnaya, M. G.; Puri, A. W.; Lidstrom, M. E. Metabolic engineering in methanotrophic bacteria. *Metab. Eng.* **2015**, *29*, 142−152.
(108) Benson, B. B.; Krause, D.; Peterson, M. A. The solubility and isotopic fractionation of gases in dilute aqueous solution. I. Oxygen. *J. Solution Chem.* **1979**, *8*, 655−690.
(109) Battino, R.; Clever, H. L. The Solubility of Gases in Liquids. *Chem. Rev.* **1966**, *66*, 395−463.
(110) Solsvik, J.; Jakobsen, H. A. The Foundation of the Population Balance Equation: A Review. *J. Dispers. Sci. Technol.* **2015**, *36*, 510−520.
(111) Aschenbrenner, O.; Styring, P. Comparative study of solvent properties for carbon dioxide absorption. *Energy Environ. Sci.* **2010**, *3*, 1106−1113.
(112) Mirzaei, S.; Shamiri, A.; Aroua, M. K. A review of different solvents, mass transfer, and hydrodynamics for postcombustion CO2 capture. *Rev. Chem. Eng.* **2015**, *31*, 521−561.
(113) White, C. M.; Strazisar, B. R.; Granite, E. J.; Hoffman, J. S.; Pennline, H. W. Separation and capture of co2 from large stationary sources and sequestration in geological formations—coalbeds and deep saline aquifers. *J. Air Waste Manage. Assoc.* **2003**, *53*, 645−715.
(114) Luis, P. Use of monoethanolamine (MEA) for CO2 capture in a global scenario: Consequences and alternatives. *Desalination* **2016**, *380*, 93−99.

https://doi.org/10.1021/acs.iecr.1c03131
Ind. Eng. Chem. Res. XXXX, XXX, XXX−XXX

Interface Mass Transfer in Reactive Bubbly Flow: A Rigorous Phase Equilibrium Based Approach

S. B. Øyen,* H. A. Jakobsen, T. Haug-Warberg, and J. Solsvik

Department of Chemical Engineering, Norwegian University of Science and Technology (NTNU), N-7491 Trondheim, Norway

E-mail: sindre.b.oyen@ntnu.no;jannike.solsvik@ntnu.no

Closure Equations to Reactor Model

Species Mass

The reaction kinetic rate expression was based on the production of one mole X and followed the Monod-Haldane equation[1,2]:

$$\mu_X = \mu_{\max,\mathrm{CH_4}}\mu_{\max,\mathrm{O_2}}\frac{c_{L,\mathrm{CH_4}}}{K_{\mathrm{m,CH_4}} + c_{L,\mathrm{CH_4}}}\frac{c_{L,\mathrm{O_2}}}{K_{\mathrm{m,O_2}} + c_{L,\mathrm{O_2}}}. \tag{1}$$

In Eq. (1), $\mu_{\max,i}$ is the maximum specific growth rate, $K_{\mathrm{m},i}$ is the saturation constant denoting the concentration at which $\mu_X = \mu_{\max,i}/2$, and $c_{L,i}$ is the molar concentration of component i in the liquid. The constants were taken from Joergensen and Degn[3] and Olsen et al.[4] and are given in Table S1.

The mass–based volumetric production or consumption of species i is related to Eq. (1) through[4–6]

$$R_i = \frac{M_{w,i}}{M_{w,\mathrm{X}}}\frac{\nu_i}{0.52}\mu_X\rho_L\omega_{L,\mathrm{X}}, \tag{2}$$

where ν_i are the stoichiometric coefficients as they are represented in the chemical reaction, and the factor 0.52 occurs as the reaction rate is based on the production of one mole of X.

The effective dispersion coefficient of the liquid was taken from the correlations of Deckwer et al.[7]:

$$D_{L,\mathrm{eff},z} = 0.678 d_{\mathrm{col}}^{1.4}(v_G\alpha_G)^{0.3}. \tag{3}$$

Here, the diameter of the reactor column is denoted d_{col}. The liquid–phase dispersion coefficient in Eq. (3) is valid in the variable ranges $v_L^s = 7.07 \times 10^{-3}\,\mathrm{m\,s^{-1}}$, $0 \leq v_G^s \leq 0.15\,\mathrm{m\,s^{-1}}$, and on columns with internal diameter 0.15 m and 0.2 m.

Furthermore, the effective dispersion coefficient of the gas was taken from the correlations of Field and Davidson[8]:

$$D_{G,\mathrm{eff},z} = 56.4 d_{\mathrm{col}}^{1.33} v_G^{3.56}. \tag{4}$$

The gas–phase dispersion coefficient in Eq. (4) is valid in the variable ranges $0 \leq v_L^s \leq 0.0135\,\mathrm{m\,s^{-1}}$, $0.0085 \leq v_G^s \leq 0.13\,\mathrm{m\,s^{-1}}$, and column diameters $0.076 \leq d_{\mathrm{col}} \leq 3.2\,\mathrm{m}$[9].

For bubbly flow, Calderbank and Moo-Young[10] parametrized the mass transfer coefficients as functions of the Schmidt number, and we adopted their method here:

$$k_{L,i} = 0.31 \left(\frac{(\rho_L - \rho_G)\mu_L g}{\rho_L^2} \right)^{1/3} \mathrm{Sc}_i^{-2/3}. \tag{5}$$

In Eq. (5), g is the specific gravity, and μ_L is the dynamic molecular viscosity of the liquid, which was assumed equal to the pure liquid H_2O viscosity[11]. The Schmidt number is denoted Sc_i and is given by

$$\mathrm{Sc}_i = \frac{\mu_L}{\rho_L D_{W,i}}. \tag{6}$$

Here $D_{W,i}$ are the multicomponent diffusivities approximated by Wilke's model

$$D_{W,i} = \frac{1 - \omega_{L,i}}{\bar{M}_{w,L} \sum\limits_{\substack{j=1 \\ j \neq i}}^{N_C} \frac{\omega_{L,j}}{M_{w,j} D_j}}, \tag{7}$$

where the molecular diffusivities in H_2O, D_j, were computed by Erkey et al.[12] with molecular diameters from Bondi[13].

Furthermore, Henry's law correlations for O_2, CH_4, CO_2, and NH_3 were taken from Benson et al.[14], Rettich et al.[15], Sander[16], and Sander[16], respectively.

The surface area separating the gas– and the liquid–phases was computed by the assumption of spherical bubbles[7]:

$$a = 6\frac{\alpha_G}{d_b}. \tag{8}$$

Here, d_b is the bubble diameter which was assumed constant throughout this work.

Momentum

For both the liquid– and the gas–phases, the Reynolds analogy was assumed valid, and hence, the effective, turbulent viscosities were

$$\mu_{L,\text{eff},z} \approx \rho_L D_{L,\text{eff},z}, \tag{9}$$

$$\mu_{G,\text{eff},z} \approx \rho_G D_{G,\text{eff},z}. \tag{10}$$

Furthermore, the drag force acting on the two phases was modeled as[17]

$$f_{\text{drag}}^{G-L} = -\frac{3}{4}\frac{\alpha_G}{d_b}\rho_L C_D |v_L - v_G|(v_L - v_G), \tag{11}$$

where C_D is the drag coefficient. Tomiyama[18] parametrized the drag coefficient for pure, uncontaminated systems as:

$$C'_D = \max\left[\min\left[\frac{16}{\text{Re}_p}\left(1 + 0.15\text{Re}_p^{0.687}\right), \frac{48}{\text{Re}_p}\right], \frac{8}{3}\frac{\text{Eö}}{\text{Eö} + 4}\right]. \tag{12}$$

When multiple bubbles flow through a liquid, a swarm effect is observed. The modified drag coefficient accounts for this effect by introducing an area fraction dependency[19]:

$$C_D = C'_D(1 - \alpha_G)^P, \tag{13}$$

in which P denotes a correction factor. The relative Reynolds and Eötvös numbers are given as

$$\text{Re}_p = \frac{\rho_L |v_L - v_G| d_b}{\mu_L} \tag{14}$$

$$\text{Eö} = \frac{g(\rho_L - \rho_G)d_b^2}{\sigma}. \tag{15}$$

In Eq. (15), σ denotes the surface tension.

The wall-to-liquid friction was modeled analogously to the gas-to-liquid drag:

$$f_{\text{fric}}^{W-L} = -\frac{1}{2}\frac{\alpha_L}{d_{\text{col}}}\rho_L f_W v_L v_L. \tag{16}$$

Petukhov[20] parametrized the wall friction coefficient[21], and we adopted their correlation here:

$$f_W = (0.79\ln \text{Re} - 1.64)^{-2}, \tag{17}$$

where

$$\text{Re} = \frac{\rho_L v_L d_{\text{col}}}{\mu_L}. \tag{18}$$

Energy

The heat capacity of the liquid–phase was assumed equal to the liquid H_2O heat capacity at $T = 25\,^{\circ}\text{C}$ and $p = 1\,\text{bar}$, i.e. $c_{p,L} = c^{\circ}_{p,\text{H}_2\text{O}}(298.15\text{K})$. Additionally, $c_{p,L}$ was assumed independent of temperature. The value is tabulated by Aylward and Findlay[22]. For the gas–phase, the heat capacity was computed from a weighted sum of the pure component contributions:

$$c_{p,G} = \sum_{i=1}^{N_C} \omega_{G,i} c_{p,G,i}. \tag{19}$$

The pure component heat capacities were taken from Aylward and Findlay[22]. Furthermore, the gas–phase heat capacity was also assumed independent of temperature.

Similar to the effective turbulent viscosity, the effective thermal conductivity was assumed to follow the Reynolds analogy:

$$\lambda_{L,\text{eff},z} = D_{L,\text{eff},z}\rho_L c_{p,L} \tag{20}$$

$$\lambda_{G,\text{eff},z} = D_{G,\text{eff},z}\rho_G c_{p,G}. \tag{21}$$

The energy transfer from the liquid to the external heat exchanger was modeled with an overall heat transfer coefficient computed by a series of resistances:

$$\frac{1}{U} = \frac{1}{h_W} + \frac{t_{\text{wall}}}{k_{\text{steel}}} + \frac{1}{h_{\text{cool}}}. \tag{22}$$

Here, h_W is the heat transfer coefficient on the liquid side of the column wall, t_{wall} is the thickness of the column wall, k_{steel} is the conductivity of steel, and h_{cool} is the heat transfer coefficient on the heat exchanger side of the column wall. Deckwer [23] parametrized h_W as

$$h_W = 0.1 \lambda_L^{0.5} \rho_L^{0.75} c_{p,L}^{0.5} \mu_L^{-0.25} g^{0.25} (v_G \alpha_G)^{0.25}, \tag{23}$$

and gave values for h_{cool} [24]. Here, λ_L denotes the molecular conductivity of the liquid, which was assumed equal to the pure H_2O conductivity given by Ramires et al. [25].

Calderbank and Moo-Young [10] parametrized the interphase heat transfer coefficient as:

$$h_L = \bar{k}_L c_{p,L} \rho_L \bar{\text{Sc}}^{2/3} \text{Pr}^{-2/3}. \tag{24}$$

Here, the average mass transfer coefficient, $\bar{k}_L$, and the average Schmidt number were computed by weighted sums:

$$\bar{k}_L = \sum_{i=1}^{N_C} \omega_{L,i} k_{L,i}, \tag{25}$$

$$\bar{\text{Sc}} = \sum_{i=1}^{N_C} \omega_{L,i} \text{Sc}_i, \tag{26}$$

and the Prandtl number is given as

$$\text{Pr} = \frac{c_{p,L} \mu_L}{\lambda_L}. \tag{27}$$

Doran [26] estimated the heat of reaction for processes with biomass production to be $\Delta_{\text{rx}} h \approx -460\,\text{kJ}\,\text{mol}^{-1}$ O_2 consumed. This heat of reaction was assumed representative for

the black–boxed chemical reaction.

Supporting Figures

For the non-reactive ternary system, Figures S1 and S2 present the simulation results of the gas– and liquid–phase velocities, gas density, and pressure.

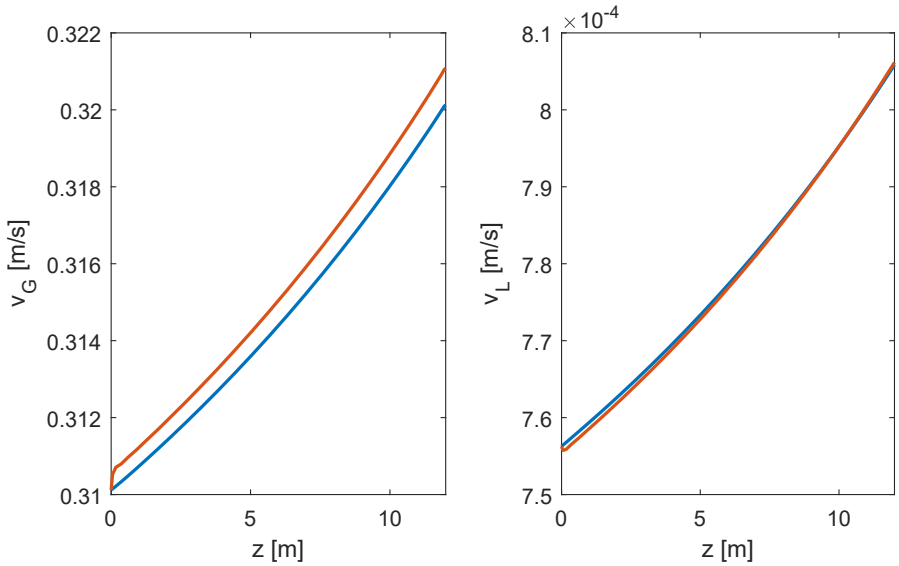

Figure S1: Local instantaneous velocities in the gas and liquid–phase in the non-reactive system. Blue lines denote results utilizing Henry's law and red lines denote results utilizing the SRK-EoS.

Supporting Tables

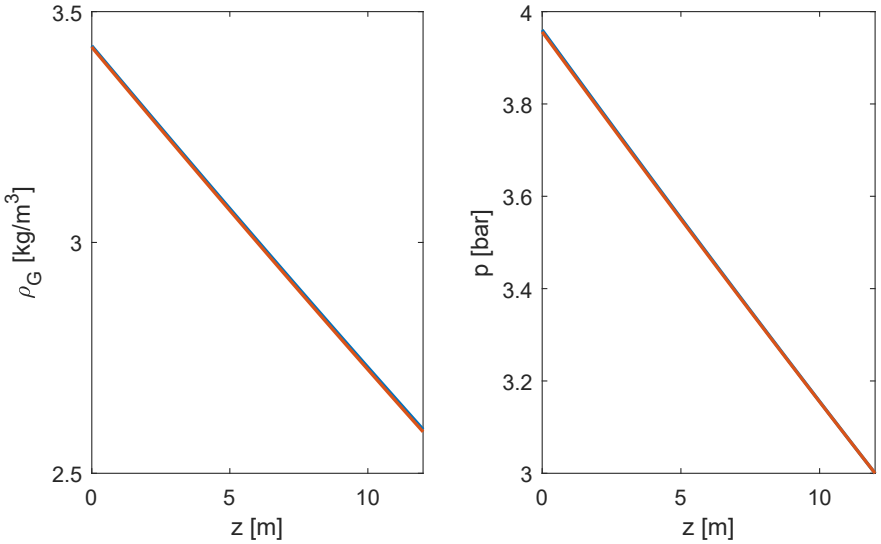

Figure S2: Density in the gas–phase and the pressure common to both phases in the non-reactive system. Blue lines denote results utilizing Henry's law and red lines denote results utilizing the SRK-EoS.

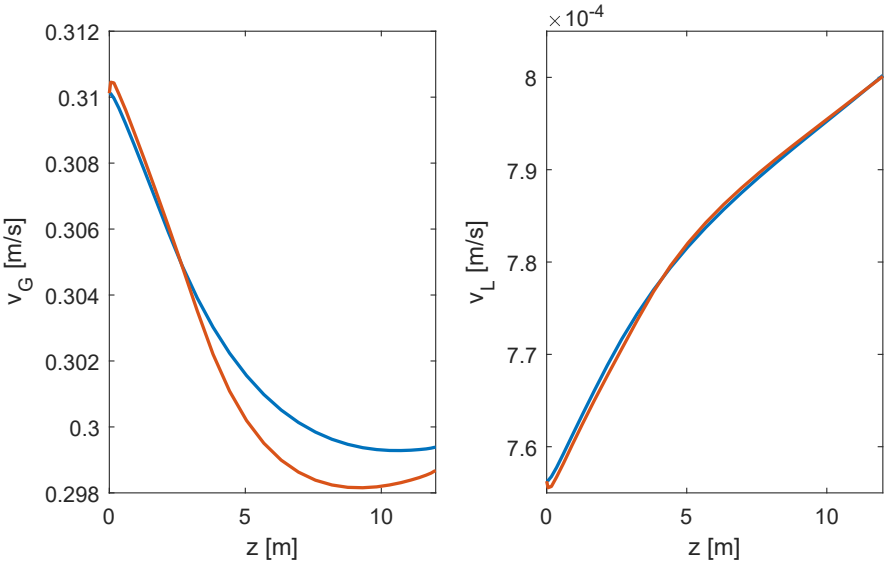

Figure S3: Local instantaneous velocities in the gas and liquid–phase in the reactive SCP system. Blue lines denote results utilizing Henry's law and red lines denote results utilizing the SRK-EoS.

Table S1: Parameters used in simulation of the bubble column bioreactor.

Variable	Value	Unit
L	12	m
d_{col}	0.2	m
t_{wall}	8.18	mm
k_{steel}	16	$\mathrm{W\,m^{-1}\,K^{-1}}$
h_{cool}	3000	$\mathrm{W\,m^{-2}\,K^{-1}}$
T_a	45	°C
ρ_L	1000	$\mathrm{kg\,m^{-3}}$
μ_L	0.8903	cP
σ	70.5	$\mathrm{mN\,m^{-1}}$
d_b	2	mm
P	2	−
$\mu_{\mathrm{max,CH_4}}$	0.37	$\mathrm{h^{-1}}$
$\mu_{\mathrm{max,O_2}}$	1	$\mathrm{h^{-1}}$
$K_{\mathrm{m,CH_4}}$	1.3	$\mathrm{\mu mol\,L^{-1}}$
$K_{\mathrm{m,O_2}}$	2.0	$\mathrm{\mu mol\,L^{-1}}$

Table S2: Critical constants and acentric factors used with the SRK-EoS.

Component	T_c [K]	p_c [MPa]	ω [−]
O_2	154.581	5.043	0.0222
CH_4	190.564	4.5992	0.0114
CO_2	304.1282	7.3773	0.2239
NH_3	405.4	11.333	0.2560
H_2O	647.096	22.064	0.3443

References

(1) Villadsen, J.; Nielsen, J.; Lidén, G. *Solvent Extr. Biotechnol.*; Springer US: Boston, MA, 2011; pp 2–51.

(2) Al Taweel, A. M.; Shah, Q.; Aufderheide, B. Effect of mixing on microorganism growth in loop bioreactors. *Int. J. Chem. Eng.* **2012**, *2012*.

(3) Joergensen, L.; Degn, H. Growth rate and methane affinity of a turbidostatic and oxystatic continuous culture of Methylococcus capsulatus (Bath). *Biotechnol. Lett.* **1987**, *9*, 71–76.

(4) Olsen, D. F.; Jørgensen, J. B.; Villadsen, J.; Jørgensen, S. B. Optimal Operating Points for SCP Production in the U-Loop Reactor. *IFAC Proc. Vol.* **2010**, *43*, 499–504.

(5) Ritschel, T. K.; Boiroux, D.; Nielsen, M. K.; Huusom, J. K.; Jorgensen, S. B.; Jorgensen, J. B. Economic Optimal Control of a U-loop Bioreactor using Simultaneous Collocation-based Approaches. *CCTA 2019 - 3rd IEEE Conf. Control Technol. Appl.* **2019**, 933–938.

(6) Ritschel, T. K.; Boiroux, D.; Nielsen, M. K.; Huusom, J. K.; Jorgensen, S. B.; Jorgensen, J. B. The Extended Kalman Filter for Nonlinear State Estimation in a U-loop Bioreactor. *CCTA 2019 - 3rd IEEE Conf. Control Technol. Appl.* **2019**, 920–925.

(7) Deckwer, W.-D. D.; Burckhart, R.; Zoll, G. Mixing and mass transfer in tall bubble columns. *Chem. Eng. Sci.* **1974**, *29*, 2177–2188.

(8) Field, R.; Davidson, J. Axial Dispersion in Bubble Columns. *Trans. Inst. Chem. Eng.* **1980**, *58*, 228–236.

(9) Fan, L.-s. *Gas-Liquid-Solid Fluidization Engineering*; Butterworth Publishers: Boston, 1989.

(10) Calderbank, P.; Moo-Young, M. The continuous phase heat and mass-transfer properties of dispersions. *Chem. Eng. Sci.* **1961**, *16*, 39–54.

(11) Korson, L.; Drost-Hansen, W.; Millero, F. J. Viscosity of water at various temperatures. *J. Phys. Chem.* **1969**, *73*, 34–39.

(12) Erkey, C.; Rodden, J. B.; Akgerman, A. A correlation for predicting diffusion coefficients in alkanes. *Can. J. Chem. Eng.* **1990**, *68*, 661–665.

(13) Bondi, A. van der Waals Volumes and Radii. *J. Phys. Chem.* **1964**, *68*, 441–451.

(14) Benson, B. B.; Krause, D.; Peterson, M. A. The solubility and isotopic fractionation of gases in dilute aqueous solution. I. Oxygen. *J. Solution Chem.* **1979**, *8*, 655–690.

(15) Rettich, T. R.; Handa, Y. P.; Battino, R.; Wilhelm, E. Solubility of gases in liquids. 13. High-precision determination of Henry's constants for methane and ethane in liquid water at 275 to 328 K. *J. Phys. Chem.* **1981**, *85*, 3230–3237.

(16) Sander, R. Compilation of Henry's law constants (version 4.0) for water as solvent. *Atmos. Chem. Phys.* **2015**, *15*, 4399–4981.

(17) Albråten, P. J. The dynamics of two-phase flow: an analysis of the momentum transport in bubble, droplet, and particulate flow. Ph.D. Thesis, Chalmers University of Technology,, Göteborg, 1982.

(18) Tomiyama, A. Struggle with computational bubble dynamics. 1998.

(19) Rampure, M. R.; Kulkarni, A. A.; Ranade, V. V. Hydrodynamics of bubble column reactors at high gas velocity: Experiments and computational fluid dynamics CFD simulations. *Ind. Eng. Chem. Res.* **2007**, *46*, 8431–8447.

(20) Petukhov, B. S. Heat Transfer and Friction in Turbulent Pipe Flow with Variable Physical Properties. *Adv. Heat Transf.* **1970**, *6*, 503–564.

(21) Bergman, T. L.; Lavine, A. S. *Fundamentals of Heat and Mass Transfer*, 8th ed.; John Wiley & Sons: Hoboken, NJ, 2017.

(22) Aylward, G.; Findlay, T. *SI Chemical Data*, 6th ed.; John Wiley & Sons Australia, Ltd: 42 McDougall Street, Milton, Qld 4064, 2008.

(23) Deckwer, W. D. On the mechanism of heat transfer in bubble column reactors. *Chem. Eng. Sci.* **1980**, *35*, 1341–1346.

(24) Vik, C. B.; Solsvik, J.; Hillestad, M.; Jakobsen, H. A. Modeling of a Slurry Bubble Column Reactor for the Production of Biofuels via the Fischer-Tropsch Synthesis. *Chem. Eng. Technol.* **2015**, *38*, 690–700.

(25) Ramires, M. L. V.; Nieto de Castro, C. A.; Nagasaka, Y.; Nagashima, A.; Assael, M. J.; Wakeham, W. A. Standard Reference Data for the Thermal Conductivity of Water. *J. Phys. Chem. Ref. Data* **1995**, *24*, 1377–1381.

(26) Doran, P. M. *Bioprocess Engineering Principles*, 2nd ed.; Academic Press: Amsterdam, 2013.

4.3 Paper III: Mass Transfer Modeling in the Fischer–Tropsch Synthesis

Chemical Engineering Science 259 (2022) 117774

Contents lists available at ScienceDirect

Chemical Engineering Science

journal homepage: www.elsevier.com/locate/ces

Mass transfer modeling and sensitivity study of low-temperature Fischer-Tropsch synthesis

S.B. Øyen *, H.A. Jakobsen, T. Haug-Warberg, J. Solsvik

Department of Chemical Engineering, Norwegian University of Science and Technology (NTNU), N-7491 Trondheim, Norway

HIGHLIGHTS

- Mass transfer models for gas–liquid systems based on rigorous phase equilibrium.
- Fischer–Tropsch synthesis operated in slurry bubble column reactor.
- Solvent specification required for Henry's law investigated.

ARTICLE INFO

Article history:
Received 21 February 2022
Received in revised form 21 May 2022
Accepted 25 May 2022
Available online 11 June 2022

Keywords:
Fischer–Tropsch
Mass transfer
Phase equilibrium
PC-SAFT
Peng–Robinson
Henry's law

ABSTRACT

An industrial-scale Fischer–Tropsch (FT) slurry bubble column reactor (SBCR) was theoretically investigated, emphasizing the mass transfer between the gas and slurry phases. In this endeavor, three different driving forces for mass transfer (the impetus behind the motion of species mass) were proposed: one based on Henry's law and two based on rigorous phase equilibrium. The mass transfer model based on Henry's law relies on the solvent, which here was specified as a paraffin with carbon chain length in the range of 16–36. The conversion level was found to increase with increasing carbon chain length. On the other hand, the mass transfer models based on phase equilibrium do not require identifying a solvent, which is advantageous for the Fischer–Tropsch synthesis (FTS) where the large number of compounds render the solvent a vague and ambiguous concept. Here, the phase equilibrium was computed with the Peng–Robinson (PR) and the perturbed-chain statistical associating fluid theory (PC-SAFT) equations of state (EoSs); however, the proposed concept is generic and easily extended to other EoSs and activity coefficient-based models. With all three mass transfer formulations, the conversion level increased with increasing pressure and decreased with increasing temperature. Furthermore, increasing the catalyst loading did not increase the conversion level, whereas increasing the mass transfer coefficient did increase the conversion level. It was concluded that the reactor operates in the mass transfer limited regime rather than the kinetically limited regime. The mass transfer model based on Henry's law was the least computationally expensive to evaluate, followed by the PR and PC-SAFT EoSs in increasing order; however, the mass transfer models based on the PR and PC-SAFT EoSs are capable of predicting the thermodynamic spontaneity of forming additional phases, which Henry's law is incapable of.

1. Introduction

In the last two centuries, the demand for fuels has increased exponentially (Smil, 2016), and while the demand is currently met, most fuels are produced through non-renewable resources, such as coal, oil, and gas. In the wake of an increasing focus on sustainable and environmentally friendly fuels, the Fischer–Tropsch synthesis (FTS) has re-emerged as a viable option to convert syngas (CO and H_2) into liquid fuels.

The FTS has been accredited to Fischer and Tropsch (1923) for their discovery of converting syngas into liquid fuels over an iron catalyst (Dry, 1989; Stranges, 2000). At that time, the syngas was obtained from coal, and the process is hence termed coal-to-liquid (CtL). Since then, two new methods have been discovered: gas-to-liquid (GtL) and biomass-to-liquid (BtL). In the GtL process, the syngas is obtained by reforming CH_4 through, e.g., steam–methane reforming, partial oxidation, or autothermal reforming. In the BtL process, the syngas is obtained by gasifying biomass into

* Corresponding author.
E-mail addresses: sindre.b.oyen@ntnu.no (S.B. Øyen), jannike.solsvik@ntnu.no (J. Solsvik).

https://doi.org/10.1016/j.ces.2022.117774
0009-2509/

Nomenclature

Latin Letters

A	Area m^2
$\mathcal{A}$	Helmholtz energy J
$\boldsymbol{A}$	Matrix of linear terms varying
a	Gas–liquid contact area $m^2 m^{-3}$
a_i	Model constants PC-SAFT, $i = \{0, 1, \ldots, 6\}$ –
a_{FT}	Reaction kinetic parameter $kmol kg_{cat}^{-1} Pa^{-2} s^{-1}$
B	Mixture excluded volume PR m^3
b_i	Model constants PC-SAFT, $i = \{0, 1, \ldots, 6\}$ –
b_{FT}	Reaction kinetic parameter Pa^{-1}
C_D	Drag coefficient varying
C_1	Compressibility expression –
C	Number of components –
CN	Carbon number –
c_p	Specific isobaric heat capacity $J K^{-1} kg^{-1}$
D	Mixture attractive term PR $Pa m^6$
$D_{eff,z}$	Effective axial dispersion coefficient $m^2 s^{-1}$
d	Diameter m
d_i	Segment diameter of component i Å
Eö	Eötvös number –
F	Source/sink term varying
f	Friction factor –
G	Molar flux $kmol m^{-2} s^{-1}$
g	Gravitational acceleration $m s^{-2}$
g_{ij}	Radial distribution function between components –
H	Henry's law constant Pa
h	Molar enthalpy $J mol^{-1}$
h_L	Liquid side heat transfer coefficient $W m^{-2} K^{-1}$
I	Dispersive integral –
$\boldsymbol{J}$	Jacobian matrix mol^{-1}
K	Phase equilibrium ratio –
k_{ij}	Binary interaction parameter –
k_B	Boltzmann constant $J K^{-1}$
k_G	Gas side mass transfer coefficient $m s^{-1}$
k_L	Liquid side mass transfer coefficient $m s^{-1}$
k	Conductivity $W m^{-1} K^{-1}$
$\mathcal{L}_i$	Lump of paraffins, $i = \{1, 2, 3, 4\}$ –
L	Reactor length m
ℓ	Lagrange interpolating polynomial –
m	Number of segments PC-SAFT –
M_w	Molar weight $kg kmol^{-1}$
N	Number of molecules –
N_A	Avogadro number –
N_i	Mass transfer flux of component i $kg m^{-2} s^{-1}$
n	Number of moles mol
$\mathcal{N}, \mathcal{M}$	Lump chain length –
P	Swarm correlation parameter –
p	Pressure Pa
Pr	Prandtl number –
R	Gas constant $J K^{-1} mol^{-1}$:
R_i	Rate of generation of component i $kg m^{-3} s^{-1}$
r_{FT}	Fischer–Tropsch reaction rate $kmol kg_{cat}^{-1} s^{-1}$
Re	Reynolds number –
S	Perimeter m
s	Scaling parameter –
Sc	Schmidt number –
T	Temperature K
t	Thickness m
U	Overall heat transfer coefficient $W m^{-2} K^{-1}$
V	Volume m^3
v	Velocity $m s^{-1}$
X	Conversion level mol%
x_i	Mole fraction of component i in liquid –
y_i	Mole fraction of component i in gas –
y	Function varying
Z	Compressibility factor –
z	z-coordinate in physical space m

Greek Letters

α	Area fraction –
α_{ASF}	Chain growth probability –
β	Initial number of moles mol
γ	Acentric factor –
Δ	Change –
δ	Kronecker delta –
ε	Well depth J
η	Modified chemical potential –
λ	Thermal conductivity $W m^{-1} K^{-1}$
μ_i	Chemical potential of component i $J mol^{-1}$
μ	Dynamic viscosity Pa s
ν	Iteration count –
ν_i	Stoichiometric coefficient of component i –
ξ_i	Auxiliary variable, $i = \{0, 1, 2, 3\}$ m^{i-3}
ρ	Mass density of mixture $kg m^{-3}$
σ	Gas–liquid surface tension $N m^{-1}$
σ_i	Segment diameter of component i Å
ϕ	Weighted area fraction ratio –
φ	Fugacity coefficient –
ψ	Area fraction ratio –
ω	Mass fraction –

Superscripts

0	Start estimate
Aq	Aqueous
assoc	Associative
$\circ$	Base case sensitivity study
disp	Dispersive
$G-I$	Gas-to-interface
$G-L$	Gas-to-liquid
hs	Hard sphere
$I-L$	Interface-to-liquid
ig	Ideal gas
m	Molar
$P-L$	Pipe-to-liquid
r,p	Residual at the same pressure
r,v	Residual at the same volume
s	Superficial
$S-L$	Solid-to-liquid
$W-L$	Wall-to-liquid
$*$	Equilibrium value
~	Reduced

Subscripts

∞	Infinite dilution limit
a	Ambient
ASF	Anderson–Schulz–Flory
NBP	Normal boiling point
b	Bubble
c	Value at critical point
col	Bubble column
cool	Cooling
D	Drag
eff	Effective
FT	Fischer–Tropsch
fric	Friction
G	Gas
i, j, k or l	Component number
ii	Pair like molecules
ij	Pair unlike molecules

in	At reactor inlet
L	Liquid
$\mathcal{L}$	Lumps
out	At reactor outlet
P	Pipe
p	Particle
pol	Polynomials
rx	Reaction
S	Solid
SL	Slurry
SiS	Solid in gas-free slurry
T	Total
W	Wall

Abbreviations

ASF	Anderson–Schulz–Flory
BtL	Biomass to liquid
CtL	Coal to liquid
EoS	Equation of state
FT	Fischer–Tropsch
FTS	Fischer–Tropsch synthesis
GLE	Gas–liquid equilibrium
GLLE	Gas–liquid–liquid equilibrium
GtL	Gas to liquid
HTFT	High-temperature Fischer–Tropsch
LTFT	Low-temperature Fischer–Tropsch
MHV2	Modified Huron/Vidal 2
PBR	Packed bed reactor
PC-SAFT	Perturbed-chain statistical association fluid theory
PR	Peng–Robinson
PSRK	Predictive SRK
SBCR	Slurry bubble column reactor
SRK	Soave–Redlich–Kwong
SSTR	Slurry stirred tank reactor
WGS	Water–gas-shift

biomass syngas (Baliban et al., 2013). The fuels produced through the FTS contain practically no nitrous, sulfuric, or aromatic compounds and are thus said to be clean fuels (Sehabiague and Morsi, 2013a). Moreover, an FTS plant utilizing the BtL technology is considered carbon–neutral (Hamelinck et al., 2004; van Steen and Claeys, 2008). Hence, the FTS can be instrumental in transitioning to clean fuel technologies.

The products from the FTS depend on the solid catalyst (usually cobalt- or iron-based). In general, the mixture consists of various n-alkanes (paraffins), n-alkenes (olefins), alcohols, acids, ketones, and aldehydes. The products exist in various carbon chain lengths and constitute both volatile and non-volatile compounds. The cobalt catalyst is found to have negligible water–gas–shift (WGS) activity (Maretto and Krishna, 2001; Hillestad, 2015), high selectivity towards paraffins (Rodrigues et al., 2011; Marano and Holder, 1997), and relatively slow deactivation (Sari et al., 2009). On the other hand, iron catalysts are active towards the WGS reaction and produce olefins and oxygenated compounds in addition to paraffins (Marano and Holder, 1997).

Two different modes of FTS operation currently exist: low-temperature Fischer–Tropsch (LTFT) and high-temperature Fischer–Tropsch (HTFT). The LTFT aims to produce waxes, while the HTFT aims to produce gasoline and α-olefins (Rauch et al., 2013). While the HTFT is usually operated in ebullated or fluidized bed reactors, the LTFT is usually operated in fixed beds or slurry reactors (Rauch et al., 2013). In fixed bed reactors operating in LTFT mode, the produced waxes inhibit the reaction rate due to diffusion limitations in the wax–catalyst region (Dry, 2004). This effect is not observed for slurry reactors where the catalyst has been crushed into fine particles before being suspended in the liquid phase. A particular slurry reactor, the slurry bubble column reactor (SBCR), also has the advantage of very high heat transfer coefficients (Kast, 1962), ensuring excellent temperature control. Moreover, the SBCR is simple in design (essentially a vertical cylinder), making it cheap and easy to construct in large scale. The most notable drawbacks of the SBCR are related to the regeneration of catalyst particles, the complicated nature of the gas–liquid mass transfer, and the hydrodynamics of the three-phase flow.

Gas–liquid mass transfer is essential in an SBCR operating at LTFT conditions. The syngas is typically sparged from the bottom of the SBCR, and a swarm of bubbles rises through the SBCR. The reactants are transported from the gas bubbles and into the liquid phase, where the solid catalyst is suspended. The driving force for gas–liquid mass transfer (the impetus behind the motion of species mass) is commonly regarded as the difference between the phase equilibrium concentration and the bulk phase concentration. Often, Henry's law data is used to close the mass transfer models (Sehabiague et al., 2008; Sehabiague and Morsi, 2013; Marano and Holder, 1997; Maretto and Krishna, 1999; Chao and Lin, 1988); however, this closure relation is inappropriate in the FTS for two reasons: (i) Henry's law is a relation for gas–liquid equilibrium (GLE) which is valid only for estimating the solubility of a volatile, poorly soluble compound, i.e., CO, H_2, H_2O, CO_2, and light hydrocarbons, in a specified solvent, and (ii) due to the vast amount of chemical compounds present, the solvent to be regarded is not uniquely defined (Derevich et al., 2008). Thus, the mass transfer of low to medium volatile compounds in the FTS cannot be estimated with Henry's law. These compounds include hydrocarbons of notable chain lengths and oxygenated compounds.

To the authors' knowledge, no mass transfer models relying on more sophisticated GLE descriptions than Henry's law exist to date in the literature for the FTS. On the other hand, efforts have been made to describe the FTS mixture when phase equilibrium has been established, and the net mass transfer is zero. In that case, the FT reactor is similar to a reactive flash calculation. For instance, some authors attempted to model the phase behavior of the FTS mixture with Raoult's law (Raje and Davis, 1996; Masuku et al., 2012; Masuku et al., 2011; Caldwell and Van Vuuren, 1986). Raoult's law is primarily a good approximation for estimating the vapor pressure of non-volatile compounds, where the compound is present in excess in the liquid phase. Hence, Raoult's law is expected to represent the GLE of the heavy, non-volatile compounds well (Marano and Holder, 1997). In an experimental study, Raje and Davis (1996) reported the opposite trend: short-chained hydrocarbons (volatile compounds) are well represented by Raoult's law, and heavy compounds (chain length > 20) deviate considerably. Masuku et al. (2012) further confirmed this trend in their experimental work. It was also concluded by Derevich et al. (2008) that Raoult's law is incapable of predicting the solubilities of CO and H_2 in FT solvents.

Sadeqzadeh et al. (2013) employed Henry's law for volatile compounds and Raoult's law for heavy compounds. Although this agrees with our intuitive understanding of the physical properties of the mixture considered, Raje and Davis (1996) concluded that Raoult's law does not represent the non-volatile, heavy compounds

well. Sadeqzadeh et al. (2013) similarly concluded that their GLE modeling approach was inadequate and that further sophisticated GLE models should be employed in FTS modeling.

Although cubic equations of state are actively used in GLE computations, they were initially fitted to vapor pressures for relatively small molecules where the reduced temperatures are above 0.6 (Bond and Dawe, 1988). Heavy compounds usually display reduced temperatures in the range 0.40–0.65; hence, utilization of cubic EoSs on heavy hydrocarbons in the FTS must be regarded as an extrapolation. Bond and Dawe (1988) and Gray et al. (1989) concluded that cubic EoSs in their original form yielded unsatisfactory results for the FTS. Wang et al. (1999) also reached similar conclusions.

Nevertheless, some investigators have employed cubic EoSs as part of a larger model to predict the phase behavior in the FTS. For instance, Ahón et al. (2005) used the Soave–Redlich–Kwong (SRK) EoS to model the gas–liquid distribution of different compounds in a well-mixed (no spatial variations), transient slurry reactor. However, Ahón et al. (2005) made no experimental comparison. On the other hand, Derevich et al. (2008) employed a *modified* PR EoS to predict the phase behavior of the gas–liquid mixture. Their results were in good agreement with the experimental results.

Zheng et al. (2019) employed the predictive Soave–Redlich–K wong (PSRK), the Soave–Redlich–Kwong/modified Huron-Vidal mixing rules (SRK/MHV2), and the PC-SAFT EoSs, in an endeavor to find the best EoS in the FTS. Their results show that the PC-SAFT EoS accurately describes the phase behavior of the complex FTS mixture over a wide range of operating conditions and successfully predicts the solubilities of syngas in the FT liquid products.

This study establishes a mass transfer model based on an accurate GLE description. The purpose is to bridge the gap in LTFT SBCRs, where current mass transfer models in the literature are solely based on Henry's law. Our contribution aims to allow for condensation of syngas and evaporation of FTS products with a sound basis in thermodynamic phase equilibrium. Furthermore, we perform a sensitivity study showing how simulation results are affected by changing the GLE modeling description, i.e., the PR and PC-SAFT EoSs, in the mass transfer driving force. Subsequently, we compare the results obtained with mass transfer based on Henry's law to the results obtained with mass transfer based on the PR and PC-SAFT EoSs. Moreover, we illustrate how the choice of solvent affects the results obtained with mass transfer based on Henry's law.

This work is divided into four parts. First, the necessary theory is provided, including a description of the SBCR, the FT mixture, reaction kinetics, and mass transfer modeling. Second, the solution strategy, numerical considerations, parameters, and initial conditions are given. Third, results and discussions are presented, and fourth, conclusions are drawn.

2. The Reactor Model

The SBCR consists of three phases: liquid, gas, and solid phase. The solid phase consists of finely ground catalyst particles suspended in the liquid phase. The gas phase consists of gas bubbles injected or sparged from the bottom of the SBCR.

Resistance to chemical conversion is assumed to be threefold. First, the reactants are transferred from the gas phase to the liquid phase. Second, the reactants are transferred from the liquid phase and onto the catalytic surface, and third, the chemical reaction occurs. The first and second resistances are related to mass transfer limitations, and the third resistance is related to reaction kinetic limitations. Since the catalyst particles used in the FTS are tinier than the gas bubbles, the solid–liquid interfacial area is larger than the gas–liquid interfacial area. Therefore, it is reasonable to assume that the mass transfer limitations are related to the gas–liquid interface rather than the solid–liquid interface. This assumption also agrees well with experimental observations (Dry, 2004), where no solid–liquid mass transfer limitations were found. Further treatment of the reaction kinetics and the mass transfer models are given in Sections 2.1, 2.2, 2.3.

The liquid, gas, and solid phases in the SBCR were modeled by a set of transport equations for each of the phases: total mass (continuity), species mass, momentum, and energy. In total, the three phases in the SBCR were represented by 12 governing equations. However, two simplifications were made: i) the liquid and solid phases were assumed to share the same temperature, T_{SL}, and ii) the solid catalyst phase was described by the continuity and momentum equations. High heat transfer coefficients have been observed for SBCRs (Kast, 1962) and the catalyst particles have a large interfacial area, thus justifying simplification i). Hence, the reactor model consists of the 10 transport equations given in Table 1. Terms representing the exchange of mass, momentum, or energy between the different phases exist as source and sink terms in the respective transport equations. Particular emphasis is placed on the reaction kinetics and the mass transfer modeling in the following sections.

The solution of the FTS SBCR model is visually displayed in Fig. 1. As seen, the FTS SBCR model is composed of the governing equations in Table 1, the mass transfer model, and the gas–liquid interface model. The mass transfer model is described in Sections 2.2 and 2.3, in which the gas–liquid interface model exists in the driving force as the reciprocal GLE ratio, that is $1/K_i$. As GLE is assumed to prevail at the gas–liquid interface, K_i is modeled by proper GLE descriptions. In this work, three GLE descriptions were employed: Henry's law, the PR EoS, and the PC-SAFT EoS.

2.1. Kinetic Modeling and Considered Species

The FTS is a chemically challenging process due to the many components and reactions. Simplifying the number of components is therefore imperative, and the procedure is, in general, carried out in two steps: i) the different classes of organic compounds (alkanes, alkenes, and oxygenated compounds) are reduced through a set of justified assumptions, and ii) the remaining organic compounds are lumped into pseudo-components. In the FTS, paraffins and olefins are produced in excess, and thus, the production of oxygenated compounds is in this work neglected. Furthermore, we employ a lumping strategy to simplify the number of components considered. The lumps considered are essential in reaction kinetics modeling, and for the mass transfer modeling in this work. The lumping strategy and reaction kinetic modeling is treated in this section. Details on the mass transfer modeling are deferred to Sections 2.2 and 2.3.

The cobalt-based catalysts are generally preferred over the iron-based catalysts in the FTS due to their high CO conversion, high selectivity towards paraffins, and low WGS activity (Petersen et al., 2019; Dry, 2004; van Steen and Claeys, 2008). Moreover, the cobalt catalyst produces mostly paraffins, and in the presence of H_2 at LTFT conditions, olefins can be further hydrogenated into paraffins (Peña et al., 2014). Therefore, it is reasonable for the cobalt catalyst to assume that the FTS produces paraffins exclusively.

In this work, all reactions are lumped into the following representative reaction (Yates and Satterfield, 1991):

$$\mathrm{CO} + \nu_{\mathrm{H_2}}\mathrm{H_2} \xrightarrow{r_{\mathrm{FT}}} \mathrm{H_2O} + \sum_{i=1}^{N_{\mathcal{L}}} \nu_{\mathcal{L}_i}\mathcal{L}_i, \tag{11}$$

where r_{FT} is the consumption rate of one mole of CO in the FT reaction in Eq. (11), $\mathcal{L}_i$ is a lump of paraffins, and $N_{\mathcal{L}}$ is the number of

Table 1
Governing equations describing the FTS SBCR.

Transport of total mass	
$\frac{d}{dz}(\alpha_L \rho_L v_L) = \sum_{j=1}^{C} N_j a$	(1)
$\frac{d}{dz}(\alpha_G \rho_G v_G) = -\sum_{j=1}^{C} N_j a$	(2)
$\frac{d}{dz}(\alpha_S \rho_S v_S) = 0$	(3)
Transport of species mass	
$\frac{d}{dz}(\alpha_L \rho_L v_L \omega_{L,i}) = \frac{d}{dz}\left(\alpha_L \rho_L D_{L,\mathrm{eff},z} \frac{d\omega_{L,i}}{dz}\right) + N_i a + \alpha_S R_i$	(4)
$\frac{d}{dz}(\alpha_G \rho_G v_G \omega_{G,i}) = \frac{d}{dz}\left(\alpha_G \rho_G D_{G,\mathrm{eff},z} \frac{d\omega_{G,i}}{dz}\right) - N_i a$	(5)
Transport of momentum	
$\frac{d}{dz}(\alpha_L \rho_L v_L v_L) = \frac{d}{dz}\left(\alpha_L \mu_{L,\mathrm{eff},z} \frac{dv_L}{dz}\right) - \alpha_L \frac{dp}{dz} - \alpha_L \rho_L g + f_{\mathrm{drag}}^{G-L} + f_{\mathrm{drag}}^{S-L} + f_{\mathrm{fric}}^{W-L} + f_{\mathrm{fric}}^{P-L}$	(6)
$\frac{d}{dz}(\alpha_G \rho_G v_G v_G) = \frac{d}{dz}\left(\alpha_G \mu_{G,\mathrm{eff},z} \frac{dv_G}{dz}\right) - \alpha_G \frac{dp}{dz} - \alpha_G \rho_G g - f_{\mathrm{drag}}^{G-L}$	(7)
$-\alpha_S \frac{dp}{dz} - \alpha_S \rho_S g - f_{\mathrm{drag}}^{S-L} = 0$	(8)
Transport of energy	
$(\alpha_L \rho_L v_L c_{p,L} + \alpha_S \rho_S v_S c_{p,S}) \frac{dT_{SL}}{dz} = \frac{d}{dz}\left(\alpha_{SL} \lambda_{SL,\mathrm{eff},z} \frac{dT_{SL}}{dz}\right) + \frac{S_i}{A} U (T_a - T_{SL}) + h_L a (T_G - T_{SL}) + \alpha_S \rho_S r_{FT} (-\Delta_{rx} h)$	(9)
$\alpha_G \rho_G v_G c_{p,G} \frac{dT_G}{dz} = \frac{d}{dz}\left(\alpha_G \lambda_{G,\mathrm{eff},z} \frac{dT_G}{dz}\right) - h_L a (T_G - T_{SL})$	(10)

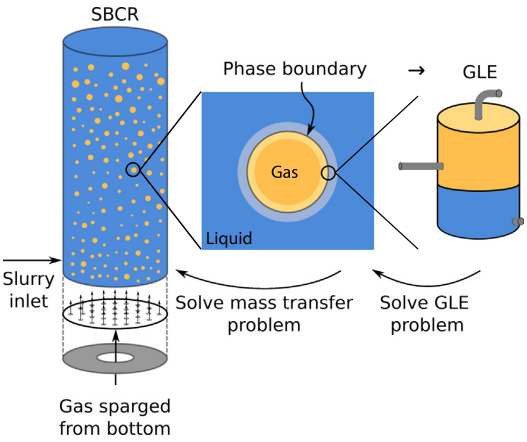

Fig. 1. Visual representation of the structure of the SBCR model.

lumps considered. Each lump $\mathcal{L}_i$ is considered one distinct species, and the paraffins contained within this lump are all treated with the same set of representative physical properties. The estimation of the physical properties of the different lumps is treated in Section 2.5.

Although the reaction occurs in the slurry phase, the reactants are supplied by mass transfer from the gaseous phase. On the other hand, the experiments by Yates and Satterfield (1991) were performed in the kinetically limited regime, and mass transfer limitations were irrelevant. Hence, their reaction rate expression of Eq. (11) was based on the partial pressures in the gas phase. However, utilizing the reaction rate expression by Yates and Satterfield (1991) in a mass transfer limited system can yield unphysical results. For instance, a non-zero consumption of reactants can be predicted due to their high partial pressures, even though the reactants need not be present in the slurry phase where the reaction occurs. The slurry phase reaction cannot proceed without dissolved reactants, and consequently, the reaction rate expression by Yates and Satterfield (1991) was modified to utilize the concentrations of the reactants in the slurry phase rather than their partial pressures. Hence, in this work, the reaction rate was expressed in terms of slurry phase concentrations of the reactants:

$$r_{\mathrm{FT}} = a_{\mathrm{FT}} \frac{K_{\mathrm{CO}}^m x_{\mathrm{CO}} K_{\mathrm{H_2}}^m x_{\mathrm{H_2}} p^2}{\left(1 + b_{\mathrm{FT}} K_{\mathrm{CO}}^m x_{\mathrm{CO}} p\right)^2}, \tag{12}$$

where a_{FT} and b_{FT} were parameter fitted constants given by Maretto and Krishna (2001) as

$$a_{\mathrm{FT}} = 8.8533 \times 10^{-3} \exp\left[4494.41\left(\frac{1}{493.15} - \frac{1}{T_{SL}}\right)\right] \times 10^{-13}, \tag{13}$$

$$b_{\mathrm{FT}} = 2.226 \exp\left[-8236\left(\frac{1}{493.15} - \frac{1}{T_{SL}}\right)\right] \times 10^{-5}. \tag{14}$$

Moreover, the molar GLE ratio is denoted

$$K_i^m = \frac{y_i^*}{x_i^*}, \tag{15}$$

where y_i and x_i are the mole fractions of component i in the gas and liquid phase, respectively, the asterisk $(*)$ denotes the phase equilibrium state, and p is the pressure. Ledakowicz et al. (1985), Deckwer et al. (1986), Withers et al. (1990), and Sehabiague et al. (2008) also gave expressions similar to Eq. (12); however, their conversions from gas partial pressures to slurry concentrations were all based on Henry's law. The volumetric reaction rate required in the transport equation for species mass is given by

$$R_i = r_{\mathrm{FT}} \rho_S \nu_i M_{w,i}. \tag{16}$$

Except for short chain lengths (carbon chain length less than 10), the product distribution of paraffins has been found to obey the Anderson–Schulz–Flory (ASF) distribution reasonably well (Sari et al., 2009; Masuku et al., 2011; Masuku et al., 2012; Todic et al., 2013). Based on the ASF distribution, Hillestad (2015) created a set of lumps, $\{C_1, C_2, C_{[3,10]}, C_{[11,\infty]}\}$, and for each lump $C_{[\mathcal{N},\mathcal{M}]}$, the stoichiometric coefficients of Eq. (11) were computed by:

$$\nu_{[\mathcal{N},\mathcal{M}]} = (1 - \alpha_{\mathrm{ASF}})\left(\alpha_{\mathrm{ASF}}^{\mathcal{N}-1} - \alpha_{\mathrm{ASF}}^{\mathcal{M}}\right). \tag{17}$$

Here α_{ASF} is the chain growth probability. Moreover, the stoichiometric coefficient of H_2 was computed consistently with Eqs. (11) and (17) as

$$\nu_{\mathrm{H_2}} = 3 - \alpha_{\mathrm{ASF}}. \tag{18}$$

Stoichiometric coefficients computed by Eqs. (17) and (18) ensure that the element balances are respected, and the mass is conserved. Furthermore, Hillestad (2015) gave the following expression for the representative carbon number of each lump:

Table 2
Straight-chained paraffins were lumped based on the carbon number (CN).

Lump	CNs lumped [-]	$\overline{CN}$ [-]	M_w [kg kmol^{-1}]	v [-]
$\mathcal{L}_1$	1 – 10	4.6466	67.0524	0.0651
$\mathcal{L}_2$	11 – 20	14.6466	207.0524	0.0227
$\mathcal{L}_3$	21 – 30	24.6466	347.0524	0.0079
$\mathcal{L}_4$	31 – ∞	40.0000	562.0000	0.0043

$$\overline{CN}_{[\mathcal{N},\mathcal{M}]} = \frac{\mathcal{N}\alpha_{ASF}^{\mathcal{N}-1} - (\mathcal{N}-1)\alpha_{ASF}^{\mathcal{N}} - (\mathcal{M}+1)\alpha_{ASF}^{\mathcal{M}} + \mathcal{M}\alpha_{ASF}^{\mathcal{M}+1}}{(1-\alpha_{ASF})(\alpha_{ASF}^{\mathcal{N}-1} - \alpha_{ASF}^{\mathcal{M}})}, \tag{19}$$

for which the lump extending to infinitely long chains reduces to

$$\overline{CN}_{[\mathcal{N},\infty]} = \mathcal{N} + \frac{\alpha_{ASF}}{1-\alpha_{ASF}}. \tag{20}$$

The lumps used here are different from those of Hillestad (2015). The lumps $\mathcal{L}_1$–$\mathcal{L}_4$ are used in this work, and their characteristics are given in Table 2.

2.2. Mass Transfer Modeling with Henry's law

The gas–liquid mass transfer model employed here is based on the two-film model. For a gaseous component i infinitely diluted in solvent j, Henry's law is appropriate:

$$py_i^* = H_{ij}x_i^*, \tag{21}$$

where H_{ij} is the Henry's law constant for solute i in solvent j. With Henry's law, the mass transfer flux is given by (see Appendix A for the derivation):

$$N_i = k_{L,i}\rho_L\left(\frac{p}{H_{ij}}\frac{\overline{M}_{w,G}}{\overline{M}_{w,L}^*}\omega_{G,i} - \omega_{L,i}\right), \tag{22}$$

where the conversion from mole fraction, x_i, to mass fraction, ω_i, given as

$$\omega_i = \frac{x_i M_{w,i}}{\sum_{j=1}^{C} x_j M_{w,j}} \tag{23}$$

has been used. Correlations for H_{ij} are given by Marano and Holder (1997) for the solutes CO, H_2, H_2O, and CO_2 in the solvent paraffins $C_{16}H_{34}$–$C_{36}H_{74}$. The molar weight of the mixture, $\overline{M}_w$, is given by Eq. (A.7).

Knowledge of the molar GLE ratio, K_i^m, is required to compute the reaction rate in Eq. (12). Assuming Henry's law is valid, K_i^m was computed by rearranging Eq. (21) and inserting into Eq. (15):

$$K_{ij}^{m,\infty} = \frac{H_{ij}}{p}. \tag{24}$$

Furthermore, the mass based equilibrium ratio is defined by

$$K_i \equiv \frac{\omega_{G,i}^*}{\omega_{L,i}^*}. \tag{25}$$

By employing the conversion formula in (23), the relation between K_i and K_i^m is given as:

$$K_i = \frac{\overline{M}_{w,L}^*}{\overline{M}_{w,G}^*}K_i^m. \tag{26}$$

The GLE ratio employing Henry's law is obtained by inserting Eq. (24) into Eq. (26):

$$K_{ij}^{\infty} = \frac{H_{ij}}{p}\frac{\overline{M}_{w,L}^*}{\overline{M}_{w,G}^*}. \tag{27}$$

The resulting mass transfer flux based on Henry's law is obtained by inserting Eq. (27) into Eq. (22):

$$N_i = k_{L,i}\rho_L\left(\frac{\omega_{G,i}}{K_{ij}^{\infty}} - \omega_{L,i}\right). \tag{28}$$

It is emphasized that the reaction rate in Eq. (12) relies on the GLE ratio. When mass transfer is computed based on Henry's law, the GLE ratio used in Eq. (12) is given by Eq. (24).

2.3. Mass Transfer Modeling with EoS

The gas–liquid mass transfer model employed here is based on the two-film model. The driving force for mass transfer was modeled as the deviation from GLE, where a complete phase equilibrium description (i.e., all components modeled, including the solvent) was used. A negative flash algorithm based on Newton–Raphson iteration was developed by Øyen et al. (2021), and their solution strategy was employed in this work to facilitate the convergence of the GLE problem. We emphasize that the heaviest lump, $\mathcal{L}_4$, ranges from chain lengths 31–∞, consequently consisting of paraffins with negligible vapor pressures (10^{-6} times that of H_2O at the same temperature, see e.g., Sehabiague and Morsi (2013)). Hence, $\mathcal{L}_4$ was assumed to remain in the slurry phase, and its mass transfer was set to zero.

The mass transfer flux obtained from the above considerations reads (see also the special case with Henry's law in Eq. (28)):

$$N_i = k_{L,i}\rho_L\left(\frac{\omega_{G,i}}{K_i} - \omega_{L,i}\right). \tag{29}$$

For mass transfer based on an EoS, the computation of K_i requires the convergence of the GLE problem, which is generally written

$$T_G = T_{SL} \tag{30a}$$
$$p_G = p_L \tag{30b}$$
$$\mu_{G,i} = \mu_{L,i}, \quad i = 1,2,\ldots,C, \tag{30c}$$

where μ_i is the chemical potential of component i. As Eq. (30c) constitute C equations in $2C$ unknowns, the solution to the GLE problem requires another C equations. These are given as a conservation of species:

$$n_{L,i} + n_{G,i} = \beta_{L,i}^0 + \beta_{G,i}^0, \tag{31}$$

where n_i denotes the mole numbers of component i. The initialization in mole numbers was based on the molar fluxes in the SBCR:

$$\beta_{L,i}^0 = \frac{G_L}{G_T}x_i \tag{32a}$$
$$\beta_{G,i}^0 = \left(1 - \frac{G_L}{G_T}\right)y_i, \tag{32b}$$

with

$$G_L = \frac{\rho_L \mid \boldsymbol{v}_L \mid \alpha_L}{\sum_{j=1}^{C} M_{w,j}x_j} \tag{33a}$$
$$G_G = \frac{\rho_G \mid \boldsymbol{v}_G \mid \alpha_G}{\sum_{j=1}^{C} M_{w,j}y_j} \tag{33b}$$
$$G_T = G_L + G_G. \tag{33c}$$

Equations (30a), (30b), (30c), (31), (32a), (32b), (33a), and (33b) were solved by the solution strategy proposed by Øyen et al. (2021). The iterative procedure is given by

$$\left[\boldsymbol{J}_L^{\nu} + \boldsymbol{J}_G^{\nu}\right]\Delta\boldsymbol{n}_L^{\nu+1} = -\left(\boldsymbol{\eta}_L^{\nu} - \boldsymbol{\eta}_G^{\nu}\right), \tag{34}$$

where

$$J_{G,ij} = \frac{\delta_{ij}}{n_{G,i}} - \frac{1}{n_G} + \left(\frac{\partial \ln \varphi_{G,i}}{\partial n_{G,j}}\right) \tag{35a}$$

$$J_{L,ij} = \frac{\delta_{ij}}{n_{L,i}} - \frac{1}{n_L} + \left(\frac{\partial \ln \varphi_{L,i}}{\partial n_{L,j}}\right), \tag{35b}$$

$$\eta_{G,i} = \ln \frac{n_{G,i}}{n_G} + \ln \varphi_{G,i} \tag{36a}$$

$$\eta_{L,i} = \ln \frac{n_{L,i}}{n_L} + \ln \varphi_{L,i}. \tag{36b}$$

Here, $\boldsymbol{J}$ denotes the Jacobian, $\Delta \boldsymbol{n}^{\nu+1} = \boldsymbol{n}^{\nu+1} - \boldsymbol{n}^{\nu}$ is the step in the vector of mole numbers, $\boldsymbol{\eta}$ is the vector of modified chemical potentials, δ_{ij} is the Kronecker delta which is one if $i = j$ and zero otherwise, and φ_i is the fugacity coefficient of component i.

After converging Eq. (34) through the aid of Eqs. (31), (32a), (32b), (33a), (33b), (33c), (35a), (35b), (36a) and (36b), the equilibrium mole fractions were extracted from the vectors of mole numbers:

$$x_i^* = \frac{n_{L,i}}{n_L}, \tag{37}$$

$$y_i^* = \frac{n_{G,i}}{n_G}. \tag{38}$$

It is emphasized that K_i^m was obtained directly through Eq. (15), which was used to compute the reaction rate of the FT reaction with Eq. (12). Furthermore, by converting the x_i^* to ω_i^* with Eq. (23), the K_i was obtained directly through Eq. (25). With knowledge of K_i, the mass transfer in Eq. (29) was computed.

A pseudo-algorithm to evaluate the mass transfer flux, N_i, is given in Algorithm 1. Here, N_i is determined after the GLE problem has converged, which requires successive evaluations of φ_i and $\left(\partial \varphi_i / \partial n_j\right)_{T,p}$ through a thermodynamic EoS of choice. In this work, the PR and PC-SAFT EoSs were chosen to model the GLE, and the details are given in Sections 2.3.1 and 2.3.2, respectively. The interested reader is referred to Øyen et al. (2021) for a detailed description and the solution strategy of the Newton–Raphson-based negative flash algorithm defined by Eqs. (31), (32a), (32b), (33a), (33b), (33c), (34), (35a), (35b), (36a) and (36b).

Algorithm 1. Evaluation of the mass transfer

1: Choose thermodynamic EoS
2: $\beta_{L,i}^0, \beta_{G,i}^0 \leftarrow$ Eqs. (32a), (32b), (33a), (33b), and (33c) ▷GLE computation start
3: **while** Not converged **do**
4: $\varphi_i \leftarrow$ thermodynamic EoS
5: $\left(\partial \varphi_i / \partial n_j\right)_{T,p} \leftarrow$ thermodynamic EoS
6: $J_{L,ij}^{\nu}, J_{G,ij}^{\nu} \leftarrow$ Eqs. (35a) and (35b)
7: $\eta_{L,i}^{\nu}, \eta_{L,i}^{\nu} \leftarrow$ Eqs.(36a) and (36b)
8: $\Delta n_{L,i}^{\nu+1} \leftarrow$ Eq. (34)
9: $n_{L,i}^{\nu+1} \leftarrow n_{L,i}^{\nu} + \Delta n_{L,i}$
10: $n_{G,i}^{\nu+1} \leftarrow n_{G,i}^{\nu} - \Delta n_{L,i}$
11: **end while** ▷GLE computation end
12: $x_i^* \leftarrow$ Eq. (37)
13: $y_i^* \leftarrow$ Eq. (38)
14: $\omega_{L,i}^*, \omega_{G,i}^* \leftarrow$ Eq. (23)
15: $K_i \leftarrow$ Eq. (25)
16: $N_i \leftarrow$ Eq. (29)

The PR and the PC-SAFT EoSs contain binary interaction parameters, k_{ij}, fitted to experimental data. The k_{ij} parameter is introduced to represent deviations from the predictive capabilities of an EoS. Graboski and Daubert (1978a) and other investigators (Graboski and Daubert, 1978b; Nishiumi et al., 1988; Heidman et al., 1985) concluded that k_{ij} for hydrocarbon–hydrocarbon interactions are zero for the SRK EoS, meaning the SRK EoS predicts the hydrocarbon-hydrocarbon interactions adequately. The PR EoS is closely related to the SRK EoS, and $k_{ij} = 0$ was therefore adopted for the PR EoS in this study. Furthermore, the PC-SAFT EoS was developed for chain-like molecules, such as straight-chained paraffins. Therefore, hydrocarbon-hydrocarbon interactions are within the predictive capabilities of the PC-SAFT EoS; hence, $k_{ij} = 0$ was employed for hydrocarbon-hydrocarbon interactions in this study. For the PR EoS, k_{ij} for non-hydrocarbon pairs were obtained from the following set of references (Gray et al., 1983; Tang and Kitagawa, 2005; Venkatramani and Okuno, 2014,; Chapoy et al., 2020; Biquiza et al., 2010; Srinivas et al., 2012; Gao et al., 1999; Rahbari et al., 2019; Petropoulou et al., 2017; mu Lin, 1984; Gasem et al., 1993; Tsonopoulos and Wilson, 1983; Meng et al., 2007; Ramdin et al., 2016). For the PC-SAFT EoS, k_{ij} for non-hydrocarbon pairs were obtained from the following set of references (Zheng et al., 2019; Gross and Sadowski, 2001; Diamantonis and Economou, 2012; Perez et al., 2017; Demetriades and Graham, 2016). Moreover, Demetriades and Graham (2016) stated that CO_2–H_2 binary GLE has not yet been computed with PC-SAFT, and thus k_{ij} is not available for the CO_2–H_2 pair. The authors have not found any work in the literature on this topic after the publication by Demetriades and Graham (2016). A full presentation of the k_{ij} employed in this study is found in Tables 3 and 4.

The mass transfer expression in Eq. (29) requires evaluation of K_i, which here was obtained through solving the GLE problem. In this context, the volume, V, was found through iteration at given $T, p, \boldsymbol{n}$. Here, the mole fractions were formally treated as mole numbers, and hence, the volume found is the molar volume. The iteration on volume was performed with Newton–Raphson iteration on the pressure equation in Eq. (B.1), see Appendix B (Michelsen and Mollerup, 2007):

$$V^{\nu+1} = V^{\nu} - \frac{\left(\frac{\partial \mathcal{A}}{\partial V}\right)_{T,\boldsymbol{n}} + p}{\left(\frac{\partial^2 \mathcal{A}}{\partial V^2}\right)_{T,\boldsymbol{n}}}. \tag{39}$$

Here, $\mathcal{A}$ is the Helmholtz energy function. A discussion on initializing the iteration procedure of Eq. (39) is found in Gross and Sadowski (2001). Note that for $n < 0$, Eq. (39) must allow $V < 0$ to yield $p > 0$. This is particularly clear for gas mixtures exhibiting ideal behavior:

$$p^{\text{ig}} = \frac{nRT}{V}. \tag{40}$$

Here RT is a positive quantity, and p^{ig} has the same sign as n/V. Thus, $p \geqslant 0$ if, and only if, $n/V \geqslant 0$, i.e., if n and V have the same sign. For the PR EoS, the volume roots were found through the built-in function `roots` in Matlab.

2.3.1. Modeling the Interface GLE by the Peng–Robinson EoS

The PR EoS has gained considerable attention over the years due to its simple structure and applicability. The EoS is explicit in pressure and is written as (Peng and Robinson, 1976)

$$p(T, V, \boldsymbol{n}) = \frac{nRT}{V - B} - \frac{D}{V(V + B) + B(V - B)}, \tag{41}$$

Table 3
Binary interaction parameters for the PR EoS.

k_{ij}	CO	H_2	H_2O	CO_2	$\mathcal{L}_1$	$\mathcal{L}_2$	$\mathcal{L}_3$	$\mathcal{L}_4$
CO	0	0.0750	0.0107	−0.0775	0.0710	0.1150	0.0708	−0.0021
H_2	0.0750	0	−0.8900	0.1650	0.1930	0.3420	0.3220	0.1509
H_2O	0.0107	−0.8900	0	−0.1207	0.6300	0.4000	0.2420	0.2420
CO_2	−0.0775	0.1650	−0.1207	0	0.1250	0.1250	0.1250	0.1250
$\mathcal{L}_1$	0.0710	0.1930	0.6300	0.1250	0	0	0	0
$\mathcal{L}_2$	0.1150	0.3420	0.4000	0.1250	0	0	0	0
$\mathcal{L}_3$	0.0708	0.3220	0.2420	0.1250	0	0	0	0
$\mathcal{L}_4$	−0.0021	0.1509	0.2420	0.1250	0	0	0	0

Table 4
Binary interaction parameters for the PC-SAFT EoS.

k_{ij}	CO	H_2	H_2O	CO_2	$\mathcal{L}_1$	$\mathcal{L}_2$	$\mathcal{L}_3$	$\mathcal{L}_4$
CO	0	0	0	−0.0103	0.0430	0.1356	0.1570	0.1623
H_2	0	0	0	0	0.0795	0.1654	0.2031	0.2194
H_2O	0	0	0	−0.0033	0.1840	0.2110	0.2167	0.2199
CO_2	−0.0103	0	−0.0033	0	0.0368	0.0787	0.0955	0.1024
$\mathcal{L}_1$	0.0430	0.0795	0.1840	0.0368	0	0	0	0
$\mathcal{L}_2$	0.1356	0.1654	0.2110	0.0787	0	0	0	0
$\mathcal{L}_3$	0.1570	0.2031	0.2167	0.0955	0	0	0	0
$\mathcal{L}_4$	0.1623	0.2194	0.2199	0.1024	0	0	0	0

where $n = \sum_{i=1}^{C} n_i$, is the total number of moles, V is the volume, $B(\boldsymbol{n})$ denotes an excluded volume, and $D(T, \boldsymbol{n})$ denotes an attractive term. A full description of the PR EoS can be found elsewhere (Peng and Robinson, 1976; Harvey, 1997; He et al., 2008; Traxinger et al., 2019; Dahm and Visco, 2014; Elliott and Lira, 2012; Michelsen and Mollerup, 2007); however, the critical constants, T_c and p_c, and the acentric factor, γ, require special attention for the lumped hydrocarbons, $\mathcal{L}_1$–$\mathcal{L}_4$. Since the lumps represent a set of paraffins rather than real compounds, data for T_c, p_c, and γ does not exist. On the other hand, Gamba et al. (2009) recognized that the paraffins exhibit an asymptotic behavior concerning the normal boiling point (NBP). A correlation was given in terms of carbon chain length as:

$$T_{\mathrm{NBP}} = 1078.7141 - \exp\left(6.9811554 - 0.11483075 CN^{2/3}\right). \quad (42)$$

The critical constants were in turn correlated to the NBP as

$$T_c = 1127.1710 - \exp(-10.635057)(1671.5921 - T_{\mathrm{NBP}})^{2.3724157}, \quad (43)$$

$$p_c = \exp\left(-15.488321 + 3.2328187\left(\frac{100}{T_{\mathrm{NBP}}}\right)^3\right)(1288.8545 - T_{\mathrm{NBP}})^{2.7447020}. \quad (44)$$

For the acentric factor, two correlations were given:

$$\gamma = \begin{cases} 1187.9291 - \exp(7.0738919)(1004.8417 - T_{\mathrm{NBP}})^{8.9643355\times10^{-4}} \\ 1185.0931 - \exp(7.0704986)(1047.5707 - T_{\mathrm{NBP}})^{1.0478687\times10^{-3}}. \end{cases} \quad (45)$$

The first equation in Eq. (45) is valid in the range $359.13 \leqslant T_{\mathrm{NBP}} \leqslant 723.59$K, and the second equation in Eq. (45) is valid in the range $723.59 < T_{\mathrm{NBP}} \leqslant 988.05$K. The correlations of Gamba et al. (2009) agree well with the experimental data of Lemmon et al. (2019) (NIST), Ambrose and Tsonopoulos (1995, 2015), Helgeson et al. (1998), and Nikitin et al. (1997), as shown in Fig. 2. Other critical constants and acentric factors are available in the literature, and a summary is presented in Table 5.

The fugacity coefficient, φ_k, and its derivative with respect to mole numbers are required to close the GLE problem in Eq. (34). The fugacity coefficient is employed in Eqs. (36a) and (36b) and is in general given by (Haug-Warberg, 2006):

$$\ln \varphi_k = \frac{1}{RT}\left(\frac{\partial \mathcal{A}^{\mathrm{r,v}}}{\partial n_k}\right)_{T,V} - \ln Z, \quad (46)$$

where $n_{i\neq k}$ has been omitted from the list of variables to be held constant under the partial derivation. The superscript "r,v" denotes that the residual Helmholtz energy potential is evaluated at the same T and V as the ideal gas Helmholtz energy potential. The compressibility factor is given by

$$Z = \frac{pV}{nRT}. \quad (47)$$

The derivative of Eq. (46) is employed in Eqs. (35a) and (35b) and is in general given by (Michelsen and Mollerup, 2007)

$$\left(\frac{\partial \ln \varphi_k}{\partial n_l}\right)_{T,p} = \frac{1}{RT}\left(\frac{\partial^2 \mathcal{A}^{\mathrm{r,v}}}{\partial n_k \partial n_l}\right)_{T,V} + \frac{1}{n} + \frac{1}{RT}\frac{\left(\frac{\partial p}{\partial n_k}\right)_{T,V}\left(\frac{\partial p}{\partial n_l}\right)_{T,V}}{\left(\frac{\partial p}{\partial V}\right)_{T,\boldsymbol{n}}}. \quad (48)$$

First and second order derivatives of $\mathcal{A}^{\mathrm{r,v}}$, first order derivatives of p, and Z are required for Eqs. (46) and (48). For the PR EoS, these five relations are given by Michelsen and Mollerup (2007, p. 87–91). Thus, φ_k and its derivative with respect to n_l in Eq. (46) and (48) can be obtained, and the GLE problem can be solved. Accordingly, K_i can be directly computed with Eqs. (15), (23) and (25), and hence, the mass transfer fluxes can be obtained with Eq. (29). See also Fig. 1 for a visual representation of how the mass transfer and GLE models are nested to solve the full FTS SBCR model.

2.3.2. Modeling the Interface GLE by the PC-SAFT EoS

The PC-SAFT EoS was shown by Zheng et al. (2019) to describe the GLE behavior of the FT mixture precisely, and hence the GLE at the interface is assumed accurately modeled by this EoS. Since the mass transfer expression in Eq. (29) relies on the GLE at the gas–liquid interface, the PC-SAFT EoS is appropriate for evaluating the mass transfer flux in Eq. (29). Moreover, the PC-SAFT EoS was based on the assumption that all molecules consist of hard, interacting chains composed of m segments. This assumption is exceptional for long-chained paraffins, where, e.g., Raoult's law was found unsuitable (Masuku et al., 2012). A full description of pure component parameters is summarized in Table 6. This includes the four considered lumps, since each lump is considered a single

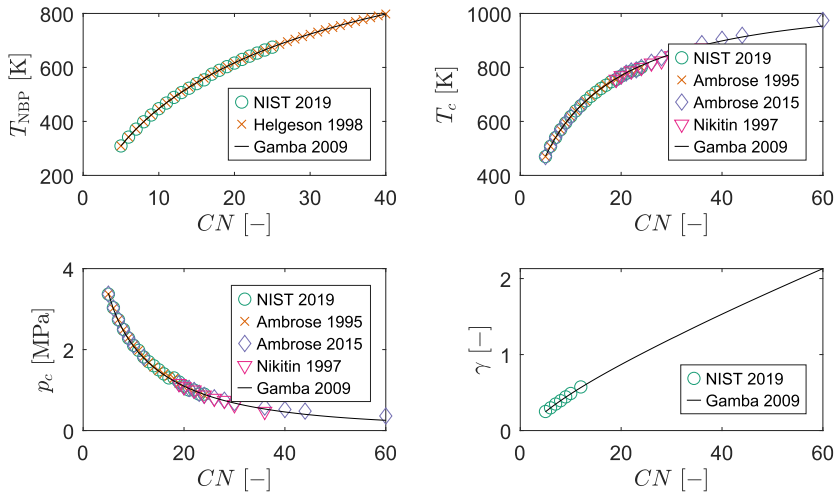

Fig. 2. Agreement of the correlations for normal boiling point, critical constants, and acentric factor by Gamba et al. (2009) with experimental investigators (Ambrose and Tsonopoulos, 1995; Helgeson et al., 1998; Nikitin et al., 1997; Ambrose et al., 2015; Lemmon et al., 2019).

Table 5
Pure component constants used for the Peng–Robinson EoS. The constants for $\mathcal{L}_1$–$\mathcal{L}_4$ are based on the correlations given by Gamba et al. (2009).

Component	T_c [K]	p_c [MPa]	γ [–]	Reference
CO	132.8600	3.4935	0.0500	(Lemmon et al., 2019)
H_2	33.1450	1.2964	−0.2190	(Lemmon et al., 2019)
H_2O	647.0960	22.0640	0.3443	(Lemmon et al., 2019)
CO_2	304.1282	7.3773	0.2239	(Lemmon et al., 2019)
$\mathcal{L}_1$	456.8924	3.5591	0.2285	(Gamba et al., 2009)
$\mathcal{L}_2$	702.4393	1.4991	0.6705	(Gamba et al., 2009)
$\mathcal{L}_3$	812.1769	0.8645	1.0309	(Gamba et al., 2009)
$\mathcal{L}_4$	898.3432	0.4599	1.5315	(Gamba et al., 2009)

Table 6
Pure component parameters used for the PC-SAFT EoS. The parameters for $\mathcal{L}_1$–$\mathcal{L}_4$ are based on the correlations given in the appendix of Gross and Sadowski (2001).

Component	m [–]	σ [Å]	ε/k_B [K]	Reference
CO	1.3097	3.2507	92.1500	(Gross and Sadowski, 2001)
H_2	1.3060	2.6010	23.4200	(Zheng et al., 2019)
H_2O	1.6619	2.4643	267.7100	(Zheng et al., 2019)
CO_2	2.0729	2.7852	169.2100	(Gross and Sadowski, 2001)
$\mathcal{L}_1$	2.6230	3.7325	226.8623	(Gross and Sadowski, 2001)
$\mathcal{L}_2$	6.1118	3.9447	254.8303	(Gross and Sadowski, 2001)
$\mathcal{L}_3$	9.5351	3.9941	260.7040	(Gross and Sadowski, 2001)
$\mathcal{L}_4$	14.7757	4.0232	264.0939	(Gross and Sadowski, 2001)

chemical species (although its properties are based on a number of hydrocarbons with different carbon chain lengths).

The PC-SAFT EoS was initially developed by Gross and Sadowski (2001) in the intensive variables $T, \rho^m = N/V$, and $x = N_i/N$. Here, ρ^m denotes the *molecular* density, $N_i = n_i N_A$ denotes the number of *molecules* of component i, N_A denotes the Avogadro constant, and $N = \sum_{i=1}^{C} N_i$ is the total number of *molecules*. However, the Helmholtz energy potential does not contain a full thermodynamic description when stated in $T, \rho^m, \boldsymbol{x}$, since it does not include the size of the system, i.e., the total amount of substance, N. Furthermore, classical thermodynamic relations and definitions are valid in the canonical variable set $T, V, \boldsymbol{N}$; for instance, Eqs. (46) and (48) are generally valid, and with molecules instead of moles as independent variables, the relations become

$$\ln \varphi_k = \frac{1}{k_B T}\left(\frac{\partial \mathcal{A}^{r,v}}{\partial N_k}\right)_{T,V} - \ln Z, \tag{49}$$

$$\left(\frac{\partial \varphi_k}{\partial n_l}\right)_{T,p} = \frac{N_A}{k_B T}\left(\frac{\partial \mathcal{A}^{r,v}}{\partial N_k \partial N_l}\right)_{T,V} + \frac{N_A}{N} + \frac{N_A}{k_B T}\frac{\left(\frac{\partial p}{\partial N_k}\right)_{T,V}\left(\frac{\partial p}{\partial N_l}\right)_{T,V}}{\left(\frac{\partial p}{\partial V}\right)_{T,\boldsymbol{N}}}, \tag{50}$$

where k_B is the Boltzmann constant. Gross and Sadowski (2001) provided the first derivatives to the Helmholtz energy potential with respect to T, ρ^m, and x_k. However, the derivatives with respect to x_k were performed without respecting $\sum_{i=1}^{C} x_i = 1$. Nevertheless, the final results made it possible to evaluate φ_k, but not $(\partial \varphi_k / \partial n_l)_{T,p}$.

Gross and Sadowski (2001) employed a different set of independent variables and gave no second derivatives, making it impossi-

ble to utilize Eqs. (39) and (50). To the authors' knowledge, the PC-SAFT EoS in the canonical variable set $T, V, \boldsymbol{N}$ is not available in the literature; hence, in this study, the PC-SAFT EoS was rewritten into the canonical variable set $T, V, \boldsymbol{N}$, and the full description with the first and second derivatives is given in Appendix C.

Eqs. (39), (49), and (50) require relations for the first order derivatives of p, and the first and second order derivatives of $\mathcal{A}^{\mathrm{r,v}}$. For the PC-SAFT EoS, the derivatives of p and the derivatives of $\mathcal{A}^{\mathrm{r,v}}$ are given in Appendix B and C, respectively. Thus, φ_k and its derivative with respect to n_l can be obtained, and the GLE problem can be solved. Accordingly, K_i can be directly computed with Eqs. (15), (23), and (25), and hence, the mass transfer fluxes can be obtained with Eq. (29).

The interactions between the governing equations, the mass transfer model, and the gas–liquid interface model is depicted in Fig. 3. Here, the shaded background indicates the three different

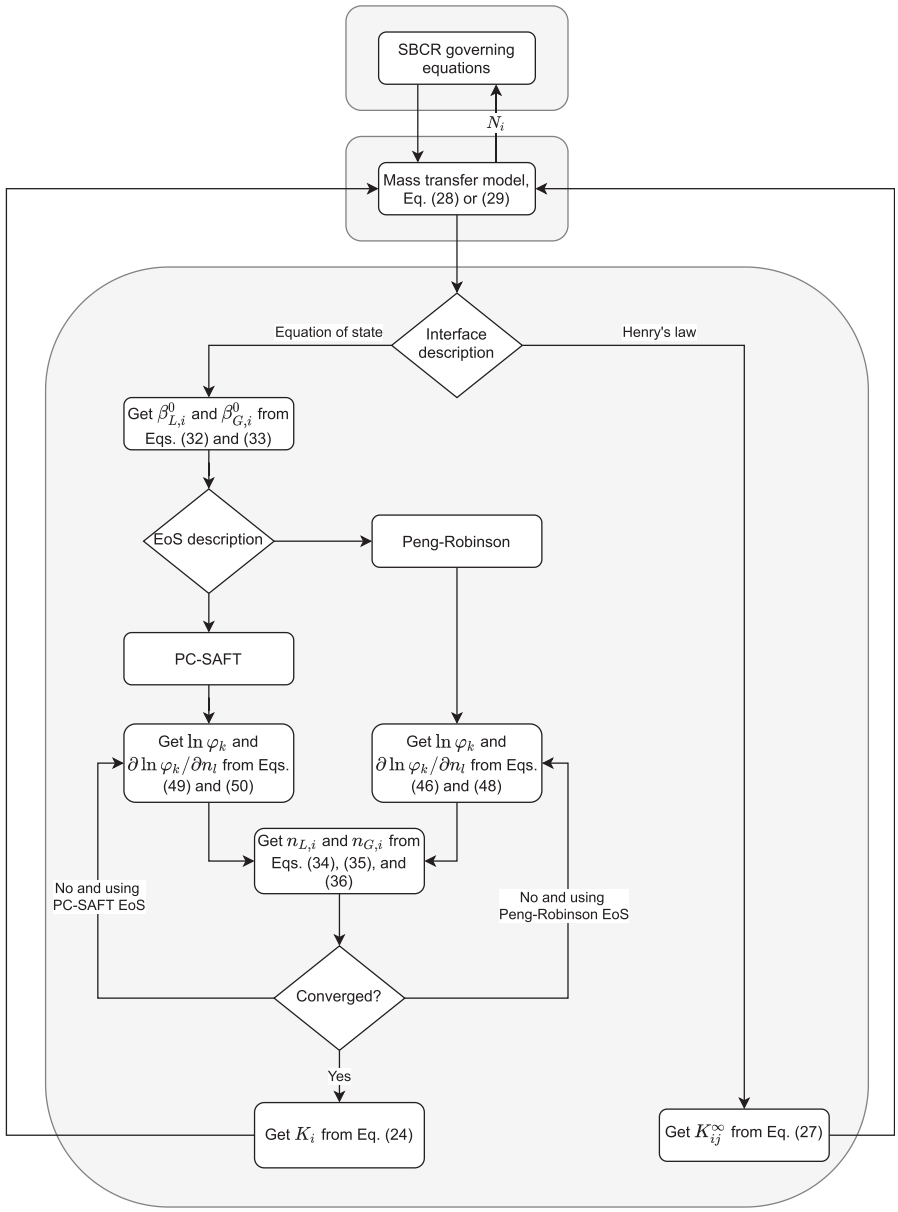

Fig. 3. Interactions between governing equations, mass transfer model and gas–liquid interface model.

parts highlighted in Fig. 1, i.e., the governing equations, the mass transfer model and the gas–liquid interface model.

2.4. Numerical Solution of the Slurry Bubble Column Reactor Model

The SBCR model equations in Table 1 were solved using the orthogonal collocation method. In this numerical method, the dependent variables are approximated by:

$$y(z) \approx \sum_{j=0}^{N_{\text{pol}}} \ell_j(z) y_j, \tag{51}$$

where the Lagrange interpolating polynomials are N_{pol}'th order polynomials given by (Kreyszig, 2011)

$$\ell_j(z) = \prod_{\substack{i=0 \\ i \neq j}}^{N_{\text{pol}}} \frac{z - z_i}{z_j - z_i}, \tag{52}$$

and $y_j = y(z_j)$ is the value of y at $z = z_j$.

Table 7
Parameters used in simulation of the FTS SBCR.

Variable	Value	Unit	Reference
L	50	m	(Sehabiague and Morsi, 2013a)
d_{col}	9	m	(Sehabiague and Morsi, 2013a)
d_{pipes}	0.114	m	(Sehabiague and Morsi, 2013a)
n_{pipes}	1200	–	(Sehabiague and Morsi, 2013a)
t_{wall}	2	mm	(Vik et al., 2015)
k_{steel}	16	W m^{-1} K^{-1}	(Hust and Lankford, 1984)
h_{cool}	3000	W m^{-2} K^{-1}	(Deckwer, 1980)
T_a	492	K	(Sehabiague and Morsi, 2013a)
ρ_L	687.2	kg m^{-3}	(Sehabiague and Morsi, 2013)
μ_L	1.05	cP	(Sehabiague and Morsi, 2013)
λ_L	0.113	W m^{-1} K^{-1}	(Maretto and Krishna, 1999)
σ	16	mN m^{-1}	(Sehabiague and Morsi, 2013)
d_b	8	mm	(Vik et al., 2015), average
P_G	2	–	(Rampure et al., 2007)
P_S	2	–	(Rampure et al., 2007)
ρ_S	3154	kg m^{-3}	(Sehabiague and Morsi, 2013a)
d_S	72	μm	(Sehabiague and Morsi, 2013a)
$c_{p,S}$	992	J kg^{-1} K^{-1}	(Maretto and Krishna, 1999)
λ_S	1.7	W m^{-1} K^{-1}	(Maretto and Krishna, 1999)
$\Delta_{\text{rx}}h$	−167	MJ kmol^{-1}	(Visconti, 2014)
α_{ASF}	0.9	–	(Maretto and Krishna, 1999), Ref. [11]
α_{SiS}	0.2	–	(Maretto and Krishna, 1999)

The Lagrange interpolating polynomials in Eq. (52) depend on the number of grid points and the location of the grid points, $\{z_j\}$. Here, $\{z_j\}$ were computed as the roots of Legendre polynomials, as this gives a dense placement of grid points near the inlet and outlet of the SBCR. In total, 30 grid points were used in a Gauss–Lobatto–Legendre grid arrangement.

The approximation in Eq. (51) reduces the problem of determining $y(z)$ to a problem of determining the set of function coefficients $\{y_j\}$. As the coefficients $\{y_j\}$ are not functions of z, the derivative is approximated as

$$\frac{\mathrm{d}y}{\mathrm{d}z} \approx \sum_{j=0}^{N_{\text{pol}}} \frac{\mathrm{d}\left(\ell_j(z) y_j\right)}{\mathrm{d}z} = \sum_{j=0}^{N_{\text{pol}}} \frac{\mathrm{d}\ell_j(z)}{\mathrm{d}z} y_j, \tag{53}$$

allowing the derivative to be written as a linear operator in y_j. Similarly, the second derivative is approximated as

$$\frac{\mathrm{d}^2y}{\mathrm{d}z^2} \approx \sum_{j=0}^{N_{\text{pol}}} \frac{\mathrm{d}^2\left(\ell_j(z) y_j\right)}{\mathrm{d}z^2} = \sum_{j=0}^{N_{\text{pol}}} \frac{\mathrm{d}^2\ell_j(z)}{\mathrm{d}z^2} y_j. \tag{54}$$

For the governing equations in Table 1, the first and second derivatives and other linear terms in y_j are gathered in the dense matrix $\boldsymbol{A}$, and the source/sink terms are gathered in the vector $\boldsymbol{F}$. Thus, for the dependent variables $\alpha_G, \alpha_S, \omega_{G,i}, \omega_{L,i}, v_G, v_S, v_L, p, T_G$, and T_{SL}, the linear system of equations is written as $\boldsymbol{Ay} = \boldsymbol{F}$. Hence, the dependent variables are integrated along the axial direction, z, by left-inverting the $\boldsymbol{A}$-matrix. Initial and boundary conditions are discussed in Section 2.5. The interested reader is referred elsewhere for detailed information on the orthogonal collocation method (Villadsen and Michelsen, 1978; Press et al., 1992; Solsvik and Jakobsen, 2012; Shen et al., 2011; Golub and Welsch, 1969; Solsvik et al., 2013; Solsvik and Jakobsen, 2013; Jakobsen et al., 2014).

2.5. Parameters and Initial and Boundary Conditions

The SBCR model requires a combination of parameters, initial conditions, and constitutive equations. The parameters and initial conditions are treated here; however, the constitutive equations are provided in Appendix D due to spatial considerations. The constitutive equations include, but are not limited to, diffusivities, viscosities, drag forces, conductivities, and heat capacities. The parameters employed for the simulations of the FTS SBCR are given in Table 7, and the initial conditions are given in Table 8 and 9.

The boundary conditions of the SBCR governing equations in Table 1 are split into four subsections: total mass, species mass, momentum, and energy.

Table 8
Initial conditions used in the simulations of the FTS SBCR.

Variable	Liquid	Gas	Solid	Unit
v_{in}^s	0.01	0.26	See α_{SiS}	m^3 m^{-2} s^{-1}
$x_{\text{CO,in}}$	0.03485	0.333	–	–
$x_{\text{H}_2\text{,in}}$	0.05632	0.667	–	–
$x_{\text{H}_2\text{O,in}}$	5.242×10^{-6}	1.103×10^{-5}	–	–
$x_{\text{CO}_2\text{,in}}$	4.736×10^{-7}	1.311×10^{-6}	–	–
$x_{\mathcal{L}_1\text{,in}}$	1.432×10^{-5}	1.035×10^{-5}	–	–
$x_{\mathcal{L}_2\text{,in}}$	0.0001265	2.038×10^{-6}	–	–
$x_{\mathcal{L}_3\text{,in}}$	0.0001532	6.288×10^{-8}	–	–
$x_{\mathcal{L}_4\text{,in}}$	0.9085	1.395×10^{-6}	–	–
p_{out}	30	30	30	bar
T_{in}	513	513	513	K

Table 9
The set of initial and boundary conditions for the SBCR governing equations in Table 1. See also Tables 7 and 8 for specific reactor inlet and outlet values of the equations below.

Conservation of total mass	
$v_L^s\|_{z=0} = v_{L,\text{in}}^s$	(55)
$v_G^s\|_{z=0} = v_{G,\text{in}}^s$	(56)
$\alpha_{SiS}\|_{z=0} = \alpha_{SiS,\text{in}}$	(57)
Conservation of species mass	
$(\alpha_L\rho_L v_L\omega_{L,i})\|_{z=0^+} - \left(\alpha_L\rho_L D_{L,\text{eff},z}\frac{d\omega_{L,i}}{dz}\right)\Big\|_{z=0^+} = (\rho_L v_L^s\omega_{L,i})\|_{z=0^-}$	(58)
$\frac{d\omega_{L,i}}{dz}\Big\|_{z=L} = 0$	(59)
$(\alpha_G\rho_G v_G\omega_{G,i})\|_{z=0^+} - \left(\alpha_G\rho_G D_{G,\text{eff},z}\frac{d\omega_{G,i}}{dz}\right)\Big\|_{z=0^+} = (\rho_G v_G^s\omega_{G,i})\|_{z=0^-}$	(60)
$\frac{d\omega_{G,i}}{dz}\Big\|_{z=L} = 0$	(61)
Conservation of momentum	
$p\|_{z=L} = p_{\text{out}}$	(62)
$v_G\|_{z=0} = v_{L,\text{in}} - \frac{1}{\frac{3}{4d_b}\rho_L C_{D,G-L}\|_{z=0}\|v_{L,\text{in}} - v_G\|_{z=0}\|}\left(\frac{dp}{dz}\Big\|_{z=0} + \rho_G\|_{z=0}g\right)$	(63)
Conservation of energy	
$[(\alpha_L\rho_L v_L c_{p,L} + \alpha_S\rho_S v_S c_{p,S})T_{SL}]\|_{z=0^+} - \left(\alpha_{SL}\lambda_{SL,\text{eff},z}\frac{dT_{SL}}{dz}\right)\Big\|_{z=0^+} = [(\rho_L v_L^s c_{p,L} + \rho_S v_S\alpha_S c_{p,S})T_{SL}]\|_{z=0^-}$	(64)
$\frac{dT_{SL}}{dz}\Big\|_{z=L} = 0$	(65)
$(\alpha_G\rho_G v_G c_{p,G}T_G)_{z=0^+} - \left(\alpha_G\lambda_{G,\text{eff},z}\frac{dT_G}{dz}\right)_{z=0^+} = (\rho_G v_G^s c_{p,G}T_G)_{z=0^-}$	(66)
$\frac{dT_G}{dz}\Big\|_{z=L} = 0$	(67)

2.5.1. Initial Conditions for the Total Mass

The initial condition for the liquid phase continuity equation was specified in terms of the superficial velocity, v_L^s, in Eq. (55). The local instantaneous velocity at the inlet, $v_{L,\text{in}}$, was obtained in terms of the other initial conditions as:

$$v_{L,\text{in}}^{v+1} = \frac{v_{L,\text{in}}^s}{1 - \alpha_{G,\text{in}}^v - \alpha_{S,\text{in}}^v}, \tag{68}$$

where $\alpha_{G,\text{in}}^v$ and $\alpha_{S,\text{in}}^v$ were updated at each iteration, v, by

$$\alpha_{G,\text{in}}^{v+1} = \frac{v_{G,\text{in}}^s}{v_{G,\text{in}}^v}, \tag{69}$$

and

$$\alpha_{S,\text{in}}^{v+1} = \alpha_{SiS}\left(1 - \alpha_{G,\text{in}}^{v+1}\right). \tag{70}$$

In Eq. (69), $v_{G,\text{in}}^v$ was updated with Eq. (63). Moreover, in Eq. (70), α_{SiS} denotes the volume fraction of solid catalyst in gas-free slurry, that is

$$\alpha_{SiS} = \frac{\alpha_S}{\alpha_S + \alpha_L}. \tag{71}$$

The initial condition for the gas phase continuity equation was specified in terms of the superficial velocity, v_G^s, in Eq. (56); however, $\alpha_{G,\text{in}}$ was updated with Eqs. (63) and (69) at each iteration. An initial guess of $\alpha_{G,\text{in}} = 0.528$ was employed.

The initial condition for the solid phase continuity equation was specified in terms of the area fraction of gas-free slurry, α_{SiS}, in Eq. (57). Since the solid phase continuity equation contains no source or sink terms, integration of Eq. (3) leads to

$$\alpha_S = \frac{\alpha_{S,\text{in}}^v v_{S,\text{in}}^v}{v_S}. \tag{72}$$

Here, $\alpha_{S,\text{in}}^v$ was iteratively updated with Eq. (70), and v_S^v and $v_{S,\text{in}}^v$ are treated in Section 2.5.3.

2.5.2. Initial and Boundary Conditions for the Species Mass

The species mass equations were solved for ω_i, and Danckwerts boundary conditions were employed (Danckwerts, 1953). In Eqs. (58) and (60), 0^- denotes the inlet from outside the SBCR, and 0^+ denotes the inlet from inside the SBCR. The axial location $z = 0^+$ is thus a part of the computational domain, whereas $\omega_L(z = 0^-)$ is the value specified in Table 8. The Danckwerts boundary conditions reflect that axial mixing is relevant even at the SBCR inlet.

2.5.3. Initial and Boundary Conditions for the Momentum

The initial condition for the gas phase momentum equation was specified as the algebraic slip model in Eq. (63). Here, $v_{L,\text{in}}$ was computed with Eq. (68).

The solid phase momentum equation was solved for v_S, and since the algebraic slip model was used, no boundary conditions are required. However, the solid phase momentum equation is implicit in v_S, and iteration is still required:

$$v_S^{v+1} = v_L - \frac{1}{\frac{3}{4d_S}C_{D,S-L}^v\rho_L \mid v_L - v_S^v \mid}\left(\frac{dp}{dz} + \rho_S g\right). \tag{73}$$

2.5.4. Initial and Boundary Conditions for the Energy

The energy equations were solved for T, and Danckwerts boundary conditions were employed (Danckwerts, 1953). The slurry and gas phase energy equations were solved simultaneously.

2.6. Program Flow

Three different mass transfer formulations were proposed in Section 2: one based on Henry's law, see Eq. (28), one based on the PR EoS, and one based on the PC-SAFT EoS. While a visual representation is given in Fig. 1, the program flow of the SBCR simulation is given in Fig. 4. As indicated on the left-hand side in Fig. 4, the main structure of the SBCR simulations is identical in the three different mass transfer formulations. The differences in mass transfer formulations are displayed on the right-hand side in Fig. 4 with a shaded background. The PR EoS and the PC-SAFT EoS share a similar structure; however, the computation of φ_k and $(\partial\varphi_k/\partial n_l)_{T,p}$ differs. In both the PR and PC-SAFT EoS cases, the complete GLE problem must be solved to evaluate N_i. On the other hand, with the mass transfer formulation based on Henry's law, only correlations for H_{ij} are required to evaluate N_i.

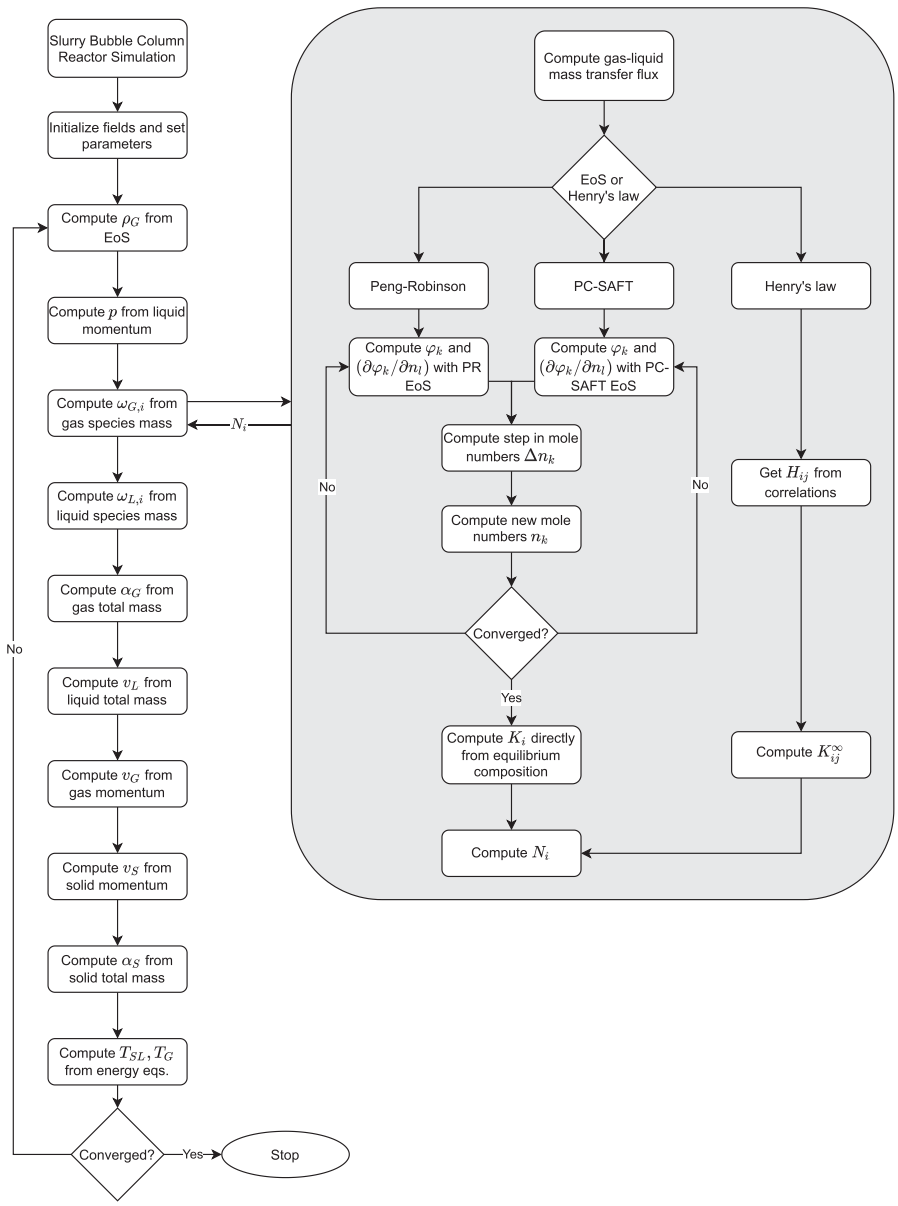

Fig. 4. Flow chart showing the program structure used for simulating the SBCR. Three different mass transfer approaches are shown on the right-hand side with a shaded background. A detailed visual representation of the different mass transfer approaches is shown in Fig. 3.

3. Results and Discussion

In this study, an industrial scale FTS SBCR was simulated with three different driving forces for mass transfer. The mass transfer expression based on Henry's law relies on the physical properties of the solvent, whereas the mass transfer expressions based on the PR and the PC-SAFT EoSs do not require the identification of a single solvent. On the other hand, the EoS-based mass transfer formulations rely on k_{ij}. In the succeeding results, emphasis is placed on i) how the EoS and the associated k_{ij} affect the mass transfer based on an EoS, ii) how the classification of the solvent affects the mass transfer based on Henry's law, iii) how the conversion level is affected by temperature and pressure, iv) whether the SBCR is kinetically or mass transfer limited, v) the computational burden of the different mass transfer formulations, and vi) justification of the assumption that no more than two phases exist at phase equilibrium.

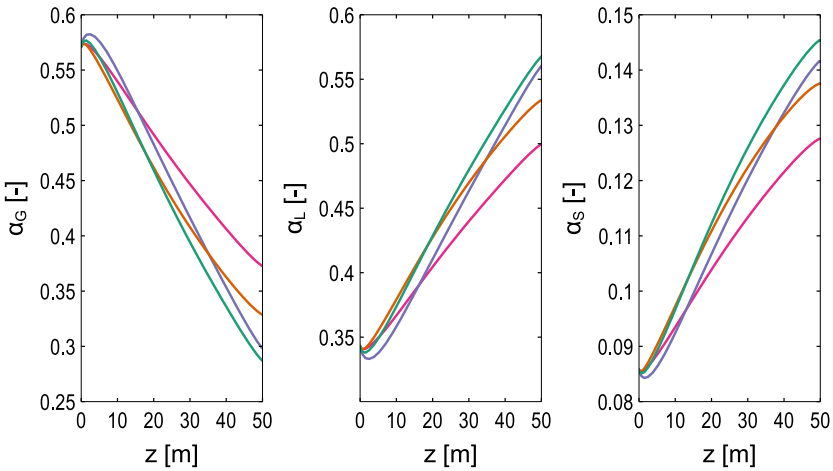

Fig. 5. Area fraction of the gas (left-hand side), liquid (middle), and solid (right-hand side) phases in the FTS SBCR. Legend: PR with $k_{ij} = 0$ (■); PR with $k_{ij} \neq 0$ (■); PC-SAFT with $k_{ij} = 0$ (■); and PC-SAFT with $k_{ij} \neq 0$ (■).

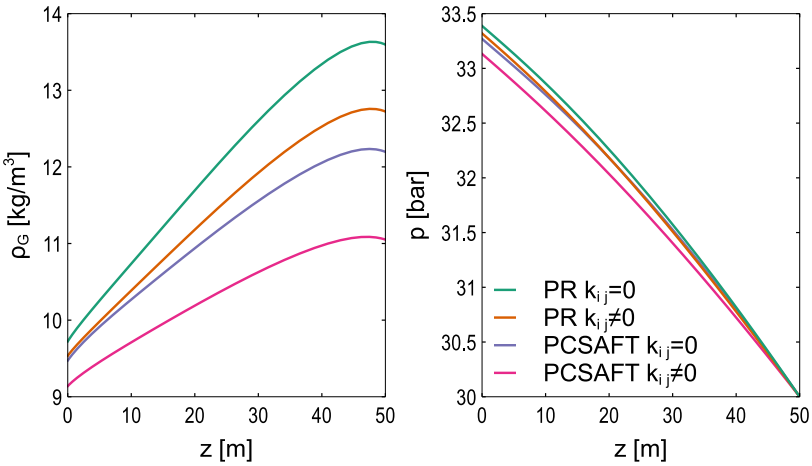

Fig. 6. Gas phase density (left-hand side) and pressure (right-hand side) in the FTS SBCR.

3.1. Mass Transfer Based on an EoS

The area fractions of the gas, liquid, and solid phases are displayed in Fig. 5. Initially, the liquid evaporates at a higher rate than the gas condenses, and consequently, α_G rises. After reaching a column height of 4 m, the condensation of CO and H_2 becomes dominant, and the net mass transfer is positive into the liquid, causing α_G to decrease. Furthermore, as the reactants are transferred out of the gas phase and into the liquid phase, the FT reactions commence. As a result, H_2O and paraffins are formed. The lighter paraffins and H_2O have high vapor pressures, and these components are thus transported back to the gas phase. This evaporation causes the molecular weight of the gas mixture to increase, and hence ρ_G increases, see Fig. 6. Moreover, v_G initially increases, and after the column height of approximately 4 m, the gas–liquid drag force causes v_G to decrease. As mass is transferred from the gas to the liquid phase, the decrease in α_G causes an increase in α_L. As α_L and v_L are inversely proportional, v_L decreases, see Fig. 7. Similarly, v_S was obtained from the algebraic slip model, which is dominated by the solid–liquid drag force and the gravitational acceleration. Since the gravitational acceleration is constant, v_S decreases as v_L decreases due to the solid–liquid drag. As a result of the balance equation for total mass of solid, α_S increases. The trends discussed for $\alpha_G, \alpha_L, \alpha_S, v_G, v_L, v_S$ and ρ_G are valid for all simulations with mass transfer based on an EoS.

It is clear from Fig. 8 that the mass transfer expressions based on an EoS rely on k_{ij}. For instance, by comparing the results based on the PR EoS with $k_{ij} = 0$ to the results based on the PR EoS with $k_{ij} \neq 0, \omega_{G,H_2}$ varies by 30 % relatively at the SBCR outlet. Similarly, by comparing the results based on the PC-SAFT EoS with $k_{ij} = 0$ to the results based on the PC-SAFT EoS with $k_{ij} \neq 0, \omega_{G,H_2}$ varies by 35 % relatively at the SBCR outlet. Furthermore, there is a wide variety of EoSs available in the literature, and the importance of choosing a suitable EoS that accurately represents the GLE is cru-

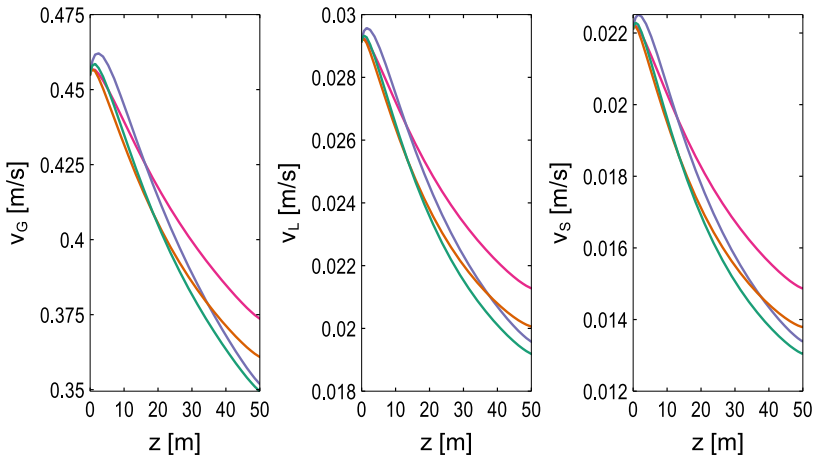

Fig. 7. Local instantaneous velocity of the gas (left-hand side), liquid (middle), and solid (right-hand side) phases in the FTS SBCR. Legend: PR with $k_{ij} = 0$ (■); PR with $k_{ij} \neq 0$ (■); PC-SAFT with $k_{ij} = 0$ (■); and PC-SAFT with $k_{ij} \neq 0$ (■).

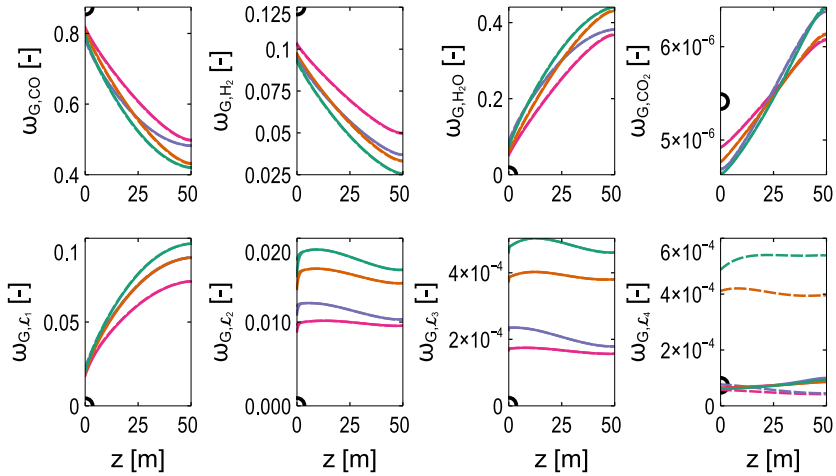

Fig. 8. Mass fractions in the gas phase in the FTS SBCR. Legend: PR with $k_{ij} = 0$ (■); PR with $k_{ij} \neq 0$ (■); PC-SAFT with $k_{ij} = 0$ (■); and PC-SAFT with $k_{ij} \neq 0$ (■). Dashed lines (– –) indicate equilibrium mass fractions, and black circles at the SBCR inlet denote boun.dary conditions.

cial in the proposed mass transfer modeling framework. For instance, by comparing the PR and PC-SAFT EoSs with $k_{ij} \neq 0, \omega_{G,H_2}$ varies by 50 % relatively. Moreover, the differences in $\omega^*_{L,i}$ displayed in Fig. 9 are significant. The reaction rate in the FTS SBCR relies on both the liquid phase composition through x_{CO} and x_{H_2}, and the gas phase composition through K^m_{CO} and $K^m_{H_2}$. Thus, the conversion of CO in the SBCR varies when the composition in the gas and liquid phases vary. From Fig. 10, the lowest conversion of CO was 63 mol% and was obtained with the PC-SAFT EoS with experimentally fitted k_{ij}. The highest conversion of CO with mass transfer based on an EoS was 74 mol% and was obtained with the PR EoS with $k_{ij} = 0$.

The equilibrium ratio, K_i, is in the denominator of the proposed mass transfer expressions based on an EoS, see Eq. (29). Consequently, the driving force becomes zero as $\omega_{G,i}/\omega_{L,i} \rightarrow \omega^*_{G,i}/\omega^*_{L,i}$. However, K_i is based on the mass fraction of both the gas and the liquid phases. As seen in Fig. 11, typically $K_i \gg 1$ or $K_i \ll 1$, except for $K_{\mathcal{L}_2} \approx 1$. Moreover, the K_i span seven orders of magnitude, that is $K_i \in \left[10^{-4}, 10^{2}\right]$. A large K_i produces a smooth driving force for mass transfer, where K_i has a dampening effect on the driving force. A smaller K_i produces a sharp gradient in the driving force for mass transfer, where the bulk concentration is quickly forced to phase equilibrium, see for instance components $\mathcal{L}_2$, and $\mathcal{L}_3$ (the mass transfer of $\mathcal{L}_4$ was set to zero). In the balance equation for total mass, the total flux term, $\sum_{i=1}^{C} N_i$, is required. Since a small K_i produces a sharp gradient, the total flux term is also expected to have a sharp gradient. Thus, the balance equation for total mass is quite sensitive to the mass transfer of non-volatile compounds. This sensitivity is counteracted by using under-relaxation factors for the balance equations for total mass. Here, an under-relaxation factor of 0.01 was used, meaning 1% of the new solution was accepted in each iteration.

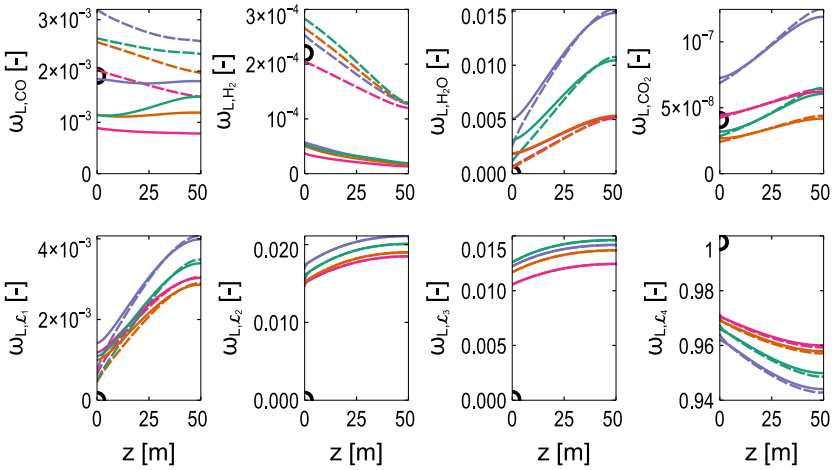

Fig. 9. Mass fractions in the liquid phase in the FTS SBCR. Legend: PR with $k_{ij} = 0$ (■); PR with $k_{ij} \neq 0$ (■); PC-SAFT with $k_{ij} = 0$ (■); and PC-SAFT with $k_{ij} \neq 0$ (■). Dashed lines (– –) indicate equilibrium mass fractions, and black circles at the SBCR inlet denote boun.dary conditions.

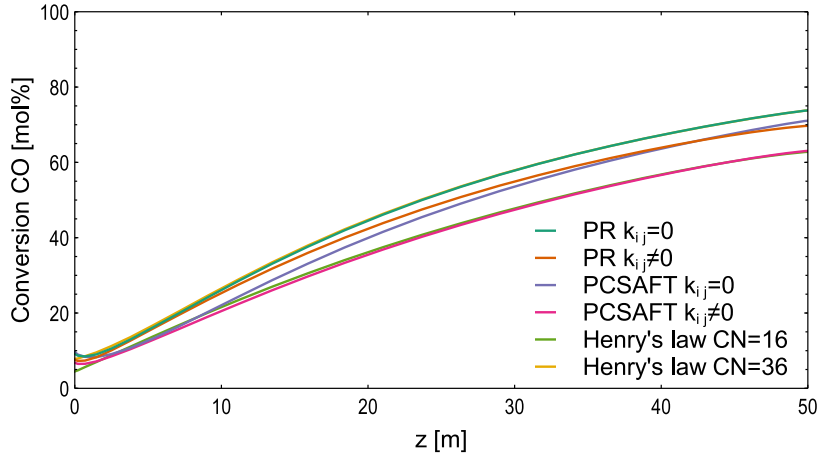

Fig. 10. Conversion of CO in the FTS SBCR. Note that the line for Henry's law with solvent carbon number 16 lies under the line for the PC-SAFT EoS with $k_{ij} \neq 0$, and the line for Henry's law with solvent carbon number 36 lies under the line for the PR EoS with $k_{ij} = 0$.

The profiles in Figs. 5-12 obtained by mass transfer based on an EoS all display the same qualitative trends with one exception: in the simulations with mass transfer based on the PC-SAFT EoS with $k_{ij} \neq 0, T_G$ and T_{SL} decrease initially. Since the FT reaction is exothermic, the reaction rate is lower in this case than for the other three simulations with mass transfer based on an EoS. The lower reaction rate originates from the lower solubility of CO and H_2, as seen from the dashed lines in Fig. 9. Furthermore, the conversion of CO in Fig. 10 also reflects the lower reaction rate obtained with the PC-SAFT EoS and $k_{ij} \neq 0$.

3.2. Mass Transfer Based on Henry's Law

The numerical solution of the FTS SBCR model with mass transfer based on Henry's law is displayed in Figs. 13-18. Clearly, the numerical solution is sensitive to the choice of solvent. In the FTS, the slurry phase consists of a vast amount of long-chained hydrocarbons, and many of them are equally qualified as solvents. For instance, in the experimental work of Sari et al. (2009), hydrocarbons with carbon chain lengths in the range 1–46 were observed, and their mass fractions were measured. The shorter hydrocarbons are volatile and are thus inappropriate as a solvent; however, hydrocarbons that have low vapor pressure have a high tendency to remain in the slurry phase. All paraffins with carbon chain lengths greater than ten have a vapor pressure lower than 5 bar at 240°C (Lemmon et al., 2019), which is less than the operating pressure of ≈ 30 bar used in this work. Hence, paraffins with carbon chain lengths greater than ten could thus be regarded as suitable solvents. Therefore, with mass transfer based on Henry's law, the solvent could be specified as a paraffin with a carbon chain length longer than ten. Thus, many choices are available, resulting in ambiguity for the FTS mass transfer modeling. In this study, solvents with carbon chain lengths in the range 16–36 were studied; however, this range only represents a small portion of the suitable solvent carbon chain lengths. Although other solvent ranges should be studied, the parametrizations of H_{ij} by Marano and Holder (1997)

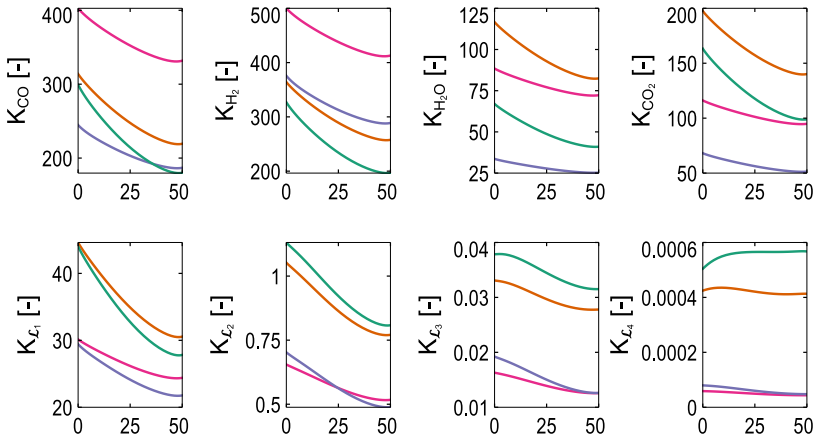

Fig. 11. Equilibrium ratios in the FTS SBCR. Legend: PR with $k_{ij} = 0$ (■); PR with $k_{ij} \neq 0$ (■); PC-SAFT with $k_{ij} = 0$ (■); and PC-SAFT with $k_{ij} \neq 0$ (■).

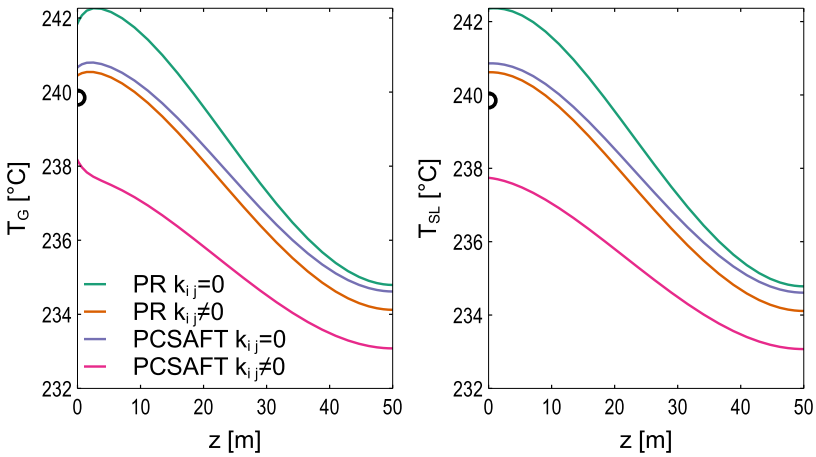

Fig. 12. Temperature in the gas and slurry phases in the FTS SBCR. Black circles at the SBCR inlet denote boundary conditions.

are not valid outside carbon chain lengths in the range 16–36. On the other hand, for the mass transfer based on an EoS, the specification of a single solvent is not required. Thus, there is no ambiguity related to the choice of solvent for mass transfer based on an EoS.

For the FTS SBCR with mass transfer based on Henry's law, the area fractions are displayed in Fig. 13. Clearly, α_G decreases by increasing the solvent carbon chain length. As the mass is transferred from the gas phase to the liquid phase, α_L consequently increases by increasing the solvent carbon chain length. The trends in α_G and α_L are related to CO and H_2: as seen in Figs. 14 and 15, the solubilities and mass transfer of CO and H_2 increase with solvent carbon chain length. Higher solubility of CO and H_2 yields a higher FT reaction rate, which is consistent with the high conversion obtained for solvent carbon chain length of 36 (see Fig. 10). As a result of the increased conversion, more H_2O is produced and subsequently transferred back to the gas phase. The main contributors to the variation of α_G are thus condensation of CO and H_2 and the evaporation of H_2O. In Fig. 13, α_G varies by 8.7 percentage points at the SBCR outlet by varying solvent carbon chain length of 16 to 36. Similarly, α_L and α_S vary by 7.1 and 1.6 percentage points at the SBCR outlet, respectively.

On the other hand, with the PR and PC-SAFT EoSs with $k_{ij} \neq 0$, α_G varies by 4.4 percentage points. However, by comparing the PR EoS with $k_{ij} = 0$ to the PC-SAFT EoS with $k_{ij} \neq 0$, α_G varies by 8.6 percentage points, which is approximately the same variation observed for mass transfer based on Henry's law by varying the solvent carbon chain length from 16 to 36.

Increasing the solvent carbon chain length increases the solubility and mass transfer of CO and H_2. In turn, the FT reaction rate and product concentration increase with increasing solvent carbon chain length. The increased reaction rate is consistent with all $\omega_{L,i}$ in Fig. 14 and T_G and T_{SL} in Fig. 16. Furthermore, the produced H_2O is transferred to the gas phase, and the ω_{G,H_2O} thus also increases as the solvent carbon chain length increases, as seen in Fig. 15. Mass transfer of $\mathcal{L}_1, \mathcal{L}_2, \mathcal{L}_3$, and $\mathcal{L}_4$ was set to zero as the H_{ij} was unavailable in the literature for these compounds. Although the four different lumps have a representative carbon chain length (see Table 2), H_{ij} was also unavailable for paraffins that match this representative carbon chain length. For instance, $\mathcal{L}_1$ is represented with carbon chain length of 4.64, that is, between n-butane and n-pentane. However, only H_{ij} for CH_4, C_2H_6, C_3H_8, and n-hexane was available from the correlations of Marano and

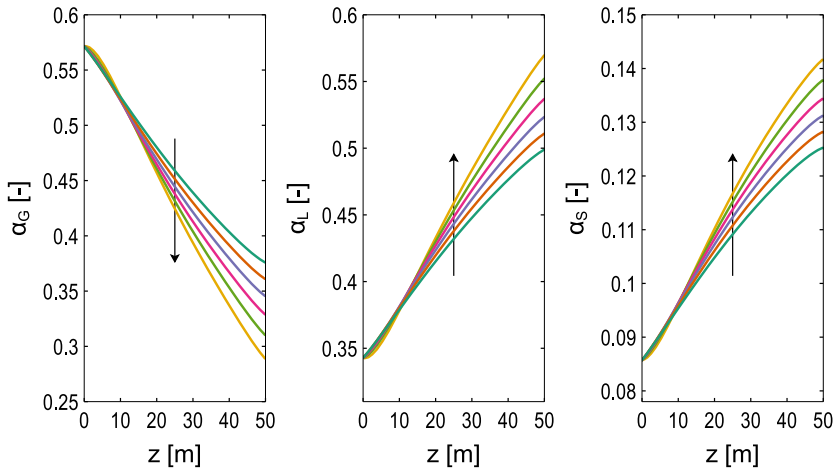

Fig. 13. Area fraction of the gas (left-hand side), liquid (middle), and solid (right-hand side) phases in the FTS SBCR. The vertical arrow indicates the direction of an increase in the solvent's carbon number. Legend: carbon number = 16 (■); carbon number = 20 (■); carbon number = 24 (■); carbon number = 28 (■); carbon number = 32 (■); carbon number = 36 (■).

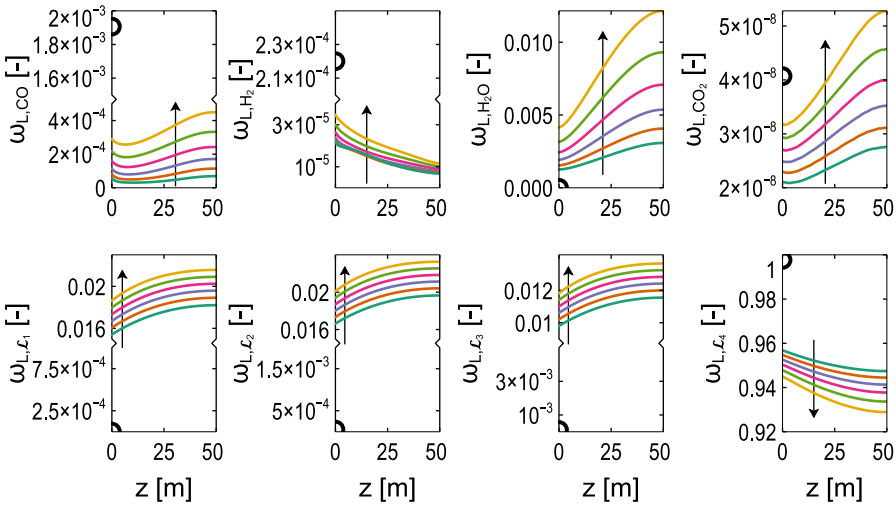

Fig. 14. Mass fractions in the liquid phase in the FTS SBCR. Black circles at the SBCR inlet denote boundary conditions. The vertical arrow indicates the direction of an increase in the solvent's carbon number. The y-axis is broken for CO, H_2, $\mathcal{L}_1$, $\mathcal{L}_2$, and $\mathcal{L}_3$. Legend: carbon number = 16 (■); carbon number = 20 (■); carbon number = 24 (■); carbon number = 28 (■); carbon number = 32 (■); carbon number = 36 (■).

Holder (1997). As the mass transfer of $\mathcal{L}_1$ could not be predicted from the mass transfer expressions based on Henry's law, $\mathcal{L}_1$ remains in the liquid phase. On the contrary, pure n-pentane is supercritical at the T and p in the FTS SBCR (Lemmon et al., 2019), and it is thus likely to evaporate. Further parametrizations are required to predict the evaporation of paraffins in the FTS SBCR with mass transfer based on Henry's law. On the other hand, the mass transfer expressions based on an EoS describe the evaporation of the paraffins, and $\mathcal{L}_1$ was here predicted to be quite volatile: $\omega_{L,\mathcal{L}_1} < 5 \times 10^{-3}$ and $\omega_{G,\mathcal{L}_1} > 0.07$. Thus, the equilibrium ratio $K_{\mathcal{L}_1} > 30$ for all four EoS cases (PR and PC-SAFT, with and without k_{ij}).

Based on the choice of solvent carbon chain length, ρ_G ranges from 10 to 11.3 kg m^{-3} at the FTS SBCR outlet. Hence, the relative difference is 12 %, exclusively from changing the solvent carbon chain length. However, the relative differences are less than those observed for mass transfer based on an EoS. By varying the EoS employed from PC-SAFT with $k_{ij} \neq 0$ to PR with $k_{ij} = 0$, ρ_G ranges from 11 kg m^{-3} to 13 kg m^{-3}, which amounts to a relative difference of 23 %. We emphasize that the EoS employed in the mass transfer expression should be based on a sound understanding of the GLE behavior of the studied compounds, and based on the studies of Zheng et al. (2019), the PC-SAFT EoS was found more suitable. In comparison, the PC-SAFT EoS predicts ρ_G=11 kg m^{-3} at

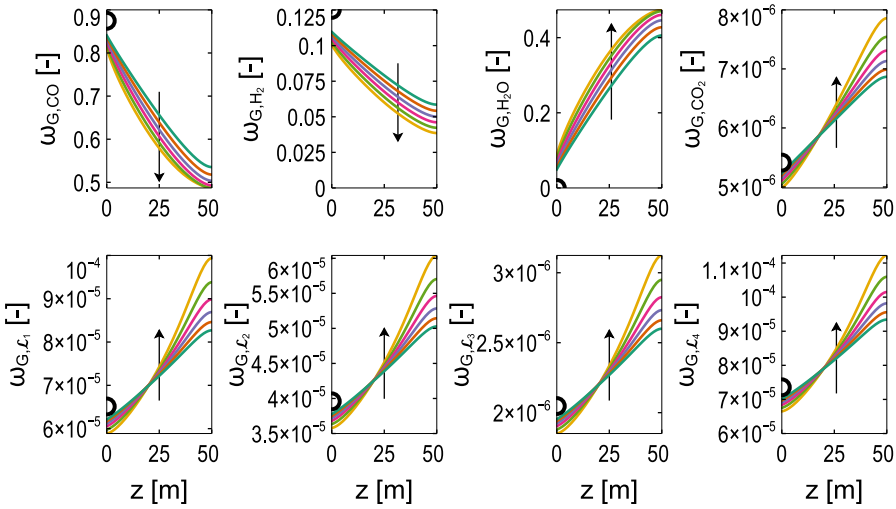

Fig. 15. Mass fractions in the gas phase in the FTS SBCR. Black circles at the SBCR inlet denote boundary conditions. The vertical arrow indicates the direction of an increase in the solvent's carbon number. Note the crossover at $z = 20$m for the lumps $\mathcal{L}_1$–$\mathcal{L}_4$. Legend: carbon number = 16 (■); carbon number = 20 (■); carbon number = 24 (■); carbon number = 28 (■); carbon number = 32 (■); carbon number = 36 (■).

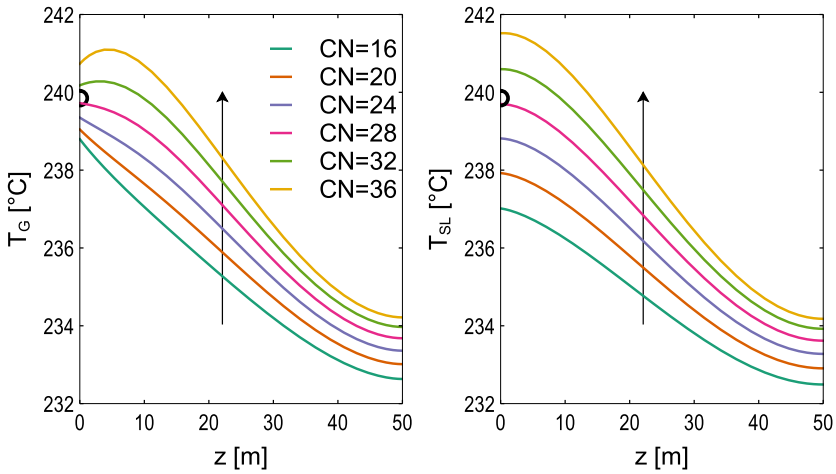

Fig. 16. Temperature in the gas and slurry phases in the FTS SBCR. Black circles at the SBCR inlet denote boundary conditions. The vertical arrow indicates the direction of an increase in the solvent's carbon number.

the SBCR outlet, which places it between the predictions using Henry's law with solvent carbon chain lengths of 28 and 36.

The pressure predictions made by using mass transfer based on Henry's law (Fig. 17) are similar to the pressure predictions made by using mass transfer based on an EoS (Fig. 6): The inlet pressure ranges from approximately 33 bar to 33.5 bar depending on the solvent carbon chain length or EoS employed. As the boundary condition was specified at the SBCR outlet, all pressure profiles join at $p_{\text{out}} = 30$bar. The velocity predictions with mass transfer based on Henry's law in Fig. 18 are similar to those based on an EoS in Fig. 7.

With mass transfer based on Henry's law, the conversion level was 63–74 mol%, based on which solvent carbon chain length was used (see Fig. 10). The conversion level is thus in the same range as with mass transfer based on an EoS, where the PR and PC-SAFT EoSs with $k_{ij} = 0$ and $k_{ij} \neq 0$ were employed. Furthermore, the conversion level increased with increasing solvent carbon chain length for mass transfer based on Henry's law. This is due to the H_{ij} of CO and H_2 decreasing with increasing solvent carbon chain length, resulting in a higher mass transfer driving force (see Eqs. (27) and (28)).

3.3. Conversion Level of the FTS SBCR

The conversion level of CO, H_2, or CO + H_2 (syngas), has become a conventional measure of the performance of FTS reactors. However, the conversion level relies on numerous parameters and the physical properties of the studied system. In Table 10, a review of experimental (Bremaud et al., 2005; Gavrilović et al., 2021; Ma et al., 2011; Masuku et al., 2012; Peña et al., 2014; Pinna et al., 2003; Rodrigues et al., 2011; Sadeqzadeh et al., 2013; Sari et al., 2009; Todic et al., 2013; Yates and Satterfield, 1991) and theoreti-

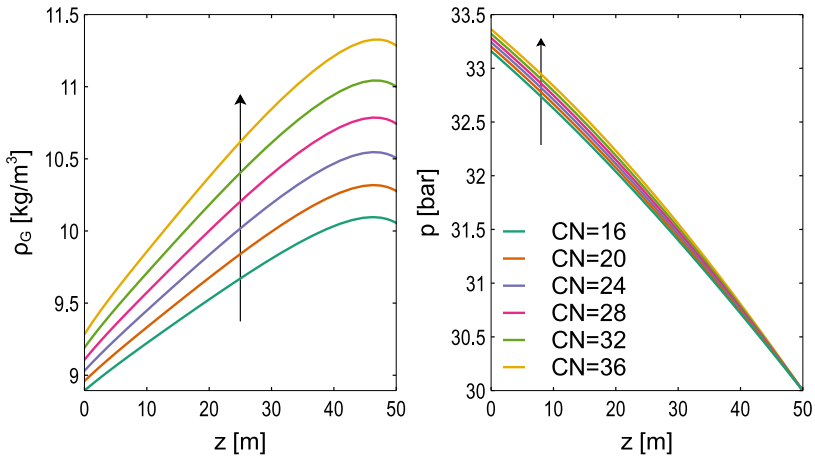

Fig. 17. Gas phase density (left-hand side) and pressure (right-hand side) in the FTS SBCR. The vertical arrow indicates the direction of an increase in the solvent's carbon number.

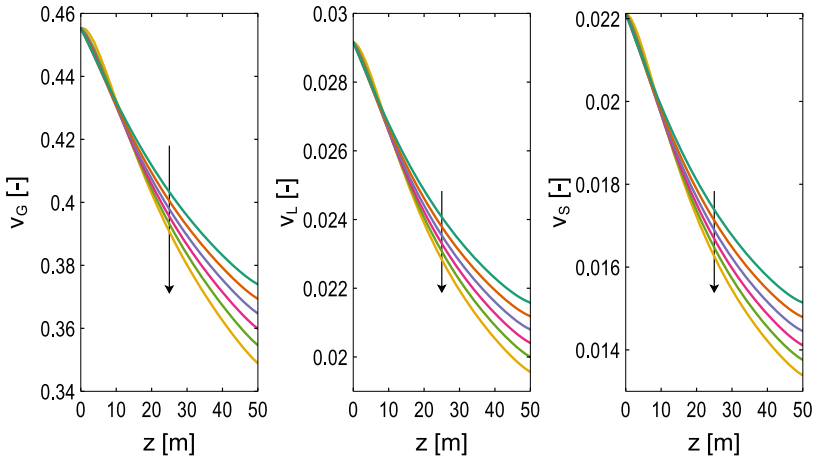

Fig. 18. Local instantaneous velocity of the gas (left-hand side), liquid (middle), and solid (right-hand side) phases in the FTS SBCR. The vertical arrow indicates the direction of an increase in the solvent's carbon number. Legend: carbon number = 16 (■); carbon number = 20 (■); carbon number = 24 (■); carbon number = 28 (■); carbon number = 32 (■); carbon number = 36 (■).

Table 10
A review of experimental and theoretical investigations in the literature. Here, Cat = Catalyst, Cat load = Catalyst loading; L = reactor length; X = conversion level; PBR = packed bed reactor; SSTR = slurry stirred tank reactor.

T [°C]	p [bar]	Cat [-]	Cat load [wt%]	L [m]	d_{col} [m]	X [mol%]	Reactor	Ref
200–240	20–35	Co/Al_2O_3	12.5	N/A	N/A	10–84	SSTR	(Sari et al., 2009)
205–230	15	Co/Al_2O_3	4.8	N/A	N/A	40–70	SSTR	(Todic et al., 2013)
210–230	20–22	Co/Al_2O_3	N/A	N/A	0.01	15–75	PBR	(Gavrilović et al., 2021)
220	15	Co/Al_2O_3	3.1–5.4	N/A	N/A	12–94	SSTR	(Ma et al., 2011)
220	20	Co/Al_2O_3	N/A	N/A	N/A	25–52	SSTR	(Masuku et al., 2012)
220	20	Co/Al_2O_3	N/A	N/A	N/A	30–50	SSTR	(Bremaud et al., 2005)
220	20	Co/Al_2O_3	4	0.1805	0.046	20–70	SSTR	(Sadeqzadeh et al., 2013)
220	20	Co/Al_2O_3	10.4–15	N/A	N/A	29–45	SSTR	(Pinna et al., 2003)
220–230	20	Co/Al_2O_3	3–8	N/A	N/A	30–75	SSTR	(Peña et al., 2014)
220–240	5–15	Co/SiO_2	4.1	N/A	N/A	11–73	SSTR	(Yates and Satterfield, 1991)
240	20	Co/SBA-15	3.3	N/A	N/A	10–80	SSTR	(Rodrigues et al., 2011)
197–267	10–50	A variety	0–50 vol%	50	9	0–99	SBCR	(Sehabiague and Morsi, 2013a)
200–260	N/A	Co/Al_2O_3	16.7	2.0	0.0508	20–40	SBCR	(Kim et al., 2009)
210–235	8–25	Co-based	N/A	N/A	N/A	30	GLE	(Visconti, 2014)
227	30	Co/Al_2O_3	25–50	30–50	6–8	50–85	SBCR	(Sehabiague et al., 2008)
240	30	Co/SiO_2	44–63	30	7	50–90	SBCR	(Maretto and Krishna, 1999)

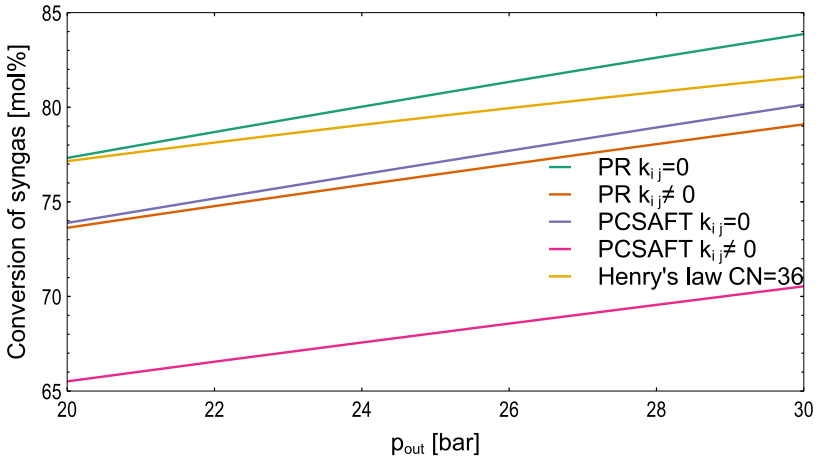

Fig. 19. Conversion level of syngas at the FTS SBCR outlet as a function of the SBCR outlet pressure.

cal (Sehabiague et al., 2008; Sehabiague and Morsi, 2013a; Maretto and Krishna, 1999; Kim et al., 2009; Visconti, 2014) studies are summarized. Despite covering a wide range of temperatures, pressures, catalyst loadings (concentrations), H_2/CO ratios, and superficial gas velocities, most of the experimental conversions peak at 70–85 mol%, and only the study of Ma et al. (2011) reach as high as 94 mol%. Maretto and Krishna (1999) suggests that catalyst concentration may be as high as $\alpha_{SiS} = 0.4$ (68 wt% for the catalyst used by Maretto and Krishna (1999)) in a commercial reactor unit before the experiments at the University of Amsterdam show complications in the downstream separation of the slurry. Most experimental studies mentioned here are well below this maximum limit. Moreover, Maretto and Krishna (1999) performed simulations at similar operating conditions to those employed here, and for an $\alpha_{SiS} = 0.2$, and $v^s_{G,in} = 0.26$, their conversion level of syngas reached approximately 50 mol%. In this study, the conversion level of syngas reached 70–84 mol%, depending on which mass transfer model has been employed. The conversion level of syngas is displayed in Fig. 19.

Sehabiague and Morsi (2013a) have performed a comprehensive theoretical sensitivity study in conversion levels of syngas, yields, selectivities, site-time yield, and mass transfer limitations. In this endeavor, effects such as choice of catalyst, catalyst loading, H_2/CO ratio in the gas phase at the SBCR inlet, superficial gas velocity, temperature, and pressure, were studied. Their results show that the conversion level of syngas can be as low as 5 mol%, but also as high as ≈ 98 mol%. In this study, the conversion level of syngas ranges from 70 to 84 mol%, based on which mass transfer model has been employed. In Table 11, the results obtained here are compared to the simulation case of Sehabiague and Morsi (2013a) that closest resembles this study. In the study of Sehabiague and Morsi (2013a), a much higher conversion level was obtained. The catalyst loading employed by Sehabiague and Morsi (2013a) is twice as high as that employed here. However, increasing $\alpha_{S,in}$ to 0.196 did not increase the conversion level any further, suggesting a mass transfer limitation in the SBCR studied here. It is also mentioned that the upper catalyst loading limit ($\alpha_{SiS} = 0.50$) studied by Sehabiague and Morsi (2013a) is higher than the recommendations ($\alpha_{SiS} = 0.40$) of Maretto and Krishna (1999) for commercial application.

Table 11
Comparison of this work and the closest resembling study of Sehabiague and Morsi (2013a).

Variable	This study	Sehabiague and Morsi (2013a)
T_{in} [°C]	240	240
p_{out} [bar]	30	30
Catalyst	Co/MgO/SiO_2	Co/MgO/SiO_2
$\alpha_{S,in}$ [−]	0.086	0.175
Kinetic expression	Eq. (12) converted from (Yates and Satterfield, 1991)	Yates and Satterfield (1991)
$v^s_{G,in}$ [m s^{-1}]	0.26	0.30
$v^s_{L,in}$ [m s^{-1}]	0.01	0.01
y_{H_2}/y_{CO} [−]	2	2
d_{col} [m]	9	9
H [m]	50	50
Conversion of syngas [mol%]	70–84	98

Experimental studies in the literature show diverging results for how the conversion level changes with operating pressure. For instance, Sari et al. (2009) show that the conversion level of CO increases as the pressure increases. Conversely, Sadeqzadeh et al. (2013) show that the conversion level of CO consistently decreases as the pressure is increased. In an extensive report by Kuo (1983), the common trend is that the syngas conversion level decreases as the pressure increases, albeit for an iron-based catalyst at an elevated temperature and significantly lower pressure and H_2/CO ratios. In another comprehensive report by Davis (2002), both iron-based and cobalt-based catalysts were tested in the same laboratory. Their findings were diverse: for the iron-based catalysts, the CO conversion level increased as the pressure rose from 13 to 25 bar at 250°C. In contrast, the CO conversion level decreased as the pressure rose from 25 to 32 bar at 230°C. On the other hand, the cobalt-based catalysts show a significant increase in the conversion level of CO (from 20 to 40 mol%) as the pressure rose from 7 to 21 bar. Increasing the pressure from 21 to 34.5 bar yielded a slight increase in the CO conversion level.

The theoretical study of Sehabiague and Morsi (2013a) shows a decreasing conversion level of syngas as the pressure is increased. This trend is interesting since they employed the reaction rate expression by Yates and Satterfield (1991) in its original form, where the consumption rate of CO is given by:

$$-r_{FT} = a_{FT}\frac{y_{CO}y_{H_2}p^2}{(1+b_{FT}y_{CO}p)^2} \tag{74}$$

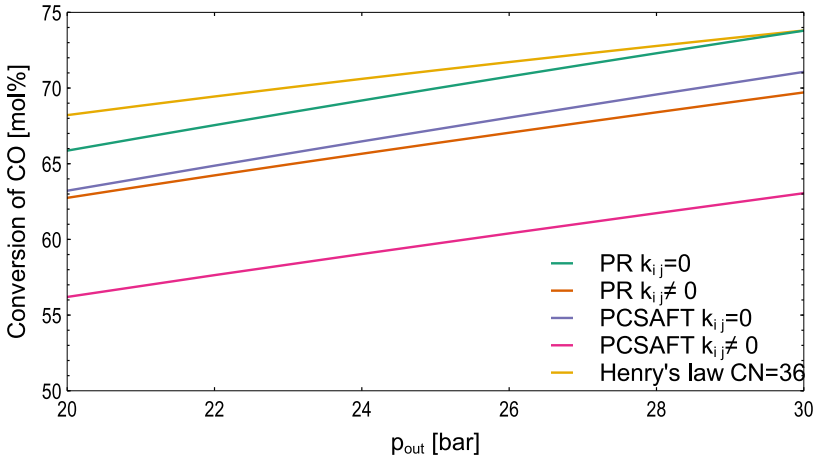

Fig. 20. Conversion level of CO at the FTS SBCR outlet as a function of the SBCR outlet pressure.

The partial change of Eq. (74) concerning pressure is:

$$\left(\frac{\partial(-r_{FT})}{\partial p}\right)_{T,y_{CO},y_{H_2}} = 2a_{FT}y_{CO}y_{H_2}\frac{p}{(1+b_{FT}y_{CO}p)^3} \tag{75}$$

Since a_{FT}, b_{FT} y_{CO}, and y_{H_2} are positive quantities, then $\partial(-r_{FT})/\partial p > 0\ \forall p > 0$. Thus, the consumption of CO increases for all positive pressures with the expression by Yates and Satterfield (1991). The decrease in the conversion level of syngas obtained by Sehabiague and Morsi (2013a) must result from other effects originating from the changed hydrodynamics obtained when the pressure field is changed. By increasing the pressure from 15 to 30 bar, Sehabiague and Morsi (2013a) report a decrease of conversion level of syngas from 70 to 45 mol%. In the experimental work of Sadeqzadeh et al. (2013), a decrease of conversion level was also reported for the same pressure change (15 to 30 bar).

In this study, opposite trends for the conversion level were found. Here, the conversion level of syngas increases as the pressure at the outlet of the SBCR increases. This trend is valid for all mass transfer models employed in this study (see Fig. 19). The results of Sehabiague and Morsi (2013a) have shown that the effects related to the hydrodynamics by increasing the pressure cannot be neglected. Nevertheless, the conversion level of syngas in this work increases as the pressure at the outlet of the SBCR increases. It is stressed that the reaction rate expression employed in this study is on the slurry phase concentration form in Eq. (12) rather than the partial pressure form in Eq. (74). This rationale was discussed previously in Section 2.1 and was based on mass transfer limitation considerations.

For mass transfer based on Henry's law, the consumption rate of CO in Eq. (12) reduces to (see also Sehabiague et al. (2008) for an identical expression):

$$-r_{FT} = a_{FT}\frac{H_{CO}x_{CO}H_{H_2}x_{H_2}}{(1+b_{FT}H_{CO}x_{CO})^2}. \tag{76}$$

Thus, the FT reaction rate with Henry's law in Eq. (76) does not directly depend on pressure. Nevertheless, the conversion level of CO and syngas increases with increasing pressure, as seen in Figs. 19 and 20. This increase in conversion level is attributed to the mass

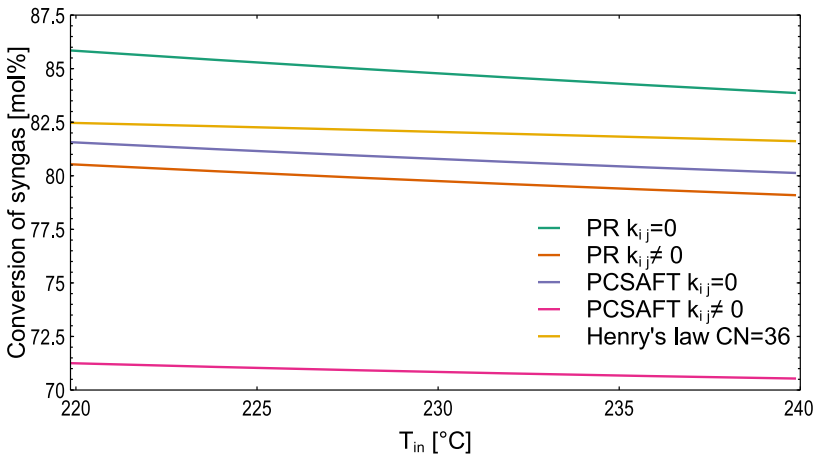

Fig. 21. Conversion level of syngas at the FTS SBCR outlet as a function of the SBCR inlet temperature. The gas and slurry phases shared the same inlet boundary condition on the x-axis.

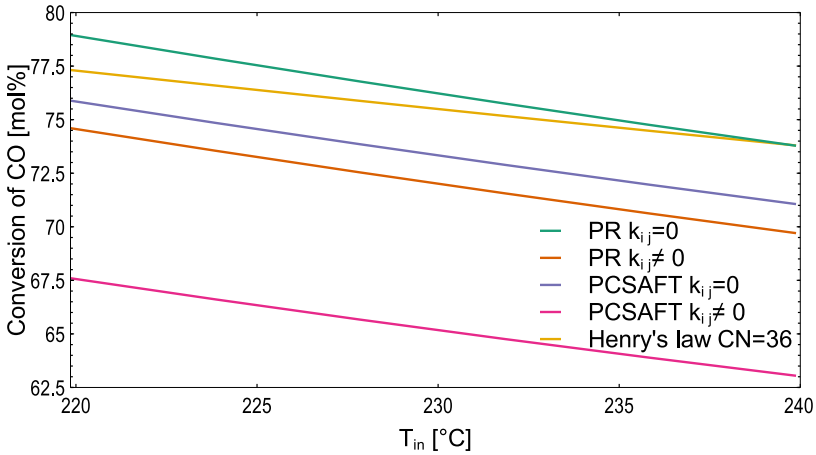

Fig. 22. Conversion level of CO at the FTS SBCR outlet as a function of the SBCR inlet temperature. The gas and slurry phases shared the same inlet boundary condition on the x-axis.

transfer expression where $K_{ij}^{m,\infty} = H_{ij}/p$ is in the denominator, see Eqs. (22) and (24). As H_{ij} is not a function of p, $1/K_{ij}^{m}$ is directly proportional to p, and the mass transfer increases with increasing p. As more reactants are dissolved in the liquid, the reaction rate increases resulting in a higher conversion level.

On the other hand, multiple effects affect the conversion level for the mass transfer expressions based on an EoS. First, the reaction rate cannot be reduced to a form that does not directly depend on pressure, such as that in Eq. (76). The reaction rate thus remains as in Eq. (12), where pressure dependencies exist directly through p and indirectly through K_i^m. Second, the mass transfer driving forces are more complicated expressions. Although K_i still exists in the denominator, K_i is deduced from a converged GLE problem, and its pressure dependency is therefore implicit. However, the overall effect is similar to the case with mass transfer based on Henry's law: the conversion level increases with increasing pressure.

Figs. 21 and 22 show, respectively, how the conversion level of syngas and CO varies with SBCR inlet temperature. Both the conversion level of syngas and CO decreases as the SBCR inlet temperature of the gas and slurry phases are increased. This trend is unintuitive, as the reaction rate of the catalyst generally increases with increasing temperature. For instance, in the experimental work of Sari et al. (2009), the conversion level of CO increases as temperature increases. However, their experiments were performed in the kinetically limited regime, where mass transfer limitations are irrelevant. Similarly, the experiments of Yates and Satterfield (1991) were also performed in the kinetically limited regime. Previously in this work, the catalyst loading was increased, and the conversion level was unaffected. Therefore, mass transfer effects were considered relevant in this study, as opposed to most experimental studies that are kinetically limited. It is deduced that there are two competing phenomena when the temperature is increased: the increased catalyst activity and the mass transfer limitations. The conversion level decreases for the studied temperature increase, suggesting that the mass transfer limitation effect is more significant than the increased catalyst activity effect. In the temperature sensitivity study performed by Sehabiague and Morsi (2013a), the reaction rate of Yates and Satterfield (1991) in

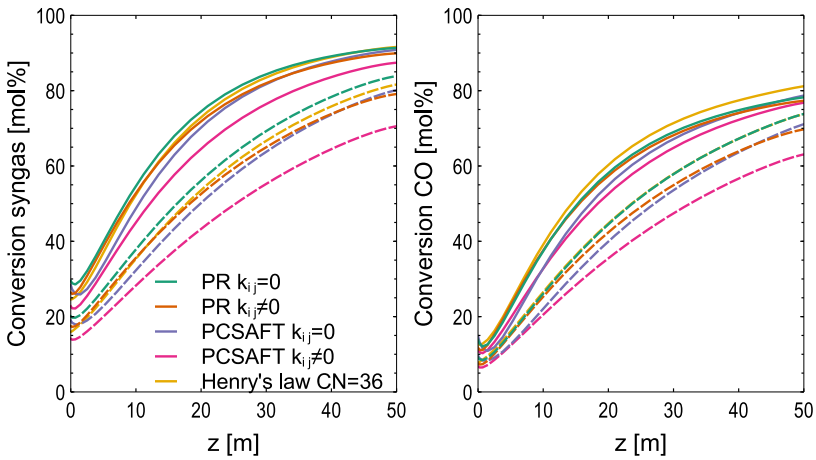

Fig. 23. Conversion level of syngas and CO. Full lines indicate $k_L = 2k_L^\circ$, and dashed lines indicate $k_L = k_L^\circ$.

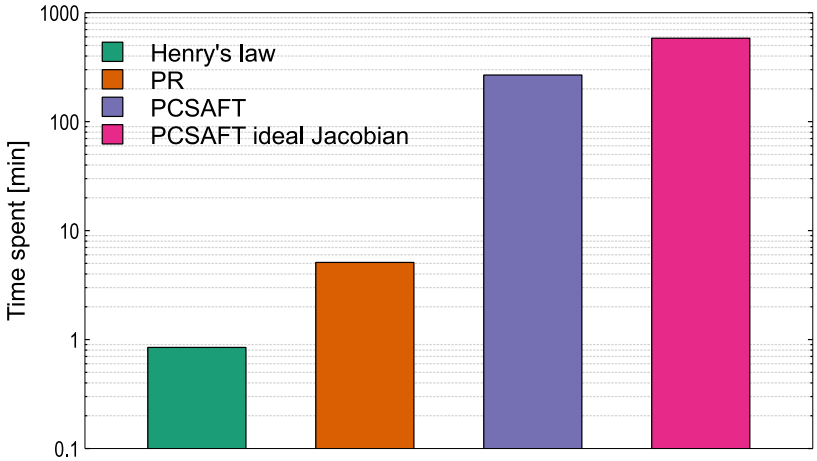

Fig. 24. Time spent to converge the FTS SBCR simulations. The y-axis is on the logarithmic scale.

the partial pressure form was employed. Sehabiague and Morsi (2013a) reported that the conversion level of syngas *increased* from 35 to 98 mol% by increasing the temperature from 220 to 240 °C. In this work, the conversion level of syngas *decreased* in the same temperature range. Thus, mass transfer effects become more prominent by converting the reaction rate expression from partial pressure form to slurry phase concentration form. This supports the claim that the FTS SBCR in this study is mass transfer limited.

3.4. Mass Transfer Limitations

Two observations have indicated that the studied FTS SBCR is mass transfer limited in this work. First, increasing the catalyst loading did not increase the conversion level. Second, increasing the temperature decreases the conversion level. Hence, a sensitivity study in the mass transfer coefficient was performed. In Fig. 23, the conversion levels of CO and syngas are displayed. The conversion levels for all studied mass transfer expressions increase when k_L is increased by a factor of two. Furthermore, the conversion level becomes less dependent on the mass transfer model as the FTS SBCR is shifted from the mass transfer limited regime into the kinetically limited regime. For instance, in Fig. 23, reasonable agreement is observed for the conversion level profiles of all mass transfer models when $k_L = 2k_L^\circ$ (full lines). On the other hand, considerable differences in the conversion level profiles are observed when k_L is computed from the correlations of Calderbank and Moo-Young (1961), that is $k_L = k_L^\circ$. With the information from this third sensitivity study, we infer that the FTS SBCR is mass transfer limited.

3.5. Simulation Time and the Formation of an Aqueous Phase

Fig. 24 displays the time spent before convergence was obtained for the FTS SBCR. Here, the mass transfer model based on Henry's law spends less than 1 min, followed by the PR EoS, which spends approximately 5 min. The mass transfer model based on the PC-SAFT EoS spends approximately 260 min and is the most computationally demanding out of the three mass transfer models evaluated here. Although the mass transfer model based on the PR and the PC-SAFT EoSs are similar in structure, the PC-SAFT EoS spends over 50 times longer than the PR EoS to converge. The differences are attributed to the GLE problem, which must be converged to obtain the K_i, see e.g., Algorithm 1 and Figure 1, 3, and 4. In the GLE problem, $(\partial\mathcal{A}/\partial V), (\partial\mathcal{A}/\partial N_k), \left(\partial^2\mathcal{A}/\partial V^2\right), (\partial^2\mathcal{A}/\partial V\partial N_k)$, and $(\partial^2\mathcal{A}/\partial N_k\partial N_l)$ are required. In general, these derivatives are computationally expensive to evaluate, especially the second order derivatives. As seen in Appendix C, the mathematical complexity of both the required first and second order derivatives is high, and the associated computational cost of evaluating them is also high. Gautam and Seider (1979) employed a solution strategy to the GLE problem where the second derivative was assumed to consist of ideal contributions solely. Adopting the procedure of Gautam and Seider (1979), the evaluation of Eq. (50) was no longer required, and thus the derivatives $(\partial^2\mathcal{A}/\partial V\partial N_k)$ and $(\partial^2\mathcal{A}/\partial N_k\partial N_l)$ need not be evaluated. Despite lowering the computational cost of evaluating the Jacobian matrix in Eqs. (35a) and (35b), the solution strategy no longer yields quadratic convergence (a part of the quadratic information is ignored). Hence, more iterations are required to converge the GLE problem. As seen in Fig. 24, the method of Gautam and Seider (1979) (PCSAFT ideal Jacobian) spends two times longer than the method using both ideal and non-ideal contributions in the Jacobian matrix. The strategy of Gautam and Seider (1979) gave identical solution profiles as including the non-ideal contribution in the Jacobian matrix; only the numerical properties of the GLE iteration procedure differed. The mass transfer expression based on Henry's law does not require convergence of the GLE problem, and the discussion related to the Jacobian matrix is not relevant. H_{ij} is computed from correlations, and the computational effort of computing the mass transfer is low. Hence, mass transfer based on Henry's law is over 5 times faster than mass transfer based on the PR EoS and over 250 times faster than the PC-SAFT EoS.

Evaluating the mass transfer expressions based on the PR and PC-SAFT EoSs relies on solving the GLE problem, which requires a fixed number of phases to be specified. In this work, only a gas and a liquid phase were considered for the GLE, that is, no solid catalyst particles were considered for solving the GLE problem in this study. The products for the FTS consist of a mixture of unpolar paraffins and polar H_2O. Furthermore, with the cobalt-based catalyst, the WGS reaction is negligible, and hence, a significant amount of H_2O is produced. It is thus worthwhile to investigate the possibility that an additional aqueous liquid phase has been erroneously disregarded. In that case, the GLE problem should be a gas–liquid–liquid-equilibrium (GLLE) problem, and a four-phase fluid flow problem is in order.

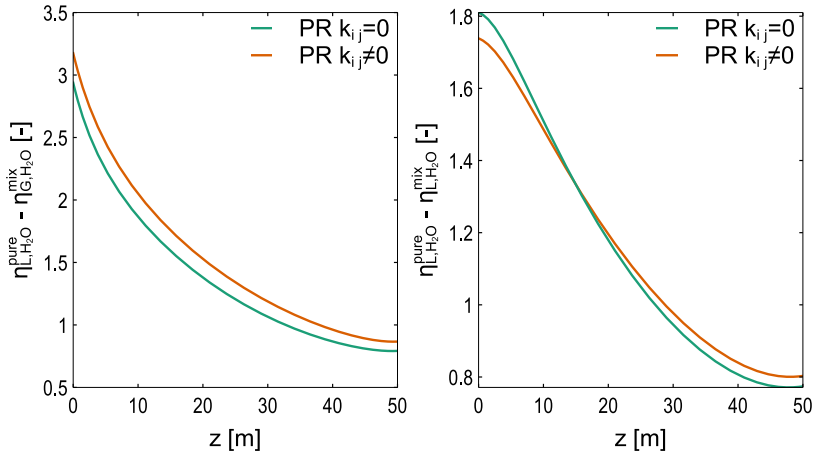

Fig. 25. The driving force for forming an aqueous phase during the operation of the FTS SBCR. The potential of H_2O condensing from the gas phase and forming an aqueous phase is on the left-hand side. The potential of H_2O separating from the organic liquid phase and forming an aqueous phase is on the right-hand side.

To investigate the possible formation of an aqueous phase, the thermodynamic spontaneity of the following reactions was considered:

$$H_2O(g, \text{mix}) = H_2O(l, \text{pure}) \tag{77}$$

$$H_2O(l, \text{mix}) = H_2O(l, \text{pure}) \tag{78}$$

The spontaneity of the phase change reactions in Eqs. (77) and (78) was characterized by the sign of the difference in modified chemical potential. For the reaction in Eq. (77), the difference is

$$\Delta\eta_G^{Aq} = \eta_{L,H_2O}^{\text{pure}} - \eta_{G,H_2O}^{\text{mix}}, \tag{79}$$

where, $\eta_{G,H_2O}^{\text{mix}}$ is the modified chemical potential in Eq. (36a), and $\eta_{L,H_2O}^{\text{pure}}$ is the modified chemical potential of pure liquid H_2O at the same T and p. Similarly, for the reaction in Eq. (78), the difference in modified chemical potential is

$$\Delta\eta_L^{Aq} = \eta_{L,H_2O}^{\text{pure}} - \eta_{L,H_2O}^{\text{mix}}, \tag{80}$$

where $\eta_{L,H_2O}^{\text{mix}}$ is the modified chemical potential in Eq. (36b). If $\Delta\eta_G^{Aq} > 0$, then Eq. (77) is *not* spontaneous. Conversely, if $\Delta\eta_G^{Aq} < 0$, then Eq. (77) *is* spontaneous. Similarly, if $\Delta\eta_L^{Aq} > 0$, then Eq. (78) is *not* spontaneous, and if $\Delta\eta_L^{Aq} < 0$, then Eq. (78) *is* spontaneous.

For the mass transfer model based on the PR EoS, $\eta_{L,H_2O}^{\text{pure}} - \eta_{G,H_2O}^{\text{mix}} > 0$, meaning Eq. (77) is *not* spontaneous, and H_2O tends to stay in the gas phase rather than forming a new pure H_2O liquid phase. Furthermore, $\eta_{L,H_2O}^{\text{pure}} - \eta_{L,H_2O}^{\text{mix}} > 0$ implies that Eq. (78) is *not* spontaneous. Thus, the H_2O dissolved in the organic liquid phase is stable and does not form a new pure H_2O liquid phase. The non-spontaneity of Eqs. (77) and (78) is seen graphically in Fig. 25.

For the mass transfer model based on the PC-SAFT EoS, a supercritical isotherm was produced in the pV-plane at the reactor temperature. Thus, no liquid root exists for the PC-SAFT EoS at the reactor temperature, and hence the formation of an aqueous phase is impossible with the PC-SAFT EoS. On the other hand, the reactor conditions are well below the critical conditions of H_2O, that is $T \approx 513\text{K} \ll 647.096\text{K} = T_c$ and $p \approx 3\text{MPa} \ll 22.064\text{MPa} = p_c$ (Lemmon et al., 2019). Attractive contributions to the Helmholtz energy potential pack molecules closer together, allowing for dense, condensed phases such as liquids. The attractive contribution is not well represented for H_2O in the current implementation. Here, the implementation of the PC-SAFT EoS was similar to the original work of Gross and Sadowski (2001); however, in a later revision (Gross and Sadowski, 2002), an associative contribution was added to the Helmholtz energy potential. Since H_2O is known to be strongly associative, the inclusion of this associative contribution is believed to be critical for representing H_2O. There are different association schemes available, and there is no consensus as to which association scheme describes H_2O better. Nonetheless, the inclusion of an associative contribution is still believed to improve the predictions of pure H_2O and correctly produce liquid roots at the reactor temperature studied here.

Last, for the mass transfer expression based on Henry's law, no GLE problem had to be solved; only a set of H_{ij} is required to determine the solubility of a solute i in a particular solvent j. Although two phases have been assumed for this mass transfer model formulation, no measure of the potential formation of an additional aqueous liquid phase exists. For the PR and the PC-SAFT EoSs, $\eta_{L,H_2O}^{\text{pure}} - \eta_{H_2O}^{\text{mix}}$ functioned as a measure of thermodynamic feasibility: for a positive difference (as observed in Fig. 25), the formation of a pure aqueous phase is *not* spontaneous. Conversely, for a negative difference the formation of a pure aqueous phase is spontaneous. For Henry's law, η is not available; hence, the possibility that an additional aqueous phase has been erroneously disregarded cannot be investigated.

In the experimental study of Loewert et al. (2019), a slurry stirred tank reactor was operated at 240°C and 30 bar, similar to the conditions in this study. Furthermore, the catalyst was cobalt-based, and thus, the product composition is similar to what was obtained in this study. Loewert et al. (2019) observed a three-phase system in the reactor unit: a gas phase, a liquid phase, and a solid catalyst phase. Downstream, a hot trap separation unit operated at 170°C separated the light hydrocarbons and unconverted reactants (gas phase) from the liquid phase. The liquid products were further separated in a cold trap operated at 6–10°C. In the cold trap, H_2O forms a dense aqueous phase that splits from the hydrocarbon phase, and the two liquid phases are separated. The use of a cold trap (6–10°C) indicates that the aqueous phase does not form in the operating temperature of the hot trap (170°C). Hence, it is not formed in the reactor (240°C) unit either. The absence of an aqueous phase is consistent with the predictions made by the PR and the PC-SAFT EoSs in this study; no aqueous phase forms in the FTS SBCR at the studied T and p.

It is also emphasized that the vapor pressure of pure H_2O at the reactor temperature (240°C) is approximately 33.5 bar (Lemmon et al., 2019). Hence, H_2O is quite volatile at the investigated temperature, and the high rate of vaporization of H_2O observed in Figs. 8, 9, 14, and 15 is reasonable.

3.6. Model Verification and Validation

The implementation of the novel mass transfer models was verified through multiple consistency tests that are inherent to all Helmholtz and Gibbs energy functions in thermodynamics. Both the PR and the PC-SAFT EoSs were implemented as Helmholtz energy libraries. Since the Helmholtz energy function is an Euler homogeneous function of degree one, the Euler theorems are applicable. The Euler theorems provide $2 + C$ consistency checks for the Helmholtz energy function:

$$\mathcal{A}^{\mathrm{r,v}} = \left(\frac{\partial \mathcal{A}^{\mathrm{r,v}}}{\partial V}\right)_{T,\boldsymbol{n}} V + \sum_{l=1}^{C}\left(\frac{\partial \mathcal{A}^{\mathrm{r,v}}}{\partial n_l}\right)_{T,V} n_l, \tag{81}$$

$$\left(\frac{\partial^2 \mathcal{A}^{\mathrm{r,v}}}{\partial V^2}\right)_{T,\boldsymbol{n}} V + \sum_{l=1}^{C}\left(\frac{\partial^2 \mathcal{A}^{\mathrm{r,v}}}{\partial V \partial n_l}\right)_{T} n_l = 0 \tag{82}$$

$$\left(\frac{\partial^2 \mathcal{A}^{\mathrm{r,v}}}{\partial n_k \partial V}\right)_{T} V + \sum_{l=1}^{C}\left(\frac{\partial^2 \mathcal{A}^{\mathrm{r,v}}}{\partial n_k \partial n_l}\right)_{T,V} n_l = 0, \quad k = 1, 2, \ldots, C. \tag{83}$$

The $2 + C$ tests made up by Eqs. (81), (82), and (83) were found to hold for both the PR and the PC-SAFT EoS implementations. Furthermore, the matrix $(\partial \mathcal{A}^{\mathrm{r,v}}/\partial N_k \partial N_l)_{T,V}$ was checked for symmetry around the diagonal. Additionally, the Gibbs–Duhem relation was confirmed to hold. Moreover, since $G = \mathcal{A} + pV$, we get $1 + C$ new tests from the Euler theorems for the Gibbs energy function:

$$G^{\mathrm{r,p}} = \sum_{l=1}^{C}\left(\frac{\partial G^{\mathrm{r,p}}}{\partial n_l}\right)_{T,p} n_l, \tag{84}$$

$$\sum_{l=1}^{C}\left(\frac{\partial^2 G^{\mathrm{r,p}}}{\partial n_k \partial n_l}\right)_{T,p} n_l = 0, \quad k = 1, 2, \ldots, C. \tag{85}$$

The $1 + C$ tests made up by Eqs. (84) and (85) were also tested, and all of them were confirmed to hold. For more information on the subject of thermodynamic consistency, the reader is referred to Michelsen and Mollerup (2007).

On the other hand, model validation is challenging in the FTS. In order to sophistically and rigorously validate the proposed mass transfer model, multiple measurements of the composition in both phases are required along the axial direction. To the authors' knowledge, this composition measurement remains to done in an FTS SBCR. Furthermore, due to the vast amount of species in the FTS, experiments generally focus on the composition at the reactor inlet or outlet, or more conveniently, the conversion level, see the comparison in Table 10. However, the effects seen on the conversion level must be seen as a combined effect of mass transfer, reaction kinetics, diffusion, dispersion effects, and superficial gas velocity. For instance, high conversion can be reached when the superficial gas velocity is low, see e.g., Gavrilović et al. (2021). The conversion level can therefore only be used as an indication for whether the mass transfer expression provides physical simulation results at flow conditions similar to those in the related experimental study. Nevertheless, in this study, a set of mass transfer expressions were compared while the other governing equations were identical. Thus, the experimental conversion levels provide a meaningful way of comparing the mass transfer models employed in this work.

4. Summary and Conclusion

In this study, an industrial scale cobalt-based FTS SBCR has been simulated, emphasizing mass transfer between gas and liquid phases. In particular, the driving force for mass transfer has been explored, in which three different driving forces were employed: one based on the PR EoS, one based on the PC-SAFT EoS, and one based on Henry's law. In the mass transfer expression based on Henry's law, the choice of solvent and its implications for the simulation results were highlighted. Here, the solvent has been specified as a paraffin with carbon chain length in the range of 16–36. For solvent carbon chain length of 16, the conversion level of CO at the SBCR outlet was 63 mol%, whereas for solvent carbon chain length of 36, the conversion level of CO at the SBCR outlet was 74 mol%. For the same carbon chain length variation, a fourfold variation in the solubility of CO was observed. Furthermore, as H_{ij} does not exist for all components, the mass transfer (evaporation) of paraffins was neglected.

In the FTS, many hydrocarbons are present in substantial amounts in the slurry phase, and identifying a single solvent is therefore ambiguous. The novel mass transfer expressions based on the PR EoS and the PC-SAFT EoS do not require the specification of a single solvent; only the different species must be specified for the mass transfer to be computed. The mass transfer expressions based on the PR and the PC-SAFT EoSs are thus advantageous regarding the solvent specification ambiguity. Moreover, the infinite dilution limit employed with Henry's law is only valid for the volatile components present in the FTS. Hence, Henry's law is only theoretically justified for predicting the mass transfer for some components. On the other hand, the mass transfer expressions based on the PR and PC-SAFT EoSs are equally valid for dilute and concentrated components, and consequently, the mass transfer of all components in the FTS can be predicted with a sound basis in thermodynamic phase equilibrium.

The conversion level of the FTS reactor has become the conventional measure of the performance of the reactor. In this study, the conversion level of CO at the SBCR outlet is in the range of 63–74 mol%, depending on the mass transfer model employed. For mass transfer based on Henry's law, the conversion level of CO was found to increase with increasing solvent carbon chain length. For the mass transfer model based on an EoS, the lowest conversion was observed for the PC-SAFT EoS with $k_{ij} \neq 0$, and the highest conversion was observed for the PR EoS with $k_{ij} = 0$. Furthermore, a sensitivity study in pressure was performed, and the conversion level of syngas was found to increase with increasing pressure. This trend is in agreement with the extensive experimental work of Davis (2002) and the experimental work of Sari et al. (2009), but in disagreement with the experimental work of Sadeqzadeh et al. (2013) and the theoretical work of Sehabiague and Morsi (2013a). More experimental work is required to fully understand the effects of pressure perturbations.

Additionally, a sensitivity study in temperature was performed. The conversion level of syngas and CO decreased with increasing temperature. This trend suggests that the SBCR is in the mass transfer limited regime, not the kinetically limited regime. Increasing the catalyst loading and the mass transfer coefficient confirmed that the studied SBCR was indeed in the mass transfer limited regime.

The three different propositions for the driving force of mass transfer were analyzed in terms of simulation time. The mass transfer expression based on Henry's law was the fastest, with a simulation time of less than 1 min. The mass transfer expression based on the PR EoS was solved in 5 min and was the second fastest proposition. The last and slowest mass transfer expression was based on the PC-SAFT EoS, which is quite computationally

demanding due to its high mathematical complexity. The simulations with mass transfer based on the PC-SAFT EoS spent 260 min. The solution of the phase equilibrium problem requires second derivatives, and since a high computational cost is associated with the second derivatives of the PC-SAFT EoS, an ideal gas approximation in the second derivatives was attempted. Although this resulted in computationally cheaper second derivatives, more iterations were required. The overall effect was simulation times of 580 min, which is more than twice as long as the simulations without the ideal gas approximation in the second derivatives.

The EoS description can predict the spontaneity of the formation of additional phases. Thus, the possible formation of an aqueous liquid phase was investigated. For the PR EoS, neither the gas phase nor the slurry phase has a chemical potential of H_2O that supports the formation of an aqueous liquid phase. For the PC-SAFT EoS, a liquid root could not be identified, as only a supercritical isotherm was produced in the *pV*-plane. Thus, also here, no aqueous liquid phase can be formed. The operating conditions investigated here do not support the supercritical isotherm for H_2O, and clearly, the associative contribution to the Helmholtz energy potential introduced in a revision (Gross and Sadowski, 2002) of the PC-SAFT EoS must be included to represent H_2O appropriately. For mass transfer based on Henry's law, the driving force measuring the spontaneity of the formation of additional phases was not available. Thus, the possibility that an aqueous phase has been erroneously disregarded could not be investigated with mass transfer based on Henry's law.

The driving force of mass transfer between gas and liquid phases was scrutinized in this study. However, the mass transfer also relies on the size of the bubbles through the interfacial area of the adjoining phases. Several correlations also suggest a bubble size dependency of the mass transfer coefficient. In this work, the bubble diameter was set constant. As a suggestion to improve the model, further work may include the population balance framework (see e.g., Vik et al. (2015)) and thereby gaining insight in the bubble size distribution and its impact on the mass transfer in the FTS SBCR.

Declaration of Competing Interest

The authors declare that they have no known competing financial interests or personal relationships that could have appeared to influence the work reported in this paper.

Acknowledgments

Funding: This project was supported by the Department of Chemical Engineering at NTNU.

Appendix A. Derivation of Mass Transfer Based on Henry's Law

In this work, the two-film model was employed. In this context, a thin film is formed on each side of the interface separating the two phases, and mass transfer flux equations can be formulated, see Fig. 26. The flux equation representing mass transfer from the gas phase to the interface is given by

$$N_i^{G-I} = k_{G,i}\rho_G\left(\omega_{G,i,I} - \omega_{G,i}\right). \tag{A.1}$$

Similarly, the flux equation representing mass transfer from the interface to the liquid phase is given by

$$N_i^{I-L} = k_{L,i}\rho_L\left(\omega_{L,i,I} - \omega_{L,i}\right). \tag{A.2}$$

In Eqs. (A.1) and (A.2), GLE is commonly assumed to prevail at the interface, i.e., $\omega_{G,i,I} = \omega^*_{G,i}$ and $\omega_{L,i,I} = \omega^*_{L,i}$. Thus,

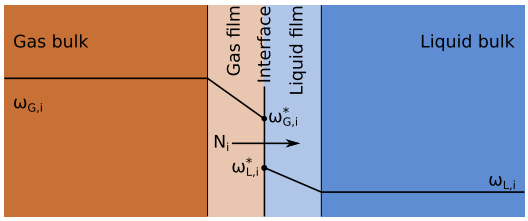

Fig. 26. An illustration of the two-film mass transfer model.

$$N_i^{G-I} = k_{G,i}\rho_G\left(\omega^*_{G,i} - \omega_{G,i}\right), \tag{A.3}$$

$$N_i^{I-L} = k_{L,i}\rho_L\left(\omega^*_{L,i} - \omega_{L,i}\right). \tag{A.4}$$

For infinitely diluted solute *i* in solvent *j*, Henry's law is given by Eq. (21). With Eq. (21), $\omega^*_{L,i}$ can be written

$$\omega^*_{L,i} = \frac{p}{H_{ij}}\frac{\overline{M}^*_{w,G}}{\overline{M}^*_{w,L}}\omega^*_{G,i}, \tag{A.5}$$

where the molar weight of the mixture is denoted $\overline{M}_w$. To represent $\overline{M}_w$ in terms of mass fractions, the conversion formula from mass fraction to mole fraction is given as

$$x_i = \frac{\omega_i/M_{w,i}}{\sum_{j=1}^{N_c}\omega_j/M_{w,j}}. \tag{A.6}$$

Hence, the molar weight of the mixture is given by

$$\overline{M}_w = \sum_{j=1}^{C} x_j M_{w,j} = \frac{1}{\sum_{j=1}^{C}\omega_j/M_{w,j}}. \tag{A.7}$$

By dividing Eq. (A.4) by $k_{L,i}\rho_L$, and utilizing Eq. (A.5), we obtain

$$\frac{N_i^{I-L}}{k_{L,i}\rho_L} = \frac{p}{H_{ij}}\frac{\overline{M}^*_{w,G}}{\overline{M}^*_{w,L}}\omega^*_{G,i} - \omega_{L,i}. \tag{A.8}$$

Next, Eq. (A.3) is divided by $k_{G,i}\rho_G\frac{H_{ij}}{p}\frac{\overline{M}^*_{w,L}}{\overline{M}^*_{w,G}}$:

$$\frac{N_i^{G-I}}{k_{G,i}\rho_G\frac{H_{ij}}{p}\frac{\overline{M}^*_{w,L}}{\overline{M}^*_{w,G}}} = \frac{p}{H_{ij}}\frac{\overline{M}^*_{w,G}}{\overline{M}^*_{w,L}}\left(\omega^*_{G,i} - \omega_{G,i}\right). \tag{A.9}$$

The mass transfer fluxes are now gathered into a single expression by recognizing that the fluxes are continuous through the interface, i.e., $N_i = N_i^{I-L} = -N_i^{G-I}$. Thus, by subtracting Eq. (A.9) from Eq. (A.8):

$$N_i\left(\frac{1}{k_{L,i}\rho_L} + \frac{1}{k_{G,i}\rho_G\frac{H_{ij}}{p}\frac{\overline{M}^*_{w,L}}{\overline{M}^*_{w,G}}}\right) = \frac{p}{H_{ij}}\frac{\overline{M}^*_{w,G}}{\overline{M}^*_{w,L}}\omega_{G,i} - \omega_{L,i}. \tag{A.10}$$

Due to the diffusivity coefficient being larger in the gas phase than in the liquid phase, the majority of the mass transfer resistance is on the liquid side of the phase boundary. Thus, the first term in the parenthesis on the left-hand side of Eq. (A.10) dominates. The second term in the parenthesis is therefore neglected. Furthermore, by assuming $\omega^*_{G,i} = \omega_{G,i}$, then $\overline{M}^*_{w,G}$ is obtained from Eq. (A.7) and $\overline{M}^*_{w,L}$ is obtained through

Eqs. (A.5) and (A.7). The resulting expression reads

$$N_i = k_{L,i}\rho_L\left(\frac{p}{H_{ij}}\frac{\overline{M}_{w,G}}{\overline{M}^*_{w,L}}\omega_{G,i} - \omega_{L,i}\right). \tag{A.11}$$

Appendix B. The pressure and its derivatives

The pressure is defined through the volume derivative of the Helmholtz energy potential:

$$p \equiv -\left(\frac{\partial \mathcal{A}}{\partial V}\right)_{T,\boldsymbol{N}}. \tag{B.1}$$

Furthermore, the Helmholtz energy potential can be split into the residual contribution and the ideal gas contribution:

$$\mathcal{A} = \mathcal{A}^{\mathrm{r,v}} + \mathcal{A}^{\mathrm{ig}}. \tag{B.2}$$

Employing Eq. (B.2) and noting that the derivative is a linear operator, Eq. (B.1) can equivalently be stated as

$$p = -\left(\frac{\partial \mathcal{A}^{\mathrm{r,v}}}{\partial V}\right)_{T,\boldsymbol{N}} - \left(\frac{\partial \mathcal{A}^{\mathrm{ig}}}{\partial V}\right)_{T,\boldsymbol{N}} = p^{\mathrm{r,v}} + p^{\mathrm{ig}}, \tag{B.3}$$

which yields

$$p = -\left(\frac{\partial \mathcal{A}^{\mathrm{r,v}}}{\partial V}\right)_{T,\boldsymbol{N}} + \frac{Nk_BT}{V} \tag{B.4}$$

With Eq. (B.4), the first derivatives in pressure are given as

$$\left(\frac{\partial p}{\partial T}\right)_{V,\boldsymbol{N}} = -\left(\frac{\partial \mathcal{A}^{\mathrm{r,v}}}{\partial T \partial V}\right)_{\boldsymbol{N}} + \frac{Nk_B}{V} \tag{B.5}$$

$$\left(\frac{\partial p}{\partial V}\right)_{T,\boldsymbol{N}} = -\left(\frac{\partial \mathcal{A}^{\mathrm{r,v}}}{\partial V^2}\right)_{T,\boldsymbol{N}} - \frac{Nk_BT}{V^2} \tag{B.6}$$

$$\left(\frac{\partial p}{\partial N_k}\right)_{T,V} = -\left(\frac{\partial \mathcal{A}^{\mathrm{r,v}}}{\partial V \partial N_k}\right)_{T} + \frac{k_BT}{V}. \tag{B.7}$$

Appendix C. The PC-SAFT EoS in Canonical Variables

In the PC-SAFT EoS, molecules are viewed as chains of hard spheres that interact. Initially, a number, $\bar{m}$, of hard spheres are given a reduced hard sphere Helmholtz energy, $\tilde{a}^{\mathrm{hs}}$. These hard sphere segments move closer by adding the reduced dispersive (attractive) Helmholtz energy, $\tilde{a}^{\mathrm{disp}}$. When the hard spheres are sufficiently close, they are assumed to form chains of segment length $\bar{m}$. The chain contribution to the reduced Helmholtz energy is denoted $\tilde{a}^{\mathrm{chain}}$. Ultimately, the molecules (hard chains) are given interaction sites where two or more molecules can associate (e.g., hydrogen bonding). The reduced associative Helmholtz energy is denoted $\tilde{a}^{\mathrm{assoc}}$.

The four different contributions are added to construct the reduced residual Helmholtz energy potential:

$$\tilde{a}^{\mathrm{r,v}}(T, v, \boldsymbol{x}) = \frac{\mathcal{A}^{\mathrm{r,v}}(T,V,\boldsymbol{N})}{Nk_BT} = \bar{m}\tilde{a}^{\mathrm{hs}} + \tilde{a}^{\mathrm{chain}} + \tilde{a}^{\mathrm{disp}} + \tilde{a}^{\mathrm{assoc}}, \tag{C.1}$$

where r, v denotes that the real fluid and the corresponding ideal gas are evaluated at the same temperature, T, volume, V, and vector of molecules, $\boldsymbol{N}$. Furthermore, $N = \sum_{i=1}^{C} N_i$ is the total number of molecules, $v = V/N$ is the molecular volume, and $\boldsymbol{x} = \boldsymbol{N}/N$ is the vector of mole fractions. $\mathcal{A}^{\mathrm{r,v}}$ denotes the extensive, residual Helmholtz energy potential.

The expression for $\tilde{a}^{\mathrm{r,v}}$ is given in Gross and Sadowski (2001). However, classical thermodynamic relations are defined through the derivatives of the $\mathcal{A}^{\mathrm{r,v}}$ and not $\tilde{a}^{\mathrm{r,v}}$. For instance:

$$S^{\mathrm{r,v}}(T,V,\boldsymbol{N}) \equiv -\left(\frac{\partial \mathcal{A}^{\mathrm{r,v}}}{\partial T}\right)_{V,\boldsymbol{N}}, \tag{C.2}$$

$$p^{\mathrm{r,v}}(T,V,\boldsymbol{N}) \equiv -\left(\frac{\partial \mathcal{A}^{\mathrm{r,v}}}{\partial V}\right)_{T,\boldsymbol{N}}, \tag{C.3}$$

$$\mu_i^{\mathrm{r,v}}(T,V,\boldsymbol{n}) \equiv \left(\frac{\partial \mathcal{A}^{\mathrm{r,v}}}{\partial n_i}\right)_{T,V,n_{j\neq i}} = N_A\left(\frac{\partial \mathcal{A}^{\mathrm{r,v}}}{\partial N_i}\right)_{T,V,N_{j\neq i}}. \tag{C.4}$$

Rewriting Eqs. (C.2), (C.3), and (C.4) in terms of $\tilde{a}^{\mathrm{r,v}}$ is a complicated task, both in terms of thermodynamic understanding and mathematical complexity. Here, we rewrite the expressions given by Gross and Sadowski (2001) in terms of the $\mathcal{A}^{\mathrm{r,v}}$ by multiplying Eq. (C.1) by Nk_BT. The resulting expression reads:

$$\mathcal{A}^{\mathrm{r,v}} = \bar{m}\mathcal{A}^{\mathrm{hs}} + \mathcal{A}^{\mathrm{chain}} + \mathcal{A}^{\mathrm{disp}} + \mathcal{A}^{\mathrm{assoc}}, \tag{C.5}$$

$$\mathcal{A}^{\mathrm{hs}}(T,V,\boldsymbol{N}) = \frac{Nk_BT}{\xi_0}\left[\frac{3\xi_1\xi_2}{1-\xi_3} + \frac{\xi_2^3}{\xi_3(1-\xi_3)^2} + \left(\frac{\xi_2^3}{\xi_3^2} - \xi_0\right)\ln(1-\xi_3)\right] \tag{C.6}$$

$$\mathcal{A}^{\mathrm{chain}}(T,V,\boldsymbol{N}) = -k_BT\sum_{i=1}^{C} N_i(m_i-1)\ln g_{ii}^{\mathrm{hs}}, \tag{C.7}$$

$$\mathcal{A}^{\mathrm{disp}}(T,V,\boldsymbol{N}) = \mathcal{A}_1 + \mathcal{A}_2, \tag{C.8}$$

$$\mathcal{A}_1(T,V,\boldsymbol{N}) = -\frac{2\pi k_BT}{V} I_1 \sum_{i=1}^{C}\sum_{j=1}^{C} N_iN_jm_im_j\left(\frac{\varepsilon_{ij}}{k_BT}\right)\sigma_{ij}^3, \tag{C.9}$$

$$\mathcal{A}_2(T,V,\boldsymbol{N}) = -\frac{\pi k_BT}{V}\bar{m}C_1I_2\sum_{i=1}^{C}\sum_{j=1}^{C} N_iN_jm_im_j\left(\frac{\varepsilon_{ij}}{k_BT}\right)^2\sigma_{ij}^3. \tag{C.10}$$

The additional relations are given by

$$\bar{m}(\boldsymbol{N}) = \sum_{i=1}^{C} x_im_i \tag{C.11}$$

$$d_i(T) = \sigma_i\left[1 - 0.12\exp\left(-3\frac{\varepsilon_i}{k_BT}\right)\right] \tag{C.12}$$

$$\xi_n(T,V,\boldsymbol{N}) = \frac{\pi}{6V}\sum_{i=1}^{C} N_im_id_i^n, \tag{C.13}$$

$$g_{ij}^{\mathrm{hs}}(T,V,\boldsymbol{N}) = \frac{1}{1-\xi_3} + \frac{d_id_j}{d_i+d_j}\frac{3\xi_2}{(1-\xi_3)^2} + \left(\frac{d_id_j}{d_i+d_j}\right)^2\frac{2\xi_2^2}{(1-\xi_3)^3} \tag{C.14}$$

$$C_1(T,V,\boldsymbol{N}) = \left[1 + \bar{m}\frac{8\xi_3 - 2\xi_3^2}{(1-\xi_3)^4} + (1-\bar{m})\frac{20\xi_3 - 27\xi_3^2 + 12\xi_3^3 - 2\xi_3^4}{(1-\xi_3)^2(2-\xi_3)^2}\right]^{-1} \tag{C.15}$$

$$I_1(T,V,\boldsymbol{N}) = \sum_{i=0}^{6} a_i\xi_3^i \tag{C.16}$$

$$I_2(T,V,\boldsymbol{N}) = \sum_{i=0}^{6} b_i\xi_3^i \tag{C.17}$$

$$a_i(\boldsymbol{N}) = a_{0i} + \frac{\bar{m}-1}{\bar{m}}a_{1i} + \frac{\bar{m}-1}{\bar{m}}\frac{\bar{m}-2}{\bar{m}}a_{2i} \tag{C.18}$$

$$b_i(\boldsymbol{N}) = b_{0i} + \frac{\bar{m}-1}{\bar{m}}b_{1i} + \frac{\bar{m}-1}{\bar{m}}\frac{\bar{m}-2}{\bar{m}}b_{2i} \tag{C.19}$$

$$\sigma_{ij} = \frac{1}{2}(\sigma_i + \sigma_j) \tag{C.20}$$

$$\varepsilon_{ij} = \sqrt{\varepsilon_i \varepsilon_j}(1 - k_{ij}) \tag{C.21}$$

C.1. Derivatives concerning T

For a generic function $f_i(x, y, \boldsymbol{z})$, we use the shorthand notation for its partial derivative:

$$f_{ix} = \left(\frac{\partial f_i}{\partial x}\right)_{y,\boldsymbol{z}}. \tag{C.22}$$

Employing Eq. (C.22), we write the temperature derivative of Eqs. (C.5), (C.6), (C.7), (C.9), (C.10), (C.11), (C.12), (C.13), (C.14), (C.15), (C.16), (C.17), (C.18), (C.19) as

$$\mathcal{A}_T^{\mathrm{r,v}} = \bar{m}\mathcal{A}_T^{\mathrm{hs}} + \mathcal{A}_T^{\mathrm{chain}} + \mathcal{A}_{1T} + \mathcal{A}_{2T}, \tag{C.23}$$

$$\begin{aligned}\mathcal{A}_T^{\mathrm{hs}} = {} & \frac{\mathcal{A}^{\mathrm{hs}}}{T} + \frac{Nk_BT}{\xi_0}\left[\frac{3\xi_{1T}\xi_2}{1-\xi_3} + \frac{3\xi_1\xi_{2T}}{1-\xi_3} + \frac{3\xi_1\xi_2\xi_{3T}}{(1-\xi_3)^2}\right. \\ & + \frac{3\xi_2^2\xi_{2T}}{\xi_3(1-\xi_3)^2} - \frac{\xi_2^3\xi_{3T}}{\xi_3^2(1-\xi_3)^2} + \frac{2\xi_2^3\xi_{3T}}{\xi_3(1-\xi_3)^3} \\ & \left. + \left(\frac{3\xi_2^2\xi_{2T}}{\xi_3^2} - \frac{2\xi_2^3\xi_{3T}}{\xi_3^3}\right)\ln(1-\xi_3) - \left(\frac{\xi_2^3}{\xi_3^2} - \xi_0\right)\frac{\xi_{3T}}{1-\xi_3}\right]\end{aligned} \tag{C.24}$$

$$\mathcal{A}_T^{\mathrm{chain}} = \frac{\mathcal{A}^{\mathrm{chain}}}{T} - k_BT\sum_{i=1}^{C} N_i(m_i - 1)\frac{g_{iiT}^{\mathrm{hs}}}{g_{ii}^{\mathrm{hs}}} \tag{C.25}$$

$$\mathcal{A}_{1T} = \frac{I_{1T}}{I_1}\mathcal{A}_1 \tag{C.26}$$

$$\mathcal{A}_{2T} = -\frac{\mathcal{A}_2}{T} + \frac{C_{1T}}{C_1}\mathcal{A}_2 + \frac{I_{2T}}{I_2}\mathcal{A}_2 \tag{C.27}$$

Furthermore, the derivatives concerning T of the additional relations are

$$d_{iT} = \frac{3\varepsilon_i}{k_BT^2}(d_i - \sigma_i), \tag{C.28}$$

$$\xi_{nT} = \frac{\pi}{6V}\sum_{i=1}^{C} N_i m_i n d_i^{n-1} d_{iT} \tag{C.29}$$

$$\begin{aligned}g_{ijT}^{\mathrm{hs}} = {} & \frac{\xi_{3T}}{(1-\xi_3)^2} \\ & + \left[\frac{d_{iT}d_j}{d_i+d_j} + \frac{d_id_{jT}}{d_i+d_j} - \frac{d_id_jd_{iT}}{(d_i+d_j)^2} - \frac{d_id_jd_{jT}}{(d_i+d_j)^2}\right]\frac{3\xi_2}{(1-\xi_3)^2} \\ & + \frac{d_id_j}{d_i+d_j}\left[\frac{3\xi_{2T}}{(1-\xi_3)^2} + \frac{6\xi_2\xi_{3T}}{(1-\xi_3)^3}\right] \\ & + \frac{d_id_j}{d_i+d_j}\left[\frac{d_{iT}d_j}{d_i+d_j} + \frac{d_id_{jT}}{d_i+d_j} - \frac{d_id_jd_{iT}}{(d_i+d_j)^2} - \frac{d_id_jd_{jT}}{(d_i+d_j)^2}\right]\frac{4\xi_2^2}{(1-\xi_3)^3} \\ & + \left(\frac{d_id_j}{d_i+d_j}\right)^2\left[\frac{4\xi_2\xi_{2T}}{(1-\xi_3)^3} + \frac{6\xi_2^2\xi_{3T}}{(1-\xi_3)^4}\right]\end{aligned} \tag{C.30}$$

$$\begin{aligned}C_{1T} = {} & -C_1^2\left[4\bar{m}\xi_{3T}\left(\frac{2-\xi_3}{(1-\xi_3)^4} + \frac{8\xi_3 - 2\xi_3^2}{(1-\xi_3)^5}\right)\right. \\ & + 2\xi_{3T}(1-\bar{m})\left(\frac{10 - 27\xi_3 + 18\xi_3^2 - 4\xi_3^3}{(1-\xi_3)^2(2-\xi_3)^2}\right. \\ & \left.\left. + \frac{20\xi_3 - 27\xi_3^2 + 12\xi_3^3 - 2\xi_3^4}{(1-\xi_3)^3(2-\xi_3)^2} + \frac{20\xi_3 - 27\xi_3^2 + 12\xi_3^3 - 2\xi_3^4}{(1-\xi_3)^2(2-\xi_3)^3}\right)\right]\end{aligned} \tag{C.31}$$

$$I_{1T} = \sum_{i=0}^{6} i a_i \xi_3^{i-1}\xi_{3T} \tag{C.32}$$

$$I_{2T} = \sum_{i=0}^{6} i b_i \xi_3^{i-1}\xi_{3T} \tag{C.33}$$

C.2. Derivatives concerning V

$$\mathcal{A}_V^{\mathrm{r,v}} = \bar{m}\mathcal{A}_V^{\mathrm{hs}} + \mathcal{A}_V^{\mathrm{chain}} + \mathcal{A}_{1V} + \mathcal{A}_{2V}, \tag{C.34}$$

$$\begin{aligned}\mathcal{A}_V^{\mathrm{hs}} = {} & -\frac{\xi_{0V}}{\xi_0}\mathcal{A}^{\mathrm{hs}} + \frac{Nk_BT}{\xi_0}\left[\frac{3\xi_{1V}\xi_2}{1-\xi_3} + \frac{3\xi_1\xi_{2V}}{1-\xi_3} + \frac{3\xi_1\xi_2\xi_{3V}}{(1-\xi_3)^2}\right. \\ & + \frac{3\xi_2^2\xi_{2V}}{\xi_3(1-\xi_3)^2} - \frac{\xi_2^3\xi_{3V}}{\xi_3^2(1-\xi_3)^2} + \frac{2\xi_2^3\xi_{3V}}{\xi_3(1-\xi_3)^3} \\ & \left. + \left(\frac{3\xi_2^2\xi_{2V}}{\xi_3^2} - \frac{2\xi_2^3\xi_{3V}}{\xi_3^3} - \xi_{0V}\right)\ln(1-\xi_3) - \left(\frac{\xi_2^3}{\xi_3^2} - \xi_0\right)\frac{\xi_{3V}}{1-\xi_3}\right],\end{aligned} \tag{C.35}$$

$$\mathcal{A}_V^{\mathrm{chain}} = -k_BT\sum_{i=1}^{C} N_i(m_i - 1)\frac{g_{iiV}^{\mathrm{hs}}}{g_{ii}^{\mathrm{hs}}}, \tag{C.36}$$

$$\mathcal{A}_{1V} = -\frac{\mathcal{A}_1}{V} + \frac{I_{1V}}{I_1}\mathcal{A}_1, \tag{C.37}$$

$$\mathcal{A}_{2V} = -\frac{\mathcal{A}_2}{V} + \frac{C_{1V}}{C_1}\mathcal{A}_2 + \frac{I_{2V}}{I_2}\mathcal{A}_2. \tag{C.38}$$

Furthermore, the derivatives concerning V of the additional relations are

$$\xi_{nV} = -\frac{\xi_n}{V} \tag{C.39}$$

$$\begin{aligned}g_{ijV}^{\mathrm{hs}} = {} & \frac{\xi_{3V}}{(1-\xi_3)^2} + \frac{d_id_j}{d_i+d_j}\left[\frac{3\xi_{2V}}{(1-\xi_3)^2} + \frac{6\xi_2\xi_{3V}}{(1-\xi_3)^3}\right] \\ & + \left(\frac{d_id_j}{d_i+d_j}\right)^2\left[\frac{4\xi_2\xi_{2V}}{(1-\xi_3)^3} + \frac{6\xi_2^2\xi_{3V}}{(1-\xi_3)^4}\right]\end{aligned} \tag{C.40}$$

$$\begin{aligned}C_{1V} = {} & -C_1^2\left[4\bar{m}\xi_{3V}\left(\frac{2-\xi_3}{(1-\xi_3)^4} + \frac{8\xi_3 - 2\xi_3^2}{(1-\xi_3)^5}\right)\right. \\ & + 2\xi_{3V}(1-\bar{m})\left(\frac{10 - 27\xi_3 + 18\xi_3^2 - 4\xi_3^3}{(1-\xi_3)^2(2-\xi_3)^2}\right. \\ & \left.\left. + \frac{20\xi_3 - 27\xi_3^2 + 12\xi_3^3 - 2\xi_3^4}{(1-\xi_3)^3(2-\xi_3)^2} + \frac{20\xi_3 - 27\xi_3^2 + 12\xi_3^3 - 2\xi_3^4}{(1-\xi_3)^2(2-\xi_3)^3}\right)\right]\end{aligned} \tag{C.41}$$

$$I_{1V} = \sum_{i=0}^{6} i a_i \xi_3^{i-1}\xi_{3V} \tag{C.42}$$

$$I_{2V} = \sum_{i=0}^{6} i b_i \xi_3^{i-1} \xi_{3V} \tag{C.43}$$

C.3. Derivatives concerning N_k

$$\mathcal{A}_k^{\mathrm{r,v}} = \bar{m}\mathcal{A}_k^{\mathrm{hs}} + \mathcal{A}^{\mathrm{hs}}\bar{m}_k + \mathcal{A}_k^{\mathrm{chain}} + \mathcal{A}_{1k} + \mathcal{A}_{2k}, \tag{C.44}$$

$$\begin{aligned}\mathcal{A}_k^{\mathrm{hs}} = {} & \frac{\mathcal{A}^{\mathrm{hs}}}{N} - \frac{\xi_{0k}}{\xi_0}\mathcal{A}^{\mathrm{hs}} + \frac{Nk_BT}{\xi_0}\left[\frac{3\xi_{1k}\xi_2}{1-\xi_3} + \frac{3\xi_1\xi_{2k}}{1-\xi_3} + \frac{3\xi_1\xi_2\xi_{3k}}{(1-\xi_3)^2}\right. \\ & + \frac{3\xi_2^2\xi_{2k}}{\xi_3(1-\xi_3)^2} - \frac{\xi_2^3\xi_{3k}}{\xi_3^2(1-\xi_3)^2} + \frac{2\xi_2^3\xi_{3k}}{\xi_3(1-\xi_3)^3} \\ & \left. + \left(\frac{3\xi_2^2\xi_{2k}}{\xi_3^2} - \frac{2\xi_2^3\xi_{3k}}{\xi_3^3} - \xi_{0k}\right)\ln(1-\xi_3) - \left(\frac{\xi_2^3}{\xi_3^2} - \xi_0\right)\frac{\xi_{3k}}{1-\xi_3}\right],\end{aligned} \tag{C.45}$$

$$\mathcal{A}_k^{\mathrm{chain}} = -k_BT(m_k-1)\ln g_{kk}^{\mathrm{hs}} - k_BT\sum_{i=1}^{C} N_i(m_i-1)\frac{g_{ik}^{\mathrm{hs}}}{g_{ii}^{\mathrm{hs}}}, \tag{C.46}$$

$$\mathcal{A}_{1k} = \frac{I_{1k}}{I_1}\mathcal{A}_1 - \frac{4\pi k_BT}{V}I_1\sum_{i=1}^{C} N_i m_i m_k\left(\frac{\varepsilon_{ik}}{k_BT}\right)\sigma_{ik}^3, \tag{C.47}$$

$$\begin{aligned}\mathcal{A}_{2k} = {} & \frac{\bar{m}_k}{\bar{m}}\mathcal{A}_2 + \frac{C_{1k}}{C_1}\mathcal{A}_2 + \frac{I_{2k}}{I_2}\mathcal{A}_2 \\ & - \frac{2\pi k_BT}{V}\bar{m}C_1I_2\sum_{i=1}^{C} N_i m_i m_k\left(\frac{\varepsilon_{ik}}{k_BT}\right)^2\sigma_{ik}^3,\end{aligned} \tag{C.48}$$

Furthermore, the derivatives concerning N_k of the additional relations are

$$\bar{m}_k = \frac{m_k - \bar{m}}{N} \tag{C.49}$$

$$\xi_{nk} = \frac{\pi}{6V} m_k d_k^n \tag{C.50}$$

$$\begin{aligned}g_{ijk}^{\mathrm{hs}} = {} & \frac{\xi_{3k}}{(1-\xi_3)^2} + \frac{d_id_j}{d_i+d_j}\left[\frac{3\xi_{2k}}{(1-\xi_3)^2} + \frac{6\xi_2\xi_{3k}}{(1-\xi_3)^3}\right] \\ & + \left(\frac{d_id_j}{d_i+d_j}\right)^2\left[\frac{4\xi_{2k}\xi_{2k}}{(1-\xi_3)^3} + \frac{6\xi_2^2\xi_{3k}}{(1-\xi_3)^4}\right]\end{aligned} \tag{C.51}$$

$$\begin{aligned}C_{1k} = {} & -C_1^2\left[4\bar{m}\xi_{3k}\left(\frac{2-\xi_3}{(1-\xi_3)^4} + \frac{8\xi_3 - 2\xi_3^2}{(1-\xi_3)^5}\right)\right. \\ & + 2\xi_{3k}(1-\bar{m})\left(\frac{10 - 27\xi_3 + 18\xi_3^2 - 4\xi_3^3}{(1-\xi_3)^2(2-\xi_3)^2}\right. \\ & \left. + \frac{20\xi_3 - 27\xi_3^2 + 12\xi_3^3 - 2\xi_3^4}{(1-\xi_3)^3(2-\xi_3)^2} + \frac{20\xi_3 - 27\xi_3^2 + 12\xi_3^3 - 2\xi_3^4}{(1-\xi_3)^2(2-\xi_3)^3}\right) \\ & \left. + 2\bar{m}_k\frac{4\xi_3 - \xi_3^2}{(1-\xi_3)^4} - \bar{m}_k\frac{20\xi_3 - 27\xi_3^2 + 12\xi_3^3 - 2\xi_3^4}{(1-\xi_3)^2(2-\xi_3)^2}\right]\end{aligned} \tag{C.52}$$

$$I_{1k} = \sum_{i=0}^{6}\left[a_{ik}\xi_3^i + i a_i \xi_3^{i-1}\xi_{3k}\right] \tag{C.53}$$

$$I_{2k} = \sum_{i=0}^{6}\left[b_{ik}\xi_3^i + i b_i \xi_3^{i-1}\xi_{3k}\right] \tag{C.54}$$

$$a_{ik} = \frac{\bar{m}_k}{\bar{m}^2}a_{1i} + \left(\frac{3\bar{m}_k}{\bar{m}^2} - \frac{4\bar{m}_k}{\bar{m}^3}\right)a_{2i} \tag{C.55}$$

$$b_{ik} = \frac{\bar{m}_k}{\bar{m}^2}b_{1i} + \left(\frac{3\bar{m}_k}{\bar{m}^2} - \frac{4\bar{m}_k}{\bar{m}^3}\right)b_{2i} \tag{C.56}$$

C.4. Derivatives concerning V, V

$$\mathcal{A}_{VV}^{\mathrm{r,v}} = \bar{m}\mathcal{A}_{VV}^{\mathrm{hs}} + \mathcal{A}_{VV}^{\mathrm{chain}} + \mathcal{A}_{1VV} + \mathcal{A}_{2VV}, \tag{C.57}$$

$$\begin{aligned}\mathcal{A}_{VV}^{\mathrm{hs}} = {} & -\frac{\xi_{0VV}}{\xi_0}\mathcal{A}^{\mathrm{hs}} - 2\frac{\xi_{0V}}{\xi_0}\mathcal{A}_V^{\mathrm{hs}} + \frac{Nk_BT}{\xi_0}\left[\frac{3\xi_{1VV}\xi_2}{1-\xi_3} + \frac{6\xi_{1V}\xi_{2V}}{1-\xi_3}\right. \\ & + \frac{6\xi_{1V}\xi_2\xi_{3V}}{(1-\xi_3)^2} + \frac{3\xi_1\xi_{2VV}}{1-\xi_3} + \frac{6\xi_1\xi_{2V}\xi_{3V}}{(1-\xi_3)^2} + \frac{3\xi_1\xi_2\xi_{3VV}}{(1-\xi_3)^2} + \frac{6\xi_1\xi_2\xi_{3V}^2}{(1-\xi_3)^3} \\ & + \frac{6\xi_2\xi_{2V}^2}{\xi_3(1-\xi_3)^2} + \frac{3\xi_2^2\xi_{2VV}}{\xi_3(1-\xi_3)^2} - \frac{6\xi_2^2\xi_{2V}\xi_{3V}}{\xi_3^2(1-\xi_3)^2} + \frac{12\xi_2^2\xi_{2V}\xi_{3V}}{\xi_3(1-\xi_3)^3} \\ & - \frac{\xi_2^3\xi_{3VV}}{\xi_3^2(1-\xi_3)^2} + \frac{2\xi_2^3\xi_{3V}^2}{\xi_3^3(1-\xi_3)^2} - \frac{4\xi_2^3\xi_{3V}^2}{\xi_3^2(1-\xi_3)^3} + \frac{2\xi_2^3\xi_{3VV}}{\xi_3(1-\xi_3)^3} \\ & + \frac{6\xi_2^3\xi_{3V}^2}{\xi_3(1-\xi_3)^4} + \left(\frac{6\xi_2\xi_{2V}^2}{\xi_3^2} + \frac{3\xi_2^2\xi_{2VV}}{\xi_3^2} - \frac{12\xi_2^2\xi_{2V}\xi_{3V}}{\xi_3^3} - \frac{2\xi_2^3\xi_{3VV}}{\xi_3^3}\right. \\ & \left. + \frac{6\xi_2^3\xi_{3V}^2}{\xi_3^4} - \xi_{0VV}\right)\ln(1-\xi_3) - 2\left(\frac{3\xi_2^2\xi_{2V}}{\xi_3^2} - \frac{2\xi_2^3\xi_{3V}}{\xi_3^3}\right. \\ & \left.\left. - \xi_{0V})\frac{\xi_{3V}}{1-\xi_3} - \left(\frac{\xi_2^3}{\xi_3^2} - \xi_0\right)\left(\frac{\xi_{3VV}}{1-\xi_3} + \frac{\xi_{3V}^2}{(1-\xi_3)^2}\right)\right],\end{aligned} \tag{C.58}$$

$$\mathcal{A}_{VV}^{\mathrm{chain}} = -k_BT\sum_{i=1}^{C} N_i(m_i-1)\left[\frac{g_{iiVV}^{\mathrm{hs}}}{g_{ii}^{\mathrm{hs}}} - \left(\frac{g_{iiV}^{\mathrm{hs}}}{g_{ii}^{\mathrm{hs}}}\right)^2\right] \tag{C.59}$$

$$\mathcal{A}_{1VV} = 2\frac{\mathcal{A}_1}{V^2} - 2\frac{I_{1V}}{I_1V}\mathcal{A}_1 + \frac{I_{1VV}}{I_1}\mathcal{A}_1, \tag{C.60}$$

$$\begin{aligned}\mathcal{A}_{2VV} = {} & 2\frac{\mathcal{A}_2}{V^2} - 2\frac{C_{1V}}{C_1V}\mathcal{A}_2 - 2\frac{I_{2V}}{I_2V}\mathcal{A}_2 + 2\frac{C_{1V}}{C_1}\frac{I_{2V}}{I_2}\mathcal{A}_2 + \frac{C_{1VV}}{C_1}\mathcal{A}_2 \\ & + \frac{I_{2VV}}{I_2}\mathcal{A}_2\end{aligned} \tag{C.61}$$

Furthermore, the derivatives concerning V, V of the additional relations are

$$\xi_{nVV} = 2\frac{\xi_n}{V^2} \tag{C.62}$$

$$\begin{aligned}g_{ijVV}^{\mathrm{hs}} = {} & \frac{\xi_{3VV}}{(1-\xi_3)^2} + \frac{2\xi_{3V}^2}{(1-\xi_3)^3} \\ & + \frac{d_id_j}{d_i+d_j}\left[\frac{3\xi_{2VV}}{(1-\xi_3)^2} + \frac{12\xi_{2V}\xi_{3V}}{(1-\xi_3)^3} + \frac{6\xi_2\xi_{3VV}}{(1-\xi_3)^3} + \frac{18\xi_2\xi_{3V}^2}{(1-\xi_3)^4}\right] \\ & + \left(\frac{d_id_j}{d_i+d_j}\right)^2\left[\frac{4\xi_{2V}^2}{(1-\xi_3)^3} + \frac{4\xi_2\xi_{2VV}}{(1-\xi_3)^3} + \frac{24\xi_2\xi_{2V}\xi_{3V}}{(1-\xi_3)^4}\right. \\ & \left. + \frac{6\xi_2^2\xi_{3VV}}{(1-\xi_3)^4} + \frac{24\xi_2^2\xi_{3V}^2}{(1-\xi_3)^5}\right]\end{aligned} \tag{C.63}$$

$$C_{1VV} = \frac{2C_{1V}^2}{C_1} - C_1^2\left[4\bar{m}\xi_{3VV}\left(\frac{2-\xi_3}{(1-\xi_3)^4}+\frac{8\xi_3-2\xi_3^2}{(1-\xi_3)^5}\right)\right.$$
$$+4\bar{m}\xi_{3V}^2\left(-\frac{1}{(1-\xi_3)^4}+8\frac{2-\xi_3}{(1-\xi_3)^5}+5\frac{8\xi_3-2\xi_3^2}{(1-\xi_3)^6}\right)$$
$$+2\xi_{3VV}(1-\bar{m})\left(\frac{10-27\xi_3+18\xi_3^2-4\xi_3^3}{(1-\xi_3)^2(2-\xi_3)^2}\right.$$
$$\left.+\frac{20\xi_3-27\xi_3^2+12\xi_3^3-2\xi_3^4}{(1-\xi_3)^3(2-\xi_3)^2}+\frac{20\xi_3-27\xi_3^2+12\xi_3^3-2\xi_3^4}{(1-\xi_3)^2(2-\xi_3)^3}\right)$$
$$+2\xi_{3V}^2(1-\bar{m})\left(\frac{-27+36\xi_3-12\xi_3^2}{(1-\xi_3)^2(2-\xi_3)^2}\right.$$
$$+2\frac{20-54\xi_3+36\xi_3^2-8\xi_3^3}{(1-\xi_3)^3(2-\xi_3)^2}+2\frac{20-54\xi_3+36\xi_3^2-8\xi_3^3}{(1-\xi_3)^2(2-\xi_3)^3}$$
$$+3\frac{20\xi_3-27\xi_3^2+12\xi_3^3-2\xi_3^4}{(1-\xi_3)^4(2-\xi_3)^2}+3\frac{20\xi_3-27\xi_3^2+12\xi_3^3-2\xi_3^4}{(1-\xi_3)^2(2-\xi_3)^4}$$
$$\left.\left.+4\frac{20\xi_3-27\xi_3^2+12\xi_3^3-2\xi_3^4}{(1-\xi_3)^3(2-\xi_3)^3}\right)\right] \tag{C.64}$$

$$I_{1VV} = \sum_{i=0}^{6} i a_i\left[(i-1)\xi_3^{i-2}\xi_{3V}^2+\xi_3^{i-1}\xi_{3VV}\right] \tag{C.65}$$

$$I_{2VV} = \sum_{i=0}^{6} i b_i\left[(i-1)\xi_3^{i-2}\xi_{3V}^2+\xi_3^{i-1}\xi_{3VV}\right] \tag{C.66}$$

C.5. Derivatives concerning V, N_k

$$\mathcal{A}_{Vk}^{\mathrm{r,v}} = \bar{m}\mathcal{A}_{Vk}^{\mathrm{hs}} + \mathcal{A}_V^{\mathrm{hs}}\bar{m}_k + \mathcal{A}_{Vk}^{\mathrm{chain}} + \mathcal{A}_{1Vk} + \mathcal{A}_{2Vk}, \tag{C.67}$$

$$\mathcal{A}_{Vk}^{\mathrm{hs}} = \left(\frac{1}{N}-\frac{\xi_{0k}}{\xi_0}\right)\mathcal{A}_V^{\mathrm{hs}} - \frac{\xi_0 V}{\xi_0}\mathcal{A}_k^{\mathrm{hs}} + \left(\frac{\xi_0 V}{Nt\xi_0}-\frac{\xi_{0Vk}}{\xi_0}\right)\mathcal{A}^{\mathrm{hs}}$$
$$+\frac{Nk_BT}{\xi_0}\left[\frac{6\xi_2^3\xi_{3V}\xi_{3k}}{\xi_3(1-\xi_3)^4}+\frac{6\xi_2^2\xi_{2V}\xi_{3k}}{\xi_3(1-\xi_3)^3}+\frac{2\xi_2^3\xi_{3V}\xi_{3k}}{\xi_3^3(1-\xi_3)^2}-\frac{4\xi_2^3\xi_{3V}\xi_{3k}}{\xi_3^2(1-\xi_3)^3}\right.$$
$$-\frac{3\xi_2^2\xi_{2k}\xi_{3V}}{\xi_3^2(1-\xi_3)^2}+\frac{6\xi_2^2\xi_{2k}\xi_{3V}}{\xi_3(1-\xi_3)^3}-\frac{3\xi_2^2\xi_{2V}\xi_{3k}}{\xi_3^2(1-\xi_3)^2}+\frac{6\xi_1\xi_2\xi_{3V}\xi_{3k}}{(1-\xi_3)^3}$$
$$+\frac{6\xi_2\xi_{2V}\xi_{2k}}{\xi_3(1-\xi_3)^2}+\left(\frac{6\xi_2\xi_{2V}\xi_{2k}}{\xi_3^2}+\frac{3\xi_2^2\xi_{2Vk}}{\xi_3^2}-\frac{6\xi_2^2\xi_{2k}\xi_{3V}}{\xi_3^3}\right.$$
$$\left.-\frac{6\xi_2^2\xi_{2V}\xi_{3k}}{\xi_3^3}-\frac{2\xi_2^3\xi_{3Vk}}{\xi_3^3}+\frac{6\xi_2^3\xi_{3V}\xi_{3k}}{\xi_3^4}-\xi_{0Vk}\right)\ln(1-\xi_3)$$
$$-\left(\frac{3\xi_2^2\xi_{2V}}{\xi_3^2}-\frac{2\xi_2^3\xi_3 V}{\xi_3^3}-\xi_{0V}\right)\frac{\xi_{3k}}{1-\xi_3}+\frac{3\xi_{1k}\xi_{2V}}{1-\xi_3}+\frac{3\xi_{1Vk}\xi_2}{1-\xi_3}$$
$$+\frac{3\xi_1\xi_{2Vk}}{1-\xi_3}+\frac{3\xi_{1V}\xi_{2k}}{1-\xi_3}-\left(\frac{\xi_2^3}{\xi_3^2}-\xi_0\right)\left(\frac{\xi_{3Vk}}{1-\xi_3}+\frac{\xi_{3V}\xi_{3k}}{(1-\xi_3)^2}\right)$$
$$+\frac{2\xi_2^3\xi_{3Vk}}{\xi_3(1-\xi_3)^3}-\frac{\xi_2^3\xi_{3Vk}}{\xi_3^2(1-\xi_3)^2}+\frac{3\xi_1\xi_2\xi_{3Vk}}{(1-\xi_3)^2}+\frac{3\xi_2^2\xi_{2Vk}}{\xi_3(1-\xi_3)^2}$$
$$+\frac{3\xi_{1k}\xi_2\xi_{3V}}{(1-\xi_3)^2}+\frac{3\xi_1\xi_{2k}\xi_{3V}}{(1-\xi_3)^2}+\frac{3\xi_{1V}\xi_2\xi_{3k}}{(1-\xi_3)^2}+\frac{3\xi_1\xi_2 V\xi_{3k}}{(1-\xi_3)^2}$$
$$\left.-\left(\frac{3\xi_2^2\xi_{2k}}{\xi_3^2}-\frac{2\xi_2^3\xi_{3k}}{\xi_3^3}-\xi_{0k}\right)\frac{\xi_{3V}}{1-\xi_3}\right], \tag{C.68}$$

$$\mathcal{A}_{Vk}^{\mathrm{chain}} = -k_BT(m_k-1)\frac{g_{kkV}^{\mathrm{hs}}}{g_{kk}^{\mathrm{hs}}}$$
$$-k_BT\sum_{i=1}^{C}Ni(m_i-1)\left(\frac{g_{iiVk}^{\mathrm{hs}}}{g_{ii}^{\mathrm{hs}}}-\frac{g_{iiV}^{\mathrm{hs}}g_{iik}^{\mathrm{hs}}}{(g_{ii}^{\mathrm{hs}})^2}\right) \tag{C.69}$$

$$\mathcal{A}_{1Vk} = \frac{I_{1k}}{I_1}\mathcal{A}_{1V} + \left(\frac{I_{1V}}{I_1}-\frac{1}{V}\right)\mathcal{A}_{1k} + \left(\frac{I_{1Vk}}{I_1}-2\frac{I_{1V}I_{1k}}{I_1^2}+\frac{I_{1k}}{VI_1}\right)\mathcal{A}_1 \tag{C.70}$$

$$\mathcal{A}_{2Vk} = \left(\frac{\bar{m}_k}{\bar{m}}+\frac{C_{1k}}{C_1}+\frac{I_{2k}}{I_2}\right)\mathcal{A}_{2V} + \left(\frac{C_{1V}}{C_1}+\frac{I_{2V}}{I_2}-\frac{1}{V}\right)\mathcal{A}_{2k}$$
$$+\left[\frac{C_{1Vk}}{C_1}-\frac{C_{1V}C_{1k}}{C_1^2}+\frac{I_{2Vk}}{I_2}-\frac{I_{2V}I_{2k}}{I_2^2}\right.$$
$$\left.-\left(\frac{\bar{m}_k}{\bar{m}}+\frac{C_{1k}}{C_1}+\frac{I_{2k}}{I_2}\right)\left(\frac{C_{1V}}{C_1}+\frac{I_{2V}}{I_2}-\frac{1}{V}\right)\right]\mathcal{A}_2 \tag{C.71}$$

Furthermore, the derivatives concerning V, N_k of the additional relations are

$$\xi_{nVk} = -\frac{\pi}{6V^2}m_k d_k^n \tag{C.72}$$

$$g_{ijVk}^{\mathrm{hs}} = 2\frac{\xi_{3k}}{1-\xi_3}g_{ijV}^{\mathrm{hs}} + 2\frac{\xi_{3V}}{1-\xi_3}g_{ijk}^{\mathrm{hs}} - 2\frac{\xi_{3V}\xi_{3k}}{(1-\xi_3)^2}g_{ij}^{\mathrm{hs}} + \frac{\xi_{3Vk}}{(1-\xi_3)^2}$$
$$+\frac{d_id_j}{d_i+d_j}\left[3\frac{\xi_{2Vk}}{(1-\xi_3)^2}+6\frac{\xi_2\xi_{3Vk}}{(1-\xi_3)^3}\right]$$
$$+\left(\frac{d_id_j}{d_i+d_j}\right)^2\left[4\frac{\xi_{2V}\xi_{2k}}{(1-\xi_3)^3}+4\frac{\xi_2\xi_{2Vk}}{(1-\xi_3)^3}+4\frac{\xi_2\xi_{2k}\xi_{3V}}{(1-\xi_3)^4}\right.$$
$$\left.+4\frac{\xi_2\xi_{2V}\xi_{3k}}{(1-\xi_3)^4}+6\frac{\xi_2^2\xi_{3Vk}}{(1-\xi_3)^4}+4\frac{\xi_2^2\xi_{3V}\xi_{3k}}{(1-\xi_3)^5}\right] \tag{C.73}$$

$$C_{1Vk} = \frac{2C_{1V}C_{1k}}{C_1} - C_1^2\left[4\bar{m}\xi_{3Vk}\left(\frac{2-\xi_3}{(1-\xi_3)^4}+\frac{8\xi_3-2\xi_3^2}{(1-\xi_3)^5}\right)\right.$$
$$+4\bar{m}\xi_{3V}\xi_{3k}\left(-\frac{1}{(1-\xi_3)^4}+8\frac{2-\xi_3}{(1-\xi_3)^5}+5\frac{8\xi_3-2\xi_3^2}{(1-\xi_3)^6}\right)$$
$$+2\xi_{3Vk}(-\bar{m}+1)\left(\frac{10-27\xi_3+18\xi_3^2-4\xi_3^3}{(1-\xi_3)^2(2-\xi_3)^2}\right.$$
$$\left.+\frac{20\xi_3-27\xi_3^2+12\xi_3^3-2\xi_3^4}{(1-\xi_3)^3(2-\xi_3)^2}+\frac{20\xi_3-27\xi_3^2+12\xi_3^3-2\xi_3^4}{(1-\xi_3)^2(2-\xi_3)^3}\right)$$
$$+2\xi_{3V}\xi_{3k}(-\bar{m}+1)\left(\frac{-27+36\xi_3-12\xi_3^2}{(1-\xi_3)^2(2-\xi_3)^2}\right.$$
$$+4\frac{10-27\xi_3+18\xi_3^2-4\xi_3^3}{(1-\xi_3)^3(2-\xi_3)^2}+4\frac{10-27\xi_3+18\xi_3^2-4\xi_3^3}{(1-\xi_3)^2(2-\xi_3)^3}$$
$$+3\frac{20\xi_3-27\xi_3^2+12\xi_3^3-2\xi_3^4}{(1-\xi_3)^4(2-\xi_3)^2}+4\frac{20\xi_3-27\xi_3^2+12\xi_3^3-2\xi_3^4}{(1-\xi_3)^3(2-\xi_3)^3}$$
$$\left.+3\frac{20\xi_3-27\xi_3^2+12\xi_3^3-2\xi_3^4}{(1-\xi_3)^2(2-\xi_3)^4}\right)+2\bar{m}_k\xi_{3V}\left(\frac{4-2\xi_3}{(1-\xi_3)^4}\right.$$
$$+4\frac{4\xi_3-\xi_3^2}{(1-\xi_3)^5}-\frac{10-27\xi_3+18\xi_3^2-4\xi_3^3}{(1-\xi_3)^2(2-\xi_3)^2}$$
$$\left.\left.-\frac{20\xi_3-27\xi_3^2+12\xi_3^3-2\xi_3^4}{(1-\xi_3)^3(2-\xi_3)^2}-\frac{20\xi_3-27\xi_3^2+12\xi_3^3-2\xi_3^4}{(1-\xi_3)^2(2-\xi_3)^3}\right)\right] \tag{C.74}$$

$$I_{1Vk} = \sum_{i=0}^{6}\left[ia_{ik}\xi_3^{i-1}\xi_{3V} + ia_i\left[(i-1)\xi_3^{i-2}\xi_{3V}\xi_{3k} + \xi_3^{i-1}\xi_{3Vk}\right]\right] \tag{C.75}$$

$$I_{2Vk} = \sum_{i=0}^{6}\left[ib_{ik}\xi_3^{i-1}\xi_{3V} + ib_i\left[(i-1)\xi_3^{i-2}\xi_{3V}\xi_{3k} + \xi_3^{i-1}\xi_{3Vk}\right]\right] \tag{C.76}$$

C.6. Derivatives concerning N_k, N_l

$$\mathcal{A}_{kl}^{r,v} = \bar{m}\mathcal{A}_{kl}^{hs} + \bar{m}_l\mathcal{A}_k^{hs} + \bar{m}_k\mathcal{A}_l^{hs} + \bar{m}_{kl}\mathcal{A}^{hs} + \mathcal{A}_{kl}^{chain} + \mathcal{A}_{1kl} + \mathcal{A}_{2kl} \tag{C.77}$$

$$\begin{aligned}\mathcal{A}_{kl}^{hs} = {}& \left(\frac{1}{N} - \frac{\xi_{0l}}{\xi_0}\right)\mathcal{A}_k^{hs} + \left(\frac{1}{N} - \frac{\xi_{0k}}{\xi_0}\right)\mathcal{A}_l^{hs} + \left(\frac{\xi_{0k}}{\xi_0 N} + \frac{\xi_{0l}}{\xi_0 N} - \frac{2}{N^2}\right)\mathcal{A}^{hs} \\ & + \frac{Nk_BT}{\xi_0}\left[\frac{3\xi_{1k}\xi_{2l}}{1-\xi_3} + \frac{3\xi_{1k}\xi_2\xi_{3l}}{(1-\xi_3)^2} + \frac{3\xi_{1l}\xi_{2k}}{1-\xi_3} + \frac{3\xi_1\xi_{2k}\xi_{3l}}{(1-\xi_3)^2} + \frac{3\xi_{1l}\xi_2\xi_{3k}}{(1-\xi_3)^2}\right. \\ & + \frac{3\xi_1\xi_{2l}\xi_{3k}}{(1-\xi_3)^2} + \frac{6\xi_1\xi_2\xi_{3k}\xi_{3l}}{(1-\xi_3)^3} + \frac{6\xi_2\xi_{2k}\xi_{2l}}{\xi_3(1-\xi_3)^2} - \frac{3\xi_2^2\xi_{2k}\xi_{3l}}{\xi_3^2(1-\xi_3)^2} \\ & + \frac{6\xi_2^2\xi_{2k}\xi_{3l}}{\xi_3(1-\xi_3)^3} - \frac{3\xi_2^2\xi_{3k}\xi_{2l}}{\xi_3^2(1-\xi_3)^2} + \frac{2\xi_2^3\xi_{3k}\xi_{3l}}{\xi_3^3(1-\xi_3)^2} - \frac{4\xi_2^3\xi_{3k}\xi_{3l}}{\xi_3^2(1-\xi_3)^3} \\ & + \frac{6\xi_2^2\xi_{3k}\xi_{2l}}{\xi_3(1-\xi_3)^3} + \frac{6\xi_2^3\xi_{3k}\xi_{3l}}{\xi_3(1-\xi_3)^4} \\ & + \left(\frac{6\xi_2\xi_{2k}\xi_{2l}}{\xi_3^2} - \frac{6\xi_2^2\xi_{2k}\xi_{3l}}{\xi_3^3} - \frac{6\xi_2^2\xi_{3k}\xi_{2l}}{\xi_3^3} + \frac{6\xi_2^3\xi_{3k}\xi_{3l}}{\xi_3^4}\right)\ln(1-\xi_3) \\ & - \left(\frac{3\xi_2^2\xi_{2k}}{\xi_3^2} - \frac{2\xi_2^3\xi_{3k}}{\xi_3^3} - \xi_{0k}\right)\frac{\xi_{3l}}{1-\xi_3} \\ & \left. - \left(\frac{3\xi_2^2\xi_{2l}}{\xi_3^2} - \frac{2\xi_2^3\xi_{3l}}{\xi_3^3} - \xi_{0l}\right)\frac{\xi_{3k}}{1-\xi_3} - \left(\frac{\xi_2^3}{\xi_3^2} - \xi_0\right)\frac{\xi_{3k}\xi_{3l}}{(1-\xi_3)^2}\right]\end{aligned} \tag{C.78}$$

$$\begin{aligned}\mathcal{A}_{kl}^{chain} = {}& -k_BT\left[(m_k-1)\frac{g_{kkl}^{hs}}{g_{kk}^{hs}} + (m_l-1)\frac{g_{llk}^{hs}}{g_{ll}^{hs}}\right. \\ & \left. -\sum_{i=1}^{C}\left[N_i(m_i-1)\frac{g_{iik}^{hs}g_{iil}^{hs}}{\left(g_{ii}^{hs}\right)^2} - N_i(m_i-1)\frac{g_{iikl}^{hs}}{g_{ii}^{hs}}\right]\right]\end{aligned} \tag{C.79}$$

$$\begin{aligned}\mathcal{A}_{1kl} = {}& \left(\frac{I_{1kl}}{I_1} - \frac{I_{1k}I_{1l}}{I_1^2}\right)\mathcal{A}_1 + \frac{I_{1k}}{I_1}\mathcal{A}_{1l} \\ & - \frac{4\pi k_BT}{V}\left[I_1m_km_l\left(\frac{\varepsilon_{kl}}{k_BT}\right)\sigma_{kl}^3 + I_{1l}\sum_{i=1}^{C}N_im_im_k\left(\frac{\varepsilon_{ik}}{k_BT}\right)\sigma_{ik}^3\right]\end{aligned} \tag{C.80}$$

$$\begin{aligned}\mathcal{A}_{2kl} = {}& \left[\frac{\bar{m}_{kl}}{\bar{m}} - \frac{\bar{m}_k\bar{m}_l}{\bar{m}^2} + \frac{C_{1kl}}{C_1} - \frac{C_{1k}C_{1l}}{C_1^2} + \frac{I_{2kl}}{I_2} - \frac{I_{2k}I_{2l}}{I_2^2}\right. \\ & \left. - \left(\frac{\bar{m}_k}{\bar{m}} + \frac{C_{1k}}{C_1} + \frac{I_{2k}}{I_2}\right)\left(\frac{\bar{m}_l}{\bar{m}} + \frac{C_{1l}}{C_1} + \frac{I_{2l}}{I_2}\right)\right]\mathcal{A}_2 \\ & + \left(\frac{\bar{m}_l}{\bar{m}} + \frac{C_{1l}}{C_1} + \frac{I_{2l}}{I_2}\right)\mathcal{A}_{2k} + \left(\frac{\bar{m}_k}{\bar{m}} + \frac{C_{1k}}{C_1} + \frac{I_{2k}}{I_2}\right)\mathcal{A}_{2l} \\ & - \frac{2\pi k_BT}{V}\bar{m}C_1I_2m_km_l\left(\frac{\varepsilon_{kl}}{k_BT}\right)^2\sigma_{kl}^3\end{aligned} \tag{C.81}$$

Furthermore, the derivatives concerning N_k, N_l of the additional relations are

$$\bar{m}_{kl} = -\frac{\bar{m}_k + \bar{m}_l}{N} \tag{C.82}$$

$$\xi_{nkl} = 0 \tag{C.83}$$

$$\begin{aligned}g_{ijkl}^{hs} = {}& \frac{2\xi_{3l}}{1-\xi_3}g_{ijk}^{hs} + \frac{2\xi_{3k}}{1-\xi_3}g_{ijl}^{hs} - \frac{2\xi_{3k}\xi_{3l}}{(1-\xi_3)^2}g_{ij}^{hs} \\ & + \left(\frac{d_id_j}{d_i+d_j}\right)^2\left[\frac{4\xi_{2k}\xi_{2l}}{(1-\xi_3)^3} + \frac{4\xi_2\xi_{2k}\xi_{3l}}{(1-\xi_3)^4} + \frac{4\xi_2\xi_{2l}\xi_{3k}}{(1-\xi_3)^4} + \frac{4\xi_2^2\xi_{3k}\xi_{3l}}{(1-\xi_3)^5}\right]\end{aligned} \tag{C.84}$$

$$\begin{aligned}C_{1kl} = {}& \frac{2C_{1k}C_{1l}}{C_1} - C_1^2\left[4\xi_{3k}\bar{m}_l\left(\frac{2-\xi_3}{(1-\xi_3)^4} + \frac{8\xi_3-2\xi_3^2}{(1-\xi_3)^5}\right)\right. \\ & + 4\xi_{3k}\xi_{3l}\bar{m}\left(-\frac{1}{(1-\xi_3)^4} + 8\frac{2-\xi_3}{(1-\xi_3)^5} + 5\frac{8\xi_3-2\xi_3^2}{(1-\xi_3)^6}\right) \\ & - 2\xi_{3k}\bar{m}_l\left(\frac{10-27\xi_3+18\xi_3^2-4\xi_3^3}{(1-\xi_3)^2(2-\xi_3)^2} + \frac{20\xi_3-27\xi_3^2+12\xi_3^3-2\xi_3^4}{(1-\xi_3)^3(2-\xi_3)^2}\right. \\ & \left. + \frac{20\xi_3-27\xi_3^2+12\xi_3^3-2\xi_3^4}{(1-\xi_3)^2(2-\xi_3)^3}\right) \\ & + 2\xi_{3k}\xi_{3l}(1-\bar{m})\left(\frac{-27+36\xi_3-12\xi_3^2}{(1-\xi_3)^2(2-\xi_3)^2} + 4\frac{10-27\xi_3+18\xi_3^2-4\xi_3^3}{(1-\xi_3)^3(2-\xi_3)^2}\right. \\ & + 4\frac{10-27\xi_3+18\xi_3^2-4\xi_3^3}{(1-\xi_3)^2(2-\xi_3)^3} + 3\frac{20\xi_3-27\xi_3^2+12\xi_3^3-2\xi_3^4}{(1-\xi_3)^4(2-\xi_3)^2} \\ & \left. + 3\frac{20\xi_3-27\xi_3^2+12\xi_3^3-2\xi_3^4}{(1-\xi_3)^2(2-\xi_3)^4} + 4\frac{20\xi_3-27\xi_3^2+12\xi_3^3-2\xi_3^4}{(1-\xi_3)^3(2-\xi_3)^3}\right) \\ & + 2\bar{m}_k\xi_{3l}\left(\frac{4-2\xi_3}{(1-\xi_3)^4} + 4\frac{4\xi_3-\xi_3^2}{(1-\xi_3)^5} - \frac{10-27\xi_3+18\xi_3^2-4\xi_3^3}{(1-\xi_3)^2(2-\xi_3)^2}\right. \\ & \left. - \frac{20\xi_3-27\xi_3^2+12\xi_3^3-2\xi_3^4}{(1-\xi_3)^3(2-\xi_3)^2} - \frac{20\xi_3-27\xi_3^2+12\xi_3^3-2\xi_3^4}{(1-\xi_3)^2(2-\xi_3)^3}\right) \\ & \left. + \bar{m}_{kl}\left(\frac{8\xi_3-2\xi_3^2}{(1-\xi_3)^4} - \frac{20\xi_3-27\xi_3^2+12\xi_3^3-2\xi_3^4}{(1-\xi_3)^2(2-\xi_3)^2}\right)\right]\end{aligned} \tag{C.85}$$

$$I_{1kl} = \sum_{i=0}^{6}\left[a_{ikl}\xi_3^i + ia_{ik}\xi_3^{i-1}\xi_{3l} + i\xi_{3k}\left[(i-1)a_i\xi_3^{i-2}\xi_{3l} + a_{il}\xi_3^{i-1}\right]\right] \tag{C.86}$$

$$I_{2kl} = \sum_{i=0}^{6}\left[b_{ikl}\xi_3^i + ib_{ik}\xi_3^{i-1}\xi_{3l} + i\xi_{3k}\left[(i-1)b_i\xi_3^{i-2}\xi_{3l} + b_{il}\xi_3^{i-1}\right]\right] \tag{C.87}$$

$$a_{ikl} = \frac{\bar{m}_{kl}}{\bar{m}^2}a_{1i} + \left(\frac{3\bar{m}_{kl}}{\bar{m}^2} - \frac{4\bar{m}_{kl}}{\bar{m}^3} + \frac{4\bar{m}_k\bar{m}_l}{\bar{m}^4}\right)a_{2i} - \frac{2\bar{m}_l}{\bar{m}}a_{ik} \tag{C.88}$$

$$b_{ikl} = \frac{\bar{m}_{kl}}{\bar{m}^2}b_{1i} + \left(\frac{3\bar{m}_{kl}}{\bar{m}^2} - \frac{4\bar{m}_{kl}}{\bar{m}^3} + \frac{4\bar{m}_k\bar{m}_l}{\bar{m}^4}\right)b_{2i} - \frac{2\bar{m}_l}{\bar{m}}b_{ik} \tag{C.89}$$

Appendix D. Constitutive Equations

D.1. Species Mass

The effective dispersion coefficient of the liquid was taken from the correlations of Deckwer et al. (1974). However, the experiments of Deckwer et al. (1974) were performed in columns with internal diameters 0.15 m and 0.2 m. The internal diameter of the column in this work was 9 m, and thus, appropriate scaling techniques were employed. The scaling was based on the work of Yang and Fan (2003):

$$D_{L,\mathrm{eff},z} = 0.678 d_{\mathrm{col}}^{s} (v_G \alpha_G)^{0.3}, \tag{D.1}$$

where the diameter of the reactor column is denoted d_{col}. The scaling parameter was given by Sehabiague and Morsi (2013a) as:

$$s = s_0 \left(1 - 0.11 \ln \frac{\rho_G}{\rho_{G,0}}\right). \tag{D.2}$$

Here, $s_0 = 1.4$ and $\rho_{G,0}$ is the gas density at ambient conditions, i.e., at $T = 298.15$K and $p = 1$bar.

Furthermore, the effective dispersion coefficient of the gas was related to $D_{L,\mathrm{eff},z}$ as (Sehabiague and Morsi, 2013a):

$$D_{G,\mathrm{eff},z} = D_{L,\mathrm{eff},z} \left(1 - \frac{d_b^{2.5}}{d_{b,0}^{2.5} + d_b^{2.5}}\right), \tag{D.3}$$

where the bubble diameter $d_{b,0} = 10$mm was classified as the transition to large bubbles.

The mass transfer coefficient was estimated based on the experiments on bubbly flow performed by Calderbank and Moo-Young (1961):

$$k_{L,i} = 0.31 \left(\frac{(\rho_L - \rho_G)\mu_L g}{\rho_L^2}\right)^{1/3} \mathrm{Sc}_i^{-2/3}. \tag{D.4}$$

In Eq. (D.4), g denotes the specific gravity, and μ_L denotes the dynamic molecular viscosity of the liquid, given in Table 7. The Schmidt number of component i is given by

$$\mathrm{Sc}_i = \frac{\mu_L}{\rho_L D_{\mathrm{Wilke},i}}, \tag{D.5}$$

where $D_{\mathrm{Wilke},i}$ are the multicomponent diffusivities approximated by Wilke's model

$$D_{\mathrm{Wilke},i} = \frac{1 - \omega_{L,i}}{\overline{M}_{w,L} \sum_{\substack{j=1 \\ j \neq i}}^{N_C} \frac{\omega_{L,j}}{M_{w,j} D_j}}. \tag{D.6}$$

Here the molecular diffusivities, D_j, were computed by Erkey et al. (1990) with molecular diameters from Bondi (1964). The parameter N in Eq. (7) of Erkey et al. (1990) was back-calculated by Vik et al. (2015) as $N = 0.605$.

The gas–liquid interfacial area was computed by the assumption of spherical bubbles (Deckwer et al., 1974):

$$a = 6 \frac{\alpha_G}{d_b}. \tag{D.7}$$

Here, d_b is the bubble diameter assumed constant throughout this work.

D.2. Momentum

The Reynolds analogy was employed to estimate the effective turbulent viscosities:

$$\mu_{L,\mathrm{eff},z} \approx \rho_L D_{L,\mathrm{eff},z}, \tag{D.8}$$

$$\mu_{G,\mathrm{eff},z} \approx \rho_G D_{G,\mathrm{eff},z}. \tag{D.9}$$

Furthermore, the drag force between the gas and liquid phases was modeled as (Albråten, 1982)

$$f_{\mathrm{drag}}^{G-L} = -\frac{3}{4} \frac{\alpha_G}{d_b} \rho_L C_{D,G-L} \mid v_L - v_G \mid (v_L - v_G), \tag{D.10}$$

where C_D is the drag coefficient. Tomiyama (1998) parametrized the drag coefficient for pure, uncontaminated systems as:

$$C_{D,G-L}\prime = \max\left[\min\left[\frac{16}{\mathrm{Re}_p}\left(1 + 0.15\mathrm{Re}_p^{0.687}\right), \frac{48}{\mathrm{Re}_p}\right], \frac{8}{3}\frac{\mathrm{Eö}}{\mathrm{Eö} + 4}\right]. \tag{D.11}$$

To account for the swarm effect observed when multiple bubbles rise through the liquid phase, a correction is introduced (Rampure et al., 2007):

$$C_{D,G-L} = C_{D,G-L}\prime (1 - \alpha_G)^{P_G}, \tag{D.12}$$

in which P_G denotes the correction factor. The relative Eötvös number is given as

$$\mathrm{Eö} = \frac{g(\rho_L - \rho_G) d_b^2}{\sigma}, \tag{D.13}$$

where σ denotes the surface tension. Furthermore, the relative Reynolds number is given by

$$\mathrm{Re}_p = \frac{\rho_L \mid v_L - v_G \mid d_b}{\mu_L} \tag{D.14}$$

The drag force between the solid and liquid phases was modeled by the same functional form as the drag between the gas and liquid phases:

$$f_{\mathrm{drag}}^{S-L} = -\frac{3}{4} \frac{\alpha_S}{d_S} \rho_L C_{D,S-L} \mid v_L - v_S \mid (v_L - v_S), \tag{D.15}$$

where the drag coefficient was obtained from the correlations of Morsi and Alexander (1972):

$$C_{D,S-L} = \frac{24}{\mathrm{Re}_S}, \quad \mathrm{Re}_S < 0.1 \tag{D.16a}$$

$$C_{D,S-L} = \frac{22.73}{\mathrm{Re}_S} + \frac{0.0903}{\mathrm{Re}_S^2} + 3.690, \quad 0.1 < \mathrm{Re}_S < 1 \tag{D.16b}$$

$$C_{D,S-L} = \frac{29.1667}{\mathrm{Re}_S} - \frac{3.8889}{\mathrm{Re}_S^2} + 1.222, \quad 1 < \mathrm{Re}_S < 10 \tag{D.16c}$$

$$C_{D,S-L} = \frac{46.50}{\mathrm{Re}_S} - \frac{116.67}{\mathrm{Re}_S^2} + 0.6167, \quad 10 < \mathrm{Re}_S < 100 \tag{D.16d}$$

$$C_{D,S-L} = \frac{98.33}{\mathrm{Re}_S} - \frac{2778}{\mathrm{Re}_S^2} + 0.3644, \quad 100 < \mathrm{Re}_S < 1000 \tag{D.16e}$$

$$C_{D,S-L} = \frac{148.62}{\mathrm{Re}_S} - \frac{47500}{\mathrm{Re}_S^2} + 0.357, \quad 1000 < \mathrm{Re}_S < 5000 \tag{D.16f}$$

$$C_{D,S-L} = -\frac{490.546}{\mathrm{Re}_S} + \frac{578700}{\mathrm{Re}_S^2} + 0.46, \quad 5000 < \mathrm{Re}_S < 10000 \tag{D.16g}$$

$$C_{D,S-L} = -\frac{1662.5}{\mathrm{Re}_S} + \frac{5416700}{\mathrm{Re}_S^2} + 0.5191, \quad 10000 < \mathrm{Re}_S < 50000. \tag{D.16h}$$

Here, the Reynolds number of the solid was computed as

$$\mathrm{Re}_S = \frac{\rho_L \mid v_S - v_L \mid d_S}{\mu_L} \tag{D.17}$$

The wall-to-liquid friction was modeled analogously to the gas-to-liquid drag:

$$f_{\mathrm{fric}}^{W-L} = -\frac{1}{2} \frac{1}{d_{\mathrm{col}}} \rho_L f_W v_L v_L. \tag{D.18}$$

Petukhov (1970) parametrized the wall friction coefficient (Bergman and Lavine, 2017), and we adopted their correlation here:

$$f_W = (0.79 \ln \mathrm{Re} - 1.64)^{-2}, \tag{D.19}$$

where the liquid Reynolds number is given by

$$\mathrm{Re} = \frac{\rho_L v_L d_{\mathrm{col}}}{\mu_L}. \tag{D.20}$$

The friction force between the liquid and the cooling pipes was modeled analogously to the friction force between the liquid and the wall:

$$f_{\mathrm{fric}}^{P-L} = -\frac{1}{2}\frac{n_{\mathrm{pipes}}}{d_{\mathrm{pipes}}}\rho_L f_P v_L v_L, \tag{D.21}$$

where (Petukhov, 1970; Bergman and Lavine, 2017)

$$f_P = (0.79\ln \mathrm{Re}_P - 1.64)^{-2}, \tag{D.22}$$

$$\mathrm{Re}_P = \frac{\rho_L v_L d_{\mathrm{pipes}}}{\mu_L}. \tag{D.23}$$

D.3. Energy

The liquid phase heat capacity, $c_{p,L}$, was assumed equal to the heat capacity of pure $C_{40}H_{82}$ and was computed from the asymptotic behavior correlations of Marano et al. (1997b) at $T = 513$k. Moreover, $c_{p,L}$ was assumed independent of temperature. Although the correlation of Marano et al. (1997b) is valid for $3 \leqslant CN \leqslant 18$, their results were in good agreement with different polyethylenes which constitute long-chained alkenes, and thus the extrapolation to $CN = 40$ is reasonable. The solid phase heat capacity was obtained from Maretto and Krishna (1999) and was assumed independent of temperature.

The gas phase heat capacity was computed as a weighted sum of the pure component contributions:

$$c_{p,G} = \sum_{i=1}^{N_C} \omega_{G,i} c_{p,G,i}. \tag{D.24}$$

The pure component heat capacities of CO, H_2, H_2O, and CO_2 were obtained at $T = 500$K from the tables given by Chase (1998). For the lumps $\mathcal{L}_1$–$\mathcal{L}_4$, the heat capacities were obtained from the asymptotic behavior correlations of Marano et al. (1997b). All gas phase heat capacities were assumed ideal and independent of temperature.

Although $c_{p,L}, c_{p,G,i}$, and $c_{p,S}$ were all computed at temperatures relevant for the FTS, they were all assumed independent of temperature. No real fluid contributions were employed for the liquid or gas phases. As the bubble columns have a remarkable heat transfer coefficient, the temperature variations are minor. Thus, the assumption of temperature invariant heat capacities is not believed to be the weakest link in the model description. The differences between ideal gas heat capacity and real fluid heat capacity could provide further insights on the behavior of the FTS SBCR; nevertheless, the study of real fluid heat capacities is left for future work.

Similar to the effective turbulent viscosity, the effective thermal conductivity was assumed to follow the Reynolds analogy:

$$\lambda_{L,\mathrm{eff},z} = D_{L,\mathrm{eff},z}\rho_L c_{p,L} \tag{D.25}$$

$$\lambda_{G,\mathrm{eff},z} = D_{G,\mathrm{eff},z}\rho_G c_{p,G}. \tag{D.26}$$

The energy transfer from the liquid to the external heat exchanger was modeled with a perimeter-to-surface area ratio and an overall heat transfer coefficient. The perimeter was computed by

$$S_I = \pi(d_{\mathrm{col}} + n_{\mathrm{pipes}} d_{\mathrm{pipes}}), \tag{D.27}$$

and the surface area available to fluid flow was computed by

$$A = \frac{\pi}{4}\left(d_{\mathrm{col}}^2 - n_{\mathrm{pipes}} d_{\mathrm{pipes}}^2\right) \tag{D.28}$$

The overall heat transfer coefficient was computed by a series of resistances:

$$\frac{1}{U} = \frac{1}{h_W} + \frac{t_{\mathrm{wall}}}{k_{\mathrm{steel}}} + \frac{1}{h_{\mathrm{cool}}}. \tag{D.29}$$

Here, h_W is the heat transfer coefficient on the liquid side of the cooling pipe wall, t_{wall} is the thickness of the cooling pipe wall, k_{steel} is the conductivity of steel, and h_{cool} is the heat transfer coefficient on the heat exchanger side of the cooling pipe wall. Deckwer (1980) parametrized h_W as

$$h_W = 0.1\lambda_{SL}^{0.5}\rho_L^{0.75}c_{p,SL}^{0.5}\mu_{SL}^{-0.25}g^{0.25}(v_G\alpha_G)^{0.25}, \tag{D.30}$$

and gave values for h_{cool} (Vik et al., 2015). Here, λ_{SL} denotes the molecular conductivity of the liquid, which was given by (Tareef, 1940)

$$\lambda_{SL} = \lambda_L \frac{2\lambda_L + \lambda_S - 2\psi_S(\lambda_L - \lambda_S)}{2\lambda_L + \lambda_S + \psi_S(\lambda_L - \lambda_S)}, \tag{D.31}$$

where λ_L and λ_S were taken from Maretto and Krishna (1999), and

$$\psi_S = \frac{\alpha_S}{\alpha_L}. \tag{D.32}$$

Furthermore, the slurry phase heat capacity is given by

$$c_{p,SL} = \phi_S c_{p,S} + \phi_L c_{p,L}, \tag{D.33}$$

where

$$\phi_S = \frac{\rho_S \alpha_S}{\rho_{SL}\alpha_{SL}}, \tag{D.34}$$

$$\phi_L = 1 - \phi_S. \tag{D.35}$$

The liquid and solid phase densities were taken from Sehabiague and Morsi (2013) and Maretto and Krishna (1999), respectively. The slurry volume fraction is

$$\alpha_{SL} = \alpha_L + \alpha_S, \tag{D.36}$$

and the slurry density is

$$\rho_{SL} = \frac{\alpha_S\rho_S + \alpha_L\rho_L}{\alpha_{SL}}. \tag{D.37}$$

Moreover, the slurry viscosity was parametrized by Vand (1948) as:

$$\mu_{SL} = \mu_L \exp\left(\frac{2.5\psi_S}{1 - 0.609\psi_S}\right). \tag{D.38}$$

Calderbank and Moo-Young (1961) parametrized the interphase heat transfer coefficient as:

$$h_L = \bar{k}_L c_{p,L}\rho_L \bar{\mathrm{Sc}}^{2/3}\mathrm{Pr}^{-2/3}. \tag{D.39}$$

Here, the average mass transfer coefficient, $\bar{k}_L$, and the average Schmidt number were computed by weighted sums:

$$\bar{k}_L = \sum_{i=1}^{N_C} \omega_{L,i} k_{L,i}, \tag{D.40}$$

$$\bar{\mathrm{Sc}}^{2/3} = \sum_{i=1}^{N_C} \omega_{L,i} \mathrm{Sc}_i, \tag{D.41}$$

and the Prandtl number is given as

$$\mathrm{Pr} = \frac{c_{p,L}\mu_L}{\lambda_L}. \tag{D.42}$$

References

Ahón, V.R., Costa, E.F., Monteagudo, J.E.P., Fontes, C.E., Biscaia, E.C., Lage, P.L.C., 2005. A comprehensive mathematical model for the Fischer-Tropsch synthesis in

well-mixed slurry reactors. Chem. Eng. Sci. 60 (3), 677–694. https://doi.org/10.1016/j.ces.2004.08.039.
Albråten, P.J., 1982. The dynamics of two-phase flow: an analysis of the momentum transport in bubble, droplet, and particulate flow, Ph.d. thesis, Chalmers University of Technology,, Göteborg, 1982.
Ambrose, D., Tsonopoulos, C., 1995. Vapor-Liquid Critical Properties of Elements and Compounds. 2. Normal Alkanes. J. Chem. Eng. Data 40 (3), 531–546. https://doi.org/10.1021/je00019a001.
Ambrose, D., Tsonopoulos, C., Nikitin, E.D., Morton, D.W., Marsh, K.N., 2015. Vapor-Liquid Critical Properties of Elements and Compounds. 12. Review of Recent Data for Hydrocarbons and Non-hydrocarbons, J. Chem. Eng. Data 60 (12) (2015) 3444–3482, doi:10.1021/acs.jced.5b00571.
Baliban, R.C., Elia, J.A., Floudas, C.A., 2013. Biomass to liquid transportation fuels (BTL) systems: Process synthesis and global optimization framework. Energ. Environ. Sci. 6 (1), 267–287. https://doi.org/10.1039/c2ee23369j.
Bergman, T.L., Lavine, A.S., 2017. Fundamentals of Heat and Mass Transfer, John Wiley & Sons, Hoboken, NJ, 8th edn., ISBN 978-1-119-32042-5, 2017.
Biquiza, L.D., Claeys, M., Van Steen, E., 2010. Thermodynamic and experimental aspects of 'supercritical' Fischer-Tropsch synthesis. Fuel Process. Technol. 91 (10), 1250–1255. https://doi.org/10.1016/j.fuproc.2010.04.005.
Bond, R.N., Dawe, R.A., 1988. Heavy component and fraction properties at low reduced temperatures for petroleum mixtures. Chem. Eng. J. 38 (3), 195–204. https://doi.org/10.1016/0300-9467(88)80078-9.
Bondi, A., 1964. van der Waals Volumes and Radii. J. Phys. Chem. 68 (3), 441–451. https://doi.org/10.1021/j100785a001.
Bremaud, M., Fongarland, P., Anfray, J., Jallais, S., Schweich, D., Khodakov, A.Y., 2005. Influence of syngas composition on the transient behavior of a Fischer-Tropsch continuous slurry reactor. Catal. Today 106 (1–4), 137–142. https://doi.org/10.1016/j.cattod.2005.07.126.
Calderbank, P.H., Moo-Young, M.B., 1961. The continuous phase heat and mass-transfer properties of dispersions. Chem. Eng. Sci. 16 (1–2), 39–54. https://doi.org/10.1016/0009-2509(61)87005-X.
Caldwell, L., Van Vuuren, D.S., 1986. On the formation and composition of the liquid phase in Fischer-Tropsch reactors. Chem. Eng. Sci. 41 (1), 89–96. https://doi.org/10.1016/0009-2509(86)85201-0.
Chao, K.C., Lin, H.M., 1988. Synthesis gas solubility in Fischer-Tropsch slurry: Final report, Tech. Rep., National Energy Technology Laboratory, Pittsburgh, PA, and Morgantown, WV, doi:10.2172/5218250.
Chapoy, A., Ahmadi, P., de Oliveira Cavalcanti Filho, V., Jadhawar, P., 2020. Vapour-liquid equilibrium data for the carbon dioxide (CO_2) + carbon monoxide (CO) system, J. Chem. Thermodyn. 150 (2020) 106180, doi:10.1016/j.jct.2020.106180.
Chase, M.W., 1998. NIST-JANAF Thermochemical Tables, J. Phys. Chem. Ref. Data Monograph 1.
Dahm, K., Visco, D., 2014. Fundamentals of Chemical Engineering Thermodynamics, Cengage Learning, Stamford, CT, USA, 1st edn., ISBN 1111580707, 2014.
P.V. Danckwerts, Continuous flow systems. Distribution of residence times, Chem. Eng. Sci. 2 (1) (1953) 1–13, doi:10.1016/0009-2509(53)80001-1.
B.H. Davis, Technology Development for Iron and Cobalt Fischer-Tropsch Catalysts, Tech. Rep., National Energy Technology Laboratory, Pittsburgh, PA, Morgantown, WV, and Albany, OR (United States), 2002, doi:10.2172/806693.
Deckwer, W.-D., 1980. On the mechanism of heat transfer in bubble column reactors. Chem. Eng. Sci. 35 (6), 1341–1346. https://doi.org/10.1016/0009-2509(80)85127-X.
Deckwer, W.-D., Burckhart, R., Zoll, G., 1974. Mixing and mass transfer in tall bubble columns. Chem. Eng. Sci. 29 (11), 2177–2188. https://doi.org/10.1016/0009-2509(74)80025-4.
Deckwer, W.-D., Kokuun, R., Sanders, E., Ledakowicz, S., 1986. Kinetic studies of Fischer-Tropsch synthesis on suspended iron/potassium catalyst - rate inhibition by carbon dioxide and water. Ind. Eng. Chem. Process Des. Dev. 25 (3), 643–649. https://doi.org/10.1021/i200034a008.
Demetriades, T.A., Graham, R.S., 2016. A new equation of state for CCS pipeline transport: Calibration of mixing rules for binary mixtures of CO_2 with N_2, O_2 and H_2. J. Chem. Thermodyn. 93, 294–304. https://doi.org/10.1016/j.jct.2015.07.045.
Derevich, I.V., Ermolaev, V.S., Mordkovich, V.Z., 2008. Liquid-vapor thermodynamic equilibrium in Fischer-Tropsch synthesis products. Theor. Found. Chem. Eng. 42 (2), 216–219. https://doi.org/10.1134/S0040579508020152.
Diamantonis, N.I., Economou, I.G., 2012. Modeling the phase equilibria of a H_2O-CO_2 mixture with PC-SAFT and tPC-PSAFT equations of state. Mol. Phys. 110 (11–12), 1205–1212. https://doi.org/10.1080/00268976.2012.656721.
Dry, M.E., 1989. Commercial conversion of carbon monoxide to fuels and chemicals. J. Organomet. Chem. 372 (1), 117–127. https://doi.org/10.1016/0022-328X(89)87082-2.
Dry, M.E., 2004. FT catalysts. Stud. Surf. Sci. Catal. 152, 533–600. https://doi.org/10.1016/S0167-2991(04)80464-6.
J.R. Elliott, C.T. Lira, Introductory Chemical Engineering Thermodynamics, Prentice Hall, Upper Saddle River, NJ, 2nd edn., ISBN 0136068545, 2012.
Erkey, C., Rodden, J.B., Akgerman, A., 1990. A correlation for predicting diffusion coefficients in alkanes. Can. J. Chem. Eng. 68 (4), 661–665. https://doi.org/10.1002/cjce.5450680418.
Fischer, F., Tropsch, H., 1923. The preparation of synthetic oil mixtures (synthol) from carbon monoxide and hydrogen. Brennst. Chem. 4, 276–285.
Gamba, S., Soave, G.S., Pellegrini, L.A., 2009. Use of normal boiling point correlations for predicting critical parameters of paraffins for vapour–liquid equilibrium calculations with the SRK equation of state. Fluid Phase Equilib. 276 (2), 133–141. https://doi.org/10.1016/j.fluid.2008.10.014.
W. Gao, R.L. Robinson, K.A.M. Gasem, High-pressure solubilities of hydrogen, nitrogen, and carbon monoxide in dodecane from 344 to 410 K at pressures to 13.2 MPa, J. Chem. Eng. Data 44 (1) (1999) 130–132, doi:10.1021/je9801664.
Gasem, K.A.M., Ross, C.H., Robinson, R.L., 1993. Prediction of ethane and CO_2 solubilities in heavy normal paraffins using generalized-parameter soave and peng-robinson equations of state. Can. J. Chem. Eng. 71 (5), 805–816. https://doi.org/10.1002/cjce.5450710520.
Gautam, R., Seider, W.D., 1979. Computation of phase and chemical equilibrium: Part I. Local and constrained minima in Gibbs free energy. AIChE J. 25 (6), 991–999. https://doi.org/10.1002/aic.690250610.
Gavrilović, L., Jørgensen, E.A., Pandey, U., Putta, K.R., Rout, K.R., Rytter, E., Hillestad, M., Blekkan, E.A., 2021. Fischer-Tropsch synthesis over an alumina-supported cobalt catalyst in a fixed bed reactor – Effect of process parameters. Catal. Today 369 (July), 150–157. https://doi.org/10.1016/j.cattod.2020.07.055.
Golub, G.H., Welsch, J.H., 1969. Calculation of Gauss quadrature rules. Math. Comp. 23 (106). https://doi.org/10.1090/S0025-5718-69-99647-1. 221–221.
M.S. Graboski, T.E. Daubert, A Modified Soave Equation of State for Phase Equilibrium Calculations. 1. Hydrocarbon Systems, Ind. Eng. Chem. Process Des. Dev. 17 (4) (1978a) 443–448, doi:10.1021/i260068a009.
M.S. Graboski, T.E. Daubert, A Modified Soave Equation of State for Phase Equilibrium Calculations. 2. Systems Containing CO_2, H_2S, N_2, and CO, Ind. Eng. Chem. Process Des. Dev. 17 (4) (1978b) 448–454, doi:10.1021/i260068a010.
Gray, R.D., Heidman, J.L., Hwang, S.C., Tsonopoulos, C., 1983. Industrial applications of cubic equations of state for VLE calculations, with emphasis on H_2 systems. Fluid Phase Equilib. 13 (April), 59–76. https://doi.org/10.1016/0378-3812(83)80082-X.
Gray, R.D., Heidman, J.L., Springer, R.D., Tsonopoulos, C., 1989. Characterization and property prediction for heavy petroleum and synthetic liquids. Fluid Phase Equilib. 53, 355–376. https://doi.org/10.1016/0378-3812(89)80103-7.
Gross, J., Sadowski, G., 2001. Perturbed-Chain SAFT: An Equation of State Based on a Perturbation Theory for Chain Molecules. Ind. Eng. Chem. Res. 40 (4), 1244–1260. https://doi.org/10.1021/ie0003887.
Gross, J., Sadowski, G., 2002. Application of the Perturbed-Chain SAFT Equation of State to Associating Systems. Ind. Eng. Chem. Res. 41 (22), 5510–5515. https://doi.org/10.1021/ie010954d.
Hamelinck, C.N., Faaij, A.P.C., den Uil, H., Boerrigter, H., 2004. Production of FT transportation fuels from biomass; technical options, process analysis and optimisation, and development potential. Energy 29 (11), 1743–1771. https://doi.org/10.1016/j.energy.2004.01.002.
Harvey, A.H., 1997. On the suitability of the virial equation for modeling the solubility of solids in supercritical fluids. Fluid Phase Equilib. 130 (1–2), 87–100. https://doi.org/10.1016/S0378-3812(96)03228-1.
T. Haug-Warberg, Den termodynamiske arbeidsboken, Kolofon, Forlag AS, Fornebu, 1st edn., ISBN 978-82-300-0205-6, 2006.
He, M.G., Yang, Y.J., Zhang, Y., Zhang, X.X., 2008. Theoretical estimation of the isobaric heat capacity c_p of refrigerant. Appl Therm Eng 28 (14–15), 1813–1825. https://doi.org/10.1016/j.applthermaleng.2007.11.007.
Heidman, J.L., Tsonopoulos, C., Brady, C.J., Wilson, G.M., 1985. High-temperature mutual solubilities of hydrocarbons and water. Part II: Ethylbenzene, ethylcyclohexane, and n-octane. AIChE J. 31 (3), 376–384. https://doi.org/10.1002/aic.690310304.
Helgeson, H.C., Owens, C.E., Knox, A.M., Richard, L., 1998. Calculation of the Standard Molal Thermodynamic Properties of Crystalline, Liquid, and Gas Organic Molecules at High Temperatures and Pressures. Geochim. Cosmochim. Acta 62 (6), 985–1081. https://doi.org/10.1016/S0016-7037(97)00219-6.
Hillestad, M., 2015. Modeling the Fischer-Tropsch Product Distribution and Model Implementation. Chem. Prod. Process Model. 10 (3), 147–159. https://doi.org/10.1515/cppm-2014-0031.
Hust, J.G., Lankford, A.B., 1984. Update of thermal conductivity and electrical resistivity of electrolytic iron, tungsten and stainless steel. National Bureau of Standards Special Publication 260, 71.
H.A. Jakobsen, Chemical Reactor Modeling: Multiphase Reactive Flows, Springer International Publishing, Cham, 2nd edn., ISBN 978-3-319-05091-1, 2014, doi:10.1007/978-3-319-05092-8.
Kast, W., 1962. Analyse des wärmeübergangs in blasensäulen. Int. J. Heat Mass Transfer 5 (3–4), 329–336. https://doi.org/10.1016/0017-9310(62)90022-4.
Kim, Y.H., Jun, K.-W., Joo, H., Han, C., Song, I.K., 2009. A simulation study on gas-to-liquid (natural gas to Fischer-Tropsch synthetic fuel) process optimization. Chem. Eng. J. 155 (1–2), 427–432. https://doi.org/10.1016/j.cej.2009.08.018.
E. Kreyszig, Advanced engineering mathematics, Wiley, Hoboken, NJ, 10th edn., ISBN 9780470646137, 2011.
J.C.W. Kuo, Slurry Fischer-Tropsch/Mobil two stage process of converting SYNGAS to high octane gasoline. Final report, Tech. Rep., Mobil Research and Development Corporation, Paulsboro, New Jersey (United States), doi:10.2172/6838947, 1983.
Ledakowicz, S., Nettelhoff, H., Kokuun, R., Deckwer, W.-D., 1985. Kinetics of the Fischer-Tropsch synthesis in the slurry phase on a potassium promoted iron catalyst. Ind. Eng. Chem. Process Des. Dev. 24 (4), 1043–1049. https://doi.org/10.1021/i200031a025.
E.W. Lemmon, M.O. McLinden, D.G. Friend, Thermophysical Properties of Fluid Systems, in: P.J. Linstrom, W.G. Mallard (Eds.), NIST Chemistry WebBook, NIST Standard Reference Database Number 69, National Institute of Standards and

Technology, Gaithersburg MD, 20899, USA, 2019, doi:https://doi.org/10.18434/T4D303.
Loewert, M., Hoffmann, J., Piermartini, P., Selinsek, M., Dittmeyer, R., Pfeifer, P., 2019. Microstructured Fischer-Tropsch Reactor Scale-up and Opportunities for Decentralized Application. Chem. Eng. Technol. 42 (10), 2202–2214. https://doi.org/10.1002/ceat.201900136.
Ma, W., Jacobs, G., Ji, Y., Bhatelia, T., Bukur, D.B., Khalid, S., Davis, B.H., 2011. Fischer-Tropsch synthesis: Influence of CO conversion on selectivities, H_2/CO usage ratios, and catalyst stability for a ru promoted Co/Al_2O_3 catalyst using a slurry phase reactor. Top. Catal. 54 (13–15), 757–767. https://doi.org/10.1007/s11244-011-9699-5.
Marano, J.J., Holder, G.D., 1997. Characterization of Fischer-Tropsch liquids for vapor-liquid equilibria calculations. Fluid Phase Equilib. 138 (1–2), 1–21. https://doi.org/10.1016/s0378-3812(97)00166-0.
J.J. Marano, G.D. Holder, A general equation for correlating the thermophysical properties of n-paraffins, n-olefins, and other homologous series. 3. Asymptotic behavior correlations for thermal and transport properties, Ind. Eng. Chem. Res. 36 (6) (1997b) 2399–2408, doi:10.1021/ie9605138.
Maretto, C., Krishna, R., 1999. Modelling of a bubble column slurry reactor for Fischer-Tropsch synthesis. Catal. Today 52 (2–3), 279–289. https://doi.org/10.1016/S0920-5861(99)00082-6.
Maretto, C., Krishna, R., 2001. Design and optimisation of a multi-stage bubble column slurry reactor for Fischer-Tropsch synthesis. Catal. Today 66 (2–4), 241–248. https://doi.org/10.1016/S0920-5861(00)00626-X.
Masuku, C.M., Hildebrandt, D., Glasser, D., 2011. The role of vapour–liquid equilibrium in Fischer-Tropsch product distribution. Chem. Eng. Sci. 66 (23), 6254–6263. https://doi.org/10.1016/j.ces.2011.09.005.
Masuku, C.M., Ma, W., Hildebrandt, D., Glasser, D., Davis, B.H., 2012. A vapor–liquid equilibrium thermodynamic model for a Fischer-Tropsch reactor. Fluid Phase Equilib. 314, 38–45. https://doi.org/10.1016/j.fluid.2011.10.020.
Meng, L., Duan, Y.Y., Wang, X.D., 2007. Binary interaction parameter k_{ij} for calculating the second cross-virial coefficients of mixtures. Fluid Phase Equilib. 260 (2), 354–358. https://doi.org/10.1016/j.fluid.2007.07.044.
M.L. Michelsen, J.M. Mollerup, Thermodynamic Models: Fundamentals & Computational Aspects, Tie-Line Publications, Holte, 2nd edn., ISBN 8798996118, 2007.
Morsi, S.A., Alexander, A.J., 1972. An investigation of particle trajectories in two-phase flow systems. J. Fluid Mech. 55 (2), 193–208. https://doi.org/10.1017/S0022112072001806.
H. mu Lin, Peng-Robinson equation of state for vapor-liquid equilibrium calculations for carbon dioxide + hydrocarbon mixtures, Fluid Phase Equilib. 16 (2) (1984) 151–169, doi:10.1016/0378-3812(84)85028-1.
Nikitin, E.D., Pavlov, P.A., Popov, A.P., 1997. Vapour-liquid critical temperatures and pressures of normal alkanes with from 19 to 36 carbon atoms, naphthalene and m-terphenyl determined by the pulse-heating technique. Fluid Phase Equilib. 141 (1–2), 155–164. https://doi.org/10.1016/S0378-3812(97)00202-1.
Nishiumi, H., Arai, T., Takeuchi, K., 1988. Generalization of the binary interaction parameter of the Peng-Robinson equation of state by component family. Fluid Phase Equilib. 42 (C), 43–62. https://doi.org/10.1016/0378-3812(88)80049-9.
Øyen, S.B., Jakobsen, H.A., Haug-Warberg, T., Solsvik, J., 2021. Interface Mass Transfer in Reactive Bubbly Flow: A Rigorous Phase Equilibrium-Based Approach. Ind. Eng. Chem. Res. 60 (48), 17705–17732. https://doi.org/10.1021/acs.iecr.1c03131.
Peña, D., Griboval-Constant, A., Lancelot, C., Quijada, M., Visez, N., Stéphan, O., Lecocq, V., Diehl, F., Khodakov, A.Y., 2014. Molecular structure and localization of carbon species in alumina supported cobalt Fischer-Tropsch catalysts in a slurry reactor. Catal. Today 228, 65–76. https://doi.org/10.1016/j.cattod.2013.10.005.
Peng, D.-Y., Robinson, D.B., 1976. A New Two-Constant Equation of State. Ind. Eng. Chem. Fund. 15 (1), 59–64. https://doi.org/10.1021/i160057a011.
Perez, A.G., Coquelet, C., Paricaud, P., Chapoy, A., 2017. Comparative study of vapour-liquid equilibrium and density modelling of mixtures related to carbon capture and storage with the SRK, PR, PC-SAFT and SAFT-VR Mie equations of state for industrial uses. Fluid Phase Equilib. 440, 19–35. https://doi.org/10.1016/j.fluid.2017.02.018.
Petersen, A.P., Claeys, M., Kooyman, P.J., van Steen, E., 2019. Cobalt-Based Fischer-Tropsch Synthesis: A Kinetic Evaluation of Metal-Support Interactions Using an Inverse Model System. Catalysts 9 (10), 794. https://doi.org/10.3390/catal9100794.
Petropoulou, E., Pappa, G.D., Voutsas, E., 2017. Modelling of phase equilibrium of natural gas mixtures containing associating compounds. Fluid Phase Equilib. 433, 135–148. https://doi.org/10.1016/j.fluid.2016.10.028.
Petukhov, B.S., 1970. Heat Transfer and Friction in Turbulent Pipe Flow with Variable Physical Properties. Adv. Heat Transf. 6 (C), 503–564. https://doi.org/10.1016/S0065-2717(08)70153-9.
Pinna, D., Tronconi, E., Lietti, L., Zennaro, R., Forzatti, P., 2003. Wax composition transients during Fischer-Tropsch synthesis. J. Catal. 214 (2), 251–260. https://doi.org/10.1016/S0021-9517(02)00151-3.
W.H. Press, S.A. Teukolsky, W.T. Vetterling, B.P. Flannery, Numerical Recipes in Fortran 77: The Art of Scientific Computing, Cambridge University Press, Cambridge, UK, 2nd edn., ISBN 0-521-43064-X, 1992.
Rahbari, A., Brenkman, J., Hens, R., Ramdin, M., Van Den Broeke, L.J.P., Schoon, R., Henkes, R., Moultos, O.A., Vlugt, T.J.H., 2019. Solubility of water in hydrogen at high pressures: A molecular simulation study. J. Chem. Eng. Data 64 (9), 4103–4115. https://doi.org/10.1021/acs.jced.9b00513.
Raje, A.P., Davis, B.H., 1996. Effect of vapor-liquid equilibrium on Fischer-Tropsch hydrocarbon selectivity for a deactivating catalyst in a slurry reactor. Energ. Fuel. 10 (3), 552–560. https://doi.org/10.1021/ef950213n.
Ramdin, M., Becker, T.M., Jamali, S.H., Wang, M., Vlugt, T.J.H., 2016. Computing equation of state parameters of gases from Monte Carlo simulations. Fluid Phase Equilib. 428, 174–181. https://doi.org/10.1016/j.fluid.2016.06.012.
Rampure, M.R., Kulkarni, A.A., Ranade, V.V., 2007. Hydrodynamics of bubble column reactors at high gas velocity: Experiments and computational fluid dynamics CFD simulations. Ind. Eng. Chem. Res. 46 (25), 8431–8447. https://doi.org/10.1021/ie070079h.
R. Rauch, A. Kiennemann, A. Sauciuc, Fischer-Tropsch Synthesis to Biofuels (BtL Process), in: The Role of Catalysis for the Sustainable Production of Bio-fuels and Bio-chemicals, Elsevier, 397–443, ISBN 9780444563309, 2013, doi:10.1016/B978-0-444-56330-9.00012-7.
Rodrigues, J.J., Lima, L.A., Lima, W.S., Rodrigues, M.G.F., Fernandes, F.A.N., 2011. Fischer-Tropsch Synthesis in Slurry-Phase Reactors using Co/SBA-15 Catalysts. Braz. J. Pet. Gas 5 (3), 149–157. https://doi.org/10.5419/bjpg2011-0015.
Sadeqzadeh, M., Chambrey, S., Piché, S., Fongarland, P., Luck, F., Curulla-Ferré, D., Schweich, D., Bousquet, J., Khodakov, A.Y., 2013. Deactivation of a Co/Al_2O_3 Fischer-Tropsch catalyst by water-induced sintering in slurry reactor: Modeling and experimental investigations. Catal. Today 215, 52–59. https://doi.org/10.1016/j.cattod.2013.03.022.
Sari, A., Zamani, Y., Taheri, S.A., 2009. Intrinsic kinetics of Fischer-Tropsch reactions over an industrial Co-Ru/γ-Al_2O_3 catalyst in slurry phase reactor. Fuel Process. Technol. 90 (10), 1305–1313. https://doi.org/10.1016/j.fuproc.2009.06.024.
Sehabiague, L., Morsi, B.I., 2013. Hydrodynamic and Mass Transfer Characteristics in a Large-Scale Slurry Bubble Column Reactor for Gas Mixtures in Actual Fischer-Tropsch Cuts. Int J Chem React Eng 11 (1), 83–102. https://doi.org/10.1515/ijcre-2012-0042.
Sehabiague, L., Morsi, B.I., 2013a. Modeling and Simulation of a Fischer-Tropsch Slurry Bubble Column Reactor Using Different Kinetic Rate Expressions for Iron and Cobalt Catalysts. Int J Chem React Eng 11 (1), 309–330. https://doi.org/10.1515/ijcre-2012-0017.
Sehabiague, L., Lemoine, R., Behkish, A., Heintz, Y.J., Sanoja, M., Oukaci, R., Morsi, B.I., 2008. Modeling and optimization of a large-scale slurry bubble column reactor for producing 10,000 bbl/day of Fischer-Tropsch liquid hydrocarbons. J. Chin. Inst. Chem. Eng. 39 (2), 169–179. https://doi.org/10.1016/j.jcice.2007.11.003.
J. Shen, T. Tang, L.-L. Wang, Spectral Methods, vol. 41 of Springer Series in Computational Mathematics, Springer, Berlin Heidelberg, Berlin, Heidelberg, 1st edn., ISBN 978-3-540-71040-0, 2011, doi:10.1007/978-3-540-71041-7.
V. Smil, Energy Transitions: Global and National Perspectives, ABC-CLIO, LLC, Westport, ISBN 144085324X, 2016.
J. Solsvik, H.A. Jakobsen, Solution of the Pellet Equation by use of the Orthogonal Collocation and Least Squares Methods: Effects of Different Orthogonal Jacobi Polynomials, Int J Chem React Eng 10 (1) (2012) Article A40, doi:10.1515/1542-6580.2702.
Solsvik, J., Jakobsen, H.A., 2013. On the solution of the population balance equation for bubbly flows using the high-order least squares method: implementation issues. Rev Chem Eng 29 (2), 63–98. https://doi.org/10.1515/revce-2012-0018.
Solsvik, J., Tangen, S., Jakobsen, H.A., 2013. Evaluation of weighted residual methods for the solution of the pellet equations: The orthogonal collocation, Galerkin, tau and least-squares methods. Comput. Chem. Eng. 58, 223. https://doi.org/10.1016/j.compchemeng.2013.07.002.
Srinivas, S., Field, R.P., Watanasiri, S., Herzog, H.J., 2012. Correlation to predict solubility of hydrogen and carbon monoxide in heavy paraffins. Fluid Phase Equilib. 320, 11–25. https://doi.org/10.1016/j.fluid.2012.02.008.
A. Stranges, Germany's synthetic fuel industry, 1927–1945, in: J. Lesch (Ed.), The German Chemical Industry in the Twentieth Century, chap. 7, Springer, Netherlands, Dordrecht, 147–216, 2000.
Tang, H., Kitagawa, K., 2005. Supercritical water gasification of biomass: Thermodynamic analysis with direct Gibbs free energy minimization. Chem. Eng. J. 106 (3), 261–267. https://doi.org/10.1016/j.cej.2004.12.021.
Tareef, B.M., 1940. Thermal conductivity of colloidal systems. Colloid J. USSR 6 (545), 1.
Todic, B., Bhatelia, T., Froment, G.F., Ma, W., Jacobs, G., Davis, B.H., Bukur, D.B., 2013. Kinetic model of Fischer-Tropsch synthesis in a slurry reactor on Co-Re/Al_2O_3 catalyst. Ind. Eng. Chem. Res. 52 (2), 669–679. https://doi.org/10.1021/ie3028312.
Tomiyama, A., 1998. Struggle with Computational Bubble Dynamics. Multiph. Sci. Technol. 10 (4), 369–405. https://doi.org/10.1615/MultScienTechn.v10.i4.40.
Traxinger, C., Pfitzner, M., Baab, S., Lamanna, G., Weigand, B., 2019. Experimental and numerical investigation of phase separation due to multicomponent mixing at high-pressure conditions. Phys. Rev. Fluids 4 (7), 6–8. https://doi.org/10.1103/PhysRevFluids.4.074303.
Tsonopoulos, C., Wilson, G.M., 1983. High-temperature mutual solubilities of hydrocarbons and water. Part I: Benzene, cyclohexane and n-hexane. AIChE J. 29 (6), 990–999. https://doi.org/10.1002/aic.690290618.
Vand, V., 1948. Viscosity of solutions and suspensions. I: Theory. J Phys Colloid Chem 52 (2), 277–299. https://doi.org/10.1021/j150458a001.
van Steen, E., Claeys, M., 2008. Fischer-Tropsch catalysts for the biomass-to-liquid process. Chem. Eng. Technol. 31 (5), 655–666. https://doi.org/10.1002/ceat.200800067.
A.V. Venkatramani, R. Okuno, Modeling of Multiphase Behavior for Water/n-Alkane Mixtures by Use of the Peng-Robinson EOS, in: Day 2 Wed, June 11, Canada Heavy Oil Conference, SPE, 2014, doi:10.2118/170100-ms.

Vik, C.B., Solsvik, J., Hillestad, M., Jakobsen, H.A., 2015. Modeling of a Slurry Bubble Column Reactor for the Production of Biofuels via the Fischer-Tropsch Synthesis. Chem. Eng. Technol. 38 (4), 690–700. https://doi.org/10.1002/ceat.201400647.

J. Villadsen, M.L. Michelsen, Solution of Differential Equation Models by Polynomial Approximation, Prentice-Hall International, Prentice-Hall, Englewood Cliffs, NJ, ISBN 0138222053, 1978.

Visconti, C.G., 2014. Vapor-Liquid Equilibria in the Low-Temperature Fischer-Tropsch Synthesis. Ind. Eng. Chem. Res. 53 (5), 1727–1734. https://doi.org/10.1021/ie4015638.

Wang, Y.-N., Li, Y.-W., Bai, L., Zhao, Y.-L., Zhang, B.-J., 1999. Correlation for gas–liquid equilibrium prediction in Fischer-Tropsch synthesis. Fuel 78 (8), 911–917. https://doi.org/10.1016/S0016-2361(99)00020-4.

Withers, H.P., Eliezer, K.F., Mitchell, J.W., 1990. Slurry-Phase Fischer-Tropsch Synthesis and Kinetic Studies over Supported Cobalt Carbonyl Derived Catalysts. Ind. Eng. Chem. Res. 29 (9), 1807–1814. https://doi.org/10.1021/ie00105a011.

Yang, G.Q., Fan, L.S., 2003. Axial liquid mixing in high-pressure bubble columns. AIChE J. 49 (8), 1995–2008. https://doi.org/10.1002/aic.690490810.

Yates, I.C., Satterfield, C.N., 1991. Intrinsic kinetics of the Fischer-Tropsch synthesis on a cobalt catalyst. Energ. Fuel. 5 (1), 168–173. https://doi.org/10.1021/ef00025a029.

Zheng, K., Yang, R., Wu, H., Wang, G., Yang, Y., Li, Y., 2019. Application of the Perturbed-Chain SAFT to Phase Equilibria in the Fischer-Tropsch Synthesis. Ind. Eng. Chem. Res. 58 (19), 8387–8400. https://doi.org/10.1021/acs.iecr.9b00174.

Chapter 5

Concluding Remarks and Suggestions for Further Work

5.1 Concluding Remarks

Transport phenomena have a solid foundation in mathematics, where the transport equations are derived rigorously through tensor calculus. However, the transport equations require additional relations referred to as constitutive equations. It is common for these constitutive equations to rely on thermodynamics.

In this work, emphasis has been placed on two constitutive equations, and new formulations with roots in thermodynamic equilibrium theory were established. The two constitutive equations investigated are i) the reaction rate and ii) the mass transfer flux. The reaction rate is commonly correlated as a function of concentration and temperature in experimental investigations. These formulations yield reaction rates well suited for the transport phenomena framework. On the other hand, thermodynamics offers another alternative for computing the extent of reaction, namely through chemical equilibrium. This framework does not provide insight into the transient behavior of the reaction but is commonly used in feasibility/process design studies.

In the first part of this work, the transport phenomena framework was combined with the chemical equilibrium framework to improve models currently employed in feasibility studies. The transport equations were solved in a sequential approach, and the chemical compositions were obtained by minimizing Gibbs or Helmholtz energy rather than from reaction kinetics. The energy minimization was performed while keeping temperature and pressure constant for the Gibbs energy approach, while the minimization was

performed keeping temperature and volume constant for the Helmholtz energy approach. With the Helmholtz energy approach, two different volume approaches were attempted for the energy minimization, that is, one where the volume was computed from the EoS (orthogonal collocation method) and one where the volume was selected from the numerical grid (finite volume method). The results were identical. In terms of computational cost, the Gibbs energy approach came out superior to the Helmholtz energy approach.

The differential Gibbs and Helmholtz reactor models were exemplified by the Soave–Redlich–Kwong EoS and the virial expansion truncated after the second term. Furthermore, two chemical processes were used in the analysis of the reactor models, and the simulations revealed that the reactor models converged well for both EoSs applied to both of the processes. It is mentioned in paper I that for large amounts of heat released/absorbed, the instantaneously established equilibrium will likely yield significant variations in the dependent variables at the reactor inlet. This is inevitable and an inherent property of neglecting the dynamic nature of the reaction.

The new reactor model based on chemical equilibrium is not aimed to replace reactor models with reaction kinetics but rather to provide an alternative in the absence of expressions for species reaction rates. Rather, it provides an improvement of the current approach applied in chemical process feasibility studies due to including flow conditions such as temperature and pressure gradients along with the chemical equilibrium calculations.

In the second part of this work, a set of mass transfer equations were derived based on a complete phase equilibrium description, incorporating all components, including what is commonly referred to as the solvent (the component in excess). This is different from common practice, where Henry's law is employed to close the set of mass transfer equations. The novel mass transfer concept provides a flexible framework that allows for selecting a thermodynamic model that best fits the components in the process investigated with the same, relatively simple expression for mass transfer. Furthermore, the term solvent is no longer required, as the phase equilibrium can be computed without knowledge of this concept. This proved advantageous in the Fischer–Tropsch synthesis, where the large number of components was shown to leave the solvent a vague and ambiguous concept.

The mass transfer equations are commonly closed by employing Henry's law. In this dissertation, the underlying assumptions of Henry's law were scrutinized and compared to a more rigorous approach, namely the complete phase equilibrium based approach. The assumptions and weaknesses of the Henry's law approach include

- The solutes are infinitely diluted in a component in excess (solvent).

- The mass transfer of the solvent cannot be directly computed, since its Henry's law coefficient does not exist.

- The solvent is a vague and ambiguous concept.

In the single cell protein process, a mixture of both volatile, slightly volatile, and non-volatile species was present, and it was shown that when the non-volatile compound cannot be selected as the solvent, its mass transfer must be ignored due to the second bullet point above. Furthermore, in the Fischer–Tropsch synthesis process, several chemical components were present in the liquid phase in substantial amounts. Hence, they are not infinitely diluted in a specific solvent. Additionally, multiple components are equally qualified as solvents, resulting in ambiguity in selecting solvent. The results show that the numerical solution of the transport equations relies significantly on which solvent is chosen, and an a priori choice of the optimal solvent is a complicated task. Moreover, the assumption of infinitely diluted solutes is violated in this system. The novel mass transfer expressions suggested here rely on a complete phase equilibrium description and can provide a rigorous alternative to methods based on Henry's law without suffering the same assumption violations.

5.2 Suggestions for Further Work

All parts of this dissertation employ minimization routines in the form of Gibbs or Helmholtz energy. For convex objective functions (Gibbs or Helmholtz energy functions) together with convex constraints, it has been proven that, if a minimum is located, then it is the global minimum [Nocedal and Wright, 2006]. This is not necessarily the case for non-convex objective functions or non-convex constraints, where multiple local minima may exist while only one global minimum exists.

In terms of thermodynamics, the constraints are linear and thus convex. Considering thermodynamic models, the ideal gas EoS yields a convex Gibbs and Helmholtz energy surface. For non-ideal gas EoSs, it must be proven that the thermodynamic model yields a convex energy surface or if it contrarily yields a non-convex energy surface. The work in this dissertation has not performed any proof of this kind, and the located minima may therefore be local minima rather than global minima. Albeit disregarded in this dissertation, it should be further explored if the differential Gibbs and Helmholtz reactor models, or the mass transfer expressions derived here are to be further developed. The topic of global optimization is discussed

by Floudas and Pardalos [2014] or, more generally, in the *Journal of Global Optimization*.

Mass transfer expressions have an explicit dependency on the interfacial area separating the two adjoining phases. Furthermore, several investigators suggest a bubble size dependency in their correlations for the mass transfer coefficient. It is clear that the bubble size is crucial in mass transfer modeling; however, in this dissertation, the focus was to improve the driving force of mass transfer, and hence, the interfacial area was ignored and set constant. Changes to the gaseous phase were thus modeled only as a change in the area fraction. In order to improve on the physical description of the model, the population balance equation could be employed for the dispersed gaseous phase.

The developed mass transfer expressions are based on phase equilibrium; hence, the underlying assumptions of phase equilibrium must hold. In this work, the temperature and pressure differences between the two phases were negligible. In other chemical processes, the differences might be substantial, violating the equilibrium assumptions. Therefore, it is essential to only employ the mass transfer expressions for systems where the temperature and pressure of the two phases are not too different. To further develop the novel mass transfer expressions derived here, balance equations for energy and momentum can also be formed around the interface separating the two phases. An interface temperature and an interface pressure (respectively) can thus be computed, allowing the phase equilibrium, and hence the mass transfer, to be computed for any system with two adjoining phases. The computational effort required to resolve the spatial scale of these calculations in addition to the spatial scale of the reactor itself is foreseen to be considerable.

As a final note, it is mentioned that verification in mass transfer modeling is a complicated matter. Mass transfer models are commonly built on the assumption that local phase equilibrium prevails at the interface of the adjoining phases. However, as shown in this work, equilibrium relies on the composition of both phases. To date, experiments are yet to be performed and reported where the composition of both gas and liquid phases are measured at multiple heights/locations in a bubble column. Experiments of this kind remain vital for verifying the mass transfer models proposed in this dissertation.

Bibliography

R. A. Adams and C. Essex. *Calculus: a complete course*. Pearson Canada, Toronto, 8th edition, 2013. ISBN 9780321781079.

D. Berthelot. Sur le Mélange des Gaz. *Comptes Rendus des Séances de L'Académie des Sciences*, 126:1703–1706, 1898.

R. B. Bird, W. E. Stewart, and E. N. Lightfoot. *Transport Phenomena*. John Wiley & Sons, New York, 2nd edition, 2002. ISBN 0471410772. doi: 10.1017/CBO9781107415324.004.

E. Brunner. *Reaktionsgeschwindigkeit in heterogenen Systemen*. PhD thesis, Georg-Augusts-Universitat, Gottingen, 1903.

E. Brunner. Auszug aus Reaktionsgeschwindigkeit in heterogenen Systemen. *Z. Phys. Chem.*, 47U(1):56–102, 2017. doi: 10.1515/zpch-1904-4705.

H. B. Callen. *Thermodynamics and an Introduction to Thermostatics*. Wiley, New York, 2nd edition, 1985. ISBN 0471862568.

P. V. Danckwerts. Significance of Liquid-Film Coefficients in Gas Absorption. *Ind. Eng. Chem.*, 43(6):1460–1467, 1951. doi: 10.1021/ie50498a055.

J. R. Elliott and C. T. Lira. *Introductory Chemical Engineering Thermodynamics*. Prentice Hall, Upper Saddle River, NJ, 2nd edition, 2012. ISBN 0136068545.

L. F. Epstein. Constants in the Equation of State of a Gas. *J. Chem. Phys.*, 20(12):1981–1982, 1952. doi: 10.1063/1.1700373.

L. Euler. *Foundations of Differential Calculus*. Springer New York, New York, NY, 2000. ISBN 9780387226453.

J. H. Ferziger and M. Perić. *Computational Methods for Fluid Dynamics*. Springer Berlin Heidelberg, Berlin, Heidelberg, 3rd edition, 2002. ISBN 978-3-540-42074-3. doi: 10.1007/978-3-642-56026-2.

A. Fick. Ueber Diffusion. *Annalen der Physik*, 170(1):59–86, 1855. doi: https://doi.org/10.1002/andp.18551700105.

C. A. Floudas and P. M. Pardalos. *Recent Advances in Global Optimization*, volume 176 of *Princeton Readings in Religions ;*. Princeton University Press, Princeton, NJ, course book. edition, 2014. ISBN 0-691-60237-9.

H. S. Fogler. *Elements of Chemical Reaction Engineering*. Prentice Hall, Boston, 5th edition, 2016. ISBN 978-0-13-388751-8.

J. Gross and G. Sadowski. Perturbed-Chain SAFT: An Equation of State Based on a Perturbation Theory for Chain Molecules. *Ind. Eng. Chem. Res.*, 40(4):1244–1260, 2001. doi: 10.1021/ie0003887.

J. Gross and G. Sadowski. Application of the Perturbed-Chain SAFT Equation of State to Associating Systems. *Ind. Eng. Chem. Res.*, 41(22):5510–5515, 2002. doi: 10.1021/ie010954d.

A. J. Haslam, A. Galindo, and G. Jackson. Prediction of binary intermolecular potential parameters for use in modelling fluid mixtures. *Fluid Phase Equilib.*, 266(1-2):105–128, 2008. doi: 10.1016/j.fluid.2008.02.004.

M. Helbæk and S. Kjelstrup. *Fysikalsk kjemi*. Fagbokforlaget, Bergen, 2nd edition, 2006. ISBN 9788245004045.

R. Higbie. The Rate of Absorption of a Pure Gas into a Still Liquid during Short Periods of Exposure. *T. Am. Inst. Chem. Eng.*, 31:365–389, 1935.

J. O. Hirschfelder, C. F. Curtiss, and R. B. Bird. *Molecular Theory of Gases and Liquids*. Wiley, New York, corrected edition, 1964. ISBN 0471400653.

F. London. The general theory of molecular forces. *Trans. Faraday Soc.*, 33 (0):8b, 1937. doi: 10.1039/tf937330008b.

H. A. Lorentz. Ueber die Anwendung des Satzes vom Virial in der kinetischen Theorie der Gase. *Ann. Phys. (Berl.)*, 248(1):127–136, 1881.

M. L. Michelsen and J. M. Mollerup. *Thermodynamic Models: Fundamentals & Computational Aspects*. Tie-Line Publications, Holte, 2nd edition, 2007. ISBN 8798996118.

J. Nocedal and S. Wright. *Numerical Optimization*. Springer Series in Operations Research and Financial Engineering. Springer New York, New York, 2nd ed. edition, 2006. ISBN 978-0-387-30303-1. doi: 10.1007/978-0-387-40065-5.

D.-Y. Peng and D. B. Robinson. A New Two-Constant Equation of State. *Ind. Eng. Chem. Fund.*, 15(1):59–64, 1976. doi: 10.1021/i160057a011.

R. Privat, R. Gani, and J.-N. Jaubert. Are safe results obtained when the PC-SAFT equation of state is applied to ordinary pure chemicals? *Fluid Phase Equilibria*, 295(1):76–92, 2010. ISSN 0378-3812. doi: https://doi.org/10.1016/j.fluid.2010.03.041.

R. C. Reid, J. M. Prausnitz, and B. E. Poling. *The properties of gases and liquids*. McGraw-Hill, New York, 4th edition, 1987. ISBN 0070517991.

H. A. Schwarz. *Gesammelte Mathematische Abhandlungen*. Springer Berlin Heidelberg, Berlin, Heidelberg, 1890. ISBN 978-3-642-50356-6. doi: 10.1007/978-3-642-50665-9.

G. Soave. Equilibrium constants from a modified Redlich-Kwong equation of state. *Chem. Eng. Sci.*, 27(6):1197–1203, 1972. doi: 10.1016/0009-2509(72)80096-4.

B. W. Taylor. *Introduction to management science*. Pearson, Boston, 10th edition, 2010. ISBN 9780132457576.

R. Taylor and R. Krishna. *Multicomponent mass transfer*. John Wiley & Sons, New York, NY, 1993. ISBN 0-471-57417-1.

J. D. van der Waals. Reprint of: The equation of state for gases and liquids. *J. Supercrit. Fluids*, 55(2):403–414, 2010. doi: 10.1016/j.supflu.2010.11.001.

H. K. Versteeg and W. Malalasekera. *An introduction to computational fluid dynamics: the finite volume method*, volume 7. Pearson/Prentice Hall, Harlow, 2nd edition, 2007. ISBN 9780131274983.

C. B. Vik, J. Solsvik, M. Hillestad, and H. A. Jakobsen. Interfacial mass transfer limitations of the Fischer-Tropsch synthesis operated in a slurry bubble column reactor at industrial conditions. *Chem. Eng. Sci.*, 192:1138–1156, 2018. doi: 10.1016/j.ces.2018.08.018.

W. G. Whitman and J. L. Keats. Rates of Absorption and Heat Transfer between Gases and Liquids. *J. Ind. Eng. Chem.*, 14(3):186–191, 1922. doi: 10.1021/ie50147a004.